JOURNAL OF THE Electrochemical Society

VOL. 117 NO. 5 MAY 1970

Chlor-Alkali Producers can count on the

PROVEN PERFORMANCE OF GLC GRAPHITE ANODES

under "Upset Conditions"

GRAPHITE PRODUCTS DIVISION

GREAT LAKES CARBON CORPORATION

299 Park Avenue • New York, N.Y. 10017

Offices and Agents Coast-to-Coast and Around the World

PRODUCTS YOU CAN TRUST® GLC

Great Lakes Carbon Corporation is one of the world's largest manufacturers of graphite for electrothermic and electrochemical processes—and for aerospace, nuclear, metallurgical and other industrial uses.

IMPROVE

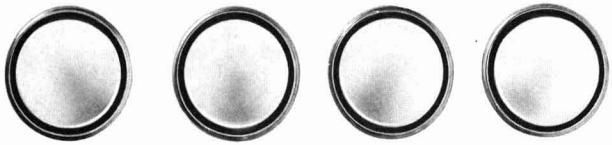

BATTERY

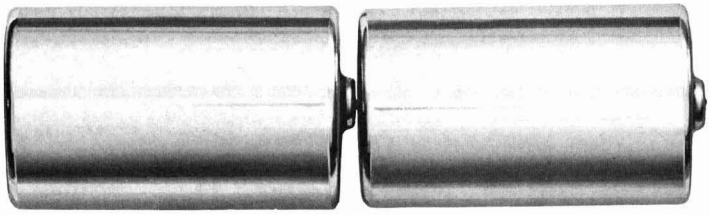

PERFORMANCE

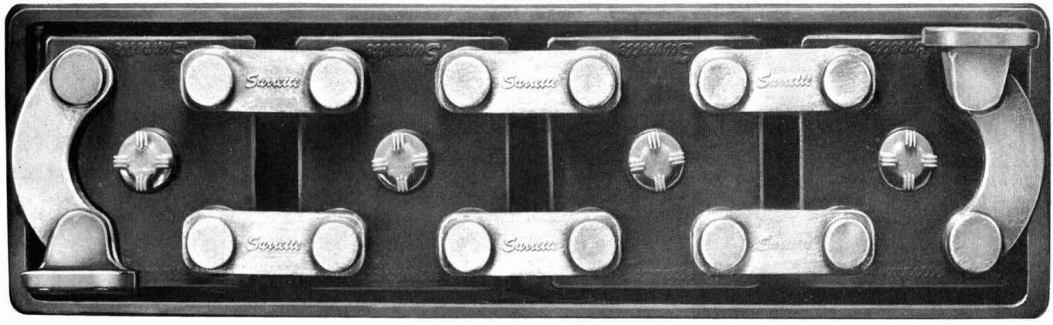

Battery performance gets a boost when you use Webril® nonwoven fabrics for separators and absorbers. For a number of very good reasons.

If primary and secondary battery systems are to perform much more reliably, they must inhibit dendrite growth and passage. Permit free ionic passage. Remain unaffected by acid or alkali. Loss of active plate material must be minimized. And electrolyte contact with plates must be assured. Webril nonwoven fabrics can do all this.

They have been performance-tested for over millions of hours in mercury-zinc, zinc-air, lead-acid, cuprous chloride, and nickel-cadmium systems. The unusually broad line of fine Webril products gives you greater design flexibility . . . even in fuel cells. You can choose from polypropylene, Dynel*, nylon, highly purified cotton, modified cellulose, and other fibers.

Find out more today. Write to Mr. P.N. Dangel, Electrical Specialties Department.

KENDALL

The Kendall Company
Fiber Products Division Walpole, Mass. 02081

*Union Carbide Corp. trademark for its modacrylic fiber.

MAY 1970

ELECTROCHEMICAL SCIENCE

TECHNICAL PAPERS

TECHNICAL NOTES

ELECTROCHEMICAL SOCIETY

Vol. 117 • No. 5

SOLID STATE SCIENCE

TECHNICAL PAPERS

Manuscripts submitted to the Journal should be sent, in triplicate, to the Editorial Office at 30 East 42 St., New York, N. Y., 10017. They should conform to the revised "Instructions to Authors" available from Society Headquarters. Manuscripts so submitted, as well as papers presented before a National technical meeting, become the property of the Society and may not be published elsewhere in whole or in part without written permission of the Society. Address such requests to the Editor.

The Electrochemical Society does not maintain a supply of reprints of papers appearing in its Journal. A photoprint copy of any particular paper may be obtained from University Microfilms, 300 North Zeeb Road, Ann Arbor, Michigan 48106.

Inquiries re positive microfilm copies of volumes should be addressed to University Microfilms, Inc., 300 N. Zeeb St., Ann Arbor, Mich. 48106.

Walter J. Johnson, Inc., 111 Fifth Ave., New York, N. Y., 10003, have reprint rights to out-of-print volumes of the Journal, and also have available for sale back volumes and single issues, with the exception of the current calendar year. Anyone interested in securing back copies should correspond direct with them.

Published monthly by The Electrochemical Society, Inc., at 215 Canal St., Manchester, N. H.; **Executive Offices, Editorial Office, and Circulation Dept.,** and **Advertising Office** at 30 East 42 St., New York, N. Y., 10017, combining the JOURNAL and TRANSACTIONS OF THE ELECTROCHEMICAL SOCIETY. Statements and Opinions given in articles and papers in the JOURNAL OF THE ELECTROCHEMICAL SOCIETY are those of the contributors, and The Electrochemical Society assumes no responsibility for them.

Claims for missing numbers will not be allowed if received more than 60 days from date of mailing plus time normally required for postal delivery of JOURNAL and claim. No claims allowed because of failure to notify the Circulation Dept., The Electrochemical Society, 30 East 42 St., New York, N. Y., 10017, of a change of address, or because copy is "missing from files." Subscription to members as part of membership service; subscription to nonmembers $40.00 plus $3.00 for postage outside U.S. and Canada. Single copies $2.50 to members, $4.00 to nonmembers. Second Class Postage Paid at New York, New York, and Manchester, N. H. Printed in U.S.A.

SOLID STATE SCIENCE (Cont.)

TECHNICAL NOTES

ELECTROCHEMICAL TECHNOLOGY

TECHNICAL PAPERS

TECHNICAL NOTE

BRIEF COMMUNICATION

REVIEWS AND NEWS

REVIEW SECTION

NEWS SECTION

Puzzle Me This*

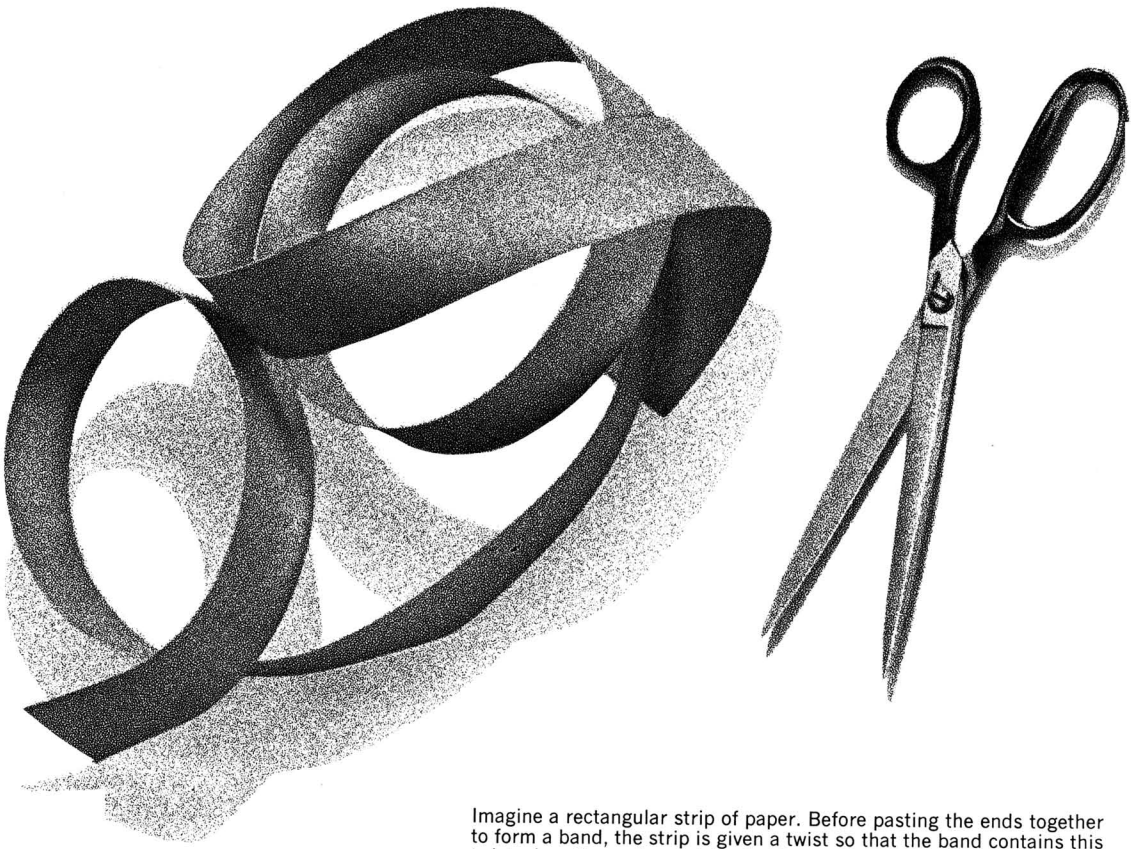

Imagine a rectangular strip of paper. Before pasting the ends together to form a band, the strip is given a twist so that the band contains this twist when the ends are joined. (The twist referred to above can also reasonably be described as a half-twist. To make the operation clear imagine that one side of the strip is white and the other black; the twist is such that when the ends are joined there will be a different color on each side of the joint.)

If the band is now cut lengthwise down the middle, when the cut is completed there will not be 2 bands but one, twice the length of the original band and containing 2 twists.

What would happen if the original band (containing one twist) is cut not down the middle, but nearer to one side than the other, let's say ⅓ of the way from one side to the other?

HINT: When cutting down the middle, once around the band will complete the cut. This is not so when the cut is made nearer one side than the other.

* The solution to this puzzle is on page 184C

Multiple choice MOS in one pass.

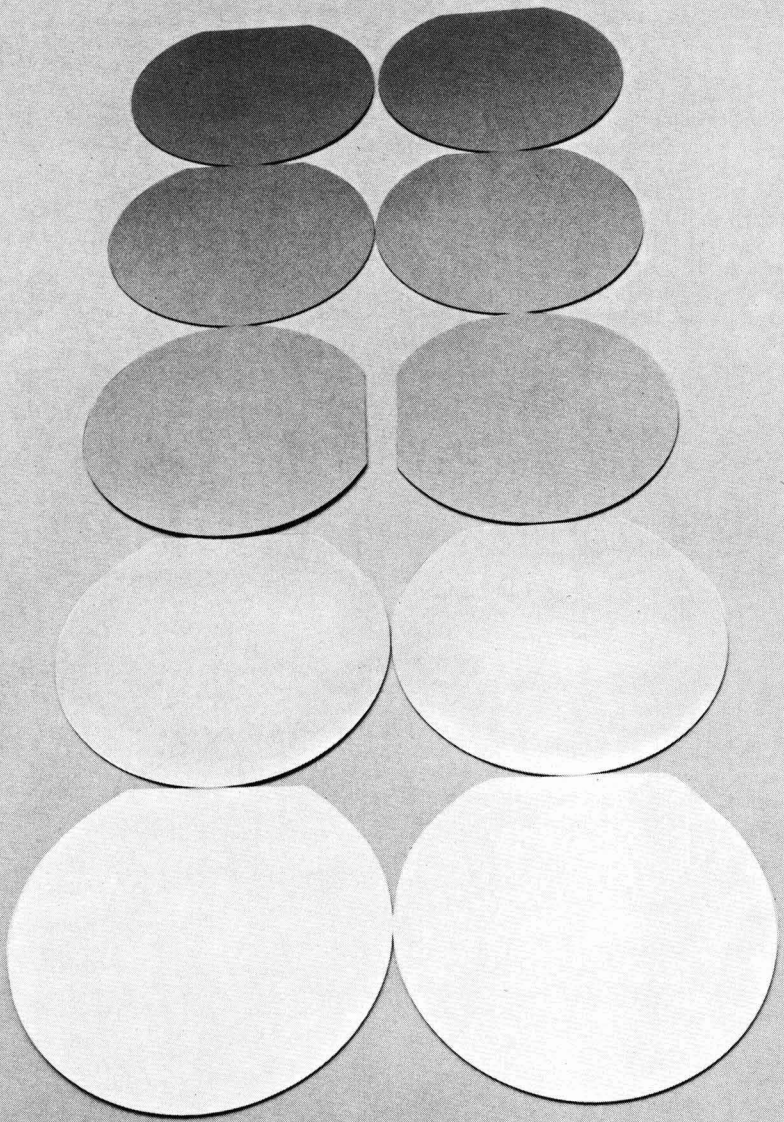

Deposit any sequence of silicon dioxide, silicon nitride and polycrystalline silicon. Without wafer handling. Without removal from the reactor chamber.

Layer these films in any combination. Build the most advanced MOS circuits, even silicon gate technologies. With the AMN-700 series of vapor deposition systems. The first non-RF powered, high-temperature, cold wall reactors for the deposition of dielectric films.

The AMN-700 can handle up to twenty 2″ wafers per station, producing films of unparalleled uniformity. Typical thickness variation is less than ±5% wafer-to-wafer within a run. Typical properties of Si_3N_4 films deposited in the AMN series are: etch rate (HF) 4-6 Å/sec; deposition rate 100-500 Å/minute; refractive index 2.0. Operating temperatures range from 650° to 900°C.

There is no RFI noise. That makes the AMN-700s completely compatible with diffusion processing and testing operations. Call collect for immediate requirements.

Applied Materials Technology, Inc., 2999 San Ysidro Way, Santa Clara, California 95051, (408) 738-0600 Telex: 34-6332 • 63 Route 206, Somerville, N. J. 08876, (201) 722-3300 Telex: 83-3439 • In Europe: Advanced Semiconductor Materials, Wokingham, U. K. Bilthoven, Netherlands; München, West Germany. In Japan: Kanematsu-Gosho, Tokyo.

applied materials

ELECTROCHEMICAL BOOKS IN PRINT

John Wiley Publications In-Print

The following are books developed and sponsored by The Electrochemical Society and published by John Wiley & Sons Inc., 605 Third Ave., New York, N. Y., 10016. Members of the Society can receive a 33% discount by ordering from Society Headquarters. Book and invoice mailed by the publisher. Nonmembers (including subscribers) must order direct from the publisher.

Corrosion Handbook. Edited by Herbert H. Uhlig. Published 1948, 1188 pages, **$21.00.**

Modern Electroplating, Second Edition. Edited by Frederick A. Lowenheim. Published 1963, 769 pages, **$16.00.**

Electrochemistry in Biology and Medicine. Edited by Theodore Shedlovsky. Published 1955, 369 pages, **$12.50.**

Arcs in Inert Atmospheres and Vacuum. Edited by W. E. Kuhn. Published 1956, 188 pages, **$7.50.** A 1956 Spring Symposium.

Ultrafine Particles, Editor-in-Chief—William E. Kuhn. Published 1963, 561 pages, **$15.00.**

First International Conference on Electron and Ion Beam Science and Technology. Edited by R. Bakish. Published 1965, 945 pages, **$24.50.** (Sponsored by the Electrothermics and Metallurgy Division of The Electrochemical Society and the Metallurgy Society of AIME.)

The Electron Microprobe. Edited by T. D. McKinley, K. F. J. Heinrich, and D. B. Wittry. Published 1966, 1035 pages, **$27.50.** A 1964 Fall Symposium.

Chemical Physics of Ionic Solutions. Edited by B. E. Conway and R. G. Barradas. Published 1966, 622 pages. **$25.00.** A 1964 Spring Symposium.

Vapor Deposition. Edited by C. F. Powell, J. H. Oxley, and J. M. Blocher, Jr. Published 1966, 725 pages, **$19.95.**

The Stress Corrosion of Metals by Hugh I. Logan. Published 1966, 306 pages; **$13.95.**

High Temperature Oxidation of Metals by Per Kofstad. Published 1966, 340 pages; **$13.50.**

The Corrosion of Light Metals, by H. P. Godard, W. B. Jepson, M. R. Bothwell, and R. L. Kane. Published 1967, 360 pages; **$13.95.**

High-Temperature Materials and Technology. Edited by I. E. Campbell and E. M. Sherwood. Published 1967, 1022 pages, **$27.50.**

Alkaline Storage Batteries, by S. Uno Falk and Alvin J. Salkind. Published 1969, 672 pages; **$32.50.**

SOCIETY SOFTBOUND SYMPOSIUM SERIES

[a] **Surface Chemistry of Metals and Semiconductors.**
H. C. Gatos, J. W. Faust, Jr., and W. J. La Fleur, Editors.
A 1959 symposium. 526 p. $21.50

[a] **Electrode Processes.** First Conference.
E. Yeager, Editor.
A 1959 symposium. 374 p. $15.50

[a] **Mechanical Properties of Intermetallic Compounds.**
J. H. Westbrook, Editor.
A 1959 symposium. 435 p. $17.50

[a] **Zirconium and Its Alloys.**
J. P. Pemsler, E. C. W. Perryman, and W. W. Smeltzer, Editors.
A 1965 symposium. 205 p. $10.00

[a] **Electrolytic Rectification and Conduction Mechanisms in Anodic Oxide Films.**
P. F. Schmidt and D. M. Smyth, Editors.
A 1967 symposium. 230 p. $7.00

[a] **Vapor Plating.**
C. F. Powell, I. E. Campbell, and B. W. Gonser.
1955. 158 p. $6.50

[a] **Iodide Metals and Metal Iodides.**
R. F. Rolsten.
1961. 441 p. $18.00

[a] **Technology of Columbium (Niobium).**
B. W. Gonser and E. M. Sherwood, Editors.
1958. 120 p. $5.00

[a] **The Structure of Electrolytic Solutions.**
Walter J. Hamer, Editor.
A 1957 symposium. 441 p. $18.00

[a] **Electrets and Related Electrostatic Charge Storage Phenomena.**
L. M. Baxt and M. M. Perlman, Editors.
A 1967 symposium. 150 p. $11.00

[a] **Electron and Ion Beam Science and Technology.** Third Conference.
R. Bakish, Editor.
A 1968 symposium. 725 p. $21.00

[b] **Measurement Techniques for Thin Films.**
B. Schwartz and N. Schwartz, Editors.
1965 and 1966 symposia. 347 p.
$12.00 (softbound) $15.00 (hard bound)

[b] **Electrode Processes.** Second Conference.
E. Yeager, H. Hoffman, and E. Eisenmann, Editors.
A 1966 symposium. 190 p. $5.00

[c] **Vacuum Metallurgy.**
J. M. Blocher, Jr., Editor.
A 1954 symposium. 216 p. $5.00

[c] **Dielectrophoretic and Electrophoretic Deposition.**
E. F. Pickard and H. A. Pohl, Editors.
A 1967 symposium. 138 p. $9.00

[a] **Optical Properties of Dielectric Films.**
N. Axelrod, Editor.
A 1968 symposium. 325 p. $9.00

[a] **Thin Film Dielectrics.**
Fredrick Vratny, Editor.
A 1968 symposium. 680 p. $27.40

[a] **Ohmic Contacts to Semiconductors.**
Bertram Schwartz, Editor.
A 1968 symposium. 356 p. $14.75

[c] **Semiconductor Silicon.**
Rolf R. Haberecht and Edward L. Kern, Editors.
A 1969 symposium. 750 p. $10.00

[c] **Chemical Vapor Deposition.**
Second Conference.
John M. Blocher, Jr. and James C. Withers, Editors.
A 1970 symposium. 872 p. $15.00.

Iron Ore Reduction.
R. R. Rogers, Editor.
A 1960 symposium. 359 p. $12.50
Order from the MacMillan Co., 60 Fifth Ave., New York, N. Y. 10003

Rhenium.
B. W. Gonser, Editor.
A 1960 symposium. 225 p. $12.50
Order from American Elsevier Publishing Co., 52 Vanderbilt Ave., New York, N. Y. 10017

---

[a] Order from University Microfilms, Inc., 300 N. Zeeb St., Ann Arbor, Mich. 48103. Enclose payment with order. Specify an Electrochemical Society volume.

[b] Order from Johnson Reprint Co., 111 Fifth Ave., New York, N. Y. 10003. Specify an Electrochemical Society volume. Prices subject to change without notice.

[c] Orders filled at the list price given, subject to availability, from The Electrochemical Society, Inc., 30 East 42 St., New York, N. Y. 10017. Enclose payment with order.

JOURNAL OF THE ELECTROCHEMICAL SOCIETY

ELECTROCHEMICAL SCIENCE

MAY 1970

ES

Polarization Characteristics of a Cupric Chloride Cathode in a Lewis Acid Organic Electrolyte

M. Eisenberg,* R. E. Kuppinger, and K. M. Wong

Electrochimica Corporation, Menlo Park, California

ABSTRACT

The polarization characteristics of copper-cupric chloride electrodes in Lewis acid-type organic electrolytes, using propylene carbonate as an aprotic solvent, were studied. Two experimental techniques were used: a multireference polarization cell (MRP) and a rotating disk electrode (RDE). For the latter, a range of rotational velocities from 25 to 2000 rpm was covered. Following elimination or accounting for concentration polarization, the remaining polarization is considered to be attributable not only to charge transfer steps, but also to chemical steps such as a slow dissolution of the cupric chloride crystal in this electrode of the second kind. Apparent exchange current density values in the range of 3-6 x 10^{-5} A/cm^2 have been determined for the reduction of $CuCl_2$ to copper.

The interest in high energy battery systems employing organic nonaqueous electrolyte with aprotic solvents has focused attention on metal halides as cathode materials (1). Little is known about the polarization behavior of electrodes of this type in Lewis acid-type electrolytes in cyclic ester solvents such as propylene carbonate. The purpose of this study was to develop and adopt two techniques for a steady-state determination of the polarization characteristics of metal halide electrodes in nonaqueous media, and as an initial study to determine the cathodic polarization of a copper-cupric chloride electrode in LiCl-$AlCl_3$-propylene carbonate electrolyte.

Apparatus and Experimental Procedure

Cathodic polarization of copper-cupric chloride electrodes has been determined by the use of two galvanostatic methods in which the steady-state polarization is achieved at successively increased levels of current density. One of the methods is based on the employment of a cell with a precise, uniform geometry and equipped with a multiplicity of sidewall reference electrodes (MRP cell); the other is based on the use of the rotating disk electrode in a closed system cell specifically developed for work with nonaqueous electrolytes.

Multireference polarization cell (MRP cell).—The MRP cell was designed as a symmetrical cell of cylindrical uniform cross section in which the working electrode (under investigation) is located centrally between two auxiliary electrodes, completing the basic cell. A schematic presentation of this cell is shown in Fig. 1. Figure 2 shows an exploded view of the cell components. The uniform cylindrical geometry of the cell, the mounting of the electrodes to the accurately machined polypropylene sections of the cell, and the

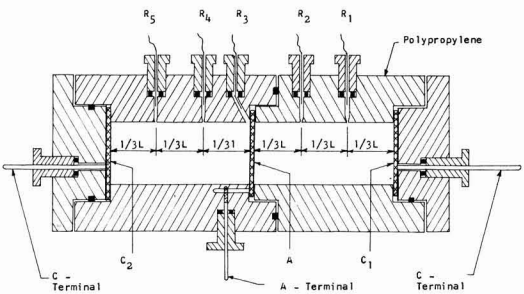

Fig. 1. Multireference polarization cell (MRP cell)

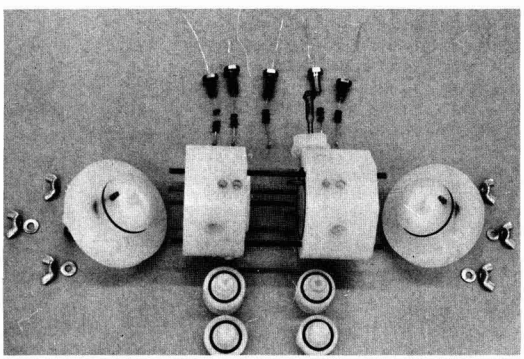

Fig. 2. MRP cell, exploded view

* Electrochemical Society Active Member.

equidistant position of the electrode under study between the two auxiliary electrodes provides a uniform primary current distribution at the surface of the electrode.

Several silver-silver chloride reference electrodes are located at precise distances, on both sides, from the plane of the electrode under study. The capillary leading to each reference electrode compartment is built into the side wall of the polypropylene cell without any protrusions or indentations; thus, the primary current distribution remains undisturbed, and there are no shielding effects commonly involved in kinetic work where protruding glass capillaries are used. The location of the capillary openings for references R_1, R_2, R_4, and R_5 (see Fig. 1) is such as to divide each half-cell compartment exactly into 1/3 lengths. Thus a measurement of the emf while current is passing through the cell between references R_1 and R_2, or R_4 and R_5 provides a direct value for the iR-drop involved for the distance 1/3 L.

There are several different ways in which the MRP cell can be employed for galvanostatic polarization studies. As can be seen in Fig. 1, it is possible to omit an electrode in position, *A*, place the working electrode under study, *e.g.*, in position C_2, place a suitable counterelectrode in position C_1, thus spacing current from one end of the cell to the other end. Through the use of reference electrodes R_5, R_4, and R_3 obtaining and carrying out measurements between the working electrode, C_2 and reference R_5, as well as between the other references, the extrapolative method may be used to correct for the iR drop included in the measurement between C_2 and R_5, since the same iR drop is involved in the distance C_2-R_5 as in the distance R_5-R_4.

It is also possible to employ the cell by placing the electrode under investigation in the center and employ the two end electrodes as counterelectrodes. In this case, a balanced polarizing circuit is employed to assure that the same amount of current flows to both sides of the electrode under investigation. This is illustrated in Fig. 3. It should be noted that in this case, by the use of reference electrode R_3, which is connected by means of a 45° capillary directly to the face of the working electrode (or a similar reference electrode R_6 on the other side), it is possible to reduce the iR drop involved in the measurement to a very small value, depending on how small and properly machined the capillary is. At the same time, if the diagonal capillary R_3 is small, it indeed comes very close to the surface of electrode A.

The polarization of the central electrode, A can be determined by employing all references, R_3, R_4, and R_5. It should be noted that the potential difference between R_3 and R_4 includes not only the iR drop, but also the effects of any concentration changes at the surface of the working electrode. Thus, the measurement employing reference, R_3, offers the means for assessing reasonably closely the effects of concentration polarization. Consequently, another way to express activation polarization is offered by the relation

$$\Delta E_{act} = (AR_4)_{net} - \Delta(R_5R_4)_{net} - [\Delta(R_4R_3) - \Delta(R_5R_4)] \quad [1]$$

where the last term in the square bracket represents the major portion of concentration polarization component, ΔE_{conc} (depending on the accuracy of the R_3 location). In the experimental studies reported here, the method expressed by Eq. [1] was employed. Lithium electrodes were used as counter-working electrodes to avoid any gas or undesirable by-product generation which would disturb the experiment.

The silver-silver chloride reference electrodes were constructed of silver wires, 0.020 in. diameter, terminating with a small loop. The wires were carefully cleaned to remove any surface oxides and coated with silver chloride by dipping in a melt of AgCl. The reference electrodes were equilibrated by immersion in the electrolyte prior to insertion into the reference electrode compartments of the MRP cell. The cell was assembled and filled with electrolyte in an argon drybox. It was then removed from the drybox and used in the normal laboratory environment. A Keithley Model 621 electrometer and a Hewlett-Packard Model 405CR digital voltmeter were used for the emf measurements. During the run a current was set and emf measurements performed until steady state was achieved. Subsequently, a larger current density level was set. During the run, reference to reference emf measurements were taken at several current values.

Rotating disk electrode.—In order to work with nonaqueous electrolyte systems under exclusion of air and moisture, a special housing was constructed for the rotating disk electrode using polypropylene materials which are inert to the cyclic esters, and a gastight construction with "O" rings for the top and bottom plates of the cell. The cell has a large ID (6.35 cm) to accommodate a variety of rotating disk diameters. A schematic diagram of the cross section of the cell is shown in Fig. 4. The diagram illustrates the relative positions of the rotating disk electrode (RDE) and of the Luggin capillary leading to an Ag/AgCl reference electrode. The distance of the tip of the capillary, which is in the same plane as the RDE from the

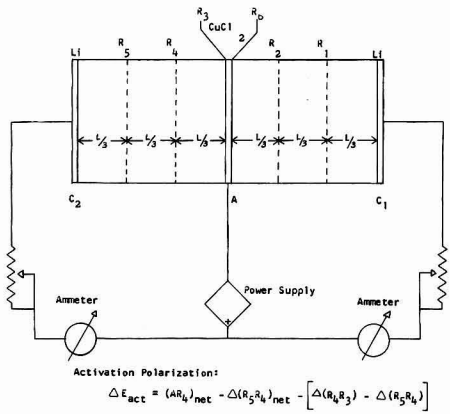

Fig. 3. Schematic presentation of MRP cell and technique (cupric chloride cathode in the center).

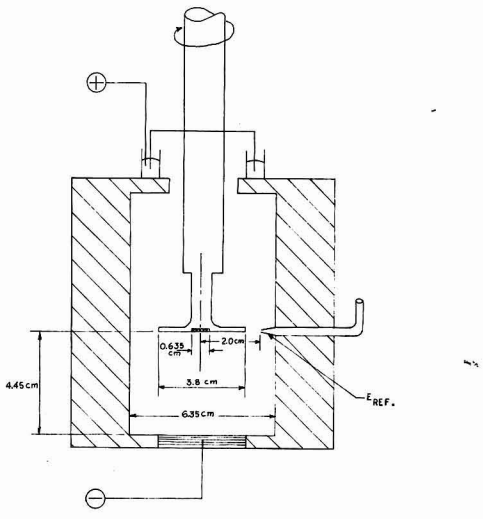

Fig. 4. Schematic diagram of RDE electrode

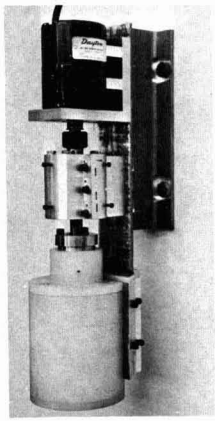

Fig. 5. Rotating disk electrode, assembled

access of the latter, is an important parameter since it affects the iR drop through the solution included in the steady-state measurement. Figure 5 shows the assembled cell in operation in the normal laboratory environment following its assembly inside an argon drybox. A mercury well is employed on top of the cell to provide both electrical contact to the RDE and a seal from the air atmosphere. The emf measurements between the RDE and the Ag/AgCl reference electrode (prepared similarly to those for the MRP cell) were made with a Keithley Model 621 electrometer and with a Hewlett-Packard Model 405CR d-c digital voltmeter. The RDE cell is constructed in such a way that the distance between the center of the active area of the RDE and the tip of the Luggin capillary can be adjusted over a range of values. For these experiments this radial distance was set at 0.635 cm, and the radius of the active area of the electrode was $R_O = 0.318$ cm. Thus, the surface area of the RDE was 3.16 cm^2.

The elimination of the iR drop between the working electrode and the Luggin capillary tip of the reference electrode is an important matter for consideration, especially due to the relatively lower conductivity of the electrolyte employed. Under favorable experimental circumstances, it is possible to obtain the value of the resistance involved by experimental means, such as the use of an interruptor and an analysis of the emf decay trace obtained on an interruption of the current. Efforts to employ an interruptor consisting of a mercury wetted Reed relay activated by an oscilloscope (Tektronix 535) sweep pulse were not successful in obtaining the iR drop at a fixed current load, because of the surface resistance of the copper chloride layer on the electroformed electrode. Different values were obtained depending on the thickness of the electroformed layer. For this reason, the method of calculation of the iR drop in the cell developed by Newman and Hsueh (2) was employed, using an experimentally determined value of the specific conductivity of the electrolyte, K. When the Luggin capillaries are located in the plane of the RDE, their relation can be expressed as

$$R = \frac{\tan^{-1}\lambda_o}{2\pi r_o K} = \frac{0.523}{K} = 102.0 \qquad [2]$$

where

$$\lambda_o = \sqrt{\frac{r}{r_o} - 1} \text{ at } z = 0$$

and the values applicable to this study are:

K = specific conductivity (5.13×10^{-3} mhos/cm^2)
r_o = radius of disk electrode (0.318 cm)
r = radial distance to Luggin capillary of reference electrode (0.635 cm)

Using the resistance value $R = 102$ ohms, the iR drops were calculated for each level of current density employed during the polarization run and subtracted to obtain net total polarization values.

The experimental procedure consisted of fixing a given rotational speed, obtaining the open-circuit emf difference between the copper-copper chloride RDE, and the Ag/AgCl reference electrode. Subsequently, a given current density was applied, held constant until steady state was achieved, and the emf determined at each level. Three levels of rotational velocity were employed throughout this study: 25, 300, and 2000 rpm. The rotational speed was determined by using a magnetic pickup, sensing the passage of a small magnet attached to the rotating shaft. The speed of the electrode, driven by a d-c series motor (1/5 hp), was controlled by a d-c regulated power supply (Power Designs Inc. Model 5015-S).

Electrolyte and electrode preparation.—The electrolyte was prepared from propylene carbonate (Jefferson Chemical Company), twice vacuum distilled at 50 mm of mercury and a temperature of 150°C. Anhydrous aluminum chloride (Matheson, Coleman and Bell) was dissolved in it to yield a molality of 0.8*M*. Lithium chloride (J. T. Baker), additionally dried in a vacuum oven overnight at 150°C, was added to yield a molality of 0.7*M*. At the LiCl:$AlCl_3$ ratio of 0.7:0.8, the solution is essentially saturated in respect to LiCl. The solution was stored in a glass stoppered Erlenmeyer inside an argon drybox. The physical properties of this electrolyte were determined by conventional methods to be as follows

Specific conductivity: 25°C
$K = 5.13 \times 10^{-3}$ mhos/cm (± 0.1)
Viscosity: $\mu = 4.05$ Hz
Density: $d = 1.243$ g/cc
Kinematic viscosity: $\nu = 3.25 \times 10^{-2}$ cm^2/sec

As far as the copper-cupric chloride cathode is concerned, it was deemed necessary to employ a simple, essentially nonporous electrode in which only the species copper and cupric chloride would be present. Initial efforts to paste a suspension of anhydrous cupric chloride in acetone onto a copper foil were unsuccessful, since poor adhesion resulted after drying of the electrode. It was consequently decided to prepare the electrode by anodic electroforming of a surface layer of $CuCl_2$ in an organic electrolyte essentially of the same nature as the electrolyte in which the electrode is to be studied. This approach was found successful and the final procedure adopted consisted of cleaning a copper foil (0.015 in. thick) to remove oxides, rinsing with acetone and subsequently with propylene carbonate, and then electroforming by making the foil anodic in a 1.5*M* $AlCl_3$ solution in propylene carbonate, using platinum electrodes and applying a current density of 0.5 mA/cm^2 for time periods of 24-48 hr. These electrodes, in the form of a circular disk of the proper diameter, could then be inserted into the MRP cell in such a way that an active surface area of 4 cm^2 presented itself to the electrolyte inside the MRP cell.

For the RDE studies, the electrode was prepared by subjecting the exposed and cleaned end of the solid copper electrode-rotor to the same electroforming treatment. Care was taken to provide a sufficient amount of electroformed cupric chloride to cover the consumption occurring during the cathodic polarization runs and provide for a safe margin.

While the electroformed cathodes represent the basic approach taken in this study, it was of some interest to investigate the comparative behavior of a porous pressed electrode. These could only be studied in the MRP cell, since a reliable attachment of a pressed layer to the rotor electrode of the RDE cell could not be achieved. The pressed electrode for the MRP cell was prepared to provide an equimolar ratio of Cu-metal and $CuCl_2$. This corresponded to a weight per cent ratio of 67% $CuCl_2$ and 32% Cu, to which 1% (by weight) of a polyethylene binder was added. The copper was added as a metal powder (No. MD 151). The $CuCl_2$ (J. T. Baker) was dehydrated by treatment

Table I. Sample calculation of ΔE_{act} (run 16, Fig. 6) according to Eq. [1]

1 Current density, mA/cm²	2 $(AR)_{4\,net}$, V	3 $\Delta(R_5R_4)_{net}$, V	4 $\Delta(R_1R_3)_{net}$, V	5 $[\Delta(R_1R_3)_{net} - \Delta(R_5R_4)_{net}]$, V	6 ΔE_{act}, V
0.15	0.107	0.029	0.033	0.004	0.074
0.25	0.179	0.044	0.058	0.014	0.121
0.50	0.312	0.070	0.106	0.036	0.206
1.25	0.592	0.164	0.237	0.073	0.355
3.00	1.485	0.436	0.587	0.151	0.898

with thionyl chloride and vacuum oven removal (at 150°C) of SO_2 and HCl by-products. Electrodes 0.035 in. thick were produced by pressing this mixture onto a 24-mesh copper screen. The resulting volume porosity was 26%.

The counterelectrodes employed in both the MRP and the RDE cells were lithium pressed to a nickel foil.

Results

MRP cell studies.—A sample calculation for the activation polarization, ΔE_{act}, using Eq. [1] is given in Table I. As discussed previously, to the extent that R_3 is small and accurately located, the bracketed expression given in column 5 of Table I represents all or a major portion of the concentration polarization. This polarization remains small at lower current densities and reaches 14.4% (0.15V out of a total of 1.049V) at an apparent current density of 3 mA/cm². A comparison of column 3 (which expresses the iR-drop involved in the polarization measurement of column 2) and of columns 5 and 6 serves to give an appreciation of the importance of iR corrections and concentration polarization corrections for the accuracy of a Tafel plot. With an appreciation of these limitations, Eq. [1] appears to offer a reasonable approach to a determination of net electrode polarization.

The results for electroformed copper-copper chloride cathodes are shown in Fig. 6 in the form of a Tafel plot. Four runs are presented, each with a fresh electrode; two for the cathode positioned in the center of the cell, and two for the cathode positioned at one end. The polarization, expressed in the form of activation polarization, was calculated from Eq. [1], or an equivalent form of it. The curve in Fig. 6 was drawn through the points for the cathode position in the center of the cell, since these results were somewhat more reproducible. It may be noted, however, that for the other two runs the polarization values are only slightly higher. It should be noted from the data that a straight Tafel line would only apply over a limited range of current density values (approximately up to 1 mA/cm²).

The results for the pressed (26% porous) electrodes are given in Fig. 7 which shows independent runs; two

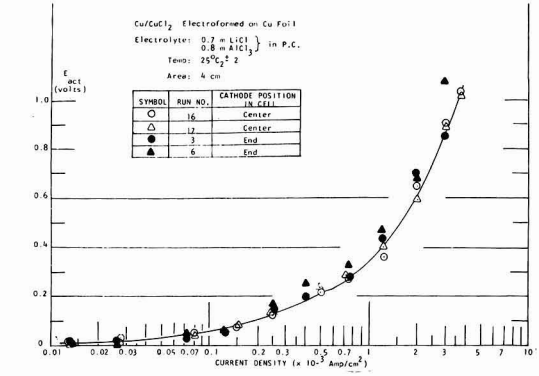

Fig. 6. Polarization of $Cu/CuCl_2$ electroformed cathode, MRP cell.

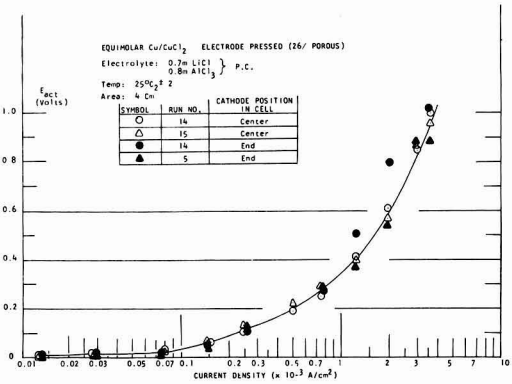

Fig. 7. Polarization of the pressed $Cu/CuCl_2$ cathode, MRP cell

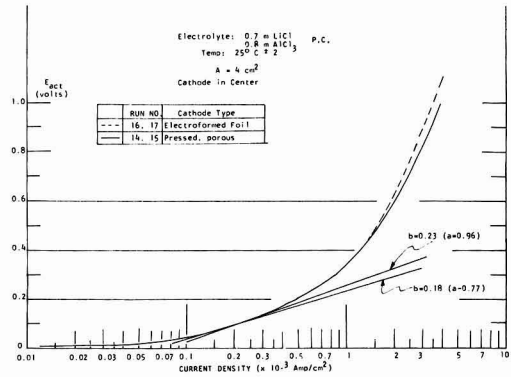

Fig. 8. Comparison of electroformed and pressed $Cu/CuCl_2$ cathode polarization, MRP cell.

for the cathode position in the center, and two for the end of the cell. Here, again, the runs with the electrode in the center are more reproducible and, consequently, the line was drawn through these data. However, in general, the results are in agreement for both electrode positions in the cell. A comparison of the results obtained for the two types of cathodes is shown in Fig. 8. The relatively close agreement of the results was at first considered surprising, since a lower polarization for the same apparent current density was expected for the pressed electrode. The results indicate that the porosity of the pressed electrode, produced in this case at a pressure of 6 tons/in.², must have been of the same order of magnitude as the natural porosity of the $CuCl_2$ layer on the surface of the anodically formed electrode. In the current density range of 0.1-0.5 mA/cm², Tafel slopes in the range $b = 0.18$ to $b = 0.23$ appeared to be applicable. However, deviation from linearity for current density of 1 mA/cm² or above, was significant. It should be remembered that the polarization values as plotted in Fig. 8 are already those obtained after subtraction of the concentration polarization component represented by the bracketed expression of Eq. [1]. As can be seen from the sample data shown in Table II, this concentration polarization (columns 2a and 2b) is subtracted from the total polarization (columns 1a and 1b) before the activation polarization, ΔE_{act} (columns 3a and 3b) is plotted in the figure. It should be noted that the concentration polarization values (columns 2a and 2b) for the two types of electrodes do not agree too well for a given current density. However, this may be due to the drift of the reference electrode potential which often occurred during a run. Such references

Table II. Sample data from the MRP cell studies

Current density, mA/cm²	Electroformed foil (Run 16) Total polar., 1a	ΔE_{conc}, 2a	ΔE_{act}, 3a	Pressed electrode (Run 14) Total polar., 1b	ΔE_{conc}, 2b	ΔE_{act}, 3b
0.25	0.135	0.014	0.121	0.119	0.009	0.110
0.5	0.242	0.036	0.206	0.202	0.013	0.189
1.25	0.428	0.073	0.355	0.457	0.041	0.416
2.00	0.754	0.103	0.651	0.683	0.068	0.615
3.00	1.049	0.151	0.898	0.946	0.104	0.842

had to be replaced from time to time. The difference may also, however, be due to the different natures of the electrode and its effect on the surface concentration of the chloride ion (see discussion in next section).

RDE cell studies.—The polarization values obtained in the RDE cell after the iR correction formally still contain a mass transfer or concentration polarization component. There is no direct way for its assessment, the way this could be done in the MRP cell. However, it can be readily estimated that for an electrode process which is productive, rather than consumptive (*i.e.*, in which a concentration build-up occurs at the interface; in this case, a build-up of Cl^- ions or $AlCl_4^-$ ions), concentration polarization is usually negligibly small. Furthermore, it should be noted that in the RDE cell the diffusional mass transport is practically of a radial nature (considering the small size of the electrode compared to the shape of the electrolyte volume in the cell). Thus, a more uniform steady state is produced in the RDE cell than in the case of the stationary electrodes in the MRP cell.

Figure 9 shows the total polarization (iR free) obtained for two runs at 25 rpm. Unlike the MRP cell, the data here are in agreement with the Tafel line over a wider range of current densities. Both curves in Fig. 9 give a slope of $b = 0.18$, although somewhat different a values have resulted. The results at 300 rpm (Fig. 10) are, again, not completely reproducible, but they fall within a fairly narrow range of slopes of $b = 0.18$-0.23. The same can be said about the results obtained at 2000 rpm (Fig. 11) where, however, one run yielded significantly higher values of the constant, a. It may be interesting to know that by comparing the results of Fig. 9, 10, and 11, increased rotational velocity did not diminish the total polarization. This, indirectly, verifies the previously discussed estimate of negligible concentration polarization in the MRP cell results.

Discussion

It is interesting to compare the RDE cell results with those of the MRP cell. It can be seen in Fig. 8 for the straight lines with slopes $b = 0.18$ and $b = 0.23$

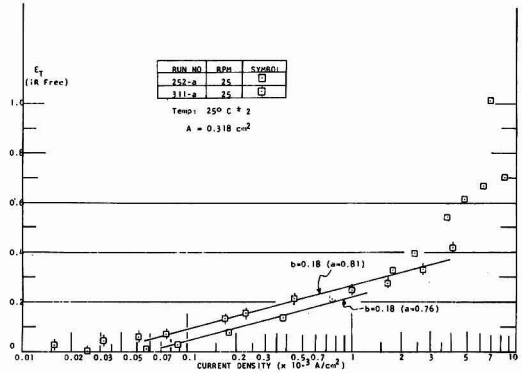

Fig. 9. Total polarization of $Cu/CuCl_2$ electroformed cathode in the RDE at 25 rpm.

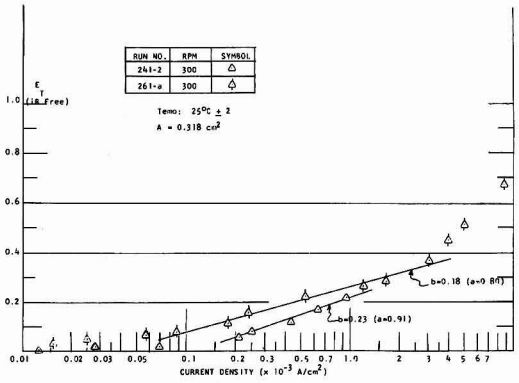

Fig. 10. Total polarization of $Cu/CuCl_2$ electroformed cathode in the RDE at 300 rpm.

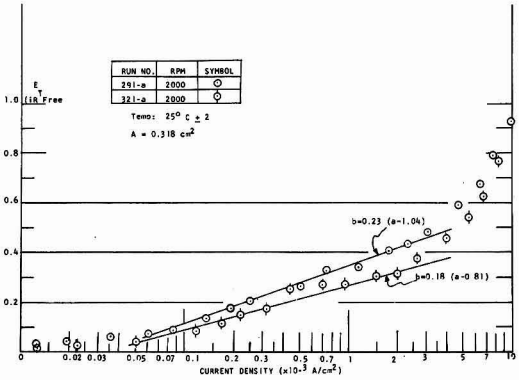

Fig. 11. Total polarizaton of $Cu/CuCl_2$ electroformed cathode in the RDE at 2000 rpm.

(and with a range of a-values bracketing the results of the RDE cell) that fair agreement is obtained in the lower ranges of current density, but serious deviation of linearity is indicated for the MRP cell above 0.5 mA/cm², while linearity is preserved for the RDE cell data up to 4 or 5 mA/cm². This indicates that possibly ohmic effects resulting in a resistance type polarization are important for the stationary cathode in the MRP cell, and that these effects can become very significant. For instance, at 3 mA/cm², Fig. 10 indicates a polarization of the order of 0.35V for the RDE cell. The corresponding value for the MRP cell is 0.84V (see Fig. 8). In light of the fact that the MRP cell method already subtracts the bulk solution concentration polarization, this large typical difference can only be attributed to ohmic effects on the surface of the cathode itself, as may result from a possible crystallization of lithium chloride as the discharge of $CuCl_2$ (and consequently, local build-up of chloride ions) proceeds in the electrolyte layer immediately adjacent to the cathode and already saturated in respect to LiCl. Another possibility is that the larger polarization is not due to an ohmic effect, but to a "reaction polarization" associated with an increased resistance to the dissolution of $CuCl_2$ which may be a chemical step preceding the charge transfer step in the over-all kinetics (see discussion further). In any event, the MRP cell should not be employed for appreciable current densities and in runs with prolonged duration. On the other hand, the RDE cell, with a small electrode area compared to a large volume of electrolyte and with a uniform and high rate of mass transfer, is conducive to obtaining overvoltage data free of resistance polarization components associated

with partial or total surface coverage by lithium chloride, or any other species which may be involved in the mechanism.

The over-all reaction in the discharge of the cupric chloride electrode can obviously be stated as

$$CuCl_{2(s)} + 2e^- \rightarrow Cu^{o}_{(s)} + 2Cl^- \qquad [3]$$

This is an electrode of the second kind, the kinetic treatment of which is complex, since the over-all process involves not only charge transfer, but also several chemical reactions. Not only is a solid phase $CuCl_2$ involved, but also the possibility of complex ion formations which the cupric or cuprous state of the copper may enter into with Cl^- ions or with Lewis-acid ions, $AlCl_4^-$. A theoretical treatment of electrodes of this general type involves, according to Jaenicke (4, 5) and Vetter (6), the reaction velocity of the chemical step, namely, the dissolution of the ionic crystal immediately at the phase boundary with the metal conductor (here, $CuCl_2$) prior to the charge transfer step in the following scheme

$$\begin{aligned} &1.\ Cu^{++}(\text{crystal}) + 4Cl^- \rightleftharpoons [CuCl_4]^{-2}{}_{soln.} \\ &2.\ [CuCl_4]^{-2}{}_{soln.} \rightarrow Cu^{o} + 4Cl^- + 2e^- \end{aligned} \qquad [4]$$

In reactions of this type the rate-determining step is usually the first one. This has, of course, not yet been established specifically for the reaction investigated here. As far as step 2 is concerned, it may in reality consist of two sequential steps, namely, a reduction, first, of Cu^{++} to the cuprous state, and then to the metallic state. The possibility of further interactions between the Cu^{++} state and Cu^{o} state may also need consideration.

In this first study an elucidation of the detailed mechanism was not undertaken. From a realization of the complexity of the kinetics, the limited theoretical significance of an over-all exchange current density, i_o, and of the transfer coefficient, α, is appreciated. These values should be regarded as apparent values. On the other hand, from the point of view of an assessment of over-all reversibility of the processes involved, their calculations appear to be of interest. The values as obtained from the individual methods and under specific conditions are given in Table III.

The effective or apparent exchange current density, i_o, would appear to be predominantly of the order 6×10^{-5} A/cm^2 for the results of the MRP cell, and predominantly of the order of 3×10^{-5} A/cm^2 for the RDE cell. A statement of these effective values amounts to a statement that the electrochemical reduction of $CuCl_2$ in the organic electrolyte under study does not proceed very reversibly and that the predominant mode of polarization one can expect would be activation polarization, by which we mean all modes of polarization other than that attributable to mass transfer resistance in the electrolyte. Obviously, when the geometric relationship in the cell, the quantity of available electrolyte, and a limited rate of mass transfer of the chloride ion away from the surface of the $Cu/CuCl_2$ cathode, combined with an appreciable build-up of surface crystallization of lithium chloride (or of other possible compounds in the particular electrolyte, *e.g.*, $LiAlCl_4$), an appreciable component of resistance polarization or of "reaction polarization" associated with inhibition of step 1 may result, as was clearly demonstrated by the results of the MRP cell, compared to those of the RDE cell. In the discharge of a galvanic cell, where the limitations of mass transfer may be even more severe than they were in the MRP cell, the importance of this phenomenon must be fully appreciated.

Table III. Values from individual methods, under specific conditions

	Slope b	α	App. trans coefficient, α	App. exchange curr. density, i_o, A/cm^2
MRP cell	0.18	0.77	0.164	5.3×10^{-5}
	0.23	0.96	0.128	6.75×10^{-5}
RDE	0.18	0.76	0.164	6.02×10^{-5}
25 rpm	0.18	0.81	0.164	3.16×10^{-5}
RDE	0.18	0.80	0.164	3.6×10^{-5}
300 rpm	0.23	0.91	0.128	11.2×10^{-5}
RDE	0.18	0.81	0.164	3.16×10^{-5}
2000 rpm	0.23	1.04	0.128	3.02×10^{-5}

Manuscript submitted Jan. 16, 1968; final revised manuscript received Jan. 15, 1970. This was Paper 6 presented at the Chicago Meeting of the Society, Oct. 15-19, 1967.

Any discussion of this paper will appear in a Discussion Section to be published in the December 1970 JOURNAL.

REFERENCES

1. R. E. Kuppinger and M. Eisenberg, Paper 54 presented at the Philadelphia Meeting of the Society, Oct. 9-14, 1966.
2. L. Hsueh, MS Thesis, U.C., Berkeley, UCRL 16607 (Jan. 1966).
3. D. P Gregory and A. C. Riddiford, *J. Chem. Soc.*, **1956**, 3756.
4. W. Jaenicke, *Z. Elektrochem.*, **56**, 473 (1952)
5. W. Jaenicke and M. Haase, *ibid.*, **63**, 521 (1959).
6. K. J. Vetter, "Elektrochemische Kinetik," Springer Verlag, p. 573, *et seq.* (1961).

Charge Acceptance of the Cadmium-Cadmium Hydroxide Electrode at Low Temperatures

Y. Okinaka* and C. M. Whitehurst

Bell Telephone Laboratories, Incorporated, Murray Hill, New Jersey

ABSTRACT

Premature hydrogen evolution occurs when a discharged cadmium hydroxide electrode is brought to a low temperature and charged at a moderate rate. It was found that, in addition to various other known factors, the discharge rate and the temperature during discharge just prior to the temperature lowering greatly affect the charge acceptance in the first low temperature charge. Light and electron microscopic examination and BET surface area measurement showed that the cadmium hydroxide crystals formed at lower discharge rates and at higher temperatures are larger in size and more difficult to reduce. The results are interpreted on the basis of the mechanism involving a soluble intermediate species in both the charging and the discharging reactions. X-ray and electron diffraction analyses of the cadmium hydroxide crystals formed on discharge in 6.9*N* KOH at temperatures below −18°C showed the presence of γ-$Cd(OH)_2$ in addition to the ordinary β-$Cd(OH)_2$. Electrodes containing γ-$Cd(OH)_2$ have a greater low-temperature charge acceptability than those containing β-$Cd(OH)_2$ alone.

When a sealed nickel-cadmium battery is brought to a low temperature in the discharged state and charged, hydrogen gas may evolve from the negative electrode before the positive electrode is fully charged (1). Since the rate of hydrogen recombination in the cell is practically negligible, it accumulates on repeating the low-temperature charge and eventually leads to a high internal pressure and a failure due to explosion. This is one of the serious limitations in the applicability of sealed nickel-cadmium batteries.

Gottlieb (2) made an extensive investigation of various factors affecting the charge acceptance of the negative cadmium hydroxide electrode and found that the charge acceptance decreases with increasing charge rate, decreasing temperature during the charge, and increasing temperature during the preceding charge-discharge cycles. He interpreted these results on the assumption that larger and/or more perfect cadmium hydroxide crystals are formed on discharge at higher temperatures and they are difficult to reduce on charge at lower temperatures and at higher rates. Popat and Rubin (3) reported experimental results similar in some respects to Gottlieb's, but they proposed an entirely different interpretation. It was postulated by them and Rubin (4) that "active" and "inactive" forms of cadmium hydroxide are formed during discharge, and they are reduced at different potentials on charge.

The main purpose of this communication is to present experimental evidence supporting Gottlieb's assumption and showing that there is a close correlation between the low-temperature charge acceptance and the size of the cadmium hydroxide crystals. Experimental results are also presented showing that, in addition to the three factors studied by Gottlieb, the discharge rate and the temperature during the discharge immediately preceding the low-temperature charge have a profound effect on the size of cadmium hydroxide crystals formed and, consequently, on the charge acceptance in the first low temperature charge. An incidental finding made during the course of this investigation was that γ-$Cd(OH)_2$, the monoclinic modification, is formed preferentially on discharge at lower temperatures rather than β-$Cd(OH)_2$, the ordinary hexagonal modification.

* Electrochemical Society Active Member.

Key words: cadmium, cadmium hydroxide, battery, nickel-cadmium battery.

Experimental Methods

All experiments were performed in flooded cells with 6.9M KOH. The cadmium hydroxide impregnated sintered nickel plate electrodes had a theoretical capacity ranging from 543 to 575 mA·hr. Their dimensions were approximately $5.6 \times 2.5 \times 0.076$ cm. The electrodes were prepared by a vacuum impregnation method consisting of impregnation in 4M $Cd(NO_3)_2$, reduction in hot 25% KOH, washing, and drying in nitrogen. This sequence was repeated five times. The electrodes were then subjected to eleven forming charge-discharge cycles at various currents. After final full discharge they were washed, dried, and stored under nitrogen atmosphere. The test cell contained one cadmium electrode, two nickel sheet counterelectrodes, and a 6.9M KOH salt bridge connecting the cell to a Hg/HgO (6.9M KOH) reference electrode. In each experiment, the cadmium electrode was first "conditioned" by repeating the following cycle three times: charge at 200 mA with approximately 50% overcharge and then a full discharge to −0.5V against the reference electrode at the same current. Finally the electrode was charged fully at 200 mA before it was subjected to a study of various experimental variables. This conditioning was carried out at room temperature.

Optical photomicrographs were taken with polarized light with a Unitron Metallograph BNX-11 using a xenon illuminator. Electron photomicrographs were obtained on specimens prepared by transferring cadmium hydroxide crystals from the electrode surface to a collodion film. X-ray diffraction data were obtained by using CuK_α radiation. Electron diffraction analysis was made by Ladd Research Industries, Inc., Burlington, Vermont, on carbon replicas prepared from collodion film specimens. BET surface area measurements were made by Numec Instruments and Controls Corporation, Monroeville, Pennsylvania, using an Orr surface-area pore-volume analyzer. Krypton was used as the adsorbate. The samples were degassed at 50°C for 24 hr.

Results and Discussion

To illustrate the problem, a potential-time curve obtained on charge and discharge at −18°C is compared in Fig. 1 with the curve obtained at 25°C before the temperature lowering. Both curves were obtained at a constant current of 200 mA. It is seen that the

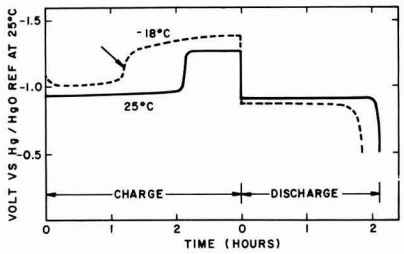

Fig. 1. Charge-discharge curves of cadmium hydroxide electrode at 25° and at —18°C after discharge at 25°C.

rise in potential at —18°C toward the hydrogen evolution range occurs after only about 60% of the 25°C discharge capacity is returned to the electrode. The arrow sign indicates where the gas bubble formation begins to become visible. The term "charge acceptance" is defined here as the ratio of the charge that the electrode accepted before this point to the charge capacity found in the discharge prior to the lowering of temperature. It is true that the charging reaction at the low temperature continues after the potential has reached the hydrogen evolution region, as is evidenced by the fact that the capacity found on the subsequent discharge was considerable greater than the charge that the electrode accepted before the onset of hydrogen evolution. However, it is the charge acceptance defined above that is important in sealed nickel-cadmium batteries because no hydrogen gas can be permitted to accumulate. Two distinct plateaus on potential-time curves, which were reported by Popat and Rubin (3) and Rubin (4) and attributed by them to the reduction of "active" and "inactive" cadmium hydroxides, were not observed under our experimental conditions.

In the previous study, Gottlieb (2) mentioned that the charge acceptance at low temperatures is not affected by the current used for the preceding cycles at a higher temperature. We found the contrary to be true, *i.e.*, the low-temperature charge acceptance is greatly affected by the magnitude of the current used for the discharge prior to the charge. Results are shown in Fig. 2. The experiments were carried out in the following manner. After the conditioning cycles described in the preceding section, the cell was placed in a bath maintained at a desired temperature and, after temperature equilibration, discharged fully to —0.5V at a specific rate. The test electrode was then removed from the cell, and a small portion of it was cut off for microscopic and other examination purposes, while the remainder of the electrode was immediately placed back into the cell. The cell was then

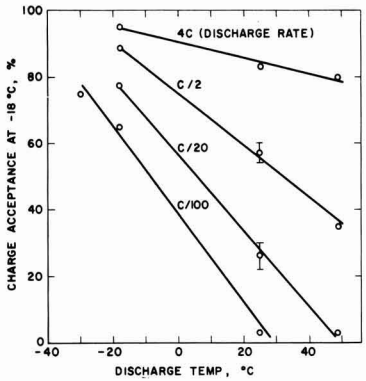

Fig. 2. Charge acceptance of cadmium hydroxide electrodes at —18°C at C/2 after discharging at various rates and temperatures. Small vertical lines indicate the reproducibility of measurement.

transferred into a —18°C bath and, after a 2-hr open-circuit stand, charged at the C/2 rate. The charging current was adjusted on the basis of the capacity found in the preceding discharge appropriate correction having been made for that portion of the electrode which had been cut off. The reproducibility of the charge acceptance measurement was found to be about ±4% for the discharge rates of C/2 and C/20 at room temperature. This is indicated by the vertical lines on the two points in Fig. 2.

Figure 2 shows that the low-temperature charge acceptance is higher after the electrode is discharged at higher rates and at lower temperatures. The charge acceptance values were found to be independent of the extent of loading of the electrode with the active material in the range between 75 mA·hr/plate and 896 mA·hr/plate. On the other hand, it is striking that the charge acceptance varies from almost 0 to 100% depending on the conditions during discharge. It is of interest to note in Fig. 2 that the charge acceptance found when the electrode was first discharged at —30°C and then charged after raising the temperature to —18°C was greater than the value found when both discharge and charge were carried out at the same temperature of —18°C.

These results can be accounted for qualitatively on the basis of the mechanism involving a soluble intermediate species in both the discharging and the charging reactions. In the potential range of interest, these reactions may be represented by the following simple equations (5, 6)

Discharge:

$$Cd + 3\,OH^- \rightarrow Cd(OH)_3^- + 2e^- \quad [1]$$

$$Cd(OH)_3^- \rightarrow Cd(OH)_2 + OH^- \quad [2]$$

Charge:

$$Cd(OH)_2 + OH^- \rightarrow Cd(OH)_3^- \quad [3]$$

$$Cd(OH)_3^- + 2e^- \rightarrow Cd + 3\,OH^- \quad [4]$$

There is some evidence indicating that anodically produced cadmium hydroxide crystals can also be reduced directly without going through the soluble intermediate (6). It will be shown in this paper that all experimental results described here can be accounted for without depending on a direct reduction mechanism. The dissolution-precipitation mechanism for the discharge reaction [1] and [2] predicts the size of $Cd(OH)_2$ crystals to be larger when they are formed at lower discharge rates. The reasoning is as follows. At lower discharge rates the rate of formation of the soluble complex $Cd(OH)_3^-$ is slower, and this should cause the precipitation reaction [2] to proceed more slowly from a more dilute, and hence less supersaturated solution. As a general rule, it is known that particles of crystalline precipitates formed from more dilute solutions are larger in size (7). The dissolution-precipitation mechanism also predicts that larger $Cd(OH)_2$ crystals should form on discharge at higher temperatures, because the degree of supersaturation of the electrolyte with the soluble complex $Cd(OH)_3^-$ should be less at higher temperatures owing to an increased solubility. This predicted relation between the crystal size and the discharge conditions has been substantiated experimentally, as will be described in the subsequent section. From considerations of surface area effects in conjunction with the solution-reduction mechanism [3] and [4], it can easily be understood why large $Cd(OH)_2$ crystals yield a poor charge acceptance. This mechanism also predicts that for a given electrode with $Cd(OH)_2$ crystals of a given size, the charge acceptance should decrease with increasing charging current and with decreasing charging temperature. These relations have been found experimentally by Gottlieb (2).

Size and shape of $Cd(OH)_2$ *crystals.*—A large number of electron and optical photomicrographs were taken in order to establish the effect of discharge rate

and temperature on the size of cadmium hydroxide crystals. Some examples of transmission electron photomicrographs of actual crystals (dark areas) are reproduced in Fig. 3. Although the crystal size in each plate varies over a wide range, it is clearly seen that the crystals formed at C/20 are much larger on the average than those formed at C/2. It is also seen that the crystals formed at higher temperatures are larger. The crystals produced at C/100 were so large that they were very clearly observable under the light microscope (see Fig. 4).

In both photomicrographs it is seen that the electrodes discharged at −18° and at −30°C contained long, needle-shaped crystals, while the crystals in the electrodes discharged at higher temperatures were all hexagonal and flat. X-ray and electron diffraction analyses showed conclusively that the needlelike crystals are γ-$Cd(OH)_2$, the monoclinic modification (8), while the normal hexagonal ones are β-$Cd(OH)_2$. Typical x-ray diffraction intensity diagrams are shown in Fig. 5. It is seen that no lines corresponding to γ-$Cd(OH)_2$ appeared in the pattern obtained with the electrode discharged at 25°C, while the electrodes discharged at −18° and at −30°C showed many distinct lines corresponding to γ-$Cd(OH)_2$. It is also apparent that more γ-$Cd(OH)_2$ formed at −30° than at −18°C. This is clearly seen also from the light photomicrographs shown in Fig. 4. γ-$Cd(OH)_2$ was identified in all electrodes discharged at −18°C regardless of the rate of discharge (4C to C/100).

Recently, Breiter and Vedder (9) reported that γ-$Cd(OH)_2$ was identified on solid polycrystalline cadmium electrodes oxidized in 1M and 5M KOH at room temperature. In 6.9M KOH and with sintered-plate type electrodes, we found no γ-$Cd(OH)_2$ at room temperature and also at 49°C at all discharge rates studied. In 1M KOH, however, a large number of γ-$Cd(OH)_2$ crystals were formed even at room temperature. As already reported by Breiter and Vedder, γ-$Cd(OH)_2$ is unstable and slowly converted to β-$Cd(OH)_2$ on open-circuit stand in contact with KOH. The conversion is, however, quite slow at room temperature. For example, the appearance of the electrode surface discharged at C/100 at −30°C (Fig. 4, top) did not change appreciably after 10 days' open-circuit stand at room temperature. At 49°C, however, the conversion was considerably accelerated, and no γ-$Cd(OH)_2$ remained only after 3 days' open-circuit stand.

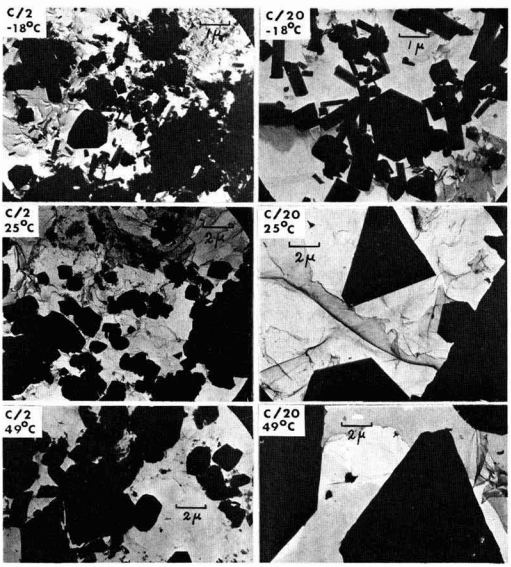

Fig. 3. Transmission electron photomicrographs of $Cd(OH)_2$ crystals formed at various temperatures and discharge rates.

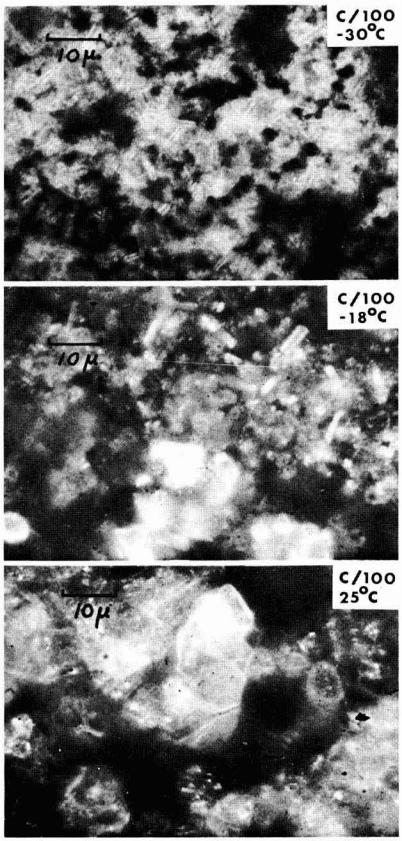

Fig. 4. Optical photomicrographs of $Cd(OH)_2$ crystals formed at the discharge rate of C/100 at various temperatures. Magnification 750 X

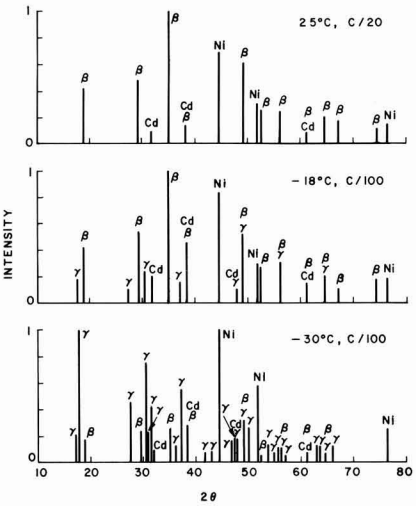

Fig. 5. X-ray diffraction intensity diagrams obtained with electrodes discharged at rates and temperatures shown.

BET surface area.—The information obtained by the microscopic observation pertains only to the surface of the electrode, and there is no assurance that the same relation between crystal size and charge accept-

ance holds for the crystals within the pores of the electrode. Measurement of the total surface area by the BET method should provide a means of comparing the size of crystals within the electrodes. With some samples brown coloration apparently due to the oxidation of undischarged cadmium occurred under the degassing conditions used (50°C, 24 hr). The data for such samples were discarded. In Fig. 6 the charge acceptance at −18°C is plotted against the BET surface area for only those samples which showed no discoloration. The surface area is expressed per gram of the electrode and not of the cadmium hydroxide crystals, since the contribution of cadmium metal particles left undischarged to the total surface area did not vary very much from electrode to electrode. The discharge capacity of all of the electrodes for which the BET measurement was made ranged approximately from 75 to 90% of the theoretical capacity. Thus, the trend shown in Fig. 6 is believed to be attributable to cadmium hydroxide crystals.

It is seen that at constant temperatures (25° and −18°C) the surface area and the charge acceptance were both smaller for electrodes discharged at lower rates. Also, the surface area of the electrode discharged at C/20 at 49° was less than that of the electrode discharged at 25°C at the same rate. The observed effect of discharge rate and temperature on the surface area parallels that on the crystal size, and undoubtedly the general conclusion drawn from the microscopic observation holds also for the crystals within the electrode.

It is significant to note in Fig. 6 that the electrodes discharged at −18° and −30°C had a considerably smaller surface area than those discharged at 25°C and yet exhibited a good charge acceptability. It appears that γ-$Cd(OH)_2$ is more readily chargeable than β-$Cd(OH)_2$ for the same surface area. Breiter and Vedder's experiments with a solid cadmium electrode also indicated that γ-$Cd(OH)_2$ is more easily reduced than β (9). In practical sealed cells, however, there seems to be no way of utilizing the favorable characteristics of γ-$Cd(OH)_2$ because of its instability at higher temperatures. With an electrode containing both β- and γ-phases, it was found that γ-$Cd(OH)_2$ crystals were all converted into the β-form after only a few 50% depth charge-discharge cycles at room temperature. It has been suggested that the active and inactive cadmium hydroxides postulated by Rubin (4) might correspond to the γ- and β-forms. With electrodes containing both γ- and β-$Cd(OH)_2$, however, we failed to observe such two separate potential plateaus as reported by Rubin.

As already described by Gottlieb (2), the greatly reduced charge acceptance is observed only in the first charge after temperature lowering. If the electrode is continuously cycled at the low temperature, the charge acceptance in the second and subsequent charge cycles becomes almost normal. This can be expected from the crystal size effect, because the $Cd(OH)_2$ crystals formed on the second and subsequent cycles should be small since these cycles are carried out at the low temperature. The formation of γ-$Cd(OH)_2$ may also be responsible for the increased charge acceptance.

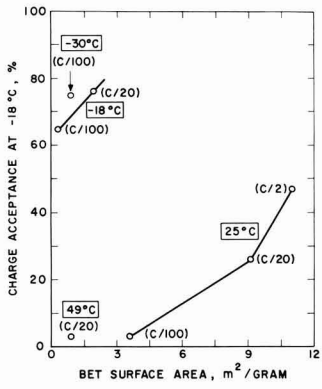

Fig. 6. Relation between charge acceptance and BET surface area. Temperatures and rates shown refer to discharge conditions.

Effect of partial cycles.—All experimental results discussed in the previous sections were obtained with electrodes discharged completely following a full charge. In sealed nickel-cadmium cells, the cadmium hydroxide electrode is not cycled in this fashion but only partially cycled, because the cells are constructed with a large excess capacity in the negative electrode. Effects of such partial cycles on the low-temperature charge acceptance were studied to simulate more closely the conditions encountered by sealed cells. Results are tabulated in Table I. In these experiments, electrodes previously charged completely at the C/2 rate were first discharged at C/20 (exp. 1 to 4) or C/2 (exp. 5 to 8), charged at C/2 until 50% of the discharge capacity was returned, and then fully discharged at various rates. This partial cycle was given at room temperature and only once except for exp. 2, in which 9 partial cycles were given. After the final full discharge, the cells were left on open circuit in a bath maintained at −18°C for 2 hr and charged at the C/2 rate.

The results of exp. 1 to 4 show that under these conditions, the charge acceptance is determined by the rate used for the initial discharge prior to the partial cycle (C/20) rather than the discharge rate used in the partial cycle. These results can be explained in the following manner. Suppose that the size of the $Cd(OH)_2$ crystals formed after the initial C/20 discharge was distributed according to a certain distribution law, for example, the normal law. On partial charge, the size of each crystal must have decreased regardless of the extent of the charge and the "tightness" (the magnitude of the standard deviation) of the distribution, whereas the total number of crystals may or may not have decreased depending on these two factors. Under the present experimental conditions, the total number of crystals appears to have remained essentially unchanged before and after the partial charge, and the $Cd(OH)_2$ crystals of reduced size which existed at the end of the partial charge appear to have grown back to the initial size on completion of the final discharge. This explains the fact that the charge acceptance observed after the partial cycle was nearly the same as that found after the full, straight C/20 discharge. The observed independence of the charge acceptance on the discharge rate used in the partial cycle probably indicates that no new nuclei were formed during the final discharge.

The same explanation applies also to exp. 5 and 6, in which the initial discharge was carried out at C/2. When the final discharge rate used in the partial cycle was very low as compared to the rate used for the initial discharge (exp. 7 and 8), the charge acceptance was considerably lower than that observed after

Table I. Effect of partial cycle (50%) at room temperature on charge acceptance at −18°C (Charge acceptance measured at C/2 rate)

Exp. No.	Rate used for full discharge prior to partial cycle	Partial cycle: Charge rate	Partial cycle: Discharge rate	Charge acceptance found, %: After partial cycle	Charge acceptance found, %: Without partial cycle
1	C/20	C/2	C/2	25	26
2	C/20	C/2	C/2 (9 cycles)	20	
3	C/20	C/2	C/26	33	
4	C/20	C/2	C/50	22	
5	C/2	C/2	C/2	51	57
6	C/2	C/2	C/25	53	
7	C/2	C/2	C/46	37	
8	C/2	C/2	C/100	3	

a straight, full discharge at C/2. This result appears to indicate that the very low rate discharge caused the small crystals initially formed at C/2 to either agglomerate or grow into large crystals.

All results listed in Table I were obtained after 50% depth partial cycles. If the depth of partial cycle is increased sufficiently when the initial discharge rate is low and the final discharge rate is high (*e.g.*, in exp. 1), a better charge acceptance is expected because of the possibility of forming small new nuclei during the final high rate discharge. Experimentally, this was found to occur, but the effect was relatively small until the depth of partial cycle was increased to about 90%. For example, the charge acceptance measured after an 87% partial cycle (C/20 full initial discharge, 87% charge at C/2, and full discharge at C/2) was found to be 36% as compared to 25% after a half depth cycle and 57% after a full depth cycle.

Practical significance of crystal size effect.—Practical significance of various experimental results described here can be summarized as follows:

1. The low-temperature charge acceptance of the negative electrode in sealed cells containing a large excess negative capacity is determined by the size of the excess cadmium hydroxide crystals, and no significant improvement in charge acceptance can be expected by high rate cycles. Consequently, sealed cells should be constructed using negative electrodes with small cadmium hydroxide crystals. Fast rate, low-temperature forming cycles should help produce small crystals.

2. Even if the negative electrode initially contains small crystals, they grow large on open-circuit stand by recrystallization. Since the rate of recrystallization is slower at lower temperatures, cells should be stored at a low temperature if they are not to be used for an extended period of time.

3. Cells in the charged state should not be left on open circuit for a long time, because the charged positive electrode self-discharges slowly to give off oxygen, and the latter discharges the negative electrode at a slow rate, which leads to the formation of large $Cd(OH)_2$ crystals.

4. Extremely low rate discharge should be avoided. This produces large $Cd(OH)_2$ crystals and possibly agglomerates of small crystals.

5. If conditions permit, temperature should be lowered when the cell is in the fully charged state rather than in the discharged state, so that the first operation at the low temperature becomes a discharge and not a charge.

Conclusion

There is little doubt that the size and the structure of $Cd(OH)_2$ crystals play an important role in determining the low-temperature charge acceptance of cadmium hydroxide electrodes. A number of experimental results can be accounted for in terms of these effects in conjunction with the reaction mechanism involving a soluble intermediate species in both the charging and the discharging reactions. However, it cannot be stated that the crystal size and structure effect explains all results. For example, we observed that the charge acceptance decreases to some extent with increasing number of charge-discharge cycles given to the electrode prior to the low temperature charge. This may be due to a redistribution of the active material within the electrode which is known to occur as a result of use (10). More complete understanding of the phenomenon would require a further investigation.

Acknowledgment

The authors are indebted to D. R. Turner and P. C. Milner for suggestions and discussions, and to Miss S. E. Koonce and F. B. Koch for their help in electron microscopy and x-ray diffraction studies.

Manuscript submitted July 28, 1969; revised manuscript received *ca.* Dec. 15, 1969.

This was Paper 50 presented at the Chicago Meeting of the Society, Oct. 15-20, 1967.

Any discussion of this paper will appear in a Discussion Section to be published in the December 1970 JOURNAL.

REFERENCES

1. M. H. Gottlieb and T. H. Willis, *Electrochem. Technol.*, **4**, 515 (1966).
2. M. H. Gottlieb, *ibid.*, **5**, 12 (1967).
3. P. V. Popat and E. J. Rubin, Abstract 47 in Extended Abstracts of Papers Presented at the Philadelphia Meeting of the Society, Oct. 9-14, 1966.
4. E. J. Rubin, Abstract 51 in Extended Abstracts of Papers Presented at the Chicago Meeting of the Society, Oct. 15-19, 1967.
5. P. C. Milner and U. B. Thomas, in "Advances in Electrochemistry and Electrochemical Engineering," C. W. Tobias, Editor, Vol. 5, Interscience Publishers, New York, 1967.
6. Y. Okinaka, *This Journal*, **117**, 289 (1970).
7. See, for example, I. M. Kolthoff and E. B. Sandell, "Textbook of Quantitative Inorganic Analysis," Chap. VII, The Macmillan Co., New York (1952).
8. P. M. de Wolff, *Acta Cryst.*, **21**, 432 (1966).
9. M. W. Breiter and W. Vedder, *Trans. Faraday Soc.*, **63**, 1042 (1967).
10. E. Lifshin and J. L. Weininger, *Electrochem. Technol.*, **5**, 5 (1967).

The Effect of Lead Ions on the Dissolution and Deposition Characteristics of a Zinc Single Crystal in 6*N* KOH

F. Mansfeld*[1] and S. Gilman*

National Aeronautics and Space Administration, Electronics Research Center, Cambridge, Massachusetts

ABSTRACT

Dissolution of the basal plane of single crystal zinc and deposition of zinc on the same material in alkaline solutions in the presence of 10^{-4}M lead ion, has been studied using *in situ* microscopy and the scanning electron microscope (SEM). It was found that in the presence of lead ions, most of the surface was protected against dissolution when polarized as much as 100 mV positive to the rest potential. Dissolution occurs initially in the form of a limited number of hexagonal etch pits that grow in size and number with time. The pits appear to correspond to sites of macroscopic crystalline imperfection.

In the absence of Pb ions, deposition of Zn on the basal plane of a zinc crystal tends toward epitaxial growth at low overpotentials. In the presence of Pb ions, at both high and low overpotentials, Zn deposition tends to initiate mainly at the few sites not protected by the microscopically smooth Pb film. At high overpotentials, growth tends to be cylindrical and microcrystalline, rather than dendritic. It is shown that, under the present conditions, no increase in the cathodic current is to be expected with increase of time.

The alkaline zinc electrode is encountered in several commercial and proposed aqueous battery devices. Its attractiveness as a uniquely high-energy anode material (for aqueous systems) is diminished by such concomitant problems as poor quality of the electrodeposit (secondary battery application) and corrosion of zinc. The use of additives incorporated into the anode, or dissolved in solution, has been proposed over the years and evaluated empirically. Most of the research effort in this area has been concentrated at industrial laboratories.

The use of Pb and Sn ion additions to the electrolyte as suggested earlier by Kudryavtsev is quoted in (1). The use of Pb ions was again investigated by Oxley and Fleischmann (2) who found that the deposit adherency on polycrystalline Zn increased when lead acetate was added at an optimum concentration of 0.5 g/l to a solution of 43% KOH, 1.13M in zinc ions. The reason for the influence of lead on deposit adherency was unclear.

Recently Bockris *et al.* (3) claimed that "the presence of 10^{-4} molar lead completely suppresses dendrites." This conclusion was reached, however, only from the change of the total current density with time without microscopical observation of the actual deposit.

At this laboratory an investigation of the effect of additives, especially lead, on dissolution and deposition characteristics of single crystal zinc has been carried out using the light microscope in a way similar to Powers' experiments (4, 5) and the scanning electron microscope as demonstrated by Naybour (6, 7). Powers studied deposition of zinc on the basal plane of a single crystal of zinc and on polycrystalline material (4) and, with Breiter (5), dissolution and passivation of the basal plane. Naybour investigated the effect of substrate orientation on growth (6) as well as the effect of electrolyte flow on the morphology of zinc deposits (7). Both optical methods have not been used previously in investigations of the effects of additives.

The effect of metal cations, anions and neutral molecules on the hydrogen evolution rate of polycrystalline zinc in 6*N* KOH and rate of hydrogen evolution of Zn-Pb and Zn-Al alloys will be reported in a separate paper. (12).

* Electrochemical Society Active Member.

[1] Present address: North American Rockwell, Thousand Oaks, California 91360.

Experimental

The zinc electrodes were obtained by cleavage from single crystal rods grown from 99.9995% pure zinc. The crystal was cooled to liquid nitrogen temperature and then cleaved and rewarmed in a drybox under argon. The cell used for microscopic observation under polarization was similar to that used by Powers (4), with the only significant modification being to the window of the optical coverglass. The coverglass was fused to the Pyrex sleeve thereby avoiding the use of adhesives which dissolve more or less rapidly in KOH. The reference electrode was a zinc rod (99.95%), the counterelectrode was gold foil. The zinc electrode potential was controlled by a Tacussell potentiostat and monitored by a Keithley electrometer. The current was recorded on a Moseley strip-chart recorder. The microscope was by Reichert, Austria, used mainly with Nomarski interference contrast.

The solution of 6*N* KOH + 20 g/l ZnO was made up from reagent grade KOH and bidistilled water using a quartz still and ZnO, "pure" (99.9%). Lead was added in the form of the acetate salt in a concentration of 1×10^{-4}M. Previous experiments with addition of 10^{-4}M acetic acid had shown that the acetate ion has no effect on deposition characteristics.

Results

Anodic dissolution.—In the investigation of the effect of lead on anodic dissolution of the basal plane of zinc, a constant potential of +75 or +100 mV *vs.* zinc in the same solution was applied after the specimen had been in contact with the solution for 5 min. In the absence of lead the surface changes in the same way as on cathodic deposition (4), the difference of course being dissolution of the surface. This indicates that dissolution and deposition occur at the same sites, probably screw dislocations. After about 60 sec one observes pits in the form of hexagonal pyramids (Fig. 1). These hexagonal pits cannot be observed with dark field methods and are consequently not visible in the paper of Powers and Breiter (5), (Fig. 2). Addition of 10^{-4}M lead to the electrolyte does not result in a perceptible coating of lead on the zinc surface (*c.f.*,

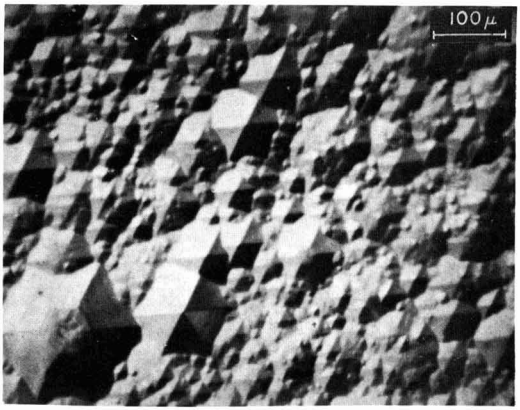

Fig. 1. Anodic dissolution of zinc, (0001) plane at +100 mV in 6*N* KOH + 20 g/l ZnO after 60 sec. Nomarski Interference Contrast (NIC), 110X.

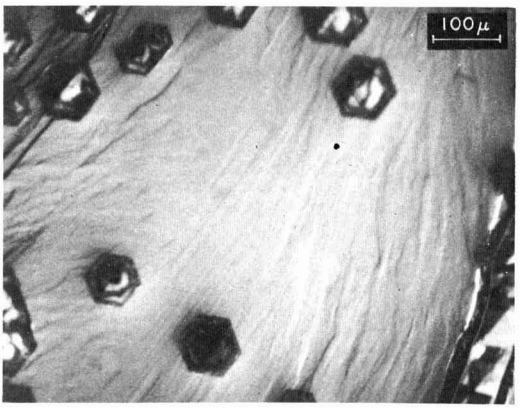

Fig. 2. Anodic dissolution of zinc, (0001) plane at +100 mV in 6*N* KOH + 20 g/l ZnO + 10^{-4}M PbAc after 240 sec. NIC, 110X.

Fig. 2), but does have a profound effect on the anodic dissolution characteristics. After applying the anodic potential hexagonal pits are observed which grow in size and number (Fig. 2). They are very numerous at more macroscopic defects of the crystal such as cracks introduced by cleavage (see right corner of Fig. 2). This difference in dissolution is also reflected in the different change of current with time (Fig. 3). With no additions, the current rises sharply and then decays; with additions, it increases slowly with the number

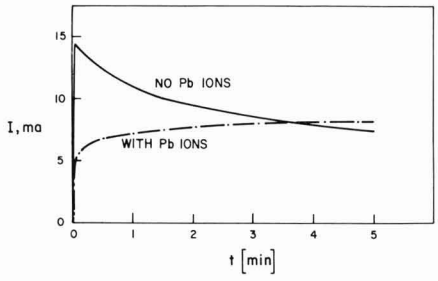

Fig. 3. Anodic dissolution of zinc, (0001) plane at +100 mV. Solid line, 6*N* KOH + 20 g/l ZnO; dashed line, 6*N* KOH + 20 g/l ZnO + 10^{-4}M PbAc. Geometric area of electrode = 0.178 cm^2.

and size of pits. Observation with the scanning electron microscope (SEM) shows that the pits are shallow, have a flat bottom and stepped sides (Fig. 4). The sides of all pits are parallel to [$11\bar{2}0$]. These pits occur probably on sites with macroscopic damage or irregularities of the crystal as can be seen from Fig. 5. The crystal was left at the open-circuit potential for 2 hr. A number of hexagonal pits were observed; they were

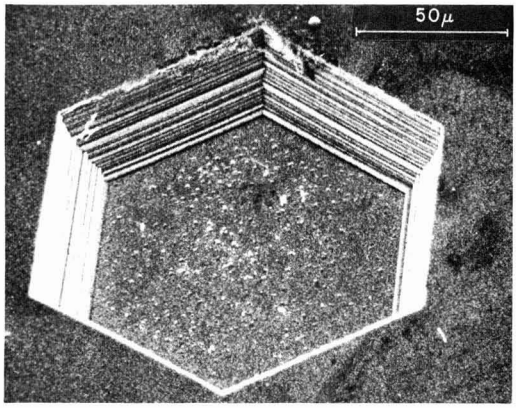

Fig. 4. Pit produced in experiment of Fig. 2 after 300 sec scanning electron microscope (SEM), 480X, 45°.

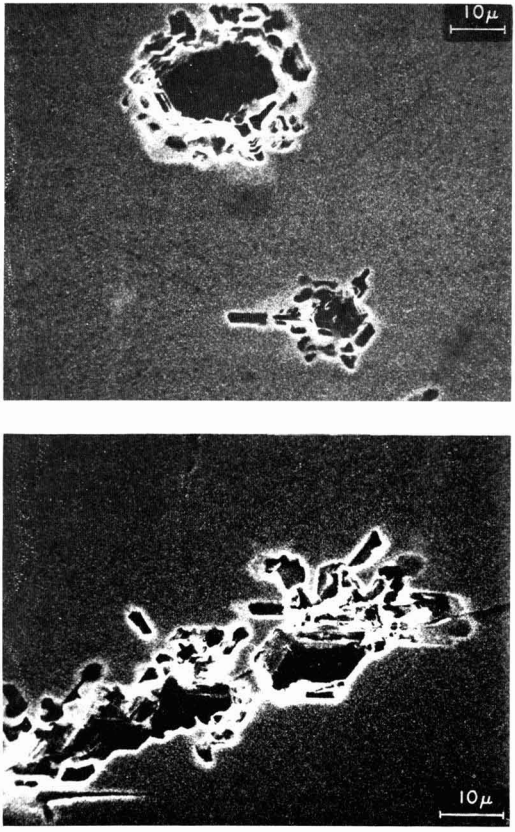

Fig. 5. Pits formed at the corrosion potential after 2 hr in 6*N* KOH + 10^{-4}M PbAc. SEM. (a) (top) 840X; (b) (bottom) 1000X.

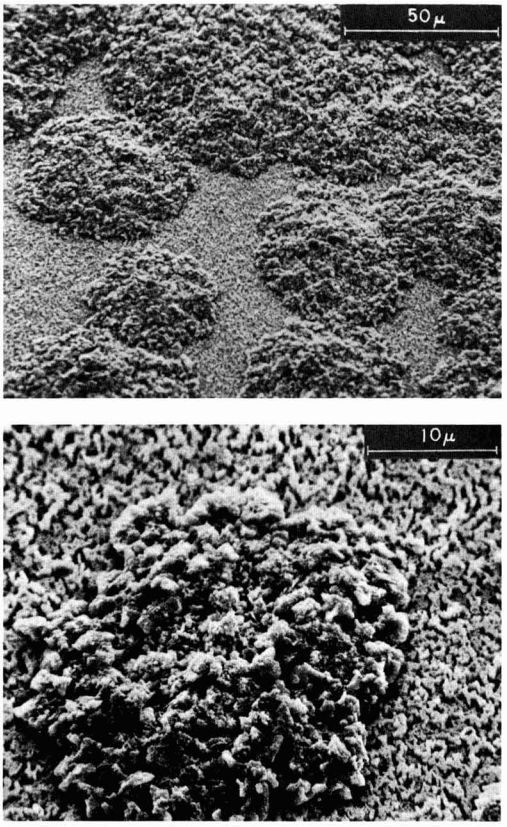

Fig. 6. Deposit at −100 mV from 6*N* KOH + 20 g/l ZnO + 10^{-4}M PbAc after 617 sec, SEM, 45°. (a) (top) 500X; (b) (bottom) 2080X.

concentrated at cracks in the surface like the one in Fig. 5b. These macroscopic defects serve as anodes, where zinc dissolves, while Pb (and hydrogen) plate out on the cathodes.

Cathodic deposition.—Cathodic deposition on the basal plane of zinc was carried out from a solution of 6*N* KOH + 20 g/l ZnO with or without additions of 10^{-4}M lead acetate at potentials of −100 or −200 mV *vs.* zinc in the same solution. The results without additions of lead were the same as already shown by Powers (4): at −100 mV the deposit was in the form of pyramids, the number of which declines with time as the more active pyramids cover the less active ones. No classical dendrites were observed at this potential even after 1 hr of plating, although a number of small protrusions were observed.[2] At −200 mV the number of growth centers was much larger and after a short time dendrites with side branches occurred. If the potential is held at −100 mV for about 30 min and then changed to −200 mV, a large number of new growth centers appear on the sides of the previously formed pyramids. After some time dendrites are observed. If the potential is brought back to −100 mV after 1 or 2 min at −200 mV, the growth centers formed at −200 mV disappear while the pyramids continue to grow.

The effect of lead additions is shown in Fig. 6 for deposition at −100 mV. It can be seen from Fig. 6a that two different types of deposit are obtained: little bumps or hills consisting of many little crystallites and flat areas consisting of a very large number of pipes growing perpendicular to the surface. Figure 6b shows both types at a higher magnification.

Figure 7 shows the deposit at −200 mV from the same solution. The deposit is completely different from that obtained in the absence of lead (classical dendrites), it reminds one of corals. The deposit consists of a very large number of crystallites, the structure of the protrusions and of the flat areas of the surface seem to be the same. Figure 7c is a magnification of one of the flat areas. The depression corresponds to blockage of deposition by a hydrogen bubble. In order to obtain additional information about the effect of lead additions, an experiment was conducted with

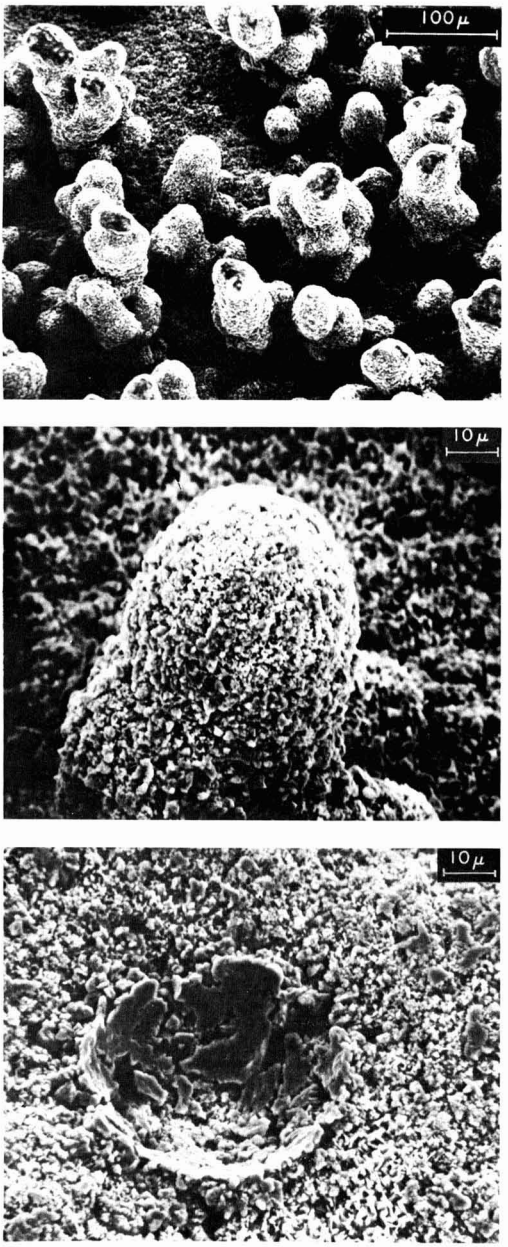

Fig. 7. Deposit at −200 mV from 6*N* KOH + 20 g/l ZnO + 10^{-4}M PbAc after 3600 sec, SEM, 45°. (a) (top) 180X; (b) (center) and (c) (bottom) 800X.

[2] The nature of these protrusions has been studied in more detail in (13).

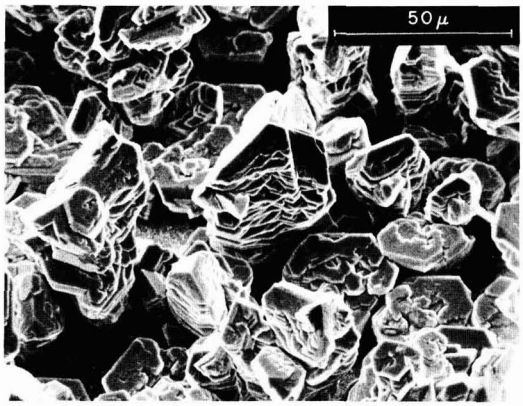

Fig. 8. Deposit at −100 mV: 60 sec in 6*N* KOH + 20 g/l ZnO + 10^{-4}M PbAc, followed by 3600 sec in 6*N* KOH + 20 g/l ZnO, SEM, 45°. 560X.

deposition at −100 mV for 1 min in a solution containing 10^{-4}M of lead, followed by additional deposition in lead-free solution. Figure 8 shows the deposit obtained at −100 mV after 1 hr of plating in the latter solution. The deposit is different from that obtained with addition of lead ions; it is similar to the protrusions observed in lead-free solutions after longer plating times (13). The protrusions are clearly crystalline with layer growth parallel to the surface but also with planes having an angle to the main crystallographic axis (center of Fig. 8).

Experiments where deposition at −100 mV in 6*N* KOH and 20 g/l ZnO was followed by deposition in the same solution with addition of lead ions produced deposits very similar to the ones shown in Fig. 6. The flat areas of the surface are again covered with pipe-shaped growths of varying length (Fig. 9). Deposition at −200 mV produced deposits similar to the ones shown in Fig. 7.

Discussion

Our results clearly show that the addition of lead ions to a solution of KOH containing zincate strongly affects anodic dissolution of the basal plane of a zinc single crystal and deposition of zinc on the same specimen. Without an externally applied potential, a microscopically smooth lead coating is deposited on the zinc surface while zinc dissolves on the anodic sites, which are thought to be major defects of the crystal (Fig. 4). If an anodic potential is applied, the crystal only dissolves at these latter sites, the other sites, which are active during dissolution in lead-free solutions (Fig. 1), are blocked and protected by lead. The pits observed after dissolution for 5 min are all rather shallow and all seem to have the same width. They are oriented with their edges parallel to $[11\bar{2}0]$ which implies that $(11\bar{2}0)$ dissolves faster than $(10\bar{1}0)$ and this in turn faster than (0001), in parallel with increasing packing density. Ashton and Hepworth (8) came to the same conclusion by measuring anodic polarization curves on the (0001), $(10\bar{1}0)$, and $(11\bar{2}0)$ plane of zinc in 0.5 NaOH.

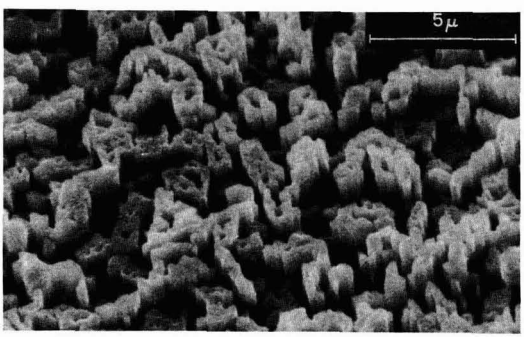

Fig. 9. Deposit at −100 mV: 150 sec in 6*N* KOH + 20 g/l ZnO followed by 1200 sec in 6*N* KOH + 20 g/l ZnO + 10^{-4}M PbAc, SEM, 45°. 4600X.

The results of deposition in lead-free solutions suggest that at the less negative potential (−100 mV) and lower deposition currents, the zinc particles diffuse on the surface to growth sites leading to pyramid growth. At more negative potentials (−200 mV) and higher deposition currents, the rate of arrival of zincate ions is higher than the rate of diffusion to growth sites, the zinc adatoms "inhibiting" their own diffusion. This results in dendritic growth. The results obtained by switching the potential from −100 to −200 mV (new nuclei, dendritic growth) and switching from −100 to −200 mV and after a short time back to −100 mV (disappearance of nuclei formed at −200 mV) support this scheme.

From our observations of the anodic dissolution of zinc in the presence of lead it follows that most of the sites for dissolution are blocked by lead. If it can be assumed that the sites for deposition and dissolution are the same, namely screw dislocations (9), then one would expect that growth on these sites is also blocked by lead. In addition it is possible that the presence of lead changes deposition characteristics from the crystallographic form of dendrites (according to Naybour (7) both tip and side branches of a dendrite grow in the $[11\bar{2}0]$ direction, the main stem and the side branches being monocrystalline) to protrusions which are no longer monocrystalline but consist of a large number of small crystals. In fact, the results of Fig. 6 and 7 show that parts of the surface are inactive for growth; the areas of larger growth consist of a large number of very small crystallites. The results of Fig. 8 show indeed that lead blocks parts of the surface, subsequent growth in lead-free solution exhibits crystalline growth again, the deposit growing mainly in the vertical direction, while large areas remain active. The nature of the sites for growth under these conditions is not known, but it seems possible that the same physical defects (or impurity centers) that act as anodes on dissolution in the presence of lead act as growth sites in deposition. Vaughan and Pick (10) assumed that copper nucleation sites were impurity centers, physical defects acting as preferred sites for impurity segregation. Although Naybour (6) showed that the number of surface defects on a zinc crystal was less than the number of growth sites, conditions are different in the present case where more surface defects are produced through local action currents. Figure 7 also shows that no classical dendrites are obtained when lead is present in the solution most likely due to incorporation of lead. There seems to be no major difference in the structure of the deposit at −100 and −200 mV in solution containing lead (Fig. 6b and 7b), the little bumps growing to larger protrusions with time under diffusion control. The nature of the pipe-like structure in Fig. 6 and Fig. 9 is not known at the present.

The conclusion of Bockris *et al.* (3) that lead addition suppresses dendrites is correct only in so far as the protrusion is not a monocrystal anymore but consists of many small crystallites. The lack of a parabolic increase of current with time as observed in (3) might be due to a lack of dependency of the diffusion current upon a radius of curvature of the substrate (11) in the case of lead additions, growth probably being linear-diffusion controlled for the type of protrusions shown in Fig. 7. A parabolic or exponential increase of current with time as observed by Bockris and co-workers (3, 11) seems questionable, however, since it was not observed by Powers (4) and in the present work in solutions free of lead ions. It could

result from the special preparation of the electrodes in (11) which consist of zinc electrodeposited on small Pt spheres and which are quite different from the much larger (0.495 cm^2) single crystal plane used in (4) and the present work. It should be remembered also that the parabolic increase of current with time in the treatment of Bockris *et al.* (11) results from the assumption that dendrite initiation is continuous, but from Naybour's (6) work it seems that dendrite initiation is instantaneous.

The small increase of current with time while dendrites grow in lead-free solutions observed in (4) and the present work results most likely only from an increase in total area as the dendrites penetrate the diffusion layer. In the presence of lead the current does not change appreciably after about 60 sec of deposition at −200 mV. The protrusions produced in this experiment have a cylindrical shape and grow perpendicular to the base contrary to real dendrites. From Table I which gives some average parameters of those protrusions it can be seen that the largest protrusions have reached a length comparable to the thickness of the diffusion layer, which is calculated to be 0.03 to 0.003 cm by using a limiting c.d. of 35 mA/cm^2 and a value of the diffusion coefficient of 2×10^{-5} to 2×10^{-6} cm^2 sec^{-1} (2). It follows that no substantial increase in area and therefore in current is expected as protrusions grow.

Conclusion

The presence of small amounts of lead ions in an alkaline solution markedly changes the anodic dissolution behavior of the basal plane of zinc by blocking most of the active sites for dissolution. Its presence also changes deposition characteristics from monocrystalline dendrites to protrusions consisting of many small crystals while large parts of the surface are inactive for deposition. It is concluded that, in the presence of lead, dissolution and deposition occurs at more macroscopic physical defects of the crystal.

It is possible that other metal ions which have a reversible potential sufficiently more noble than zinc act in a similar way. It is not entirely clear at the present how the above results apply to secondary batteries. The change in deposit morphology is certainly beneficial since no sharp dendrites result which would penetrate separators. It remains to determine what happens to the lead additions through cycling of a battery. The beneficial effect of lead ions in the electrolyte or lead alloyed in small amounts to zinc on hydrogen evolution will be reported in a separate paper (12).

Table I. Typical parameters for protrusions in experiment Fig. 7

Height	$(1.6 \pm 0.1) \times 10^{-2}$ cm
Radius	$(2.0 \pm 0.2) \times 10^{-3}$ cm
Particles/cm^2	$(1.5 \pm 0.2) \times 10^4$

Acknowledgment

One of the authors (F.M.) wishes to acknowledge support under a National Academy of Sciences Research Associateship. Scanning electron micrographs were taken with the help of Mr. J. Herman of Professor Ogilvie's laboratory, Massachusetts Institute of Technology. We are grateful to Mr. A. Pinella for metallurgical services and for helpful discussions, and to Dr. R. W. Powers for providing drawings of the Teflon cell used in light microscopy.

Manuscript submitted Oct. 8, 1969; revised manuscript received Jan. 19, 1970.

Any discussion of this paper will appear in a Discussion Section to be published in the December 1970 JOURNAL.

REFERENCES

1. J. E. Oxley, NASA Contract Report NASA CR-377, Contract NAS 5-3908, February 1966.
2. J. E. Oxley and C. W. Fleischmann, Quarterly Report No. 3, NASA Contract No. NAS 5-9591, March 1966.
3. J. O'M. Bockris, J. W. Diggle, and A. Damjanovic, First Quarterly Report to NASA, Contract NGR 39-010-002, 1-1-69 to 3-31-69.
4. R. W. Powers, *Electrochem. Technol.*, **5**, 429 (1967).
5. R. W. Powers and M. W. Breiter, *This Journal*, **116**, 719 (1969).
6. R. D. Naybour, *Electrochim. Acta*, **13**, 763 (1968).
7. R. D. Naybour, *This Journal*, **116**, 520 (1969).
8. R. F. Ashton and M. F. Hepworth, *Corrosion*, **24**, 50 (1968).
9. H. Gerischer and R. P. Fischer, *Z. Elektrochem.*, **61**, 1159 (1957).
10. F. B. Vaughan and H. J. Pick, *Electrochim. Acta*, **2**, 179 (1960).
11. J. W. Diggle, A. R. Despic, and J. O'M. Bockris, Paper 375 presented at the Montreal Meeting of the Society, Oct. 6-11, 1968.
12. F. Mansfeld and S. Gilman, submitted for publicational in *This Journal*.
13. F. Mansfeld and S. Gilman, Short communication, in preparation.

Direct Current-Voltage Characteristics of Calcia Stabilized Zirconia with Porous Platinum Electrodes

Hiroaki Yanagida,[1] R. J. Brook,[2] and F. A. Kröger*

University of Southern California, Los Angeles, California

ABSTRACT

The direct current-voltage characteristics of symmetrical cells Pt, O_2(I), $|Zr_{0.85}Ca_{0.15}O_{1.85}|$Pt, O_2(II), with pO_2(I) = pO_2(II), were measured at 560°C under oxygen pressures from 1 to 10^{-20} atm. The characteristics were nonohmic, the deviation from ohmic law being mainly due to the potential drop at the cathode interface between the solid electrolyte and the gas ambient. The characteristics consist of two parts. The first is characterized by a marked oxygen pressure dependence and is observed at voltages lower than approximately 2V (weak polarization). In this range, the rate-determining process is the diffusion of oxygen atoms (resulting from dissociation of O_2 or H_2O) through the platinum of the Pt paste electrode. The second part of the characteristic is almost independent of the oxygen pressure and is observed at voltages higher than approximately 2V (strong polarization). Here the rate-determining step is the process in which neutral oxygen atoms, adsorbed at the cathode surface of the electrolyte, combine with effectively neutral oxygen vacancies V_O^x, (oxygen ion vacancies which have trapped two electrons) to form a normal O^{2-} lattice ion (O_O^x). This process utilizes the part of the electrolyte surface not in contact with the platinum, but close to points where the platinum makes contact, and involves migration of electrons from the platinum over the surface of the electrolyte.

Stabilized zirconia with the composition $Zr_{0.85}Ca_{0.15}O_{1.85}$ crystallizes in the CaF_2 structure (1, 2) and contains 7.5% extrinsic vacant oxygen sites (2, 3). The electrical conduction at high temperature in air or oxygen is ionic in nature and is due to the migration of oxygen ions by a vacancy mechanism (2-4). The vacancies involved are oxygen ion vacancies with an effective charge +2, $V_O^{\cdot\cdot}$ (5). At lower oxygen pressures, however, electronic conduction sets in (2, 5, 6). An ionic transference number t_i is defined by

$$t_i = \sigma_i/(\sigma_i + \sigma_e) \qquad [1]$$

where σ_i is the ionic and σ_e the electronic conductivity. The value of the oxygen pressure at which this transference number is 0.5 is a function of temperature (2, 6) and varies from sample to sample (4). Typical values of $(pO_2)_{0.5}$ for stabilized zirconia of the composition given above are 10^{-42} atm at 560°C, 10^{-32} atm at 800°C, 10^{-26} atm at 940°C (2). A galvanic cell with platinum electrodes and stabilized zirconia as a solid electrolyte operated with different oxygen pressures at the two sides, gives an open circuit emf E_{open} given by (2, 7)

$$E_{open} \equiv E_{II} - E_I = \frac{1}{4F}\int_I^{II} t_i(\mu O_2)\, d\,\mu O_2 = \frac{RT}{4F}\int_I^{II} t_i\,(pO_2)\, d \ln pO_2 \qquad [2]$$

where $\mu O_2 = RT \ln pO_2$. The cell can be used as a fuel cell or a solid-state battery (8) and also as an oxygen pressure monitor (7).

The emf arises as a consequence of the simultaneous migration of ionic and electronic defects. In the stationary state, the total electrical current carried by these defects at open-circuit voltage must be zero, and therefore the electronic current j_e and the ionic current j_i must be equal and opposite

$$J = j_e + j_i = 0 \text{ or } j_e = -j_i \neq 0 \text{ at } V = E_{open} \qquad [3]$$

The ionic current is stopped by the application of a voltage E_{stop} (9, 10) given by

$$E_{stop} = \frac{1}{4F}[\mu O_2(II) - \mu O_2(I)] \qquad [4]$$

Since $t_i \leq 1$ comparison of [2] and [4] shows that

$$E_{stop} \geqslant E_{open} \qquad [5]$$

Application of a voltage higher than E_{stop} causes oxygen ions to move through the electrolyte from the lower oxygen pressure side toward the higher pressure side, and thus oxygen gas is pumped from the side of lower oxygen pressure to the side of high oxygen pressure (11-13). The oxygen pump not only pumps O_2, but can also decompose H_2O (11) and CO_2 (13). If ionic currents flow, and as seen above this is true in all cases unless $V = E_{stop}$, the chemical potential of oxygen in the electrolyte at the cathode surface (where oxygen is taken up) is lower than that of its gas ambient, and the chemical potential of oxygen in the electrolyte at the anode surface (where oxygen gas is evolved) is higher than that of its gas ambient. These potential drops, if appreciable, must be expected to reduce the accuracy of oxygen pressure monitor cells and the efficiency of fuel cells or oxygen pump cells. Their presence is indicated by the nonohmic character of the current-voltage characteristics; such nonohmic effects have been observed with several ionic conductors (12-15). It is the purpose of the present study to investigate the current-voltage characteristics of calcia stabilized zirconia in order to gain insight into the processes taking place at the electrodes. In this study, mainly symmetrical cells with pO_2(I) = pO_2(II) and $J = 0$ at $E_{stop} = 0 = E_{open}$ have been used. This was done to avoid possible complications arising from the ionic current inside the electrolyte in asymmetrical cells at $J = 0$ [see (3)]. Asymmetrical cells were only used to separate the effects of anodic and cathodic potential drops. The oxygen pressure of the gas ambient under which the measurements were made was between 10^{-20} and 1 atm.

* Electrochemical Society Active Member.
[1] Present address: Department of Industrial Chemistry, University of Tokyo, Hongo, Tokyo, Japan.
[2] Present address: British Atomic Energy Authority, Harwell, England.

Experimental Procedures

Sample preparation.—Zirconium dioxide was made by slow calcination of zirconium tetra-acetyl-acetate (supplied by Matheson Coleman and Bell Company) at 800°C in air. Major impurities present in the acetate were [in weight per cent (w/o)]: 0.15 SiO_2, 0.005 Fe_2O_3, 0.003 Al_2O_3, 0.003 MgO, 0.003 TiO_2, 0.004 (Na_2O + K_2O). The ignition loss was 71.23 w/o. Calcium carbonate supplied by Mallinckrodt was used as a source of calcia. For this, the maximum limits of major impurities, given in weight per cent, are: 0.10 Na, 0.10 Sr, 0.02 Mg, 0.01 K, 0.005 Ba. Zirconium dioxide and calcium carbonate powders were weighed to give the composition (0.15 CaO + 0.85 ZrO_2), mixed in an agate mortar for 2 hr, and pressed to pellets. The pellets were heated in dry Argon gas at 1900°C for 2 hr in an induction furnace with a graphite crucible. The pellets as fired showed a brown color. The color disappeared on heat-treatment in air at 800°C. X-ray analysis showed the diffraction pattern of the fluorite structure only. The pellets in their final state were 1 mm thick and 10 mm in diameter.

Experimental set-up.—The specimen, whose characteristic was to be studied, was kept in a stabilized zirconia tube through which a carrier gas (5 ml/sec) containing various amounts of oxygen was circulated. The experimental set-up is shown schematically in Fig. 1. Nitrogen gas was used as the carrier gas and was found to contain $\approx 10^{-4}$ oxygen as an impurity. In addition water vapor was present. The oxygen content was varied by passing the gas through an oxygen pump cell consisting of stabilized zirconia as a solid electrolyte with platinum paste electrodes (11-13). The oxygen pressure was reduced by applying to the pump cell, operated at 670°C, a voltage higher than E_{stop} corresponding to the two oxygen pressures, $pO_2(I) \approx 10^{-4}$ atm (N_2) and $pO_2(II) \approx 0.2$ atm (air). The oxygen pressure was increased by applying a voltage smaller than E_{stop}. To reduce the amount of water vapor in the gas ambient around the test specimen, a liquid nitrogen cold trap was used with the trap usually at position A. Some measurements were carried out without the trap to find the effects of water vapor.

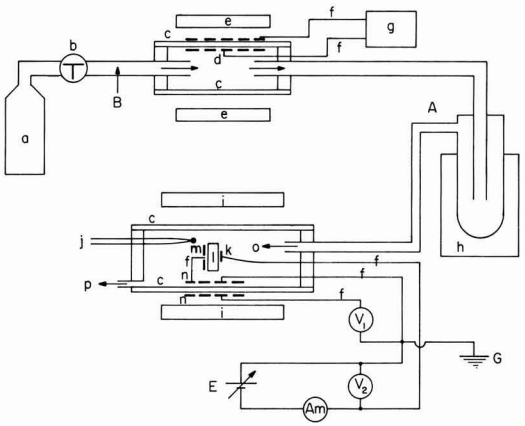

Fig. 1. Experimental set-up. a, inert gas bottle; b, cock and flow meter; c, stabilized zirconia tube; d, platinum paste electrodes for oxygen pump; e, oxygen pump furnace; f, platinum leads; g, d-c power supply for oxygen pump; h, liquid nitrogen cold trap; i, furnace for *I-V* characteristic measurements; j, thermocouple; k, platinum paste cathode; l, test specimen; m, platinum paste anode; n, platinum paste electrodes for oxygen pressure monitoring; o, gas input; p, gas outlet; V_1, volt meter for oxygen pressure monitoring (Cary 31); V_2, volt meter for *I-V* characteristic measurements (Cary 31); Am, d-c power supply and voltage regulator; G, ground; A, position of the liquid nitrogen trap used in most of the experiment; B, alternative position of the cold trap.

Some measurements were also done with the trap at position B rather than at A. The oxygen pressure around the specimen was monitored by a zirconia cell using the wall of a commercial Zircoa B grade stabilized zirconia tube with the composition $(ZrO_2)_{0.90}(CaO)_{0.10}$ as the electrolyte.

The test specimen was provided with platinum paste electrodes at the two sides. The platinum paste was prepared using a submicron platinum powder and an organic suspending medium. At one side the paste covered much of the surface specimen (5-20 mm²); at the other side the electrode had an area of ≤ 1 mm². Contact to the electrodes was made by spring loaded platinum wires (0.01 in. diameter) which were dipped in platinum paste prior to their application to the electrodes.

The specimen with electrodes and contacts in place was heated to 800°C for about ½ hr in order to remove the organic material and to sinter partially the platinum powder. The microscopic configuration of the contact is shown schematically in Fig. 2. The platinum has a spongelike structure with interconnected gas channels. It makes direct contact with the zirconia over part of the surface, leaving a gas-zirconia contact over the remaining surface area. Lines where the triple contact platinum-zirconia-gas occurs are indicated by T. Usually only half of the characteristic will be reported, *viz.*, that half for which the small area electrode is the cathode.

The voltage differences between the electrodes of the oxygen pressure monitor cell and between those of the test specimen (pellet) were measured with a vibrating reed electrometer (Cary 31, Applied Physics Corporation). The current through the specimen was measured with the aid of a Keithley 610B multipurpose electrometer. The voltage applied over the specimen was changed with a voltage divider, Dekavider DV-412 (Electro-Measurements, Inc.). A Burgess 5156 (Clevite Corporation) dry battery was used as a direct current source. Most of the measurements were carried out at 560°C, a temperature chosen to be high enough to keep the resistance at a reasonable level, but low enough to reduce F center migration from the cathode into the electrolyte which complicates the analysis.

In one instance, measurements were made on an asymmetric cell, *i.e.*, where $pO_2(I) = 10^{-20}$ atm and $pO_2(II) = 0.2$ atm. For this experiment, the sample was cemented to the end of a zirconia tube and placed in a furnace containing an air atmosphere. The interior of the tube was filled with flowing nitrogen which had been purified to $pO_2 = 10^{-20}$ atm by the zirconia pump, this value being measured by the open-circuit emf of the sample itself. Paste electrodes and platinum wire contact probes were used for this experiment in the same way as described above for the symmetric cells, except in that both electrodes were of the same area ~ 1 mm².

Minimum oxygen pressures around the test specimen.—The lowest oxygen pressure monitored near the test specimen was 10^{-20} atm at 560°C. This is well above the values (16) monitored within the oxygen pump cell itself (11). The pressure increase is due to

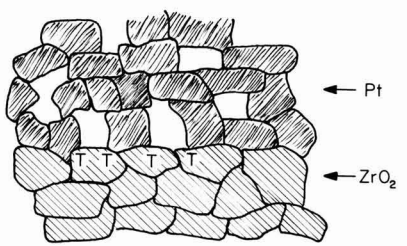

Fig. 2. Schematic representation of the contact between the electrolyte and a sintered Pt contact made by sintering Pt paste at 800°C.

leakage through the wall or release of oxygen from the wall of the glass tube connecting the pump to the measuring vessel. An alternative experimental arrangement with the cold trap at the position B in Fig. 1 gave pressures in the measuring cell well above those found with the trap in the usual position A. The difference is due to the buffering action of hydrogen (11). If water vapor present in the tank nitrogen is still present when the gas enters the pump cell (*i.e.*, the set-up with the trap at A), the water is decomposed with the formation of an equivalent amount of hydrogen. Drying the gas at A then removes most of the residual water and leads to a certain value of the water-hydrogen pressure ratio $(pH_2O/pH_2)_A$. On the other hand, with the cold trap in position B, the water is largely removed before the gas enters the cell, and therefore the amount of H_2 that can be formed is largely reduced. This leads to a higher value of the water-hydrogen pressure ratio $(pH_2O/pH_2)_B$. If no leakage would occur, each would give rise to an oxygen pressure given by the ratio

$$pO_2^{1/2} = K_{H_2O} pH_2O/pH_2 \qquad [6]$$

with $(pO_2)_A < (pO_2)_B$. Moreover, leakage of oxygen occurs and this will have a much stronger effect if the H_2 pressure is low (case of position B) than if it is high (case of position A). As a result, the value of pO_2 finally measured in the monitor cell is again smaller in case A than in case B.

Experimental Results and Discussions

Hysteresis.—If at a given oxygen pressure the current is measured as a function of applied voltage, first increasing the voltage from zero to 6V at a rate of 1 v/min, and then decreasing it to zero at the same rate, hysteresis is observed. Figure 3 shows the result for a measurement with the cell in air. Both the decrease of current wtih time (4, 9, 17) and the increase of current with time (9, 11) were previously reported. The hysteresis, however, has not been satisfactorily explained (9). The present authors believe that the increase is due to the injection of F centers into the electrolyte from the cathode at voltages $\geq$2V, and that the decrease is due to the time required for the completion of polarization or, if it is after a considerable number of F centers have been formed, the time required for these centers to disappear. The most reproducible curves were obtained with measurements taken during the decrease of the applied voltage from 6 to 0V at a rate of 1 V/min (the solid curve in Fig. 3) after the voltage had been increased from 0 to 6V beforehand at the same rate and held at 6V for half a minute. The times involved are supposed to be long enough to build up space charges characteristic of polarization, but are still short enough to keep F centers, formed at the cathode at high voltages, from drifting into the electrolyte to an appreciable extent. From here on, only the characteristics obtained according to this schedule will be discussed.

Oxygen pressure dependence of the direct-current vs. voltage characteristics.—Some examples of current-voltage characteristics measured at various oxygen pressures are shown in Fig. 4. It is seen that variation of the oxygen pressure affects the characteristic in different ways. At $V > 2V$ the current slightly decreases with increasing oxygen pressure in the range $10^{-14.5}$ to $10^{-4.3}$ atm and hardly changes with the oxygen pressure in the range $pO_2 > 10^{-4.3}$ atm. This behavior is more easily seen from a plot of the slope of the *I-V* characteristic, *i.e*, the dynamic conductance $(\partial I/\partial V)$, as a function of applied voltage. The inverse of this derivative, $(\partial V/\partial I)$, is of the dimension of a resistance and is called dynamic resistance. Figure 5 shows the relation between $(\partial V/\partial I)$ and applied voltage for various oxygen pressures. The effect of oxygen pressure upon the dynamic resistance is strongest where applied voltage is zero, and weakest at voltages higher than 2V. This behavior suggests that the characteristic is determined by two different mechanisms, the effect of one being dominant at $V < 2V$, the other being dominant at voltages >2V.

A difference in mechanism is also indicated by a difference in the effect of the presence of water vapor (Fig. 6). The effect of a variation in pH_2O is seen only at low O_2 pressures where oxygen atoms are present mainly as water molecules, and at $V < 2V$; at higher voltages there is practically no effect.

Finally the time dependence in the high and low voltage regions is different: the current at high voltages increases with time probably as a result of the occurrence of electronic conduction, increasing when F centers formed at the cathode drift into the electrolyte. That at low voltages tends to decrease.

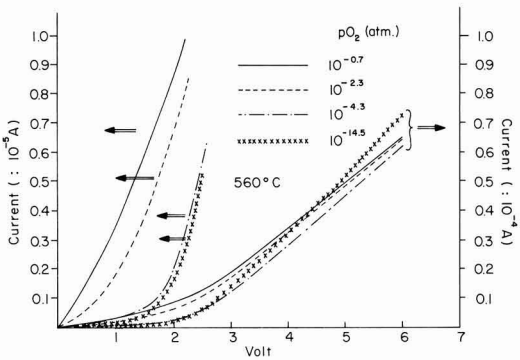

Fig. 4. Effect of oxygen pressure on *I-V* characteristics

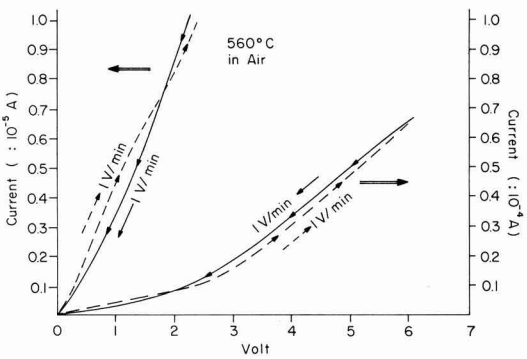

Fig. 3. Example of the direct current-voltage characteristic and hysteresis.

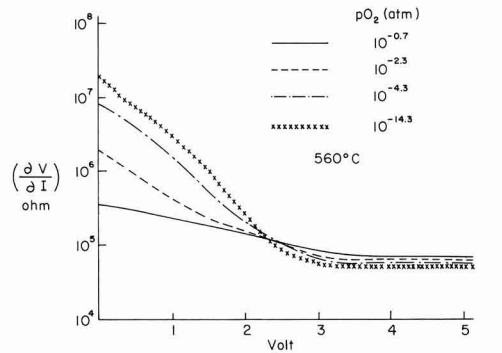

Fig. 5. Interface dynamic resistance as a function of applied voltage and oxygen pressure.

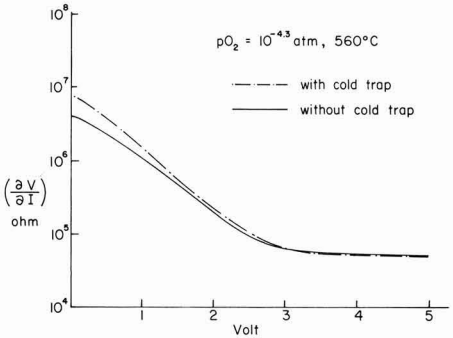

Fig. 6. Effect of water vapor on the dynamic resistance as a function of voltage.

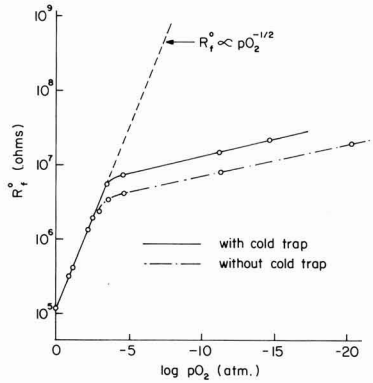

Fig. 7. R_f^0 as a function of oxygen pressure ($R_b = 5 \times 10^5$ ohm)

Low voltage section of the characteristic.—Dynamic resistance at zero volts.—Since the test specimen was operated with the same oxygen pressures at the two sides, E_{stop} as given by [4] is zero. Since no ionic current occurs when the applied voltage is E_{stop}, no potential drop can be present at the electrolyte-gas ambient interfaces. Furthermore, since the applied voltage is zero in this case, there is no oxygen chemical potential drop across the electrolyte.

The equivalent circuit consists of three resistances in series: one, R_c represents the resistance between the electrolyte and its gas ambient at the cathode side, the second, R_b, the bulk resistance of the electrolyte, and the third, R_a, the resistance between the ambient and the solid electrolyte at the anode side interface. The relation

$$\left(\frac{\partial V}{\partial I}\right)_{V=0} = R_b^0 + R_c^0 + R_a^0 \qquad [7]$$

holds, where the superscript 0 indicates that the applied voltage is zero. Or, introducing the total interface resistance R_f, defined by

$$R_f^0 = R_c^0 + R_a^0 \qquad [8]$$

and noting that R_b is ohmic so that $R_b^0 \equiv R_b$, [7] can be written

$$\left(\frac{\partial V}{\partial I}\right)_{V=0} = R_b + R_f^0 \qquad [9]$$

The resistance across the electrolyte is practically independent of oxygen pressure since the concentration of anion vacancies responsible for ionic conduction is fixed and determined by the calcium oxide content; also the electronic contribution to the conductivity across the electrolyte is hardly measurable in the oxygen pressure range 1 to 10^{-20} atm covered in this study, so that $t_i \approx 1$. Hence, the change in the dynamic resistance $(\partial V/\partial I)_{V=0}$ with pO_2 must be mainly due to a change in the interface resistance R_f^0. Equation [9] tells us that if a constant ($=R_b$) is subtracted from the observed dynamic resistances, the residue should be the R_f^0, which is a function pO_2. Trial and error shows that a plot of log R_f^0 *vs.* log pO_2 is linear for the oxygen pressure range from 10^{-4} atm up to 1 atm if $R_b = 5 \times 10^5$ ohms; the line has a slope of $-1/2$, indicating that $R_f^0 \propto pO_2^{-1/2}$ (Fig. 7). The value of R_b found in this manner should be compared with reported values for the resistivity of stabilized zirconia. According to Kingery *et al.* (3), $\rho(560°C) \approx 2.9 \times 10^4$ ohm cm. For a sample thickness, t, of ≈ 1 mm, a gross cathode contact area, S_g, of ≈ 1 mm^2, an anode area of 5 mm^2, and thus for an effective cross section of the conduction path of $S_{eff} = (5 - 1)/\ln 5 = 2.5$ mm^2, the calculated value of the bulk resistance $\left(\rho \frac{t}{S_{eff}}\right)$ is 1.16×10^5 ohms. The fact that the characteristic leads to a slightly larger value may be due to the fact that the actual contact area for the low voltage mechanism, S_L, is less than S_g. For $S_L/S_g = 1/4.3$, the two resistance values agree. This phenomenon, described here in terms of S_L and S_g has been discussed elsewhere (19) in terms of a "constriction resistance."

The plot of log R_f^0 *vs.* log pO_2 shown in Fig. 7 has a sharp change in slope near $pO_2 = 10^{-4}$ atm, indicating that R_f^0 is only weakly dependent on the oxygen pressure for $pO_2 < 10^{-4}$ atm. This sharp change in behavior requires a distinction between R_f^0 for high and for low oxygen pressure, *i.e.*, between $R_{f,h}^0$ and $R_{f,l}^0$. Comparison of the results of experiments with and without the liquid nitrogen cold trap (*i.e.*, with gas of the same oxygen pressure but containing different amounts of water vapor) shows that $R_{f,l}^0$ is variable, but $R_{f,h}^0$ is not affected. This indicates that $R_{f,h}^0$ involves oxygen atoms deriving from O_2 molecules, but that $R_{f,l}^0$ involves oxygen atoms deriving from buffer molecules, *e.g.*, H_2O or CO_2 (in the present case probably the former). It indicates also that we are dealing with a different rate-limiting process. We shall deal with the oxygen process and with the water process below.

The relative importance of the two terms, R_c^0 and R_a^0, may be shown by noting that a change in the gross anode surface area from 5 to 20 mm^2 did not give any alteration of the observed characteristics whereas changing the cathode area did alter the behavior. This indicates that R_f^0 is determined mainly by R_c^0: it is mainly the cathodic processes that determine the current-voltage characteristics. Consequently

$$R_f^0 \approx R_c^0 \qquad [10]$$

and

$$R_c^0 >> R_a^0 \qquad [11]$$

The same feature is indicated by a comparison of the *I-V* characteristic of an asymmetrical cell, for which $pO_2(I) = 10^{-20.0}$ atm and $pO_2(II) = 0.2$ atm, with the *I-V* characteristics of symmetrical cells operated at these two pressures. As shown in Fig. 8, the section of the asymmetrical characteristic for $V > E_{open}$ (curve 1a) where the electrode at the low pO_2 side is the cathode, is almost identical with the symmetrical characteristic for $pO_2 = 10^{-20.0}$ atm (curve 2) if the latter is shifted by E_{open} (curve 2). Similarly the section of the asymmetric characteristic for $V < E_{open}$ (curve 1b) where the electrode at the high pO_2 side is the cathode, is almost identical with the characteristic of the symmetrical cell having $pO_2 = 0.2$ atm (curve 3) similarly shifted (curve 3'). Thus the gas present at the cathode (negative relative to E_{open}) determines the shape of the characteristic.

If the cathode process determines R_f^0, the pressure dependence of R_f^0 mainly arises from the pressure dependence of R_c^0. Since $R = C^{-1}$, where C is the conductance, the pO_2^{-n} dependence of R_c^0 corresponds to the following relation for the conductance C_c^0 at the cathode side interface

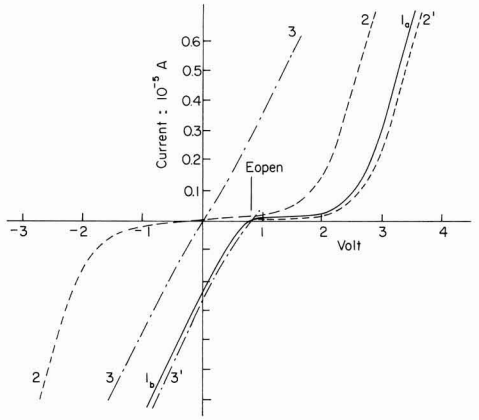

Fig. 8. Comparison of the *I-V* characteristic of an asymmetrical cell with those of symmetrical cells. 1_a, asymmetrical characteristic for $V \geqq E_0$ (E_0 = 810 mV, at 560°C, $pO_2(I) = 10^{-20.0}$ atm and $pO_2(II) = 10^{-0.7}$ atm.); 1_b, asymmetrical characteristic for $V \leq E_0$; 2, symmetrical characteristic for $pO_2 = 10^{-20.0}$ atm; 2', 2 shifted to the right by 810 mV; 3, symmetrical characteristic for $pO_2 = 10^{-0.7}$ atm; 3', 3 shifted to the right by 810 mV.

$$C_c^0 = \frac{1}{R_c^0} \propto pO_2^n \qquad [12]$$

where $n = \frac{1}{2}$ at high oxygen pressures and $n \approx 0$ at low oxygen pressures. The conductance is given by

$$C_c^0 = \left(\frac{\partial I}{\partial V}\right)_{V=0} \qquad [13]$$

The current I is given by the number of O^{2-} ions formed per second from $O_2(g)$ or $H_2O(g)$ at the cathode and transferred to the solid electrolyte (15). This may happen in various ways, each involving a number of steps, one of which is the rate-determining one.

Determination of the rate-limiting step: $pO_2 >> pH_2O$.—At relatively high oxygen pressures, when $pO_2 >> pH_2O$, the over-all cathode process consists of the dissociation and ionization of oxygen and its incorporation into the zirconia

$$\tfrac{1}{2}\,O_2(g) + 2e^-(Pt) \rightarrow O^=(ZrO_2) \qquad [14]$$

It has been argued (13) that since species in three phases are involved in this process, it has to occur at a triple contact where these three phases meet (Fig. 2,T). It should be understood, however, that this triple contact is one-dimensional and cannot carry any current. Although the actual process will occur more or less close to T, it must take place across a two-dimensional surface, *e.g.*, an area either at the Pt side or at the zirconia side (or at both sides) of T. In the first case the process must involve diffusion of an oxygen species through or over the platinum; in the latter case it must involve electron diffusion from the Pt at T over the free zirconia surface. It is proposed that the first mechanism is responsible for the low-voltage behavior and that the second mechanism accounts for the high-voltage behavior. We shall now proceed with a discussion of the former. The following steps, indicated schematically in Fig. 12 are supposed to be involved.

$$\tfrac{1}{2}\,O_2(g) \rightleftarrows \tfrac{1}{2}\,O_2(Pt/g) \qquad [15]$$

$$\tfrac{1}{2}\,O_2(Pt/g) \rightleftarrows O(Pt/g) \qquad [16]$$

$$O(Pt/g) \rightarrow O(Pt/ZrO_2) \qquad [17]$$

$$O(Pt/ZrO_2) + V_O^{\cdot\cdot} \rightleftarrows O_O^x + 2h^{\cdot} \qquad [18]$$

$$2e^-(Pt) + 2h^{\cdot} \rightleftarrows 0 \qquad [19]$$

Here $O_2(Pt/g)$ are oxygen molecules adsorbed at the interfaces between the platinum crystals and the gas phase either at the outer surface of the paste electrode or inside the platinum sponge; $e^-(Pt)$ are electrons of the platinum, with energies corresponding to its Fermi surface; $O(Pt/g)$ are oxygen atoms in the platinum at the platinum-gas interface (the formation of charged forms of oxygen in the platinum, *e.g.*, O^- or $O^=$, is not energetically favored), $O(Pt/ZrO_2)$ are oxygen atoms in the platinum near the Pt, ZrO_2 interface, $V_O^{\cdot\cdot}$ are the oxygen ion vacancies present in the zirconia at a concentration given by that of calcia (2, 3), O_O^x is the structure element symbol for a normal $O^=$ ion in the zirconia, and $h^{\cdot}$ are electron holes formed in the ZrO_2 surface by solution of the oxygen atoms from the platinum.

Each of the steps in the reaction sequence must be considered as a possible rate-limiting step. To treat them in turn, reaction [15] represents access of the oxygen gas to the platinum surface and could be the rate-limiting step if diffusion of oxygen molecules through a boundary layer were slow. The oxygen flux would then be

$$J_0 = \frac{2D'}{\eta}\,[pO_2(g) - pO_2(Pt/g)] \qquad [20a]$$

where η is the boundary layer thickness and D' the diffusion coefficient for oxygen in the boundary layer.

By an analysis similar to that used in the next section, it can be shown that this leads to an equation for the interface resistance of the form

$$R_f^0 = \frac{RT}{4\mathbf{F}B'}\,pO_2^{-1}(g) \qquad [20b]$$

where $\mathbf{F}$ is the Faraday and B' is a constant (cf. Eq. [35]). The resistance thus varies linearly with $pO_2^{-1}(g)$ whereas the experimental observations (Fig. 7) vary with $pO_2^{-1/2}(g)$. Thus [15], which has been recognized in the literature (19) as a possibly important rate-limiting process (gas phase polarization), is not the rate-controlling step in any of the present experiments.

In a similar manner, reaction [16] can be eliminated as a rate-limiting step since it also shows a conductance proportional to $pO_2(g)$. Of all the reactions, only [17] and [18] have the required $pO_2^{1/2}$ dependence through the equilibrium of [16] combined with [17]. Of these two, [18] has no voltage dependence since the activity of $V_O^{\cdot\cdot}$ may be considered constant as determined by the calcium concentration. If the current capable of being given by [18] is greater than $I_b = V/R_b$ given by the ohmic bulk resistance, R_b, and this must be expected to occur close to the origin of the I-V curve where I_b is small, the over-all current must be limited by R_b and be independent of pO_2. On the other hand, if the current given by [18] is the smaller one so that [18] becomes the rate-limiting step it leads to a voltage independent current $I_m \propto pO_2^{1/2}$. The resulting I-V characteristic near the origin would be as shown in Fig. 9. The experimental results in the present work show, however, that in the area where the dynamic resistance is proportional to $pO_2^{-1/2}$, the current near $V = 0$ is dependent on both $pO_2^{1/2}$ and V. Therefore [18] cannot be rate limiting, and [17] is indicated as the rate-determining step.

Low voltage I-V characteristic for $pO_2 >> pH_2O$.—The fact that [17] is the rate-determining step leads to an expression for $(\partial V/\partial I)_{V=0}$ which may be compared with the data. As mentioned earlier, in any situation in which ionic current flows, *i.e.*, where $V \neq E_{stop}$, the chemical potential of oxygen at the cathode surface of the electrolyte is lower than that of its gas ambient. For $pO_2(I) = pO_2(II)$ as holds for the cells investigated in the present study, and in accordance with the experimental results which indicate that the cathode resistance $R_c >> R_a$ the anodic resistance, the variation of the chemical potential of oxygen through

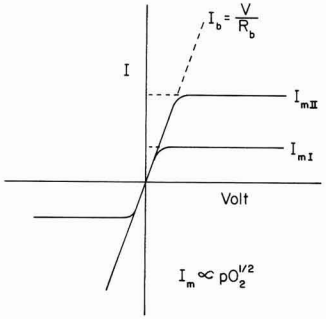

Fig. 9. Schematic diagram for the case where the process [18] would be the rate-determining step. It would be expected that $(\partial V/\partial I)_{V=0} = R_b$ near the origin; $I_m \propto pO_2^{1/2}$.

the cells can be shown schematically as in Fig. 10. As shown, the drop in μO_2 at the cathode is much larger than the increase in μO_2 at the anode: $\mu O_2(g) - \mu O_2(c) >> \mu O_2(a) - \mu O_2(g)$

$$\Delta\mu O_2 = \mu O_2(a) - \mu O_2(c) \approx \mu O_2(g) - \mu O_2(c)$$

The induced potential difference $\Delta\mu O_2$ over the electrolyte represents an emf

$$E_{a-c} \approx E_{g-c} = \frac{\Delta\mu O_2}{4F} \qquad [21]$$

which is almost of the magnitude and sign to stop the migration of ions under the influence of the outer field. The ionic conduction processes may be represented by the equivalent circuit (Fig. 11). The limitation of electronic conduction may be represented by a resistance, R_e, parallel to the others which represent the resistance to ionic conduction. In this equivalent circuit, the polarization emf (21) works over the resistance $R_f \approx R_c$. Since there is practically no electronic conduction under the conditions of the experiments, $R_e \approx \infty$. A small ionic current is kept going if the applied voltage is larger than the polarization voltage (21)

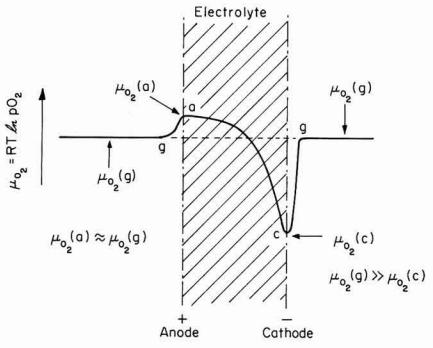

Fig. 10. Schematic diagram of the oxygen chemical potential across the circuit (electrode-electrolyte) if ionic current flows.

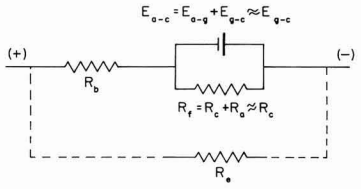

Fig. 11. Equivalent circuit for the situation depicted in Fig. 10

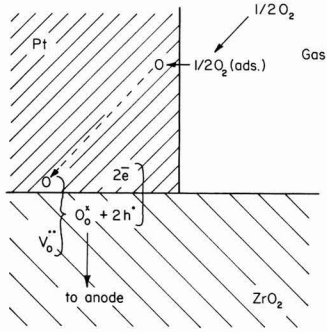

Fig. 12. Reaction steps in the low-voltage mechanism. The dotted line indicates the rate-controlling step.

$$V = I \cdot R_b + E_{a-c} \qquad [22]$$

$$E_{a-c} = \frac{RT}{4F} \ln \frac{pO_2(a)}{pO_2(c)} = \frac{RT}{4F} \ln \frac{pO_2(g)}{pO_2(c)} \qquad [23]$$

If [17] is the rate-determining step, the rate is given by a diffusion flux equation

$$J_O = D \frac{\partial}{\partial x} [O(Pt)] \qquad [24]$$

where D is the diffusion constant of O atoms for diffusion through the platinum from the Pt/gas surface to the Pt/ZrO_2 interface along any of the paths pp', qq', rr', tt' in Fig. 13; it may include diffusion along the Pt/ZrO_2 interface (path Ts in Fig. 13) but not diffusion along the Pt/gas interface (p → q → r → t → T), since the latter would be effected faster by a diffusion of O_2 molecules through the gas phase. (This is true in particular in pure oxygen where concentration gradients cannot occur, and since there is no indication of a change in mechanism on going from pure oxygen to inert gas-O_2 mixtures, the same appears to hold for operation in these mixtures also. Gas diffusion of O_2, if rate determining, would also give a rate $\propto pO_2$.)

The maximum contact area for the proposed process is the total area S of the Pt/ZrO_2 interfaces (wT in Fig. 13). As we saw in the section on Dynamic resistance at zero voltage, the contact area for the low voltage mechanism $S_L \approx (1/4.3)S_g$. The total ZrO_2 surface becomes accessible only if the ZrO_2 becomes sufficiently conductive at its surface to transport electrons from the platinum over the ZrO_2 surface.

Assuming a linear gradient, [24] can be changed to

$$J_O = \frac{D}{\partial} \{[O(Pt/g)] - [O(Pt/ZrO_2)]\} \qquad [25]$$

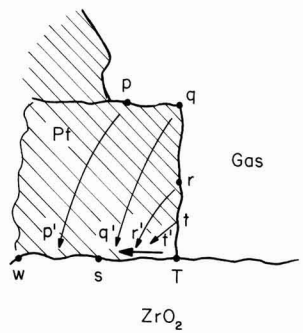

Fig. 13. Various diffusion paths for O in Pt

Here ∂ is the effective length of the diffusion path, *i.e.*, in Fig. 13, the appropriate average of the lengths of paths pp' to tt'.

The equilibrium for [15] and [16] leads to

$$[O(Pt/g)] = K_1 pO_2^{1/2}(g) \quad [26]$$

and one can also write (Fig. 10)

$$[O(Pt/ZrO_2)] = K_1 pO_2^{1/2}(Pt/ZrO_2) \equiv K_1 pO_2^{1/2}(c) \quad [27]$$

Consequently

$$J_O = \frac{D}{\partial} K_1 \{pO_2^{1/2}(g) - pO_2^{1/2}(c)\} \quad [28]$$

At the interface Pt/ZrO_2, O atoms are transformed into $O^=$ ions by reaction [18]. Therefore the particle current [28] ultimately represents an equivalent electrical current through the ZrO_2 of

$$I_h = 2\mathbf{F}S_L J_O \quad [29]$$

Here S_L is the effective area of the Pt/ZrO_2 interface, **F** is the Faraday, and the subscripts h and L are used to indicate respectively relatively high O_2 pressure ($pO_2 >> pH_2O$) and a low voltage. Combining [29] with [22], [23], and [28], we find

$$V = I_h R_b + \frac{RT}{4\mathbf{F}} \ln pO_2(g)/pO_2(c) \quad [30]$$

and

$$I_h = 2\mathbf{F}S_L \frac{D}{\partial} K_1 \{pO_2^{1/2}(g) - pO_2^{1/2}(c)\} = B\{pO_2^{1/2}(g) - pO_2^{1/2}(c)\} \quad [31]$$

where

$$B = 2\mathbf{F}S_L(D/\partial)K_1 \quad [32]$$

Eliminating $pO_2(c)$ from [30] and [31] we get

$$V = I_h R_b + \frac{RT}{4\mathbf{F}} [\ln pO_2(g) - 2 \ln \{pO_2^{1/2}(g) - I_h/B\}] \quad [33]$$

and, by differentiation

$$\frac{\partial V}{\partial I} = R_b + \frac{RT}{2\mathbf{F}B} \{pO_2^{1/2}(g) - I_h/B\}^{-1} \quad [34]$$

or, for zero voltage where $I_h = 0$

$$\left(\frac{\partial V}{\partial I}\right)_{V=0} = R_b + \frac{RT}{2\mathbf{F}B} pO_2^{-1/2}(g) \quad [35]$$

This is just the form observed for R_f^0 at $pO_2 > 10^{-4}$ atm (Fig. 7). The current by this mechanism cannot exceed a limiting value given by [31] with $pO_2(c) = 0$, *i.e.*

$$(I_h)_{lim} = BpO_2^{1/2}(g) \quad [36]$$

This limiting value is approached when $V \to \infty$; $\partial V/\partial I$ as given by [34] approaches ∞, or $\partial I/\partial V$ approaches zero. In the present experiments the saturation level is not reached, a different mechanism with a larger current taking over at large voltages. This new mechanism is discussed below.

Low-voltage characteristic for $pO_2 << pH_2O$.—At lower oxygen pressures and in an incompletely dried gas where $pO_2 < pH_2O$, oxygen atoms are present mainly in the form of water molecules, and the O atoms in the platinum will be mainly formed from these. The successive steps of the entire cathodic process are then

$$H_2O(g) \to H_2O(g/Pt) \quad [37]$$

$$H_2O(g/Pt) \rightleftarrows H_2O(Pt/g) \quad [38]$$

$$H_2O(Pt/g) \rightleftarrows O(Pt/g) + H_2\uparrow \quad [39]$$

followed by [17]-[19]. The fact that the voltage dependence of the current is similar to that in the O_2 governed case and different from the dependence shown in Fig. 9 suggests that we are again dealing with a diffusion controlled process. If it is assumed that [17] is again the rate-limiting step, then the concentration of $O(Pt/g)$ depends on the activity of H_2O and H_2 through [38] and [39] and the current may be represented by

$$I_l = 2\mathbf{F}S_L \frac{D}{\partial} K_2 \left[\frac{pH_2O}{pH_2}(g) - \frac{pH_2O}{pH_2}(c)\right] \quad [40]$$

K_2 being the equilibrium constant of [38] and [39] combined. But since $pH_2O/pH_2 = K_{H_2O} pO_2^{1/2}$, this would make I_l again $\propto pO_2^{1/2}$, whereas a much weaker dependence was observed (see Fig. 7). Thus [17] cannot be the rate-limiting step. The observed behavior is found if diffusion across a boundary layer in the gas phase, *i.e.*, [37], is the rate-limiting process. This leads to a current

$$I_l = 2\mathbf{F}K_3 \{pH_2O(g) - pH_2O(g/Pt)\} \quad [41]$$

dependent on pH_2O in the gas and pH_2O at the gas-Pt surface, the latter depending on the applied field in a manner similar to that found for $O(Pt/ZrO_2)$ in the oxygen governed case.

The weak pO_2 dependence seen in Fig. 7 is at least qualitatively explained by the way in which pH_2O is linked to pO_2, in that a lowering of pO_2 results from the decomposition of H_2O with the formation of H_2. Thus a decrease of pO_2 is tied to a decrease of pH_2O and increase of pH_2. But whereas pO_2 is determined by pH_2O/pH_2, the rate of [37] depends on pH_2O alone, and the latter may vary only slightly while the former varies considerably. However, a quantitative fit on the basis of this model with $(K_{H_2O})_{560°C} = 7.6 \times 10^{12}$ atm$^{1/2}$ is not obtained, and further experiments with well-defined buffer mixtures are required to clarify the mechanism operating in this range.

High-voltage section of the characteristic.—At voltages above 2V a new mechanism becomes operative. It might be assumed that the change in mechanism is due to a change from ionic conduction, dominant at low voltages, to electronic conduction at high voltages. This, however, cannot be the case. The electronic conductivity σ_e and the concentration of free electrons [e'] in calcia stabilized zirconia vary with the oxygen pressure as (2, 6)

$$\sigma_e \propto [e'] \propto pO_2^{-1/4} \quad [42]$$

whereas the high-voltage conductivity $(\partial I/\partial V)_H$ is practically independent of pO_2. Thus apparently the current remains largely ionic. This conclusion is also supported by the fact that the dynamic resistance, $(\partial V/\partial I)_H$, shown in Fig. 5 and 6, has a value of 5-8 x 10^4 ohms which is close to the value 1.16 x 10^5 ohms calculated on the basis of the published ionic conductivity (3) and the dimensions of the cell, assuming the cathode electrode to be active over its whole surface. The following mechanism is proposed.

As shown in Fig. 10, the chemical potential of oxygen at the cathode surface of the ZrO_2 (point c) is lower than that of the gas ambient. This is the result of the slow process at the interface and represents polarization. Although a certain amount of polarization takes place at all voltages, its extent increases with applied voltage. Increasing the strength of polarization results in a lowering of μO_2 at point c. Since the concentration of electronic defects is related to pO_2 by [42], types of oxygen vacancies different from the ones present under normal conditions can be formed

$$V_O^{\cdot\cdot} + e^- \rightleftarrows V_O^{\cdot} \quad [43]$$

$$V_O^{\cdot} + e^- \rightleftarrows V_O^{x} \quad [44]$$

where $V_O^{\cdot}$ and V_O^{x} are oxygen ion vacancies with one and two trapped electrons respectively. Once V_O^{x} vacancies are present, it is possible for the oxygen adsorbed at the surface of the ZrO_2 to enter the lattice directly by the reaction

$$O(ZrO_2/g) + V_O^x \rightarrow O_O^x \qquad [45]$$

The O_O^x can then pass to the anode.

This model relies on having V_O^x close to the ZrO_2-gas interface. Since the polarization occurs at the platinum cathode, the V_O^x occurs initially at that point and diffuses away with longer times of polarization as shown in Fig. 14. As a result of the sideways diffusion of the F-centers (V_O^x), path a in Fig. 14, the free ZrO_2 surface next to the platinum becomes electronically conductive and becomes available to the adsorbed oxygen for the reaction of Eq. [45].

The spreading of an area with increased, probably electronic, conductivity has been observed by Kleitz (13). Also, inspection of samples used in the present work revealed F-centers (a purple coloration) over the entire contact area if the samples were subjected to voltages >6V. The high voltage characteristic is time dependent, with current increasing with time; this is predicted by the model (*i*) because F-centers diffuse into the zirconia away from the interface (path b in Fig. 14) causing some electronic conduction in the bulk (this is the effect that was minimized in the design of the experiments; section on Experimental set-up), and (*ii*) because the sideways diffusion increases the surface area that can take part in the O transport of Eq. [45] (the distance vT in Fig. 14 increases with time). In the present experiments the maximum sideways diffusion path length is of the order of the radius of the platinum particles, *i.e.*, small relative to the thickness of the sample. Therefore, a state is very quickly reached where the entire free surface is active. From then on the only time dependence is due to process (*i*).

Once the entire free surface area is available for reaction [45], the sequence of processes involved in the incorporation of oxygen is (Fig. 15)

$$\tfrac{1}{2}O_2(g) \rightleftarrows \tfrac{1}{2}O_2(ZrO_2/g) \qquad [46a]$$

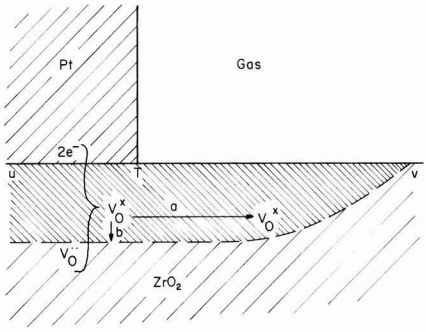

Fig. 14. Diffusion of F-centers away from the platinum electrode region into the zirconia.

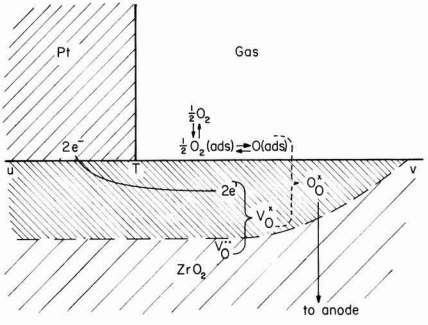

Fig. 15. Reaction steps for the high-voltage mechanism. The dashed lines indicate the rate-controlling step.

$$\tfrac{1}{2}O_2(ZrO_2/g) \rightarrow O(ZrO_2/g) \qquad [46b]$$

$$2e^-(Pt) \rightarrow 2e'(ZrO_2) \qquad [47a]$$

$$2e'(ZrO_2) + V_O^{\cdot\cdot} \rightarrow V_O^x \qquad [47b]$$

together with reaction [45]. The rate-controlling step in this sequence can be determined in much the same way as for the low voltage case. Experimentally, the high voltage characteristic is voltage dependent but not oxygen pressure dependent. Since [46a] and [46b] and [47a] are oxygen pressure dependent, and [47b] is voltage independent, the indication is that [45] is the rate-controlling step.

The oxygen pressure independence of reaction [45] may be shown as follows. The number of neutral oxygen atoms adsorbed on the zirconia surface is

$$O(ads)_H = K_4 S_H p O_2^{1/2}(g) \qquad [48]$$

where K_4 is the equilibrium constant of [46a] and [46b] combined, and S_H is the effective surface area for the mechanism. The concentration of V_O^x vacancies is given by [43], [44], with equilibrium constants K_5, K_6, and [42]

$$[V_O^x(c)] = K_5 K_6 [V_O^{\cdot\cdot}] p O_2^{-1/2}(c) \qquad [49]$$

The current generated by the high voltage mechanism with [45] as the rate-limiting step is equivalent to the number of O_O^x lattice ions formed per second

$$I_H = 2\mathbf{F}\frac{dO_O^x}{dt} = 2\mathbf{F}AS_H[V_O^x]O(ads) \qquad [50]$$

where A is the rate constant for reaction [45]. Using [48] and [49]

$$I_H = C\,[pO_2(g)/pO_2(c)]^{1/2} \qquad [51]$$

with $C = 2\mathbf{F}AK_4K_5K_6S_H[V_O^{\cdot\cdot}]$. Or using [23]

$$I_H = C \exp\frac{2\mathbf{F}}{RT}E_{a-c} \qquad [52]$$

From [22] and [52]

$$V = I_H R_b + \frac{RT}{2\mathbf{F}}\ln(I_H/C) \qquad [53]$$

and

$$\frac{\partial V}{\partial I_H} = R_b + \frac{RT}{2\mathbf{F}}I_H^{-1} \qquad [54]$$

These expressions do not contain pO_2 and thus give the required independence from oxygen pressure. They also represent a voltage dependent current as required. The dynamic resistance [54] approaches R_b with increasing current, *i.e.*, at large voltages, as is observed (Fig. 5 and 6).

Since the bulk resistivity of the electrolyte, ρ_b, is independent of voltage, the bulk resistance applicable to the low voltage mechanism is

$$R_{b,L} = \rho_b \frac{y}{S_L}$$

and the bulk resistance applicable to the high voltage mechanism is

$$R_{b,H} = \rho_b \frac{y}{S_H}$$

where y is the sample thickness, and S_L, S_H are the active contact areas appropriate to the two mechanisms. From above, $R_{b,L} = 5 \times 10^5$ ohms, and from Fig. 5 and 6, $R_{b,H} \approx 2 \times 10^5$ ohms. Thus, as an approximate figure

$$\frac{S_H}{S_L} \approx 2.5$$

or in other words, the platinum crystals physically cover about 30% of the zirconia surface "covered" by the paste.

Transition from the low- to the high-voltage mechanism.—Although we have spoken about low-voltage and a high-voltage mechanism with a transition at $\approx$ 2V, in reality both mechanisms occur at all voltages: only the ratio in which they contribute varies. The total ionic current is the sum of the current generated by the two mechanisms, *i.e.*, that from the low voltage mechanism, I_L, and that from the high voltage mechanism, I_H. Then

$$I = I_L + I_H \qquad [55]$$

I_L in turn involves two types of oxygen atom source, one at high oxygen pressures, I_h, and one at low oxygen pressures, I_l. These are given by [31] and [41]. Then

$$I_L = I_h + I_l \qquad [56]$$

Consequences of the proposed models.—The models proposed here have been developed on the basis of experiments on moderately sintered Pt-paste contacts. They are sufficiently general, however, to be applied to other types of contacts and contact configurations, *e.g.*, Pt, Au, and Ag point contacts as used by Kleitz (13), evaporated or sputtered Pt contacts as used by Heyne (9) and Karapachev *et al.* (18). The oxygen dominated low-voltage regime was found to depend on diffusion of O through the platinum and was characterized by a diffusion coefficient D and an effective thickness ∂. As shown in [32]-[34], the resistance is greater than the bulk electrolyte resistance and is proportional to ∂ as long as ∂ is not too small; a decrease of ∂ will decrease the resistance until a constant resistance R_b is reached. For large ∂, the resistance is quasi-ohmic but polarization occurs; for small ∂, the resistance is truly ohmic, and no polarization occurs. The conclusions only hold if other rate-limiting steps are avoided.

Absence of polarization with thin sputtered Pt cathodes and the occurrence of polarization with thicker Pt layers was actually observed by Heyne (9). An increase of the current, attributable to a decrease of the effective diffusion path, was observed by Karapachev *et al.* (18) in experiments in which they made scratches in evaporated Pt layers, thus creating 3-phase boundaries with small effective ∂. In terms of Fig. 13, the unscratched layer corresponds to $\partial \approx$ pp', while the scratched one reduces ∂ to the average of pp'-tt'. An almost ohmic characteristic was also found by Yuan *et al.* (11) who used a thinly spread paste cathode in pumping experiments.

An investigation of the electrode characteristics in the O_2 dominated low-voltage range should show a material dependence through the solubility of O and its diffusion constant. This may account for the differences observed between Pt, Au, and Ag point contacts (13). The high-voltage mechanism was based on the utilization of free ZrO_2 surface. Therefore, a cathode geometry which reduces the free surface area (*e.g.*, evaporated or sputtered platinum) should suppress the current based on this mechanism and may make an increase in current due to electronic conduction (characterized by a $pO_2^{-1/4}$ dependence) observable.

A transition from a low- to a high-voltage mechanism has been observed by others, *e.g.*, Kleitz (13) and Guillou *et al.* (15). These authors used point contacts and therefore must have observed ionic effects of the type discussed here. Experiments with porous cathodes as employed in the present investigation but with zirconia doped with donors (5) should show a high-voltage mechanism as discussed in the present paper, but setting in at a lower voltage. The discussion given so far applies to densely sintered zirconia. With porous zirconia other models become possible in which oxygen may reach the Pt/ZrO_2 interface by diffusion as O_2 through the pores in the zirconia. This as the rate limiting step would lead to a current $\propto pO_2$.

Determination of transference numbers by polarization techniques.—It is interesting to consider in the light of the results presented in this paper, the use of polarization experiments to determine the extent of electronic conduction in stabilized zirconia. In the technique of Vest and Tallan (4), the time dependence of the voltage needed to drive a constant current across the sample is measured, and the electronic transport number obtained from the relation

$$t_e = \frac{E(0)}{E(\infty)} \qquad [57]$$

where $E(0)$ is the voltage at time = 0, and $E(\infty)$ is that at time = ∞. This relation is as pointed out, valid only when the electrodes are blocking to the passage of oxygen. With the electrodes used in the present paper, blocking behavior was not observed, and values of t_e deduced from the time effects would not be correct; that Vest and Tallan were able to observe isolated electronic conduction may well be due to their use of "fluxed" platinum paste electrodes, *i.e.*, electrodes with a glass additive used to improve adhesion. The presence of the glass would seem to improve the blocking effect of the electrode, presumably by sealing gas permeation channels and thus increasing ∂ in Eq. [25]; at any rate the different behavior with at first sight similar (both Pt) electrodes, emphasizes the need to consider the details of electrode structure when interpreting observations of electrical behavior in largely ionic conductors.

Summary

The direct current-voltage characteristics of cells Pt, O_2/(Zr, Ca) O_2/Pt, O_2 with the same oxygen pressures at both sides were measured at 560°C under oxygen pressures ranging from 1 to 10^{-20} atm. The characteristics were markedly nonohmic and showed two distinct regions. One, at voltages <2V shows an oxygen pressure dependence, the conductance varying as $pO_2^{1/2}$ as long as O_2 is the major O-containing species; a weaker pO_2 dependence is found if H_2O is the main O-containing species. The rate-determining step for the O_2 case is the diffusion of O atoms through the platinum of the electrode. The high-voltage region shows practically no pO_2 dependence. Here the rate-limiting step is the combination of O atoms adsorbed at the ZrO_2 gas interface with V_O^x formed as a result of polarization.

The importance of the electrode material and the electrode geometry is stressed.

Acknowledgment

This work was supported by the Directorate of Chemical Science, Air Force Office of Scientific Research under Contract AF-AFOSR-68-1405.

Manuscript submitted Aug. 22, 1969; revised manuscript received *ca.* Jan. 21, 1970.

Any discussion of this paper will appear in a Discussion Section to be published in the December 1970 JOURNAL.

REFERENCES

1. R. C. Garvie, *J. Am. Ceram. Soc.*, **51,** [10], 553 (1968).
2. Hermann Schmalzried, *Z. Elektrochem.*, **66** [7], 575 (1962).
3. W. D. Kingery, James Pappis, M. E. Doty, and D. C Hill, *J. Am. Ceram. Soc.*, **42** [8], 393 (1959).
4. R. W. Vest and N. M. Tallan, *J. Appl. Phys.*, **36** [2], 543 (1965).
5. F. A. Kröger, *J. Am. Ceram. Soc.*, **49** [4], 215 (1966).
6. J. W Patterson, E. C. Bogren, and R. A. Rapp, *This Journal*, **114** [7], 752 (1967).
7. G. G. Charette and S. N. Flengas, *ibid.*, **115** [8], 796 (1968).
8. D. P. Clark and R. E. Meridith, *Electrochem. Technol.*, **5** [9/10], 446 (1967).
9. L. Heyne, "Ionic Conductivity in Oxides," pp. 149-164 of "Mass Transport in Oxides," J. B. Wachtman, Editor, National Bureau of Standards, Special Publication No. 296 (1968).
10. F. A. Kröger, *Proc. Brit. Ceram. Soc.*, **1**, July, p. 167 (1964).

11. Daniel Yuan and F. A. Kröger, *This Journal*, **116**, [5], 594 (1969).
12. J. Besson, C. Deportes, and M. Kleitz, Brevet Francais, No. Provisoire 128-327 (Nov., 1967).
13. M. Kleitz, "Electrode Reactions in Solid Oxide Electrolytes," Thesis, University of Grenoble (May, 1968).
14. C. J. Devane and E. L. Holverson, *J. Appl. Phys.*, **38** [13], 5421 (1967).
15. M. Guillou, J. Millet, and S. Palous, *Electrochim. Acta*, **13** [6], 1411 (1968).
16. Hiroaki Yanagida, cited in ref. (11) as private communication. To be published elsewhere.
17. D. W. Strickler and W. G. Carlson, *J. Am. Ceram. Soc.*, **47** [3], 120 (1964).
18. S. V. Karapachev and A. T. Filyaev, *Elektrokhimiya*, **2** [11], 1330 (1966).
19. C. S. Tedmon, Jr., H. S. Spacil, and S. P. Mitoff, *This Journal*, **116** [9], 1170 (1969).

Electrodeless Electrolysis

Abner Brenner* and John L. Sligh, Jr.*

National Bureau of Standards, Washington, D. C.

ABSTRACT

Solid ionic conductors and fused salts were electrolyzed without contact of solid electrical leads. The current was carried to the materials to be electrolyzed either by means of electrons emitted by a hot filament or by a glow discharge. The materials were made the separating wall between the anode and cathode compartments of an apparatus constructed of glass or fused silica. Electrolysis of glass produced a white opaque material which did not seem to differ chemically from the original glass. Dendrites of several metals were obtained in the glow discharge electrolysis of fused salts. The results of the latter process resembled conventional electrolysis with metal electrodes and was not similar to the glow discharge electrolysis of aqueous electrolytes.

In electrodeposition or electrolysis as ordinarily practiced, the electrodes are metals or graphite, and the products of electrolysis form at the interface between the electrode and the electrolyte. Most of the data of electrolysis have been obtained with the use of such electrodes, and their characteristics have entered into the theories. Thus, the cathode provides a pathway by means of which electrons can flow to the electrolyte-cathode interface. However, the electric current is conducted by other kinds of systems, such as the electron beam and rarified gases; and the question arises as to whether electrochemical reaction will occur with such systems in contact with an electrolyte.

The purpose of this investigation was to call attention to prior work that showed that electrolysis could be accomplished without the use of conventional electrodes and to explore further the variety of unconventional ways in which electrolysis could be accomplished.

Electrolysis in the absence of the conventional electrode-electrolyte interface will in this paper be called, for brevity, "electrodeless electrolysis," although it is recognized that the electron beam, rarified gas, or other conducting phase in contact with the electrolyte is performing the function of the conventional electrode.

The subject of electrodeless electrolysis has not previously been unified in the literature as a single topic or branch of electrochemistry. For that reason the introductory part of this paper has been amplified beyond the customary scope of an introduction, so as to present a survey of the field. We define electrodeless electrolysis as the occurrence of an electrochemical reaction, such as those resulting in deposition of metal or evolution of gas, at locations in the system which are remote from the metallic conductors which bring the current to the system. Electrodeless electrolysis has been observed in a variety of experiments, and the nature and, hence, the explanation of the phenomena, are not necessarily the same for all. Probably the first example of electrodeless electrolysis was that reported by Grotthuss (1) in 1819 who passed a current through a crack in a glass vessel which was wet on both sides by a silver nitrate solution. Silver separated out in the vicinity of the crack. The phenomena was studied in detail by Braun (2) in 1891 who gave it the name electrostenolysis. Metal deposition or evidence of a chemical reaction also was observed by a number of electrochemists at an organic membrane, such as a pig bladder or at an inorganic membrane, such as copper ferrocyanide, on the passage of current through systems consisting of a membrane separating solutions of heavy metal salts:

Anode/salt solution//membrane//salt solution/cathode

Electrostenolysis differed from deposition at membranes in that the former required 20V or more, whereas the latter process occurred with the low voltages used in ordinary electrodeposition. The subject of the electrolytic processes at membranes has been capably reviewed and discussed by Söllner (3) and, thus, there is no need for further treatment here.

Electrodeless electrolysis of an entirely different kind occurred with the glow discharge above an aqueous solution. The phenomenon was first reported by Gubkin in 1887 (4). In an evacuated vessel containing an electrolyte (and water vapor) he passed a current between an electrode suspended in the vapor and an electrode situated beneath the surface of the electrolyte. A potential of several hundred volts was required. This phenomena was studied in some detail by several workers some 50 or 60 years later [(5), no attempt is made here to give a complete bibliography of glow discharge electrolysis].

Glow discharge electrolysis is very different from conventional electrolysis. Either reduction (for example, of permanganate ion) or oxidation (for example, of ferrous ion) can occur and the yield may be several times greater than that expected from Faraday's law. Furthermore, in some experiments it makes little difference whether the anode or cathode is placed in the electrolyte (5b) (the other electrode being in the space above the electrolyte) or whether direct or alternating current is used. The separation of metal was reported in two instances (5a, 5c), but this seems to be a rare occurrence and the observations are open to question. One explanation of the glow discharge electrolysis is that water vapor is decomposed in the

* Electrochemical Society Active Member.

Key words: electrolysis, electrodeless electrolysis, glow discharge, electrolysis of fused salts, electrolysis of glass, electron beam electrolysis.

discharge into free radicals which then react with the dissolved salt.

Although the term "glow discharge electrolysis" has been used almost invariably in the literature as the name of the phenomena described in the preceding paragraph, it is unlikely that the phenomena involve the mechanism of conventional electrolysis. Hence, the use of the word "electrolysis" in connection with the action of the glow discharge of aqueous solutions is a little unfortunate.

Couch and Brenner (6a) observed a green corona above a copper solution and a blue corona above an indium solution with the glow discharge. Sastry (6b) observed similarly colored corona with some other salt solutions but not with fused salts. He concluded that the presence of water was necessary and that the decomposition of water vapor into free radicals in the cathode fall was involved in the mechanism.

A very different type of electrodeless electrolysis was described by Burt in 1925 (7a, 7b) and by Selenyi (7c) in 1927. They placed an ordinary (evacuated type) light bulb in a bath of fused sodium nitrate in which a wire was placed and served as anode. The filament of the lamp was made incandescent by passage of an a-c current. Then a d-c potential was placed between the wire serving as anode in the sodium nitrate and the filament, which was made negative. Current passed through the glass bulb and pure sodium collected on the upper cool walls of the interior of the bulb. The yield was exactly in accordance with Faraday's law. The explanation of the phenomena was that sodium ions migrated through the bulb from the sodium nitrate and were discharged on the inner surface of the bulb by the stream of electrons from the hot filament.

We have extended electron beam electrolysis to materials other than glass; this work is described in a subsequent section. The fused salt bath, which presumably served as a source of sodium ions, we found not to be an essential part of the experiment, as electrolysis could be performed with the bulb immersed in distilled water instead of fused sodium nitrate or with the electrical contact established through copper, plated on the outside of the bulb. Thus, the glass was actually electrolyzed to yield sodium.

The systems described in the previous examples of electrodeless electrolysis all possessed a sharp discontinuity between an electrolyte and another phase, for example, between a membrane and an electrolyte or between a gaseous phase and an electrolyte. Milicka (8) described an unusual example of electrodeless electrolysis in which both phases were aqueous. In a U-tube a concentrated solution of potassium iodide was placed and above it, in one limb, distilled water was placed. Current was passed through the liquids in the U-tube, and iodine was observed to separate out at the interface between the two liquids. Substitution of copper sulfate for the iodide resulted in the deposition of copper or copper hydroxide at the interface. Milicka stated that these experiments were well known to the earlier electrochemists, but gave no reference.

Since nothing in the current theories of electrolysis would lead one to expect electrolysis to occur at the boundary of two aqueous liquids, we attempted to verify the report. In our experiment the amount of iodine was very slight, and it was necessary to introduce starch into the liquids to make its presence visible. A blue color did occur on passing a current of 50 mA at about 1000V through the column. It appeared to form chiefly next to the wall of the glass tube. It is likely that the phenomenon is not as simple as it seems, and the presence of the glass wall may be essential to the electrolysis.

The most recent example of electrodeless electrolysis was described by Palit (9) in 1968. He observed that gas collected in a salt bridge which was used to connect a vessel of catholyte to a vessel of anolyte. The gas began to appear after about 6 hr of electrolysis, and the composition of the gas ranged from 60% to 90% oxygen. The formation of the gas was attributed to the production of charged water molecules which migrated away from the electrodes and reacted with either hydroxyl or hydrogen ions.

Our experiments on electrodeless electrolysis which are described below dealt mainly with the electrolysis of solid materials and fused salts. Aqueous solutions were not involved. The phase contacting the material to be electrolyzed was a partial vacuum ranging from about 1.0 to 10^{-5} Torr/(133 to 0.00133 N/m^2). It will be noted that in some of these experiments materials have been electrolyzed almost in free space, as the only electrical contact with the specimen was an electron beam and/or a gas at low pressure.

Electron Beam Electrolysis

Apparatus and procedure.—A schematic diagram of the apparatus is shown in Fig. 1. It is taken from U.S. Patent 3,366,562 in which it is fully described. The apparatus consisted of a glass envelope, 10 and 12, which was provided with a large port, 17, for evacuation by an oil diffusion pump, 18, and with vacuum-tight seals, 20, 21, and 28, for introducing the electrical leads, 26 and 30. The tungsten filament, 25, was heated by alternating current and could carry up to 17A. The specimen to be electrolyzed took a number of forms, but for some of the work it was a solid, cast around the end of the anode lead and was placed in the top of the holder shaped like a long stem funnel. The latter was made from fused silica or mullite. The stem of the holder protruded through a vacuum-tight seal to the outside and served both as a conduit for the positive lead and to prevent short circuiting of the latter by the electron beam. The voltage for electrolysis was applied between the tungsten filament, 25, and the positive lead, 30. The pressure in the vessel was about 10^{-5} Torr.

The solid materials which were electrolyzed had to be heated to attain a conductivity sufficient for electrolysis. For example, glass required about 400°C and selected ceramics still higher temperatures. In some experiments the tungsten filament was placed only a centimeter or two distant from the electrolyte, and the heat from the filament was sufficient to raise the temperature of the electrolyte to a point that it became conducting. However, this was not adequate for

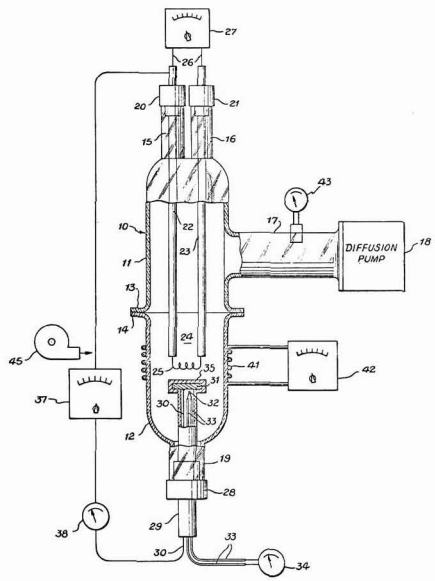

Fig. 1. Diagram of apparatus for electron beam electrolysis. Figure taken from U.S. Pat. No. 3,366,562. The numbers refer to the description in the patent.

some materials, and it was necessary to use a noninductively wound resistance heater which was placed inside of the glass envelope around the solid electrolyte. Heating by induction with a metal susceptor placed around the electrolyte was not successful, as the magnetic field of the induction coil apparently dispersed the stream of electrons and no current could be made to pass through the system.

In a typical experiment the apparatus was pumped down to 10^{-5} Torr and as a check on the system the high voltage, 1000-1500V d.c., was applied between filament and the positive lead with the resistance heater off. The absence of current flow was evidence that there was no electrical leakage. The heating element was next energized to make the solid conductive. As the latter became hot, current began to flow. Usually the current was held below 50 mA as a higher current (and a higher voltage) occasionally caused perforation of the specimen, in which case all the current flowed through the pore and electrolysis ceased.

The main difficulty with electron beam electrolysis was establishing a good electrical connection between the anode lead and the solid electrolyte. A solid metallic connection was unsatisfactory. A number of methods were evaluated using glass as a representative solid electrolyte. In the electrolysis of glass it was well known before 1900 that solid contacts were unsatisfactory, but that molten salts or sodium amalgam could be used. Markin (10) showed that the difficulty with solid electrodes was that the contact that it made with a solid electrolyte occurred only at isolated points and resulted in a very high local current density. This caused either arcing through or the formation of dendrites, which soon extended through the solid and shorted the electrodes.

In Burts' light bulb experiment the anode lead to the glass was a fused salt. However, this is not generally applicable, because so few materials are readily obtainable in the form of a bulb. We, therefore, gave up the attempts to find a suitable solid positive contact and turned to conduction through a rarified gas to establish the electrical contact with the electrolyte. This subject is treated in a later section of this paper.

Materials for electrolysis.—Preparation of a solid electrolyte in a shape suitable for electrodeless electrolysis, whether by electron beam or by the glow discharge method, was a difficulty that we did not completely overcome. In these methods of electrolysis high voltages had to be used because even the heated solid materials were not very conductive. Consequently, the slightest pore which traversed a solid electrolyte allowed the circuit to be completed without passage of current through the electrolyte. Solid electrolytes made by fusing a salt and allowing it to solidify all seemed to have cracks. Very slow cooling, particularly in a metal container made of foil, helped to eliminate some of the stresses arising from contraction on cooling. However, to obtain a sound disk of a salt, it seemed that cutting a slice from a single crystal was the only solution. The solid materials which could be obtained readily for electrolysis, therefore, were silver chloride, which is plastic at room temperature, glass, ceramic materials commercially available in the form of plates or impervious tubes closed at one end, and single crystals.

Results of experiments with electron beam electrolysis.—In our apparatus the "light bulb" experiment of Burt was easily carried out as follows. A glass test tube filled with an easily fusible salt mixture was placed near the tungsten filament. The open end of the tube extended through a vacuum-tight seal to the outside. The positive lead was inside of the test tube. Under these circumstances the outside wall of the glass tube was exposed to the electron beam and readily electrolyzed. The sodium could not be collected because it was spread as a mist or film over the extensive inner surface of the chamber. However, the film was dissolved in water and titrated. The alkalinity corresponded to over 90% of the amount of sodium predicted by Faraday's law.

A similar experiment with a mullite tube resulted in the formation of a dark layer on the outside of the tube, but the nature of the transformation was not investigated.

In other experiments the arrangement shown in Fig. 1 was used, which involved direct contact of the materials with the positive metallic lead. Copper and nickel dendrites were obtained from their chlorides which had been melted with potassium chloride and cooled. Silver dendrites were obtained from solid silver chloride. The deposition occurred on the surface facing the heated filament, and dendrites extended into the body of the solid. Here is a clear instance of an electron beam acting as a cathode exactly as would be expected of a metal or any other electronically conducting cathode, *i.e.*, the dendrites formed at the cathode-electrolyte interface and grew into the electrolyte.

In one experiment solid sodium tetraborate was electrolyzed, but the heat of the filament and the IR drop caused the salt to melt, and consequently the experiment was actually electrolysis of the fused salt. At the conclusion of the experiment a lump of transparent boric oxide was found on top of the melt; the sodium liberated by the electrolysis had volatilized. Materials which normally did not electrolyze, also did not undergo electrolysis with the electron beam. For example, molybdenum disulfide, which is an electronic conductor, did not undergo any observable change in the electron beam experiment.

Glow Discharge Electrolysis of Solid Electrolytes

Development of process, apparatus, and procedure.—The difficulty of obtaining a satisfactory electrical contact of the positive lead to the solid electrolyte in electron beam electrolysis led to the investigation of glow discharge electrolysis. The first experiment was a hybrid type of electrolysis—a modification of the one with a glass tube described earlier. In that experiment the outside surface of the tube was exposed to the electron beam for electrolysis; the inside contained a molten salt for making a good electrical connection to the positive lead wire. In the modified experiment with glow discharge the fused salt was not used. Instead, the interior of the tube was evacuated to a low pressure at which a good glow discharge occurred. The path of the current thus went from the positive lead through the rarified gas to the inside wall of the glass tube, and finally through the wall to the electron beam. Satisfactory operation of the glow discharge as a positive lead to the solid electrolyte suggested using the glow discharge also on the outside wall of the glass tube to carry the current instead of the electron beam. Thus, in essence, a body would be electrolyzed without any palpable contact with metallic electrical connections.

The first experiment in which the glow discharge was used to make electrical contact to both sides of a glass wall was performed with simple equipment. A 96% silica glass[1] tube about 5 cm in diameter and 75 cm in length served as one electrode chamber. At one end of the tube was a connection to a vacuum pump and a graphite electrode which passed through a vacuum-tight seal. The other electrode chamber was simply a long glass test tube about 2.5 cm in diameter which extended into the larger tube through a vacuum-tight seal. This smaller tube likewise was provided with a graphite electrode and a vacuum connection. The central part of the apparatus was heated by a tube furnace to 400°-500°C. On placing a potential of about 1400V across the two graphite electrodes (both vessels being evacuated to between 0.1 and 1.0 Torr) a glow discharge occurred and a current of about 40 mA flowed. The path of the current was from one graphite electrode, through the rarified gas,

[1] Vycor, Registered TM, Corning Glass Works.

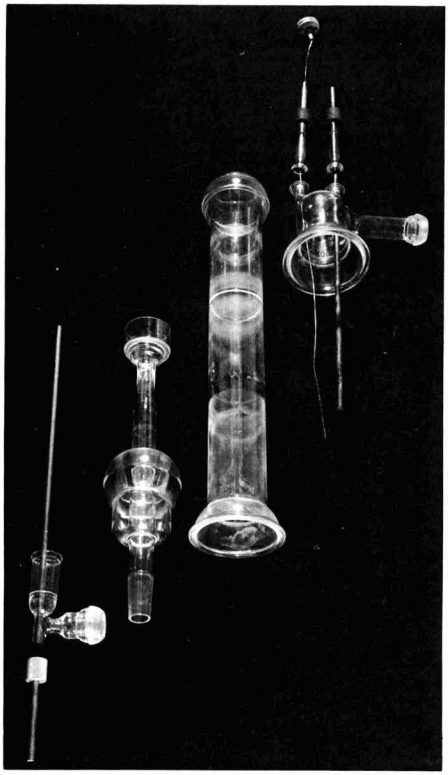

Fig. 2. Disassembled apparatus for glow discharge electrolysis

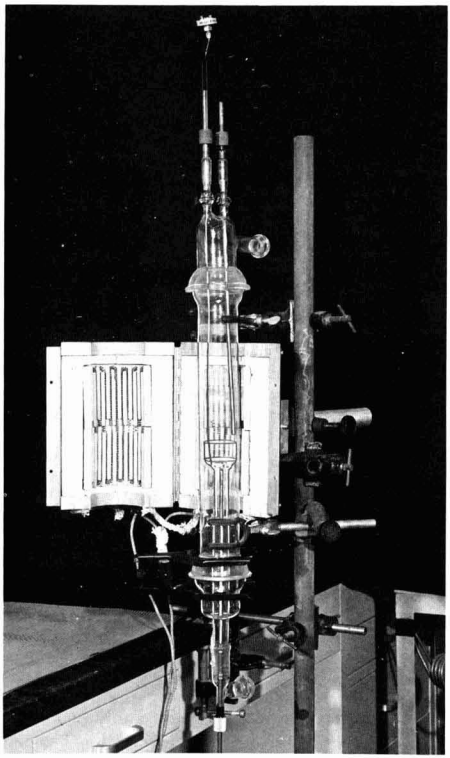

Fig. 3. Photograph of apparatus for glow discharge electrolysis

through the glass wall and through rarified gas on the other side to the other graphite electrode. The appearance of the glass after electrolysis was similar to that of the tube electrolyzed by the hybrid glow discharge-electron beam procedure described in the preceding paragraph.

The next step in the development of the apparatus was to provide for the electrolysis of solid materials in the form of a slab or disk because, as already mentioned, we had difficulty in obtaining materials in the form of a thin-walled tube (1-3 mm thick). The apparatus which was designed is shown disassembled in Fig. 2 and assembled in Fig. 3. It was essentially a modification of the electron beam apparatus with the filament and the positive lead replaced by a graphite rod.

The main envelope was again a silica glass tube about 6 cm in diameter with spherical joints at each end. The glass fixture which was attached to the upper end of the envelope carried a side tube for attachment to an ordinary vacuum pump (a high vacuum was not necessary) and two tubulations which were provided with vacuum-tight seals. One tubulation carried a graphite rod (6 mm in diameter) which served as an electrode and the other carried a sheathed thermocouple, about 1.5 mm in diameter. The glass fixture attached to the lower end of the envelope also was provided with a side tube for connection to a vacuum pump and a vacuum-tight seal for a graphite electrode.

The part of the apparatus which needs further elaboration is the funnel shaped part which projected upward to about the middle of the main chamber. It is shown schematically in Fig. 4. It was made of fused silica, and it was integral with the lower fixture, just described. It may be noted that, by closing the mouth of the funnel with a disk, the apparatus became divided into two chambers, the large outer

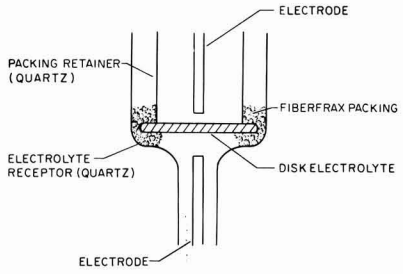

Fig. 4. Diagram of funnel shaped holder of electrolyte in glow discharge electrolysis.

chamber and the smaller chamber consisting of the fused silica funnel.

As with electron beam electrolysis, one of the most significant problems was to prevent short circuiting by flow of current between the edges of the disk and the mouth of the funnel. The key to the solution of the problem was the observation that the glow discharge would not penetrate through a tortuous path, even though it was porous enough for gas to flow through. For example, powdered magnesium oxide (which is a good insulator even at elevated temperatures) packed in a tube so as to make a compact about 1 cm thick prevented the glow discharge. A fibrous mineral material[2] was also satisfactory and easier to use. To prevent leakage around the disk of solid electrolyte, which was inserted into the mouth of the funnel, the fibrous mineral was packed underneath the outer perimeter of the disk and around its sides so as to fill the space between the disk and the funnel wall. To still further increase the length of the tortuous path, a fused silica cylinder was placed on the sur-

[2] Fiberfrax, Registered TM, Carborundum Company.

face of the disk and fibrous mineral packed around it, as shown in the diagram, Fig. 4. This arrangement prevented current from leaking, even up to an applied potential of 6000V.

The packing was useful also for preventing electrical leakage between the electrodes via the tubing connected to the vacuum pump. The vacuum connections at the top and bottom of the apparatus were connected to a T-joint which led to the vacuum pump. In some instances the discharge took the path of going from one side tube, through the rubber tubing and the T-connection to the other side tube, thus, effectively short-circuiting the flow of current through the disk. This short-circuiting was prevented by packing fibrous material lightly in the tubing between the T-joint and the apparatus. The glow discharge was thereby discouraged from traversing this path.

In the first experiments the residual air sustained the glow discharge. Replacement of the residual air by argon (at low pressure) was found necessary in the electrolysis of silver chloride, because otherwise the silver formed was oxidized to silver oxide. In most experiments, therefore, argon was introduced through a tube which ended in the vicinity of the disk. The flow of gas was controlled simply by manipulating a screw clamp on the rubber tubing and observing the bubbling of the gas as it flowed through oil in a U-tube. Argon gave a glow discharge over a wider range of pressure than air, namely, between 0.05 and 8 Torr at a voltage between 1000 and 3000.

In comparison with electron beam electrolysis, the glow discharge experiments were much easier to perform because (*i*) a higher pressure was satisfactory (as much as 1.0 Torr could be used as compared to less than 10^{-4} Torr for the electron beam process), (*ii*) contamination from a filament was eliminated (in the electron beam procedure some tungsten evaporated from the filament); (*iii*) short circuiting between the cathode and anode chambers was minimized.

Usually an electrolysis current of about 25 mA was desired. This required from 1000 to 3000V. Heating of the specimen was necessary to obtain sufficient conductivity for passage of current, and the tube furnace used is shown in Fig. 3. It permitted a temperature of about 800°C to be obtained, but this temperature was inadequate for obtaining conductivity of some ceramics.

The source of voltage in the glow discharge experiments was a commercial instrument which delivered a maximum of 30 kV at 35 mA. During the glow discharge experiments, particularly those in which a gas flowed through the system, regulation of the pressure was necessary. This was accomplished by a commercial electronic instrument which had a thermocouple type of pressure gauge as a sensing device. The instrument automatically turned the vacuum pump on and off so as to keep the pressure between two prescribed limits, for example, between 0.1 and 0.2 Torr.

Results of experiments with solid electrolytes.— Silver chloride was the electrolyte which we used for exploring the variables of operation and the modifications of equipment. Silver chloride is easily melted, gives a sound ingot on solidification, and is plastic, so that it does not develop pores and cracks. In electrolysis, the side facing the negative lead became covered with silver. On long electrolysis (an hour or more) silver dendrites eventually grew through the disk and shorted out the flow of current through the silver chloride. Silver iodide electrolyzed similarly to silver chloride. In a quantitative experiment, we found that the silver chloride disk lost weight about equal to the amount of chlorine that should have been liberated on the basis of Faraday's law. No silver was observed on the anode side unless the experiment was run long enough for the dendrites formed on the cathode side to penetrate completely through the electrolyte. This further demonstrates that the process which occurred was truly an electrolysis between plasma electrodes and not a thermal decomposition. We believe this to be the first reported example of an electrolysis between two gas plasma electrodes.

The most interesting results were obtained with the electrolysis of glass. In an electrolysis performed (as described earlier) with a fused salt bath serving as the anode connection, the glass did not change its appearance, even though sodium was liberated.

In the electrolysis of glass with the glow discharge (or with the glow discharge on one side and the electron beam on the other, as in an earlier section) the side of the glass facing the cathode became dull and developed some blisters, while the side toward the anode developed an opaque white layer which readily flaked off, as shown in Fig. 5. The chemistry of the change was not elucidated, as the opaque material gave an x-ray pattern similar to that of the original glass and the content of silica in the materials seemed to be almost the same as that in the original glass. The dramatic change in the appearance of the glass on electrolysis warrants further investigation.

Thin disks of some titanates, such as barium titanate which were initially light yellow in color became brown or black on electrolysis, the discoloration occurring throughout the thickness of the disk. The disk also became electrically conductive. A similar phenomenon resulted on heating a disk of the titanate to 700°C in an atmosphere of hydrogen.

Several other materials in the form of disks sawed from a single crystal were electrolyzed and, although they changed in appearance, no clear evidence was obtained of the nature of the chemical change. It is thought that in some of these instances, the conductivity of the material was too low at the temperature of the experiment, and that the flow of current may have been through pores or cracks which developed as a result of thermal shock. A single crystal disk of sodium chloride became opaque on the side facing the cathode and a thin white film deposited on the surface of the containing vessel. The film gave an alkaline reaction and probably was derived from vaporized sodium. Similar results were obtained with a disk of potassium bromide. Calcium fluoride did not allow enough current to pass, even at 750°C, to permit an adequate amount of electrolysis for qualitative examination.

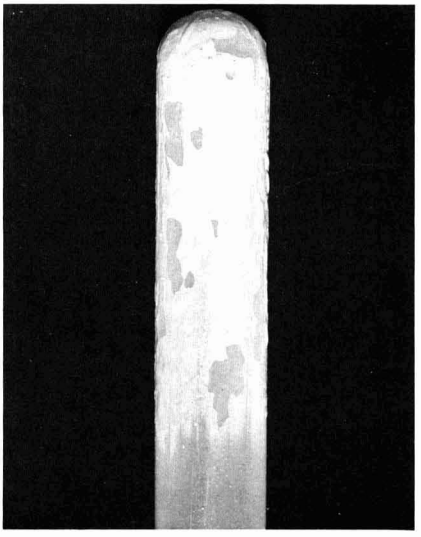

Fig. 5. Glass test tube electrolyzed by the glow discharge method.

Glow Discharge Electrolysis of Fused Salts

Background.—It was pointed out in the introduction and survey that the glow discharge electrolysis of aqueous solutions differed from conventional electrolysis with metal electrodes in that the products were not those usually obtained (metals were seldom reported as having been deposited) and the yields were several times greater than those expected on the basis of Faraday's law. This kind of electrolysis involves complexities in the vapor phase. By contrast the glow discharge electrolysis of fused salts is simpler, resembling conventional electrolysis in products formed and their yields. The fact that the current is conducted to the molten electrolyte by a gas at low pressure instead of metal conductors appears to make no difference in the results, except that reaction or alloying of the product with a metallic electrode can be avoided.

Of the various types of electrodeless electrolysis which have been described, the glow discharge electrolysis of fused salts was the process most easily performed and seems to be the one most likely to have any practicable use.

Apparatus.—The most obvious kind of apparatus to use for the glow discharge electrolysis of fused salts is a U-tube, such as shown in Fig. 6. The tube was made of glass or fused silica. The fused salt, B, was contained in the bend of the U-tube and was separated into two portions by the porous diaphragm, D. The U-tube was constructed with a considerably reduced diameter at the bend, which was occupied by the fused salt (diameter at the bend about 2 mm), so as to restrict the amount of melt electrolyzed to about 1 or 2 ml. This was necessary because the amount of metal formed in electrolysis was small (amounting to 10-50 mg in a typical experiment) and, consequently, was very difficult to recover from a large mass of fused salt. After each experiment, the U-tube was sawed through at the diaphragm in order to separate the cathode and anode compartment and make possible the working up of the salt for the products of electrolysis.

Most of the experiments in fused salt electrolysis were done with the simple apparatus shown in Fig. 7. Since in all of the experiments the main interest was in the metal deposit, the cathode chamber, A, was made small, and it was immersed in a larger amount of fused salt, B. The chamber A was introduced empty into the test tube C at the beginning of an experiment. On lowering the chamber into the melt, the latter entered through the porous disk D. The purpose of the disk was to filter the fused melt which was to be electrolyzed and to prevent loss of products which formed

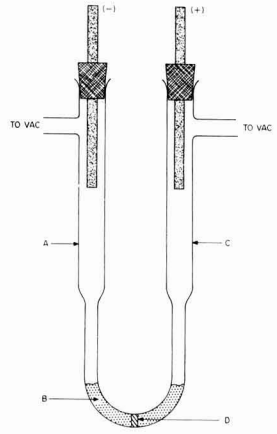

Fig. 6. U-tube for glow discharge electrolysis of fused salts

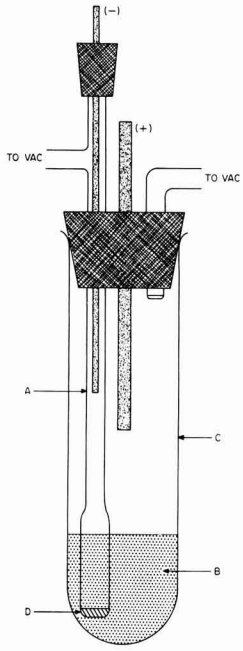

Fig. 7. Apparatus with a test tube envelope for the glow discharge electrolysis of fused salts.

in A during electrolysis. At the conclusion of the electrolysis, the chamber A was removed and the molten salt allowed to drain out. The chamber was then sawed through a short distance above the frit so as to expedite the collection of the product.

In all of the experiments the degree of vacuum was the same as that used for the glow discharge electrolysis of solid electrolytes. Care had to be taken in evacuating the vessel to prevent an inequality in pressure from forcing the melt completely from one chamber into the other.

In these experiments the phenomena in the anode chamber were not investigated and were not of concern, particularly since the diaphragm prevented any products from the anode compartment from entering the cathode compartment. Therefore, in most experiments a metallic anode was used is the anode chamber instead of a glow discharge. However, in at least one experiment, the electrolysis of molten silver chloride, the glow discharge was used in both chambers to demonstrate that solid electrodes were not essential.

Results of experiments with fused salts.—The glow discharge electrolysis of fused cupric chloride in potassium chloride yielded no deposit, probably because the electrolysis resulted only in a reduction of cupric ion to cuprous. The electrolysis of molten cuprous chloride at first also yielded no deposit. However, it was surmised that the presence of a small concentration of cupric ion was responsible for this failure. The molten cuprous chloride (in potassium chloride melt) was then treated with copper powder in the anode compartment prior to the electrolysis and then forced through the porous diaphragm in the cathode compartment. A yield of copper dendrites was obtained in the cathode compartment on electrolysis.

Silver chloride was electrolyzed in the U-tube without difficulty. After electrolysis, the solidified melt was obtained in the form of a rod after breaking away the glass tubing. On compressing the plastic chloride into a thin, transparent sheet, silver dendrites were readily visible, as shown in Fig. 8. The yield was roughly in accord with Faraday's law.

Tin dendrites were obtained from stannous chloride, cobalt dendrites from cobalt chloride, and nickel dendrites from nickel chloride. These products were separated from the solidified melts by dissolving the latter with water.

In the electrolysis of magnesium chloride, small, shining crystals collected in the tube above the level of the melt, thus indicating that the metal had been liberated at the surface of the melt as a vapor and had then subsequently condensed on the cooler portion of the apparatus.

Conclusion

This investigation of electrodeless electrolysis is only of an exploratory nature. The glow discharge electrolysis of ceramics and solid materials warrants further investigation. We suggest that the apparatus be designed to permit the ceramic electrolyte to be heated to much higher temperatures than we used, in order to promote a higher conductivity. If vessels could be constructed of a transparent, high melting material like yttrium oxide (mp 2410°C), the work would be greatly facilitated. Further work is in order to explain the curious change produced in glass on electrolysis.

The high voltages required for electron beam or glow discharge electrolysis militates against their use for any but a highly specialized application. The residual electrical conduction imparted to ceramics by the glow discharge electrolysis might be of some practicable use. The glow discharge electrolysis of fused salts might be of advantage in a situation in which the contamination of the deposit by a metallic cathode could not be permitted.

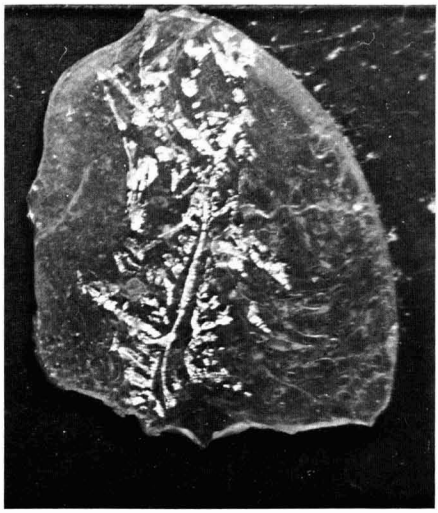

Fig. 8. Dendrites of silver in silver chloride which had been electrolyzed in the fused state.

The main interest in these exploratory experiments in electrodeless electrolysis, however, is in calling for a broader understanding of electrochemical phenomena by calling attention to the wide variety of situations in which chemical changes can be produced by the electric current.

To generalize as to the common denominator underlying all these curious examples of electrolysis, it seems that the presence of a metallic conductor is not it. Rather it seems that the essential factors are (assuming the presence of at least one ionic conductor) that the two materials in contact be different phases (gas, liquid, solid) and /or differ greatly in electrical conductivity.

Acknowledgment

The authors wish to express appreciation for the financial support of this research by the National Aeronautics and Space Administration under Contract No. R-09-022-052.

Manuscript submitted Aug. 1, 1969; revised manuscript received Jan. 8, 1970. This was Paper 153 presented at the Detroit Meeting of the Society, Oct. 5-9, 1969.

Any discussion of this paper will appear in a Discussion Section to be published in the December 1970 JOURNAL.

REFERENCES

1. Grotthuss, *Ann. Physik* (Gilbert), **61,** 65 (1819).
2. F. Braun, *ibid.*, **278,** 450 (1891); *ibid.*, **280,** 471 (1891); *ibid.*, **280,** 501 (1891).
3. K. Söllner, *Z. Elektrochem.*, **35,** 789 (1929).
4. J. Gubkin, *Ann. Physik*, **268,** 114 (1887).
5a. O. M. Corbino, *Atti Accad. Lincei*, **5** [6], 377 (1927).
5b. A. Klemenc, *Chimia*, **6,** 177 (1952).
5c. A. Klemenc and W. Kohl, *Monatsh. Chem.*, **84,** 498 (1953).
5d. M. Haissinsky and A. Coche, *J. Chim. Phys.*, **51,** 581 (1954).
5e. A. Banege-Nia, *Compt. rend.*, **245,** 1421 (1957).
5f. A. R. Denaro and A. Hickling, *This Journal*, **105,** 265 (1958).
5g. A. Hickling and M. D. Ingram, *Trans. Faraday Soc.*, **60,** 783 (1964).
5h. K. O. Hough and A. R. Denaro, *J. Sci. Instr.*, **43** [7], 488 (1966).
5i. A. R. Denaro and P. A. Owens, *Electrochim. Acta*, **13,** [2], 157 (1968).
6a. D. E. Couch and A. Brenner, *This Journal*, **106,** 628 (1959).
6b. B. S. R. Sastry, *J. Electroanal. Chem.*, **10** [3], 248 (1965).
7a. R. C. Burt, *J. Opt. Soc. Am.*, **11,** 87 (1925).
7b. R. C. Burt, U.S. Pat. 1,776,993, Sept. 30, 1930.
7c. P. Selenyi, *Ann. Phys.*, **84,** 111 (1927); **85,** 643 (1928).
8. L. Milicka, *Z. Physik. Chem.*, **210,** 23 (1959).
9. S. R. Palit, *J. Indian Chem. Soc.*, **45** [3], 286 (1968).
10. B. I. Markin, *J. Gen. Chem. USSR* (English Trans. of Consultants Bureau) **22,** 1137 (1952).

Current Distribution During the Electrodeposition of Gold

H. Y. Cheh

Bell Telephone Laboratories, Incorporated, Murray Hill, New Jersey

ABSTRACT

The phenomenon of macro- and microcurrent distribution in plating systems is studied. At high current densities where mass transport of the reacting species is rate controlling, the plating process will yield relatively uniform macro- but nonuniform microcurrent distribution. At low current densities where depletion of the reacting species is negligible, relatively uniform micro- but nonuniform macrocurrent distribution will be observed. The effect of surface roughness and current density on the microcurrent distribution of gold plated from a citrate bath is studied experimentally. The microcurrent distribution is found to improve considerably by reducing the surface roughness and by performing the deposition process at a lower current density. Due to the low gold content of most gold baths, practical gold plating is performed under conditions where mass transport limitations of the reacting species are significant.

The electrodeposition of gold is becoming increasingly important due to its wide applications in electronics equipment. The purpose in plating a thin layer of gold over certain parts of a substrate surface is to protect the parts from corrosion, reduce the electrical contact resistance, or provide a conducting path between devices. More uniform deposition both on a macro- and microscale and deposits with lower porosity and better mechanical properties are the goals pursued by the modern plating industry.

In this paper, the current distribution of a gold plating system is considered. The theoretical aspects of macro- and microcurrent distributions concerning systems involving only one electrochemical reaction are first examined. The conclusions from these considerations can be applied to many practical plating systems. Experimental observations on the microcurrent distribution of gold plated from a citrate gold bath are then reported.

Phenomenological Description of Macro- and Microcurrent Distribution

A typical linear dimension for a microprofile on a surface is in the order of 50μ whereas the linear dimension for a macroprofile is about 1000μ or larger. Transition between micro- and macrodimensions occurs between these limits. These definitions are somewhat arbitrary. The dimension of micro- *vs.* macroprofiles suggested here falls in the range used by most electroplaters. A rigorous definition can be established from the concept of the diffusion layer thickness. This will be treated in a later section.

Many investigators have found that a fundamental difference of current distribution occurs on macro- and microprofiles. For instance, Meyer (1) and Gardam (2) found that, in acid copper bath, uniform plating into the pores of the basis metal occurred although the macrocurrent distribution was poor. In a cyanide copper bath, the filling of microgrooves was poor whereas the macrocurrent distribution was relatively uniform. Reinhard (3), Foulke and Kardos (4), and Kardos (5) all found that the microcurrent distribution for all baths became less uniform with increasing current density. It is well known to electroplaters that (6), as a common rule, in the absence of a leveling agent, a bath having relatively uniform macrocurrent distribution generally has nonuniform microcurrent distribution and *vice versa*.

Fundamental Transport Processes in Plating Systems

A general theory of current distribution on electrodes is based on a consideration of the phenomenological theory of transport processes in electrochemical systems. The fundamental transport equations in dilute solutions have been discussed in detail by Levich (7) and more recently by Newman (8). Application of these equations has followed two main courses. At low current densities where change of concentration near the electrode-solution interface can be neglected, the transport equations reduce to the Laplace equation (9)

$$\nabla^2\phi = 0 \qquad [1]$$

and the current density is given by

$$\vec{i} = -\kappa\nabla\phi \qquad [2]$$

where ϕ is the potential in the solution, $\vec{i}$ is the current density vector, and κ is the electrical conductivity of the solution. An extensive review of the solution of the Laplace equation for electrochemical systems has been completed by Fleck (10). At high current densities and when electrical migration is neglected, the mass transport of the reacting species becomes rate controlling and the transport equations reduce to the convective diffusion equation (9)

$$\frac{\partial c_i}{\partial t} + \vec{v}\cdot\nabla c_i = \nabla\cdot(D_i\nabla c_i) \qquad [3]$$

and

$$\vec{i} = -z_i\mathbf{F}D_i\nabla c_i \qquad [4]$$

where c_i, D_i, z_i are the concentration, differential diffusion coefficient, and valency of species i, $\vec{v}$ is the fluid velocity, and $\mathbf{F}$ is the Faraday constant. Methods of solving the convective diffusion equation have been treated in detail by Levich (7).

These two limiting cases play an important role in electroplating. The application to the phenomenon of macro- and microcurrent distribution is given below.

Application to the Phenomenon of Macro- and Microcurrent Distribution

An important parameter used in systems where mass transport is slow is the Nernst diffusion layer thickness δ_N. For a single electrode reaction, it is defined by

$$i = -z_i\mathbf{F}D_i\left(\frac{\partial c_i}{\partial y}\right)_{\text{at electrode}} \equiv z_i\mathbf{F}D_i\frac{c_{iB} - c_{iI}}{\delta_N} \qquad [5]$$

where y is a distance coordinate normal to the electrode surface, c_{iB} and c_{iI} are the concentration of the reacting species i in the bulk and at the interface, respectively. δ_N is a function of Reynolds number and Schmidt number in forced convection systems and a

Key words: electrodeposition, current distribution, gold.

function of Grashof number and Schmidt number in free convection systems (11). Typical values of δ_N in gently stirred solutions range from 50 to 100μ (12). δ_N can be used conveniently to establish an operational definition of macro- and microprofiles (4, 5, 14). When the linear dimension of a surface profile is in the same range or slightly smaller than δ_N, the profile is considered to be microscopic. When the linear dimension is at least one order of magnitude larger than δ_N, the profile becomes macroscopic. Since δ_N depends on both the flow condition and physical properties of the system, the dimension of macro- and microprofiles varies accordingly. The local variation of δ_N determines the characteristics of local mass transport. For instance, a faster transport results from a thinner diffusion layer. Consequently, from the standpoint of mass transport, microprofiles are "rough" whereas macroprofiles are "smooth." On the other hand, when mass transport of the reacting species is not rate controlling, ohmic drop in the solution and electrode overpotential at the interface are the important parameters to consider. Let us now examine the two cases.

Ohmic drop and electrode overpotential controlling.—This is the case where low current density is applied. The concentration gradient of the reacting species at the interface is negligible. On a macroprofile, the effect of ohmic drop in the solution is predominant in determining the current distribution. Primary current distribution results when electrode overpotential is negligible. The current distribution depends only on geometrical factors concerning the electrochemical cell and electrode arrangements. On a microprofile, the effect of ohmic drop in the solution is outweighed by the electrode overpotential at the interface. The microcurrent distribution is governed by the secondary current distribution. A linear electrode overpotential-current density relation exists when the electrode overpotential is small

$$i = \frac{i_o n \mathbf{F}}{RT} \eta \qquad [6]$$

where i_o is the exchange current density for the reaction, n is the number of electrons transferred for the reaction, η is the electrode overpotential, R is the gas constant, and T is the absolute temperature. The current distribution depends on the same geometrical factors as to the primary current distribution and, in addition, to the dimensionless parameter (9, 13) $(L/\kappa)(di/d\eta)$ where L is a characteristic length of the microprofile. For large cathodic overpotentials, the electrode overpotential-current density relation is given by the Tafel equation

$$\eta = -\frac{RT}{(1-\alpha)n\mathbf{F}} [\ln(-i) - \ln i_o] \qquad [7]$$

where α is the transfer coefficient. The current distribution now depends on the parameter (9, 13) $|i_{avg}|(1-\alpha)n\mathbf{F}L/RT\kappa$, where i_{avg} is the average current density. It has been confirmed in numerous cases (14, 15) that, at low current densities, the secondary current distribution on a microprofile is uniform due to the high overpotential of the deposition reactions and the high conductivity of most plating baths. This is the reason for the statement (6) "a bath of poor macrocurrent distribution has good microcurrent distribution."

Mass transport controlling.—At high current densities when mass transport of the reacting species becomes rate controlling, the Nernst diffusion layer thickness is the most important parameter to consider. A relatively uniform distribution of current is seen on the macroprofile due to the uniform thickness of the Nernst diffusion layer over the profile whereas the local variation of the diffusion layer thickness over the microprofile is responsible for the poor microcurrent distribution. Of course, current distribution can be highly nonuniform at electrode edges. For instance, the theoretical current density is infinite at the leading edge of a flat plate in the direction of electrolyte flow (16). Therefore, the above statement is only valid at regions where both the momentum and the diffusion boundary layers are fully developed.

For most plating baths, the metal ion concentration is so high that the two limiting cases can readily be distinguished and consequently lead to the interesting observation of macro- and microcurrent distribution. However, the gold content in a gold plating bath is usually so low (approximately 10-20 g/l) that under most operating conditions, the process is influenced by both electrode potential, ohmic drop and mass transport. To study the applicability of the above theoretical considerations, experimental investigation on the microcurrent distribution of a gold plating system was carried out.

Experimental

Electrolyte.—The Ehrhardt acid citrate bath (17) which contained 21.3 g/l potassium gold cyanide and 50 g/l ammonium citrate (dibasic) was chosen for these experiments. At 60°C, the pH of the bath was 5 and the conductivity of the bath was 0.063 ohm^{-1} cm^{-1} measured by a conductivity bridge which supplied 1000 Hz bridge current.

Electrodes.—Two types of cathodes were used to study the effect of the dimension and geometry of surface inhomogeneities. Electroformed nickel with a wavy surface of amplitude approximately 25μ and polished planar OFHC copper plates were chosen to study the microcurrent distribution. The surface area for both electrodes was 1 cm^2. Three identical V-shaped grooves, 2.5 mm apart, were cut into the copper plates. The angles of the grooves were 30°, 60°, and 90°, and the groove depths were approximately 50, 125, and 250μ. The anode was a platinum coil.

Experimental procedures.—Prior to plating, both the nickel and the copper electrodes were cleaned and degreased using acetone and trichloroethylene, respectively. The copper electrodes were then bright-dipped for approximately 10 sec in a solution containing 250 ml H_2SO_4, 125 ml HNO_3, 4 ml HCl, and 250 ml water. Both electrodes were then rinsed with distilled water. The plating cell was cylindrical in shape with a volume of 200 ml. For each plating, 150 ml of the citrate gold solution was used. Oxygen-free nitrogen was bubbled through the solution for 30 min prior to electrolysis, and a nitrogen atmosphere was maintained above the solution during electrolysis. No stirring was applied. The plating was performed at 60°C. The applied cathodic current density was 2, 4, and 6 mA/cm^2. The limiting current density for gold deposition in this experiment was found to be 6.3 mA/cm^2. The Tafel slope for the system was measured under galvanostatic condition using a rotating disk electrode at a constant rotational speed of 1730 rpm. The value was found to be 130 mV at 60°C. Depending on the depths of these grooves and the current density used, the duration of electrolysis was varied between 1 to 6 hr for optimum observation. To protect the gold surface for sectioning, approximately 12μ of Watts nickel was plated over the gold coating.

These electrodes were then mounted in epoxy, sectioned, polished, and etched in an equivolume mixture of acetic acid, nitric acid, and phosphoric acid. The microcurrent distribution of the citrate gold was determined by microscopic examination.

Results

Typical results from photomicrographs are shown in Fig. 1 to Fig. 5. They can be summarized as follows:

1. The microcurrent distribution is relatively uniform on the electroformed nickel electrode.

2. On the copper electrode, the microcurrent distribution becomes less uniform at increasing cathodic current densities and sharpening V-angles.

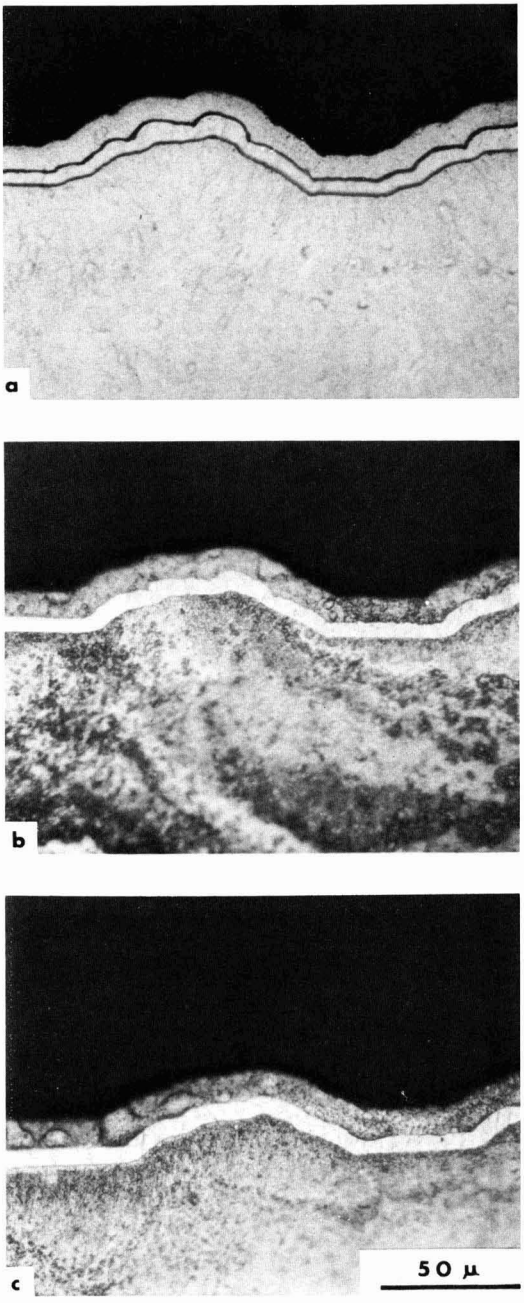

Fig. 1. Photomicrographs of gold deposits on nickel substrates with wavy surfaces: (a) 2 mA/cm^2; (b) 4 mA/cm^2; (c) 6 mA/cm^2.

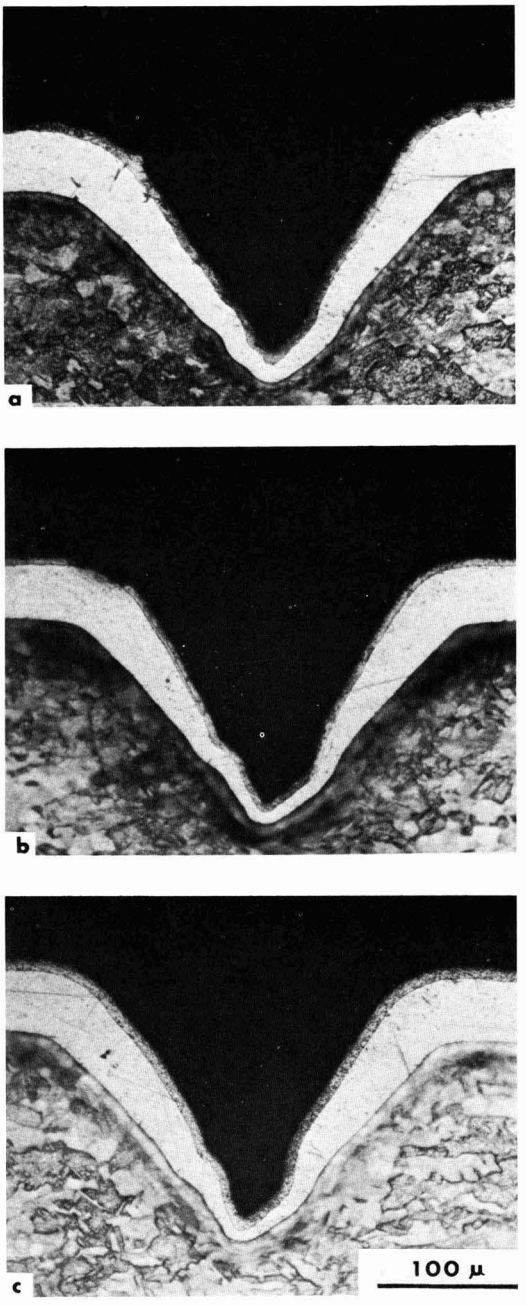

Fig. 2. Photomicrographs of gold deposits on copper substrates with triangular grooves: (a) 2 mA/cm^2; (b) 4 mA/cm^2; (c) 6 mA/cm^2.

3. On the copper electrode, the microcurrent distribution becomes less uniform at increasing groove depth.

Quantitative information on the microcurrent distribution of citrate gold plating are plotted in Fig. 6 to Fig. 8. The current distribution is represented by a gold plating thickness ratio h_1/h_2 where h_1 is the average deposit thickness on a planar surface and h_2 is the thickness at the bottom of a triangular groove. Geometrical factors used in these figures are the groove depth d and groove angle θ, and the operating variable chosen here is the current density.

Discussion

It has been concluded that the secondary current distribution depends heavily on the dimensions and geometry of the surface profile that is being plated. It is, therefore, not surprising to find that, on electro-

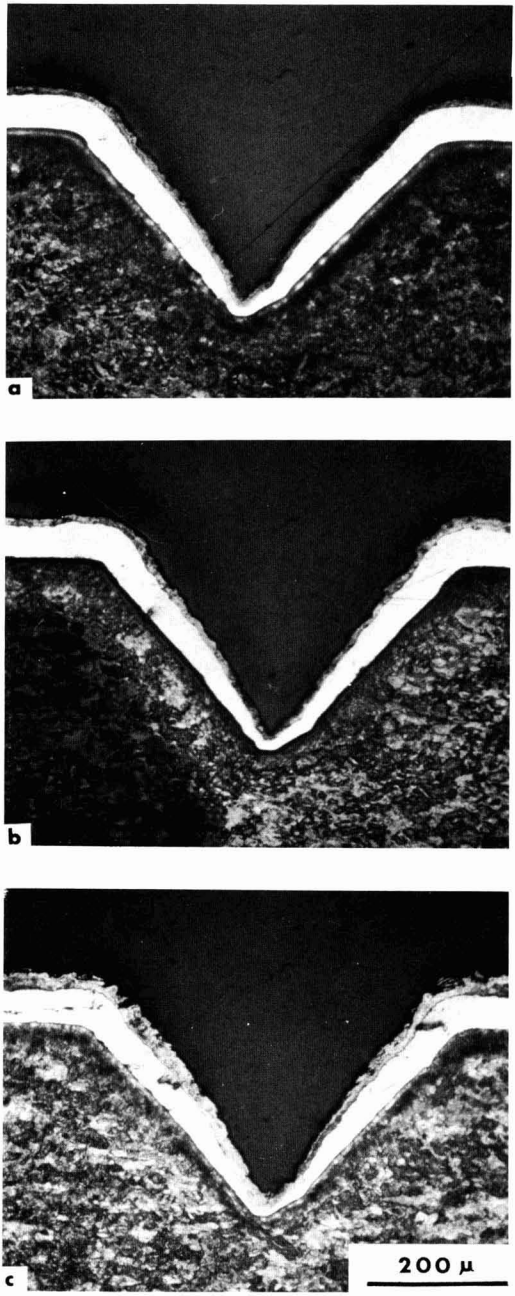

Fig. 3. Photomicrographs of gold deposits on copper substrates with triangular grooves: (a) 2 mA/cm^2; (b) 4 mA/cm^2; (c) 6 mA/cm^2.

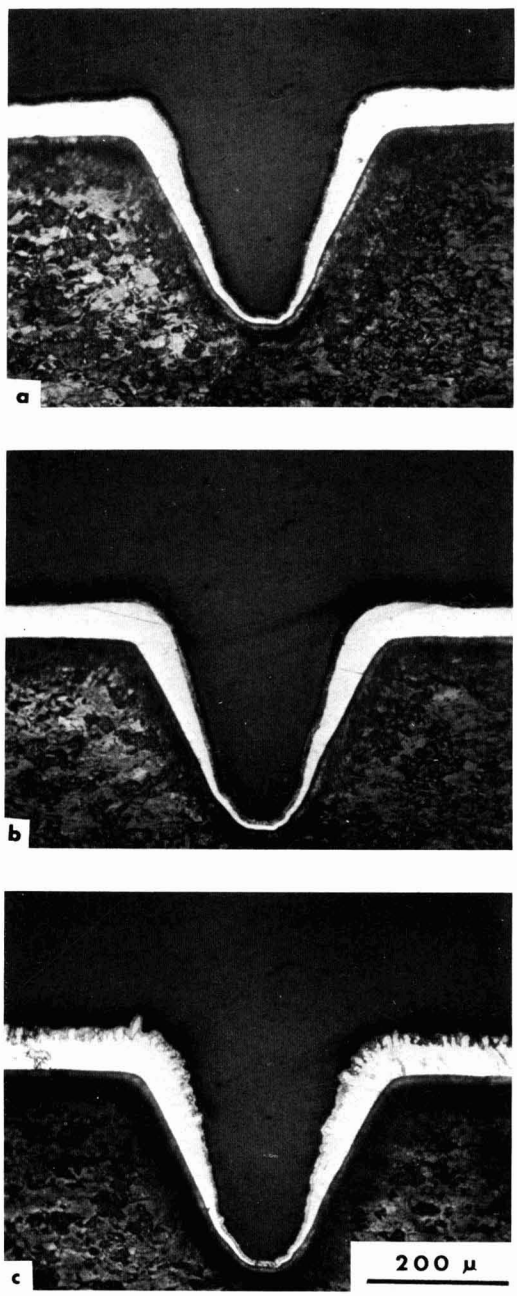

Fig. 4. Photomicrographs of gold deposits on copper substrates with triangular grooves: (a) 2 mA/cm^2; (b) 4 mA/cm^2; (c) 6 mA/cm^2.

formed nickel surface which is relatively smooth, the microcurrent distribution is rather uniform.

At increasing cathodic current densities, the process becomes increasingly mass transport limited and consequently, the microcurrent distribution becomes less uniform. At the limiting current density, gassing is observed at the electrode. The deposit becomes incoherent and frequently rough or powdery.

Wagner (18) has calculated theoretically the secondary current distribution on a triangular wave surface when the counterelectrode is far removed from the working electrode. The geometrical parameter is shown to be 1/2 (cos $\theta/2$/sin $\theta/2$) where θ is the angle between the two adjacent sides of the triangle. For linear polarization,

$$\frac{i_p - i_r}{i_{avg}} = \frac{L}{\kappa}\frac{di}{d\eta}\frac{1}{2}\frac{\cos\theta/2}{\sin\theta/2} \qquad [8]$$

whereas for Tafel polarization

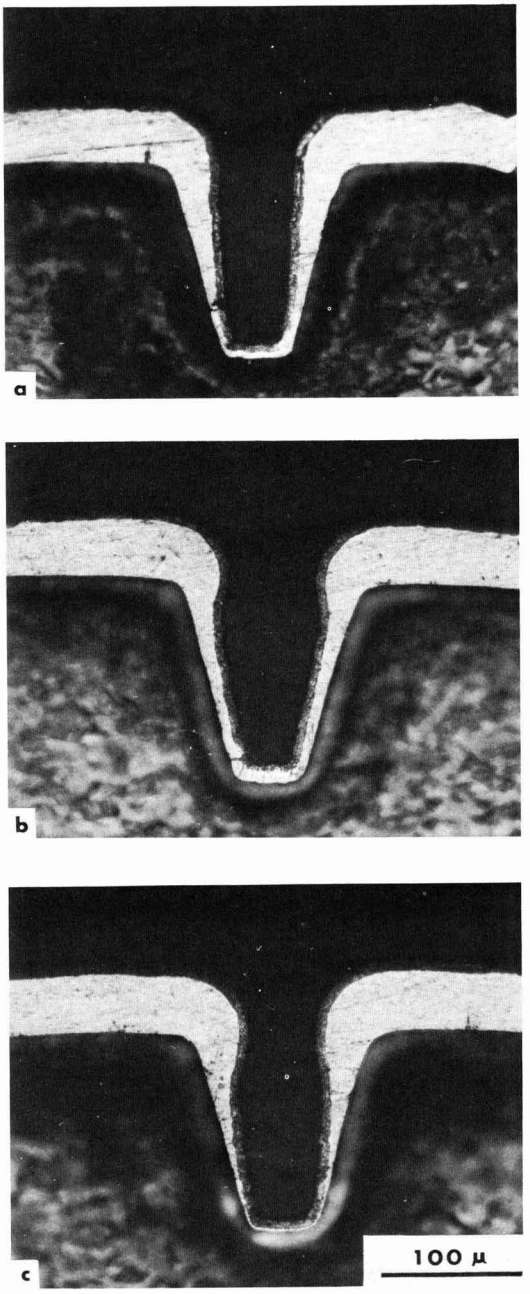

Fig. 5. Photomicrographs of gold deposits on copper substrates with triangular grooves: (a) 2 mA/cm^2; (b) 4 mA/cm^2; (c) 6 mA/cm^2.

$$\ln \frac{i_p}{i_r} = \frac{|i_{avg}| L(1-\alpha) n\mathbf{F}}{\kappa RT} \frac{1}{2} \frac{\cos \theta/2}{\sin \theta/2} \qquad [9]$$

where i_p is the current density at the peak, i_r is the current density at the recess, and L is the distance between two adjacent peaks. Varying θ from 90° to 30°, the geometrical parameter increases by approximately a factor of ten. Therefore, the microcurrent distribution is very sensitive to the value of this angle. This conclusion is also amply demonstrated in the present investigation as shown in Fig. 6-8.

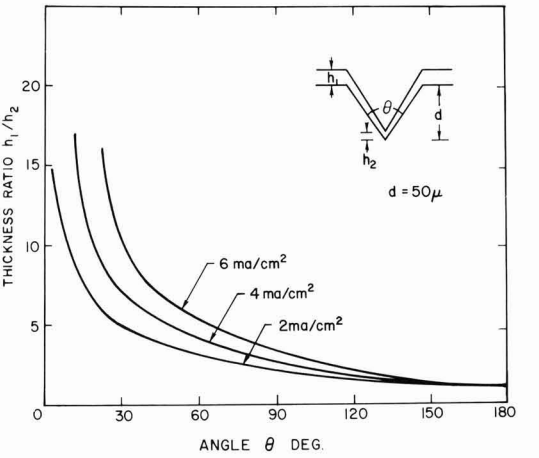

Fig. 6. Microcurrent distribution of gold deposits on copper substrates.

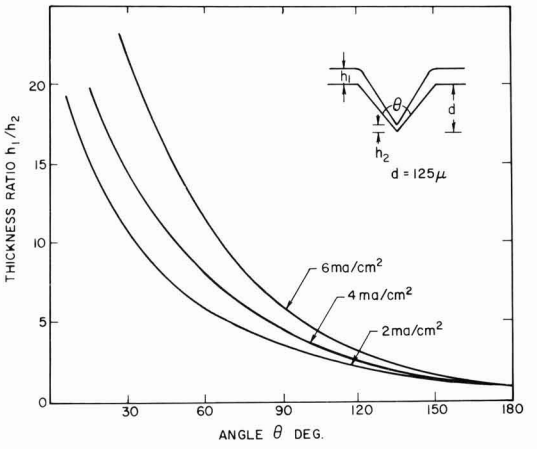

Fig. 7. Microcurrent distribution of gold deposits on copper substrates.

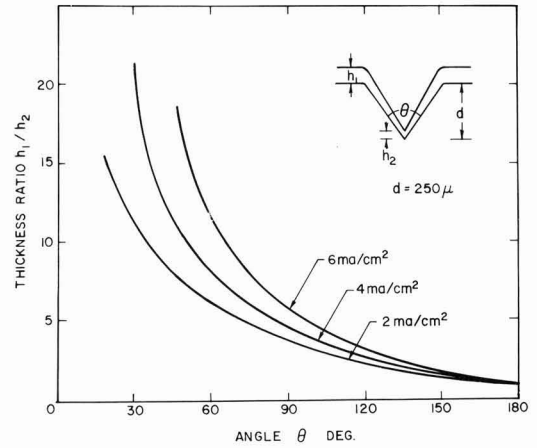

Fig. 8. Microcurrent distribution of gold deposits on copper substrates.

Considering the effect of groove depth from these figures, a significant increase in the thickness ratio is seen when groove depth is increased from 50 to 125μ but less change is found from 125 to 250μ. This can be explained by a consideration of the mass transfer aspect. Using the limiting current density of 6.3 mA/cm^2 and assuming the diffusion coefficient of gold ion as 9×10^{-6} cm^2/sec, δ_N is calculated from Eq. [5] to be 100μ. The difference between the diffusion path is, therefore, greater when d is changed from 50 to 125μ than from 125 to 250μ. Ignoring the effect of electrical migration, the interfacial concentration of gold ion is 10 g/l at a cathodic current density of 2 mA/cm^2 and 5.7 g/l at 4 mA/cm^2. Comparing these values to the bulk concentration of gold (15 g/l), it is seen that even at 2 mA/cm^2, the effect of mass transport is appreciable. It is therefore concluded that for most gold baths, due to the low gold content, the plating process is performed under conditions where mass transport limitations cannot be ignored.

Conclusions

Theoretical aspects of macro- and microcurrent distribution are presented. Two operating regimes for plating systems are established. At low current densities where concentration gradients near the electrode-solution interface can be neglected, a plating bath with no leveling agents will have relatively uniform microcurrent distribution but nonuniform macrocurrent distribution. At high current densities where mass transport of the reacting species is rate controlling, the plating bath will have nonuniform microcurrent distribution but relatively uniform macrocurrent distribution.

Quantitative information on the microcurrent distribution of a citrate gold plating system have been obtained. Effect of surface roughness as well as operating conditions such as metal concentration and current density on the current distribution has been established. It is also confirmed that most gold plating systems are operated under conditions where the effect of mass transport of the reacting species cannot be neglected.

In order to improve the microcurrent distribution, reduction of surface roughness and application of low current densities are both essential. An alternative approach will be either to search for suitable leveling agents or to raise the gold content of the bath thereby reducing the mass transfer controlling effect on microcurrent distribution.

Acknowledgment

The author wishes to thank D. R. Turner for his interest and encouragement during the course of this work.

Manuscript submitted Aug. 20, 1969; revised manuscript received Dec. 18, 1969.

Any discussion of this paper will appear in the Discussion Section to be published in the December 1970 JOURNAL.

List of Symbols

c_i,	Concentration of species i, moles/cm^3
c_{iB}, c_{iI},	Concentration of species i in the bulk and at the interface, respectively, moles/cm^3
D_i,	Differential diffusion coefficient of species i, cm^2/sec
d,	Depth of a triangular grove, cm
$\mathbf{F}$,	Faraday's constant, coulomb/equiv
h_1, h_2,	Deposit thickness on a planar surface and at the recess of a triangular groove, respectively, cm
$\vec{i}$, i,	Current density vector and measured current density, A/cm^2
i_{avg}, i_p, i_r,	Average current density, current density at the peak and current density at the recess of a triangular wave surface, A/cm^2
i_o,	Exchange current density, A/cm^2
L,	A characteristic length, cm
L,	Wave length of a triangular wave, cm
n,	Number of electrons transferred in a reaction
R,	Gas constant, joule/mole °K
T,	Temperature, °K
$\vec{v}$,	Fluid velocity, cm/sec
y,	Distance normal from electrode, cm
z_i,	Valency of species i
α,	Transfer coefficient in polarization equation
δ_N,	Nernst diffusion layer thickness, cm
η,	Electrode overpotential, V
κ,	Conductivity, mho/cm
ϕ,	Electrostatic potential, V

REFERENCES

1. W. R. Meyer, *Proc. Am. Electroplaters' Soc.*, **23**, 116 (1935).
2. G. E. Gardam, *J. Electrodepositors' Tech. Soc.*, **22**, 155 (1947).
3. C. E. Reinhard, *Proc. Am. Electroplaters' Soc.*, **37**, 171 (1950).
4. D. G. Foulke and O. Kardos, *ibid.*, **43**, 172 (1956).
5. O. Kardos, *ibid.*, **43**, 18 (1956).
6. E. Raub and K. Müller, "Fundamentals of Metal Deposition," Elsevier, Amsterdam, (1967).
7. V. G. Levich, "Physicochemical Hydrodynamics," Prentice Hall, Englewood Cliffs, N. J. (1962).
8. J. Newman, "Transport Process in Electrolytic Solutions," C. W. Tobias, Editor, Advances in Electrochem. and Electrochem. Eng., **5**, 87 (1967).
9. J. Newman, *Ind. Eng. Chem.*, **60** [4], 12 (1968).
10. R. N. Fleck, "Numerical Evaluation of Current Distribution in Electrochemical Systems," M. S. Thesis, University of California, Berkeley, 1964.
11. N. Ibl, *Electrochim. Acta*, **1**, 117 (1959).
12. N. Ibl, *Chem.-Ing.—Tech.*, **35**, 353 (1963).
13. T. P. Hoar and J. N. Agar, *Discussions Faraday Soc.*, **1**, 162 (1947).
14. O. Kardos and D. G. Foulke, "Applications of Mass Transfer Theory: Electrodeposition on Small Scale Profiles," C. W. Tobias, Editor, Advances in Electrochem. and Electrochem. Eng., **2**, 145 (1962).
15. N. Ibl, "Diffusion Layers; Influence on Mass Transport on the Structure of Electrolytic Deposits," Protection Against Corrosion by Metal Finishing, Zürich, Forster Verlag A. G., p. 48 (1966).
16. C. W. Tobias and R. G. Hickman, *Z. Physik. Chem.* (Leipzig), **229**, 145 (1965).
17. R. A. Ehrhardt, *Proc. Am. Electroplaters' Soc.*, **47**, 78 (1960).
18. C. Wagner, *This Journal*, **98**, 116 (1951).

Electroless Deposition of Certain Metal Oxides

I. Alpha-PbO_2

W. Mindt*[1]

Bell Telephone Laboratories, Incorporated, Murray Hill, New Jersey

ABSTRACT

Electroless deposition of α-PbO_2 films by oxidation of lead(II) acetate with peroxydisulfate is described. Investigations into the mechanism of this reaction show it to be a mixed electrolytic process with the two partial reactions $Pb^{++} + 2H_2O \rightarrow \alpha\text{-}PbO_2 + 4H^+ + 2e^-$ and $S_2O_8^= + 2e^- \rightarrow 2SO_4^=$. The variation of mixed potential and growth rate with the *p*H of the electrolyte is studied and interpreted in terms of the *p*H dependence of both partial reactions. A mechanism of the reduction of $S_2O_8^=$ at PbO_2 is proposed.

The anodic oxidation of some metal ions in aqueous solutions leads under certain conditions to the deposition of an oxide at the anode, according to the electrode reaction

$$mMe^{z+} + nH_2O \rightarrow Me_mO_n + 2nH^+ + (2n - mz)e^- \quad [1]$$

(in acid solutions). Some well-known examples are the systems Pb^{++}/PbO_2, Mn^{++}/MnO_2, $Ni^{++}/$"NiO_2", Tl^+/Tl_2O_3 and Ag^+/AgO. If the oxidation of the metal ion is carried out as a controlled heterogeneous reaction by a suitable oxidizing agent instead of an external electrical current, the deposition of the metal oxide can be called "electroless" in analogy to the corresponding process known for metals.[2] In general, the conditions under which electroless deposition of metal oxides is possible are equivalent to those for metals: The oxidizing agent must have, of course, a higher redox potential than the equilibrium potential of reaction [1], and its reduction at the metal oxide must be kinetically possible. The reduced species should be soluble in the electrolyte and should not interfere with the anodic process, *e.g.*, due to adsorption at the metal oxide. Nucleation of the metal oxide in the solution should be prevented since this results in an uncontrolled precipitation. Finally, since oxidation and reduction steps occur at different locations, charge transport within the metal oxide must be possible, *i.e.*, the metal oxide has to be an electrical conductor.

In the present work some systems are investigated in which these conditions are fulfilled. In the first part, deposition of α-PbO_2 is described. Films of this oxide are of interest for use as counterelectrodes in solid valve metal oxide capacitors, since they have a considerably higher conductivity than MnO_2 films which are used so far, and capacitors with PbO_2 coatings show similar self-healing properties (2, 3).

The oxidizing agent used in our experiments is peroxydisulfate (persulfate). The studied over-all reaction is

$$Pb^{++} + 2H_2O + S_2O_8^= \rightarrow \alpha\text{-}PbO_2 + 4H^+ + 2SO_4^= \quad [2]$$

This reaction was described earlier by Rüetschi and Cahan (4). The authors obtained α-PbO_2 as precipitate from solution by a homogeneous reaction. Occasionally, the formation of PbO_2 films at the walls of the glass beakers in which the reaction was carried out was observed (5); however, this effect was not further studied. In the experiments described here, reaction [2] was carried out heterogeneously on PbO_2 substrates under conditions where no precipitation of PbO_2 in the solution occurred.

It is of some practical interest to be able to deposit adherent α-PbO_2 films on insulating substrates. In electroless metal deposition, this is usually accomplished by treating the substrate surface in such a way that it acts as catalyzer during the deposition of an initial metal layer. We did not investigate an equivalent procedure of surface activation. As an alternative method, an initial PbO_2 layer of a few hundred angstroms was precipitated from solution by catalyzing reaction [2] with Ag^+, as will be described in the experimental part. Further growth of PbO_2 was carried out by electroless deposition. α-PbO_2 films obtained in this way showed good adherence up to a thickness of 1μ on various substrates, such as glass, quartz, ceramics, or Ta_2O_5.

Experimental

All experiments were carried out in a supporting electrolyte of M $NH_4C_2H_3O_2$ which was prepared from 30% NH_4OH and glacial acetic acid (both Baker "electronic grade"). Lead acetate was added to this solution in the form of PbO (Fisher "certified") and an equivalent amount of acetic acid. In most experiments, a concentration of lead acetate of 50 mM was used. $S_2O_8^=$ was added from a freshly prepared aqueous solution of ammonium persulfate (Fisher "certified") which was brought to the *p*H of the studied solution by addition of NH_4OH.

The PbO_2 electrodes used for the current/potential measurements were prepared by anodic deposition of a *ca.* 0.5μ thick layer on a 0.25 cm^2 Pt electrode. The deposition was carried out immediately before each measurement in the same electrolyte, applying a current density of 0.5 mA/cm^2. Weight measurements of the deposited PbO_2 were carried out on electrodes of larger surface area to achieve a higher accuracy. For this purpose, 3 x 1 in. glass slides were used, on which an initial layer of 500Å PbO_2 was precipitated in the following way: Glass slides were exposed in a vertical position to a solution prepared by mixing 100 ml of 50 mM lead acetate dissolved in M $NH_4C_2H_3O_2$ with 100 ml of 2M $(NH_4)_2S_2O_8$, both brought to a *p*H of 6. To this solution, $AgNO_3$ was added as catalyst in a concentration of 5 x 10^{-5}M. After an induction time of about 15 min, the solution turned slowly brown, and after 45 to 90 min, a continuous film of 500Å PbO_2 was precipitated on the glass slides. After washing with distilled water and drying at room temperature, the slides were used for the weight and open-circuit potential measurements. Results of these measurements should be, of course, independent of the way in which the initial PbO_2 layer was obtained. This was confirmed by experiments carried out on 20 cm^2 Pt elec-

* Electrochemical Society Active Member.

[1] Present address: C/O F. Hoffmann-La Roche and Company, CH 4002 Basel, Postfach, Switzerland.

[2] Electroless deposition of a metal oxide is known so far only in the case of MnO_2. Films of this oxide are deposited by reduction of MnO_4^- (1). It is, however, doubtful if the term "electroless" can be applied to this process, since it is precipitation from solution rather than a controlled heterogeneous reaction.

trodes, on which PbO_2 was electrodeposited, as well as by using glass substrates on which PbO_2 was deposited by hydrolysis of lead tetraacetate as described by Robinson (2).

The potential/current measurements were carried out potentiostatically, using a 1*N* calomel reference electrode (NCE) and a Pt counterelectrode. Stationary conditions were achieved after a few minutes at low current densities (< 10 $\mu A/cm^2$) and after several seconds at higher current densities. The electrolyte was stirred. All experiments were carried out at 25°C.

Results

In Fig. 1, stationary current/potential curves are shown which demonstrate that the nature of the deposition is a mixed electrolytic process. Curve 1 was obtained in a solution of 50 mM lead acetate in M $NH_4C_2H_3O_2$ at *p*H 8.5. In this solution, where the lead ions are solubilized by complexing with acetate, the anodic reaction is

$$Pb^{++} + 2H_2O \rightarrow \alpha PbO_2 + 4H^+ + 2e^- \qquad [3]$$

with cathodic currents, PbO_2 is reduced to a lower oxide. Curve 2 was obtained after addition of 50 mM ammonium persulfate to the above solution. The net current results from the superposition of reaction [3] and the reduction of $S_2O_8^=$

$$S_2O_8^= + 2e^- \rightarrow 2SO_4^= \qquad [4]$$

By subtraction of curve 1 from curve 2, the partial current voltage curve of reaction [4] is obtained (curve 3). At open circuit, deposition of PbO_2 occurs at the mixed potential U_m with the partial current density i_d. Independent determinations of i_d by weight measurements of the deposited PbO_2 give the same result. This can be seen in Fig. 2 which shows i_d and U_m as a function of *p*H. The electrolyte was again 50 mM lead acetate and 50 mM ammonium persulfate in M ammonium acetate. The *p*H was varied between 5 and 10 by addition of $HC_2H_3O_2$ or NH_4OH, respectively. i_d was determined from the stationary anodic current at the potential U_m in the absence of $S_2O_8^=$ as described before as well as by weight measurements. The results of both methods were reproducible with deviations not larger than 10%. A current density of 1 mA/cm^2 corresponds to a deposition rate of 760 Å/min. The deposition current increases with *p*H, following the relationship

$$\log i_d = \text{const} + 0.81\,\text{pH} \qquad [5]$$

U_m was determined on PbO_2 films deposited on Pt and on glass substrates. With increasing *p*H, U_m shifts in negative direction by (59 ± 5) mV per *p*H unit.

The observed *p*H dependence of i_d and U_m results from influences of both anodic and cathodic reactions.

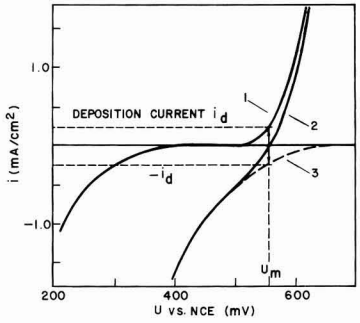

Fig. 1. Stationary current/potential curves at PbO_2 electrode. Curve 1, anodic partial reaction [3], measured in a solution of 50 mM lead acetate in 1M ammonium acetate at *p*H 8.5; curve 2, over-all reaction [3] + [4], measured after addition of 50 mM ammonium persulfate; curve 3, cathodic partial reaction [4], calculated by subtraction of curve 1 from curve 2.

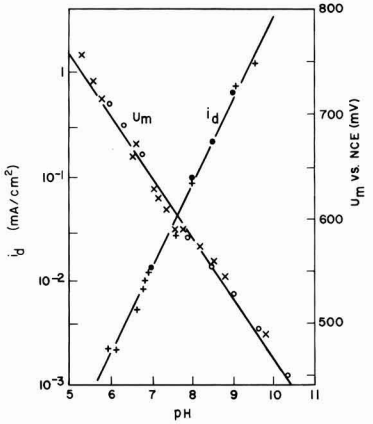

Fig. 2. Deposition current i_d and mixed potential U_m as function of *p*H. Electrolyte: 50 mM lead acetate + 50 mM ammonium persulfate in 1M ammonium acetate. ●, i_d from current at U_m in absence of $S_2O_8^=$; +, i_d from weight measurements; o, U_m at PbO_2 deposited on platinum; x, U_m at PbO_2 deposited on glass (1 mA/cm^2 corresponds to 760 Å/min).

This becomes evident from Fig. 3 in which the partial current/potential curves of the two reactions are plotted at different *p*H values. The anodic curves were determined in a solution of 50 mM lead acetate in M ammonium acetate. The *p*H was varied as before. The reduction of $S_2O_8^=$ could not be studied in a similar way in a solution containing $(NH_4)_2S_2O_8$ only. Under this condition, the PbO_2 electrode turned slowly into a passivated state, and the current measurements were irreproducible. It is assumed that this is the effect of adsorption of the reaction product, $SO_4^=$. Apparently, the PbO_2 surface which is freshly formed during the deposition shows a different behavior with regard to the kinetics of the $S_2O_8^=$ reduction. The partial current/potential curves of the $S_2O_8^=$ reduction near U_m were determined from the difference between the currents of the Pb^{++} oxidation and the over-all reaction [2] as described for Fig. 1. The intersections between anodic and cathodic curves at the same *p*H represent open-circuit conditions (zero net current), *i.e.*, give the values of i_d and U_m. The dotted line is obtained from the experimental data of i_d and U_m in Fig. 2. The log i/U curves of the Pb^{++} oxidation approach at higher current densities and low *p*H a Tafel slope of 118 mV which is expected for this reaction if the trans-

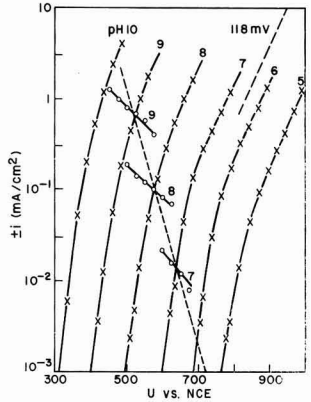

Fig. 3. Partial current/potential curves at various *p*H. x, anodic reaction [2]; o, cathodic reaction [4]; dotted line, i_d vs. U_m from data in Fig. 2.

fer coefficient α is 0.5. In the region studied here (dotted line), the slopes are generally smaller. The Tafel slopes of the reduction of $S_2O_8^=$ vary between 210 and 270 mV, corresponding to transfer coefficients between 0.28 and 0.22. The low transfer coefficient is typical for this reaction, *e.g.*, a value of $\alpha = 0.32$ was obtained by Müller (6) in alkaline solutions at Pt electrodes.

In Fig. 4, the partial cathodic current is plotted as a function of the $S_2O_8^=$ concentration at constant electrode potentials. This experiment was carried out again in a solution of 50 mM lead acetate in 1M $NH_4C_2H_3O_2$, to which $(NH_4)_2S_2O_8$ was added from a 2M aqueous solution. The *p*H was kept constant at 8.50. At low concentrations, the current is proportional to the square root of the persulfate concentration indicating a reaction order of 0.5 for the $S_2O_8^=$ ion. The deviation from linearity at higher concentrations is probably the effect of the presence of $SO_4^=$ ions which seem to inhibit the reaction. This assumption is supported by the fact that an addition of 0.1M $(NH_4)_2SO_4$ to the solution results in a decrease of the current to nearly zero.

Properties of the PbO_2 *films.*—The electron diffraction pattern of the PbO_2 films deposited on glass substrates showed only lines of the α-modification. There was no evidence for the presence of lower lead oxides. In some cases, the crystallites had a slight orientation with the (100)-plane parallel to the substrate as is observed also on electrodeposited α-PbO_2 (7). The crystallite size of a 5000Å thick film deposited at *p*H 8 is about 2000Å as determined by electron microscopy.

The electrical properties are, in general, similar to those of electrodeposited α-PbO_2 (8). Hall effect measurements showed that the carrier density is about 10^{21} cm^{-3} and is nearly independent of the *p*H at which the films were deposited. There is, however, an effect on the resistivity with increasing *p*H, *e.g.*, a 5000Å thick film deposited at *p*H 7 had a resistivity of 2×10^{-3} ohm cm, whereas at *p*H 10 a resistivity of 3×10^{-2} ohm cm was obtained.

Discussion

The result that the deposition occurs at the rate expected from the stationary current potential relations indicates that the deposition is a pure electrochemical process, *i.e.*, that no "chemical" deposition due to a reaction without charge exchange at the interface is involved. The deposition rate is controlled by the potential U_m which is a function of the composition of the electrolyte.

The variation of U_m with *p*H was found to be linear in the studied *p*H region with a slope of −59 mV/*p*H. An interpretation of this result is difficult since it arises from a complex *p*H dependence of the current potential relations of both partial reactions, as was seen in Fig. 3. In the following, the origins of the *p*H dependence of the two reactions are discussed.

The drift of the anodic current potential curves with *p*H is mainly the effect of the variation of the equilibrium potential of the anodic reaction. The equilibrium potential of reaction [3] is

$$U_o = 1.450 - 0.0296 \log (Pb^{++}) - 0.1183\, pH \quad [6]$$

Measurements of the open-circuit potential of a PbO_2 electrode in a solution of 50 mM lead acetate in 1M ammonium acetate are shown in Fig. 5 (dotted line). The variation with *p*H is linear and has a slope of −90 mV/*p*H instead of −118 mV/*p*H which would be expected for reaction [3]. Better agreement with this result would be given by the reaction

$$Pb(OH)^+ + H_2O \rightleftharpoons PbO_2 + 3H^+ + 2e^- \quad [7]$$

with

$$U_o = 1.270 - 0.0296 \log [Pb(OH)^+] - 0.0887\, pH \quad [8]$$

It is, however, not certain what composition the lead acetate complex has in this solution. The assumption that a complex of the type $Pb(OH)(C_2H_3O_2)_n^{(n-1)-}$ exists is not unreasonable, since $Pb(OH)^+$, respectively $Pb_4(OH)_4^{4+}$, is the hydrolyzed form stable in this *p*H region in perchlorate medium according to Olin (12). It should be mentioned that the absolute values of the open-circuit potentials in Fig. 5 cannot be compared with the calculated equilibrium potentials, since no liquid junction potentials and activity coefficients have been taken into account. The fact that the deviation is as high as 150 mV indicates that the activity coefficient of lead(II) in this solution is very low.

Besides the *p*H dependence of the equilibrium potential, there is also an effect of the *p*H on the rate of the anodic reaction, as can be seen in Fig. 3. At higher *p*H, the current potential curves are steeper. It is unlikely that this is an effect of an increase of the exchange current of reaction [3], since the influence of the reverse current should be negligible at overpotentials more than about 120 mV. It may be suggested that the mechanism of the reaction changes at higher *p*H, possibly due to the formation of $Pb(OH)_2$ or a complex of this with acetate.

The result that the cathodic curves are *p*H dependent is at first surprising, since $S_2O_8^=$ as well as the reaction product $SO_4^=$ are almost completely dissociated in the studied *p*H region. The mechanism of the $S_2O_8^=$ reduction on platinum electrodes in alkaline solution, as proposed by Müller (6)

$$S_2O_8^= \rightleftharpoons (2SO_4^{\cdot-})_{ads} \quad [9]$$

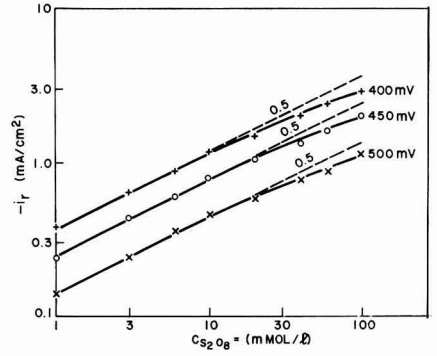

Fig. 4. Partial current of $S_2O_8^=$ reduction at PbO_2 *vs.* concentration of $S_2O_8^=$. Electrolyte: 50 mM lead acetate + x mM ammonium persulfate in 1M ammonium acetate, *p*H 8.50.

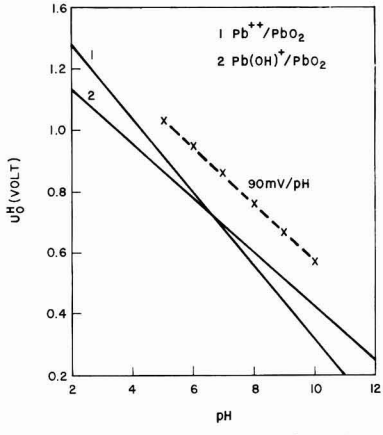

Fig. 5. Equilibrium potentials calculated from thermodynamic data (9) *vs. p*H. x, open-circuit potentials of PbO_2 electrodes measured in a solution of 50 mM lead acetate in 1M ammonium acetate.

$$2(SO_4^{\cdot-})_{ads} + 2e^- \rightarrow 2SO_4^= \quad [10]$$

does also not explain the pH dependence found here. It has been proposed by several authors (10) that the sulfate radical is converted to the OH· radical, according to

$$SO_4^{\cdot-} + H_2O \rightleftharpoons OH\cdot + SO_4^= + H^+ \quad [11a]$$

or

$$SO_4^{\cdot-} + OH^- \rightleftharpoons OH\cdot + SO_4^= \quad [11b]$$

Recent investigations on the photolysis of persulfate ions (11) showed that between pH 8.5 and 10.8 the stability of the $SO_4^{\cdot-}$ radical decreases rapidly, indicating the existence of a pH dependent equilibrium like Eq. [11]. Although the path of the conversion of $SO_4^{\cdot-}$ into OH· is not yet clarified, the following mechanism of the reduction of $S_2O_8^=$ at PbO_2 can be proposed

$$S_2O_8^= \rightleftharpoons 2SO_4^{\cdot-}{}_{ads} \quad [9]$$

$$2SO_4^{\cdot-}{}_{ads} + 2\,OH^- \rightleftharpoons 2\,OH\cdot_{ads} + 2SO_4^= \quad [11]$$

$$2\,OH\cdot_{ads} + 2e^- \rightarrow 2\,OH^- \quad [12]$$

The steady-state conditions for $SO_4^{\cdot-}{}_{ads}$ and $OH\cdot_{ads}$ are

$$\frac{d[SO_4^{\cdot-}]}{dt} = 2k_9\,[S_2O_8^=] - k_9'\,[SO_4^{\cdot-}]^2 - k_{11}\,[SO_4^{\cdot-}][OH^-] + k_{11}'\,[SO_4^=][OH\cdot] = 0 \quad [13]$$

$$\frac{d[OH\cdot]}{dt} = k_{11}\,[SO_4^{\cdot-}][OH^-] - k_{11}'\,[SO_4^=][OH\cdot] - k_{12}\,[OH\cdot] = 0 \quad [14]$$

and

$$i = \mathbf{F}\,k_{12}\,[OH\cdot] \quad [15]$$

Assuming that the equilibrium of reaction [11] is on the left side in the studied pH region, $k_{11}'/k_{11} >> 1$, and that $k_{12} << k_{11}'$, the following relation is obtained for the current at a constant potential

$$i = -\mathbf{F}\,\frac{k_{11}\,k_{12}}{k_{11}'}\sqrt{2\,\frac{k_9}{k_9'}}\,\frac{[OH^-][S_2O_8^=]^{1/2}}{[SO_4^=]} \quad [16]$$

This result is in agreement with the reaction order of 0.5 found for the $S_2O_8^=$ ion at low concentrations (Fig. 4). Furthermore, it gives an explanation for the pH dependence of reaction [4], although the experimental data in Fig. 3 are not sufficient to determine if the reaction order of OH^- is actually one. Finally, Eq. [16] shows that an increase of the sulfate ion concentration will decrease the current. This was also observed in the experiments; however, a passivation of the PbO_2 surface by formation of lead(II) sulfate may have a similar effect.

Acknowledgments

The author would like to thank U. B. Thomas and P. C. Milner for their interest in this work and many helpful discussions. He is also indebted to H. C. Montgomery for the provision of facilities for the Hall effect measurements and to G. W. Kammlott for carrying out the electron diffraction and electron microscopic studies.

Manuscript submitted Sept. 30, 1969; revised manuscript received Jan. 9, 1970.

Any discussion of this paper will appear in a Discussion Section to be published in the December 1970 JOURNAL.

REFERENCES

1. R. W. Berry, P. M. Hall, and M. T. Harris, "Thin Film Technology," p. 388, D. van Nostrand Co., Inc., Princeton, (1968).
2. P. Robinson, U.S. Pat. 3,066,247, Nov. 27, 1962.
3. W. Mindt, G. I. Parisi, Patent pending.
4. P. Rüetschi and B. Cahan, *This Journal*, **104,** 406 (1957).
5. B. Cahan, Private communication.
6. L. Müller, *J. Electroanal. Chem.*, **13,** 275 (1967).
7. A. T. Zaslavskii and S. S. Tolkachev, *Z. Fiz. Khim., SSSR*, **26,** 743 (1952).
8. W. Mindt, *This Journal*, **116,** 1076 (1969).
9. "Selected Values of Chemical Thermodynamic Properties," National Bureau of Standards Circular 500, Part 1, p. 158 (1961).
10. D. A. House, *Chem. Rev.*, **62,** 185 (1962), review article.
11. L. Dogliotti and E. Hayon, *J. Phys. Chem.*, **71,** 2511 (1967).
12. A. Olin, *Acta Chem. Scand.*, **14,** 126, 814 (1960).

Electrochemical Behavior of Selenium and Tellurium in Fused LiCl-KCl Eutectic

F. G. Bodewig and James A. Plambeck***

Department of Chemistry, University of Alberta, Edmonton, Alberta, Canada

ABSTRACT

Liquid selenium has been reduced coulometrically in fused LiCl-KCl eutectic at 400°C. Nernstian behavior is observed for the cell C,Se(1)/$Se^=$, LiCl-KCl//Pt^{++},LiCl-KCl/Pt. The standard potentials of the selenium/selenide couple at 450°C with respect to the appropriate standard platinum reference electrode are −1.141, −1.172, and −1.252V on the molar, molal, and mole fraction scales, respectively. Voltammetric studies showed an anodic wave at +0.05V ascribed to $2Se + 2Cl^- \rightarrow Se_2Cl_2(g) + 2e^-$ and a cathodic wave at −1.07V ascribed to $Se + 2e^- \rightarrow Se^=$. For tellurium an anodic wave at −0.15V is ascribed to Te → Te(II) + $2e^-$ and a cathodic one at −1.40V to the plating of lithium into tellurium; the formation of free telluride does not appear to occur. The standard potential for the couple Te(II)/Te is estimated at −0.1V.

A recent publication from this laboratory (1) reported the electrochemical behavior of sulfide in the fused LiCl-KCl eutectic. The present paper extends this study to selenium and tellurium.

The literature on selenium and tellurium in fused salt media is scanty. Verdieck and Yntema (2) measured the deposition potential of tellurium from solutions of tellurium dioxide in fused $AlCl_3$-NaCl-KCl at 218°C. The solid electrolyte cells Ag(s)/AgI(s)/Ag in Te or Se have been investigated by Kiukkola and

** Electrochemical Society Active Member.
* Electrochemical Society Student Member.

Wagner (3). Foster and Liu (4) employed the cell $Li_3Bi(s)$, Li in Bi(l)/LiCl-LiF/Li in Te(l), Li_2Te to obtain the free energy of formation of Li_2Te by emf measurements, and a similar cell has been used in the Bi-Te system by Liu and Angus (5). Selenium and tellurium have been used as cathode materials in secondary cells with fused salt electrolytes at Argonne National Laboratory (6, 7).

Experimental

Apparatus.—Potentials were measured with a digital voltmeter (Model 3440A, Hewlett-Packard). Coulometric generations employed a Model IV Coulometric Current Source (E. H. Sargent and Company). An Anotrol Model 4100 Potential Controller was used for voltammetric investigations.

A Lindberg Hevi-Duty Model 54381A furnace with a Model 59344 temperature controller was employed. Temperatures were measured with a chromel-alumel thermocouple calibrated at the melting point of zinc.

The electrolytic cell was essentially the same as described previously (8).

Solvent.—The preparation of the LiCl-KCl eutectic solvent (59.5 m/o LiCl, mp 352°C) has been described previously (1).

Chemicals.—Reagent grade LiCl (Fisher Scientific Company) and KCl (Fisher Scientific Company or Shawinigan Chemicals) were used. Selenium (99.99%) was obtained in ¼ x 2 in. rods from A. D. Mackay, Inc. Tellurium (99.999%) was obtained from Atomergic Chemetals Company. Graphite electrodes were Special Spectroscopic Electrodes ⅛ in. in diameter (National Carbon Company). Argon was dried by passage through a magnesium perchlorate column and two traps cooled by a dry ice-acetone bath.

Electrodes.—A reference electrode based on the Pt(II)/Pt couple (about 0.03M) was generated coulometrically for each experiment by anodization of a coil of platinum wire.

The selenium electrode consisted of a small Pyrex cup (7 mm diameter, 5 mm long) containing pieces of selenium. Contact with the selenium (liquid at operating temperature) was made with a graphite rod attached to Nichrome leads well above the melt level. The Pyrex cup rested on the bottom of the isolation compartment and was totally immersed in the melt.

The tellurium electrodes were made by melting lumps of tellurium in a 4 mm Pyrex tube under argon. A tungsten wire was inserted into the liquid tellurium which was then allowed to solidify. The electrode was removed by carefully breaking the glass.

A graphite rod in an isolation compartment was used as the counterelectrode.

Procedure.—The crucible containing the frozen eutectic, isolation compartments, and electrodes was placed inside the outer glass jacket of the electrolytic cell which could be connected to a vacuum pump. Transfers of frozen eutectic to the crucible were made inside a dry box under nitrogen. The outer jacket was closed to the atmosphere by means of a Pyrex cap connected to it with a 75 mm O-ring joint. On this cap were blown five 14/20 ground-glass joints which were used to insert a thermocouple, an argon inlet tube, and the electrodes. The isolation compartments were made of 10 mm Pyrex sealing tubes with 10-20μ frits (D porosity; Ace Glass Inc.) The temperature of the cell was slowly raised to 370°C under vacuum in order to dry the glass equipment and electrodes before fusion of the eutectic. After fusion of the eutectic, argon was introduced and bubbled through the melt during all experiments. The compartments were allowed to fill with eutectic during a period of 8-10 hr. The selenium or tellurium was added as a final step. Ionic species were generated by anodization or cathodization of the selenium or tellurium. The cells were operated at 400° ± 2°C to minimize loss of volatile materials from the melt, which was still the most serious problem encountered in the investigation.

Electrode potentials were measured against the platinum reference electrode and corrected to the Pt(II), 1.0 *M*/Pt standard molar platinum electrode (SMPE) of Laitinen and Liu (9); they are reported in conformance with the IUPAC "Stockholm" sign convention. The thermoelectric potential of the graphite and leads was measured as +10 mV with respect to platinum. It was essentially invariant with temperature from 400° to 450°. The potentials were corrected for this effect. They were then converted from 400° to 450°C using the experimentally determined potential-temperature relationships (see below) and the actual temperature of each potential measurement. The amount of solvent in each isolation compartment was determined by a potentiometric chloride titration; when necessary, selenide was removed by acidification (in a hood). The concentrations of $Se^{=}$ and Pt^{++} were determined from the coulombs passed and solvent volume (9). The least-square calculations were done on the University of Alberta IBM/360 computer, and copies of the programs used are available in the thesis of one of the authors (F.G.B.).

The voltammetric procedure was as described previously (1).

Results

Voltammetric results.—The voltammetric curves obtained for selenium and tellurium are shown in Fig. 1, denoted respectively by triangles and circles. In the absence of selenium and tellurium, the only electrochemical phenomena observed are anodic chlorine evolution (+0.3V) and cathodic lithium deposition (>−2.1V) as in previous work (1, 9).

The cathodic branch observed with selenium is ascribed to $Se(l) + 2e^- \rightarrow Se^=$. A red-brown color was observed leaving the electrode until the entire compartment contents were colored when cathodic current was passed. Extrapolation of the linear part of the curve to zero current gave −1.07 ± 0.02V for the "decomposition" potential, in good agreement with the potentiometric results given below. The anodic wave is ascribed to $2Se(l) + 2Cl^- \rightarrow Se_2Cl_2(g) + 2e^-$, analogous to the reaction $2S(l) + 2Cl^- \rightarrow S_2Cl_2(g) + 2e^-$ observed previously (1). The "decomposition" potential was +0.05 ± 0.02V. Colorless gas bubbles were observed forming on the electrode at this potential and leaving the melt. No attempt was made to trap the gas since Se_2Cl_2 is reported as unstable at considerably lower temperatures than those employed here. Stable potentials could not be obtained, as is expected when the species produced electrochemically volatilizes from the melt.

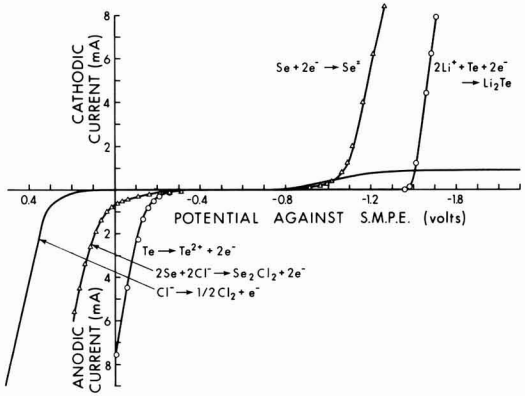

Fig. 1. Voltammetric curves of LiCl-KCl containing selenium (triangles) or tellurium (circles). Temperature 400°C, reference potential SMPE. Area of selenium pool approximately 0.4 cm^2, of tellurium rod 1.1 cm^2. Voltammetric curve of pure melt on graphite electrode is line without symbols.

Voltammetric curves were also taken with selenium electrodes in compartments in which selenide had been generated. Two typical curves are shown in Fig. 2. Identical straight lines were always obtained regardless of the direction of voltage change as long as precautions were taken to prevent significant changes in the ion concentration between measurements. These precautions included stirring and, when necessary, oxidation or reduction such that the zero current potential remained within 3 mV of its original value. The slope of these lines was approximately 15 ohms and represents the cell resistance. These curves show the $Se/Se^{=}$ couple to be reversible in this solvent system.

The cathodic branch observed with tellurium (Fig. 1) is ascribed to the formation of stable lithium-tellurium intermetallic compounds whose limiting composition is Li_2Te (4); the reaction written as $Te(s) + 2Li^+ + 2e^- \rightarrow Li_2Te(s)$ is probably an oversimplification. The potential characteristic of this reaction was -1.40 ± 0.02V. Liquid alloys were observed to form on the tellurium rod on cathodization beyond this potential. Such alloy formation on cathodization has been observed in previous studies of the Li-Te system (4, 10). The anodic wave is ascribed to $Te \rightarrow Te(II) + 2e^-$. An orange-brown color was observed leaving the electrode upon anodization. The "decomposition" potential for this reaction was -0.15 ± 0.03V, in good agreement with the potentiometric measurements given below.

Potentiometry of selenium.—Three complete experiments, each involving multiple cells, were carried out with new compartments, electrodes, and eutectic charge used in each. A total of 52 data points were taken at 400° ± 2°C. For each point, the emf became constant, within 0.5 mV, 30-90 min after completion of coulometric reduction of selenium and stirring. The potential was thereafter constant, within 1 mV, over several hours.

The effect of temperature on the emf was determined in several experiments over the temperature range 380°-420°C, with both increasing and decreasing temperature. The measured potential was, for a fixed selenide concentration, linearly dependent on temperature. A plot of $\Delta E/\Delta T$ against the logarithm of the molar concentration (as moles $Se^{=}$/liter of eutectic at 450°C) was linear (Fig. 3). Least square analysis of this plot gives $\Delta E/\Delta T = +0.123 \log [Se^{=}] - 0.510$ mV/°C, with a relative standard error of 6% in the slope and 1.5% in the intercept, for the temperature dependence of the cell (−)C, Se(l)/$Se^{=}$, LiCl-KCl// Pt(II), LiCl-KCl/Pt (+). This equation is identical to that obtained for the analogous sulfide cell (1) within experimental error. It was used to extrapolate all measured potentials to 450°C. This temperature is accepted as standard for potential measurements in this fused salt system [(11), and references cited therein].

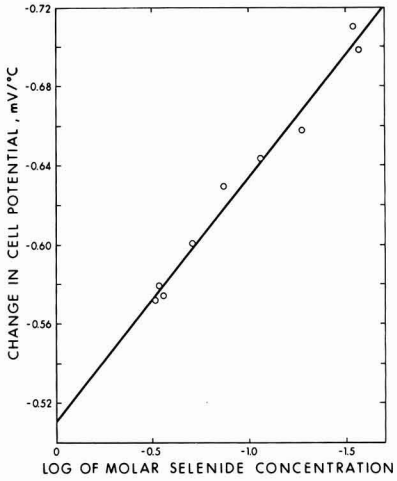

Fig. 3. Temperature dependence of potential as a function of selenide ion concentration. Line is that given by least-squares analysis. Temperature range 380°-420°C.

These extrapolated potentials gave linear Nernst plots over the concentration range 0.015-0.35M selenide. A typical plot of potentials against the logarithm of selenide concentration (Fig. 4) shows that Henry's law is obeyed over the concentration range studied. A summary of all runs is given in Table I; the original data are available in the thesis of F.G.B. Least square analysis of all points gave a standard potential of -1.141V for the Se(l)/$Se^{=}$ couple (molarity scale) at 450°C, with a standard error of 0.002V. This corresponds to values of -1.172 and -1.252V, with the same standard error, on the molality and mole fraction scales, respectively (11), all potentials being with respect to the appropriate standard platinum electrode. The slope of the Nernst plot was -0.0660 V/log unit with a standard error of 0.0014, corresponding to 2.17 ± 0.05 electrons taking part in the reaction. This is in agreement with the theoretical value of 2 expected for $Se + 2e^- \rightarrow Se^{=}$.

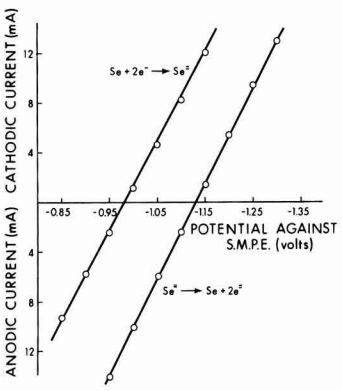

Fig. 2. Current-potential curves for different selenide concentrations in the same compartment. Reference potential SMPE, temperature 400°C.

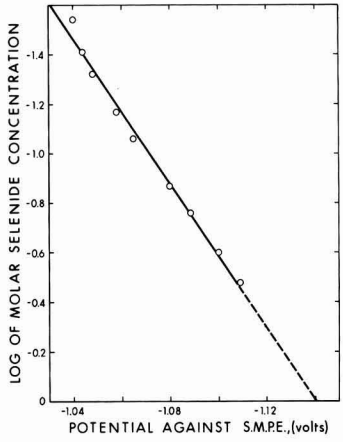

Fig. 4. Electromotive force of selenide electrode (*vs.* SMPE) as a function of selenide concentration in a typical run, showing obedience to Henry's law. Temperature (extrapolated) 450°C.

Table I. Standard emf determinations for the $Se/Se^{=}$ couple*

Selenide molarity	No. of points	$E_{M^{\circ}}$, V	Standard deviation, mV	Exper. n
0.015-0.10	7	−1.136	2.6	2.22
0.024-0.24	9	−1.141	1.1	2.27
0.018-0.16	9	−1.144	1.2	2.21
0.029-0.32	9	−1.143	2.4	2.08
0.029-0.33	9	−1.140	2.8	2.10
0.039-0.35	9	−1.143	2.3	2.10
Least square analysis of all points	52	−1.141	1.5	2.17

* Values corrected to 450°C and SMPE; each entry is a separate compartment, the first being run 1, the next two being run 2, and the remainder being run 3.

Stable potentials could not be obtained on anodization of selenium electrodes, for the reasons discussed above.

Potentiometry of tellurium.—Attempts were made to measure the standard potential of the Te(s)/$Te^{=}$ couple. These attempts were unsuccessful because the solubility of "Li_2Te" in the LiCl-KCl eutectic in the presence of excess tellurium is very low; even an attempt to produce $2 \times 10^{-3}M$ $Te^{=}$ resulted in the formation of liquid on the surface of the tellurium electrode. The potentials obtained in this manner were quite stable. They correspond, after correction for reference electrode, to those observed by Foster and Liu (4) for very tellurium-rich alloys of lithium and tellurium in a similar system, and therefore cannot be considered as true tellurium/telluride electrode potentials.

Anodization of tellurium produced an orange-brown solution. Long needles of tellurium were observed extending from the electrode. The potentials measured were unstable, however, and drifted in the negative direction continuously after anodization was completed. At the same time, the color of the solution slowly disappeared. A yellow powder sometimes condensed in the cooler top of the isolation compartment. This behavior would be expected if a volatile species such as $TeCl_2$ (bp 327°C) escaped from solution at 400°. The experiment was repeated at 375°, but the species formed still volatilized from solution.

Attempts to produce meaningful Nernst plots from the potential data for this system were unsuccessful. The slope varied between 0.067 and 0.134 V/log unit. Since 0.033 V/log unit would be expected for a four-electron process, the ionic species produced should be Te(II) rather than Te(IV). From these plots and the voltammetric curves the standard potential (molarity scale) of the Te(II)/Te(s) couple is estimated as -0.10 ± 0.03V, placing it between Rh(III)/Rh and Ir(III)/Ir couples in this medium (11). Attempts to further oxidize the Te(II) species at a graphite electrode were unsuccessful.

Discussion

The potential between selenium and lithium electrodes, using literature data for lithium (11) and the result of the present study for selenium, is 2.2V at 450°C. This is in good agreement with the open-circuit potentials of 2.3-2.4V obtained from the Li/Se secondary cell between 350° and 400°C (7) and implies that at nearly full charge the selenium electrode potential of that cell may well be determined by soluble $Se^{=}$ in the electrolyte rather than electrode composition. The free energy of the reaction $2Se(l) + Cl_2 \rightarrow Se_2Cl_2(g)$ can be estimated as −11 kcal/mole from the voltammetric curves. No literature data could be found with which to compare this value; it seems reasonable, however, as it is similar to that for the formation of gaseous S_2Cl_2 (1).

The Li/Te secondary cell is reported (4, 6) to have an open-circuit voltage of 1.7-1.8V which is in agreement with the value of 1.9V obtained from the voltammetric curves of the present study.

There is a significant point raised in the present work related to lithium-chalcogen cells. Clearly, a soluble selenide species determines the potential of the selenium electrode under the conditions of the present study. Such a species, whether $Se^{=}$ or Li_2Se, can be expected to be present in Li/Se cells (6) and to diffuse to the lithium electrode if cell construction so permits. This will lead to reduced cell efficiency and eventual cell failure. The problem appears less significant in the Li/Te system due to lower solubility of the species produced.

Acknowledgment

The authors are grateful to the National Research Council of Canada for financial assistance in the form of an Operating Grant (to J.A.P.). This paper is taken from the thesis of one of the authors (F.G.B.) submitted to the Faculty of Graduate Studies, University of Alberta, in partial fulfilment of the requirements for the Ph.D. degree.

Manuscript submitted Sept. 29, 1969; revised manuscript received Dec. 20, 1969.

Any discussion of this paper will appear in a Discussion Section to be published in the December 1970 JOURNAL.

REFERENCES

1. F. G. Bodewig and J. A. Plambeck, *This Journal*, **116**, 607 (1969).
2. R. G. Verdieck and L. F. Yntema, *J. Phys. Chem.*, **48**, 268 (1944).
3. K. Kiukkola and C. Wagner, *This Journal*, **104**, 379 (1957).
4. M. S. Foster and C. C. Liu, *J. Phys. Chem.*, **70**, 950 (1966).
5. C. C. Liu and J. C. Angus, *This Journal*, **116**, 1054 (1969).
6. H. Shimotake, G. L. Rogers, and E. J. Cairns, Paper 18 presented at the Chicago Meeting of the Society, Oct. 15-19, 1967; Extended Abstracts of the Battery Div., J-1, **12**, 42 (1967).
7. H. Shimotake and E. J. Cairns, Paper 282 presented at the Boston Meeting of the Society, May 5-9, 1968.
8. H. A. Laitinen and J. A. Plambeck, *J. Am. Chem. Soc.*, **87**, 1202 (1965).
9. H. A. Laitinen and C. H. Liu, *ibid.*, **80**, 1015 (1958).
10. J. A. Plambeck and C. C. Liu, Unpublished data.
11. J. A. Plambeck, *J. Chem. Eng. Data*, **12**, 77 (1967).

Kinetics of the Hydrogen Evolution Reaction on Titanium

N. T. Thomas* and Ken Nobe*

School of Engineering and Applied Science, University of California, Los Angeles, California

ABSTRACT

The kinetics of the hydrogen evolution reaction on titanium in sulfuric acid solutions between pH 0.25 to 2.25 have been investigated. The Tafel slope of the HER was 150 mV at all pH values, and the electrochemical reaction order was 0.6 with respect to the hydrogen ions. The corrosion potential varied negligibly with pH; $(\partial \log i_{corr}/\partial \text{ pH}) = -0.57$; $(\partial \log i_o/\partial \text{ pH}) = -0.23$. If it is assumed that a thin incipient oxide film covers the surface of active titanium, a mechanism for the HER based on Temkin adsorption behavior, electrochemical desorption as the rate-determining electrode reaction step, and the dual barrier model is consistent with the experimental results.

There have been a number of investigations of the hydrogen evolution reaction (HER) on titanium in aqueous solutions. However, a mechanistic study of the HER on titanium has not been reported thus far.

Hackerman and Hall (1) reported an HER Tafel relationship of $\eta' = 1.30 + 0.154 \log i$, volts, for titanium in sodium chloride solutions. Straumanis *et al.* (2) and Andreeva (3) obtained HER Tafel slopes of 175 and 160 mV for titanium in 0.5*N* and 40% H_2SO_4, respectively. Kolotyrkin and Petrov (4) observed the Tafel behavior of $\eta' = 0.82 + 0.135 \log i$, volts, and a first order dependence on the concentration of hydrogen ions for the HER on titanium in sulfuric acid solutions. Petrenko (5) and Artemova (6) obtained Tafel relationships of $\eta' = 0.97 + 0.119 \log i$ and $\eta' = 0.97 + 0.135 \log i$, volts, for titanium in 2*N* H_2SO_4, respectively.

This work is an investigation of the kinetics and mechanism of the HER on titanium in sulfuric acid solutions of pH ranging from 0.25 to 2.25 at room temperature. Experimental details have been given elsewhere (7).

Results

Figure 1 shows the results of the cathodic polarization of titanium in sulfuric acid solutions. The HER Tafel slope was 150 mV for all pH values. It should be observed that deviations from the Tafel behavior occurred at about −1.0V *vs.* SCE for all pH values. At more active potentials, the current density was greater than the value obtained by extrapolating the Tafel line. This behavior suggests the possible commencement of a second reduction process.

As shown in Table I, the corrosion potential did not vary significantly with the pH. The corrosion current at each pH was determined by extrapolating the Tafel line to the corrosion potential. These values and the exchange current densities are also given in Table I.

Figure 2 is a cross plot of the data in Fig. 1. The log i *vs.* pH lines at constant potential ψ, in the Tafel region, are all parallel with slope

$$\left(\frac{\partial \log i}{\partial \text{pH}}\right)_{\psi} = -0.60 \qquad [1]$$

Similarly, the ψ *vs.* pH lines at constant current i, in the Tafel region, are all parallel as shown in Fig. 3. The slopes were

$$\left(\frac{\partial \psi}{\partial \text{pH}}\right)_{i} = -90 \text{ mV} \qquad [2]$$

Figure 4 gives the dependence of the corrosion current on the pH of the solution and shows that

$$\frac{\partial \log i_{corr}}{\partial \text{pH}} = -0.57 \qquad [3]$$

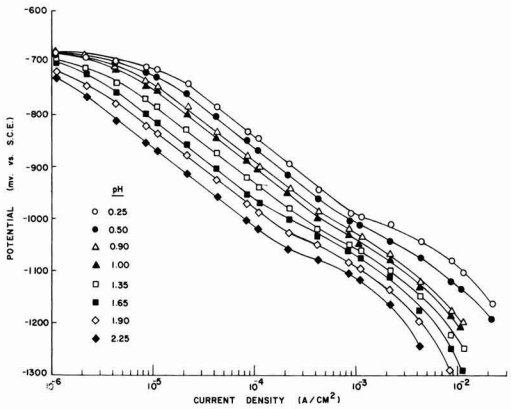

Fig. 1. Cathodic polarization curves of titanium in H_2SO_4

The dependence of the exchange current of the HER on the pH is given in Fig. 5 and shows that

$$\frac{\partial \log i_o}{\partial \text{pH}} = -0.23 \qquad [4]$$

Values of the Tafel slopes and the exchange current densities for the HER obtained in this investigation are comparable to the values reported by other investigators (1, 2, 4-6). The corrosion rates are in reasonable agreement with the values reported by Millaway (8).

In the Tafel region, the rate of the HER can be expressed as

$$i = k a_{H^+}{}^n \exp\left(\frac{-\alpha \mathbf{F} \psi}{RT}\right) \qquad [5]$$

where k is the rate constant, a_{H^+} is the activity of the hydrogen ions, α is the over-all transfer coefficient, and n is the electrochemical reaction order with respect to the hydrogen ions. The over-all transfer coefficient, $\alpha = 0.4$, is determined from the cathodic Tafel slope of 150 mV. The slope of the curves in Fig. 2

Table I. Cathodic parameters of titanium in H_2SO_4

pH	Active corrosion potential, mV *vs.* SCE	Tafel slope, mV	Corrosion current, μA/cm^2	Exchange current, μA/cm$^2 \times 10^3$	$R_p \times 10^{-3}$, ohm-cm^2
0.25	−680 ± 10	150	9.0 ± 0.7	15.4 ± 1.2	4.0 ± 0.5
0.50	−675	150	6.0	13.5	5.7
0.90	−670	150	3.4	11.5	8.0
1.00	−665	150	2.9	10.5	11.0
1.35	−678	150	2.0	8.8	14.0
1.65	−675	150	1.4	7.5	23.0
1.90	−680	150	1.0	6.5	34.0
2.25	−685	150	0.6	5.5	51.0

* Electrochemical Society Active Member.

Key words: hydrogen evolution, titanium, kinetics, corrosion, Temkin isotherm, dual-barrier.

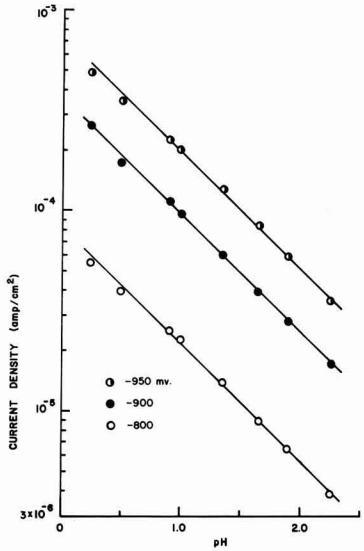

Fig. 2. Plot of logarithm of current density *vs.* pH in the Tafel region of the HER.

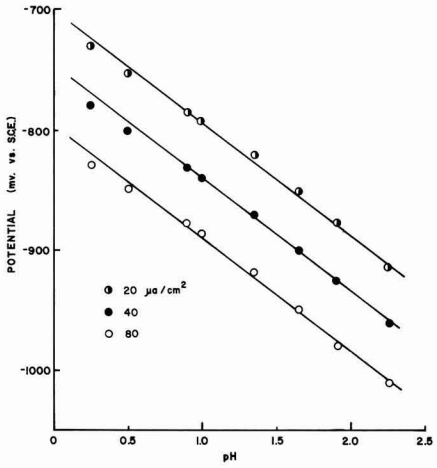

Fig. 3. Plot of potential *vs.* pH in the Tafel region of the HER

gives the reaction order

$$n = -\left(\frac{\partial \log i}{\partial p\mathrm{H}}\right)_{\psi} = 0.60 \qquad [6]$$

Equation [5] shows that $(\partial\psi/\partial \mathrm{pH})_i = -2.303\ RT/\mathbf{F}$ $n/\alpha = -90$ mV which agrees with the experimental value of Eq [2]. The equation for the exchange current density can be obtained from Eq. [5]

$$i_o = k a_{\mathrm{H}^+}{}^n \exp\left(\frac{-\alpha \mathbf{F}\psi_o}{RT}\right) \qquad [7]$$

It follows from Eq. [7] and the Nernst equation, $\psi_o = -2.303\ RT/\mathbf{F} \log a_{\mathrm{H}^+}$ that $i_o = k a_{\mathrm{H}^+}{}^{n-\alpha}$. Thus

$$\frac{\partial \log i_o}{\partial p\mathrm{H}} = -0.20 \qquad [8]$$

which is in good agreement with Eq. [4]. The equation for the corrosion current can also be obtained from Eq. [5]

$$i_{\mathrm{corr}} = k a_{\mathrm{H}^+}{}^n \exp\left(\frac{-\alpha \mathbf{F}\psi_{\mathrm{corr}}}{RT}\right) \qquad [9]$$

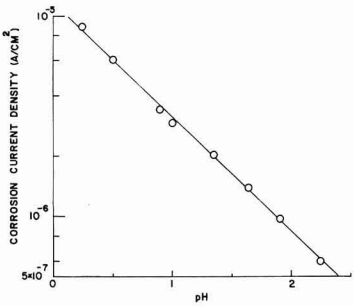

Fig. 4. Dependence of corrosion current on pH

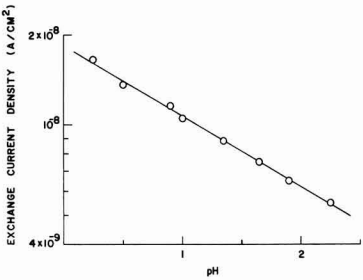

Fig. 5. Dependence of the HER exchange current on pH

From Eq. [9], the pH dependence of the corrosion current can be determined

$$\frac{\partial \log i_{\mathrm{corr}}}{\partial p\mathrm{H}} = -n + \frac{\alpha \mathbf{F}}{2.3RT}\left(\frac{\partial \psi_{\mathrm{corr}}}{\partial p\mathrm{H}}\right) \qquad [10]$$

Since it has been shown that $\partial\psi_{\mathrm{corr}}/\partial \mathrm{pH} \approx 0$

$$\frac{\partial \log i_{\mathrm{corr}}}{\partial p\mathrm{H}} \approx -n = -0.60 \qquad [11]$$

and this value agrees well with Eq. [3].

Since a single anodic process and a single cathodic process can describe the corrosion of titanium in sulfuric acid, the polarization current can be expressed as

$$i = i_{\mathrm{corr}}\left[\exp\left(\frac{\alpha_a \mathbf{F}\eta}{RT}\right) - \exp\left(\frac{-\alpha_c \mathbf{F}\eta}{RT}\right)\right] \qquad [12]$$

where α_a and α_c are the over-all transfer coefficients of the anodic and cathodic processes, respectively, and $\eta = \psi - \psi_{\mathrm{corr}}$. From Eq. [12] the relation between the polarization resistance, R_p, and the corrosion rate, i_{corr}, can be determined (9)

$$R_p = \left(\frac{\partial \eta}{\partial i}\right)_{\eta \to 0} = \frac{RT}{i_{\mathrm{corr}}(\alpha_a + \alpha_c)\mathbf{F}} \qquad [13]$$

Figure 6 shows a linear plot of $(\psi - \psi_{\mathrm{corr}})$ *vs.* the applied current for titanium in sulfuric acid of various pH values. The slope of each curve is the polarization resistance which is given in Table I. A plot of log R_p *vs.* log i_{corr} is shown in Fig. 7. It is seen that a slope of -1 correlated the data well. The polarization resistance-corrosion current values were comparable to those values obtained for a number of different metals as shown in Fig. 5 of ref. (10).

The $R_p - i_{\mathrm{corr}}$ data and $\alpha_c = 0.40$ indicates that $\alpha_a = 0.44$. Thus, an anodic Tafel slope of 136 mV for titanium electrodissolution can be estimated.

Equation [5] can be expressed as

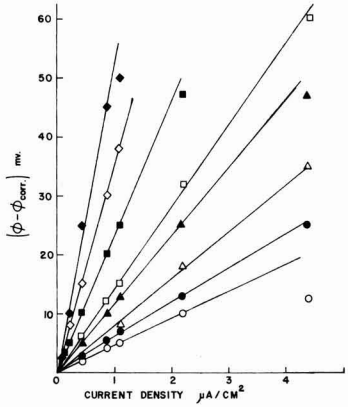

Fig. 6. Linear plot of $(\psi-\psi_{corr})$ *vs.* current density. Same symbols as in Fig. 1.

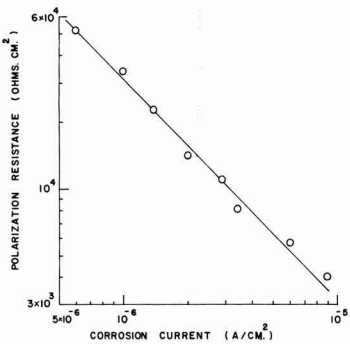

Fig. 7. Log. polarization resistance (ohm cm^2) *vs.* log corrosion current (A/cm^{-2}).

$$i_{corr} = k a_{H^+}{}^n \exp\left(\frac{-\alpha_c \mathbf{F}\psi_{corr}}{RT}\right) \quad [14]$$

Equations [13] and [14] can be used to express the pH dependence of the polarization resistance as shown in Eq. [15]

$$\frac{\partial \log R_p}{\partial pH} = n + \frac{\alpha_c \mathbf{F}}{2.303\,RT}\left(\frac{\partial \psi_{corr}}{\partial pH}\right) \quad [15]$$

Since it has been shown that $\partial\psi_{corr}/\partial pH \approx 0$

$$\frac{\partial \log R_p}{\partial pH} \approx n = 0.60 \quad [16]$$

Figure 8 shows a plot of log R_p *vs.* pH. The slope of the straight line which best fits the experimental points is 0.57 and agrees well with Eq. [16]. The slope of Fig. 8 is also consistent with the results given in Eq. [3]. The above analysis has shown that the experimental results of this investigation are self-consistent.

The rate of the HER on titanium in sulfuric acid between pH 0.25 to 2.25 can be expressed by the equation

$$i = k a_{H^+}{}^{0.6} \exp\left(\frac{-0.40\mathbf{F}\psi}{RT}\right) \quad [17]$$

Figure 9 shows the results of the measurements of the differential capacitance of titanium in pH 0.25 solutions as a function of potential. At potentials more negative than the active corrosion potential, the capacitance decreased with decrease in potential. A minimum capacitance value is attained at approximately

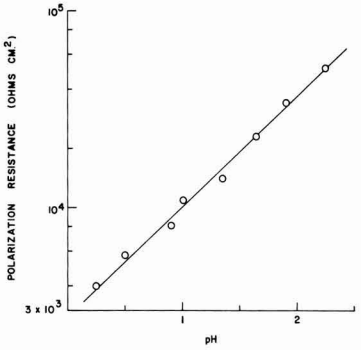

Fig. 8. Dependence of the polarization resistance on pH

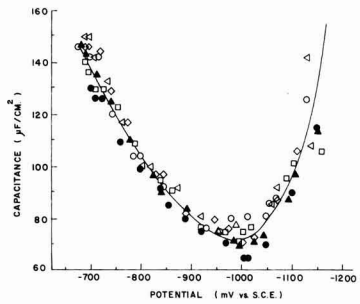

Fig. 9. Differential capacitance of titanium in 1*N* H_2SO_4 as a function of potential.

−1.0V. The capacitance increased again with further decrease in potential.

Discussion

The reaction steps in the HER which are generally considered are Eq. [18], [19], and [20]:

$$H^+ + e^- \rightarrow H_{ads} \quad [18]$$

and

$$H^+ + H_{ads} + e^- \rightarrow H_2 \quad [19]$$

or

$$H_{ads} + H_{ads} \rightarrow H_2 \quad [20]$$

A detailed account of the mechanisms of the HER on metals, assuming the applicability of the Langmuir isotherm for the adsorption of hydrogen atoms, is given by Bockris (11). Parsons (12), Thomas (13), and Conway and Salomon (14) have considered the kinetics of the HER using the Temkin isotherm for the adsorbed hydrogen atoms.

The experiments of Tomashov *et al.* (15) show that a mixed oxide film of TiO_2 and Ti_2O_3 is present on the surface of passive titanium. The thermodynamic data of these oxides indicate their possible presence even on active titanium in the Tafel region of the HER

$$Ti + 2H_2O = TiO_2 + 4H^+ + 4e^-; \quad \psi^o = -1.100\text{V } vs.\text{ SCE} \quad [21]$$

and

$$2Ti + 3H_2O = Ti_2O_3 + 6H^+ + 6e^-; \quad \psi^o = -1.405\text{V } vs.\text{ SCE} \quad [22]$$

The presence of other titanium oxides are also possible in the HER Tafel region, and it is surmised that in this region a thin oxide film is always present on the surface of titanium.

Meyer (16) has utilized a dual barrier model to develop electrode kinetic equations for metals covered with thin oxide films. Meyer (16, 17) and Posey *et al.* (18) interpreted the kinetics of reduction reactions on

zirconium and passive steel, respectively, in terms of the dual barrier model. MacDonald and Conway (19) used this model to analyze the kinetics of the oxygen evolution reaction on gold. The electrode reaction rates for this model are dependent on the potential across the oxide film, ψ_f, and across the double layer in the electrolyte, ψ_d. Thus

$$\psi = \psi_f + \psi_d \quad [23]$$

The rate of electron transport through the thin oxide film can be described by Eq. [24]

$$i = k_f \exp\left(\frac{-\alpha_f \mathbf{F}\psi_f}{RT}\right) \quad [24]$$

where α_f is the transfer coefficient for the electromigration of electrons in the film and k_f is the film rate constant. It is assumed that the charge transfer across the film and the electrolyte double layer are both rate determining. Analysis has shown that experimental data is consistent with the electrochemical desorption step, Eq. [19], as the rate-determining step for the HER and with Temkin behavior for adsorbed hydrogen atoms. For this case

$$i = k' a_{H^+}^{(1+\beta)} \exp\left(-\frac{2\beta \mathbf{F}\psi_d}{RT}\right) \quad [25]$$

Equations [24] and [25] lead to Eq. [26]

$$i = k'' a_{H^+}^{\frac{(1+\beta)\alpha_f}{2\beta+\alpha_f}} \exp\left[-\frac{2\beta\alpha_f \mathbf{F}\psi}{(2\beta+\alpha_f)RT}\right] \quad [26]$$

Expressions for the reaction order and the HER Tafel slope can be determined from Eq. [26]

$$n = \frac{(1+\beta)\alpha_f}{2\beta+\alpha_f} \quad [27]$$

$$\frac{\partial\psi}{\partial \log i} = -2.303\frac{RT}{\mathbf{F}}\frac{(2\beta+\alpha_f)}{2\beta\alpha_f} \quad [28]$$

By substituting the experimental values, $n = 0.60$ and $\partial\psi/\partial \log i = 150$ mV, one obtains $\alpha_f = 0.67$ and $\beta = 0.5$. These derived values indicate that a mechanism consistent with the experimental results of the HER on titanium in sulfuric acid can be based on Temkin adsorption, electrochemical desorption as the rate-determining electrode reaction step, and the dual barrier model.

Bockris and Srinivasan (20) present a plot of log i_o of the HER *vs.* the work function of metals. This plot shows that the metals fall into three groups, those with high hydrogen overpotentials, medium hydrogen overpotentials, and low hydrogen overpotentials. The rate-determining step for the HER on these three groups of metals was ascribed to be ion discharge, electrochemical desorption, and recombination, respectively. This correlation shows that titanium is included in the medium hydrogen overpotential group, that is, the electrochemical desorption step is the rate-determining step which is in accord with the analysis of the experimental results of this work. In the present study, the values of log i_o for the HER on titanium in H_2SO_4 were between -7.8 to -8.3 for solutions of *p*H between 0.25 and 2.25 which is in good agreement with the data used in the correlation reported by Bockris and Srinivasan (20).

It was observed in the polarization of titanium in sulfuric acid that, at approximately -1.0V, deviations from Tafel behavior commenced with an anomalous increase in the cathodic current. A possible explanation of this phenomenon is the complete reduction of the incipient oxide film at this potential and the subsequent hydrogen ion discharge on oxide-free titanium. This interpretation seems to be in accord with the results of Beck (21) who reported that the rate of the HER on an oxide-free titanium surface in 12M HCl was greater than on an oxide-covered surface.

A second feasible explanation of the nonlinearity in the ψ-log i curve is the possible titanium hydride formation from the hydrated oxides Ti_2O_3 and TiO_2, at about -1.0V, as indicated by calculations based on thermodynamic data obtained from Pourbaix (22, 23)

$$Ti_2O_3 + 10H^+ + 10e^- = 2TiH_2 + 3H_2O; \quad \psi^o = -1.027\text{V } vs.\text{ SCE} \quad [29]$$

$$TiO_2 + 6H^+ + 6e^- = TiH_2 + 2H_2O; \quad \psi^o = -0.910\text{V } vs.\text{ SCE} \quad [30]$$

It should be noted that Pourbaix's calculations (22) were based on the standard free energy of formation of titanium hydride reported by Baymakov and Lebedev (24), ΔG_f^o (TiH_2) = 10.00 kcal/mole. On the other hand, thermodynamic data reported by Stalinski and Bieganski (25) indicate a value, ΔG_f^o (TiH_2) = -20.6 kcal/mole. Based on the latter value, the standard potentials of TiH_2 formation from Ti_2O_3 and TiO_2 are as follows

$$Ti_2O_3/TiH_2;\ \psi^o = -0.764\text{V } vs.\text{ SCE} \quad [31]$$

$$TiO_2/TiH_2;\ \psi^o = -0.692\text{V } vs.\text{ SCE} \quad [32]$$

It is also seen that, at approximately -1.0V, a minimum in the differential capacitance of titanium in 1*N* H_2SO_4 occurred as shown in Fig. 9. The potential of zero charge of titanium, -942 mV *vs.* SCE, was calculated from the work function by Petrenko (5). At present, no significance is attached to this apparent agreement between the potential of the capacitance minimum and the calculated potential of zero charge.

Acknowledgment

This work is part of a continuing University of California program in sea water desalination.

Manuscript submitted Aug. 22, 1969; revised manuscript received Jan. 5, 1970.

Any discussion of this paper will appear in a Discussion Section to be published in the December 1970 JOURNAL.

LIST OF SYMBOLS

a_{H^+},	hydrogen ion activity
F,	Faraday constant
i,	current density, A/cm^2
i_o,	exchange current density for HER, A/cm^2
i_{corr},	corrosion current density, A/cm^2
k,	rate constant in Eq. [5]
k',	rate constant in Eq. [25]
k'',	rate constant in Eq. [26]
k_f,	film rate constant in Eq. [24]
n,	electrochemical reaction order with respect to hydrogen ion
R,	gas constant
R_p,	polarization resistance, ohm cm^2
T,	absolute temperature, °K
α,	over-all charge transfer coefficient
α_a,	anodic charge transfer coefficient
α_c,	cathodic charge transfer coefficient
α_f,	charge transfer coefficient for electromigration of electrons in film
β,	charge transfer coefficient for electrochemical desorption step, Eq. [19]
η,	($\psi - \psi_{corr}$), V
η',	hydrogen overpotential ($\psi - \psi_o$), V
ψ_{corr},	corrosion potential, V
ψ_o,	equilibrium potential for HER, V
ψ^o,	standard electrode potential, V
ψ_d,	potential across double layer
ψ_f,	potential across oxide film

REFERENCES

1. N. Hackerman and C. D. Hall, *This Journal*, **101**, 321 (1954).
2. M. E. Straumanis, S. T. Shih, and A. W. Schlecten, *J. Phy. Chem.*, **59**, 317 (1955).
3. V. V. Andreeva and V. I. Kazarin, *Proc. Acad. Sci. USSR, Phy. Chem. Sec.*, **121**, 577 (1958).
4. Ya. M. Kolotyrkin and P. S. Petrov, *Zhur. Fiz. Kim.*, **31**, 659 (1957).
5. A. T. Petrenko, *Russ. J. Phy. Chem.*, **36**, 815 (1962).

6. V. M. Artremova, *Soviet Electrochem.*, **3**, 1089 (1967).
7. N. T. Thomas and Ken Nobe, *This Journal*, **116**, 1748 (1969).
8. E. E. Millaway, *Mater. Protec.*, **8**, 16 (1965).
9. M. Stern and A. L. Geary *This Journal*, **104**, 56 (1957).
10. M. Stern and E. Weisert, *Proc. Am. Soc. Testing Mat.*, **59**, 1280 (1959).
11. J. O'M. Bockris, "Modern Aspects of Electrochemistry," Vol. 1, Chap. 4 Butterworth, London (1954).
12. R. Parsons, *Trans. Faraday Soc.*, **54**, 1053 (1958).
13. J. G. N. Thomas, *ibid.*, **57**, 1603 (1961).
14. B. E. Conway and M. Salomon, *Electrochim. Acta*, **9**, 1599 (1964).
15. N. D. Tomashov, R. M. Al'tovskii, and M. Ya. Kushnerev, *Proc. Acad. Sci. USSR, Phy. Chem. Sec.*, **141**, 927 (1961).
16. R. E. Meyer, *This Journal*, **107**, 847 (1960).
17. R. E. Meyer, *ibid.*, **110**, 167 (1963).
18. F. A. Posey, G. H. Cartledge, and R. P. Yaffe, *ibid.*, **106**, 582 (1959).
19. J. J. MacDonald and B. E. Conway, *Proc. Roy. Soc.*, **A269**, 419 (1962).
20. J. O'M. Bockris and S. Srinivasan, *J. Electroanal. Chem.*, **11**, 350 (1966).
21. T. R. Beck, *This Journal*, **15**, 890 (1968).
22. M. Pourbaix, Cebelcor report, R. T. 146, May 1968.
23. M. Pourbaix, "Atlas of Electrochemical Equilibria in Aqueous Solutions," pp. 213-22, Pergamon Press, New York (1966).
24. Y. V. Baymakov and O. A. Bieganski, U. S. Dept. of Commerce Report AD 613.519, MT 64-317 (1966).
25. B. Stalinski and Z. Bieganski, *Bull. Acad. Polanaise Sci.*, **X**, 247 (1962).

Specular Reflection Studies of Gold Electrodes *in situ*

T. Takamura, K. Takamura, W. Nippe, and E. Yeager*

Department of Chemistry, Case Western Reserve University, Cleveland, Ohio

ABSTRACT

Multiple specular reflection has been used to examine the gold electrode in acid and alkaline solutions. Reflectivity-potential and linear sweep voltammetry curves have been recorded simultaneously. The wavelength dependence indicates that reflectivity changes with potential arise principally because of the interaction of the d-c electric field at the interface with the internal photoelectric effect in gold corresponding to a 5d → 6s band transition. The results demonstrate that multiple specular reflection techniques are particularly well suited to *in situ* studies of the specific adsorption of ions, the formation of mono- and polylayer oxides, and the Faraday adsorption of ions such as lead and cadmium to form monolayers of these metals on gold.

Substantial interest has been expressed by electrochemists recently in the use of optical techniques for the examination *in situ* of electrode-solution interfaces. Ellipsometry and reflectance measurements have received the principal attention.

The purpose of this publication is to demonstrate how a simple multiple specular reflection technique can be used to obtain interesting information concerning adsorption phenomena, oxide formation, and the electronic properties of metal electrode surfaces. McIntyre (1) also has called attention to the suitability of specular reflection methods for *in situ* studies of adsorption and the formation of various layers. Holden and Ullman (2) have used specular reflectance to study anodic film formation interferometrically. Walter (3, 4) has used a grazing-angle specular reflection technique for *in situ* examination of electrode surfaces.

Gold electrodes were chosen for study not only because of their importance to electrochemistry but also because of the marked wavelength dependence of reflectance in the visible portion of the spectrum. An internal photoelectric effect (5-7) involving a 5d → 6s band transition ($L_{32} \rightarrow L_2$) leads to an edge in the optical reflectivity at approximately 2.3 eV or 5500Å. This transition should be sensitive to the interaction of surface orbitals with adsorbed species and the electric field at the interface. The plasmon excitation in gold is at ~8 eV, far in the vacuum ultraviolet.

Apparatus and Experimental Procedure

The measurement cell (Fig. 1) consisted of two flat gold electrodes mounted parallel with a 2-mm separation and backed by glass plates. These electrodes were connected in parallel and a third gold electrode (E in Fig. 1) was used as the counterelectrode in a compartment separated from the main compartment by a fritted glass disk. The potential of the parallel working electrodes was measured relative to a saturated calomel electrode in a separate vessel connected by a Luggin capillary whose tip was placed near the center of the parallel gold working electrodes but outside of the optical path. This arrangement is satisfactory provided the current density on the working electrodes is sufficiently small for no appreciable ohmic drop to occur in the electrolyte between them. Such was true for all of the work reported here with the exception of the cathodic peak associated with oxide reduction.

This cell was not gas tight and hence should be considered a preliminary model. Air-saturated solutions were used rather than having the solutions contaminated with some unknown amount of O_2 from the air. The electrolyte solutions were prepared from

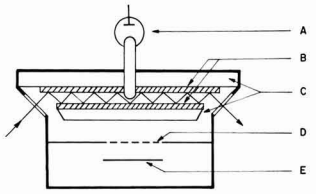

Fig. 1. Schematic diagram of specular reflection electrochemical cell. A, reference electrode (SCE): B, gold plates (working electrode).

* Electrochemical Society Active Member.

high-purity reagent grade chemicals and triply distilled water. The $HClO_4$ and H_2SO_4 solutions were pre-electrolyzed with gold electrodes. The NaOH solutions were not pre-electrolyzed and hence were contaminated with iron and other species.

The flat gold plates used as working electrodes were 99.99% pure, 0.5 mm thick, 25 mm high, and about 40 mm in length. They were polished on a flat glass plate with 5μ alumina grinding powder followed by 0.3μ chromic oxide grinding powder. After final polishing, the plates were cleaned with acetone, hot sodium hydroxide-ethanol mixture, and pure concentrated nitric acid, and finally rinsed with triply distilled water.

A monochromatic beam from a Beckmann DU spectrophotometer with a tungsten source was passed through the optically flat cell windows (Fig. 1) into the electrolyte and externally reflected approximately 20 times between the working electrodes at an angle of incidence near 50°. The reflected light was detected by a photomultiplier (RCA 1P28) and the signal then amplified with a chopper amplifier (Beckmann Model 5800) and fed to an X-Y plotter (Mosley Model 7000A) on which was also displayed the potential of the parallel gold electrodes *vs.* the reference electrode. The linearity of the photomultiplier-amplifier system with respect to optical intensity was checked by comparison with the detection-readout system ordinarily used with the Beckmann DU spectrophotometer. No polarizer was used in the optical system, but after a few specular reflections from the gold the light became plane polarized perpendicular to the plane of incidence.

Linear sweep cyclic voltammetry curves were recorded simultaneously on a second X-Y plotter in the usual manner with a Wenking potentiostat and Hewlett-Packard function generator (Model 3300A) at voltage sweep rates normally between 33 and 100 mV/sec. All potentials in this paper are relative to the saturated calomel reference electrode. The temperature was 22°-23°C.

Results

A typical reflectivity-potential curve at 5400Å and corresponding linear sweep voltammetry curve are given in Fig. 2 for a 0.2*M* $HClO_4$ solution. Small variations occur in the reflectivity and reflectivity dependence on potential from sample to sample, depending on the quality of the surface finish, but the shapes of the curves are invariant. Specific adsorption effects should be relatively small in this solution. The reflectivity-potential curve consists of two regions: linear characterized by slight hysteresis; and nonlinear corresponding to formation of an oxide layer and characterized by large hysteresis. Formation of stable gold oxide begins at about +1.1V on the anodic sweep branch (8-12) and at the same potential the reflectivity begins to decrease rapidly. The over-all decrease in Fig. 2 amounts to about 1% per single reflection. During the reverse potential sweep the reflectivity remains constant until the oxide layer starts to be reduced at about 1.0V. The large peak in the cathodic sweep in the voltammetry curve at 0.98V is attributed to the reduction of the oxide. Similar reflectivity-potential curves were obtained at all wavelengths (4800-8000Å) in both $HClO_4$ and H_2SO_4 solutions, although at wavelengths longer than 6000Å the plots showed some curvature in the region from 0 to 1.0V.

In Fig. 3 are superimposed the curves for the potential dependence of charge and reflectivity changes associated with formation and reduction of the oxide layer in 0.2*M* $HClO_4$. The charge-potential curve was obtained by integrating the voltammetry curve of Fig. 2. The reflectivity changes plotted in this figure correspond to the difference between the observed relative reflectivity in Fig. 2 and the value obtained by a linear extrapolation of the reflectivity change-potential curve recorded while scanning anodically in the potential range 0-1.0V. The two curves, including the hysteresis effects, correlate fairly well providing further evidence of the formation of the oxide layer and the attending reflectivity changes. At more anodic potentials in Fig. 3, the oxide layer is certainly more than a monolayer. Curves similar to those given in Fig. 3 have been obtained in 0.5*M* NaOH. Both the reflectivity and charge curves in Fig. 3 may be somewhat distorted by IR drop within the solution and nonuniform current distribution on the electrode surfaces.

The reflectivity change-potential curve in Fig. 3 resembles corresponding plots of the relative amplitude and phase retardation *vs.* potential obtained by Sirohi and Genshaw (12) from ellipsometric measurements on gold at 5500 and 6328Å in acid solutions at potential steps of 0.1V.

The relationship between the change in reflectivity and the extent of oxidation of the surface has been further examined by recording simultaneously the change in reflectivity and the charge passed as a function of time when the potential is stepped from a value just below that at which oxide starts to form (0.96V) to a value sufficient to form a multilayer oxide (*e.g.*, 1.20V). The plots of the change in reflectivity *vs.* charge associated with formation of oxide indicate two linear regions (Fig. 4) with the change in slope occurring at ~500 μcoul/cm^2, which probably corresponds to the completion of monolayer coverage.

The reflectivity-potential and voltammetry curves for an alkaline solution are shown in Fig. 5. The presence of oxygen in the solution contributed waves associated with the O_2-HO_2^- couple in the anodic and cathodic sweeps at potentials in the range 0 to −0.20V. The hysteresis in this potential range is probably caused by this couple. In contrast to the results in acid solution at wavelengths shorter than 6000Å, the non-oxide portion of the reflectivity-potential curve in NaOH solution is no longer characterized by a single linear region but rather appears to consist of two approximately linear portions intersecting at about −0.40V for the sweep in either the anodic or cathodic direction. This potential value corresponds to the point

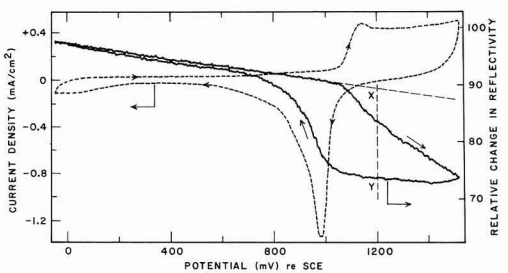

Fig. 2. Relative reflectivity change-potential (—) and current-potential (- -) curves of the gold electrode in 0.2M $HClO_4$ at 22°C. Potential sweep rate, 108 mV/sec; wavelength, 5400Å; electrode area, 23 cm^2; incident angle, 50°.

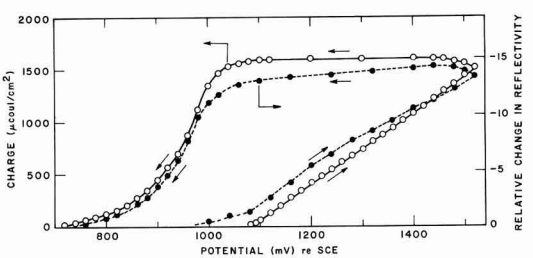

Fig. 3. Relative reflectivity change-potential (—●—) and charge-potential (—○—) curves for the formation of gold oxide layer obtained in 0.2M $HClO_4$. Conditions same as for Fig. 2.

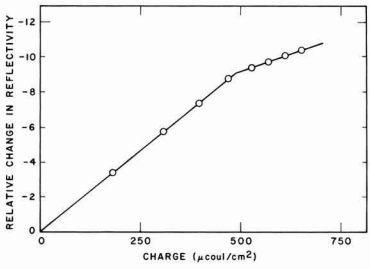

Fig. 4. Relative reflectivity changes *vs.* charge associated with oxide formation in 0.1M H_2SO_4 at 22°C. Wavelength, 6750Å; potential, +1.20V re SCE.

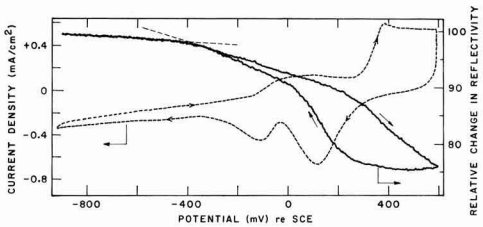

Fig. 5. Relative change in reflectivity-potential (—) and current-potential (- -) curves of gold in 0.5M NaOH at 22°C. Potential sweep rate, 104 mV/sec; wavelength, 5400Å; exposed electrode area, 23 cm^2; incident angle, 50°; number of reflections, 18.

of zero charge (pzc) reported by Eyring and coworkers (13) for gold in NaOH solutions. According to these workers, the pzc for gold in the 0.2*M* $HClO_4$ solutions used for the measurements in Fig. 2 is approximately −0.05V which is more cathodic than the voltage regions scanned in this figure.

To obtain further information on the relation of the reflectivity to the pzc, iodide ions were added to 0.5*M* NaOH solution (Fig. 6). The specific adsorption of I^- shifts the pzc to more negative values. The potential (E_A) of the intersection of the two linear portions of the reflectivity-potential curves is likewise shifted. A plot of E_A *vs.* log C_{I^-} is given in Fig. 6. Linearity is expected on the basis of the Esin-Markov effect (14). Three points in the semilog plot in Fig. 6 fall on a straight line with a slope of −0.060V/decade.

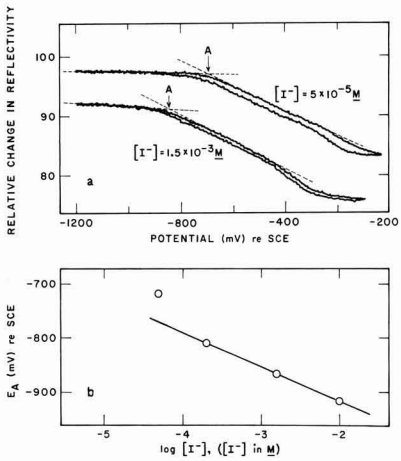

Fig. 6. Effect of iodide ions on the reflectivity-potential curves of gold: (a) in 0.5M NaOH and the shift of the potential of intersection of the two linear regions (E_A) with iodide concentration (b). Wavelength, 5600Å; other conditions same as in Fig. 5.

Some of the small hysteresis observed in Fig. 6 may be associated with the slow adsorption-desorption of I^-.

The sensitivity of the reflectivity curves to the pzc and specific ionic adsorption cannot be readily explained on the basis of the dependence of the reflectivity on the refractive index of the ionic double layer. The calculations of Stedman (15) and Prostak and Hansen (16) have shown that such effects should be too small to cause changes in the reflectivity of the magnitude observed in the present work.

The adsorption of ions on the electrode surface, however, can produce changes in the charge on the metal surface and the penetration of the electric field into the surface of the metal. These in turn would lead to changes in the carrier concentration in the surface of the metal as well as to changes in the photon energies required for the 5d → 6s band transition. Both of the effects would produce a change in the complex refractive index and hence the reflectivity of the interface.

The wavelength dependence of the reflectivity at various potentials provides further insight into the mechanism by which reflectivity changes with change in electrode potential. The wavelength dependence of the reflectivity, however, could not be recorded directly at given electrode potentials because the intensity of the light reaching the photomultiplier changes far too rapidly with wavelength after the large number of reflections involved in the present system. Consequently the wavelength dependence of the slopes of the reflectivity-potential curves has been examined instead. In Fig. 7 are plotted the relative rates of change of the reflectivity with respect to potential expressed in per cent $[(100/R)\ (dR/dE)]$ evaluated at 0.27V and +0.70V at 0.2*M* $HClO_4$. The slopes are the same at these two potentials for $\lambda \leq 5500$Å since the reflectivity-potential plot is linear in this region. Also plotted in this figure is the change in reflectivity associated with the formation of the oxide at a potential of +1.20V (taken as the distance X-Y in Fig. 2). The maxima in all three curves occur at 5500Å where the reflectivity of gold changes rapidly due to the 5d → 6s band transition (see insert drawing in Fig. 7). This implies that the maximum in these curves is caused by the rapid change in reflectivity of the gold. Feinleib (17), using an a-c modulation technique obtained a peak at the same wavelength in his electrochemical reflectance studies of gold. The slopes plotted in Fig. 7 correspond to the a-c signal obtained by Feinleib, who used a modulation potential of 2V which probably encompassed the linear region of Fig. 2, the oxide region, and perhaps the H_2 evolution region. Thus the quantitative significance of his results is in doubt.

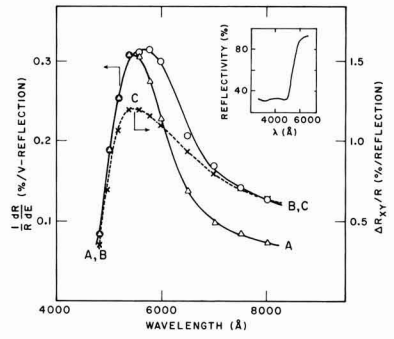

Fig. 7. Wavelength dependence of reflectivity change. Curve A, $(1/R)\ (dR/dE)$ at $E = +0.27$V re SCE. Curve B, $(1/R)\ (dR/dE)$ at $E = +0.78$V re SCE. Curve C, relative reflectivity change (X-Y in Fig. 2) for oxide formation. Conditions same as for Fig. 2. Insert figure, reflectivity of gold in air (17).

The relative slope *vs.* wavelength plot for +0.27V in Fig. 7 indicates that the effects of potential become relatively small at wavelengths remote from the maximum. Even when these relative slopes are converted to absolute values by multiplying by the absolute reflectivity, the absolute slope for +0.27V still passes through a pronounced maximum at 5500Å. This means that the principal effect of changing the electrode potential on the reflectivity-wavelength curve at potentials from 0 to ~+0.4V is to translate the curve along the wavelength scale with the change in reflectivity negligible at wavelengths shorter than the threshold for the 5d → 6s band transition. The direction of the shift along the wavelength scale indicates that the photon energies required for the transition become lower with increasing anodic potential. Such a decrease in the minimum photon energy required for this transition is in accord with the idea that the transition is from the top of the 5d band to the Fermi level and that the top of the 5d level bends upward (higher energy) at the surface, while the Fermi level is relatively invariant.

Prostak and Hansen (16) calculated the change in reflectivity for the gold-electrolyte (1*M* KCl) interface assuming a 0.5Å thick surface layer in the metal phase in which the optical constants have been modified by an amount equivalent to a photon energy of 0.1 eV due to penetration of the electric field into the metal. By applying Maxwell's equations to a three-layer structure, these authors obtain a change in reflectivity (100 $\Delta R/R$) at normal incidence of 0.07% at 5500Å, compared with a value of $(1/R)dR/dE = 0.3\%/$V per reflection observed at this wavelength in the present work at an angle of incidence of 50° for an applied potential +0.27V. The four-fold discrepancy is not surprising since the comparison is valid only if the penetration depth is 0.5Å and 10% of the change in applied potential occurs within this layer, aside from the difference in angle of incidence. The calculated change in reflectivity should be larger for a deeper penetration and for a larger electric field within the metal. Therefore, the experimental values appear reasonable in terms of a model involving the penetration of the field into the metal to a depth of the order of 1Å.

The shift in the slope of the linear portion of the reflectivity-potential curve associated with passing through the pzc can be explained on the basis of a change in the fraction of the applied electric field which penetrates into the metal surface. Such a change in the distribution of the potential at the interface is certainly to be expected when the ions predominating in the plane of closest approach to the electrode surface are changed from anions to cations and the solvent dipoles at the interface probably reorient.

The maximum in the curve in Fig. 7 corresponding to the reflectivity change for the oxide can be interpreted in terms of a shift in the threshold frequency of the 5d → 6s band transition resulting from the interaction of the oxide ions with the surface orbitals of the metal. An alternate view of the same phenomenon is that the local field produced by the oxide ions penetrates into the metal phase thus shifting the threshold frequency of the 5d → 6s transition. The decrease in reflectivity caused by the oxide, however, persists at longer wavelengths (see Fig. 7) and hence the reflectivity is decreased by some other mechanism at longer wavelengths. One possibility is a change in carrier concentration and mobility in the surface layers of the metal due to the local field of the oxide ions.

Various workers (12, 18-20) have proposed that the chemisorption of an oxygen species; *i.e.*, AuO or AuOH, occurs on gold at potentials more cathodic than those of oxide layer formation. Sirohi and Genshaw (12) have explained the changes in phase retardation and amplitude in their ellipsometric studies of gold at relatively cathodic potentials in terms of the chemisorption of an oxygen species, which modifies the optical constants of the metal phase. Without some kind of relatively slow adsorption-desorption process, these authors find it difficult to explain the observed time dependence.

Unfortunately the present results do not provide strong evidence for or against such chemisorption at potentials cathodic to the oxide region although it may cause the curvature noted in the reflectivity-potential curves in the potential range +0.3 to 1.0V at $\lambda > 6000$Å. Why this curvature is not evident at shorter wavelengths remains to be explained.

The Faradaic adsorption of lead and cadmium on the gold electrodes has been examined using the present apparatus. Lead or cadmium ions strongly adsorb on gold at far more positive potentials than the standard electrode potentials of these ions (21, 22). Reflectivity-potential and current-potential curves for gold in 0.2*M* $HClO_4$ containing 5 x 10^{-4} *M* Pb^{2+} are shown in Fig. 8. The Faradaic adsorption and desorption peaks for Pb occur at +0.10V in the voltammetry curve. The surface concentration of adsorbed Pb estimated from the area under the voltammetry peaks corresponds to 400 μcoul/cm^2, providing further evidence for monolayer formation. The reflectivity-potential curve shows a marked change on adsorption or desorption of the lead atoms and is quite wavelength-dependent (Fig. 9). At shorter wavelengths, *e.g.*, 5000Å, the reflectivity increases on the formation of the Pb monolayer, whereas at longer wavelengths, *e.g.*, 7500Å, the reflectivity decreases. A similar situation has been found with cadmium (Fig. 9).

The wavelength dependence of the change in reflectivity attending the formation of lead and cadmium monolayers remains to be explained but is not sur-

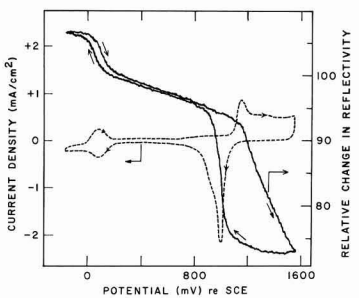

Fig. 8. Relative change in reflectivity-potential and current-potential curves for gold in the presence of Pb^{+2} ions. Electrolyte: 5 x 10^{-4}*M* Pb^{2+} + 0.2*M* $HClO_4$. Potential sweep rate, 105 mV/sec; wavelength, 5200Å; other conditions same as for Fig. 6.

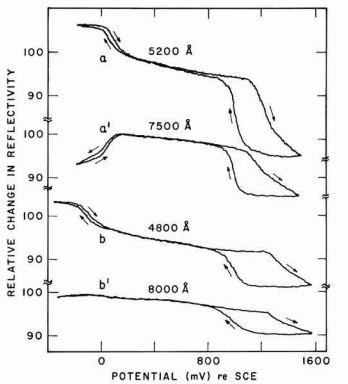

Fig. 9. Relative change in reflectivity-potential curves at various wavelengths in the absence of Pb^{2+} or Cd^{2+}. Electrolyte: curves a, a'; 5x10^{-4}*M* Pb^{2+} + 0.2*M* $HClO_4$. Curves b, b'; 1x10^{-3}*M* Cd^{2+} + 0.2*M* $HClO_4$. Potential sweep rate, 105 mV/sec; other conditions same as for Fig. 2.

prising since a monolayer of foreign metal atoms on the gold surface has specific electronic and hence optical properties. This wavelength dependence should provide an important tool in studying the electronic properties of such monolayers.

The work reported here is preliminary. It has demonstrated, however, that specular reflection techniques can be used to: (*i*) establish the point of zero charge for solid metal electrodes, (*ii*) follow adsorption and desorption, and (*iii*) obtain information concerning the surface electronic properties of metal electrodes and the penetration of the electric field into the metal phase.

Acknowledgment

The authors are pleased to acknowledge the support of this research by the U.S. Office of Naval Research.

Manuscript submitted Oct. 17, 1969; revised manuscript received *ca.* Dec. 22, 1969. This was Paper 257A presented at the New York Meeting of the Society, May 4-9, 1969.

Any discussion of this paper will appear in a Discussion Section to be published in the December 1970 JOURNAL.

REFERENCES

1. J. D. McIntyre, Paper 232 presented at the New York Meeting of the Society, 135th National Meeting, Electrochemical Society, May 4-9, 1969; Extended Abstracts, pp. 578-579.
2. B. J. Holden and F. G. Ullman, Papers 52, *ibid.*; Extended Abstracts, pp. 61-4.
3. D. C. Walter, *Can. J. Chem.*, **45**, 807 (1967).
4. D. C. Walter, *Anal. Chem.*, **39**, 896 (1967).
5. R. Zallen in "Optical Properties and Electrical Structures of Metals and Alloys," p. 164, F. Abeles, Editor, John Wiley and Sons, Inc., New York (1966).
6. D. Beaglehale and T. J. Hendrickson, *Phys. Rev. Letters*, **22**, 133 (1969).
7. A. Mooradian, *ibid.*, **22**, 185 (1969).
8. F. G. Will and C. A. Knorr, *Z. Electrochem.*, **64**, 270 (1960).
9. H. A. Laitinen and M. S. Chao, *This Journal*, **108**, 726 (1961).
10. S. B. Brummer and A. C. Makrides, *ibid.*, **111**, 1122 (1964).
11. G. Gruneberg, *Electrochim. Acta*, **10**, 339 (1965).
12. R. S. Sirohi and M. A. Genshaw, *This Journal*, **116**, 910 (1969).
13. D. D. Bode, T. N. Anderson, and H. Eyring, *J. Phys. Chem.*, **71**, 792 (1967). See also, G. M. Schmid and N. Hackerman, *This Journal*, **109**, 243 (1962); M. Green and H. Dahms, *ibid.*, **110**, 466 (1963).
14. O. A. Esin and B. F. Markov, *Acta Physiochim. URSS*, **10**, 353 (1939).
15. M. Stedman, *Chem. Phys. Letters*, **2**, 457 (1968).
16. A. Prostak and W. N. Hansen, *Phys. Rev.* **160**, 600 (1967).
17. J. Feinleib, *Phys. Rev. Letters*, **16**, 1200 (1966).
18. J. P. Hoare, *This Journal*, **110**, 245 (1963).
19. J. P. Hoare, *Electrochim. Acta*, **9**, 1289 (1964).
20. G. M. Schmid and R. N. O'Brien, *This Journal*, **111**, 832 (1964).
21. E. Schmidt and H. R. Gygax, *J. Electroanalyt. Chem.*, **13**, 378 (1967); **14**, 126 (1967).
22. E. Schmidt, Paper B5, 19th Meeting of CITCE, Detroit, September 1968; Extended Abstracts, pp. 43-46.

Galvanostatic Overpotential Transients and Electrocrystallization Processes on Copper Single Crystals in Solutions of Cupric Perchlorate

L. H. Jenkins*

Solid State Division, Oak Ridge National Laboratory, Oak Ridge, Tennessee

ABSTRACT

Overpotential transients have been measured on copper single crystal surfaces oriented (100), (110), (111), and (321) undergoing galvanostatic dissolution or deposition in acidic solutions of $Cu(ClO_4)_2$. In the current density range 1-400 $\mu A/cm^2$ it is shown that maximum values observed in overvoltage-time relationships respond to analytical treatment. For the (100) and (110) the anodic and cathodic overpotential maxima *vs.* current density relationships were symmetric about the equilibrium point, but not for the (111) and (321). From plots of certain functions of overvoltage maxima *vs.* current density, orientation sensitive quantities similar to exchange current densities could be calculated. At the low and intermediate current densities it was established that a "deposition anomaly" was observed on all orientations. Deposited material did not seem to occupy crystal lattice positions, and moreover, affected subsequent anodic overpotential-time relationships in a manner related to the extent of the deposition. *In situ* photomicrography and goniometric observations were used to determine the orientations and rates of facet development on the various surfaces when subjected to long term deposition or dissolution, and these results are discussed in terms of the relative ease of movement of monatomic steps over the various orientations. A model is proposed of a sequence of events on the surface and in the diffusion layer which provides a self-consistent explanation of all the experimental data.

The behavior of copper serving as electrodes in acidic solutions of cupric perchlorate have previously been studied by Piontelli, Poli, and Serravalle (1) and by Bockris and Enyo (2). Among other things, both studies attempted to relate kinetic parameters of the systems to structural characteristics of various electrode surfaces. Also, Shanefield and Lighty (3) have observed the changes in growth forms on copper (100) surfaces produced by electrodeposition from cupric perchlorate solutions containing various impurities.

The report of Piontelli *et al.* concerned data for copper single crystal surfaces oriented (100), (110), and (111) in which the "quasi-steady" overvoltages observed under galvanostatic conditions at current

* Electrochemical Society Active Member.

densities of ~ 1-10 mA/cm^2 were orientation dependent. Anodic and cathodic data were not symmetric about the equilibrium point for any one orientation, nor were the relative differences between orientations the same for anodic and cathodic processes. Employing spherical electrodes ~ 0.1 cm in diameter, Bockris and Enyo determined kinetic parameters for surfaces prepared by melting in helium or by electrodeposition. In ~ 0.1M $Cu(ClO_4)_2$ at current densities $\gtrsim$ 10 mA/cm^2 the data indicated charge transfer to be the rate-controlling step, but it was suggested that at lower current densities surface diffusion was the slow process. Certain differences observed between the two types of electrodes were thought to arise from differences in dislocation densities.

Data such as these indicate that perhaps the determination of pertinent kinetic parameters at current densities lower than those studied previously would, when augmented by observations of changes in surface structure resulting from long-term dissolution or deposition, yield information regarding the effects of structure on the reactivity of a metal surface. Obviously there are many other relevant reports in the literature concerning the behavior of copper electrodes in solutions of copper ions. As a matter of fact, data regarding systems of copper sulfate far exceed that related to perchlorates. However, the work previously cited regarding the latter provides an adequate basis to discuss the research reported here, and similar work in sulfate systems which is currently being prepared for publication will provide opportunity later for discussion of other systems.

Materials.—Preferentially oriented cylindrical copper single crystal slugs approximately 25 mm diameter x 100 mm were grown in this laboratory by seeding 99.999+% metal from the melt in graphite crucibles. From such crystals coin-shaped specimens ~ 7 x 25 mm were cut with an acid string saw, and the flat surface chemically polished on a soft cloth polishing wheel using an aqueous solution containing $CuCl_2$, HCl, and H_3PO_4. Finally, the crystals were electropolished in a copper-containing phosphoric acid bath, rinsed in dilute phosphoric acid, and washed in distilled water. [Details of these procedures have been published previously (4, 5).] The manipulations introduced no new dislocations into the crystals, and the average dislocation density in as-grown material was ~ 5 x 10^4-10^6 cm^{-2}. The large surfaces prepared in this manner were not absolutely flat, but rather contained a few gentle undulations such that the average orientation was within ± 0.1° of that desired.

Solutions of $Cu(ClO_4)_2$ were prepared from doubly recrystallized material and stored in rack reservoirs in the manner previously described (6). All solutions used in this study were 0.20M in $Cu(ClO_4)_2$ with *p*H adjusted to ~ 1 by addition of $HClO_4$. When introduced into the Teflon cells they were free of dissolved oxygen, under an atmosphere of hydrogen, and in equilibrium with polycrystalline metallic copper. Ultrapure grade (99.999+%) tank hydrogen was passed through a platinum catalytic purification system and then through magnesium perchlorate drying towers before using.

Experimental methods.—Two types of reaction cells were used. One type, illustrated in Fig. 1, was used to obtain galvanostatic current-potential data. The apparatus consisted of a large brass support plate with a flat surface and an O-ring groove. On this was mounted a pipe flange-type reaction flask cover with fine ground face and standard taper outer joints. A shallow dish of Teflon sat within this enclosure. Four ports with thin, beveled lips in the bottom of the Teflon dish provided for isolation of the crystal orientation of interest. The copper specimens were pressed against the lips of the port and held in place by gentle pressure from the mounting screws in the manner shown. The diameter of the ports was such that 2 cm^2 geometric

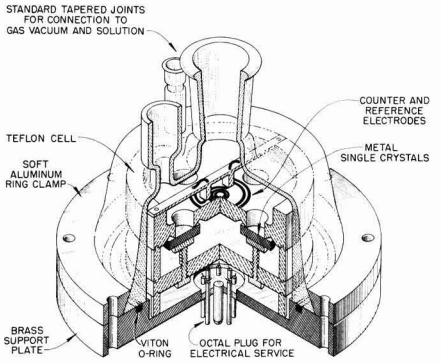

Fig. 1. Cell for isolating single orientations and determining current-overpotential characteristics.

area of each crystal surface was exposed to the solution. Infrequently, crystals of different orientation were mounted in each of the four available ports. Usually only three orientations were used in order to obtain duplicate data for one of them. Polycrystalline copper wires suspended from a cross member over the dish served as counter and reference electrodes. Electrical access was provided through a vacuum tight octal plug welded in the brass support plate. After the crystals were mounted and appropriate electrical connections made, the flask cover was placed over the dish and secured to the plate by a ring clamp. The entire apparatus was then attached to the solution flask and hydrogen and vacuum lines on a mounting rack. Usually a glass electrode inserted through the small standard taper port served as an auxiliary reference electrode. After repeated evacuation and flushing with hydrogen over a period of at least two days, solution was admitted to the system. Appropriate stopcocks were then closed, the entire system detached from the rack, and placed in an air bath maintained at 23.00° ± 0.02°C and which was surrounded by a Faraday cage. Potential measurements were made with either vibrating reed electrometers or a Philbrick P-2 operational amplifier, and data were recorded either on a strip chart recorder or by photography of oscilloscope traces, respectively.

The second type of reaction cell is shown in Fig. 2. The main body of the cell was machined from 99.99+% copper. After the viewing glass was attached, an electropolished crystal was mounted and pressed against the lower Viton O-ring. (Since all O-rings contacted the solution, they previously had been soaked for many hours in hot solutions of the same composition as the test solution.) Solution was introduced to the system through the small side port in the main body of the

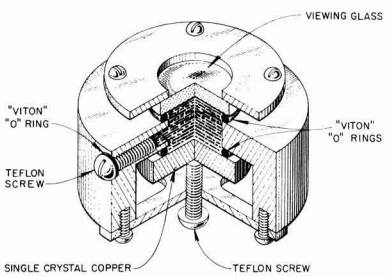

Fig. 2. Cell permitting microscopic observation and time-lapse photomicrography of surfaces. Main cell body of 4/9s copper serves as counterelectrode.

cell with the aid of a pipette drawn to a needle tip capillary. Obviously, it was impossible to maintain an inert atmosphere within the cell while filling the system. Because of this, the solutions used in the 2-ml capacity cells were not free of dissolved oxygen, nor certainly were they initially at equilibrium with copper metal. As in the previous cell, 2 cm^2 geometric surface area of the crystal was exposed to the solution. The cell was filled to the top of the port such that insertion of the closure screw with O-ring seal caused overflow and prevented entrapment of air within the system. After filling and sealing, the cell was set aside for a period of at least two weeks so that equilibrium could be established. The cell was then placed on a microscope stage, and using the body of the cell as a counterelectrode, changes in single crystal surface structures due to dissolution or deposition process concomitant with the passage of current through the system were observed and recorded by time lapse photomicrography. A few systems were closed with a Teflon screw which contained a polycrystalline copper wire sealed through its length to serve as a reference electrode, but usually no attempts were made to measure potentials within these cells. All the data discussed here were obtained under galvanostatic conditions. The current source was a dry cell pack, and current flow was regulated by fixed in-line resistors with resistance values very large compared with those of the various cells.

In all cases when the reaction cells were opened, crystals were examined and photographed under the microscope. Orientations of surface facets were determined with a two-circle reflection goniometer. In instances in which deposition had been to an extent great enough to make the observations valid, Laue back reflection x-ray techniques were used to establish the orientation of the deposited metal.

Experimental Results

Changes in surface structure.—Using the copper body cells, observations were made on surfaces oriented (100), (110), (111), and (321). Data were taken at constant currents of 4, 40, and 400 $\mu A/cm^2$ original surface area for all orientations during both dissolution and deposition, and a few observations were made at other current densities also. Under any given combination of experimental conditions the changes observed in a surface structure were reproducible. Data always were obtained from duplicate systems, and in many cases from triplicate, so that the results discussed below derive from more than 60 different crystals. In all cases tested, deposits were single-crystalline and oriented like the substrate.

(100).—Under all experimental conditions dissolution of the (100) was completely uniform and regular, and resulted in the formation of square pits. Figure 3 shows that rapid removal produced a more regular and well-defined pit than removal of a like amount of material at a lower rate. At lower current densities sides of pits were less well defined and apparently relatively more material was removed by motion of steps over the original surface than at higher current densities. Nevertheless, in general, such differences were of degree rather than kind.

By comparison, deposition on the (100), although accompanied by the formation of four-sided pyramids, did not occur in as regular and uniform a manner. At higher current densities pyramids of a uniform size developed, but at current densities $\lesssim$ 100 $\mu A/cm^2$ (although initial deposition and growth occurred uniformly) some pyramids soon began to develop at a much greater rate than others. A few of these larger pyramids, appearing dark to the viewer, had sides $\sim$ 22° from the (100), but they were outnumbered approximately 10:1 by the lighter appearing large kind with sides $\sim$ 8° from the original surface. The number of large pyramids, both light and dark, comprised less than 1% of the total number on the surface. However, initial deposition occurred uniformly, and the formation of large pyramids seemed apparently a random fluctuation. As a first approximation, growth rates of topographic features were linear in time. Deposition growth forms occurred in an even less uniform manner at 4 $\mu A/cm^2$. Again, although nucleation of small pyramids apparently occurred over the entire surface, random large growths began to develop. At this low current density much of the material seems to have been deposited by step motion over the original surface, similar to the case for dissolution, for the volume of material contained in the pyramids was calculated to be only $\sim$ 20% of the total deposited.

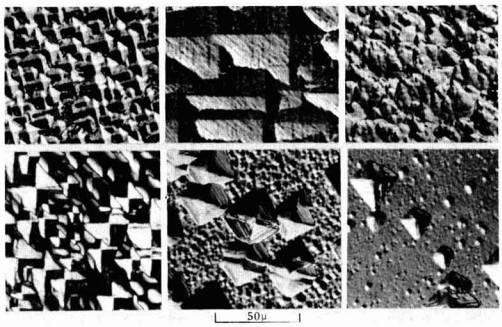

Fig. 3. Structures developed on (100) due to long-term galvanostatic processes. Upper photographs represent features developed by anodic process after removal of the equivalent of $\sim$ 4.5 coulombs cm^{-2} at current densities (left to right) of 4000, 40, and 4 $\mu A\ cm^{-2}$, respectively. Lower photographs after deposition equivalent to $\sim$ 1.0 coulombs cm^{-2} at (left to right) 400, 40, and 4 $\mu A\ cm^{-2}$.

Facets formed by both pyramids and pits always were oriented along <100> zones, and no facets on any other zones were ever obtained under the stated conditions. As in the case previously reported (7) pit bottoms always were within $\sim$ 5° of the original (100), but as indicated above, deposition-formed facets exhibited more varied orientations.

(110).—Structures developed on the (110) were very similar under all conditions. Reaction always occurred in a uniform manner and invariably resulted in the formation of a well-defined series of sharp-topped ridges separated by equally sharp-bottomed valleys, as illustrated in Fig. 4. Ridge sides were never formed other than along the <100> zone, and faceting was more or less continuous along this zone out to $\sim$ 40° from the (110).

(111).—The (111) also seemed to react in a completely uniform manner. Either dissolution or deposition apparently occurred by the removal of material at submicroscopic steps on the surface. In early stages, these

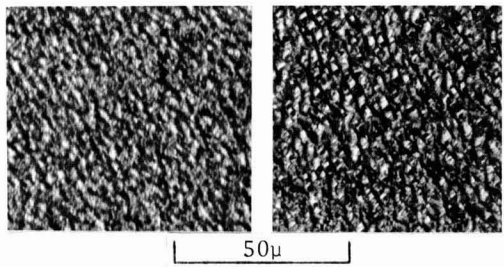

Fig. 4. Typical structures developed on the (110), left, and (321) right. Former shown after dissolution of $\sim$1.5 coulombs cm^{-2} at 4 $\mu A\ cm^{-2}$, and the latter after equivalent deposition at 400 $\mu A\ cm^{-2}$.

steps interacted to form small ledges of such great density that the entire surface appeared roughened. As the process continued, small ledges interacted to form large ledges separated by apparently flat (111) surfaces, such that the surface appeared as smooth over local areas as at initiation of reaction. Figure 5 is a series of photomicrographs, some taken *in situ* of the same area, which illustrates this process. The large ledges formed in all cases were, of course, highly faceted.

(321).—This surface also seemed to react in a uniform manner with no appreciable difference in the facets produced by dissolution or deposition. A great deal of (111) faceting was always observed (see Fig. 4), and this was accompanied by the development of companion facets along the two <100> zones, such that nonsymmetrical, triangular shaped pits or pyramids were formed. At high current densities facets developed along these zones approached within 4° of the (100). At lower current densities faceting along the <100> zones tended to be further removed from the (100) and nearer the (210).

Potential vs. time data.—Data obtained in the Teflon cells at all current densities (1-400 μA/cm^2), both anodic and cathodic, and on all four orientations studied revealed that potential *vs.* time curves of working electrodes exhibited maxima generally of the shape observed by Roiter *et al.* (8) on zinc single crystals in solutions of zinc sulfate. However, one important difference must be noted: The times to formation of the maxima reported here are much too long (generally by an order of magnitude) to be associated with charging of the double layer. True steady-state overpotentials could not be established on any of the crystals, in that, following establishment of a maximum value, if the current passed long enough, the measured overpotential gradually decreased. Ultimately microscopic changes in surface structure could be observed without a true steady state being established, although pseudo-steady states frequently were observed shortly after maxima were established. Figure 6 illustrates typical potential-time curves of overvoltages for the orientations studied. The excellent reproducibility of the values of the potential maxima, as well as times to formation, for successive anodic pulses is clearly indicated. Cathodic overpotential-time relationships were equally reproducible. As shown, excellent agreement between the absolute values of anodic and cathodic maxima were obtained, although at current densities $\lesssim$ 100 μA/cm^2 slightly longer times were often required to establish the latter. Note also at the lower current density shown the post-maximum overvoltage-time relationship is quite different in the anodic and cathodic cases. At higher current densities times to formation of maxima were approximately equal for both processes, but again over-all overvoltage-time relationships were not precisely similar.

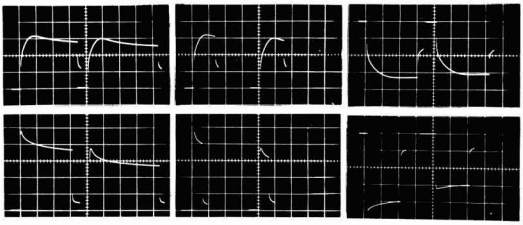

Fig. 6. Oscilloscope traces of "normal" overpotential-time relationships. Top row all at 30 μA/cm^2, 5 mV/div vertical scale, 2 sec/div horizontal scale, from left to right: anodic (110), (321); anodic (110), (321); cathodic (110), (321). Bottom row all at 150 μA/cm^2, 10 mV/div vertical scale, 1 sec/div horizontal scale, from left to right: anodic (100), (111); anodic (100), (111); cathodic (100), (111).

The most interesting feature of the deposition process was its effect upon a subsequent anodic pulse. Overvoltage-time relationships were altered drastically for an anodic process which had been preceded by a cathodic pulse. [Similar phenomena have been observed on other single crystalline material (9).] This is illustrated in Fig. 7 which, when compared with Fig. 6, shows that such anodic maxima can take much longer to become established than under postanodic conditions. Also, the absolute values of these overpotential maxima are greatly reduced at higher current densities, and in all cases the entire overvoltage-time relationship is altered. Interestingly enough, only very slight differences were observed between postanodic and postcathodic overpotential-time relationships during deposition, and the value of a cathodic overpotential maximum rarely showed noticeable effects of previous electrode processes. Due to excessively long decay times following cathodic current interruption, an exhaustive study of postdeposition cathodic overpotential-time relationships was not undertaken. These observations will be of considerable significance in later discussions concerning interpretation of all the data.

The extent of this postdeposition anomaly was dependent on the current density, deposition time, orientation of the surface to some extent, and the time lapse

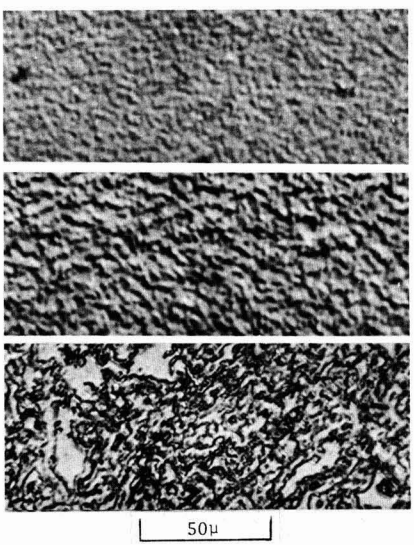

Fig. 5. A (111) surface undergoing dissolution at 400 μA/cm^{-2}. Top and middle are *in situ* views of the same area after 6- and 15-min reaction, respectively. Lack of definition is due to the difficulty of lighting and focusing through the cell and solution. Bottom illustrates a view of the same crystal after removal from the cell following 1 hr of reaction.

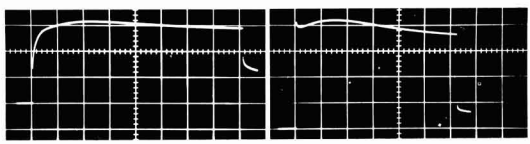

Fig. 7. Oscilloscope traces of postcathodic, anodic overpotential-time relationships ½ hr after a cathodic process at the same current density. Left: (110) at 30 μA/cm^2, 5 mV/div vertical scale, 2 sec/div horizontal scale. Right: (100) at 150 μA/cm^2, 10 mV/div vertical scale, 1 sec/div horizontal scale. Compare with extreme left trace, top and bottom, respectively, of Fig. 6.

between deposition and subsequent dissolution. The effect was more pronounced at low current densities, < 25 $\mu A/cm^2$, than at high, > 150 $\mu A/cm^2$. Consequently, effects of deposition time were also more pronounced at lower current densities. In general, low current density deposition, as indicated in Fig. 8, increased the time to formation of the succeeding anodic maximum by an amount proportional to the extent of deposition. At current densities > 200 $\mu A/cm^2$ even slight deposition effects were not detectable after periods more than one hour. At extremely low current densities, < 5 $\mu A/cm^2$, the effect could be observed for periods of many hours.

Other ambiguous potential-time relationships were observed. Whether the electrode supported an anodic or cathodic process at higher current densities, about 10 min were required to re-establish equilibrium potential after the flow of current was interrupted. However, at low current densities recovery time was much longer. For example, a current of 300 $\mu A/cm^2$ flowing for 1 sec typically would establish an overvoltage maximum near 50 mV in ~ 0.03 sec, and would regain rest potential within 10 min following current interruption. After 60 sec at 5 $\mu A/cm^2$ (equal charge passed) a maximum typically would not have yet been established, the observed overvoltage would not have exceeded ~ 10 mV, and still it could require hours for the rest potential to become re-established. Therefore, it appears that the rate of potential decay was not directly related to the absolute value of the observed overvoltage, nor, in a simple manner, to the quantity of current flowing. In general, recovery time following a cathodic process would exceed that following an exactly similar anodic pulse.

Current potential data.—At this point it is important that it be understood that, unless otherwise indicated, the overpotentials quoted in the presentations which follow are always values of the postanodic maxima. That is to say, every cathodic pulse applied in systems in which current-potential characteristics were being determined was followed by an anodic pulse of equivalent magnitude and duration. This latter pulse was disregarded, and equilibrium allowed to become established in the system. Only then was the next electrode process of interest initiated and data recorded.

Figure 9 illustrates the current-potential relationships obtained on the various surface orientations in this study. The following experimental observations are shown by the figure: (*i*) The curves for (100) and (110) are symmetrical about zero current and overpotential. (*ii*) While it is not obvious from this figure, the (321) data are not exactly symmetric about zero. (*iii*) The (111) data are obviously asymmetric in that at any given current density the absolute value of the cathodic maximum is smaller than that of its anodic counterpart. (*iv*) At any current density the absolute value of the overvoltage associated with the process was a function of crystal orientation, increasing in the order (321) $<$ (110) $<$ (100). The (111) obviously cannot be included in this generalization because of the asymmetric character of the data. (*v*) Since the step densities on the (100), (110), and (111) must be approximately equal and much smaller than that of the (321), measured overvoltage maxima are independent of the surface step density.

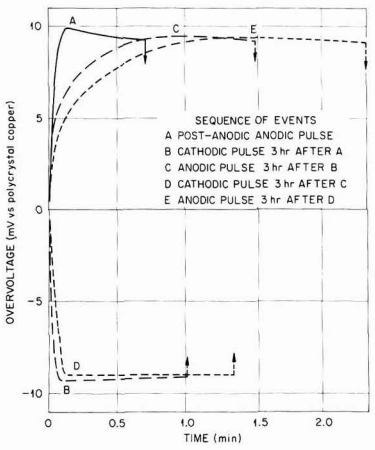

Fig. 8. Effects of deposition on overvoltage-time relationships on the copper (321) orientation at 15 $\mu A/cm^2$.

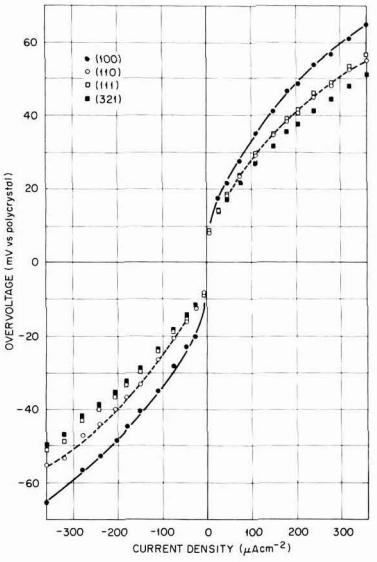

Fig. 9. Overvoltage maxima for variously oriented copper single crystals as a function of current density in solutions of 0.2M $Cu(ClO_4)_2$ and $HClO_4$ ($pH \sim 1$) at 23°C.

Discussion

Surface structure.—The classic model of electrocrystallization processes assumes that, after crossing the double layer and undergoing stepwise discharge, atoms ultimately are incorporated into the crystal lattice at kink sites on steps. Whether this is accomplished by diffusion of adatoms over the surface to steps or by direct action at step and/or kink sites, deposition or dissolution ultimately may be described as occurring by the "motion of steps" over the crystal surface, and use of the phrase here does not imply a choice as to the mechanistic detail. Sources of steps are crystal edges, dislocations, new steps nucleated during the processes, and departures from close-packed arrangements due to crystal orientation. It is difficult to assess the exact number of steps arising from dislocations, but if it is assumed that all dislocations have a screw component and that an equal distribution of dislocations of equal and opposite sign exists, the maximum number of steps generated by dislocations should be of the order of the square root of the dislocation density. On the other hand, a misorientation of only $\sim 0.1°$ from a close-packed arrangement will produce $\sim 10^5$ steps cm^{-1}. It is readily seen that, since the surfaces used in this study could not be prepared with orientations better than $\pm 0.1°$, the density of orientation related steps was approximately two orders of magnitude greater than that produced by the maximum dislocation density, $\sim 10^6$ cm^{-2}. Furthermore, although apparently it is not generally recognized, the major

source of steps on a large number of noncleaved metal surfaces employed in studying electrocrystallization phenomena is just such slight misorientations. One other fact is most helpful in discussing the structures developed on the surfaces reported here: Young and Hulett (10) have demonstrated that steps on a copper (111) surface arising from misorientations of $\sim 0.1°$ can sustain a current density as great as 10 mA/cm^2 over long periods of time without nucleation of new steps becoming necessary. This is a current density two orders of magnitude greater than the highest employed in these studies.

It could be assumed that facets developed on (321) surfaces are the end products of complex step interactions and reflect more of the nature of such interactions than of the model substrate supporting the steps. On the other hand the interaction on the (111) of steps to form ledges, which in time aggregated to form larger ledges separated by apparently flat (111), does indicate something of the nature of that orientation. First it is clear that bunched steps constitute a reasonably stable array. Their rapid rates of formation suggest material is as easily added or removed on this surface from such an array as from the initial configuration. Ledges formed are large enough to be considered discreet areas of orientation other than (111), which in turn suggests that step motion over the (111) occurs with some difficulty. At lower current densities on the (100) observations clearly indicated a large portion of the process had to be sustained by step motion since all material was not accountable by pit or pyramid formation. However, as kinetic demands increased, it appears step motion was insufficient to support the reaction, and facets over which steps could move with greater facility were formed. The absolute failure ever to develop facets within $\sim 5°$ of the (100) would indicate that step motion over this orientation is most difficult of any orientation studied. The same type of argument can be used to explain formation of a ridge-valley structure on the (110). In summary, it is proposed that facet development on close-packed orientations is a consequence of the relative difficulty with which steps move over such surfaces. However, facets of close-packed arrangements can be developed as a result of step motion on surfaces with large step densities, such as (321), since the latter contain components of the former within their structure. As a consequence of this argument it must be concluded that, once facets are developed on a surface, little reaction occurs on the areas covered by low index facets, and the surface is in a true sense no longer acting in a uniform manner.

The fact that regardless of initial orientation a large proportion of the total facets formed were oriented along <100> zones suggest that steps move along the <100> zone with relative ease. The low angle facets developed on (100) indicate that the degree of faceting is related to the rate of the surface process in that only those facets necessary to support the reaction are formed. This proposal is substantiated by the observation that at high current densities facets on the (321) formed orientations near the (100), while those formed at lower current densities were further removed from the (100) along the two <100> zones.

Finally, it should be stated there was no evidence that the defect structure of the copper crystals played a significant role in crystal growth or dissolution. Even the pits and pyramids on the (100) could not be related to the crystal defect density.

Overpotential-time data.—Before discussing the overpotential-time data, it is helpful to consider the entire system in the manner employed by Bertocci (11). Although he treated steady-state conditions, the concepts should be applicable to transient processes. Three reactions must be considered: a redox reaction

$$Cu^+ \rightleftarrows Cu^{++} + e \qquad \text{(i)}$$

the reaction between adatoms and cuprous ions

$$A \rightleftarrows Cu^+ + e \qquad \text{(ii)}$$

and the exchange of adatoms with the metal lattice

$$M \rightleftarrows A \qquad \text{(iii)}$$

Bertocci, in treating the general case, assumed the concentration of adatoms always to be the equilibrium value so considerations here are a bit less specific. At any rate, however, it can be shown that the equilibrium potential can be expressed as

$$E_{eq} = E^o_{Cu^+/Cu^{2+}} + \frac{RT}{F} \ln \frac{(a_{Cu^{2+}})_{eq}}{(a_{Cu^+})_{eq}} = E^o_{A/Cu^+} + \frac{RT}{F} \ln \frac{(a_{Cu^+})_{eq}}{(a_A)_{eq}} \qquad [1]$$

and that when activities of the various species at the interface depart from equilibrium values, the potential of the electrode may be expressed as a sum of the reversible potential of the pertinent reaction and the overvoltage for that reaction

$$E = E_{Cu^+/Cu^{2+},\,rev} + \eta_i = E_{A/Cu^+,\,rev} + \eta_{ii} \qquad [2]$$

Using the notation that $E_i \equiv E_{Cu^+/Cu^{2+},\,rev}$, etc., it follows that

$$E_i - E_{eq} = \frac{RT}{F} \ln \frac{(a_{Cu^{2+}}) \times (a_{Cu^+})_{eq}}{(a_{Cu^{2+}})_{eq} \times (a_{Cu^+})} \qquad [3]$$

$$E_{ii} - E_{eq} = \frac{RT}{F} \ln \frac{(a_{Cu^+}) \times (a_A)_{eq}}{(a_{Cu^+})_{eq} \times (a_A)} \qquad [4]$$

Since electrocrystallization processes must be associated with reaction (iii), the electrocrystallization overvoltage, will be noted as η_{iii}. It has been defined by Vetter (12) as

$$\eta_{iii} \equiv \frac{RT}{F} \ln \frac{(a_A)_{eq}}{(a_A)} \qquad [5]$$

Note that this expression for η_{iii} is contained in Eq. [4] so that also

$$E_{ii} - E_{eq} = \frac{RT}{F} \ln \frac{(a_{Cu^+})}{(a_{Cu^+})_{eq}} + \eta_{iii} \qquad [6]$$

Still following the method of Bertocci it can be shown from Eq. [2], [3], [4], and [5] that, since

$$E - E_{eq} \equiv \eta \qquad [7]$$

$$\eta = \frac{RT}{F} \ln \frac{(a_{Cu^{2+}}) \times (a_{Cu^+})_{eq}}{(a_{Cu^{2+}})_{eq} \times (a_{Cu^+})} + \eta_i = \frac{RT}{F} \ln \frac{(a_{Cu^+}) \times (a_A)_{eq}}{(a_{Cu^+})_{eq} \times (a_A)} + \eta_{ii} \qquad [8]$$

and that

$$2\eta = \frac{RT}{F} \ln \frac{(a_{Cu^{2+}}) \times (a_A)_{eq}}{(a_{Cu^{2+}})_{eq} \times (a_A)} + \eta_i + \eta_{ii} = \frac{RT}{F} \ln \frac{(a_{Cu^{2+}})}{(a_{Cu^{2+}})_{eq}} + \eta_i + \eta_{ii} + \eta_{iii} \qquad [9]$$

Among others, Bertocci considered the special case in which $2\eta = \eta_i$. He pointed out such circumstances required that $(a_{Cu^{2+}}) = (a_{Cu^{2+}})_{eq}$ and that reaction (ii) occur completely reversibly (that is $\eta_{ii} = 0$). These requirements also were those necessary for Bockris and Enyo to interpret their data obtained under conditions of charge transfer control. However, Eq. [8] indicated such circumstances also require that $(a_A) = (a_A)_{eq}$, a limitation which would seem obtainable only if, under the stated conditions, adatoms are indistinguishable from those occupying lattice sites, and therefore, that the adatom concentration equal the number

of surface lattice sites. This relationship will be explored more fully in discussions which follow.

Bertocci's model can be used to explore situations in which charge transfer is not the rate-controlling process, and it is necessary that this be done, for Bockris and Enyo also clearly demonstrated that the redox reaction could not be rate limiting under the experimental conditions reported here. It could be thought, for example, that premaxima overvoltage transients resulted solely from the occurrence of the redox reaction within the diffusion layer without a net flux of material across the interface prior to the establishment of maxima. Since the equilibrium constant for the reaction, $Cu^{o} + Cu^{++} \leftrightarrows 2Cu^{+}$, is approximately 10^{-6} (13), it can readily be demonstrated there were sufficient cuprous ions within the diffusion layer to support the necessary current. This mechanism dictates that, during the time of the premaximum transients, reactions (ii) and (iii) do not occur. From the data of others it is only reasonable to assume that also $(a_{Cu2+}) = (a_{Cu2+})_{eq}$. However, a consequence of the mechanism is that concentrations of cuprous ions in the diffusion layer are smaller than at equilibrium for anodic processes and larger for cathodic. The second portion of Eq. [8] reveals that such circumstances require either that anodic processes exhibit negative overpotentials or $\eta_{iii} \neq 0$. Since either choice is unacceptable the proposed mechanism must be considered most implausible. Moreover, it does not aid in understanding the deposition anomaly. However, as is indicated below, this situation related to cuprous ion activities within the diffusion layer is permissible if surface adion concentrations depart from the equilibrium value.

All the time dependent characteristics of overpotentials reported here cannot be explained on the basis of the classic model of adatom diffusion over the surface to steps where they eventually can be incorporated into the crystal lattice. The data are easier understood if it is assumed that surface diffusion coefficients are much smaller than those for similar processes in solutions. Also, it is necessary to make one alteration in the assumptions generally made regarding the classic model: It will not be assumed that exchange of adatoms at steps occurs more rapidly than other surface processes, but rather that the action is hindered in some manner, and a barrier to exchange exists.

The formation of maxima, the dependence of the rate of decay of overpotential on the current density prior to opening the circuit and on the total charge passed, as well as the inverse relationship between current density and total charge passed at overpotential maxima formation suggest the following interpretation of the data. On closing a circuit at a higher current density the initial current was carried largely without reaction at steps. As the surface concentration of adatoms changed rapidly from the equilibrium value, other necessary events occurred such that the conditions required for steps to act as sources or sinks for adatoms were established. Thereafter, reaction began to occur at steps, and continued reaction produced gradual changes in surface adion concentrations toward the equilibrium value in efforts to establish desired steady-state concentrations. However, under the given experimental conditions, the net flux of adatoms at steps was such that the theoretical steady-state surface adion concentration was slow in being established since most of the adatom flux at steps served largely to support the net reaction rather than to change the average surface concentration of the species. (As will be seen later, it is also proposed that voltage-time relationships are influenced by events occurring at the metal-solution interface.) Obviously such a mechanism assumes the occurrence of time-dependent phenomena. Consequently, if it is assumed that at higher current densities overvoltage maxima were formed before significant reaction occurred at steps, premaxima current flow can be expressed in terms of adion activities

$$(a_A)_{eq} - (a_A)_t = kit/\mathbf{F} \qquad [10]$$

where (a_A) = activity of surface adions at equilibrium or time, t, as designated,

i = current density,
k = fraction of the total current carried by adion reaction,
$\mathbf{F}$ = the Faraday.

By combining Eq. [5] and [10] one obtains the expression

$$\exp(-z\mathbf{F}\eta_{iii}/RT) + kit/\mathbf{F}(a_A)_{eq} = 1 \qquad [11]$$

Consequently, the shape of premaxima portions of overvoltage-time curves at higher current densities should reflect the indicated relationship between overvoltage and time. For the few conditions tested, this was found to be the case, but effects of orientation, current density, polarity, etc., were such that additional studies of these phenomena are being conducted. Shapes of postmaxima portions of overvoltage-time curves should be a complex function of, among other things, the rate of change of surface adion concentration toward equilibrium values, events in the diffusion layer, and changes in surface structures produced by the process under observation. The absolute values of maxima resulting from such a reaction mechanism could, as experimentally observed, be independent of the surface step density, although postmaxima overvoltage-time relationships should not necessarily be.

The failure to establish a true steady-state potential at higher current densities over reasonable times suggests the time required for such an event is of the order of that for significant alterations in initial surface structure. Data shown in Fig. 10 clearly indicate that "normal," postanodic maxima were established before the equivalent of a monolayer of copper had reacted. The high current density data suggest that the equilibrium concentration of adatoms is at least two orders of magnitude less than the total number of lattice sites, if as previously suggested, the initial current flow was largely supported without reaction at steps.

Such a mechanism also accounts satisfactorily for the more rapid establishment of equilibrium conditions following termination of high current density pulses as compared with low decay rates of overpotential

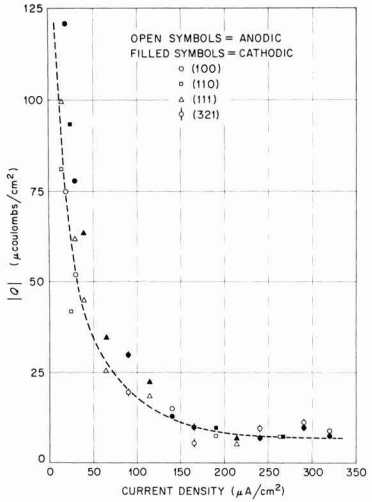

Fig. 10. Total charge passed before overpotential maxima formed on different orientations as a function of current density.

after low current density processes. On interruption of large currents, the potential for a short time, although rapidly decaying, was still sufficient to exceed the barrier to exchange at steps such that they still could act as sources or sinks for adatoms. During this time the total number of adatoms approached the equilibrium value, and additional time was required only for the proper equilibrium distribution to become established.

Anodic pulses at low current densities apparently followed the same general pattern. However, the data in Fig. 9 and 10 suggest that at current densities $\lesssim 25$ $\mu A/cm^2$ "normal" anodic maxima were formed by a current flow supported extensively by reaction at steps. Otherwise, the surface adatom concentration would have been so depleted that much higher overpotentials should have been observed. Also, since early, premaxima stages of current flow were accompanied by a slow monotonic increase in overpotential at low current densities, it would appear that at least a portion of the barrier to reaction at steps was indeed due to the occurrence of some sort of time dependent phenomena. The extremely slow rate of decay to equilibrium potential following interruption of a low current density pulse suggests that related processes at steps also were dependent on the overpotential. On interruption of small anodic currents, overpotentials during decay apparently were of such a relatively small magnitude that the barrier to reaction at steps was not exceeded sufficiently to produce adatoms at a rate necessary to satisfy rapidly the equilibrium requirements. Therefore, rates of potential decay during open circuit following low current density anodic processes were slower because they reflected the rate of production of adatoms at steps rather than, as at higher current densities, attainment of an equilibrium distribution by an adequate adion concentration. It will be seen that cathodic processes at low current densities can be understood on the basis of the same general model, although slight, but significant, alterations must be made.

Since Piontelli (14), as well as others, questions the validity of overpotential maxima and generally attributes their existence to the presence of impurities, perhaps some comments on the systems reported here would be useful. Admittedly neither the data of others obtained at higher current densities nor present theories of electrocrystallization phenomena are too helpful in assessing these results. It seems highly unlikely they can be dismissed as an impurity effect because it is difficult to propose a model of surface processes involving impurities which accounts satisfactorily for all the experimental results reported here.

At this point it is informative to discuss in some detail a part of the data reported by Bockris and Enyo (2). Although they were concerned primarily with the determination of kinetic parameters for copper electrodes exposed to various acidic solutions of different copper salts under conditions such that charge transfer was the slow process, only that portion of the data gathered when such conditions were not met ($i \lesssim 10$ mA/cm^2) is considered here. As much as is possible reference is made only to data concerned with cupric perchlorate systems. However, unless specifically excluded by the authors, it is assumed their general remarks drawn from all the data apply equally to perchlorate solutions. Using spherical copper electrodes they obtained different current-overpotential relationships for electrodes prepared by melting in helium and others of similar origin which were subjected to electrodeposition before use. In general, electrodes of the latter type acted in a much more consistent and understandable manner. For example, cathodic Tafel behavior was obtained for the latter, but not the former type, and values of anodic overpotentials gathered from the two kinds of electrodes did not agree completely. It was proposed that such behavior resulted from the different surface properties of the electrodes. They suggested that electrodes melted in helium contained an oxide film which, on exposure to acidic solutions, dissolved to expose a "new (clean) copper surface" on which the exchange current density would be expected to be greater than on a surface formed by electrodeposition. Further, they assumed a dislocation density of $\sim 10^9$ cm^2 for the former type and that of the latter to be greater, and concluded, therefore, that because electrodes melted in helium had this lower density of growth sites a surface process (diffusion) could become rate determining. It was also concluded that, at the lower current densities studied, surface diffusion was the rate-controlling step on both types of surfaces, which also helped explain the observation that rise times of overpotentials were greater than expected and differed for the two types of electrodes, as well as in anodic and cathodic cases for a single type.

The surface processes suggested by Bockris and Enyo are not unreasonable, but more credible alternatives do exist. From considerations of elementary geometry it can be shown that surfaces of spherical copper electrodes must have an average step density of $\sim 10^7$ cm^{-1} due solely to the intersection of crystallographic planes by the circumference of the sphere. Since, as previously discussed, the number of steps generated by dislocations intersecting a surface surely cannot exceed the square root of the dislocation density, defect related steps on the electrodes of Bockris and Enyo most probably did not number more than $\sim 10^5$ cm^{-1}. Therefore, growth sites produced by electrode geometry far outnumbered those associated with line defects in both types of electrodes, and it appears highly improbable that surface diffusion processes were affected to any significant extent by dislocations present in either type of electrode. Since average step densities on the two electrodes must have been approximately equal, it is much more reasonable to assume that differences measured on the two surfaces were not related to the average number of steps, but rather to the arrangement and distribution of this number of steps due to the different methods of surface preparation. This suggestion is compatible with the changes they observed on "new (clean)" helium-melted surfaces as more data was gathered on them. Presumably the net reaction on such electrodes in time would produce a surface similar to that resulting from electrodeposition, which, because of the method of preparation (15), surely must have consisted of ledges, facets, etc., formed by the bunching of steps.

It is not the primary purpose of this discussion to argue whether the interpretation presented here for the data of Bockris and Enyo is preferable to that of the authors, but rather to demonstrate that data gathered by others under entirely different conditions than those described in this report can reasonably be interpreted in a manner to lend support to the argument that a surface can yield vastly different current-potential and potential-time characteristics depending upon the arrangement of steps on that surface. The surfaces reported in this study upon which current-potential data were gathered contained steps distributed, as previously indicated, in a more or less continuous manner. The reactions performed on these surfaces were conducted at such low rates that the initial step distribution was changed very little during the course of the measurements, and it is certain these data are representative of structures quite different from those of Piontelli *et al.* and Bockris and Enyo. Therefore, it is not surprising that apparently little correlation can be made between any of these experimental results.

Before attempting an analytical treatment of observed overpotential maxima, it would be informative to discuss the data illustrated in Fig. 9 in more gen-

eral terms. It is conceivable that current-potential data for (100), (110), and (111) alone could support an argument that the differences observed on different orientations were related to the relative ease of direct reaction at steps on these orientations. However, the similarity of cathodic data for (321) and (111) preclude the possibility of direct discharge at steps on these orientations, since under such conditions the magnitude of the overvoltages should be proportional to the orientation related step densities which are $\sim 10^7$ and 10^5/cm, respectively. Moreover, the nearly perfect symmetry of the anodic and cathodic branches of the (321) data indicates that the mechanism also is not operable during dissolution from the (321). Then because of their relationships to the (321) and to each other [relative differences between (100) and (110) are greater than between (110) and (321)] and because of their perfect symmetry in anodic and cathodic branches, the (100) and (110) also appear unlikely to react by such a mechanism.

In considering the possibility of nucleation phenomena occurring, it is helpful again to compare cathodic data for the (321) and (111) with their structures. While the idealized (111) is a familiar structure, the ball model of a fcc (321) is perhaps not so well known. The model shows that 40% of the atoms on this surface are located along continuously kinked steps, and on the average, of course, a step occurs every 2½ atom rows. The only "nucleus" capable of existence on the model surface would be a long chain of single atoms at the half position between steps. Placement in any other lattice position would constitute direct growth at steps. Although a real crystal surface most surely does not have that of the idealized model, the arrangement must be such that $\sim$ 40% of the atoms, on the average, represent a kink stepped arrangement. Otherwise, the real surface area of the (321) would have to increase due to formation of preferred orientations, an occurrence which has previously been shown not to happen (5). Therefore, regardless of the real structure of the (321), the similarity of its cathodic current-potential maxima to those of the (111) argue against nucleation as a major event on these surfaces. It would seem then that data concerning the current-potential maxima relationships do not offer any objections to the modified model of surface processes previously proposed.

It does appear strange, however, that overpotential-current relationships should show such a pronounced orientation effect but apparently be free from any influence of step density. This is especially true in view of the relationship between current and step densities derived from the theoreies of electrocrystallization overvoltage. Several authors have considered surfaces from which material is added or removed by step motion, and they have arrived at expressions which relate step density to the average current density and overpotential. Bertocci *et al.* (16) have discussed these models and have shown that it is possible that a proportionality between step and current densities could be observed for misorientations an order of magnitude greater than those of surfaces used in these studies. However, all such models assume that adatom exchange at steps is unhindered. Because of this and also because effects obviously related to crystal orientation were observed, it is unreasonable to conclude that overvoltage characteristics reported here are unrelated to electrocrystallization phenomena. This argument is strengthened further by treating the data for (100) and (110) as indicated in Fig. 11. That similar results are not obtained by treating (321) and (111) data in this manner is demonstrated in Fig. 12. The assumption of indicated values for certain parameters leads to a slight misfit for (321) and a gross misfit for (111) data. Figure 13 shows that a better fit for the (111) is obtained if the value of α is assumed to be 0.46 for this orientation. The slight misfit observed for (321) data suggests an

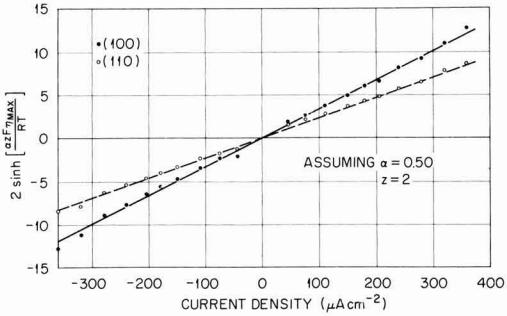

Fig. 11. Relationships between overpotential maxima and current densities on the (100) and (110) at 23°C in 0.2M $Cu(ClO_4)_2$ + $HClO_4$ (pH ~ 1).

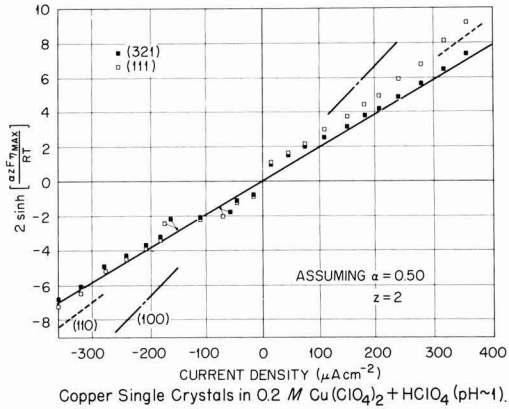

Fig. 12. Relationships between overpotential maxima and current densities on the (111) and (321) if same parameters assumed which permit proper fitting of (100) and (110) data.

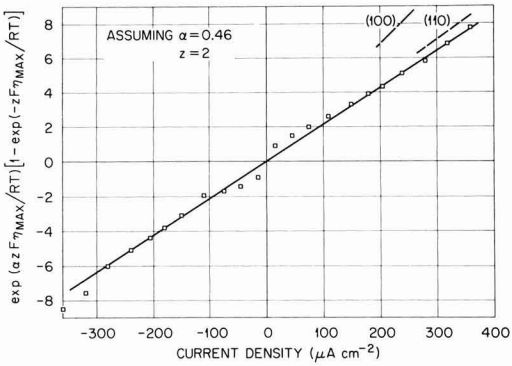

Fig. 13. Relationships between overpotential maxima and current densities on the (111) at 23°C in 0.2M $Cu(ClO_4)_2$ + $HClO_4$ (pH ~ 1) at indicated values assumed for α and Z.

α value of $\sim$ 0.49 for this surface, and further calculations are judged to be not worthwhile. From such plots it is readily seen that the relationship between values of overpotential maxima and the current flowing in the system can be described by the expression

$$i = K\left\{\exp\left[\frac{\alpha z\mathbf{F}\eta_*}{RT}\right] - \exp\left[\frac{-(1-\alpha)z\mathbf{F}\eta_*}{RT}\right]\right\} \quad [12]$$

where η_* = value of overpotential maximum
α = an orientation sensitive transfer coefficient having the values (100) and (110) = 0.50; (321) = 0.49; (111) = 0.46.
z = a factor relating the electrocrystallization overvoltage to the measured overvoltage.
K = a pre-exponential function having the dimensions of current density. The orientation dependent values measured from the slopes of the lines in Fig. 11, 12, and 13 are: (100) = 30; (110) = 40; (111) = 45; (321) = 50 μA/cm^2
i = current density.

The remaining terms have the significance previously indicated.

Previously it has been postulated that premaxima currents were accompanied by changes in surface adatom concentrations without concomitant action at steps. This is, of course, in agreement with the requirements that surface adatom concentrations be less than the equilibrium value during anodic processes when $\eta_{iii} \neq 0$. A cursory examination of Eq. [9] reveals that data of others regarding $(a_{Cu^{2+}})$ and η_{ii} define conditions such that $2\eta = \eta_i + \eta_{iii}$. The preceding analytical treatment of current-overpotential maxima data requires that $\eta_{iii} = 2\eta$. Therefore, it is necessary to determine conditions under which η_i can approach zero, and to decide if those conditions can be established. Again referring to Eq. [8] and considering the anodic case, it is obvious that η_i can approach the limiting zero value only under the circumstances previously discussed when $(a_{Cu^+})_{eq} > (a_{Cu^+})$. This, in turn, is permissible in the specific case considered when $(a_A)_{eq} > (a_A)$. Therefore, it appears the analytical treatment is reasonable in terms of a model reaction sequence which requires that $(a_{Cu^{2+}}) = (a_{Cu^{2+}})_{eq}$, $\eta_{ii} = 0$, $\eta_i \rightarrow 0$, and that reaction (i) occur within the diffusion layer at a rate greater than reaction (iii) occurs on the surface during the time of the transient. Apparently voltage time characteristics resulted from complicated interactions due to these latter two reactions, and in view of such processes even the twin maxima often observed during postcathodic anodic transients illustrated in Fig. 7 seem reasonable and comprehensible.

At current densities higher than those reported here it would appear that $\eta_i >> 0$ and $\eta_{iii} < 2\eta$. Eventually at still higher current densities the conditions become established whereby, as reported by others, $\eta_{iii} = 0$ and $\eta_i = 2\eta$. It is interesting to note that the data of Piontelli *et al.* were obtained in just this transitional range of current densities where it is suggested that the relationship between η_i and η changes with current density.

Figures 11 to 13 indicate that overpotential values obtained at current densities $\lesssim$ 100 μA/cm^{-2} do not agree with the proposed mechanism and treatment as well as those obtained at higher current densities. However, this effect is consistent with the assumption that maxima occurring under the former conditions were not established before significant reaction had occurred at steps. The significance of the pre-exponential constants determined for each orientation depends on the validity of the suggested model of events on the surface and in the diffusion layer. If the proposals advanced to explain the experimental observations are correct, and if the adatom concentrations at equilibrium are about equal on all orientations, then K values could closely approximate the values of the exchange current density of adatoms and ions in solution. It is interesting to compare them with the value of 20 μA cm^{-2} obtained by Roiter *et al.* (8) on single crystalline zinc in zinc sulfate solutions. Anodic and cathodic maxima were symmetric about the equilibrium point in the zinc system, and it was determined that observed values of maxima depended upon the nature of the preceding electrode process. Unfortunately, no reference is made to the orientation(s?) of zinc crystals used in the study so analogies regarding orientations cannot be drawn. Obviously K values are lower by factors of $\sim$ 200 than the exchange current densities determined by Bockris and Enyo under conditions of charge transfer control. However, as previously noted, such experimental conditions require that adatoms and metal atoms be indistinguishable, a condition not demanded of the systems reported here. This suggests the possibility that excessive removal rates so alter copper surfaces that measurements determined thereon are concerned with surfaces of marked physical differences, in the sense of geometric arrangements, adsorbed species, identity of nearest neighbors, etc., from those on which removal rates are low enough that a surface process may be rate controlling.

Anomalous deposition effects.—The previous treatment accounts in a self-consistent manner for most of the experimental phenomena mentioned earlier, but it still must be shown that the proposed model accommodates equally well the observed effects of deposition on a succeeding dissolution process. If material is incorporated into the metal lattice at steps, it must become identified with, and indistinguishable from, the rest of the crystal. Therefore, no "deposition effect" should be observed following such a process. By the same token, if nucleation occurred and the deposit formed over the old substrate, only the new steps bounding deposits should serve as possible sources of different effects since material bounded by the steps should be identical with the substrate. However, data shown in Fig. 9 indicate that the deposition process was independent of step density in the range $\sim 10^5$-10^7 cm^{-1} since almost identical cathodic branches of current-overpotential data were obtained for the (321) and (111). Therefore, it is difficult to believe that nucleation phenomena could account for the observed deposition anomaly. A reasonable alternative is suggested by the shapes of anodic overpotential-time curves of the type illustrated in Fig. 8. If, as proposed, the shape of low current density "normal" anodic overpotential-time curves reflect both reaction at steps as well as depletion of surface adatoms, then the relationships between cathodic and subsequent postcathodic, anodic curves indicate that material deposited at low and intermediate current densities had more the characteristics of adatoms than of the crystalline substrate. (Although it is not to be assumed that the process is completely independent of the substrate.) Moreover, these characteristics were retained over long periods of time. Therefore, it is suggested that much of the material deposited at low current densities over relatively short periods of time did not occupy half-crystal positions, and in this sense could not be distinguished from adatoms. Since, as indicated in Fig. 8, the anomaly could be observed for the total deposit equivalent to much more than a monolayer of material, such deposits probably have extremely open structures with high vacancy concentrations. This is equivalent to proposing that under these conditions crystal growth occurred more or less by direct addition of atoms at random sites, with little subsequent surface diffusion. While conceptually the idea lacks a certain appeal, it appears that, following a low current density cathodic process, the observed smaller values of anodic maxima and increases in times to establishment can be explained on the basis of an increased concentration of adatom-like material under conditions of "pseudo-equilibrium."

A further indication of the differences in dissolution and deposition processes at low and intermediate current densities is seen by comparing the post-maxima shapes of overpotential-time curves of Fig. 6. Such dif-

ferences were more difficult to detect at current densities in excess of $\sim$ 200 μA/cm^2, and with the exception of the (111) and possibly the (100), at higher current densities overpotential-time relationships were almost precisely similar for anodic and cathodic processes at the same current density on any one orientation.

A somewhat more 'quantitative discussion of the deposition anomaly is possible. The data in Fig. 10 show clearly that "normal" maxima for both anodic and cathodic processes at the indicated current densities were established on all orientations well before the equivalent of a monolayer of copper had reacted. But as indicated in Fig. 8 the deposition effect was not restricted to the charge passed in establishing a maximum, but rather to the total amount of material deposited. The highest current density at which it was established that ensuing anodic maxima formed only when the total previous deposit had been removed was 160 μA/cm^2. Six hours following depositions lasting 1 min at this current density, dissolution produced anodic maxima only after one minute at the same current density. ("Normal" anodic maxima under such conditions were established in $\sim$ 0.1 sec on all orientations and had larger absolute values than observed in postcathodic instances.) These depositions corresponded approximately to the equivalent of 15 atom layers. At lower current densities the largest deposit which was precisely duplicated in a succeeding anodic overvoltage-time to maximum curve corresponded to $\sim$ 50 atom layers. Neither of the examples cited here were established as limiting cases, nor indeed were any of the limiting conditions precisely defined. However, it was observed that at current densities $\gtrsim$ 200 μA/cm^2 the effect diminished as the current density increased, and a relationship between the total amount of deposit and the amount removed at the time of anodic maximum formation could not be established at higher current densities.

A most intriguing aspect of the overpotential data is that the (321) and (111) have nearly identical cathodic but quite different anodic branches. Previously it has been pointed out that, as illustrated in Fig. 6, on any orientation postmaxima anodic and cathodic overpotential-time relationships are not always identical for any one reaction rate, even at the highest current densities studied. This indicates that immediately after the maximum change in adion concentration had been established, subsequent surface events were not precisely equivalent for dissolution and deposition. The suggested model of reaction seems suitable for anodic processes, but further discussion is required in the cathodic case. The relative step densities on the (321) and (111) suggest that the lack of symmetry in the (111) overpotential data resulted from lower values for cathodic processes rather than excessively high values for the anodic. If so, it was not diffusion over the surface which limited the maximum cathodic overpotential developed on the (111), otherwise the (321) surfaces would not have produced data identical to that obtained for the (111). At higher current densities it is possible that unusual growth processes might have occurred on the (111). It could be that diffusion was such a relatively slow process that growth was accomplished on the flat surface areas rather than by diffusion to step sites. However, there is insufficient evidence to suggest nucleation processes occurred, and furthermore, by analogy to observations on all orientations at low current densities, it seems preferable to think of growth on the (111) as being accomplished by rather ill-defined methods which produced atom layers with a very high vacancy content.

A more plausible reason for the asymmetric behavior of the (111) and (321) could be a consequence of the fact that the (111) is the close packed plane in copper. In face-centered cubic systems such as copper the close packed planes are stacked in the sequence ABCABC-AB . . ., etc., but it is not at all certain that adatoms on a (111) area are restricted to sites representing proper crystal sequential orders. So while there are two types of geometrically similar sites available to adatoms on this surface, in terms of permanent occupancy of such sites one of them is crystallographically improper. Growth occurring in such unsuitable arrays, rather than by movement of crystallographically correct steps over the surface, could have been responsible for the asymmetric behavior observed. The slight asymmetric property of the (321) data emphasizes the fact that a tremendously high step density was incapable of causing complete obliteration of this effect, and that perhaps it is indeed an intrinsic property of the close-packed arrangement. Therefore, it is not at all certain that the "deposition anomaly" observed on all orientations at lower current densities did not also occur undetected on all orientations at higher current densities. It is possible that diffusion over any orientation was relatively so difficult that initial growth at all the current densities reported here occurred in such a way that structures with very high vacancy content always were formed.

Manuscript submitted Jan. 27, 1969; revised manuscript received *ca.* Dec. 24, 1969. The data reported here were presented in part as Paper 110 at the Washington Meeting, Oct. 11-15, 1964, and in part as Paper 72 at the Philadelphia Meeting, Oct. 9-14, 1966. The research on this paper was sponsored by the USAEC under contract with Union Carbide Corporation.

Any discussion of this paper will appear in a Discussion Section to be published in the December 1970 JOURNAL.

REFERENCES

1. R. Piontelli, G. Poli, and G. Serravalle, "*Transactions of the Symposium on Electrode Processes*," E. Yeager, Editor, John Wiley & Sons, New York (1961).
2. J. O'M. Bockris and M. Enyo, *Trans. Faraday Soc.*, **58,** 1187 (1962).
3. D. Shanefield and P. Lighty, *This Journal,* **110,** 973 (1963).
4. F. W. Young, Jr. and T. Wilson, *Rev. Sci. Inst.*, **32,** 559 (1961).
5. L. H. Jenkins and U. Bertocci, *This Journal,* **112,** 517 (1965).
6. L. H. Jenkins and J. Stiegler, *ibid.*, **109,** 467 (1962).
7. L. H. Jenkins, *ibid.*, **113,** 75 (1966).
8. W. Roiter *et al.*, *Acta Physicochem. USSR*, **10,** 845 (1939).
9. W. Krebs and D. Roe, *This Journal,* **114,** 892 (1967).
10. F. W. Young, Jr. and L. D. Hulett, Jr., "Metal Surfaces," W. Robertson *et al.*, Editors, Am. Soc. for Metals, Metals Park, Ohio (1963).
11. U. Bertocci, *Electrochim. Acta,* **11,** 1261 (1966).
12. K. J. Vetter, "Electrochemical Kinetics," Academic Press, New York (1967).
13. F. Fenwick, *J. Am. Chem. Soc.*, **48,** 860 (1926).
14. R. Piontelli, *Electrochimica Metallorum,* **1,** 5 (1966).
15. J. O'M. Bockris *et al.*, *J. Sci. Inst.*, **33,** 400 (1956).
16. U. Bertocci, L. D. Hulett, Jr., L. H. Jenkins, and F. W. Young, Jr., "Reactivity of Solids," J. W. Mitchell *et al.*, Editors, Wiley-Interscience, New York (1969).

Oxygen Reduction on Active Platinum in 85% Orthophosphoric Acid

A. J. Appleby*

Institute of Gas Technology, Chicago, Illinois

ABSTRACT

The oxygen reduction reaction on platinum that has been anodized, followed by reduction at 500 mV, has been studied in 85% orthophosphoric acid over a wide temperature range. This anodized platinum surface is more active for oxygen reduction than annealed reduced platinum in the 850-950 mV potential range and has a higher Tafel slope (1.79 $RT/\mathbf{F}$ at 25°C, compared to 1.04 $RT/\mathbf{F}$ for the annealed surface). Activation energy at the reversible potential is 14.9 ± 1.5 kcal. It is suggested that the rate-determining step on this surface is

$$S + O_2 + H^+ + e^- \rightarrow SO_2H$$

under conditions in which the adsorption of the product is close to Langmuirian. Hydrogen peroxide is not appreciably involved in the reduction mechanism. These results are interpreted in terms of the surface structure of the electrode after oxide reduction.

It is well-known that platinum that has been freshly anodized behaves as a more effective catalytic surface for a wide range of electrochemical processes. This effect has been explained by Kolthoff and Nightingale (1) and by Davis (2) as being due to facilitated electron transfer from the oxidized platinum surface by an oxygen-bridge mechanism. Other workers, on the other hand, have argued that a chemical mechanism is responsible in which reagents react directly with the oxidized surface, which is unstable under reducing conditions (3, 4).

Anson (5) considered that platinum that has been oxidized then reduced by a redox system is covered by a thin, platinized layer, and behaves as a specially active surface. This argument is supported by the observation that marked roughening of the surface occurs under a-c conditions (6). However, Gilman (7) has shown that only a small increase in area is produced by one polarization cycle, and this is true only if reduction of the oxidized surface is rapid. An alternative explanation was advanced by Feldberg, Enke, and Bricker (8) who attributed the enhanced activity of oxidized and reduced platinum to an adsorbed layer of PtOH.

In general, no special increase in activity other than that which may be attributed to impurity adsorption (9, 10) is observed by pulsing platinum to 1.6V (11). Under these conditions, approximately one monolayer of adsorbed oxygen on the platinum surface is involved (12). At higher potentials, more than one monolayer of oxide may form (13-15).

In this paper, the reduction of oxygen in 85% orthophosphoric acid is studied on reduced platinum that has been previously anodized at high potentials. Kinetics and mechanism on this active surface are compared with those occurring on a reduced, annealed platinum surface (10).

Results are interpreted in terms of surface modification due to partial reduction of the oxide layer, with the formation of a strained lattice containing dissolved oxygen and with a high density of surface defects (16).

Experimental

The all-silica cell in which the experiments were carried out has been described in a previous publication (17). The working electrode consisted either of one of a number of 1-cm² platinum foils suspended from wires, or of the disk of a rotating ring-disk electrode. Electrodes (zone-refined grade, nominal 99.999% purity) were degreased and washed in concentrated HCl, conductivity water, and the electrolyte itself before use. The reference electrode was a dual bubbling hydrogen system equipped with a Luggin capillary. Hydrogen for the reference electrode and oxygen or oxygen-nitrogen mixtures (reproducibly mixed to the required P_{O_2} by capillary flowmeters) were led to the cell via presaturators. All measurements throughout this work were carried out by conventional galvanostatic methods, although with the ring-disk electrode a potentiostat was used. The latter electrode was used to study the formation of hydrogen peroxide intermediates in the reaction and to obtain polarization data over a longer activation-controlled range.

The electrolyte was purified by treatment with hydrogen peroxide in a manner previously described (17). All potentials throughout this paper are expressed relative to the bubbling hydrogen electrode in the same solution (HRE potentials).

Electrode pretreatment.—Electrodes were anodized at a potential of 2V HRE for 2 min and were then allowed to reduce galvanostatically at a current density of 20 μA/cm² until the potential reached 500 mV. Following this treatment the cathodic galvanostatic current was switched off and the electrode was allowed to attain its equilibrium rest potential.

Rest potentials.—Rest potentials of the electrodes were approximately 990-1010 mV. The values were not significantly temperature dependent; initial experiments, carried out by adding small quantities of analytical grade 85% orthophosphoric acid to the pure electrolyte, established that small traces of impurities resulted in lowered values.

Tafel plots were obtained as soon as the electrode had reached an open-circuit potential whose value had changed by less than 5 mV in the previous 2 min. It was noted, however, that the potentials of electrodes left on open circuit slowly rose over a period of hours to a maximum of 1020-1030 mV.

Tafel plots.—Galvanostatic Tafel plots were made using a conventional battery-operated, high impedance circuit allowing sufficient time (up to 5 min at low current density, 1-2 min at higher current density) for equilibrium to be reached at each point. Steady-state readings were taken when the potential changed by less than 2 mV in the previous interval of 1 min. Plots were obtained in this way at 25.1°, 52.1°, 76.1°, 95.9°, 116.0°, and 136.1°C (Fig. 1). In general, they could be traced forward and backward with very little hysteresis.

Each potential-log current plot shows a gently sloping region extending from the rest potential, followed

* Electrochemical Society Active Member.

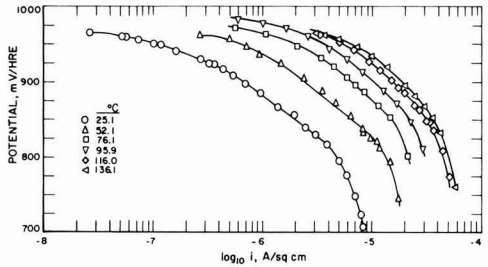

Fig. 1. Galvanostatic Tafel plots of oxygen reduction on active platinum, temperature dependence.

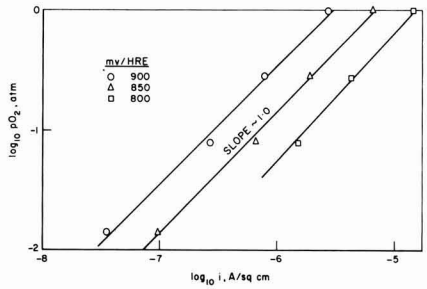

Fig. 2. Effect of oxygen partial pressure on polarization at 52.1°C

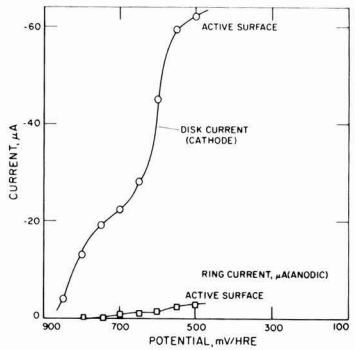

Fig. 3. Ring-disk electrode data, 4840 rpm at 76.1°C

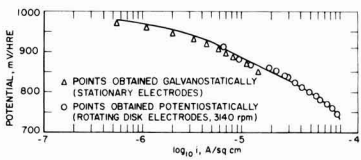

Fig. 4. Tafel plot at 76.1°C on active platinum: stationary and rotating disk electrode data.

by a Tafel region starting at about 925 mV. The Tafel slopes and $1/\alpha$ values at each temperature studied are given in Table I. In addition, Table I contains exchange current values obtained by extrapolating the Tafel line to the calculated reversible potential at each temperature (assuming $P_{O_2} = 1$ and $P_{H_2} = 1\text{-}p$ atm, where p is the water vapor pressure above phosphoric acid).

In each case the experimentally obtained exchange current has been corrected to 1 atm oxygen partial pressure assuming a first order mechanism (see below).

Order of reaction for oxygen.—A series of Tafel plots was made at different oxygen partial pressures. At the lower partial pressures it was necessary to wait for some time to elapse before the first point was taken to allow oxygen evolved during electrode pretreatment by anodizing to disperse before reproducible results could be obtained. Tafel plots at four oxygen partial pressures on active platinum electrodes at 52.1°C have been previously published (18). A log-log plot of polarization data in the Tafel range of these plots is shown in Fig. 2, which indicates that the chemical reaction order for oxygen reduction is unity.

Hydrogen peroxide.—A rotating ring-disk electrode was used to determine the percentage of hydrogen peroxide produced, either as the end product of a parallel mechanism or as an intermediate in the overall process of oxygen reduction to water. In these experiments the disk electrode was prepared by anodizing followed by reduction in the same way as the platinum foil working electrodes referred to previously. The lightly platinized ring of the electrode was maintained at a constant potential of 1.3V HRE; at this potential hydrogen peroxide oxidation is diffusion controlled. Experiments were carried out at 76.1° and 116.0°C in 85% orthophosphoric acid purified by hydrogen peroxide treatment. Disk current and the corresponding anodic ring current were determined at various cathodic potentials applied to the disk by means of a potentiostatic circuit. A typical reduction wave for oxygen at 76.0°C is shown on Fig. 3, for a rotational velocity of 4840 rpm. Unlike the corresponding case on oxide-free annealed platinum (10), little effect of impurity adsorption on oxygen reduction kinetics in the double layer region was noted.[1] At 76.1°C, small quantities of hydrogen peroxide were detected at the electrode ring. The collection factor of the electrode used was 35%; on this basis hydrogen peroxide accounted for less than 10% of the total reaction product or detectable intermediate. At the same temperature on annealed oxide-free platinum, hydrogen peroxide accounted for a greater proportion, approximately 16% of the total product or intermediate. At 116°C, no hydrogen peroxide could be detected at the ring when the disk was in the "active" state.

The ring disk electrode at 3140 rpm was used to confirm the Tafel slope at 76.1°C over a greater range than was possible in the electrolyte stirred by gas bubbling. At this rotation speed, the linear Tafel range at the electrode was increased by approximately a further decade. Figure 4 shows that there is good agreement between the Tafel slope for platinum foil electrodes under stirring by gas bubbling and a rotating disk electrode at a high rate of hydrodynamic stirring.

Activation energy.—Figure 5 shows an Arrhenius plot of the extrapolated i_o values (corrected for oxygen partial pressure). Activation energy at the reversible potential on this basis is about 14.9 ± 1.5 kcal (10), and the value on active platinum is close to that observed on oxidized platinum (13.1 kcal) (17).

The higher temperature i_o values lie somewhat off the line; this is probably due to the uncertainty in measuring the Tafel slope (assumed to be about 125 mV/decade) at the higher temperatures.

Table I. Kinetic data for oxygen reduction on active platinum in 85% orthophosphoric acid

Temp, °C	i_o, A/cm² (atm O_2)	Tafel slope, mV/decade	$1/\alpha$
25.1	2.7×10^{-10}	106	1.79
52.1	3.4×10^{-9}	119	1.85
76.1	1.5×10^{-8}	120	1.76
95.9	4.0×10^{-8}	124	1.69
116.0	1.2×10^{-7}	125	1.62
136.1	2.8×10^{-7}	125	1.52

[1] This deactivation is attributed by Bockris *et al.* (19) to $H_2PO_4^-$ ion adsorption.

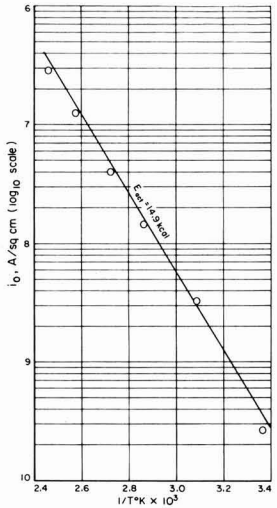

Fig. 5. Arrhenius plot of extrapolated exchange currents for oxygen reduction on active platinum in 85% orthophosphoric acid.

Discussion

Nature of the active platinum surface.—Platinum which has been anodized at high potential has on its surface a phase oxide film at least two monolayers thick (13-15). In addition, the outer layers of the platinum lattice appear to contain "dermasorbed" oxygen, that is, oxygen dissolved in the first two or three atomic layers of the platinum. Evidence for the existence of the latter type of dissolved oxygen has been given by Schuldiner and Warner (20), and is implicit in the observation that the anodic charge in galvanostatic transients is always greater than the cathodic charge in the platinum oxidation reduction cycle. The evidence for this has been reviewed by Vetter (21) and Hoare (22). This observation has been explained by Gilman (23) in terms of an impurity oxidation reaction contributing to the anodic current, by Laitinen and Enke (14) in terms of oxygen evolution in the anodic cycle, and by Vetter and Berndt (24) in terms of a cathodic mechanism involving a 2-electron reduction of the oxide film so that hydrogen peroxide was the end product rather than water. The latter reaction is unlikely, in view of the ring-disk electrode data of Frumkin *et al.* (25), which indicated that no detectable hydrogen peroxide was produced during oxide-film reduction on platinum. Equally, the first two explanations are unlikely as the same phenomenon is observed under conditions of high purity (additionally oxidation of many species is strongly inhibited on oxidized platinum) (26) and oxygen evolution is not normally apparent at low potentials, at which this effect is still observed.

Feldberg *et al.* (8) offer an explanation for this phenomenon in terms of a partial reduction of the platinum oxide film [which consists of PtO (27) if the potential of the electrode is not greater than about 1.8V] to PtOH, on the assumption that the reduction of this compound is highly irreversible. This is difficult to accept on kinetic grounds, and it is hard to see how an oxide film some monolayers thick can be exactly half reduced to a PtOH film with the same thickness.

A previous publication (10) has described the kinetics of oxygen reduction on a platinum surface prepared by electrochemical reduction to remove any residue oxide followed by anodic and cathodic pulsing (at a maximum anodic potential of 1.2-1.5V) to produce a surface free of adsorbed capillary-active impurities. If PtOH is the end product of the reduction of the PtO produced in the anodic pulse, it would be expected that the electrode surface would be covered with a monolayer of this material. The surface produced by this treatment is, however, kinetically similar to platinum pretreated by hydrogen reduction at 500°C. The latter surface is unlikely to carry any oxidized platinum; in addition, it is hard to see how radicals such as O_2H or O can be adsorbed on a surface bearing a monolayer of a similar species (OH) and still obey a Temkin-type adsorption isotherm, in which the heat of adsorption of species of similar electronegativity (for example, OH, O, O_2H) falls off as the total coverage increases (28). This isotherm accurately applies only at intermediate coverages ($0.2 < \theta < 0.8$); at $\theta \rightarrow 0$ or 1, adsorption is Langmuirian. Hence, with a coverage of —OH close to unity, the adsorption isotherm for O or O_2H would be expected to be also Langmuirian.

It seems reasonable to assume that the charge imbalance in anodic and cathodic galvanostatic transients is caused by diffusion of oxide ions into the first few monolayers of the platinum lattice (20) where they become inaccessible for reduction. Because of the high energy of the platinum lattice containing interstitial oxygen, it is energetically difficult for the oxygen to diffuse out through the reduced outer one or two monolayers of platinum. The latter are envisaged to be, therefore, situated on top of a disordered highly strained lattice of Pt-O alloy, so that the surface after oxide reduction is a high-energy, randomly oriented platinum layer containing numerous vacancies and lattice defects.

It is interesting to note that the "active" surface is not produced by pulsing to 1.5V, where only one monolayer of reducible oxide is involved (12). It is necessary to strongly oxidize the surface by anodizing at high potential, followed by reduction at about 600-700 mV to remove the superficial reducible oxide layer. The disordered surface containing dissolved oxygen thus produced is not particularly stable, but is more stable than would be expected for a very lightly platinized surface, of the type suggested by Anson (5).

As Feldberg *et al.* (8) have shown, the active surface degrades very slowly above 700 mV, but is reduced relatively quickly to give a normal annealed platinum surface at 300 mV. It seems likely that the nitric-acid-treated platinum surface reported by Hoare (29) is a similar high-energy surface containing dissolved oxide ions.

Mechanism of Reaction on the Active Surface

The principal kinetic characteristics of the active surface are: (*i*) first order reduction of oxygen, and (*ii*) Tafel slopes of 1.79 $RT/\mathbf{F}$ to 1.54 $RT/\mathbf{F}$, depending on temperature. In addition, the surface is more active than annealed, oxide-free platinum, less affected by impurities, and produces less hydrogen peroxide.

On normal (annealed) platinum the Tafel slope is $RT/\mathbf{F}$, and oxygen reduction is first order. It has been shown that this is consistent with the rate-determining step (10, 11)

$$SO_2 + H^+ + e^- \rightarrow SO_2H$$

in which it is assumed that the adsorption of SO_2H follows the Temkin isotherm. This is justified on the following grounds. The rate equation for the above reaction is

$$i = \theta' k\mathbf{F} \exp(-\beta\mathbf{F}V/RT - \beta r\theta/RT)$$

where β is a symmetry factor, θ' is the coverage of molecular oxygen, θ is the total coverage of similar oxygenated compounds (—O, —OH, and —O_2H) on the electrode surface, r is the change in heat of absorption for unit change in θ, and k is the specific rate constant. $\mathbf{F}$, R, and T have their usual meanings. Only the adsorption of the product of the reaction follows the Temkin isotherm; the observation that oxygen reduction is first order implies that $pO_2 \propto \theta'$; that is, a

Langmuir isotherm (at low coverage) operates for the reactant (10).

Assuming that the oxidation products of water (—O and —OH) are in equilibrium on the electrode, and their adsorption obeys a Frumkin isotherm (Temkin approximation in the coverage range $0.2 < \theta < 0.8$) then it can be shown in this interval of θ (30)

$$\partial V/\partial\theta = \frac{r}{\mathbf{F}}$$

and $\mathbf{F}V = r\,\theta$ (29)

Hence

$$i \propto pO_2 \exp(-\mathbf{F}V/RT)$$

Damjanovic and Brusic (11) have also shown that this treatment is consistent with their observed pH dependence.

In principle, the oxygen electrode on oxide-free platinum behaves like a normal charge transfer process with a Tafel slope $2RT/\mathbf{F}$, which is progressively poisoned (*i.e.*, the rate constant decreases) by the increasing surface coverage of the oxidation products of water with increasing potential. The reduction reaction on the active surface apparently involves the same rate-determining step taking place under conditions of increased heat of adsorption of the reaction intermediate ($—O_2H$),[2] thus accounting for the increased rates, and where this effective poisoning (fall in rate constant due to change in heat of adsorption with coverage) is less apparent. We must postulate that the adsorption isotherm of O_2H is more nearly Langmuirian on the "active" surface.

If we consider a surface with a high proportion of lattice defects, it is probable that the range of energy distributions at individual defects is not too wide. On this basis, with only a small number of sites that are active at any time, approximately Langmuir conditions of adsorption at relatively low coverage are possible. The effect of $O^=$ within the lattice must not be discounted. If the Temkin isotherm on the annealed surface is caused by an induced heterogeneity effect, due to dipole interaction at the surface, then the effect of lattice oxygen may be to reduce these interactions and allow a more Langmuirian isotherm to operate.

The activation energy on the reduced annealed surface was previously determined to be approximately 22.9 kcal at the reversible potential (10). This figure contains a heat of adsorption term due to fall in bond-strength of reaction intermediates as —O coverage on the electrode rises with potential. For this reason, it is more legitimate to compare activation energies for the two surfaces at a potential where coverage by adsorbed —O is low, rather than at the reversible potential. On this basis, the difference in activation energy at about 800 mV ($\eta \sim -400$ mV) is (22.9-14.9) $-$ $(\alpha_1 - \alpha_2)\,\eta\mathbf{F}$ kcal, where α_1 and α_2 are the mean transfer coefficients on each surface. With $\alpha_1 \sim 1.0$ and $\alpha_2 \sim 0.59$, this difference amounts to approximately 2.5 kcal. If one assumes that the total increase in surface energy is equivalent to about one surface defect for every ten surface atoms, then it is possible to account for most of the activation energy decrease on this basis. If a platinum atom at a defect has extra energy available for bonding equal to 4 available Pt-Pt bonds, then the excess energy of each site (compared with normal platinum) is about 4 $Ls/6$ where Ls is the latent heat of sublimation of platinum. On the basis of Pauling's equation (31) for the strengths of polar bonds, the increase in bond strength of the reaction intermediate at each site will be approximately

$$\frac{1}{2}\frac{4Ls}{6} \sim 40 \text{ kcal/mole}$$

The net increase in bond strength over the whole surface will thus be about 4 kcal. If one assumes that the change in activation energy will be given by $\beta \times 4$ kcal where β is a symmetry factor, a change of 2 kcal might be expected, with $\beta = 1/2$.

It is also likely that the electronic work function at a defect site is not canceling, *i.e.*, it appears in the over-all rate equation. This possibility has been discussed by Damjanovic, Setty, and Bockris (32). Hence, if the electronic work function is lower at defects, an additional reduction in the activation energy may be expected.

[2] This also explains the lower proportion of H_2O_2 detected in comparison with that at the annealed oxide-free surface (10).

Conclusion

The "active" surface of platinum is kinetically different from a normal annealed platinum surface prepared by reduction. This may be attributed to the effect of dermasorbed oxygen (20) within the first few layers of the lattice, and to a high degree of surface disorder. Since the structure of the surface is not stable, eventual rearrangement and recrystallization take place with the production of a platinum surface with normal properties. The method of activation by anodizing and reducing is consequently not a promising method for long-time improvement in the electrocatalytic properties of the substrate.

Acknowledgment

The author wishes to thank the sponsors of the TARGET fuel cell program and Pratt & Whitney Aircraft Division of United Aircraft Corp. for permission to publish this work. The help of members of IGT in the preparation of this publication is also greatly appreciated.

Manuscript submitted Oct. 31, 1969; revised manuscript received *ca.* Feb. 3, 1970.

Any discussion of this paper will appear in a Discussion Section to be published in the December 1970 JOURNAL.

REFERENCES

1. I. M. Kolthoff and E. R. Nightingale, *Anal. Chim. Acta*, **17**, 329 (1957).
2. D. G. Davis, *Talanta*, **3**, 335 (1960).
3. K. I. Rozenthal and V. I. Veselovskii, *Zh. Fiz. Khim.*, **27**, 1163 (1953).
4. T. I. Borisova and V. I. Veselovskii, *ibid.*, **27**, 1195 (1953).
5. F. C. Anson, *Anal. Chem.*, **33**, 934 (1961).
6. F. C. Anson and D. M. King, *ibid.*, **34**, 362 (1962).
7. S. Gilman, *J. Electroanal. Chem.*, **9**, 276 (1965).
8. S. W. Feldberg, C. G. Enke, and C. E. Bricker, *This Journal*, **110**, 826 (1963).
9. S. D. James, *ibid.*, **114**, 1113 (1967).
10. A. J. Appleby, *ibid.*, **117**, 328 (1970).
11. A. Damjanovic and V. Brusic, *Electrochim. Acta*, **12**, 615 (1967).
12. W. Bold and M. Breiter, *ibid.*, **5**, 145 (1961).
13. A. K. N. Reddy, M. Genshaw, and J. O'M. Bockris, *J. Electroanal. Chem.*, **8**, 406 (1964).
14. H. A. Laitinen and C. G. Enke, *This Journal*, **107**, 773 (1960).
15. D. Gilroy and B. E. Conway, *Can. J. Chem.*, **46**, 875 (1968).
16. H. Dietz and H. Gohr, *Electrochim. Acta*, **8**, 343 (1963).
17. A. J. Appleby, *J. Electroanal. Chem.*, **24**, 97 (1970).
18. A. J. Appleby and A. Borucka, *This Journal*, **116**, 1212 (1969).
19. J. O'M. Bockris, Cahan, and Stoner, *Chem. Instrumentation*, **1**, 273 (1969).
20. S. Schuldiner and T. B. Warner, *This Journal*, **112**, 212 (1965).
21. K. J. Vetter, "Elecktrochemische Kinetik," pp. 500-506, Springer, Berlin (1961).
22. J. P. Hoare, "The Electrochemistry of Oxygen," pp. 24-26, Interscience Publishers, New York (1968).
23. S. Gilman, *Electrochim. Acta*, **9**, 1025 (1964).
24. K. J. Vetter and D. Berndt, *Z. Elektrochem.*, **62**, 378 (1964).
25. A. N. Frumkin, E. I. Krushcheva, M. R Tarasevich, and N. A. Shumilova, *Elektrokhimiya*, **1**, 17 (1965).
26. J. O'M. Bockris and H. Wroblowa, *J. Electroanal. Chem.*, **2**, 428 (1964).

27. J. P. Hoare, *ibid.*, **12**, 260 (1966).
28. B. E. Conway and E. Gileadi, *Trans. Faraday Soc. London*, **58**, 2493 (1962).
29. J. P. Hoare, *This Journal*, **112**, 849 (1965).
30. H. Wroblowa, M. L. B. Rao, A. Damjanovic, and J. O'M. Bockris, *J. Electroanal. Chem.*, **15**, 139 (1967).
31. L. Pauling, "The Nature of The Chemical Bond," 3rd ed., pp. 88-91, Cornell University Press, Ithaca, N. Y. (1960).
32. A. Damjanovic, T. H. V. Setty, and J. O'M. Bockris, *This Journal*, **113**, 429 (1966).

Technical Notes

Zinc-dichromate High Power Primary Cell

Gianfranco Pistoia and Bruno Scrosati*

Istituto Elettrotecnico, Universitá di Roma, Rome, Italy

It is known that the electrochemical cells so far developed, at high discharge current drains, *i.e.*, current densities greater than 0.15 A/cm^2, generally have the characteristic of showing an appreciable voltage drop at the electrodes. This makes it impossible to obtain high specific power values, *i.e.*, power densities greater than 0.25 W/cm^2, with such systems.

The characteristics necessary in an electrochemical system for the development of a high power cell, *i.e.*, a cell capable of tolerating high discharge rates, are in essence: (*a*) high values of open circuit potential (OCV), (*b*) very low internal resistance to ensure that IR drops through the cell are almost negligible, and (*c*) very low electrode polarizations even at high discharge rates.

None of the high power cells based on metallic anodes and halogens as cathodes, such as Mg/Cl_2 (1), Zn/Cl_2 (2), and Mg/Br_2 (3) has all these characteristics. In these systems, in order to dissolve the halogens, it is necessary to use electrolytes containing halide salts, such as NaCl and NaBr (1), $CaCl_2$ and $ZnCl_2$ (2), and $MgBr_2$ (3), which do not possess high specific conductivities. This results in an appreciable voltage drop under discharge and, consequently in the impossibility of obtaining high power values. Furthermore, the necessity of a continuous supply to the positive electrode of the gaseous or liquid halogen from a separate container creates enormous problems as far as both materials and techniques are concerned. Finally the high cost and the use of substances which are dangerously toxic makes this type of cell limited in its application.

It would seem more practical to use, as a cathode, a couple in which the oxidized form is present on the electrode support, as in the Zn/KIO_3 (4) and Zn/AgO (5) systems, or, alternatively, in solution. The latter has some advantage over the former, since it does not require preformation of the cathode, as it is sufficient to provide an inert electrode, such as graphite, at whose surface the oxidized species may be reduced.

One of the cells which works with a liquid depolarizer is the zinc-dichromate cell. This cell is an old concept and could in principle be discharged at high current drains (6). On the other hand the cell, in its old construction, presents serious disadvantages, such as electrode polarizations and very short shelf life, which have so far prevented its use for high power purposes. These disadvantages can be overcome by recirculating the electrolyte through the electrodes, choosing the best electrolyte concentration and working temperature and by careful design of the cell. Using a similar technique, Crowley *et al.* were able to realize a high rate performance cell based on a Mg/CrO_3 system having a recirculating acidic electrolyte (7).

In this work the characteristics and the performance of an improved zinc-dichromate cell are reported.

Experimental

Choice of electrolyte.—Before arriving at the system Zn/$Na_2Cr_2O_7$ in acidic solution, several other possible cathodic couples for the development of high power cells, were taken into consideration. Among these were

$S_2O_8^{2-}/SO_4^{2-}$	$E° = 2.01$V
Co^{3+}/Co^{+2}	$E° = 1.81$V
MnO_4^-/Mn^{2+}	$E° = 1.69$V
Ce^{4+}/Ce^{3+}	$E° = 1.61$V

The respective voltage under load of cells using each of these systems coupled with a zinc anode and in sulfuric solution was, at best, about 1V for current densities of the order of 0.05 A/cm^2.

More encouraging results were obtained with systems utilizing the $Cr_2O_7^{2-}/Cr^{3+}$ couple and therefore attention was focused on this cathodic material. The characteristics of the zinc-dichromate system were thoroughly studied, particularly as far as the composition of the electrolyte and its recirculation procedure through the electrodes were concerned.

It is known that the formal potential of the $Cr_2O_7^{2-}/Cr^{3+}$ couple varies widely with the nature and the concentration of the acid (8). In HCl and $HClO_4$ solutions, especially when dilute, the formal potential is considerably lower than in H_2SO_4 solutions. It was noted that progressively increasing the H_2SO_4 concentration up to 4.5M [32 w/o (weight per cent)] the OCV of the zinc-dichromate system correspondingly increases to a value very close to the 2.12V expected from the formal potentials of the two electrodes.

Also the dichromate concentration plays an important role especially as far as the oxidation reaction rate is concerned (9). It is known that in acidic solution the following equilibria are present

$$HCrO_4^- \rightleftharpoons H^+ + CrO_4^{2-}$$

$$2HCrO_4^- \rightleftharpoons H_2O + Cr_2O_7^{2-}$$

It appears that the most active ion in the oxidation process is $Cr_2O_7^{2-}$ which predominates at high concentrations (8). It follows that the use of concentrated dichromate solutions is necessary in order to obtain the high reaction rates that are essential to realize an electrochemical system able to work at high current drains.

* Electrochemical Society Active Member.

Several tests were performed with the system Zn/$K_2Cr_2O_7$ using a 32 w/o H_2SO_4 aqueous solution and with a $K_2Cr_2O_7$ concentration increasing from 3 to 10g for 100g of sulfuric solution. The cell performance improvement was consistent with the concentration increase. Potassium dichromate, however, is not very soluble and it was not possible to reach a concentration higher than 10 w/o of the salt in the sulfuric solution. Since sodium dichromate has greater solubility, the Zn/$Na_2Cr_2O_7$ system was examined, with the dichromate concentration increasing from 10 to 20 w/o. Since concentrations higher than 15 w/o did not improve the cell performance significantly, the solution H_2SO_4 32 w/o and $Na_2Cr_2O_7$ 15 w/o in water, was chosen as the optimum electrolyte solution.

Cell structure.—A possible cell structure is shown in Fig. 1. This cell essentially consists of a circular amalgamated zinc plate forming the anode which faces the cathode, a circular graphite plate. The surface of each electrode is 50 cm^2 and the distance between them 0.2 cm.

The electrodes are kept at the desired distance by an inert support on which are located both the inlet and the outlet for the recirculating electrolyte. The system is sealed by the external casing and by gasket rings. The cell performance improves with the temperature increase of the solution. In order to avoid an external heat source, an initial working temperature has been chosen that could be obtained simply by mixing the $Na_2Cr_2O_7$ aqueous solution with the sulfuric acid before the activation of the cell. For this purpose the sulfuric acid and the dichromate solutions are kept in two separate containers (Fig. 2). By this procedure it is possible to obtain a temperature of 75°C and an electrolytic conductivity of 0.97 $ohm^{-1} \cdot cm^{-1}$ compared with 0.66 at 20°C.

At the moment of the cell activation, known amounts of the two solutions are released and mixed together

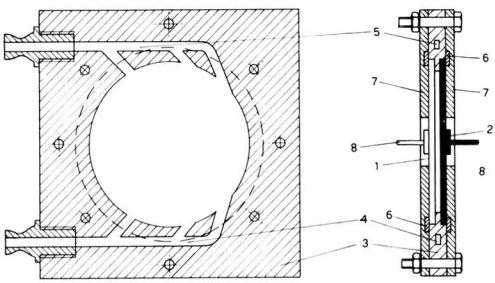

Fig. 1. Cell structure: 1, zinc plate; 2, graphite plate; 3, electrode support; 4, electrolyte inlet; 5, electrolyte outlet; 6, gasket rings; 7, external case; 8, external contacts.

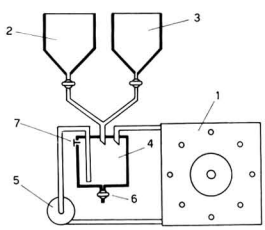

Fig. 2. Cell assembly: 1, cell; 2, sulfuric acid container; 3, dichromate container; 4, mixing container; 5, pump; 6, exhausted solution outlet; 7, valve.

Table I. Performance of the cell Zn/H_2SO_4 (32%), $Na_2Cr_2O_7$(15%)/C

Average working temperature; 60°C; OCV: 2.10-2.12V; electrode surface: 50 cm^2; electrode separation 0.2 cm.

Current density ($A/cm^2 \cdot 100$)	Average voltage at electrodes (V)	Power ($W/cm^2 \cdot 100$)	Time of discharge (min)
1.6	1.88	3.0	50
8.0	1.83	14.6	25
13.6	1.76	23.9	10
20.0	1.64	32.8	10
30.0	1.59	47.7	8
40.0	1.54	61.6	5
44.0	1.41	62.0	4
48.0	1.22	58.5	4
50.0	1.00	50.0	3

in a third container situated below. By means of a pump, the electrolyte is then continuously recycled between the electrodes. The electrolyte inlets are designed so as to ensure a uniform distribution of the liquid on the plates. At the end of the cell operation the exhausted electrolyte is eliminated from the mixing container by an outlet at the bottom of the container itself. In this way the contact between electrodes and solution is restricted solely to the period when the cell is operative. Consequently, self discharge processes are minimized. A value in the upper part of the container eliminates the possibility of any pressure build-up.

The electrolyte recirculation is extremely convenient for this type of cell, because allowing a continuous renewal of the liquid layer in contact with the electrode surfaces avoids accumulation of reaction products in the vicinity of the electrodes.

Results

The performance of the cell is reported in Table I, from which it can be seen that the values of the voltage under load remain sufficiently high even at high discharge current densities. This is due both to the very low value of the internal resistance, calculated as 0.004 ohm at the working temperature, and to the rapid renewal of the electrolytic solution. The first characteristic makes the IR drop almost negligible and the second avoids serious concentration polarization effects.

Figures 3 and 4 show the performance of this cell compared with those based on the most common system so far developed for operation at high current density rates. It can be seen that the cell is able to furnish current and power density values twice as great as those of the Mg/Br_2 cell (3) which to date has been considered the best of the high power cells operating for the periods of time shown in Table I. For instance with the zinc-dichromate cell it is possible to obtain

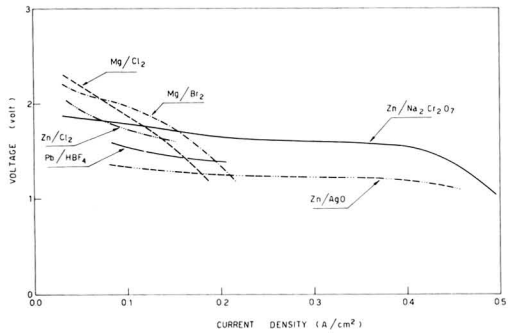

Fig. 3. Voltage-current density for the zinc/dichromate and other batteries at high drain rates. Data related to Zn/AgO and Pb/HBF_4 systems were obtained in pulse condition (10). For data related to Mg/Cl_2, Zn/Cl_2, and Mg/Br_2 see ref. (1), (2), (3), respectively.

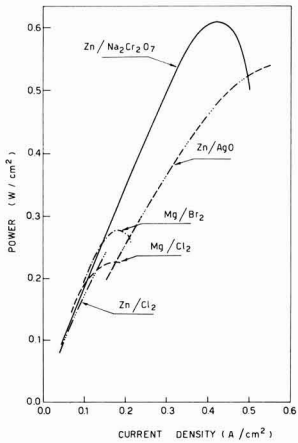

Fig. 4. Power-current density curve for the zinc-dichromate and other batteries at high drain rates. Data related to the Zn/AgO are obtained in pulse condition (10). For data related to Mg/Cl_2, Zn/Cl_2, and Mg/Br_2 see ref. (1), (2), (3), respectively.

a maximum power density value of about 0.62 W/cm² at 0.44 A/cm², while the Mg/Br_2 cell gives a maximum value of 0.28 W/cm² at 0.19 A/cm².

No attempt has yet been made on optimizing the volume and the weight of the cell and therefore no W/g or W/cm³ values are here reported.

The low cost of manufacture, the safety, and the simplicity of use represent other important advantages of the zinc-dichromate cell over the metal-halogens type.

Acknowledgment

This work was sponsored by the Consiglio Nazionale delle Ricerche under Contract No. 115/0860.0.1894.

Manuscript submitted Nov. 3, 1969; revised manuscript received Jan. 16, 1970. This was Paper 45 presented at the Detroit Meeting of the Society, Oct. 5-9, 1969.

Any discussion of this paper will appear in a Discussion Section to be published in the December 1970 JOURNAL.

REFERENCES

1. R. Blue, N. Sweeny, and M. Neipert, U.S. Pat. 3,019,279 Jan. 30, 1962.
2. P. Howard, *This Journal*, **99**, 206C (1952).
3. M. Neipert and R. Carr, U.S. Pat. 3,134,968, May 26, 1964.
4. J. Jones and A. Arranaga, *This Journal*, **115**, 435 (1968).
5. R. Jasinski, "High Energy Batteries," p. 269, Plenum Press, New York (1967).
6. L. Jumeau, "Piles et Accumulateurs Électriques," p. 37, A. Colin, Paris (1941).
7. C. Crowley, W. Langdon, D. Louzos, and J. Conolly, U.S. Pat. 2,921,111, Feb. 2, 1953.
8. H. A. Laitinen, "Chemical Analysis," p. 441, McGraw-Hill Book Co., New York (1960).
9. F. H. Westheimer, *Chem. Rev.*, **45**, 419 (1949).
10. See ref. (5), p. 211.

Electrode Overvoltages in Molten Fluorides
The Corrosion of Zirconium Electrodes in Molten KHF_2

S. Pizzini*,[1], G. Sternheim

Euratom CCR, Materials Department, Petten, North Holland

In the previous papers (1, 2) dealing with the evolution of hydrogen at bright Pt electrodes as well as in a paper of this series (3) dealing with the corrosion of aluminum electrodes in KHF_2 melts, it was shown that in anhydrous melts or in melts where the water contamination is lower than about 0.1% by weight, the limiting current for the cathodic evolution of hydrogen and accordingly, the corrosion current of aluminum, is negligibly small. Indeed, it has been felt that the cathodic deposition of the refractory metals from KHF_2 melts should be feasible if the solubility of the fluorides of the refractory metals in KHF_2 melts is sufficiently high or if the diffusion coefficient of the cations is high enough at the relatively low working temperatures. In order to obtain preliminary information on this subject, zirconium was chosen as a test material and corrosion as well as polarization experiments on zirconium electrodes were carried out.

A flanged copper cell with Viton gaskets [a slightly modified version of the graphite cells described in ref. (2)] was used. As before, Teflon was used as a container for the melt and a graphite ring as the auxiliary electrode. KHF_2, twice-crystallized in water-10% ethanol mixtures and dried under vacuum, was used.

Pure anhydrous nitrogen gas was used as cover gas to minimize the contamination of the melt. Electrodes of known geometrical dimensions (about 1 cm²) were mechanically polished, rinsed with ethanol, and then used for corrosion or polarization measurements. The electrodes used for corrosion experiments were quickly extracted from the melt and cleaned in ethanol in an ultrasonic bath. Overvoltage measurements were carried out by the galvanostatic method, as previously described (1-3). As reference electrode, an iso-electrodic zirconium or a hydrogen electrode was used. The voltage of a cell constituted by a hydrogen electrode and a zirconium electrode is about −500 mV. The solubility of ZrF_4 (added to the melt after being previously dried under vacuum) is of the order of 2×10^{-3} moles/liter at 250°C.

Figure 1 shows the ϵ *vs.* current density plot for the cathodic polarization of zirconium electrodes. From this figure one recognizes the presence of a limiting current at about 1×10^{-2} A/cm² and of small plateau at about −1700 mV.

Inspection of the electrode, after polarizing it at about −2000 mV, revealed the presence of a film of potassium metal. When anodically polarized, the electrode eventually passivates. In Fig. 2 the results of different corrosion experiments (at different cathodic polarizing currents) are reported. The experimental value of $i°_K$, the corrosion current under conditions of spontaneous corrosion, equals 3.96×10^{-2} A/cm² (average of 20 experiments). The corresponding mean square deviation is quite large (1.22×10^{-2} A/cm²), thus indicating poorly reproducible surface conditions.

* Electrochemical Society Active Member.
[1] Present address: Istituto di Elettrochimica e Metallurgia dell' Università, via G. Venezian 21, Milano, Italy.

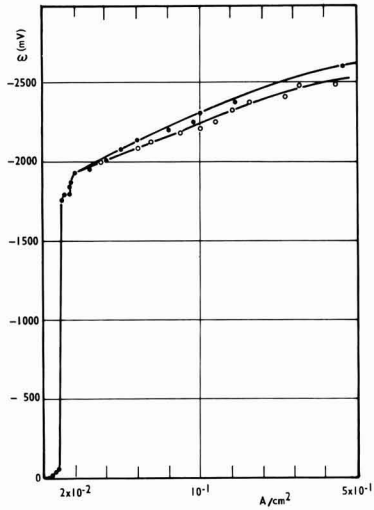

Fig. 1. ϵ *vs.* current density plot for the cathodic polarization of zirconium electrodes in KHF_2 melts. Temperature, 250°C, zirconium reference electrode.

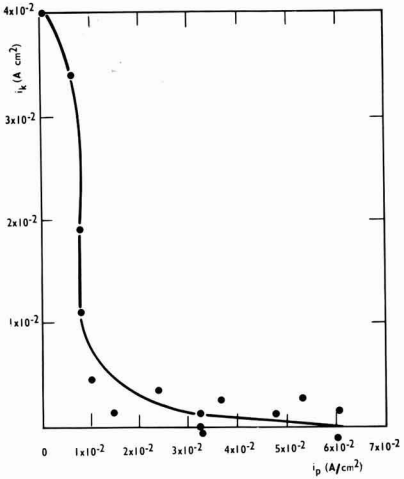

Fig. 2. Weight changes *vs.* polarization current plots for the cathodic polarization of zirconium electrodes in KHF_4 melts. Temperature, 250°C. Weight changes are expressed in terms of corrosion current.

Figures 1 and 2 show that the corrosion rate is greatly reduced and eventually suppressed at voltages between −1700 and −2500 mV. It appears, however, that when the corrosion rate is zeroed, a discharge of potassium takes place. (The negligibly small weight increase observed at the highest cathodic polarization could, however, indicate simultaneous discharge of Zr and K). The zirconium deposition rate is, however, insignificant for any technological application. As this behavior is similar to that of aluminum in the same melt (3), discussion of these present experimental results could be carried out by analogy with the aluminum case, when considering zirconium as a corrosion electrode.

Figure 3 is a picture of the possible reactions which occur at such a corrosion electrode, when the cathodic reactions are supposed to be, according to our previous papers (1, 2), the reactions

$$(\alpha)\quad HF + e \rightarrow \tfrac{1}{2}H_2 + F^-$$

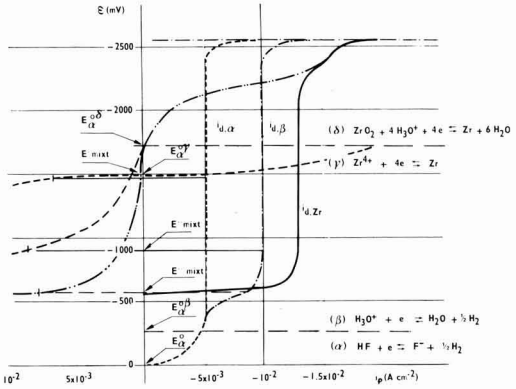

Fig. 3. Schematic diagram of the partial anodic and cathodic reactions at a zirconium electrode in steady state corrosion conditions.

and

$$(\beta)\quad H_3O^+ + e \rightarrow \tfrac{1}{2}H_2 + H_2O$$

both of which are diffusion limited. In the case of (β) reaction it has been demonstrated that the limiting current is a function of the water content (1). The overvoltage *vs.* the current density (c.d.) curves for (α) and (β) reactions, reported in Fig. 3 correspond to that measured at Pt electrodes in KHF_2 melts containing water; although the overvoltage for the H_2 discharge could be very different at the Zr electrode, the value of the limiting current must be the same in melts of the same composition.

In the same figure, a guess is also made for the shape of the overvoltage *vs.* c.d. for the possible anodic reactions

$$(\gamma)\quad Zr \rightleftharpoons Zr^{4+} + 4e$$

and [see also ref. (4) for the same reaction in aqueous solutions]

$$(\delta)\quad Zr + 6H_2O \rightleftharpoons ZrO_2 + 4H_3O^+ + 4e$$

Reaction (γ), whose standard potential (indicated in Fig. 3 as $E_\alpha^{\circ\gamma}$) has been calculated (5) from the free energy of the reaction

$$Zr + 4HF = ZrF_4 + 2H_2 \quad \Delta G^{250^\circ C} = -151.9 \text{ kcal/mole} \qquad [1]$$

for a melt saturated in KF as well as in ZrF_4,[2] should account for the free corrosion of zirconium, when the partial cathodic reaction is reaction (α)

$$(\alpha)\quad HF + e \rightarrow \tfrac{1}{2}H_2 + F^-$$

Reaction (δ), whose standard potential (indicated in Fig. 3 as $E_\alpha^{\circ\delta}$) has been calculated from the free energy value of the reaction

$$Zr + 2H_2O = ZrO_2 + 2H_2 \quad \Delta G^{250^\circ C} = -132.2 \text{ kcal/mole} \qquad [2]$$

is the usual expression for the half cell reaction of an oxide electrode (6).

In Fig. 3 the ϵ *vs.* i_P curves for reactions (γ) and (δ) have been drawn (as dotted and dashed lines) in a manner that supposes the absence of effects of overvoltages for reaction (γ)[3] and a strong hindering (due to the presence of a ZrO_2 layer, possibly nonstoichiometric) of reaction (δ).

Although reaction [1] is apparently thermodynamically favored, reaction [2] should occur as soon as

[2] The possible formation of zirconium hydride has not been accounted for, inasmuch as this effect may be considered as a slight reduction of the thermodynamic activity of zirconium metal.

[3] This condition, based on the assumption that zirconium is a "normal metal" with an exchange current of the order of 10^{-2} A/cm², is, however, unessential for the treatment which follows.

the accumulation of metal cations and water near to the electrode leads to supersaturation and consequent precipitation of the sparingly soluble ZrO_2.

In the same figure different possible values of the mixed potential of the corrosion electrode have been indicated, which only depend on the shape of the anodic overvoltage curve for reactions (γ) and (δ). Reactions (α) and (β) in fact occur under conditions of diffusion-limited current. If it is supposed that reaction (γ) occurs, coupled with reaction (β), then the value of the mixed potential E'_{mixt} closely corresponds to the $E_\alpha{}^\gamma$ value and the corrosion current i°_K can be calculated from the known value of $i_{d,\beta}$ as (3)

$$i^\circ_K = i_{d,\beta}$$

Figure 3, where the curves of Fig. 1 (solid lines) are replotted by recognizing that the inflection at −1750 mV corresponds to the zirconium deposition plateau and that the plateau at −2000 mV corresponds to potassium deposition, shows, however, that the potential which the electrode takes under current-less conditions (*i.e.*, E'''_{mixt}) is definitely more anodic than that corresponding to the E'_{mixt} value. Moreover, the corrosion current takes a value

$$i^\circ_K = 3\, i_{d,\beta} = 3\, i_{d,Zr}$$

(where $i_{d,Zr}$ is the cathodic limiting current measured at the Zr electrode, see Fig. 1) if we consider that the average content of water of a KHF_2 bath after the treatments used for the present experiments corresponds to a limiting current for the (β) reaction of about 1.3×10^{-2} A/cm² (1, 2).

From the ϵ *vs.* current density curves for the anodic polarization of a zirconium electrode reported in Fig. 3, it appears that the present experimental behavior is well accounted for, if one assumes that the electrode works according to reactions (δ) and (β), *i.e.*, as a covering layer electrode.

When considering a stationary film thickness of the order of 100Å or less [as results from the extrapolation of the data of ref. (4) to a formation voltage corresponding to the overvoltage of the partial anodic reaction (δ)] and ambipolar migration in the semiconducting[4] layer, more insight into the corrosion mechanism could be gained by using the phase-scheme of Fig. 4 for a Zr, ZrO_2 electrode. Here the electrode is represented as a "Korrosion Deckschicht Elektrode" according to Lange (9) and it is supposed that the rate-determining step for the corrosion reaction is the diffusion of H_3O^+ across the diffusion layer. Mobility of Zr^{4+} and O^{--} in the ZrO_2 film does not imply that we assume the migration of ions as a volume process via lattice defects; faults, dislocations, and grain boundaries are alternative paths (10, 11).

From Fig. 4 it is apparent that reactions (γ) and (β), subdivided in the elementary reaction steps and written as

$$(\pi + Zr^{4+} - \text{transf.} + \theta)\underset{I}{Zr^{4+}} \rightarrow \underset{II}{Zr^{4+}}$$

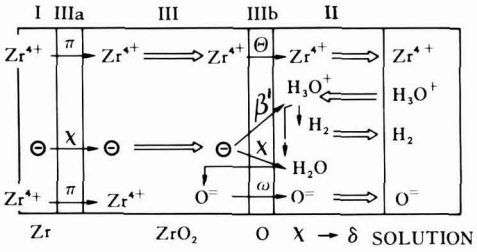

Fig. 4. Phase scheme of a "Korrosion Deckschicht Elektrode." The metal phase is indicated with I, the oxide phase with III, and the solution phase with II. δ indicates the thickness of the diffusion layer. Other Greek symbols indicate, as in the previous paper (3), reactions taking place at the interfaces IIIa and IIIb.

and

$$(\chi + e\text{-transf.} + \beta')\ \underset{II}{H_3O^+} + \underset{I}{e} \rightarrow \underset{II}{H_2O} + \underset{II}{\tfrac{1}{2}H_2}$$

(where Zr^{4+} — transf. and *e*-transf. indicate the mass and charge transfer processes across the ZrO_2 phase) occur simultaneously at a rate which equals the limiting current of β reaction.

If the coupling of reactions (γ) and (β) were the unique process responsible for the corrosion reaction, then the corrosion current i°_K should equal the value of the limiting current $i_{d,\beta}$. This is not apparently the case, because of the side reaction with H_2O, which is a product of reaction (β) and reacts with Zr according to the partial reactions

$$(\chi + e\text{-transf.} + \chi')\ \underset{II}{H_2O} + \underset{I}{2e} \rightarrow \underset{III}{O^=} + \underset{II}{H_2}$$

and

$$(\pi)\ \underset{I}{Zr^{4+}} \rightarrow \underset{III}{Zr^{4+}}$$

and occur as well with a maximum rate which equals the $i_{d,\beta}$ value. In steady state conditions we have therefore

$$i^\circ_K = i_{d,\beta} + 2\, i_{d,\beta}$$

which is a figure very close to the experimental value. This result confirms the proposed model and suggests as a reasonable explanation for the observed codeposition of Zr and K, the permanence (see Fig. 3) of a ZrO_2 layer [with the overvoltage associated with the polarization of the electrode according to reaction (δ)] at voltages higher than the discharge potential of Zr according to reaction (γ).

Nomenclature

$E^j{}_\alpha$	Potential of an electrode j, *vs.* a hydrogen electrode whose reaction is α
ϵ	Electrical potential difference measured at the terminals of the tensiometric cell
i_P	Polarizing current A/cm²
i_d	Diffusion limiting current
i°_K	Corrosion current, A/cm², when external current is zero
i_K	Corrosion current, A/cm²
${}_I Me^{z+} = {}_I Me - Z_I e$	

Subscripts I, II, III indicate the metal, solution, and oxide phases, respectively.

APPENDIX

In this paper the symbols for the electrode reactions have been written according to our previous papers (1-3) and the nomenclature used is a slightly modified version of the Lange and Göhr symbolism (6).

The arbitrary zero of the potential scale of Fig. 3 is the potential of the reaction (α) for hydrogen at 1 atm and HF at 39.8 mm Hg, which is the equilibrium pressure of a melt of KHF_2 at 250°C saturated with KF.

The potential of reaction (β) is calculated according to ref. (1) by taking into account the free energy of the reaction

$$H_2O + HF \rightleftarrows H_3O^+ + F^-$$

($\Delta G \simeq 9000$ cal/mole at 250°C) and corresponds, for H_2O at 1 atm and HF at the equilibrium partial pressure, to −263 mV.

Acknowledgments

The authors are greatly indebted to Dr. J. H. Westbrook for his valuable suggestions.

Manuscript submitted March 14, 1969; revised manuscript received Dec. 22, 1969. This was Paper 202 presented at the New York Meeting of the Society May 4-9, 1969.

Any discussion of this paper will appear in a Discussion Section to be published in the December 1970 JOURNAL.

[4] S. Aronson (8) quotes, at temperatures around 500°C, an ionic transport number of 0.35.

REFERENCES

1. S. Pizzini, G. B. Barbi, and G. Sternheim, *Electrochim. Acta*, **8**, 227 (1963).

2. S. Pizzini and A. Magistris, *ibid.*, **9**, 1189 (1964).
3. S. Pizzini, A. Magistris, and G. Sternheim, *Corr. Sci.*, **4**, 345 (1964).
4. G. C. Willis, G. B. Adams, and P. Van Ryssel-berghe, *Electrochim. Acta* **9**, 79 (1964); **9**, 93 (1964).
5. Janaf Thermochemical Tables, Clearinghouse (1965).
6. K. J. Vetter, "Elektrochemische Kinetik," Springer, Berlin (1961).
7. T. Smith, *This Journal*, **112**, 560 (1965).
8. S. Aronson, *ibid.*, **108**, 312 (1961).
9. F. Lange and H. Göhr, "Thermodynamische Elektrochemie," Hütig Verlag, Heidelberg (1962).
10. R. Cox and C. Roy, AECL-2350, October 1965.
11. E. A. Gulbransen and K. F. Andrew, *Trans. AIME*, **209**, 394 (1957).

On the Electrical Analog Circuit for the Study of Metal Solution Interfaces by the Square Wave Technique for Capacitance Measurements

R. G. Barradas*

Department of Chemistry, Carleton University, Ottawa, Ontario, Canada

and E. M. L. Valeriote*

Department of Physical Chemistry, University of Bristol, Bristol, England

In an earlier paper (1) we evaluated the technique for capacitance measurements published by McMullen and Hackerman (2) and reported that capacity *vs.* potential (*C. vs. E*) curves change in using different values of R_s [see ref. (1)]. At that time the maximum possible values of R_s were used and we argued that there was some empiricism in assuming the electrical analog of the metal-solution interface. In a subsequent communication (3) we suggested an experimental improvement in the electrode assembly to minimize the problems due to R_s. However, on further reconsideration, the following electrical analysis is now offered by way of an appendix as a more plausible explanation of some of the anomalies observed. Referring to McMullen and Hackerman's analysis and nomenclature of time-potential curves it is not necessary to assume that $R_p = \infty$ (see Fig. 1). It is to be noted that R_p should, in principle, be more rigorously represented by the complex faradaic impedance (Z_f). The representation of a faradaic process by a simple resistor (R_p) is somewhat restrictive with respect to *a priori* separation of this process from double layer charging. The exact form of Z_f depends on the model for the faradaic process. In the limiting case, when Z_f approaches infinity, the same conclusions will be reached. Hence, one could alternately replace R_p by Z_f throughout this paper, and subsequently R by Z (see Eq. [13]), where $Z = (R_s + R_c)Z_f/R_s + R_c + Z_f$, but this appears to be a less desirable choice because it would involve mixing complex quantities with purely real or imaginary ones. However, this simple treatment is limited to near ideally polarizable electrodes, where negligible faradaic processes occur, such as the hanging mercury drop electrode (3) for which the assumption that Z_f approaches infinity renders the model depicted in Fig. 1 to be valid.

If $R_c = 0$ as stated in case I [ref. (2)]

$$E_c = \frac{R_p E_i}{R_p + R_s}\left[1 - \left(\frac{\exp[-R_p + R_s]\,t}{R_p R_s C^1}\right)\right] \quad [1]$$

If the period of the square wave $\tau << \dfrac{R_p R_s C^1}{(R_p + R_s)}$ the exponential term in Eq. [1] can be linearized to give $E_c = E_i t/R_s C^1$. Following McMullen and Hackerman's analysis [case III in ref. (2)] when $R_c = 0$ one obtains

$$E_x = iR_c + E_i t/R_s C^1 \quad [2]$$

as a correct equation for E_x (the observed signal) for each half-cycle obtained on the oscilloscope. The slope of the observed linear oscilloscope trace is then given by

$$dE_x/dt = R_c\ di/dt + E_i/R_s C^1 \quad [3]$$

The first term on the right hand side of Eq. [3] is not independent of the parameters in the second term and may not be negligible in comparison. The negligence of $R_c\ di/dt$ is therefore questionable.

To investigate this point more rigorously, the circuit analysis should be carried out with the initial condition that R_c could take any value (except infinity). Assuming that R_p and R_s are finite, application of Kirchoff's laws yields the following equations

$$E_i = iR_s + E_x \quad [4]$$

$$E_x = E_c + iR_c \quad [5]$$

$$E_c = i_p\ R_p \quad [6]$$

$$dE_c/dt = i_c/C^1 \quad [7]$$

$$i = i_p + i_c \quad [8]$$

Solving Eq. [4] and [5] gives

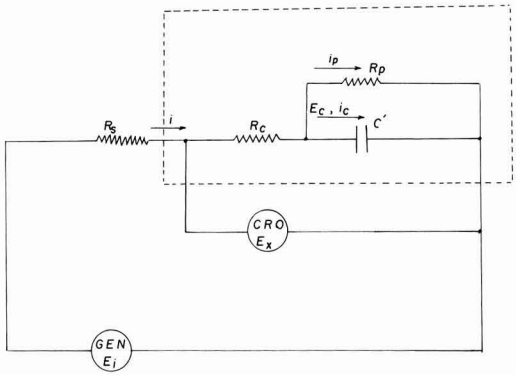

Fig. 1. Electrical analog circuit with the addition of GEN (generator) and CRO (oscilloscope) symbols.

* Electrochemical Society Active Member.

$$E_x = E_c\left(\frac{R_s}{R_s + R_c}\right) + E_i\left(\frac{R_c}{R_s + R_c}\right) \quad [9]$$

and

$$E_i = (R_s + R_c)i + E_c \quad [10]$$

From Eq. [6] and [8]

$$E_c = R_p(i - i_c) \quad [11]$$

Combination of the differentials of [10] and [11], and recalling that E_i is constant during each half cycle

$$dE_i = 0 = (R_p + R_s + R_c)di - R_p\, di_c \quad [12]$$

Integrating the right hand side of Eq. [12] using the boundary condition that at $t = 0$, $E_c = 0$; it follows from Eq. [4] and [5] that $(E_i)_{t=0} = i/(R_s + R_c)$. Setting

$$\underline{R} = (R_s + R_c)\, R_p/R_s + R_c + R_p \quad [13]$$

yields:

$$i_c = \frac{R_s + R_c}{\underline{R}}\left[i - \frac{E_i}{R_s + R_c} \right] \quad \text{and}$$

$$\frac{di_c}{dt} = \frac{R_s + R_c}{\underline{R}} \cdot \frac{di}{dt} \quad [14]$$

Combining Eq. [7] with [14] and the differential of [10] then results in

$$\frac{di_c}{i_c} = \frac{-dt}{\underline{R}C^1} \quad [15]$$

Integration of [15] from $i_c = E_i/(R_s + R_c)$ to i_c and $t = 0$ to $t = t$, and taking the exponentials of the resulting expression, one obtains

$$i_c = \frac{E_i}{R_s + R_c}\exp(-t/\underline{R}C^1) \quad [16]$$

Substitution of [16] into Eq. [7], and integrating, on substitution into Eq. [9] leads to

$$E_x = \frac{E_i}{R_s + R_c}\left\{ \frac{R_s\underline{R}}{R_sR_c}\left[1 - \exp\left(-t/\underline{R}C^1\right)\right] + R_c \right\} \quad [17]$$

t is always $\leq \tau/2$ during a half cycle, hence at large enough frequencies so that $t \leq \tau/2 << \underline{R}C^1$ the exponential in [17] can be linearized to give

$$E_x = \frac{E_iR_c}{R_s + R_c} + \frac{E_iR_s}{(R_s + R_c)^2} \cdot \frac{t}{C^1} \quad [18]$$

the condition under which linearization can be made equivalent to $\tau/2 << C^1(R_s + R_c)$, since $\underline{R} \to R_s + R_c$ as $R_p \to \infty$. This condition is realized to a good approximation as long as no faradaic process occurs. It is to be noted from Eq. [18] that as long as the wave is linear, the form of E_x is independent of the value of R_p. The slope of the output wave is given by

$$\frac{dE_x}{dt} = \frac{E_i}{C^1} \cdot \frac{R_x}{(R_s + R_c)^2} \quad [19]$$

or

$$C = \frac{C^1}{A} = \frac{E_iR_s}{A(R_s + R_c)^2} \cdot \frac{1}{(dE_x/dt)} \quad [20]$$

where A is the electrode area and C is the differential capacity. If $R_c << R_s$ then

$$C = \frac{E_i}{AR_s(dE_x/dt)} \quad [21]$$

Equation [21] is not dissimilar in essence from the one ultimately arrived at by McMullen and Hackerman (2). However, when R_c becomes significant compared to R_s, Eq. [21] will give values of C which are greater than those obtained from the more accurate Eq. [20] because $R_s/(R_s + R_c)^2$ is $< 1/R_s$ for $R_c > 0$. This analysis goes a long way toward explaining the anomalous dependence of capacities on R_s reported in ref. (1). Examination of Fig. 2, 3, and 4 in ref. (1) suggests that a potential shift is also occurring. An assumption that R_c changes as a function of potential alone could not explain the difference between cathodic and anodic branches for small values of R_s. In all likelihood, it is more probable that for small values of R_s it is reasonable to consider that there is some undesirable faradaic reaction occurring in the case of the large Hg pool electrode (5 cm^2), but the faradaic process should be minimal if not insignificant with the use of a hanging Hg electrode [ref. (1)]. R_c may well vary as a function of potential if it is not to be regarded as purely the electrolyte resistance. In any case, it is possible to incorporate the nonelectrolyte component of R_c into a term such as Z_f if R_p is replaced by it; thereby making R_c the electrolyte resistance only (6). The anomalies for large R_s values (implying constant current conditions) appears in all probability to be solely due to departure from constant current conditions at given potential if a faradaic process was occurring, in which case the simple model shown in Fig. 1 would be invalid unless the form of Z_f and its coupling with the charging impedance were considered as mentioned earlier. The present model is not intended, as stated previously, to cover such a case and the technique is not meant to be used under such conditions. Considering the availability of many other more accurate methods for determining capacitance data from slopes of oscilloscope traces [see *e.g.*, ref. (4) and (5)] the technique as published by McMullen and Hackerman (2) does not appear to warrant further complicated theoretical considerations. McMullen and Hackerman's objective was meant for a specialized application, namely to obtain electrode surface area measurements where no faradaic processes occur. The technique could indeed be useful under either constant current or constant voltage conditions.

Acknowledgment

Financial support from the National Research Council of Canada is gratefully acknowledged. We are also indebted to Professor R. S. C. Cobbold of the University of Toronto for helpful discussions.

Manuscript submitted Sept. 15, 1969; revised manuscript received *ca.* Dec. 24, 1969.

Any discussion of this paper will appear in a Discussion Section to be published in the December 1970 JOURNAL.

REFERENCES

1. R. G. Barradas and E. M. L. Valeriote, *This Journal*, **112**, 1043 (1965).
2. J. J. McMullen and N. Hackerman, *ibid.*, **106**, 341 (1959).
3. R. G. Barradas and E. M. L. Valeriote, *ibid.*, **114**, 593 (1967).
4. J. W. Hayes and C. N. Reilley, *Anal. Chem.*, **37**, 1322 (1965).
5. E. R. Brown, T. G. McCord, D. E. Smith, and D. D. DeFord, *ibid.*, **38**, 1119 (1966).
6. B. B. Damaskin, "The Principles of Current Methods for the Study of Electrochemical Reactions," pp. 68 and 73, McGraw-Hill Book Co., New York (1967).

A Simple Cell and Reference Electrode for Voltammetry in Alkaline Melts

E. Banks,* C. W. Fleischmann,*[1] and L. Meites[2]

Department of Chemistry, Polytechnic Institute of Brooklyn, Brooklyn, New York

Various techniques are used to provide conductance between two or more otherwise isolated compartments of an electrolytic cell. For molten salt studies, isolation of the compartments is usually accomplished by fritted glass, porous silica disks, or asbestos plugs. Examples are given in recent reviews (1-4). These materials, however, are severely attacked by alkaline melts. For use in such melts, particularly those of the alkali tungstates, a simple, inexpensive, and easily constructed two-compartment cell was designed. This cell employed commercial laboratory porcelain as a nonporous conductive separator between the working and reference half-cell compartments.

Sodium glasses have been employed as conductive separators in molten salts (5, 6), but the use of glass limits work to below 500°C. Labrie and Lamb (7), however, developed a reference electrode employing the Ag/Ag(I) couple in which a sodium-containing porcelain separator was used in melts up to 900°C. These workers also demonstrated the feasibility of commercial porcelain as a separator.

Reference half-cells reversible to oxygen have been employed in oxide-containing melts (1-4), but because they are inconvenient, they have not been recommended (3) for use in fused-salt voltammetry. A large Pt electrode is frequently employed as a reference for voltammetry in melts (1-4), but since it had not been demonstrated that such an electrode is well poised in tungstate melts, a metal, metal ion couple was preferred. The Ag/Ag(I) couple has been used as a reference in a number of melts (1-4), and Ag/Ag_2WO_4 was found to be a successful half-cell for use as a reference with the present cell design.

The Ag_2WO_4 used in these studies was prepared by precipitation from aqueous solutions. A filterable precipitate was obtained by mixing together 0.1-0.2*F* solutions of reagent-grade $AgNO_3$ and Na_2WO_4 and allowing the precipitate to digest, overnight, in the dark. The precipitate was washed several times with water, then acetone, and dried in air.

The cell is illustrated in Fig. 1. A 5-ml Coors porcelain crucible served both as the container for the Ag/Ag_2WO_4 reference half-cell and as the conductive septum. This crucible was placed in a 10-ml porcelain tray along with the study melt. For improved conductance, the area of the crucible in contact with the melt was increased by placing the crucible on a loose platform of alumina tubes or rods. The resistance between the reference and working electrodes was determined for each cell by means of an a-c bridge so that the recorded voltammograms could be corrected for the potential drop across the porcelain.

Reproducibility of the potential of a Ag/Ag_2WO_4 half-cell was determined to be ±10 mV from the potentials of nine cells of the composition

$$Ag/Ag_2WO_4//Na_2WO_4//Ag_2WO_4/Ag$$

Potentials were measured at 750°C with the cells under argon. A second measurement on some cells was made after 3 hr to establish the extent of the potential drift with time. Table I records the potential of cells prepared as follows: Cells 1 through 4, constructed from freshly synthesized Ag_2WO_4 and previously unused Ag-wire electrodes; Cells 5 and 6, one half-cell was prepared from Ag_2WO_4 recovered from a previous reference compartment; and in cells 8 and 9, new and previously used silver wires were opposed. In cell 7, one porcelain crucible was of more recent manufacture than the other (8).

Ag/Ag_2WO_4 half-cells are polarized only about 5 mV at 100 mA/cm² (750°C) as shown by an extrapolation of the current-voltage data in Fig. 2 to that current density. This figure gives the total polarization of the anodic and cathodic reactions at two silver wire electrodes immersed in silver tungstate. The polarization at each electrode may be taken to be 2-3 mV at 100 mA/cm² assuming that the anodic and cathodic contributions to the total polarization are equal. This assumption is supported by voltammograms obtained at silver microelectrodes in Ag_2WO_4 which did show equivalent anodic and cathodic polarizations.

Since most voltammetric studies employ a small study electrode (*e.g.*, a 1-mm diameter Pt bead), the current density at the reference would be of the order of 1 mA/cm². Such a current density would give rise to negligible polarization as may be read from Fig. 2.

* Electrochemical Society Active Member.
[1] Present address: Mallory Battery Company, Tarrytown, New York.
[2] Present address: Clarkson College of Technology, Potsdam, New York.

Key words: fused salt voltammetry cell; silver-silver tungstate reference, voltammetry fused Cd(II) tungstate.

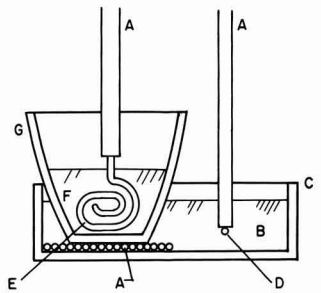

Fig. 1. Two-compartment cell for voltammetry. A, alumina tubing; B, study melt; C, 10-ml porcelain dish; D, study electrode; E, silver wire; F, Ag_2WO_4; G, 5-ml porcelain crucible.

Table I. Potentials of cells: $Ag/Ag_2WO_4//Na_2WO_4//Ag_2WO_4/Ag$, 750°C

Full-cell No.	Potential[a] of cell, V	Potential of cell, V after 3 hr	Description of cell[b]
1	0.00619	—	Both half cells were constructed from freshly synthesized Ag_2WO_4 and previously unused Ag-wire electrodes.
2	0.0148	0.0094	
3	0.00376	—	
4	0.000496	0.00175	
5	0.0388	—	One half-cell was prepared from Ag_2WO_4 recovered from a previously reference compartment.
6	0.00923	0.00845	
7	0.00150	—	New and previously used silver wires were opposed.
8	0.00507	0.0004	
9	0.0033	—	One crucible was of more recent manufacture than the other.

[a] Polarity always selected to give positive cell potentials.
[b] Otherwise as for Full-cell No. 1-4.

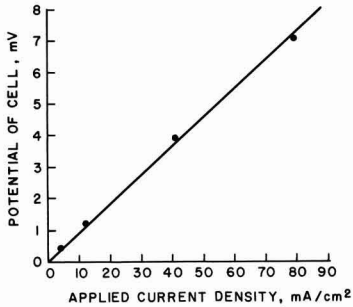

Fig. 2. Current-voltage data for two Ag electrodes in Ag_2WO_4, 750°C. Constant current applied in increasing steps; potential read after 30 sec.

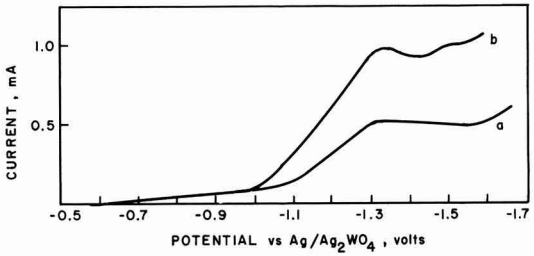

Fig. 3. Voltammograms for Pt bead (0.03 cm^2 area) in Na_2WO_4 containing: (a) 0.2 m/o Cd(II), (b) 0.4 m/o Cd(II), 750°C. Sweep rate, —250 mV/min.

The cell shown in Fig. 1 was employed to study the reduction of WO_3 and simple cations from alkali tungstate melts. As an illustration, Fig. 3 presents voltammograms obtained for the reduction of 0.2 and 0.4 m/o (mole per cent) Cd(II) from Na_2WO_4, 750°, at a Pt bead (0.03 cm^2 area).

This cell design was also employed for synthesis. For electrosynthesis at constant current when it is not desired to monitor the potential of the study electrode, any suitable couple may be employed on the other side of the porcelain membrane. As an example, tungsten bronzes were electrodeposited from polytungstate melts and a suitable anodic reaction on the other side of the porcelain was the electro-oxidation of alkali tungstate at Pt.

Acknowledgment

Special thanks are due to the National Aeronautics and Space Administration for support given under the NASA Predoctoral Traineeship Program. This paper is abstracted in part from a dissertation submitted by one of us (C.W.F.) to the Polytechnic Institute of Brooklyn in partial fulfillment of requirements for a Ph.D. degree (Chemistry).

Manuscript received Aug. 6, 1969.

Any discussion of this paper will appear in a Discussion Section to be published in the December 1970 JOURNAL.

REFERENCES

1. A. D. Graves, G. J. Hills, and D. Inman, "Advances in Electrochemistry and Electrochemical Engineering," Vol. 4, p. 117, P. Delahay, Editor, Interscience (John Wiley), New York (1965).
2. Iu. K. Delimarskii and B. F. Markov, "Electrochemistry of Fused Salts," Sigma Press, Washington, D.C. (1961).
3. C. H. Liu, K. E. Johnson, and H. A. Laitinen, "Molten Salt Chemistry," p. 681, M. Blander, Editor, Interscience (John Wiley), New York (1964).
4. R. W. Laity, in "Reference Electrodes," p. 524, D. J. G. Ives and G. J. Janz, Editors, Academic Press, New York (1961).
5. J. O'M. Bockris, G. J. Hills, D. Inman, and L. Young, *J. Sci. Instr.*, **33**, 438 (1956).
6. K. Hauffe and A. L. Vierk, *Z. Electrochem.*, **53**, 151 (1949).
7. R. J. Labrie and V. A. Lamb, *This Journal*, **106**, 895 (1959).
8. C. S. Ryland, Sales Manager, Chemical Porcelain Products Division, Coors Porcelain Co., Private communication.

JOURNAL OF THE ELECTROCHEMICAL SOCIETY

SOLID STATE SCIENCE

MAY 1970

Factors Affecting the Growth of Porous Anodic Oxide Films on Zirconium

B. Cox*

Chalk River Nuclear Laboratories, Atomic Energy of Canada Limited, Chalk River, Ontario, Canada

ABSTRACT

Although anodization of zirconium and its alloys generally results in the formation of barrier-type films, porous anodic oxide films can be produced in some electrolytes and by some preparation techniques. A survey of common electrolytes reveals that those containing nitrate, chromate, dichromate, and phosphate ions commonly lead to porous anodic films. An electron microscope study of the films produced in these electrolytes, and others giving barrier-type films, has shown that no single explanation fits all instances of porous film formation. While incorporation of the electrolyte anion in the oxide may be the primary factor influencing the formation of porous oxide films, it appears to operate primarily by affecting the local transport of oxygen ions through the films. This effect may be achieved by influencing the crystallization of the oxide during growth so that in some instances local oxidation and cracking occur at grain boundaries, while in other instances it leads to the general development of a porous structure.

Zirconium and Zircaloy-2 readily form barrier-type anodic oxide films in a wide range of electrolytes (1-4), including gaseous plasmas (5). A few instances of the formation of thick porous anodic films have been reported, generally associated with anodization at high voltages in solutions containing the nitrate ion (1, 6). We have found that porous films can be formed even at low voltages and have used such films in testing a porosimeter designed to measure pore sizes in zirconia films *in situ* (7, 8).

It was found that the capacitance, and especially the resistance, of even the barrier-type oxide films was much less than would be predicted from optical measurements of the oxide thickness and previous measurements of the resistivity of zirconia films using dry metallic contacts (9, 10). This effect was most pronounced for Zircaloy-2, an alloy containing small second phase particles, but was also present with the batch of crystal-bar zirconium used in our experiments.

It appeared that there might be a whole spectrum of degrees of porosity from electrolyte to electrolyte, and we set out to study this possibility and to correlate the effect with observable variations in the ionic transport process through the oxide film.

Experimental

Paddle shaped specimens, with 2 x 2 cm blades, were cut from one sheet of crystal-bar zirconium (Be) and one of Zircaloy-2 (Bh). Analyses of these batches of material are listed in Table I. The specimens were chemically polished in mixed nitric/hydrofluoric acids, washed in water and alcohol, and weighed prior to and after anodization.

Anodization was carried out either by the stepwise constant voltage technique, holding for different predetermined times in the range 0.5-100 min at each voltage step or by the constant current technique with applied currents between 1.0 and 5.0 mA/cm^2 and a predetermined final voltage. The electrolytes used were "normal" solutions of the following in water: H_2SO_4, Na_2SO_4, HNO_3, NH_4NO_3, KNO_3, KNO_2, KOH, NH_4OH, $K_3Fe(CN)_6$, $K_2Cr_2O_7$, $KCrO_4$, tartaric, lactic, formic, oxalic, acetic, and citric acids; saturated solutions of potassium persulfate, ammonium borate, and boric acid; 2% ammonium borate in ethylene glycol; 0.5M NH_4NO_3 in ethylene glycol; 85% phosphoric acid; a

Table I. Analysis of crystal-bar zirconium and Zircaloy-2 batches

Element	Crystal-bar Zirconium (Be), ppm	Zircaloy-2 (Bh), ppm
Al	<25	<40
B	<0.2	<0.2
C	35	80
Ca	10	—
Cd	<0.3	<0.2
Co	<5	<5
Cr	20	0.09*
Cu	<25	<20
Fe	80	0.14*
H	2	10
Hf	75	60
Mg	<10	<10
Mn	<10	<10
Mo	<10	—
N	12	20
Na	<10	—
Nb	<100	—
Ni	<10	0.05*
O	<5	1000
Pb	<40	—
Si	<40	70
Sn	<10	1.45*
Ta	<200	<200
Ti	<20	<20
V	<5	—
W	<25	—
Zn	<50	—

* Weight per cent.

* Electrochemical Society Active Member.

Key words: zirconium alloys, oxidation, anodization, oxide films, morphology, electron microscopy.

1:2:3 mixture of water, oxalic acid, and ethylene glycol, and a complex solution recommended by workers at Oak Ridge National Laboratory (4).

At the final anodization voltage and time the d-c source was disconnected and the leakage rates of the films determined by plotting the voltage decay on a high speed recorder. The anodic oxide surface was examined by optical microscopy, replica electron microscopy, and scanning electron microscopy. The metal-oxide interface was examined with the scanning electron microscope. The electrical properties of the films were determined with a GR1680A automatic impedance bridge during immersion in a molar ammonium nitrate solution; capacitative and resistive components (based on a parallel equivalent circuit) were followed as a function of immersion time. Measurements were also made using mercury and Viking alloy LS232 liquid metal contacts (8), and in a mercury porosimeter designed to measure pore sizes in insulating oxide films (7).

The "optical thickness" of the oxide films was determined by comparing the interference colors of the oxide on individual metal grains with a calibration strip prepared using the data of Wilkins (11) and checked with a spectrophotometer. The refractive index of the films was assumed to be insensitive to the forming electrolyte. The insensitivity of the refractive index to the forming electrolyte was demonstrated by Wilkins (3) for a limited range of electrolytes, and has been generally assumed to hold for all electrolytes by other investigators (4, 12). The "capacitative thickness" was determined from the capacitative component of the a-c impedance of the specimen, assuming the oxide to be effectively a parallel sided slab of dielectric. Average current efficiencies were determined from the optical thickness and the time taken to reach the final voltage. Instantaneous current efficiencies were calculated from the slope of the voltage/time plot on the assumption that the formation rate (Å/V) was constant throughout the period of film growth.

Results

Electrical measurements.—Selected measurements of optical thickness and impedance of the oxide films are presented in Table II to demonstrate the variations in the behavior observed in the various electrolytes. Further details may be obtained from the author. The oxide formation rates (based on the optical thickness of the oxide) for those electrolytes where sufficient specimens were anodized to give a meaningful average are quoted in Table III in comparison with other published values for which the formation method is known. Porous oxides could be detected electrically either by following the change in capacitance of a specimen with time after immersion in an aqueous electrolyte (Fig. 1) or by comparing the apparent thickness indicated by liquid metal and aqueous electrolytic contacts [see Ref. (8), Fig. 19]. The much greater degree of porosity of the films formed in NH_4NO_3 than in H_2SO_4 could be readily seen from the separation of the curves of apparent thickness measured in an aqueous electrolyte and in mercury. The capacitative thickness of apparently nonporous films is plotted against their optical thickness in Fig 2.

The degree of porosity of the other anodic films was also estimated from a comparison of the apparent oxide thickness measured with mercury, LS232, and an aqueous electrolyte as contacts (Table II). A consistently higher apparent thickness in the liquid metals

Table II. Properties of anodic oxide films formed on zirconium and Zircaloy-2

Specimen No.	Forming electrolyte	Final voltage, V	Forming method*	Optical thickness, Å	Impedance 1/C, cm²/μF Hg	LS232	NH_4NO_3	Specific resistance, ohm × 10^8 Hg	LS232	NH_4NO_3	Comments
Zirconium specimens											
Be 95	$KCrO_4$	25	C	500-650	3.83	3.34	2.97	34.8	28	13.2	
Be 153	Na_2SO_4	25	C	300-650	3.48	2.80	2.72	40.0	26	15.2	See Fig. 5 and 6
Be 154	Citric	25	C	300-650	4.08	4.09	2.68	51.8	21	12.7	
Be 155	NH_4NO_3	25	C	300-650	4.51	3.68	2.98	12.4	39-0.002	10.7	
Be 24	KNO_2	156	V	3350	—	17.3	16.4	—	62	60	
Be 34	KOH	144	V	3820	—	21.2	19.6	—	185	11.7	Increasing flaws or porosity in the oxide
Be 23	H_2SO_4	144	V	3350	—	19.5	17.5	—	55	42	
Be 31	ORNL	125	V	2400	—	13.4	8.6	—	49	3.89	
Be 40	NH_4NO_3	112	V	gray	313	177	8.0				
Zircaloy-2 specimens											
Bh 257	Amm. Bor.	25	C	500	3.49	3.17	3.14	64.1	15	9.54	
Bh 265	Na_2SO_4	25	C	375	3.32	3.00	2.97	7.29	40	20.4	
Bh 330	$K_2S_2O_8$	25	C	400	3.81	3.25	3.36	59.0	38	20.0	Apparent order of increasing flaws or porosity
Bh 258	$K_2Cr_2O_7$	25	C	550	5.39	6.04	4.23	5.79	53	12.4	
Bh 266	H_3PO_4	25	C	575	9.66	10.13	2.51	50.5	29	10.3	
Bh 238	NH_4NO_3	25	C	500-1400	11.5	16.2	2.44	37.3	160	1.46	
Bh 320	KOH	100	V	2550	—	13.0	12.14	—	72	39.2	
Bh 321	KNO_2	100	V	2660	32.4	15.0	12.85	0.015	47	36.7	Increasing flaws or porosity in the oxide
Bh 249	H_2SO_4	98	V	1990	11.7	12.7	9.69				
Bh 354	ORNL	100	V	1930	18.6	10.7	2.59	0.025	99	0.08	
Bh 227	NH_4NO_3	96	V	~4000	121	70	5.86				

* Forming method: V = constant voltage; C = constant current.

Table III. Formation rates of anodic oxide films on zirconium and Zircaloy-2

Electrolyte	Formation method	Formation rate, Å/V	Reference
0.5M H_2SO_4	Stepwise constant voltage, <5 min decay/step	16.8	This work
0.5M H_2SO_4	Stepwise constant voltage, 1-2 hr/step	22	This work
0.5M H_2SO_4	Stepwise constant voltage, >24 hr/step	25.5-29	This work
0.1M H_2SO_4	Stepwise constant voltage, decay to 0.2 mA/cm²	16.9	Wilkins (3)
1.0M KOH	Stepwise constant voltage, ~5 min decay/step	22.2	This work
1.0M KOH	Constant current 1.0 mA/cm², no decay	21.1	This work
1% KOH	Constant current 10 mA/cm², decay to 0.2 mA/cm²	26.5	Wilkins (3)
1% NaOH	Constant current 10 mA/cm², decay to 0.2 mA/cm²	25.3	Wanklyn (13)
ORNL solution	Stepwise constant voltage, ~5 min decay/step	16.3	This work
ORNL solution	Constant current, 1.0 mA/cm²	15.0	This work
ORNL solution	Constant voltage, 30 sec decay	14.5	Banter (4)
Sat. amm. borate	Stepwise constant voltage, ~5 min decay/step	19.5	This work
Sat. amm. borate	Stepwise constant voltage, ~1 hr decay/step	20.0	This work
Sat. amm. borate	Stepwise constant voltage, >24 hr decay/step	~30	This work
Sat. amm. borate	Stepwise constant voltage, decay to 0.2 mA/cm²	22	Wanklyn (13)
Sodium borate/ boric acid	Stepwise constant voltage, 5 min-1 hr decay	27	Salomon (14)

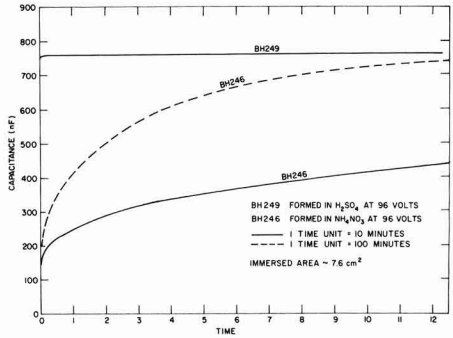

Fig. 1. Comparison of impedance vs. immersion time curves for porous and nonporous anodic oxide showing equality of barrier layer oxide thickness for both specimens.

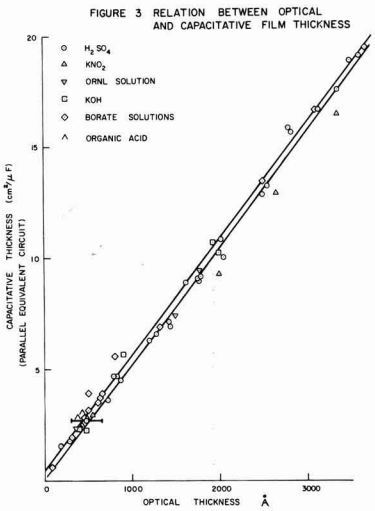

Fig. 2. Relation between optical and capacitative oxide thickness for films formed in various electrolytes.

is indicative of the total oxide thickness, while the final apparent thickness in ammonium nitrate measures the barrier thickness. The sizes of the flaws present in some films have been determined using a mercury porosimeter (Fig. 3) and the results can be correlated with the observed defects seen by electron microscopy [see Ref. (7) for details].

During forming at constant current the characteristic plateau (13) in the voltage-time curve was often observed. The duration of this plateau varied enormously with the electrolyte being used and in any given electrolyte was always longer for Zircaloy-2 specimens than for zirconium specimens. During the plateau localized oxygen evolution could be observed at a number of sites. Anodization was attempted initially at ~1 mA/cm² for all specimens; in some instances the current had to be increased as much as a factor of five before the plateau could be passed. The current was returned to 1 mA/cm² once film growth resumed. Typical examples of the shapes of the constant current curves for Zircaloy-2 are shown in Fig. 4, and for zirconium in Fig. 5. The voltage decay curves were obtained for zirconium and Zircaloy-2 specimens after formation at constant current. Examples are shown in Fig. 6. The decay currents of specimens formed at constant voltage in different electrolytes were also measured [see Ref. (8), Fig. 24].

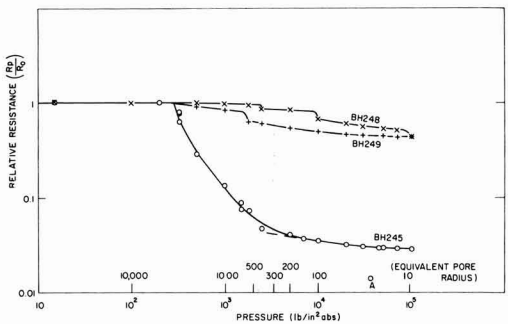

Fig. 3. Porosimeter curves for barrier-type anodic oxide films formed in sulfuric acid (Bh 248, Bh 249) and a porous anodic film formed in ammonium nitrate (Bh 245).

Visual observations.—Observation of the specimens in the optical microscope showed that (for most electrolytes) the interference colors were uniform over the zirconium matrix. Large intermetallic particles were clearly different in interference color from the surrounding matrix, but in most instances were too small for the film thickness on the intermetallics to be determined in the optical microscope, or even to estimate whether it was greater or less than the surrounding oxide thickness. Electrolytes giving porous oxide films commonly yield irregular interference colors, and some other electrolytes reproducibly gave local variations in oxide thickness.

Examination of the specimens with the electron microscope and scanning electron microscope showed that most anodic films, especially on Zircaloy-2, contained a number of flaws, even when they would be classified as good barrier-type oxide films from an examination of the electrical measurements. These flaws fell into a few characteristic types (illustrated by Fig. 7-9) which appeared commonly in a number of solutions and in the case of cracking at grain boundaries became more prominent with increasing oxide thickness.

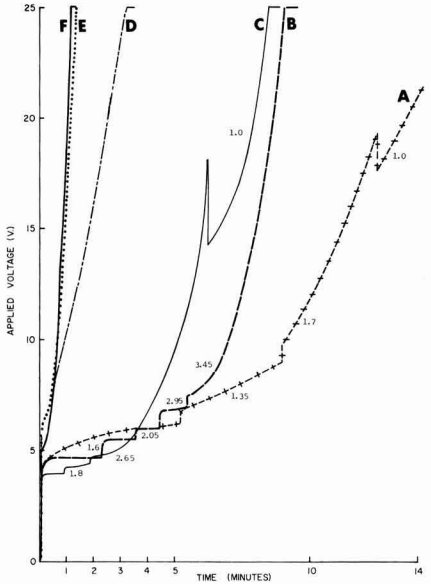

Fig. 4. Voltage-time curves for Zircaloy-2 specimens anodized in organic acid electrolytes. Numbers by curves indicate current density where this was increased above 1 mA/cm² to overcome the plateau in the anodization curve. Specimens anodized in (a) citric acid, (b) tartartic acid, (c) oxalic acid, (d) lactic acid, (e) acetic acid, (f) formic acid.

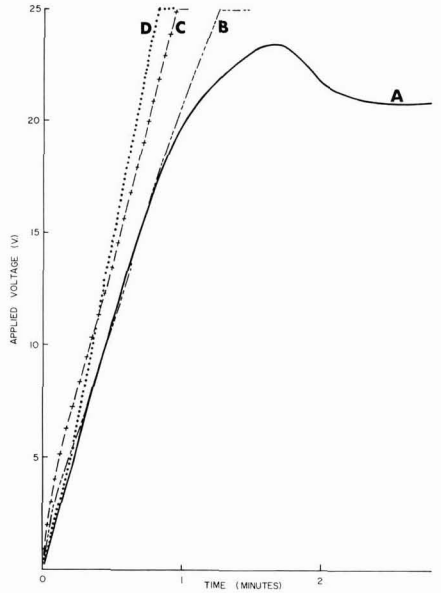

Fig. 5. Constant current anodization of unalloyed zirconium at 1 mA/cm^2. Specimens anodized in (a) $KCrO_4$, (b) NH_4NO_3, (c) citric acid, (d) Na_2SO_4.

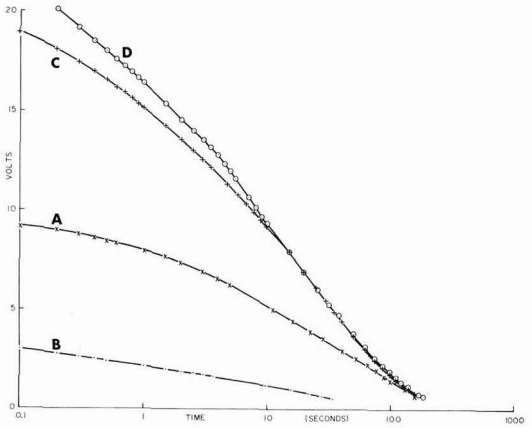

Fig. 6. Decay of the formation voltage for specimens of unalloyed zirconium shown in Fig. 5. (a) $KCrO_4$, (b) NH_4NO_3, (c) citric acid, (d) Na_2SO_4.

However, the phenomena which were studied in most detail were those leading to more severe breakdown of the oxide and to generally porous oxide films. These can be divided into three different types of failure.

1. Formation of thicker oxide along grain boundaries and around intermetallic particles leading to cracking along grain boundaries and ultimately to spalling of the oxide (see Fig. 10-12).

2. Local formation of patches of thicker rough oxide eventually leading to spalling (Fig. 13 and 14).

3. Formation of generally porous oxide films which continue to grow considerably in thickness when held at the forming voltage (Fig. 15-17).

Transmission electron microscopy of stripped oxide films from selected specimens formed in sulfate, hydroxide, tartrate, and nitrate electrolytes showed unique features associated with the films formed in nitrate. In bright and dark field illumination the

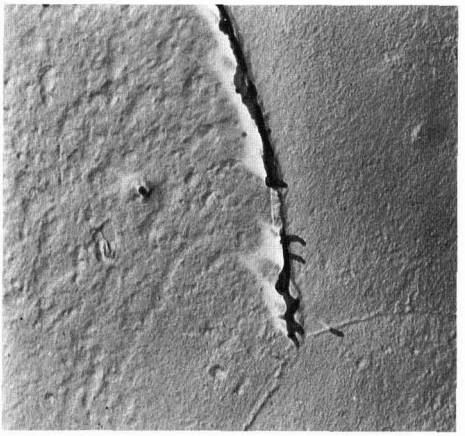

Fig. 7. Cracks forming along prior metal grain boundaries in anodic oxide film formed in sulfuric acid specimen (Bh 249, 96 V). X 20,000.

Fig. 8. Minor flaws produced by cracking of anodic oxide around intermetallic particles in a Zircaloy-2 specimen anodized in ammonium borate (Specimen Bh 306, 18 V). X 5000.

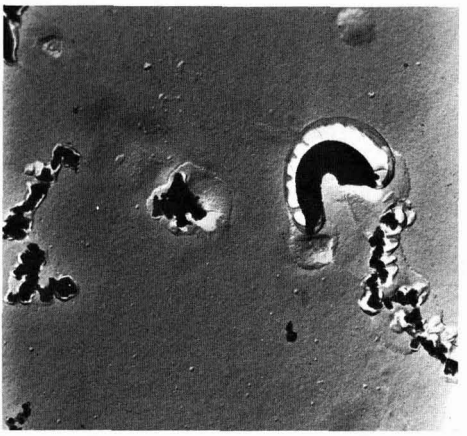

Fig. 9. Small areas of poorly adherent thicker oxide detached from specimen, anodized in ORNL solution, by the replication technique (Specimen Bh 319, 100 V). X 20,000.

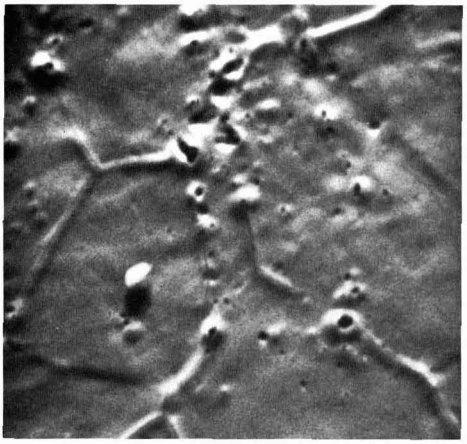

Fig. 10. Scanning electron micrograph showing later stages of development of thick oxide ridges along prior metal grain boundaries. Cracks in oxide are now visible along some boundaries (Specimen Bh 249, 96 V in H_2SO_4). X 2000.

Fig. 11. More advanced stage of growth in sulfuric acid of grain boundary ridges of thick anodic oxide (Specimen Bh 315, 132 V). SEM X 10,000.

crystallite size was clearly smaller in the nitrate films compared with films formed in the other three electrolytes (Fig. 18). In addition to being larger the crystallites were also less distorted in the barrier-type films. In the nitrate films the thickness varied in an irregular fashion not evident in the other oxides, and small thin patches, which might be the early stage of pore development, could be seen (Fig. 19). The diffraction patterns, from basal planes of the zirconium matrix, showed that the nitrate film was also unique in being essentially all monoclinic ZrO_2, whereas the other films had large percentages of cubic ZrO_2 ($\geq$75%) and only traces of the monoclinic phase (Fig. 20). There were differences between the barrier-type films in the randomness of the distribution of the cubic oxide crystallites. In some instances, especially tartaric acid, the crystallites were almost random, giving rise to complete rings (Fig. 21), whereas in the other barrier-type oxides the crystallites were highly oriented.

Fig. 12. Local oxide spalling as result of formation of thicker oxide along grain boundaries. X 1000. (Photo-emission electron micrograph).

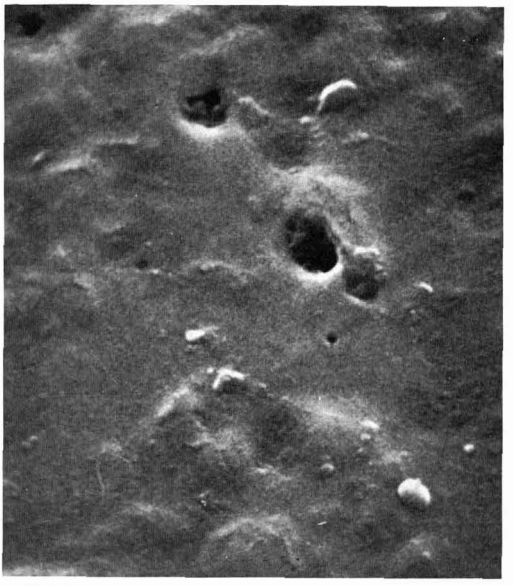

Fig. 13. Uneven growth of anodic oxide films in potassium chromate solution, X 10,000.

Scanning electron microscopy of the oxide/metal interfaces of anodic oxide films showed that considerable roughness of the interface was present for oxides known from other measurements to be porous (Fig.

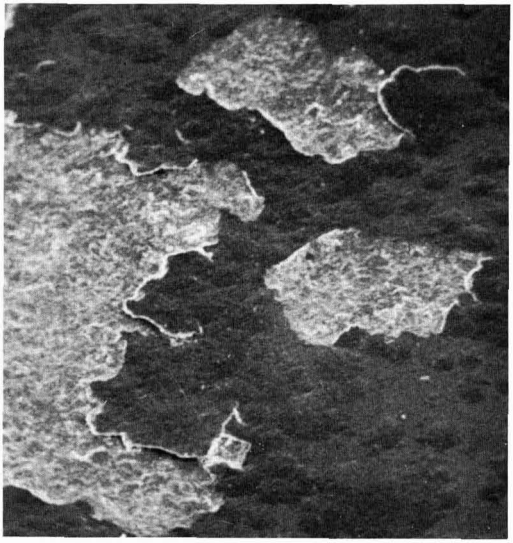

Fig. 14. Spalling of oxide resulting from multiplication and coalescence of areas of thick oxide formed in potassium chromate. X 100.

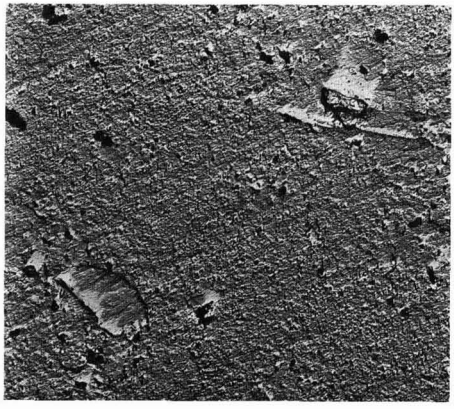

Fig. 15. Intermediate stage in development of pore network in oxide formed in ammonium nitrate (Specimen Bh 312, 18 V, 5 min). X 5000.

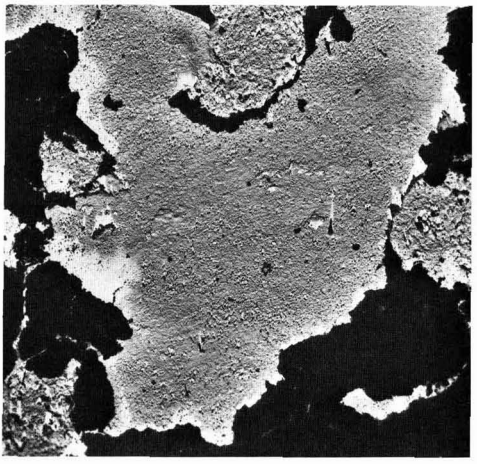

Fig. 16. Oxide spalling at a later stage in formation of thick porous oxide in ammonium nitrate (Specimen Bh 246 96 V). X 5000.

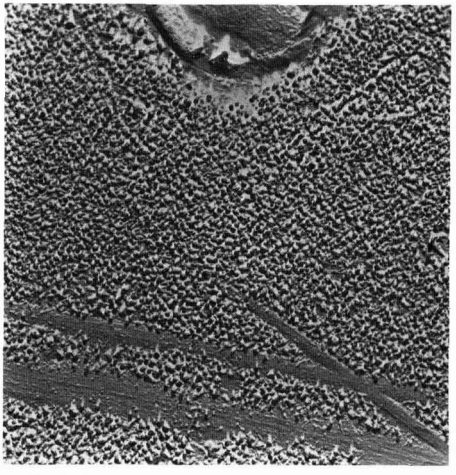

Fig. 17. Uniform pore network in anodic oxide formed in phosphoric acid (Specimen Bh 266, 25 V). X 20,000. N.B. absence of porous oxide along residual scratches.

22), whereas the interfaces of barrier-type films were generally smooth except in the vicinity of second phase particles.

Discussion

Identification of porous oxide films from electrical measurements.—A study of the impedance measurements (*e.g.*, Table II) shows that porous oxide films result for specimens formed in solutions containing the nitrate ion (NH_4NO_3, HNO_3, KNO_3) and phosphoric acid. The mode of formation has some influence on the results, however. Zircaloy-2 specimens formed at constant voltage or constant current showed little difference in the relative thickness indicated by liquid metal and aqueous contacts (*c.f.*, specimens Bh 225, 328, and 329), whereas for crystal-bar zirconium, films formed at constant current showed less evidence of porosity than those formed at constant voltage. This conclusion from the impedance measurements was confirmed by electron microscopy. The oxide surface on the zirconium specimen was found to be uneven, but not obviously porous. This conclusion might have been different had the specimen been held at the final voltage for some time after forming at constant current, if the increase in porosity found for Zircaloy-2 specimens held at constant voltage for increasing lengths of time is indicative of general behavior (Fig. 15-17).

Oxide films formed on Zircaloy-2 in chromate and dichromate solutions showed extensive areas of breakdown. There was correspondingly less evidence for breakdown on a zirconium specimen formed in potassium chromate solution at constant current, than for a comparable Zircaloy-2 specimen both from impedance measurements and electron microscopy.

Films formed in most other electrolytes showed relatively small differences between apparent thickness measurements in liquid metals and aqueous electrolytes. Of the former the measurements in LS232 are the more reliable because of its better ability to wet zirconia (8). Of those showing major differences between the impedance with aqueous and liquid metal contacts (a factor of two or more differences in apparent thickness in NH_4NO_3 and LS232) porosity, or other major flaws, were confirmed by electron microscopy and porosimetry only for films formed in phosphoric and sulfuric acids. Differences less than a factor of two can probably be explained on the basis of a

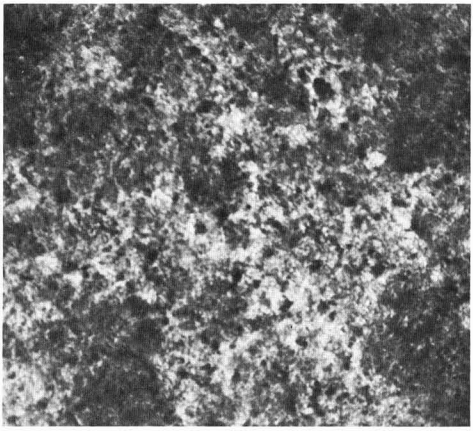

Fig. 18a

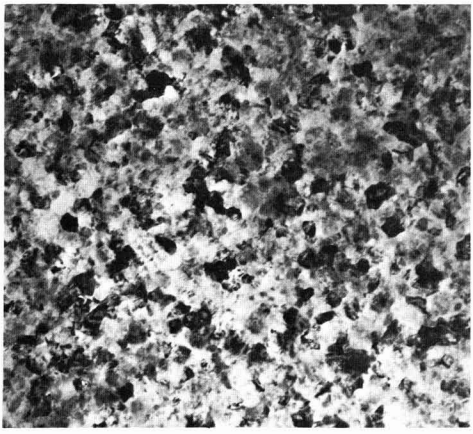

Fig. 18b

Fig. 18. Transmission electron micrographs of anodic oxide films (a) formed in ammonium nitrate (Bh 224); (b) formed in potassium hydroxide (Bh 308). X 75,000.

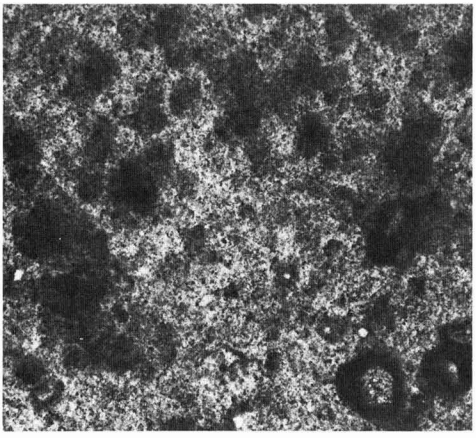

Fig. 19. Cellular structure developing in anodic oxide formed in ammonium nitrate. X 20,000.

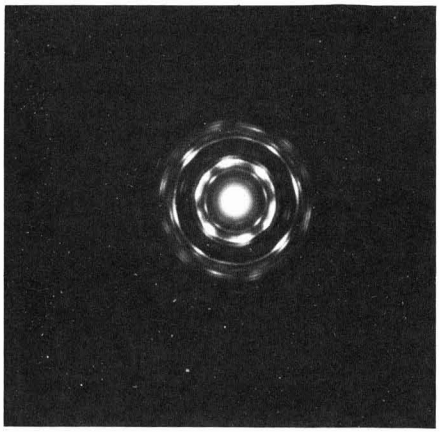

Fig. 20a

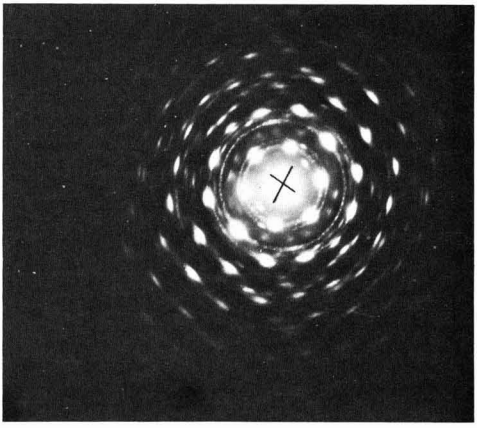

Fig. 20b

Fig. 20. Diffraction patterns from oxide formed (a) in ammonium nitrate (Bh 224), (b) in potassium hydroxide (Bh 308).

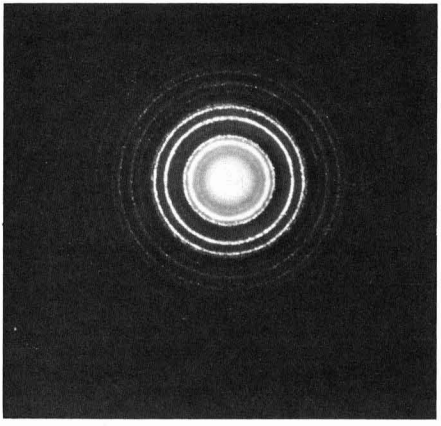

Fig. 21. Diffraction pattern from oxide formed in oxalic acid (Bh 263).

number of small flaws associated with the intermetallic particles.

Banter (4) has demonstrated for zirconium that in many electrolytes the anion is incorporated into the anodic film. However, with the exception of the organic acids, the other electrolytes for which he demonstrated this phenomenon were ones which we have found to yield porous or cracked oxide films. Thus, it

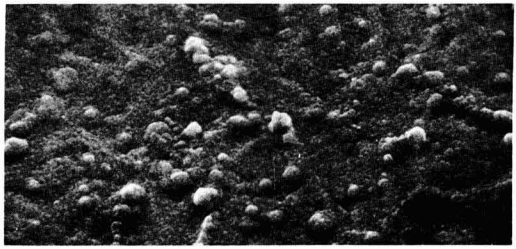

Fig. 22. Oxide metal interface of thick porous anodic oxide film formed in ammonium nitrate (Bh 247, 97 V).

is possible that anions from the electrolyte adsorbed in the porous structure rather than incorporated into the oxide lattice led to many of his observations. Nevertheless, it seems likely that anions from most if not all electrolytes are incorporated into nonporous anodic oxides (12, 15), but at levels generally below the level of detection of the methods employed by Banter.

That the incorporation of anions does not lead to any major change in the physical properties of the oxide formed is shown by the small spread of the impedance/thickness data for relatively defect free oxides in Fig. 2. The phosphate films for which Banter observed the outer layers dissolving faster than the inner ones were likely also to have been porous (Fig. 17) and the dissolution may have been due to this porosity rather than to the incorporation of a larger fraction of phosphate ions into the oxide lattice in the outer regions of the film. Absorbed phosphate would almost certainly have been more highly concentrated within the porous layer than within the inner "barrier-type" film, thus leading to the possible misinterpretation of the observations.

Current decay curves and leakage currents.—The formation of porous anodic films could also be detected in the current decay curves for specimens formed at constant voltage. An essentially constant (but fluctuating) current was observed for specimens forming porous films. Cracking and breakdown of the film can be distinguished from this process as they usually lead to discontinuous increases in the forming current. The rate of decay of the current during forming does not seem to be indicative of the quality of the final film as determined from a-c impedance measurements. Presumably the size of this current (which is probably mainly electronic at long decay times) measures the effectiveness with which the intermetallic particles are anodized, although no correlation could be found with the apparent thickness of the oxide on the intermetallic particles in those instances where this could be estimated.

Unusually high decay currents were observed for films formed in KOH. This current represents mainly oxygen evolution at intermetallic sites and might be thought to be due to lack of film formation on these intermetallics. However, electrical measurements on these films did not show them to be of significantly lower resistance than other films which did not yield such high leakage currents. The high decay currents in KOH also explain the apparent difference between our values for the formation rate in KOH (Table III) and those quoted by Wilkins (3, 11). Our specimens were held at each voltage step for a constant time whereas Wilkins' were held until a predetermined leakage current (0.2 mA/cm^2) was reached. Our data suggest that this would represent a long time at each voltage step and would be expected to yield a higher formation rate in Å/V. The good agreement when equivalent formation methods are compared is shown by the results in sulfuric acid. Wilkins' technique is equivalent to a decay time of about 1 min at each voltage, and therefore the formation rates are very close for the two equivalent conditions.

During formation at constant current, breakdown of the type observed in chromate and dichromate reveals itself as a failure of the voltage to continue to rise (Fig. 5). This feature is not observed with specimens forming porous films in nitrate or phosphate solution. These, and other, films show the normal arrest in the anodic growth curve (1, 16) at about 5V, at the current densities used here.

The height and length of this arrest varied from 3.7-6.3V and from a few seconds effectively to infinity depending on the electrolyte. In any given electrolyte the height was also a function of the current density. Extrapolation of our curves of "plateau" height *vs.* current density to the current densities of Adams *et al.* (16) gives good agreement with their data. Observation of local oxygen evolution during this plateau together with other data suggests that the plateau is caused by the presence of second phase particles in the zirconium matrix. The plateau is commonly very small or absent for unalloyed zirconium except at very low current densities, or for roughly abraded surfaces (16) where embedded abrasive particles may substitute for the intermetallic particles in Zircaloy-2.

The variation from electrolyte to electrolyte in the length of the plateau, and the current density needed to exceed it, is presumably a measure of the ability of each electrolyte to form a nonconducting film on the intermetallic particles. In Zircaloy-2 these are either Zr-Fe-Ni or Zr-Fe-Cr phases and the critical step may be the formation of an oxide film other than ZrO_2 on these particles. The big variation in the length of the plateau for different organic acids is surprising in this context since little difference would be expected in the ability of lactic, tartaric, and citric acids (for instance) to oxidize the intermetallic particles.

For unalloyed zirconium a clear distinction was found in leakage rate for porous and nonporous oxide films (Fig. 6). This distinction was not apparent with anodic films formed on Zircaloy-2, showing that in the latter instance the properties of the oxide formed on the intermetallic particles were more important in determining the leakage rate of the oxide than the porosity of the oxide formed on the majority of the surface. That this conclusion is reasonable may be judged from the fact that the porous oxide films all apparently have a barrier-layer at the oxide-metal interface, as judged from impedance measurements during immersion (Fig. 1). The intermetallic particles are large enough to short-circuit the whole oxide if the oxide over them is very thin, cracked, or more conducting (electronically) than that on the matrix. Further confirmation of this explanation may be provided by the apparent correlation between the leakage rate (estimated from the residual voltage after 10 sec) and the average current efficiency for formation (indicated by the time to reach 25V) for most of the specimens where no change in current density was needed to exceed the plateau (Table IV). Since most of the time taken to reach 25V was required to overcome the effect of the intermetallic particles the second of the above quantities probably measures the efficiency with which these particles are oxidized in a particular electrolyte.

Electron microscope studies.—Unlike anodic oxide films on many other valve metals, those formed on zirconium and its alloys are essentially microcrystalline (17) and bear a striking resemblance in the transmission electron microscope to thin thermal oxide films formed at ~300°C (18). Although marker studies using rare gas atoms indicated that the moving species during anodization is oxygen (19); the oxides used by Davies *et al.* were formed in nitrate solution and were therefore probably porous. Thus, electrolyte could have migrated past the markers via the pores. Further studies by Whitton using charged marker ions and oxides formed in borate solution have confirmed that the migrating species is oxygen but that migration is not through the bulk of the lattice

Table IV. Current efficiency and leakage rate of specimens anodized to 25V

Specimen	Electrolyte	Optical thickness (A) Matrix	Optical thickness (A) Inter-metallics	Current efficiency (%) at ~1 mA/cm² Average	Current efficiency (%) at ~1 mA/cm² Final	Leakage rate (residual voltage at time) 1.0 sec	Leakage rate (residual voltage at time) 10 sec
Bh 257	Amm. borate	500	200	22.6	40.0	—	—
Bh 258	$K_2Cr_2O_7$	550	—	Breakdown occurred			
Bh 259	$KCrO_4$	550	—	before reaching 25V			
Bh 260	Amm. borate	500	200	—	—	—	—
Bh 261	Tartaric	425	—	0*	54.3	—	—
Bh 262	Lactic	425	—	34.8	30.2	2.2	1.25
Bh 263	Oxalic	375	825	0	30.0	—	—
Bh 264	Citric	475	—	0	15.2	—	—
Bh 265	Na_2SO_4	375	—	50.4	84.0	3.8	1.90
Bh 266	H_3PO_4	575	—	0	61.3	—	—
Bh 267	1:2:3/H_2O/HOx/Gly	290	600	29.1	~100	2.45	1.52
Bh 268	Amm. bor/E. Gly	250	600	High	80.0		
Bh 269	NH_4NO_3/E. Gly	1100-3000	—	>87	~100	5.4	2.2
Bh 325	Acetic	430	—	82	~100	4.9	1.4
Bh 326	$K_3Fe(CN)_6$	500	—	59.7	70.0	2.5	0.5
Bh 328	NH_4NO_3	500-1400	—	>78	>80	3.3	1.1
Bh 329	NH_4NO_3	550-1600	—	>83	>80	3.3	1.05
Bh 330	$K_2S_2O_7$	400	—	50.0	100	2.8	0.8
Bh 331	Formic	200	—	43.5	61.8	3.1	1.4

* Specimens showing zero current efficiency did not anodize beyond the plateau at 1 mA/cm². Leakage rates are not shown for these specimens.

(15). Thus, since the latter films were probably nonporous, it appears that in anodic films, as in thermal films (20), the oxygen transport process is via the boundaries between the oxide crystallites (or any residual amorphous material between the crystallites) rather than through the bulk of the oxide lattice.

The various processes by which irregular or porous oxide films are formed in different electrolytes are thought to be related to the effect of incorporated electrolyte ions on the crystallization or recrystallization of the oxide film. Thus, transmission microscopy has shown that crystallite size and degree of orientation are affected by the electrolyte used. These effects are most readily seen in the enhanced oxidation and ultimate cracking (perhaps) due to local stresses observed at grain boundaries in sulfuric acid, and to a lesser extent in potassium nitrite. The effect of such cracks on dielectric loss in films formed in sulfuric acid has already been reported by Young (21). Disorder at grain boundaries might be expected to lead to variations in the density of easy diffusion paths and locally enhanced oxidation via local modifications in the field strength in the oxide. That this phenomenon is infrequent during anodic oxidation presumably indicates a normally greater degree of order at crystallite boundaries in anodic films than is present in thermal oxide films so that locally enhanced anodic oxidation at grain boundaries is the exception rather than the rule. The observation that barrier-type films are predominantly cubic ZrO_2, would be expected to lead to less lattice disorder in crystallite boundaries than in thermal oxide films which are predominantly monoclinic.

The electron microscope study of films formed in nitrate, phosphate, and dichromate solutions shows that the porosity originates in the growth of films having relatively rough outer and inner interfaces, and apparently associated with a high percentage of monoclinic ZrO_2 in the film. In nitrate and phosphate solutions these rough films cover virtually the whole surface, and eventually develop a network of pores. Thicker films do not form along residual scratches in the metal, which can often be seen in the optical microscope because the interference color film over them is of normal thickness (8). Presumably the distorted nature of the underlying metal prevents the formation of the thicker films at these points, although the precise reason for this is not clear. Perhaps the cold work in the surface causes the formation of cubic oxide at these sites, and this inhibits the development of roughness and porosity.

It is concluded therefore that electrolytes, which lead to the formation of porous oxides, modify the crystallization of the oxide thus permitting the development of a thick and ultimately porous oxide. The cell structure (such as it is) in the thick films formed in nitrate solutions seems to develop from a pattern of crystallization which occurs in the first few seconds of formation (Fig. 19). The manner in which the pore structure develops from this has not been elucidated. Penetration of the electrolyte into the pores and the development of a columnar crystallite structure would permit this growth process to continue. In chromate and dichromate solutions the course followed seems to be basically the same, but becomes irregular on a small scale. This leads to small local patches of thicker oxide which eventually crack and spall, presumably due to the more severe local stresses in these films than in the nitrate or phosphate films.

Previous studies of the crystal structure of anodic oxide films on zirconium by x-ray and glancing angle electron diffraction (22-25) have been unable to agree on the relative proportions of cubic, monoclinic, and amorphous oxide in the film formed in different electrolytes. Previous studies of anodic films by transmission electron microscopy have stopped short of attempted interpretations of the diffraction patterns (17).

The basic processes relating the changes in oxide morphology to the effect of the incorporated ions and changes in the crystallization process require a detailed study of the films by transmission electron microscopy. This is currently in progress but is beyond the scope of the present work.

Conclusion

A survey of the anodization of zirconium alloys in a number of electrolytes has shown that (using a forming method involving long holds at constant voltage) porous anodic films can be formed in solutions containing nitrate, chromate, dichromate, and phosphate ions. Flaws formed at intermetallic particles and by cracking of the oxide along grain boundaries are also prevalent being worst in sulfuric acid of the electrolytes tested here, but being found to a greater or lesser extent in most of the electrolytes yielding barrier-type films.

In the electrolytes yielding porous films the precise mechanism of their formation is apparently different for each electrolyte, however the underlying mechanism is believed to be associated with the incorporation of anions into the oxide and their effect on the crystallization of the oxide during anodization.

Acknowledgments

The author is indebted to R. A. Ploc for the transmission electron microscopy quoted here. This forms part of a broader study of the structure of anodic oxide films on zirconium alloys which is still in progress. The photo-emission electron microscopy was kindly performed by Balzer's Ltd. (see Fig. 12).

Manuscript submitted Oct. 7, 1969; revised manuscript received *ca.* Jan. 26, 1970. This was Paper 30 presented at the New York Meeting of the Society, May 4-9, 1969.

Any discussion of this paper will appear in a Discussion Section to be published in the December 1970 JOURNAL.

REFERENCES

1. R. D. Misch and bibliography in "Metallurgy of Zirconium," pp. 663-677, Lustman and Kerze, Editors, McGraw-Hill Book Co., New York (1955).
2. L. Young, "Anodic Oxide Films," Academic Press Inc., New York and London (1961).
3. N. J. M. Wilkins, *This Journal*, **109**, 998 (1962).
4. J. C. Banter, *ibid.*, **114**, 508 (1967).
5. N. Ramasubramanian, Atomic Energy of Canada Limited, Unpublished results.
6. I. L. Rosenfeld, E. N. Lantseva, and E. I. Kalinina, *Russ. J. Phys. Chem.*, **34**, 473 (1960).
7. B. Cox, *J. Nucl. Mater.*, **27**, 1 (1968).
8. B. Cox, Atomic Energy of Canada Limited, Report AECL-2668.
9. D. K. Dawson and R. H. Creamer, *Brit. J. Appl. Phys.*, **16**, 1943 (1965).
10. B. Cox and D. L. Speirs, Atomic Energy of Canada Limited, Report AECL-2704.
11. N. J. M. Wilkins, UKAEA Report AERE-R4666 (1964); *Corrosion Sci.*, **4**, 17 (1964); **5**, 3 (1965).
12. G. T. Rogers, P. H. G. Draper, and S. S. Wood, *Electrochim. Acta*, **13**, 251 (1968).
13. C. F. Britton, J. V. Arthurs, and J. N. Wanklyn, UK Report, AERE-4702.
14. R. E. Salomon, W. M. Graven, and G. B. Adams Jr., *J. Chem. Phys.*, **32**, 310 (1960).
15. J. L. Whitton, *This Journal*, **115**, 58 (1968).
16. G. B. Adams Jr., T. S. Lee, S. M. Draganov, and P. Van Rysselberghe, *ibid.*, **105**, 660 (1958).
17. J. N. Wanklyn, "Corrosion of Zirconium Alloys," ASTM, STP 368, pp. 58-75 (1964).
18. R. A. Ploc, *J. Nucl. Mater.*, **28**, 48 (1968).
19. J. A. Davies, B. Domeij, J. P. S. Pringle, and F. Brown, *This Journal*, **112**, 675 (1965).
20. B. Cox, *J. Nucl. Mater.*, **31**, 48 (1969).
21. L. Young, *Trans. Faraday Soc.*, **55**, 842 (1959).
22. P. H. S. Draper and J. Harvey, *Acta Met.*, **111**, 873 (1963).
23. R. K. Hart, D. I. C. Thesis, Imperial College, London (1951).
24. I. S. Kerr, Ph.D. Thesis, University of London (1955).
25. R. D. Misch and W. E. Ruther, *This Journal*, **100**, 531 (1953).

Reactions Caused by Additive Coloration of Tl^{+}- and Pb^{+2}-Doped KCl

L. Ben-Dor, A. Glasner, and A. Zudkevitz

Department of Inorganic and Analytical Chemistry, The Hebrew University, Jerusalem, Israel

ABSTRACT

Additive coloration of KCl doped with Tl^{+} may reduce the substitute $-Tl^{+}$ ions to Tl^{o} neutral centers or to negative "Tl^{-}" complex centers. In the case of Pb^{+2}-doped KCl, an intermediate Pb^{+} and a Pb^{o} netural center are formed.

Tl^{+}-Doped Alkali Halides

The spectra of Tl^{+}-doped alkali halides is well understood (1-1c) and is thought to be directly connected with electron excitations confined to the impurity ion. Additive coloration performed by heating the crystal in vacuum or low nitrogen pressure, in alkali metal vapor as well as radiative coloration, performed by x-rays or γ-rays, of the doped alkali halides have been studied (2-4), but attention was paid mainly to the effect of the impurity on F-center formation.

In the case of KBr, Tamai (5) observed the formation of two distinct bands on additive coloration by potassium vapor: a Tl neutral center (TNC) peaking at 4.1 eV (310 nm) and a Tl complex center (TCC) peaking at 3.1 eV (400 nm). The nomenclature adopted had been used earlier (2). The TNC is supposed to be a Tl^{+} ion associated with one F center, and the TCC a Tl^{+} ion associated with two F centers.

The formation of Tl^{o} as well as Tl^{+2} in KCl as a result of low-temperature γ-irradiation was studied (6). Coloration by irradiation causes both reducing and oxidizing processes. The elucidation of the resulting absorption spectra is complicated because of the simultaneous formation of a variety of V, F, and impurity centers. Also, the species thus formed are highly excited and labile, disappearing on warming above liquid nitrogen temperature. In contrast, additive coloration forms only reduced centers, which are stable to heat- and bleaching-treatments in general. It seemed advisable to carry out a further investigation to check the new "reduced-only" color centers formed and possibly confirm the existence of a negatively charged TCC center in other alkali halides besides KBr.

Pb^{+2}-Doped Alkali Halides

The absorption of Pb^{+2}-doped alkali halides, unlike the Tl^{+}-doped salts, is attributed solely to charge transfer transitions (7). The existence of Pb^{+2}-cation vacancy complexes has been reported by many investigators (8-10). In studies of X-irradiated NaCl doped with Pb^{2+}, a gray coloration caused by Pb^{o} (11) and an "atomary" lead center (12), peaking at 254 nm, were reported. Low-temperature colorability of doped KCl was also studied (13, 14), but no attention was given to uv impurity bands formed thereby. In this work, the reduced species formed on additive coloration are more closely defined.

Experimental Section

All chemicals used, KCl, TlCl, $PbCl_2$, were J. T. Baker Analyzed Reagents. Single crystals were grown by the Stockbarger method, and additive coloration was performed both in Pyrex (550°C) and in nickel (700°C) (16) containers at a pressure of ~50 Torr nitrogen. The optical absorption was recorded on a Perkin-Elmer Model 137 uv spectrophotometer, working in the double beam mode. A special holder with 1 mm slit was used in the sample beam of the spectrophotometer, so that a 1-2 mm thick crystal plate, cleaved from the center of the colored single crystal (13 mm on the edge), could be moved in front of the beam. In this manner the spectrum of a desired region of the crystal plate could be recorded at various distances from the exposed surface. The spectra were taken at room temperature.

Results and Discussion

A KCl crystal containing 0.01-0.05 m/o (mole per cent) Tl^{+} did not show F absorption on coloration as

the high impurity concentration acted as an efficient trap for electrons. Crystals containing less than 0.001 m/o Tl^+ were easily colored and showed a distinct band peaking at 290 nm, besides the well-defined F band (Fig. 1). The additively colored crystal plates cleaved from the center of the colored cube exhibited three distinct areas [cf. ref. (2)]: an outer bluish F-zone about 2.5 mm wide, a brown-yellow zone containing the reduced center (290 nm), and an innermost colorless zone containing the unreacted Tl^+ ions. The same crystals, when colored for longer periods (2 hr instead of 1 hr) and/or at higher nitrogen pressure (100 Torr instead of 50 Torr), or in the presence of thallium chloride powder added to the coloring vessel, showed another previously unobserved band peaking at 345 nm (Fig. 2). It was found that the center responsible for this latter band is formed mainly in the outer zone, overlapping the F zone, of the crystal. On the other hand, the center responsible for the 290 nm band is found in the inner square of the crystal plate, 4.5-5 mm deep inside the face exposed to the coloring alkali metal vapor. The 247 nm A band of the Tl^+ ions survives in the interior colorless square (Fig. 3). Following former nomenclature, we wish to identify the 290 nm band as being due to TNC and the 345 nm as a TCC, reasoning that the doubly reduced TCC is formed only under drastic reducing conditions in the outer zone, where the concentration of electrons is highest. Comparing the centers observed in KBr by Tamai (5) with those found by us:

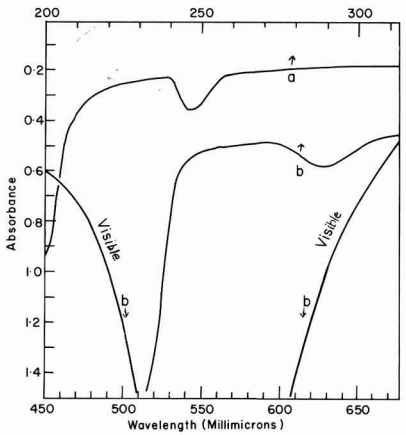

Fig. 1. Absorption spectra of Tl^+ doped KCl: (a) before coloration, (b) after additive coloration (1 hr, 700°C, 50 Torr nitrogen).

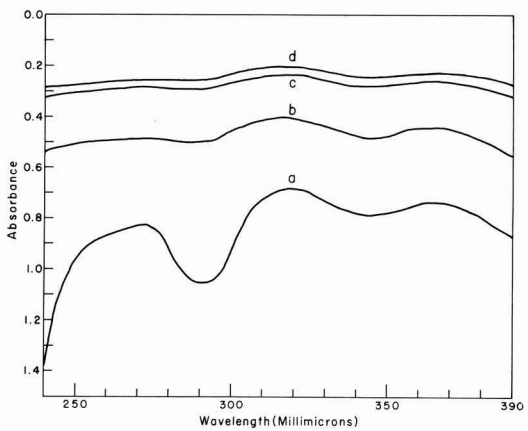

Fig. 2. Absorption spectra of additively colored Tl^+-doped KCl (2 hr, 550°C, 100 Torr nitrogen). Spectra shown in (a) to (d) were taken in progressively inner parts of the crystal.

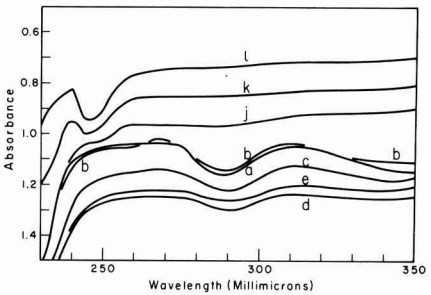

Fig. 3. Absorption spectra of additively colored Tl^+-doped KCl (conditions of coloration as in Fig. 2). Spectra shown in (a) to (d) were taken at ½ mm distances from the exposed face. Spectra (e)-(i) were omitted for clarity; (j)-(l) show spectra to 6 mm from the face.

	TNC, eV	TCC, eV
KCl	~4.3	3.6
KBr	4.0	3.1

one observes a shift in the same direction and similar magnitude when changing the matrix from KBr to KCl.

Delbecq *et al.* (6) identified a Tl^0 center in low-temperature γ-irradiated KCl, showing a weak band at ~300 nm, as well as a comparatively stronger band peaking at 380 nm, and three other extremely weak bands peaking in the visible and near IR regions. All these bands are attributed to Tl^0 centers on the basis of an analogy with the well-established Ag^0 center (17). The authors point out (7) that the 380 nm absorption is associated with a transition from the $^2P_{1/2}$ ground state to a $^2S_{1/2}$ resonant level in the conduction band. This latter excited level may be unstable at high temperatures. On the other hand, the 290 nm band prominent in our spectra may be due to a transition in the Tl^0 center from the ground state completely up to the conduction band. Thus, in the additively colored crystals only a single absorption band in the uv, arising from the Tl^0 center, was observed.

The 345 nm band produced only under more drastic conditions of coloration is attributed to a negative thallium complex, *i.e.*, a substitute Tl^0 atom associated with an F center. The Tl^0 center first produced carries an effective negative charge making its association with an anion vacancy highly probable. Under the drastic coloring conditions this associate could then capture a second electron to produce the negative complex center.

KCl single crystals containing 0.025-0.05% Pb^{+2}, as grown, showed besides the characteristic 273 nm Pb^{+2} band an absorption band at 325 nm (Fig. 4). This 325 nm band was also observed in concentrated KCl solutions containing ~100 ppm Pb^{+2} ions. Crystals absorbing in this region invariably had a yellow coloration, reminiscent of the yellow-brown coloration appearing in Tl^+ as well as in Zn^{+2}, Cd^{+2}, or Hg^{+2} doped (15) KCl crystals when additively colored. In all these cases the characteristic absorption band causing the yellow-brown coloration was attributed to the formation of neutral atomic species. Hence we suggest that, in the case of lead-doped crystals, dispersed neutral species appear to be formed by reduction in the melt, or by a photochemical decomposition, during crystal growth

$$PbCl_2 \rightarrow Pb^0 + Cl_2$$

Hence the 325 nm band is attributed to an atomary Pb^0-center. On the other hand, the gray coloration ob-

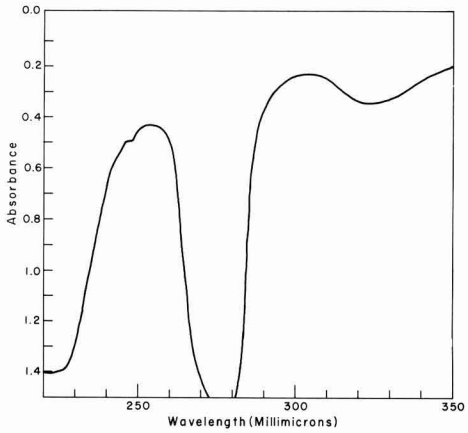

Fig. 4. Absorption spectra of Pb^{+2}-doped KCl after growth (the kink at ~250 nm should be disregarded).

served by Schulman *et al.* (11) in NaCl is indicative of colloidal lead aggregates.

On additive coloration of the Pb^{+2}-doped KCl, a further band, not well resolved, situated at ~254 nm, was obtained (Fig. 5). Since this band is different from the one described above, 325 nm, attributed to Pb^{o}, and since the crystal had neither a yellow nor a gray coloration, it must be due to another intermediary reduced species, viz., Pb^{+} center.

The Pb^{2+}-doped crystals were further studied by irradiative coloration at r.t., and it was found that with very low doping concentration (0.002 m/o Pb^{+2}), F centers are formed, but the presence of any other band is hardly discernable, although the characteristic Pb^{+2} band at 273 nm diminishes in intensity. Optical bleaching by direct sunlight renders the crystals colorless, and on further heat-treatment for 2 hr in a closed ampoule at ~200°C, the previously observed 254 nm band is formed. We claim, in accordance with Schulman *et al.* (11), that irradiation causes the formation of Pb^{o} centers (in low concentration not discernable in the spectrum) as well as immobile oxidizing species such as holes. During heat-treatment the Pb^{o} centers are partly reoxidized, causing the appearance of the band at 254 nm. This center, formed both by a reduction (additive coloration) and by an oxidizing process, could only be a Pb^{+} center.

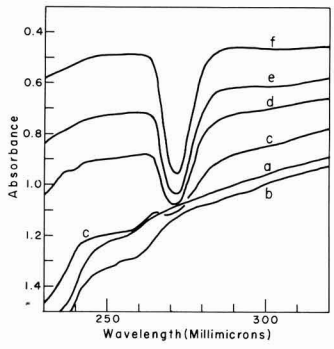

Fig. 5. Additive coloration of Pb^{+2}-doped KCl (20 hr, 550°C, 100 Torr nitrogen). Spectra shown in (a) to (f) were taken in progressively inner parts of the crystal. Note weak 254 nm band in outer parts, its disappearance toward the interior with the simultaneous appearance of the Pb^{+2} band (273 nm).

In summary, both Tl^{+} and Pb^{+2} substituted in KCl crystals act as electron traps; therefore crystals containing high concentrations of these ions do not color, *i.e.*, no F centers are formed either on irradiation or treatment with alkali metal vapor. In each case a maximum of two electrons per impurity ion may be trapped, but the impurity ions prefer to be reduced to the neutral atomary state.

In moderately doped KCl crystals the following centers were observed and may be identified as follows:

Tl^{o} (290 nm), Tl^{o}-F center complex	(345 nm)
Pb^{+} (254 nm), Pb^{o}	(325 nm)

The position of the bands is indicated in parentheses. Our results in the case of Tl^{+}-doped KCl are similar to those of Tamai (5) with KBr, but the models attributed to the respective centers are different, as shown above.

The apparent discrepancy between low-temperature irradiative coloration (6) and the results obtained on additive coloration of Tl^{+}-doped KCl is explained.

Of all the cation impurities studied, to date, only thallium was found to form a complex center formed from an association of Tl^{o} (neutral) with an F center. In the case of Pb^{2+}-doped KCl, the reduced species formed are most probably Pb^{+} and Pb^{o} centers. The 254 nm band is thus identified as a monovalent Pb^{+} center, rather than an "atomary" center as had been casually suggested (12) in the case of NaCl crystals.

Manuscript received Oct. 20, 1969; revised manuscript received *ca.* Jan. 15, 1970. This paper is based on the M.Sc. Thesis of one of the authors (A.Z.) (1965).

Any discussion of this paper will appear in a Discussion Section to be published in the December 1970 JOURNAL.

REFERENCES

1. F. Seitz, *J. Chem. Phys.*, **6**, 150 (1938).
1a. R. S. Knox, *Phys. Rev.*, **115**, 1095 (1959).
1b. J. E. A. Alderson, *Phys. Stat. Sol.*, **7**, 21 (1964).
1c. A. Fukuda, *J. Phys. Soc. Japan*, **26**, 1006 (1969); **27**, 96 (1969).
2. O. Stasiw, *Gött. Nachr.*, 1 (1936).
3. T. G. Castner and W. Känzig, *J. Phys. Chem. Solids*, **3**, 178 (1957).
4. J. J. Markham and H. N. Hersh, *J. Chem. Phys.*, **32**, 1885 (1960).
5. T. Tamai, *J. Phys. Soc. Japan*, **16**, 2463 (1961).
6. C. J. Delbecq, A. K. Ghosh, and P. H. Yuster, *Phys. Rev.*, **151**, 599 (1966); **154**, 797 (1967).
7. J. H. Schulman and W. D. Compton, "Color Centers in Solids," Pergamon Press, London, New York (1962).
8. E. Berstein, J. W. Davisson, and N. Seler, *Phys. Rev.*, **96**, 819 (1954).
9. R. A. Eppler and H. G. Drickamer, *J. Phys. Chem. Solids*, **15**, 112 (1960).
10. W. J. Fredericks and A. B. Scott, *J. Chem. Phys.*, **28**, 249 (1958).
11. J. H. Schulman, R. J. Ginther, and C. C. Klick, *J. Opt. Soc. Am.*, **40**, 854 (1963).
12. L. V. Grigoruk and I. Ya. Melik-Gaikazyan, *Optika i Spektros.*, **15**, 394 (1963).
13. W. A. Sibley, E. Sonder, and C. T. Butler, *Phys. Rev.*, **136**, A537 (1964).
14. E. Sonder and W. A. Sibley, *ibid.*, **140**, A539 (1965).
15. L. Ben-Dor, A. Glasner, and S. Zolotov, *Phys. Stat. Sol.*, **18**, 593 (1966).
16. C. Z. van Doorn, *Rev. Sci. Inst.*, **32**, 755 (1961).
17. C. J. Delbecq, W. Hayes, M. C. M. O'Brien, and P. H. Yuster, *Proc. Roy. Soc. (London)*, **271**, 243 (1963).

Physical and Electrical Investigations on Silicon Epitaxial Layers on Sapphire Substrates

J. Mercier

Section Physique des Couches Minces,
Laboratoire d'Electrostatique et de Physique du Métal, Grenoble-Gare, France

ABSTRACT

X-ray microdiffraction and special IR spectrometry techniques are used to explain the peculiarities of electrical properties of silicon thin films on sapphire substrates. Taking into account an autodoping effect due to the transfer of aluminum from the substrate into the layer, an optimum epitaxial temperature is observed. The results are interpreted in terms of misoriented regions, which are related to the presence of various Si-O bonds, the nature and the amount of which are dependent on the epitaxial temperature. It is concluded that chemical interactions between the substrate and the layer are more effective than crystallographic effects in determining the particular electrical properties of these silicon layers.

The need for physical methods is especially strong in the field of heteroepitaxy studies. This need does not arise from the number of the preparation steps, but from the intricate nature of the physical parameters involved in the process. The electrical characteristics, so useful with respect to the applications of these layers, give no physical insight. Furthermore they often involve long, sometimes destructive steps before measurements.

For these reasons, x-ray diffraction methods and IR spectrometry techniques complement the conventional electrical methods, in order to characterize thin silicon films grown by pyrolysis of silane, in hydrogen, on single crystal sapphire.

The aim of this study is an attempt to answer the following question: what are the relative contributions of fundamental factors and of incidental ones, inherent to the fact that the film properties are different from those of bulk material? The discrimination between these factors lies in the ability to improve the incidental ones, while the fundamental ones can only be optimized.

Experimental Conditions

Following Matare's general analysis presented in his excellent review paper (1), we can state some fundamental factors, optimizing in principle the experimental conditions:

1. High crystalline quality, Al_2O_3 ingots are used: they are Czochralski grown, and various tests confirm this quality (etching techniques, Borrmann effect).

2. The orientation $(01\bar{1}2)$ of the substrates gives two related advantages: (*a*) a nonpreferential *in situ* etching with H_2 at high temperature (1300°C), and (*b*) a quasi-systematic epitaxy of Si (100) as determined by x-ray and electron diffraction methods.

3. The substrate, 500 μm, and film, 5 μm, thick are chosen to minimize the strain of the layers.

4. Stresses are also avoided by a slow cooling rate after epitaxy ($\sim$ 100°/min).

5. The residual contamination level is low. With quite identical process conditions, silicon homoepitaxy is performed in the range 1000°-1200°C (2). Layers 5 μm thick are grown with N-type conductivity: when on 5-10 ohm cm P-type substrates, the layers resistivities are >100 ohm cm, and when on 0.01 ohm cm Sb doped substrates, the impurity concentration is less than 10^{14} cm^{-3}, at 1150°C.

6. The flow conditions (H_2 as a carrier gas, silane prediluted in H_2) have been determined to get low supersaturations required for epitaxy. The mean growth rate is 0.1 μm/min at 1100°C.

Electrical Results

The mean value results are shown in Fig. 1. Two processes have been used: process A, in which a chemical treatment of the substrate by hot phosphoric acid prior to insertion in the reactor is employed; and process B, without this chemical treatment. In any case, no intentional doping is performed.

From Fig. 1a, it follows that P-type doping occurs in the higher range of temperature, whatever the process, but N-type layers are grown at low temperatures, with the A process only.

Figure 1b gives the variation of Hall mobility with the epitaxial temperature. In the experimental range, a maximum value occurs at some optimum temperature (say T_o = 1100°C). But if the sensitivity is far less in the A process than in the B process, the maximum value in the former case is slightly less than in the latter one.

Figure 1c gives another picture of this last result. If, instead of absolute values, a quality factor, F expressed as follows

$$F = \frac{\text{Hall mobility (film)}}{\text{Hall mobility (bulk for the same type and conc.)}}$$

is used, the difference between both processes disappears. We note that F increases with T_{epi} and reaches 50-60% at T_o.

Using a MOS structure, the majority carrier concentration (N_S) and the minority carrier lifetime (τ_s) near the free surface of the film (3, 4) has been measured.

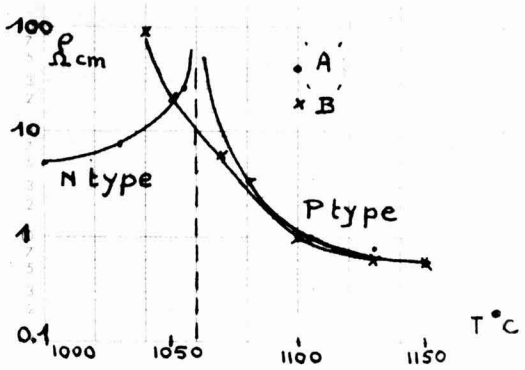

Fig. 1a. Resistivity of Si layers vs. T_{epi}

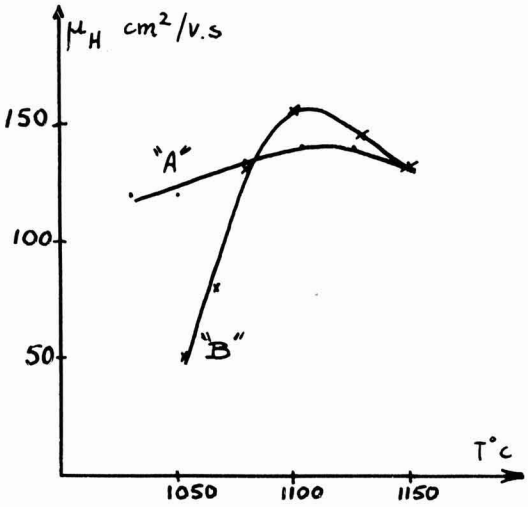

Fig. 1b. Hall mobility vs. T_{epi}

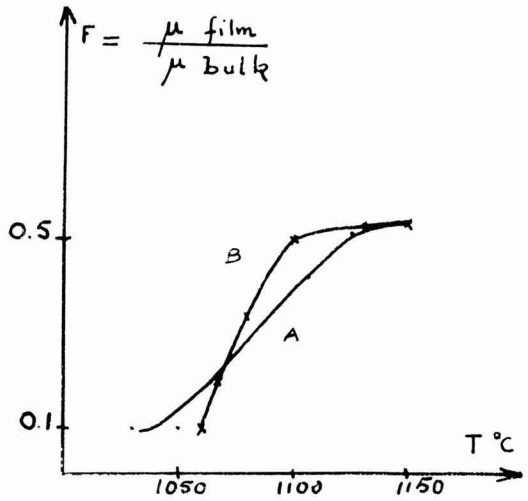

Fig. 1c. Relative factor of merit vs. T_{epi}

The variation of τ_s and its apparently high maximum value, when compared to other results (5) have been noted. The results are given in Table I.

Furthermore, some N-type layers were subjected to short time moderately high temperature, H_2 atmosphere treatments. For example, a 10 ohm cm N-type layer after 5 min at 1100°C turns to 150 ohm cm P-type. This change could not be explained in terms of usual dopant's diffusion. That it occurs only with H_2 atmosphere seems to indicate interfacial electrical states similar to those reported in ref. (6).

Table I. Electrical characteristics of Si layers

T_{epi}	Type	ρ, ohm cm	N_S, cm^{-3}	τ_S(ns)	Nature of oxide
1030	N	7.6	3.3×10^{15}	90	Pyrolitic
1055	N	23.8	1.1	7	Pyrolitic
1080	P	3.5	8.0	4	Anodic
1105	P	1	7.0	45	Anodic
1150	P	0.55	1.1×10^{16}	3	Anodic

Discussion

Some of these results can be now interpreted.

1. It has been ascertained by (7, 8) that Al from the substrate gives rise to P-type autodoping. The exact mechanism involved has not been clearly demonstrated. But from the variation of the layer resistivities, it seems reasonable to suppose that the N-type contamination is due to phosphorous residues after etching. This contamination has thus no other reason, but is inherent with the difficulties involved in the chemical surface preparation of the substrates. This result is to be compared with more subtle interfacial contamination effects (9). As a consequence, P-type layers grown at high temperature in the A process conditions are certainly electrically compensated. This explains the slightly lower maximum value of μ_f for the A process than for the B process (Fig. 1b).

2. The observed reduction of mobility (expressed by F) being independent of the type and doping level, it is plausible to explain in terms of structure defect the limitations at low temperature. This assumption must be checked by specific methods (discussed later). On the other hand, the decrease of mobility values in the higher temperature range can be attributed to impurity defects, the level of which increases with temperature.

X-ray Surface Topography

In the analysis of structural defect limitations, the first step to be considered is the state of preparation of the substrate surface. Reflection techniques as schematically described in Fig. 2 are used (10). Plate and sample under study are simultaneously moved to explore the whole surface, the resolution is fairly good (10μ).

Figure 3 shows a well polished substrate, and Fig. 4a presents a poorly polished one. An optical examination would have given in either case a very flat appearance. Then the same last wafer, after subjection to an H_2 treatment at 1300°C is seen in Fig. 4b. The efficiency of this treatment is demonstrated by the removal of

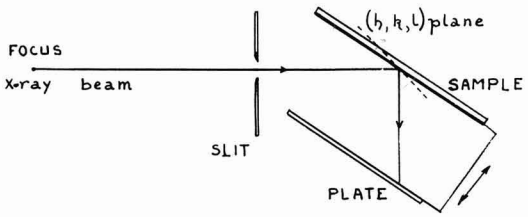

Fig. 2. X-ray surface topography arrangement

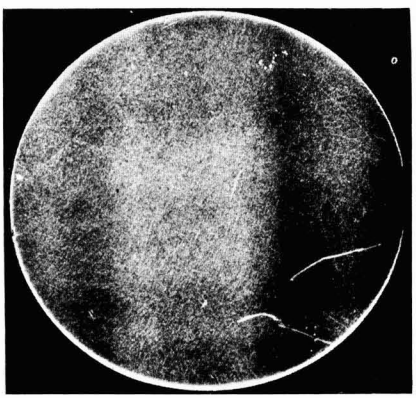

Fig. 3. X-ray surface topography of a well polished Al_2O_3 substrate.

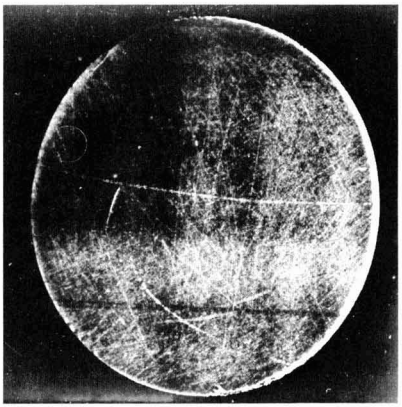

Fig. 4a. X-ray surface topography of a poorly polished Al_2O_3 substrate before H_2 treatment.

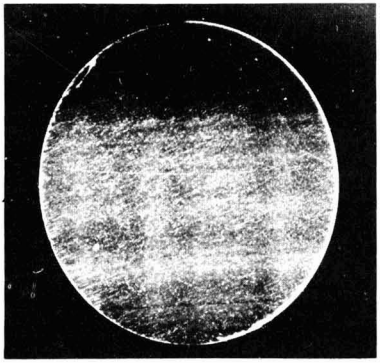

Fig. 4b. X-ray surface topography of a poorly polished Al_2O_3 substrate after H_2 treatment.

fine scratches and the smoothing of dislocation lines. Some preferential etching is indicated by the [100] direction as seen in Fig. 5, which is a G x 10 part of that substrate. This direction has been spotted with the $[0\bar{2}1]$ reference direction. This last one is the intersection of the (3.2.4) reflecting plane with the (01.2) plane.

From these results, one may say that, in spite of difficulties, mechanical and gaseous polishing give good surfaces for epitaxy.

After growing a silicon layer, it is possible, with a proper choice of film thickness to investigate during the same experiment the free surface of the silicon film and the silicon-substrate interface (obviously with different reflecting planes: for Si (440) is convenient). Generally no structure is seen. But Fig. 6a (silicon surface) and Fig. 6b (interface) are special cases: the structures' replica is apparent (see the right corner down). As these structures are visible only if a rapid cooling rate after epitaxy takes place, it may be concluded that the contrast is due to thermal stresses both in the silicon film and in the substrate.

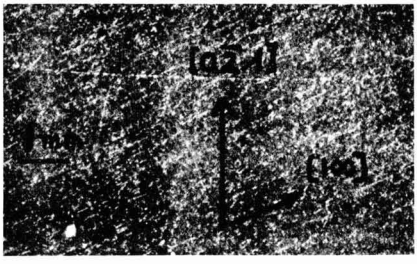

Fig. 5. Part (G x 10) of that wafer

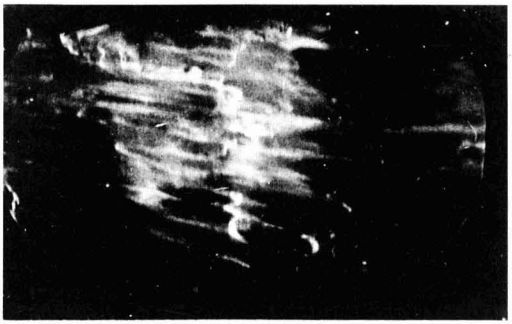

Fig. 6a. X-ray surface topography of the silicon film free surface

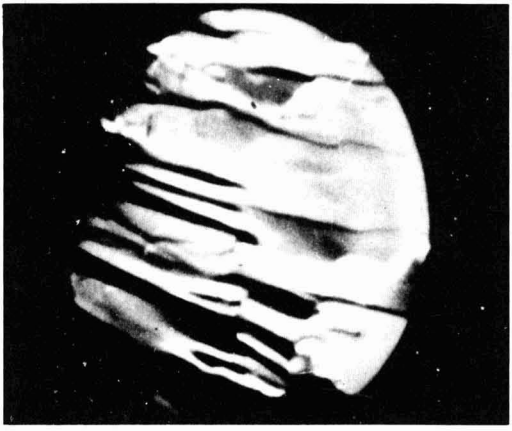

Fig. 6b. X-ray surface topography of the Si-Al_2O_3 interface

Assessment of Crystalline Quality of Films

The x-ray diffraction method is a powerful technique for this aim, its interesting features are: (*i*) nondestructive, (*ii*) analysis of net planes in the film and not only of the surface structure, and (*iii*), semiquantitative: the diffracted intensities are comparative estimates of this quality.

Table II shows relative intensities of the Cu $K\alpha_1$ radiation, diffracted on various planes for six layers (D 1 to 6), deposited at different temperatures.

The (400) plane-reflection corresponds to the predominant (100) orientation of Si films. Regardless of the position of the x-ray spot (2 x 5 mm^2) on the surface, and whatever the sample under study, this intensity is constant and is the strongest one. It will be taken as a reference, with a value of 10^6 in arbitrary unit.

The (200) plane-reflection does not normally satisfy the Bragg condition, unless some planes are missing.

Table II. Relative intensities of x-ray diffracted beam

T_{epi}, °C →	1030	1055	1080	1105	1125	1150
Plane:						
(400)	10^6	10^6	10^6	10^6	10^6	10^6
(200)	1.6×10^3	10^4	1.2×10^5	<40*	1.4×10^4	400
(220)	2×10^3	200	<40	<40	2.8×10^3	200

* 40 is the (relative) detection limit.

This means that stacking faults are present in the layers and the given figures are indicative of their density. It must be noticed that the reported values are maximum ones, for the intensity varies from place to place.

The (220) plane-reflection, which has been reported by others (11) is due to an epitaxial defect orientation (110). Its intensity is uniform for a given film.

The stressed layers as shown in Fig. 6 were (110) mono-oriented.

In conclusion, the comparison of figures in Table II, gives an optimum temperature from both the point of view of stacking fault and of misorientation densities. This temperature is the same one as for mobility values.

Substrate Layer Chemical Interactions

That chemical interaction occurs at the initial stages of the heteroepitaxial process is ascertained with a simple experiment: the selective removal of the epitaxial layer leaves a disturbed Al_2O_3 surface (12) which is not observed solely due to an H_2 heat treatment.

It has generally been assumed that heteroepitaxy occurs in this specific case, by the way of a substitution for Al atoms by Si atoms (13). A reducing action of Si itself seems to have been demonstrated (14-16) in vacuum deposition. However, these authors agree that a very low supersaturation gives this etching effect, and this condition is not generally met in normal deposition conditions. In fact, this would not allow the reversible reaction

$$2Si + Al_2O_3 \rightleftarrows 2SiO + Al_2O$$

to take place but, the following reactions

$$Si + Al_2O_3 \rightleftarrows SiO_2 + Al_2O$$

$$SiO_2 + H_2 \rightleftarrows SiO + H_2O$$

involving less silicon but also the presence of H_2 would be favored due to the extremely dry atmosphere of the experimental conditions.

In any case, however, two consequences of this reactivity are expected: (*i*) the association between the epitaxial condition and the presence of Al in the layer, and (*ii*) the introduction of various Si-O bonds at the film-substrate interface, and probably in the layer itself, due to the high solubility of oxygen in silicon.

Infrared Spectroscopy

In order to check these two points, we have conducted experiments in infrared spectroscopy.

Infrared interferences in the range 1.5-7μ are used for layer thickness measurement. But absorption lines, characteristic of specific chemical bonds are well known. For Si-O bonds they lie in the 700-1400 cm^{-1} range, and for Si-Al the optically excited line is 560 cm^{-1} (0.067 eV) (see the special references at the end of this article).

The use of IR spectrometry however gives rise to two main difficulties with respect to: (*i*) selectivity to avoid interfering effects of the substrate, and (*ii*) sensitivity due to the small amount of Si, containing a low impurity concentration (from a chemical point of view).

The attenuated total reflection method in an arrangement first proposed by Harrick (17) using multiple reflections, has been devised for this purpose. The principle is given in Fig 7. A monochromatic light of the proper wavelength hits a prism in optical contact with the sample. With a suitable refractive index of this prism, a total reflection condition is obtained, and light transfers some part of its energy to a certain depth inside the absorbing medium (Si) (18).

Experimental difficulties, with the optical contact, the low transmittance (<20%), the need for a compensating circuit in the reference beam, add to the theoretical difficulties in the interpretation of the results.

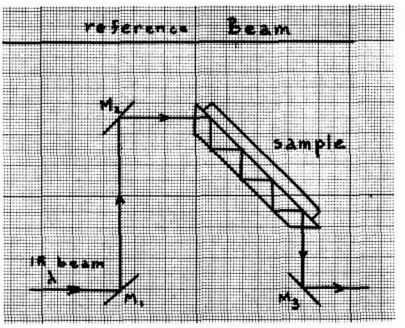

Fig. 7. Attenuated total reflection arrangement

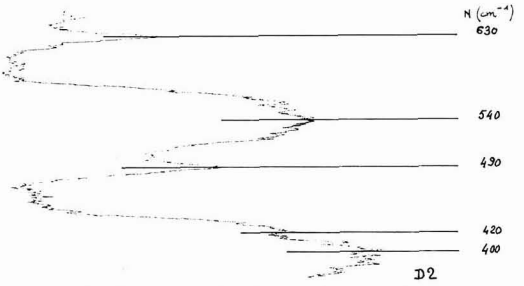

Fig. 8a. IR spectrum of D_2 layer: 390-630 cm^{-1} range

For example, difficulties inherent to the method are: (*a*) shift toward long wavelengths, (*b*) attenuation of short λ bands, and (*c*) reduction of spectrum contrast.

For the moment, only qualitative results are given in Table III. Some spectra are given for the D_2 and D_1 layers (Fig. 8 and 9) and an Al_2O_3 substrate (Fig. 10).

Discussion

1. The Si-Al bond is detected in all epitaxial layers, whatever the epi temperature process and therefore electrical type of the layer.

2. Various Si-O bonds are found, the nature and the amount of which depend on the epi temperature. No apparent continuous transition between amorphous poly- and monocrystalline forms is found when increasing T_{epi}. But for the same optimum T as before,

Table III. IR absorption spectra of Si films (10)

Wave No. cm^{-1} N	T_{epi}, °C: 1030 1055 1080 1105 1125 1150 — Sample D_1	D_2	D_3	D_4	D_5	D_6	Substrate	Reference
390	+	+	+	+	+	+	+	Al_2O_3
420-430		+	+		+		+	Al_2O_3
450-470				+	+	+		?
490	+	+	+		+	+	+	Al_2O_3
510			+	+			+	?
530-560	+	+		+	+	+		Al in Si
630	+	+	+	+	+	+		SiO (amorphous) at 620, but also Al_2O_3
700-720			+		+			
760	+	+						
780-820	+		+	+		+		α Quartz
865-895	+							SiO_2 (crystalline)
940		+		+	+			SiO_2 (vitreous)
985	+		+					
1015	+							Si-O
1050-1080		+	+		+	+		
1110-1160	+		+		+	+		α Quartz
1220-1280	+	+	+			+		α Quartz
1385						+		SiO_2 (polycrystalline)

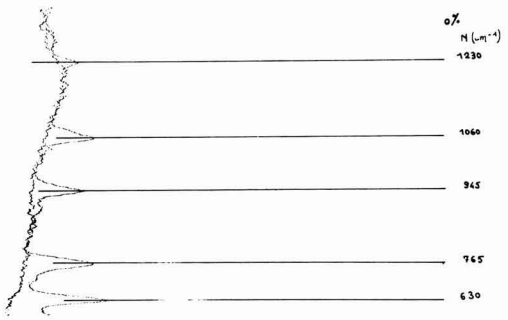

Fig. 8b. IR spectrum of D_2 layer: 630-1400 cm^{-1} range

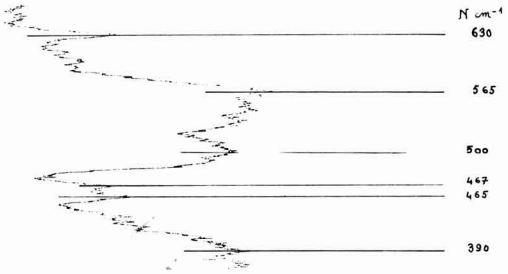

Fig. 9a. IR spectrum of D_4 layer: 390-630 cm^{-1} range

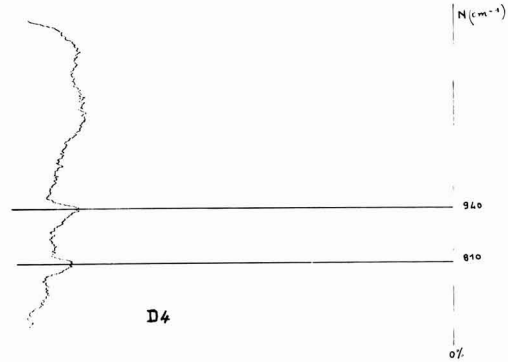

Fig. 9b. IR spectrum of D_4 layer: 630-1400 cm^{-1} range

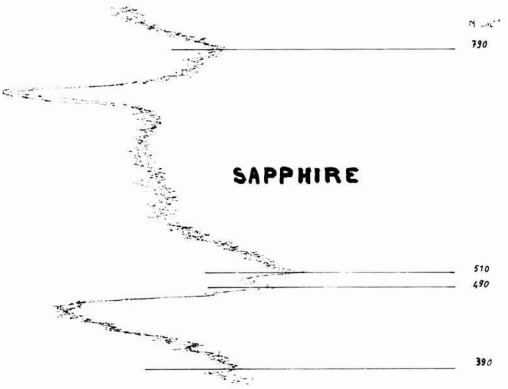

Fig. 10. IR spectrum of Al_2O_3 substrate

(a) the number of absorption lines is minimum, and (b) no amorphous SiO and SiO_2 quartz bonds are present in this layer.

Quartz as a separate phase might have its own orientation, quite independently of the substrate and as a result misorientation effects could be ascribed to its presence.

To resolve an objection against the preceding discussion, we have performed the same experiment on N/N^+ homoepitaxial silicon layers without finding any evidence of Si-O and Si-Al bonding. This removes the possible influence of impurities in silane itself.

Conclusion

Even in our optimized conditions, imperfections are always present in heteroepitaxial Si layers. The optimum range of epitaxial temperatures, around 1100°C, has been found for the majority carrier mobility and has been correlated to crystalline quality from x-ray diffraction methods. IR spectrometry has pointed out the outstanding influence of chemical bonds in explaining most of the layer properties. This conclusion does not mean that crystallographic defects are not of great importance, but it seems that their effects are essentially indirect, due to interaction between dislocations and impurities for example.

Acknowledgments

This work is partly supported by the French Délégation Générale à la Recherche Scientifique and by the French Centre National de la Recherche Scientifique. The author thanks these Administrations for permission to publish. I am grateful to Professor L. Neel for allowing this work and to Dr. B. K. Chakraverty for valuable discussions. It is a pleasure to thank Dr. G. Blet and his group of the L.R.B.G. of Thomson-Houston for his contribution to physical measurements. Without his help, I would not have so rapidly demonstrated the possibilities of infrared techniques in such studies. I also thank Mr. Jund of the C.S.F. laboratory for performing special electrical measurements.

Manuscript submitted June 18, 1969; revised manuscript received *ca.* Jan. 14, 1970. This was Recent News Paper 343 presented at the New York Meeting of the Society, May 4-9, 1969

Any discussion of this paper will appear in a Discussion Section to be published in the December 1970 JOURNAL.

REFERENCES

1. H. F. Matare, "Semiconductor Silicon," R. R. Haberecht and E. L. Kern Editors, Joint Symposium, New York Meeting of the Society, 249 (1969).
2. J. Mercier, 3rd International "Mikroelektronik Tagung," Münich (Nov. 1968), R. Oldenburg, Editor.
3. C. Jund and R. Poirier, *Solid State Electron.*, **9**, 315 (1966).
4. S. R. Hofstein, *I.E.E.E. Trans. Electron Devices*, **ED12**, 104 (1965).
5. F. P. Heiman, *ibid.*, **ED14**, 781 (1967).
6. J. Olmstead *et al.*, *ibid.*, **ED12**, 104 (1965).
7. D. J. Dumin and P. H Robinson, *This Journal*, **113**, 469 (1966).
8. J. Mercier, *Rev. Phys. Appl.*, **3**, 127 (1968).
9. F. P. Heiman, *Appl. Phys. Letters*, **11**, 132 (1967).
10. G. Blet, Private communication.
11. D. J. Dumin, *J. Appl. Phys.*, **38**, 1909 (1967).
12. R. Nolder and I. Cadoff, *Trans. Met. Soc.* AIME, **233**, 549 (1965).
13. J. L. Fraimbault, Thesis, Grenoble University, July 1967.
14. J. D. Filby, *This Journal*, **113**, 1085 (1966).
15. G. W. Cullen, Private communication.
16. S. J. Strepkoff, Thesis, Caen University, May 1968.
17. N. J. Harrick, *Phys. Rev. Letters*, **4**, 124 (1960).
18. J. Fahrenfort, *Spectrachim. Acta*, **17**, 698 (1961).
19. G. Blet, Unpublished results, PV No. 201.

Special References for the IR Study

N (cm^{-1})	*Reference*
390	Alumina (Sadtler—ref. Y 172 S) P. T. Sarjeant and R. Roy (*J. Appl. Phys.*, p. 4541, Oct. 1967) give 378
490	P. T. Sarjeant gives 440 and 485
540-560	Near 0.067 eV optical level Al/Si T. S. Moss, "Optical Properties of Semiconductors" [Butterworths, p. 123 (1961)], C. B. Collins [*Phys. Rev.*, **108**, 1049 (1957)], W. Kohn [*Solid State Phys.*, **5**, 257 (1957)], Hrostoroski and Kayser [*J. Phys. Chem. Solids*, **4**, 48, 315 (1958)]
584	P. T. Sarjeant and R. Roy [*J. Appl. Phys.*, p. 4541 (Oct. 1967)]
630	Sadtler, P. T. Sarjeant, and P. T. Sarjeant and R. Roy 620: SiO_2 amorphous (Desoto Chemical Coatings) L. C Afpemow and J. T. Vandeberg
800	B_3 line of α quartz (Plyler), E. K. Plyler [*Phys. Rev.* (2) **33**-1929-48]
777-828-809	Reflection lines α quartz B. D. Saskena [*Proc. Indian Acad. Sci.*, **A12**, 93-139 (1940); *ibid.*, **A22**, 379-182 (1945)]
790	SiO_2 Sadtler Y 1695
820	SiO_2 crystalline (Desoto Chemical Coatings 4663)
940	Silica glass (Gmelin 935) D. G. Drummond [*Nature*, **134**, 739 (1934)]
1010	SiO (Gmelin, p. 266, gives 1001) G. Hass and C. D. Salzberg [*J. Opt. Soc. Am.*, **44**, 181 (1954)]
1110	SiO_2 α quartz B_4 line (Gmelin and E. K. Plyler)
1260	2nd line twin β_4 α quartz Mean value 1220-1285
1375	Mean value 1320-1400 (Gmelin) A. H. Pfund and Silverman [*Phys. Rev.* (2), **39**, 64 (1932)], A. S. Barker, Jr., [*Phys. Rev.*, **132**, 1473 (1963)] studied the spectrum *vs.* orientation and surface state of alumina

The Role of Damage in the Annealing Characteristics of Ion Implanted Si

Billy L. Crowder

IBM T. J. Watson Research Center, Yorktown Heights, New York

ABSTRACT

Carrier concentration profiles are presented for Si which has been implanted with a low (3×10^{13} cm^{-2}), intermediate (3×10^{14} cm^{-2}) or high (8×10^{15} cm^{-2}) dose of 280 keV P^{31} ions at room temperature and subjected to a 30 min post implantation anneal in the temperature range 550°-850°C. The annealing behavior of these samples is correlated with the amount of damage produced by the room temperature implantation. If a continuous amorphous region is present, ions within this region become electrically active and uncompensated during the epitaxial recrystallization of the layer between 550° and 600°C. These results are generalized to provide a model for the annealing characteristics observed for room temperature and elevated temperature ion implanted Si layers.

Ion implantation doping of silicon at or near room temperature has been shown to produce gross structural defects consisting of amorphous (or highly disordered) regions along the path of the ion (1). Theoretical estimates of the spatial distribution of damage in "amorphous" Si have indicated that the average projected range of the ions is somewhat larger than the average damage depth and that the straggling in these quantities are comparable (2, 3). Recent experimental observations confirm these estimates for implantations of P, As, B, and Si into Si (4). Annealing is required to remove such gross lattice damage and to achieve the desired electrical activity of the implanted dopant. Previous investigations of the dose dependence of the annealing characteristics of Si doped with P or As by room temperature ion implantation have indicated a minimum in the number of carriers per implanted ion as a function of the number of implanted ions in the temperature range 500°-700°C (5, 6). The purpose of this investigation is to demonstrate that this minimum is due to three factors: (*i*) the damage distribution lies closer to the surface than the implanted ion distribution (4), (*ii*) the compensating centers remaining after the annealing of the damage clusters are thermally stable up to temperatures characteristic of diffusion processes in Si (4), and (*iii*) a continuous amorphous layer, if present, recrystallizes epitaxially onto the underlying substrate at 500°-600°C (1).

Experimental

Implantation was accomplished with a Cockcroft-Walton accelerator capable of operation to 300 kV. The P ions were obtained from gaseous PF_5. The ion beam was focused, mass analyzed magnetically, and electrostatically scanned uniformly over a 4 cm^2 area. The total dose was obtained by integrating the current from the samples. Dose rates were typically 1 μamp cm^{-2}. Accurate target alignment was not available since the beam sweep was over approximately $\pm$ 1°.

The Si substrates were <100> wafers cut from Czochralski-grown crystals, which were boron-doped and 1 ohm-cm resistivity. The substrates were lapped and chemically polished. Contact areas were diffused with As prior to implantation to facilitate good electrical contact to the implanted region.

The electrical evaluation of ion implanted layers was accomplished by Hall effect and sheet resistivity measurements on van der Pauw configurations in conjunction with removal of Si layers by anodic oxidation and HF stripping. This technique has been fully described by Mayer *et al* (7). The details of our experiments have been covered in a previous publication and will not be repeated here (8)

Experimental Results

Table I summarizes the electrical properties observed for Si implanted with 280 keV P^{31} ions at a low, inter-

Table I. Summary of electrical properties of Si implanted with 280 keV P^{31}

Dose (cm^{-2})	Annealing temperature[a] (°C)	Sheet resistivity (ohm/□)	n_s[b] (cm^{-2})	n_s[c] (cm^{-2})
3×10^{13}	550	2800	0.4×10^{13}	0.4×10^{13}
	600	680	1.6×10^{13}	2.4×10^{13}
	850	480	2.2×10^{13}	3.2×10^{13}
3×10^{14}	550	2400	0.05×10^{14}	0.07×10^{14}
	600	500	0.4×10^{14}	0.6×10^{14}
	700	175	1.3×10^{14}	2.0×10^{14}
	850	150	2.0×10^{14}	2.6×10^{14}
8×10^{15}	550	14	6.4×10^{15}	—
	600	13.6	6.7×10^{15}	7.6×10^{15}
	850	13.4	6.2×10^{15}	7.2×10^{15}

[a] Samples annealed after ion implantation for 30 min in a nitrogen atmosphere.
[b] Effective number of carriers cm^{-2} determined from the sheet Hall coefficient of the entire implanted layer.
[c] The total number of carriers cm^{-2} obtained by integrating over the distribution obtained by the anodic oxidation and HF stripping procedure in conjunction with sheet Hall coefficient and sheet resistivity measurements.

mediate, and high dose and subjected to annealing for 30 min at the temperature given in column 2. In column 4, the effective number of carriers cm^{-2} as determined from the sheet Hall coefficient of the implanted layer is presented. This number is less than the true number of carriers cm^{-2} (presented in column 5 and obtained from stripping experiments) due to the fact that it represents a weighted average which favors higher mobility carriers (7). The utilization of the implanted P ions (*i.e.*, the ratio of carriers observed to P implanted), presented in Table II, exhibits the minimum observed by previous authors (5, 6).

The depth distribution of carriers for Si implanted with P^{31} and annealed at various temperatures for 30 min are given in Fig. 1 (3×10^{13} P cm^{-2}), Fig. 2 (3×10^{14} cm^{-2}), and Fig. 3 (8×10^{15} cm^{-2}). In Fig. 3, the total P atom profile [obtained by neutron activation analysis as described in ref. (9)] is also shown. The carrier concentration after an 850°C anneal (not shown in the figure) corresponds closely to this total P profile [see ref. (8)]. It should be emphasized that no appreciable differences were observed between the total P profile obtained by neutron activation analysis for samples which were not annealed and samples which were annealed at 850°C for 30 min; *i.e.*, no appreciable diffusion occurs as a result of the annealing step (9). The low dose implant (Fig. 1) exhibits a large "tail" which is due to partially channeled P ions. As the damage produced during the course of the implantation is increased, channeling of P ions is eventually curtailed (10). Channeled P ions contribute less to the profile for the intermediate dose (3×10^{14} cm^{-2}, Fig. 2) than to that for the low dose. For the high dose implant, ions which have partially channeled represent only a small fraction of the implanted dose (Fig. 3).

The Hall mobility observed in Si implanted with 3×10^{14} cm^{-2} 280 keV P ions (see Fig. 2 for profiles) are presented in Fig. 4 as a function of the observed carrier concentration. After a high temperature anneal (850°C), the mobility of the implanted layer is comparable to that observed for bulk Si, as previously observed for well annealed ion implanted layers by Baron *et al.* (11). At lower annealing temperatures, where most of the implanted P ions are not electrically active and uncompensated, the observed mobility is lower for layers within approximately 0.5μ of the surface, presumably because of the presence of charged compensating species. Similar behavior was observed for the Hall mobility in the low dose implants (3×10^{13} cm^{-2}) in that the mobility after a 550°C anneal was lower than that observed in uncompensated bulk Si, for layers within 0.5μ of the surface.

The surface of the substrate implanted with 8×10^{15} P ions cm^{-2} exhibited the "milky" appearance characteristic of amorphous Si. The depth of this amorphous region was determined to be 0.5μ by interference fringes observed in the optical absorption spectrum of a similarly implanted wafer (12). The surface still exhibited the milky appearance after annealing at 550°C for 30 min, but the depth of the amorphous layer was only 0.1μ. This observation is consistent with the epitaxial regrowth onto the crystalline substrate previously reported (1). Annealing for 30 min at 600°C

Table II. Utilization factor for Si implanted with 280 keV P^{31}

Dose (cm^{-2})	Utilization factor[a] 550°C	600°C	700°C	850°C
3×10^{13}	0.13	0.8	~1[b]	1
3×10^{14}	0.02	0.2	0.7	0.9
8×10^{15}	~1[b]	1.0	~1[b]	0.9

[a] The utilization factor (defined as the total number of carriers observed to the number of P ions implanted) is given as a function of the temperature at which the sample was annealed for 30 min.
[b] These values are obtained from the effective number of carriers cm^{-2} (rather than the total number of carriers cm^{-2}), estimating the profile correction from the data given at temperatures for which wafers were stripped and profiled.

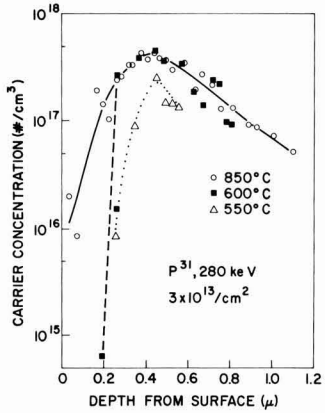

Fig. 1. Carrier concentration profile of <100> Si implanted with 3×10^{13} cm^{-2} 280 keV P^{31}. Samples were annealed for 30 min at 550°C (open triangles), 600°C (closed squares), or 850°C (open circles).

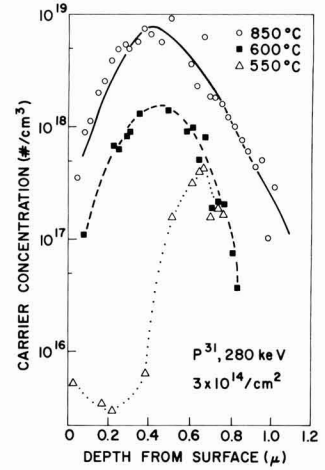

Fig. 2. Carrier concentration profile of <100> Si implanted with 3×10^{14} cm^{-2} 280 keV P^{31}. Samples were annealed for 30 min at 550°C (triangles), 600°C (squares), or 850°C (circles).

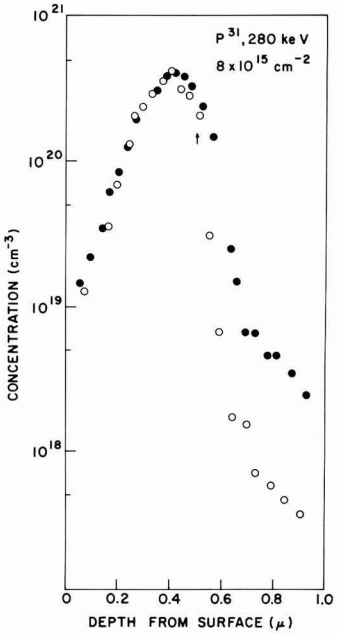

Fig. 3. Concentration profile of <100> Si implanted with 8 x 10^{15} cm^{-2} 280 keV P^{31}. Closed circles represent total P concentration as determined by neutron activation analysis. Open circles represent carrier concentration observed after a 30 min anneal at 600°C. Arrow marks depth of continuous amorphous region present after implantation and before annealing.

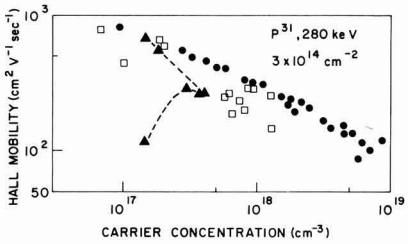

Fig. 4. Hall mobility of Si ion-implanted layers as a function of observed carrier concentration of the layer. Carrier concentration profiles of these samples are given in Fig. 3. Samples were annealed for 30 min at 550°C (triangles), 600°C (open squares), or 850°C (circles).

was sufficient to eliminate this milky appearance. These results may explain the higher annealing temperatures reported for P-implanted layers by Davies, who employed a four point probe (*i.e.*, contacting only the high resistance surface layer) to measure resistivity (13).

Discussion of Results

In a study of the electrical properties of Si implanted with 400 keV P ions, Gibson *et al.* observed essentially complete annealing at temperatures as low as 550°C for low dose (1 x 10^{13} cm^{-2}) and high dose (1 x 10^{15} cm^{-2}) implantations in a random direction (14). These authors did not report on intermediate doses, but the results of the previous section indicate that for such doses only a fraction of the implanted P ions are electrically active and uncompensated after a 550°C anneal for 30 min, in spite of the fact that the gross lattice damage produced by low dose implants anneals below 400°C (15).

Experimental investigations on the spatial distribution of damage in Si produced by P ions in the energy range 70-280 keV show that the ratio of the average damage depth (*i.e.*, the depth from the surface at which the peak in the damage distribution profile occurs) to the average projected range of the P ions (R_p) is between 0.6 and 0.7 [ref. (4)]. For 280 keV P implantations considered here, the maximum damage density occurs at 0.24-0.28μ. Since the damage increases with increasing ion dose, the amount of damage in the spatial region in which most of the P ions lie is much greater for a dose of 3 x 10^{14} cm^{-2} than for 3 x 10^{13} cm^{-2}. These factors are clearly reflected in both the profile of carrier concentration after a 550°C anneal in Fig. 1 and 2 and the low mobilities observed for carriers in this region of highest damage density. An analogous situation is observed for implantations conducted at temperatures above 400°C, where gross lattice damage anneals during implantation. Thermally stable defects remain after the annealing of isolated damage clusters, whether annealing occurs during or after implantation. The density of these defects in the vicinity of the ion distribution is higher for higher doses. Higher temperatures, at which diffusion processes can eliminate such compensating centers, are required to achieve a large fraction of the implanted ions electrically active and uncompensated.

In the case of a high dose which produces a continuous amorphous region, the annealing behavior is markedly different. After a 600°C anneal, the carrier concentration profile corresponds closely to the implanted P ion profile (Fig. 3) to a depth of 0.5μ and the Hall mobility is that expected for bulk Si of comparable doping. Beyond this point, the carrier concentration is markedly lower than the P concentration. Since most of the implanted P ions lie within 0.5μ of the surface, a 600°C anneal results in nearly complete utilization of the implanted P (Table I). The process of epitaxial regrowth of the amorphous region onto the underlying crystalline Si substrate provides a mechanism for the incorporation of most of the P atoms substitutionally and the elimination of any compensating defect centers. Annealing at 550°C also results in nearly complete utilization of the implanted P, even though the surface is still amorphous. As shown earlier, the depth of the amorphous region after a 550°C anneal is only 0.1 to 0.13μ so that most of the P ions lie within recrystallized Si. The diffused contact areas serve to make good electrical contact to this "buried" conducting region.

Similar results are obtained for high dose As implantations, as presented in Fig. 5. The depth of the continuous amorphous region was determined to be 0.35 to 0.36μ [stripping and visual observation; interference fringes (12)] as shown by the arrow. Arsenic ions which are within 0.35μ of the surface (*i.e.*, within the amorphous region) become electrically active and uncompensated after a 550°C anneal for 30 min.

In the high dose P and As implantations, the distribution of ions which lie just beyond the boundary of the amorphous layer produced by room temperature implantation are located in a region of relatively high damage density, thus requiring temperatures characteristic of diffusion processes in Si in order to become uncompensated and electrically active.

Summary

The fact that the damage distribution lies closer to the surface than the ion distribution giving rise to the damage has been shown to have interesting consequences in the low temperature annealing behavior of room temperature implantations of P into Si. These results can be generalized as follows:

1. At a sufficiently low dose, the damage density is so low in the region where the bulk of the ion distribution lies that a large fraction of the implanted species

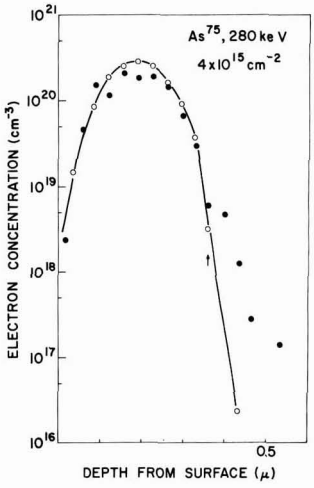

Fig. 5. Carrier concentration profile of <100> Si implanted with As^{75}, 280 keV, 4 x 10^{15} cm^{-2}. Samples were annealed for 30 min at 550°C (open circles) or 800°C (closed circles). Arrow marks depth of continuous amorphous Si region present after implantation and before annealing.

are electrically active and uncompensated after a low temperature anneal, as observed, *e.g.*, for P implants by Gibson *et al.* (14) and for low dose B implants by Seidel and MacRae (16).

2. As the dose is increased, the amount of damage in the region occupied by the ion distribution increases. A fraction of the damage centers which remain after the gross lattice damage has annealed are thermally stable to temperatures characteristic of those at which diffusion processes can occur (4). When this fraction of compensating defects is comparable to or exceeds the ion concentration, high temperatures are required to achieve a high degree of electrical activity in the implanted layer. These observations apply for the situation where annealing is accomplished during implantation as well as low temperature implantations followed by a post implantation anneal. Such behavior has been noted for B, P, and As implantations by a number of authors [see, *e.g.*, ref. (9) and (16)].

3. If the dose is sufficiently high and the temperature sufficiently low to allow the formation of a continuous amorphous region overlapping the ion distribution, the epitaxial regrowth of this amorphous region "sweeps out" the compensating defects and the ions within this regrown region are electrically active and uncompensated. At a given temperature, light ions require a higher dose to produce this amorphous layer than heavy ions, as shown, *e.g.*, for room temperature implantations of P or As (6). For a given ion, lower doses are required at lower temperatures, as demonstrated for B implantations into Si by Davies (13). The required dose may approach a limiting value at sufficiently low temperatures.

Acknowledgments

The author gratefully acknowledges the capable technical assistance of W. N. Hammer, N. A. Penebre, and R. A. Fiorio.

Manuscript submitted Oct. 13, 1969; revised manuscript received *ca.* Dec. 26, 1969.

Any discussion of this paper will appear in a Discussion Section to be published in the December 1970 JOURNAL.

REFERENCES

1. R. S. Nelson and D. J. Mazey, "International Conference on Applications of Ion Beams to Semiconductor Technology," 1967, Grenoble, France, p. 337.
2. P. Sigmund and J. Sanders, *ibid.*, p. 215.
3. P. V. Pavlov, D. I. Tetel'baum, E. I. Zorin, and V. I. Aleksev, *Soviet Phys.-Solid State (English Transl.)*, **8**, 2141 (1967).
4. B. L. Crowder, To be published.
5. V. K. Vasil'ev, E. I. Zorin, P. V. Pavlov, and D. I. Tetel'baum, *Soviet Phys-Solid State (English Transl.)*, **9**, 1503 (1968).
6. B. L. Crowder and F. F. Morehead, *Appl. Phys. Letters*, **14**, 313 (1969).
7. J. W. Mayer, O. J. Marsh, G. A. Shifrin, and R. Baron, *Can. J. Phys.*, **45**, 4073 (1967).
8. B. L. Crowder and J. M. Fairfield, *This Journal*, **117**, 363 (1970).
9. J. M. Fairfield and B. L. Crowder, *Trans. Met. Soc. AIME*, **245**, 469 (1969).
10. K. E. Manchester, *This Journal*, **115**, 656 (1968).
11. R. Baron, G. A. Shifrin, O. J. Marsh, and J. W. Mayer, *J. Appl. Phys.*, **40**, 3702 (1969).
12. B. L. Crowder, R. S. Title, M. H. Brodsky, and G. D. Pettit, *Appl. Phys. Letters*, 16 (1970).
13. E. Davies, *Appl. Phys. Letters*, **14**, 227 (1969).
14. W. M. Gibson, F. W. Martin, R. Stensgaard, F. Palmgren Jensen, N. I. Meyer, G. Galster, A. Johansen, and J. S. Olsen, *Can. J. Phys.*, **46**, 675 (1968).
15. J. A. Davies, J. Denhertog, L. Eriksson, and J. W. Mayer, *ibid.*, **45**, 4053 (1967).

Ionic Instabilities in Pyrolytically Deposited SiO_2 Films

P. M. Dunbar[1] and J. R. Hauser

North Carolina State University, Raleigh, North Carolina

ABSTRACT

Forms of ionic instability in pyrolytic SiO_2 layers are investigated through movements of the flat band voltage. The films were in the thickness range of 1000Å, deposited at 725°C, and annealed at 800°C in a steam atmosphere. As deposited, the films exhibited the presence of both positive and negative charge. This charge was also found to be highly mobile. The annealed films exhibited only positive ionic charge but high flat band voltages with instability present only after long term bias.

The process of pyrolytic deposition has become quite widely used in semiconductor device fabrication. Basically, the process concerns the deposition of thin insulator films such as SiO_2 for both diffusion and electrical insulation. Some of the initial work with this process was performed by Jordan (1) in his attempt to apply the process as a suitable method for diffusion masking on germanium. Klerer (2, 3) expanded on Jordan's work and studied the chemical

[1] Present address: Howard University, Washington, D. C. 20001.

reactions involved in a pyrolytic deposition. Other evaluations showed densified pyrolytic films to be quite comparable to thermally grown SiO_2. However, ionic instability usually occurred in the films. These instabilities have been noted briefly (4), and this present work expands on this problem.

Experimental Techniques and Results

The apparatus used in this work was similar to that used by Jordan (1). A diagram of the complete system is shown in Fig. 1. This system allows the three basic operations of purging, deposition, and annealing in a steam atmosphere. The nitrogen purge takes place prior to any deposition and while the furnace is heating or cooling. When the slice obtained proper temperature, the deposition was initiated by introducing nitrogen into the bubbler which contains liquid tetraethyoxysilane. The tetraethyoxysilane was standard reagent grade material. This flow rate and the purge rate can be controlled by flowmeters 1 and 2. The bubbler was held at 32°C in order to regulate the absorption rate of the tetraethyoxysilane into the nitrogen carrier. This allowed an improvement in repeatability by excluding room temperature as a process parameter. The substrates used were n-type silicon slices. The resistivity was in the 10 ohm-cm range, and the crystal orientation was [100]. The slices were approximately 3 cm in length by 1.5 cm in width.

The substrates were stored in methyl alcohol prior to deposition, and placed wet into a 200°C furnace at the outset of a run. The system was then purged with a nitrogen flow rate of 1.0 l/min for about 15 min. When proper temperature was reached, deposition was begun by diverting 0.5 l/min of nitrogen through the tetraethyoxysilane while allowing 0.5 l/min of nitrogen to flow freely into the furnace, giving a total deposition flow rate of 1.0 l/min. This combination yielded the best results, because a higher or lower rate through the bubbler detracted from the uniformity of the films. At the end of the desired deposition time, the bubbler flow was cut off and the purge flow of 1.0 l/min was returned. After allowing 2 min for the system to clear of tetraethyoxysilane vapors, the power to the furnace was shut off. The slice was then removed after the temperature dropped to 300°C. Deposition temperatures were in the 700°C range with deposition rates of 60 to 160 Å/min. This range of deposition rates had no detectable effect on the stability results.

The resulting films were clear in appearance and the thicknesses, estimated from the film color, were in the 1000Å range. Although the films suffered from a thickness nonuniformity in the range of 20%, the region over which metal was evaporated had no more than a 5% variation. The annealed films were processed identically except that a 15 min steam treatment at 800°C was included.

To fabricate the capacitors, 17 mil diameter dots were evaporated onto the slice. Both gold and aluminum were used, but the metal thickness was 4000Å throughout. Electrical contact was made to these devices with a probing technique.

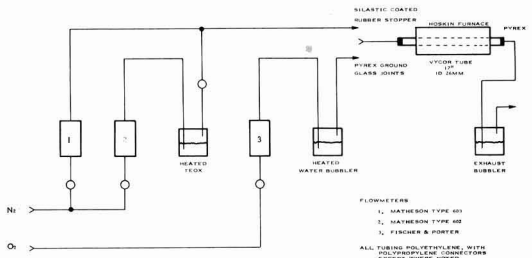

Fig. 1. Apparatus for pyrolytic deposition of thin insulating films

Evaluation

Studies of these devices showed the steam annealed films to be quite similar to thermal oxides with respect to dielectric strength and structural qualities such as pinhole characteristics. Although the unannealed devices had both high leakage currents and pinhole counts, the breakdown strength of all the devices were in the 10^7 V/cm range. The relative permeativity values were quite scattered, but generally were 20% higher than in thermal oxides.

It is known that pyrolytic oxides obtained from tetraethyoxysilane can contain considerable concentrations of impurities which can dope the silicon either p- or n-type. No doping effect on the silicon was noted for the temperatures and times used in the present work. The possible presence of a p-type layer was checked by etching the oxide from several wafers after testing and checking for the conductivity type which remained n-type. Similar deposits on p-type wafers of about 10 ohm·cm resistivity have also failed to show the presence of a thin n-type layer due to diffusion from the pyrolytic oxide during the temperatures and time employed in this work.

The apparatus used to determine the capacitance *vs.* voltage characteristics involved a standard capacitance bridge outfitted so that the voltage could be automatically swept across the device. A block diagram of this system is shown in Fig. 2. A 50 msec ramp voltage from the oscilloscope was used to sweep the device voltage. The ramp was 50V in height but the beginning and end points could be adjusted by means of the series bias. The scope could be triggered externally or allowed to free run, depending on the mode of sweep voltage desired. Comparisons of the curve shifts were made by photographs of the scope face.

The initial curves were obtained by single sweeps of the ramp voltage across the device. After the initial curve was obtained, the ramp voltage was allowed to free run across the device for several thousand cycles to detect any rapid movements of the curve. The bridge was then disconnected, and a 9V d-c bias was connected across the device for a 4-hr period with the metal positive. At the end of this time, the battery was disconnected and the bridge reconnected, and another "initial" curve was obtained. As before, the ramp was then set on free run to detect any rapid changes. This was then repeated for the opposite polarity for the 4-hr bias.

The need to bias the ramp voltage resulted from the need to sweep the device voltage in a bipolar method. This bias, however, resulted in a d-c component of voltage placed across the device whenever a sweep was made. Although this d-c component had no detectable effect in the single sweep mode, the effect was quite appreciable during the free run time. The voltages applied to the devices during the free running mode are shown in Fig. 3. Typical initial curves for both types of devices are shown in Fig. 4 and 5. The flat band voltage for this oxide thickness and substrate doping occurred when C/C_{max} was in the order of 0.7. These curves depict the movements somewhat typical of unstable oxides. Note however, that the unannealed films exhibited positive flat band voltages after negative stress. This indicates the presence of a fairly large negative charge density in the layer.

Note also, that after annealing in a steam atmosphere the effect of this negative charge could also explain the low flat band voltage of the unannealed films

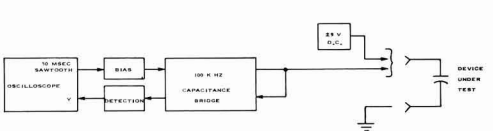

Fig. 2. Capacitance *vs.* voltage apparatus

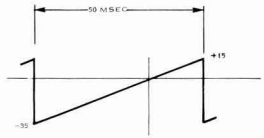

A. Ramp voltage employed after negative stress.

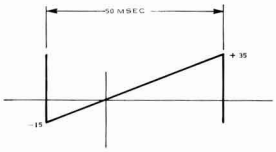

B. Ramp voltage employed after positive stress.

Fig. 3. Sweep voltage

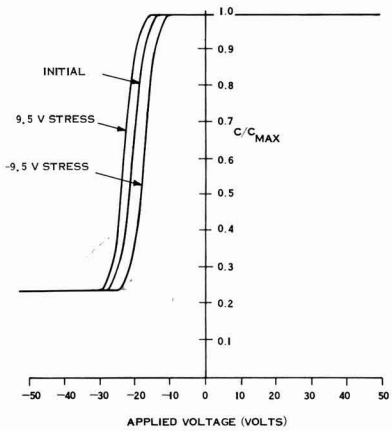

Fig. 4. Capacitance *vs.* voltage for annealed devices before and after stress.

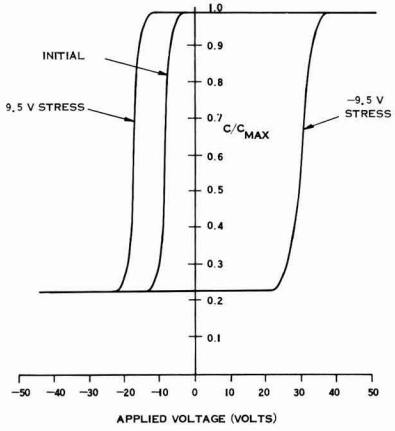

Fig. 5. Capacitance *vs.* voltage for unannealed devices before and after stress.

as compared to the annealed films, since the negative charge would counteract any positive charge present in the layer, thus lowering the flat band voltage. Since the annealing seems to eradicate these charge centers, the counteracting effect would not be present in the annealed films, allowing the now free positive charge to raise the flat band voltage. The positive charge and its related high flat band voltage could, of course, have been caused by a contamination entering at some point in the process; however, the apparent nulling of the negative charge by annealing suggests that this negative charge is inherent in the unannealed pyrolytically deposited SiO_2 films.

Another major difference between the annealed and unannealed devices was exhibited when the sweep voltage was set to free run in order to detect any rapid movements. The unannealed devices, as shown in Fig. 6 and 7, exhibited a very rapid flat band movement, indicative of a highly mobile charge species. Two factors indicate that the mobile charge causing this is the negative charge. Primarily, this type of rapid hysteresis was not present after annealing. This, when coupled to the indication that the negative charge was eliminated by annealing points to this charge as the cause of the rapid shifts.

A close examination of the rapid instability also indicates that negative charges can explain the rapid shifts in flat band voltage. Note that after positive stress, the positive charge would be near the SiO_2-Si interface, having a more pronounced effect in V_{FB} than the negative charges which are at the SiO_2-metal interface. The d-c component of the free running sweep, then would move the negative charges to the SiO_2-Si interface but the positive charges would remain comparatively unmoved, thus counteracting the negative charge movement, slowing down any hysteresis effects. The case of negative stress points this out in somewhat more dramatic fashion. After stress, the positive charge is now at the metal-SiO_2 interface,

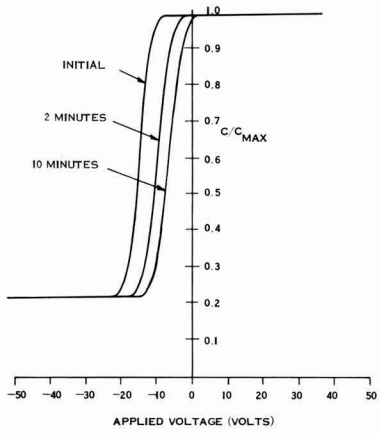

Fig. 6. Capacitance *vs.* voltage showing rapid charge movement after positive stress in unannealed devices.

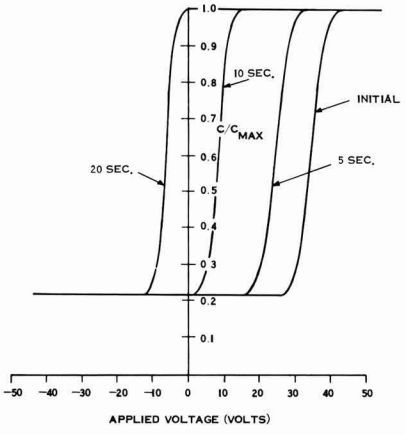

Fig. 7. Capacitance *vs.* voltage showing rapid charge movement after negative stress in unannealed devices.

where it has little effect on V_{FB}, and the negative charge, now at the SiO_2-Si interface, is the controlling factor. So, when the free run component occurs, this negative charge now moves rapidly to the metal-SiO_2 interface, lowering the V_{FB} just as rapidly, causing the rapid movement as seen in Fig. 7.

These results, however, were somewhat scattered. Although the characteristics shown in Fig. 6 and 7 were quite typical, the speed of the movements varied widely, indicating a somewhat unpredictable mobility of the negative charge. Another factor of note is that these rapid changes did not occur until after the devices were put under a long term bias.

Summary and Conclusions

Stability studies showed the films to be unstable with high flat band voltage as compared to good thermally grown oxides. Both the annealed and unannealed films exhibited the effects of charge movement indicative of positive ionic charge in the oxide layer. The unannealed devices indicated the presence of both positive and negative charge in the oxide layer.

The presence of the negative total charge in the oxide differs from that of thermal oxides where positive ionic charges are observed. The origin of the negative charge can only be speculated on at this point. Ionic instabilities in SiO_2 have been studied in considerable detail (5, 6). The rapid movement of the negative charges in the present study would require, however, a much larger mobility than has previously been reported for ions. Hofstein (7) has reported on a hydrogen ion trapping instability in SiO_2 which gives times more consistent with the rapid shifts observed in this work. The hydrogen ion, however, is a positive charge whereas the present observations indicate a rapid movement of negative charges. The negative charges may in fact be just electronic motion within the pyrolytic SiO_2 layer. A thin higher quality thermal oxide at the silicon interface could prevent the electrons from flowing out of the pyrolytic oxide into the silicon, resulting in their accumulation at the pyrolytic-thermal oxide interface.

The improvement in the C-V shifts following annealing in a stream atmosphere appear to be due largely to the elimination of the rapid negative charge movements within the oxide. The steam annealing process can have two effects on the insulating layer. Previous work (2-4) has indicated this process results in a densification of the pyrolytic oxide films. Also, there is likely some increase in the thickness of the thermal oxide between the silicon and the pyrolytic oxide. Both of these processes may contribute to the improved electrical properties following annealing.

Manuscript received May 3, 1969; revised manuscript received *ca.* Jan. 26, 1970.

Any discussion of this paper will appear in a Discussion Section to be published in the December 1970 JOURNAL.

REFERENCES

1. E. L. Jordan, *This Journal*, **108**, 478 (1961).
2. J. Klerer, *ibid.*, **108**, 1070 (1961).
3. J. Klerer, *ibid.*, **112**, 503 (1965).
4. J. Oroschnik and J. Kraitchman, *ibid.*, **115**, 649 (1968).
5. W. Leighton, *IEEE Proc.*, **55**, 214 (1967).
6. E. H. Snow *et al.*, *J. Appl. Phys.* **36**, 1664 (1965).
7. S. R. Hofstein, *IEEE Trans. Electron Devices*, **ED-13**, 222 (1966).

Water Contamination in Thermal Oxide on Silicon

G. L. Holmberg,[1] A. B. Kuper,[2] and F. D. Miraldi

School of Engineering, Case Western Reserve University, Cleveland, Ohio

ABSTRACT

Wet-grown, baked 5400Å films were controllably hydrated in tritiated-water vapor under conditions approximating device operation (50°-250°C, 0.25-8 hr, 25-400 Torr water vapor pressure). Fast penetration and fast outdiffusion suggest a micropore diffusion mechanism. This conclusion is supported by a low diffusion activation energy (0.3 eV) and exponential profiles in the bulk oxide. Strong surface peaking of the hydrogen tracer in both indiffusion and outdiffusion is attributed to surface energy lowering (Gibbs effect). "Water" under these conditions gave negligible MOS ΔQ_{ox} or ΔQ_{is} even with a hydrogen concentration of 5×10^{18} cm^{-3} at the silicon. Sodium contamination gave an order higher water entry rate. Water, likewise, increased sodium entry rate and charge production by the sodium.

Water has long been considered a serious contaminant in oxide-passivated silicon planar devices. Since it is not possible to eliminate it in device manufacture or, except by hermetic sealing, in device use, it is desirable to study its effects under likely contamination conditions.

In previous studies (1, 2), fused silica was hydrated at high temperatures (600°-1200°C) to measure the diffusion coefficient and the activation energy for water diffusion in silica. The same studies indicated that water interacted with bridging oxygens to form silanol (Si-OH) groups on entering the silica.

Oxides on silicon have been grown in tritiated steam at 1000°C (3, 4). The diffusion coefficient (3, 4) and activation energy (3) determined from bakeout were comparable to those determined for water diffusion in fused silica, but bakeout data were not taken below 500°C. Only one study (5) has produced a hydrogen profile associated with water contamination; the sample was contaminated by boiling in tritiated water.

Electrical effects of water contamination in thermal oxide on silicon have been studied. Water has been shown (6) to promote channel conduction on p-type surfaces. Water under certain conditions is believed (5, 7) to act as a positively charged species, probably due to formation of H^+ ions. Water also acts to annihilate interface states (8-10) and is known to increase dielectric loss in bulk silica (11). Water introduced during oxidation appears to have no charge associated with it as evidenced by the fact that the hydrogen in

[1] Present address: 3508 Wilson St., Fairfax, Virginia 22030.
[2] On leave 1969-1970 to Electrical Engineering, Technion, Haifa, Israel.

tritiated-steam grown oxides (3, 4) did not redistribute under bias-temperature stress.

Since data were not available on the diffusion of water in silica below 600°C, we had to extrapolate fused-silica data to the lower temperatures of interest in our work. The validity of the extrapolation from 600°C is questionable; in addition, significant differences exist between the oxide and bulk silica. The oxide is very thin and therefore may be dominated by surface effects. It is under large compressive stress, contains concentration gradients of silicon and oxygen, and has a different thermal history than the fused silica; in particular, the oxide film is formed below its softening point. Evidence recently summarized (12) also suggests a micropore structure in the oxide.

A number of experiments have demonstrated the interaction of water with sodium in silica. Increased sodium transport in the presence of water (13) and increased wet oxidation rates in the presence of sodium (12) have been shown. Sodium is thought to release hydrogen (5) in the oxide. Glass corrosion studies indicate (14) that water can release sodium in silica.

In our study, oxides were hydrated in tritiated-water vapor under controlled conditions approximating device operating conditions. Sets of hydrogen profiles were developed with time, temperature, and water vapor pressure as parameters. Outdiffusion and other experiments further characterized the hydration. Models are presented for the hydration process. MOS measurements of charge and interface-state density were made to assess the electrical effects of the water.

Radioactive sodium and water were diffused together in some samples; profiles and MOS electrical effects were measured to determine interactions between the two diffusants.

Experimental

Samples were 1 or 10 ohm-cm, n-type, {111}-oriented silicon. They were wet-oxygen oxidized in a quartz-tube furnace at 1200°C to a thickness of 5400Å, then baked for 30 min at 1000°C in dry nitrogen.

Hydrations were carried out in the apparatus shown in Fig. 1. The sample cell was a solid aluminum cylinder into the top of which several slots had been milled; the remainder of the apparatus was stainless steel, sealed to the cell by a Viton O-ring. Oxidized wafers were dropped into the slots and held in good thermal contact with the aluminum by means of Teflon strips at their edges. The source vial contained 0.5 cc of tritiated water with specific activity of approximately 250 mc/g. The tubing and valves were wrapped with heating tape and kept well above the temperature of the source vial to prevent water condensation anywhere except in the source vial.

The tritiated-water source vial was valved off while loading the samples. The source vial was then cooled with liquid nitrogen, the source valve opened, and the apparatus evacuated with a mechanical forepump. After evacuation, the source valve was closed, the cell and samples brought to temperature in a thermostated oven, and the source vial thermostated at a temperature corresponding to the desired water vapor pressure.

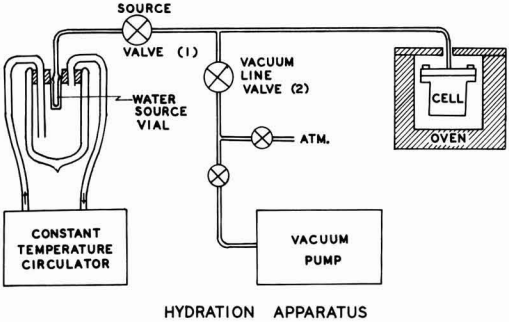

HYDRATION APPARATUS

Fig. 1. Apparatus for tritiated-water hydrations

When source and samples were at the proper temperature, the vacuum line valve was closed, the source valve opened, and timing started. At the end of the desired hydration time, these operations were reversed to recondense the water into the source vial and to remove the samples.

An experiment was done to test pressure equilibration. With a glass plate in place of the sample cell, it was found that water immediately condensed onto the glass on opening the source valve. A calculation confirmed that pressure in the apparatus should equilibrate within a second after opening the source valve. Thus we felt it unnecessary to have a manometer in the system, and pressures are based on source vial temperature.

The apparatus allowed close control of hydration conditions. Accuracy and precision of temperature were within 1°C, pressure was within 1%, and time was accurate within a few seconds. Also, the cell allowed several samples to be loaded simultaneously and exposed to identical hydration conditions.

Samples were etched in dilute HF and the etchants were liquid-scintillation counted. Since the efficiency of liquid scintillation counting is degraded by large amounts of aqueous material in the solution, an apparatus was built to minimize etchant volume. The apparatus allowed etching with 0.5 cc of acid and rinsing in 1 cc of water with good reproducibility.

Samples were washed in water before sectioning to exchange off adsorbed tritiated water from the surface and thus to avoid contaminating the first section with adsorbed activity. Samples were also washed between sections to avoid cross-contamination between adjacent sections.

The etchant was neutralized with calcium hydroxide, then solubilized with a xylene-PBD mixture by means of Beckman Biosolve BS-3 solubilizer. Counting was done in a Picker Ansitron II liquid scintillation counter. Counting efficiency was approximately 25% and background about 25 counts per minute. Sufficiently long counts were taken to keep one-sigma counting errors below 5%.

Counting efficiency was determined by counting a standard along with the etchants. The standard had the same chemical composition as the unknowns, and its activity was known to ±3%. Accuracy of relative concentrations (for profile shapes or for comparisons of profiles) was equal to the 5% counting error. However, uncertainty in the specific activity of the tritiated water in the source vial limited accuracy of absolute hydrogen concentrations to about 20%.

Sodium-water interactions were studied with a $Na^{22}Cl$ tracer. Samples were either baked or else equilibrated with a wet ambient (nitrogen, 95°C dew point) at 800°C. They were next contaminated by dipping them into a methanol solution of the tracer and air drying them. The samples were then sandwiched between two bare silicon wafers to minimize sodium evaporation during the diffusion and were diffused in a tube furnace. The dry (baked) oxides were diffused in a dry nitrogen ambient and the wet oxides in a wet (95°C dew point) nitrogen ambient.

The sodium-contaminated samples were sectioned in dilute HF. The etchant was gamma scintillation counted with a 4 x 4 in. NaI(Tl) crystal and a multichannel analyzer. A counting standard (±3%) was again used.

Some samples were diffused both with $Na^{22}Cl$ and with tritiated water. These samples were etched like other hydrated samples and liquid scintillation counted. Two analysis channels were set up on the liquid scintillation counter to count the two isotopes in the presence of each other. Counting efficiencies and the interferences of the isotopes on each other were determined from counting standards. Sodium concentrations were also checked by gamma scintillation counting.

Aluminum dots were evaporated onto some of the samples, and 1-MHz C-V curves were run. Room temperature flatband voltage was used to measure fixed charge in the oxide. Interface state density was measured by the Gray-Brown (15) technique of determining the shift in flatband voltage between room temperature and liquid nitrogen temperature.

Hydration Results

A typical hydration profile is shown in Fig. 2. The profile is made up of three regions: at the air interface is a sharp spike of hydrogen; in the bulk oxide the profile is rather flat; at the silicon interface there is a slight peak with a dip just before the peak. The spike at the air interface is present in all profiles, the peak and dip at the silicon only in some profiles. This profile and others to be presented are simply drawn through the data points and represent no theoretical fit.

Figure 3 shows the time development of the hydration profile at constant temperature and pressure (hydration time was the time during which tritiated water vapor was actually in contact with the samples). The spike at the air interface is present in all profiles. In the bulk oxide the profile is roughly exponential (*i.e.*, linear on the semilog plot). The effect of increasing hydration time is to fill and flatten the profile in the bulk oxide. Concentration in the oxide near the air interface increases with increasing hydration time, but penetration of the spike remains roughly constant.

For 15-min hydrations, not shown in the figure, the hydration profile is nonreproducible and shows anomalous peaking near the silicon. Even for the profiles shown, however, the penetration is much faster than expected. A diffusion coefficient estimated from the profiles in Fig. 3 is 10^{-13} cm^2/sec, more than an order larger than estimated by extrapolating fused silica hydration data (1) from 600°C.

The effect of hydration temperature at constant time and pressure is shown in Fig. 4. The effect of increasing hydration temperature is similar to the effect of increasing hydration time. The profile fills and flattens in the bulk, and the surface spike rises in amplitude at constant penetration.

The anomalous peaking in the 50° and 100°C profiles is similar to that at short times. It appears that there is some defect in the oxide which interacts with

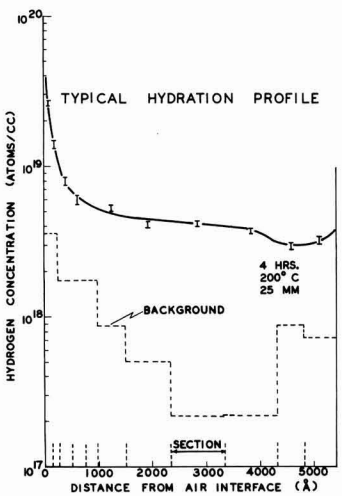

Fig. 2. Typical hydration profile. Counting errors ($\pm 1\sigma$) are shown by error bars. Concentration equivalent of counting background is represented by dashed curve and sectioning by vertical dashed lines. Reproducibility on individual data points was about ±10% from sample to sample.

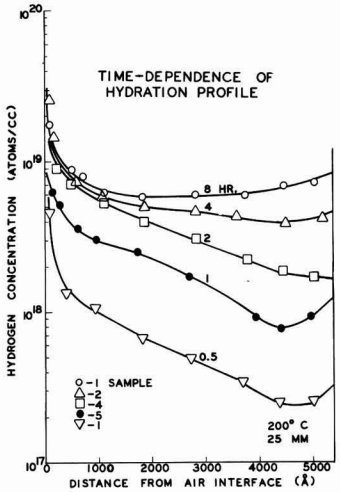

Fig. 3. Time development of hydration profile at constant temperature and pressure. Profiles are in reasonable agreement with Hofstein's (5) profile for a dry oxide. Data are averages of one or more samples, as indicated.

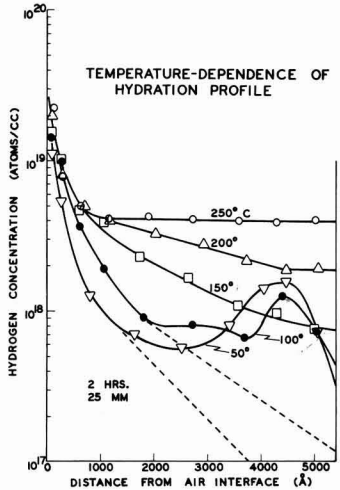

Fig. 4. Effect of temperature on hydration profile at constant time and pressure. Anomalous peaking at low temperature is similar to that seen for short times. Activation energy for diffusion was about 0.3 eV.

the "water" and then saturates. At higher temperatures (or longer times) the hydrogen profile levels itself out.

For error-function profiles, either the total hydrogen in the oxide (N) or the intercept (x) of the profile with a given concentration level should have the same temperature dependence as $D^{1/2}$ (D is the diffusion coefficient). Although the profiles are not actually error functions, Arrhenius plots were made for N and x (from Fig. 4) and the slope used to approximate the energy dependence of $D^{1/2}$. The former method estimated an activation energy of 0.25 eV for D (0.13 eV for $D^{1/2}$), and the latter gave 0.3 eV.

An activation energy of 0.3 eV is less than half of the activation energies found for fused silica hydration (1, 2), steam oxidation (16), or wet-oxygen oxidation (17) of silicon, or for outdiffusion of water from steam-grown oxides (3). The low activation energy suggests that hydration rates could be appreciable at room temperature.

The effect of hydration pressure is shown in Fig. 5. Increase in pressure shifts the hydration profile uniformly to higher concentrations. Concentration of hydrogen in the oxide varies as the square root of hydration pressure, as expected from fused silica hydration data (1, 2), which indicates the breakup of the water molecule into two independently diffusing fragments on entering the oxide. The square root pressure dependence throughout the oxide implies that little of the hydrogen tracer exists as water molecules in the oxide.

Several experiments were done to characterize the hydrogen surface spike. As shown in Fig. 3-5, the amplitude of the spike increased with time, temperature, and pressure with no significant increase in penetration. It was considered possible that the surface region of the oxide was different from the remainder of the oxide, possibly due to local stress-relief.

In order to test this hypothesis, 1000Å of oxide was etched from the surface. The etched oxide and an unetched oxide were then hydrated together for 4 hr. The surface spike was still present in the oxide which had been etched before hydration. The same result was obtained in the same experiment with a 1-hr hydration.

It was also considered possible that the spike was an experimental artifact. As mentioned previously, the sample surface was thoroughly washed before the first section was taken in order that adsorbed surface activity not be contained in the first section, thus making its concentration incorrectly high. Also, samples were soaked overnight in concentrated HCl and washed overnight in running water with no noticeable effect on the spike. Thus, the spike was apparently actually present in the oxide surface region.

An outdiffusion experiment was done to characterize further both the surface spike and the bulk diffusion mechanism. Three samples were hydrated simultaneously. One was etched immediately as a control (profile A in Fig. 6) and showed good agreement with other samples hydrated previously under the same conditions.

A second sample was vacuum-baked after hydration. After baking, it had the profile shown as profile B in Fig. 6. Note that roughly half of the hydrogen outdiffused in 4 hr at 200°C. Extrapolation of bake-out data for tritiated-steam grown oxides (3) would give a negligible outdiffusion rate at 200°C. This suggests that water diffused at 200°C is incorporated differently into the oxide than it is incorporated during a steam oxidation.

The first 1250Å of the third sample was sectioned (profile C in Fig. 6). This profile agreed well with the profile in the surface region of the control. We assume

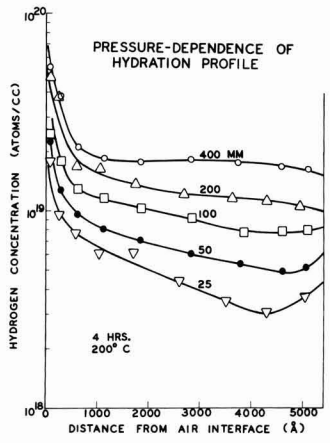

Fig. 5. Effect of pressure at constant time and temperature. Concentration varied as square root of pressure.

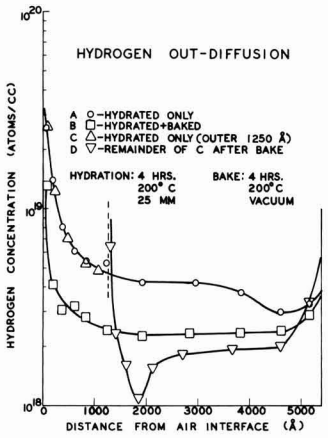

Fig. 6. Outdiffusion behavior of hydrated oxides

that the remainder of the profile in this sample was similar to that in the control. After vacuum baking, the partially etched sample had the profile shown as profile D in Fig. 6. Again the outdiffusion rate is large. Of greater significance, however, is the fact that the surface spike reformed in the outdiffusion. In fact, the dip in the profile just beyond the spike suggests that hydrogen was preferentially segregated from this region into the surface region.

It should perhaps be emphasized that these results were obtained on single samples, and reproducibility was therefore not checked. Similar results have, however, been obtained (18) for a similar outdiffusion experiment with sodium in an oxide film.

There were essentially no MOS electrical effects from hydrations at 200°C or below, even though hydrogen concentrations as high as 5×10^{18} cm^{-3} were measured at the silicon. Room-temperature flatband voltage showed a positive shift of about 1V (4×10^{10} electrons cm^{-2}), attributed to annealing. No measurable change in interface state density was observed. Annihilation of states was complete for hydrations at 800°C, however, suggesting that temperature is important to the annihilation.

Interpretation of Results

To interpret the hydration data two models are considered, one for bulk oxide profiles, one for the surface spike.

In bulk oxide, hydration is characterized by fast in- and outdiffusion, exponential profiles, low activation energy, and anomalous peaking for "gentle" hydrations (as in Fig. 4, 50° and 100°C). It is possible that extrapolation from high temperature data underestimates the diffusion coefficient. This would explain "fast" penetration. However, it would not explain the anomalous peaking, nor the fact that the profile does not have the expected error-function shape.

A model in which the oxide is assumed to contain a network of micropores could explain the observations. A "network of micropores" as used here does not mean actual pinholes through the oxide. Rather it means an interconnected network of small (probably a few atom diameters) disturbed regions which have a somewhat higher diffusivity than the bulk oxide. Such a model for oxide structure has been previously suggested (12).

We considered diffusion in such a micropored structure to be analogous to grain boundary diffusion and applied Fisher's (19) diffusion model to the hydration data. In Fisher's treatment, the diffusant is considered to penetrate very quickly along the high diffusivity path and then to side-diffuse. The model predicts exponential profiles, as observed, and appears consistent with the fast diffusion, low activation energy, and even the anomalous peaking which was observed.

Such a high diffusivity path would, of course, show up most strongly at low temperatures where bulk diffusion is slow. At high temperatures, such as in steam oxidations, bulk diffusion would be expected to dominate, as has been observed (3, 4, 17).

Several explanations were considered for the surface spike. We first thought that the spike represented a second, slower-diffusing hydrogen species. However, the shape of the spike and the change in amplitude with no penetration change were not consistent with this interpretation.

Surface rate limitation would give the observed behavior of the spike for indiffusions. However, it could not explain reformation of the spike from a flat profile in outdiffusion.

The remaining possibility was enhanced solubility in the surface region, either electrically or chemically caused. Electrical binding was rejected since no evidence was found of charge associated with the "water."

In keeping with the micropore model, it was considered possible that the surface region had a higher pore density and therefore retained more water than the bulk oxide. However, to explain the experiments in which the oxide surface was etched before in- and outdiffusion, it would be necessary to assume that the heavily pored region reformed in hours at 200°C.

The model which we favor has recently been described in papers on near-surface effects in metal-metal diffusions (20, 21) and is referred to as the Gibbs effect. In a diffusion system such as water-silica, where the reaction between the diffusant and the host matrix is exothermic, segregation of the diffusant near the surface of the host matrix leads to lowering of surface free energy. Thus, water segregates near the surface of the oxide simply because this lowers the energy of the system. The penetration of the spike in our profiles (a few hundred angstroms) is in good agreement with the penetration in the profiles shown in ref. (21).

With this model it would be expected that surface concentration would rise with bulk concentration, as observed. The constant penetration and the shape of the spike are reasonable. The reformation of the spike in outdiffusion would be expected.

Sodium-Water Interactions

Sodium chloride was diffused wet and dry as previously described, and sodium distributions and their electrical effects were measured. Although the diffusion length was orders greater than the oxide thickness (11) for dry diffusions at 600°C, profiles were steeply falling and diffusion time (1 to 60 min) had little effect on the profile. It appeared that the sodium was being preferentially segregated in the surface region of the oxide. This segregation could possibly be explained again by the Gibbs effect (20, 21). An alternative explanation, given by Fowkes and Burgess (18), is a surface layer of negative oxide ions which attract the sodium ions and bind them near the surface.

In wet diffusions the profile showed a definite development with time, *i.e.*, a filling and flattening with increasing time. Furthermore, profiles for wet diffusions peaked at the silicon, which has been associated with image charge in the silicon (22). Profiles for 1 hr wet and dry diffusions are shown in Fig. 7. In addition to the other differences noted between wet and dry diffusions, the water had the effect of significantly increasing the quantity of sodium transported. Such an effect has been previously noted (13).

Electrically, a definite sodium-water interaction is also seen. Charge production in the silicon is shown in Fig. 8 as a function of diffusion time. In dry diffusions at 600°C charge buildup was slow as expected from the sodium profiles. At 800°C charge buildup also behaved as expected [the decrease for long diffusion times has been attributed to anion compensation (23)].

Charge buildup in the wet diffusions, however, was very rapid. This is expected from the larger amount of sodium transported in the wet diffusions. However,

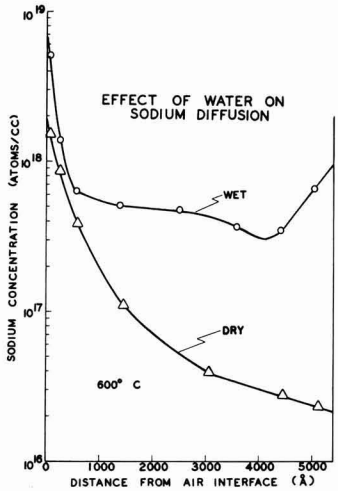

Fig. 7. Comparison of sodium profiles for 1-hr wet and dry diffusions of $Na^{22}Cl$ at 600°C.

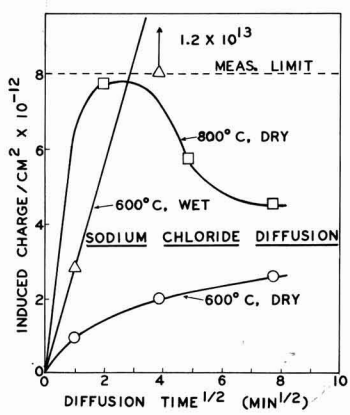

Fig. 8. Variation of MOS-measured charge with diffusion time for NaCl. Wet diffusions at 800°C gave charge beyond measurement limit for all diffusion times.

the larger sodium transport alone does not appear sufficient to explain the magnitude of charge production. The same amount of sodium can easily be transported in a dry diffusion (by increasing diffusion temperature, for example) as was transported in these wet diffusions without producing as large a charge (22). This implies that water enhances the charge production of sodium. The mechanism of such enhancement has not been ascertained.

It was noted in the wet diffusions that the sample coverplates were oxidized several times faster where they were in contact with the contaminated samples than they were on areas remote from the contamination (the covers were larger than the samples). Since the water in the wet nitrogen ambient was necessarily the oxidant, this observation implied that sodium also enhanced the transport of water into the oxide. Such sodium-enhanced oxidation has been previously observed (12) and could possibly be explained by Charles' (14) proposed mechanism for the sodium-enhanced corrosion of silica.

The hypothesis that sodium enhanced the water transport was directly checked in a 200°C hydration. Sodium-contaminated and uncontaminated samples were hydrated together and sectioned. The profiles are shown in Fig. 9. The sodium level in the contaminated

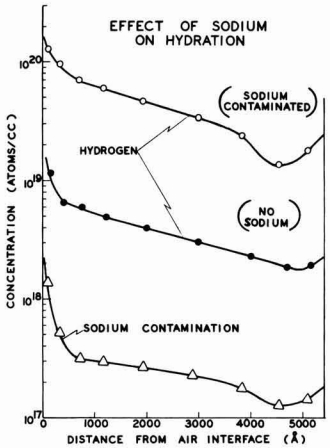

Fig. 9. Effect of sodium contamination on hydration at 200°C. Lowest profile represents sodium contamination in contaminated samples. Other profiles are hydration profiles in uncontaminated and contaminated samples, respectively.

oxides was rather low, a few times normal residual levels. However, this small amount of sodium was sufficient to increase "water" transport by roughly an order of magnitude as shown by the hydrogen profiles for contaminated and for uncontaminated oxides.

Electrically, however, water still appeared to have no effect at 200°C, even in a sodium-contaminated oxide. Room-temperature flatband voltage and interface state density were measured on samples after sodium diffusion. Hydration of these samples had no measurable effect on interface state density and gave the same slight positive shift of room-temperature flatband voltage as noted in hydration of clean oxides.

Summary

1. At "device" temperatures (200°C) hydration of a thermal oxide appears to occur via micropores; this may help to elucidate the structure of the oxide.

2. The diffusing species is not known, but water molecules separate into two independently diffusing fragments on entering the oxide.

3. Peaking of hydrogen in the surface region of the oxide is characteristic of the water-silica system and is explained by the Gibbs effect (surface energy lowering).

4. Water enhances sodium transport and positive charge production at moderate temperatures (600°-800°C).

5. Sodium enhances water transport at "device" temperatures (200°C).

6. At the device temperatures of interest in this study, diffused water has negligible effect on silicon surface potential or on interface-state density.

Acknowledgments

This work was supported by Grant NGR 36-003-067, NASA Electronics Research Center, Cambridge, Massachusetts. We gratefully acknowledge the contributions of Professors A. H. Heuer and E. T. Yon, as well as those of C. J. Slabinski, H. P. Caban-Zeda, and J. Hoel in experimental assistance and helpful advice. This paper was submitted by one of us (G.L.H.) in partial fulfillment of requirements for the Ph.D. degree in Engineering to Case Western Reserve University.

Manuscript submitted June 27, 1969; revised manuscript received Jan. 5, 1970. This was Paper 113 presented at the New York Meeting of the Society, May 4-9, 1969.

Any discussion of this paper will appear in a Discussion Section to be published in the December 1970 JOURNAL.

REFERENCES

1. A. J. Moulson and J. P. Roberts, *Trans. Faraday Soc.*, **57**, 1208 (1961).
2. T. Drury and J. P. Roberts, *Phys. Chem. Glasses*, **4**, 79 (1963).
3. P. J. Burkhardt, *This Journal*, **114**, 196 (1967).
4. T. E. Burgess and F. M. Fowkes, *ibid.*, **113**, 63C (1965).
5. S. R. Hofstein, *I.E.E.E. Trans. Electron Devices*, **ED-14**, 749 (1967).
6. A. B. Kuper and E. H. Nicollian, *This Journal*, **112**, 528 (1965).
7. S. R. Hofstein, *I.E.E.E. Trans. Electron Devices*, **ED-13**, 222 (1966).
8. E. H. Nicollian and A. Goetzberger, *Appl. Phys. Letters*, **7**, 216 (1965).
9. E. Kooi, *Philips Res. Rept.*, **21**, 477 (1966).
10. D. M. Brown and P. V. Gray, *This Journal*, **115**, 760 (1968).
11. A. E. Owen and R. W. Douglas, *J. Soc. Glass Tech.*, **43**, 159 (1959).
12. A. G. Revesz and K. H. Zaininger, *R. C. A. Rev.*, **29**, 22 (Mar. 1968).
13. T. E. Burgess *et al.*, *This Journal*, **116**, 1005 (1969).
14. R. J. Charles, *J. Appl. Phys.*, **29**, 1549 (1958).
15. P. V. Gray and D. M. Brown, *Appl. Phys. Letters*, **8**, 31 (1966).
16. V. A. Pliskin, *IBM J. Res. Develop.*, **10**, 198 (1966).
17. B. E. Deal and A. S. Grove, *J. Appl. Phys.*, **36**, 3770 (1965).
18. F. M. Fowkes and T. E. Burgess, *Surface Sci.*, **13**, 184 (1969).
19. J. C. Fisher, *J. Appl. Phys.*, **22**, 74 (1951).
20. T. S. Lundy and R. A. Padgett, *Trans. Met. Soc. AIME*, **242**, 1897 (1968).
21. A. J. Mortlock, *ibid.*, **242**, 1963 (1968).
22. E. Yon, W. H. Ko, and A. B. Kuper, *I.E.E.E. Trans. Electron Devices*, **ED-13**, 276 (1966).
23. A. B. Kuper, C. J. Slabinski, and E. T. Yon, *Phys. Failure Electron.*, **5**, 232 (RADC 1967); also A. B. Kuper, *Surface Sci.*, **13**, 172 (1969).

Epitaxial GaAs Kinetic Studies: {001} Orientation

Don W. Shaw*

Texas Instruments, Incorporated, Dallas, Texas

ABSTRACT

Gallium arsenide deposition rate studies were conducted with an open tube, chloride transport system which permitted independent control of the reactant input partial pressures. A recording microbalance was adapted to the deposition apparatus so that the epitaxial growth rates could be continuously measured during the actual deposition process. At low temperatures and high reactant partial pressures the process appears to be kinetically controlled. The rate then becomes inversely proportional to the gallium monochloride partial pressure and may indicate the presence of a competitive adsorption process. At high temperatures and low partial pressures the rates may be described in terms of a "quasi-equilibrium" model where a fraction of the incoming gas stream equilibrates with the condensed phase.

Studies of the influence of substrate temperature on GaAs epitaxial growth rates in the $Ga/HCl/As/H_2$ system have indicated that at low temperatures the process operates under kinetic control (1). Under such conditions the growth rate is independent of the total gas flow rate but is strongly dependent on the crystallographic orientation of the substrate. In addition the rate increases rapidly with increasing substrate temperature contrary to the behavior predicted from thermodynamic considerations. The epitaxial growth rates as well as the electrical characteristics of the deposits are also known to be significantly influenced by the composition of the vapor from which the layers are grown (2, 3). These facts indicate the utility of a detailed investigation of the influence of the gas phase composition on the kinetics of GaAs epitaxial growth.

Kinetic studies in gas flow systems are often limited by lack of precision of the rate data. Usually the studies are conducted by deposition for a fixed time period with subsequent measurement of the layer thickness. Although this approach is straightforward, it is time consuming and relatively imprecise. Implicit in its use is the assumption that the deposition rate is constant over the time interval used for deposition of the layer. An effort was made in the present investigation to eliminate these problems by use of an apparatus which permitted continuous measurement of the epitaxial growth rate as the layer was being deposited. This consisted of a recording microbalance adapted to the epitaxial deposition system. By suspension of the substrate crystal from one arm of the microbalance, the weight of the crystal was continuously measured. The details of this approach are described in the following section.

Experimental

Under proper conditions the growth of GaAs from a $GaCl/As_4/HCl/H_2$ ambient is a surface catalyzed process (1). This is a critical requirement to the study of epitaxial growth kinetics since it permits growth on the substrate only. Extraneous growth on the tube walls or the substrate holder would greatly complicate the results due to depletion of the gas stream of reactants. Obviously, if the epitaxial growth rate is to be obtained by continuous gravimetric measurements of the crystal, extraneous growth on the specimen hangdown and support must be eliminated. The GaAs system to be described meets these requirements, particularly if a small excess of HCl is added to the reactant gas phase (1).

The experimental apparatus is illustrated in Fig. 1. It consists principally of two parts: a microbalance, from one arm of which the specimen is suspended, and the fused silica reactor assembly. The microbalance is a Cahn RG Electrobalance (Cahn Instrument Company, Paramount, California) which uses the null balance principle. As the specimen weight changes, the deflection of the beam from its equilibrium point is detected. Attached to this beam is a coil positioned in a magnetic field. As the beam is deflected, a current is applied to the coil which restores the beam to the equilibrium position. From the measured current the specimen weight is obtained. Ideally, the balance is sensitive to 0.1 μg with a maximum capacity of 1g. As the specimen weight changes, it does not move vertically within the reaction apparatus. Consequently the length of the flat profile region of the furnace is minimized. The temperature variation over the length of the substrate crystal was found to be $< 2°C$. Both the weight and growth or etch rates are continuously measured. The latter data are obtained by electronically differentiating the balance output with time using a Cahn Mark II Time Derivative Computer. Usually the rate was displayed on one channel of a dual pen recorder, while the variable under study (temperature, partial pressure, etc.) was displaced simultaneously on the other channel. The noise level for both the rate and the weight outputs was minimized by electronic filtering.

The materials employed in construction of the balance mechanism are not inert to the corrosive gases used in deposition. Consequently, it was necessary to protect the balance by use of a hydrogen counterflow. This flow entered the center arm of the balance chamber, passed over the balance mechanism, and then flowed downward. The protective hydrogen flow rate

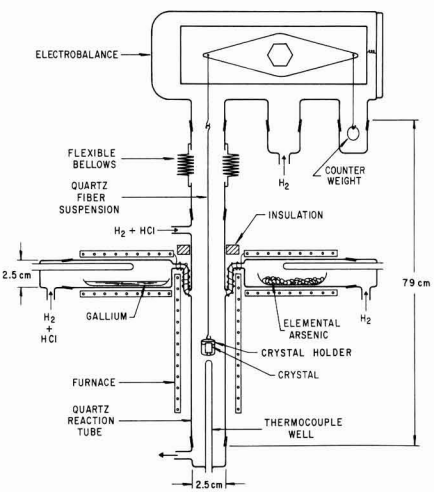

Fig. 1. Diagram of experimental apparatus

* Electrochemical Society Active Member.

amounted to one half of the total flow rate passing over the specimen. Coupling of the balance chamber to the actual epitaxial apparatus was achieved with a flexible Teflon bellows attached to the standard taper joints with heat shrinkable tubing. Initially a fused silica tube was used in the coupling, but mating of fused silica tapers between the balance chamber, deposition apparatus, and the coupling tube required very precise axial alignment. The use of a flexible Teflon bellows eliminated this problem.

Specimen removal and replacement was accomplished by movement of the balance chamber while the deposition apparatus was held in a fixed position. In this case the balance chamber was mounted on a rack and pinion device which permitted vertical movement. In addition, the balance chamber and mount could be translated in the horizontal direction. In order to change samples, the balance was moved upward, thus detaching it from the coupling tube. The hangdown fibers were unhooked at the opening and the balance then shifted horizontally. Finally, the lower hangdown fiber was extracted together with the specimen. The reverse procedure was followed in loading a new specimen.

Gaseous gallium monochloride and arsenic were the reactants. As mentioned earlier, some hydrogen chloride was added to retard nucleation and growth of extraneous material on the specimen hangdown or the tube walls. Gallium monochloride is formed by reaction of HCl with liquid gallium at 925°C. Earlier experiments (1) showed that the reaction goes essentially to completion at temperatures as low as 900°C. Thus the gallium monochloride input partial pressure was calculated from the total flow rate, the H_2-HCl flow rate over the gallium source, and the HCl partial pressure in the latter flow. Experimentally the gallium monochloride partial pressure was varied by changing the HCl partial pressure in the gas stream passing over the gallium source. This HCl partial pressure as well as that entering the tube as free HCl were continuously monitored with thermistor type thermal conductivity cells. Pure H_2 flowed through the reference sides of these cells. The arsenic input was obtained by passing hydrogen over elemental arsenic. The arsenic partial pressure was empirically determined from independent measurements of arsenic weight loss as a function of temperature. The same carrier gas flow rate over the arsenic source was used for all experiments, and the arsenic partial pressure was varied by changing the arsenic source temperature. All temperatures were monitored with thermocouples inside fused silica tubes. The thermocouple measuring the substrate temperature extended to just below the suspended substrate. Furnace profiles permitted determination of the actual substrate temperature from the thermocouple reading. Kanthal wound resistance furnaces were used throughout. Since gallium monochloride is unstable at low temperatures, it was necessary to prevent the gas temperature from falling below the substrate temperature between the gallium source and the substrate. Failure to do so would result in premature disproportionation of GaCl. This was prevented by heating the GaCl inlet tube with resistance wire wound as shown in Fig. 1.

The flow rates measured at room temperature were as follows:

Protective H_2 flow through balance chamber	300 ml/min
H_2-HCl flow over Ga source	100 ml/min
H_2-HCl flow—free HCl input	100 ml/min
H_2 flow over arsenic source	100 ml/min

Since the GaAs epitaxial growth rate is often dependent on the substrate orientation, under the experimental conditions it was necessary to expose essentially only one surface orientation to growth. For the {001} orientation used in this study this was achieved by using very thin specimens polished on both sides. Typical substrate dimensions were 1 × 1 × 0.02 cm. The slices were cleaved into squares, which exposed very smooth {110} sides. This resulted in 96% of the geometrical surface area being the {001} orientation while the remainder was {110} [which is typically a slower growing orientation (4)]. The samples were supported in a sample basket constructed of fused silica fibers. This was suspended from the balance by a fused silica hangdown fiber 125 μm in diameter. Usually, the sensitivity of the apparatus was determined by the noise level, which resulted from mechanical vibrations, thermal effects, or the aerodynamic drag (5) exerted on the specimen and the hangdown by the flowing gas. The latter is very significant, although not so severe as to prevent successful results. A change in the total flow rate results in an immediate change in the zero position of the balance. However, if the flow is held constant the drag is constant and the new zero position remains stable. For epitaxial kinetic studies a precise determination of the actual weight is unnecessary. Only the rate of change is important; thus zero shifts due to the gas flow effects are of little significance since they do not result in long term drifts. Under typical experimental conditions a change in rate of 0.005 mg/min may be detected. For a 2 cm^2 GaAs specimen, this corresponds to a change in rate of 0.275 μm/hr, which exceeds the sensitivity of the usual rate determination methods in open flow systems.

The rate-partial pressure experiments were conducted in such a manner as to gain simultaneously information concerning the sensitivity of the growth rate to temperature and reactant partial pressure. This was accomplished by very slowly cooling the substrate at a fixed gas phase composition. The deposition rate, as determined from the balance output, was plotted on one axis of an x-y recorder, while the output of the substrate thermocouple was measured on the other. This, in effect, yielded a rate-temperature plot for a given gas composition. The partial pressure of one of the reactants would then be changed and the experiment repeated. This would be continued until the rate-temperature curves were obtained for a range of reactant partial pressures. Isothermal sections from these curves yielded the rate-partial pressure curves for any desired temperature in the experimental range studied. Usually the previous deposit was removed by *in situ* etching between cycles so that each cycle represented growth on a similar surface. Since the weight gain during a temperature cycle represented the deposit thickness, the amount necessary for removal by etching between cycles was always known. After etching, at the beginning of each new cycle, an isothermal, steady-state growth rate was established before cooling to minimize effects of variations in the initial growth rates due to the freshly vapor etched surface.

Results

Figure 2, which was constructed from x-y plots of rate *vs.* thermocouple reading, summarizes the influence of deposition temperature on the {001} growth rate. Several curves are illustrated, each representing a different arsenic partial pressure. Constant values of the GaCl and HCl partial pressures were maintained for all runs. In general shape, the curves agree with the preliminary results reported in ref. (1), which were obtained by a set of fixed time depositions at various temperatures. Previous evidence (1) identifies the low-temperature regions, where the rate increases with increasing temperature, as kinetically or surface limited regions. Here the rate is limited principally by a relatively slow surface step which might be an adsorption or desorption process or an actual surface reaction. At higher temperatures each curve passes through a maximum, beyond which the rate begins to decrease with further increases in temperature. Figure 2 shows that the actual value of the temperature, T_{max}, where the maximum rate is observed, is a function of the arsenic partial pressure.

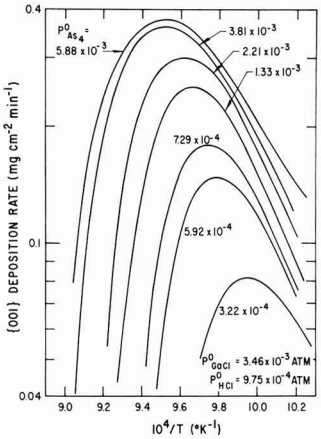

Fig. 2. Growth rate as a function of reciprocal temperature at several arsenic input partial pressures in atmospheres.

A similar set of rate *vs.* $1/T$ curves at various gallium monochloride partial pressures is given in Fig. 3. For these experiments the arsenic and hydrogen chloride partial pressures were held constant. Again the same basic curve shape is observed. As in Fig. 2, the value of T_{max} is a function of the gas phase composition. Apparent activation energies measured in the kinetic regions exhibit good agreement among the various runs and yield an average value of 48.7 ± 3.5 kcal/mole. No dependence of the activation energy on gas phase composition was evident.

If the deposition temperature is continually reduced, a point is ultimately reached at which the growth rate actually passes through a minimum. Additional temperature reductions result in an apparently increasing growth rate. Termination of the experiment after the temperature had been reduced below the minimum and examination of the crystal and its support revealed that extraneous GaAs deposits were beginning to form on the fused silica crystal support and hangdown fiber. Thus the apparent increase in growth rate was the result of the increased surface area and weight which accompanied the nucleation of these extraneous deposits. As the substrate temperature is lowered in the kinetic region, the growth rate decreases, even though the gas phase supersaturation is increasing, due to a reduction in the rate of some activated surface process. This will continue until the supersaturation exceeds the critical value necessary for nucleation on fused silica; then an apparent rate increase would be observed with our technique for rate measurement. The earlier stages of this effect are apparent in Fig. 3 for the curves corresponding to the three highest gallium monochloride partial pressures. Although this particular experiment was not extended so far as to produce an actual minimum in rate, a decrease in slope of the curves is evident at very low temperatures. The decrease occurs at higher temperatures as the gallium monochloride partial pressure is increased since the critical value of gas phase supersaturation is reached at higher temperatures.

Figure 4 illustrates the influence of the arsenic initial partial pressure on the deposition rate at several selected temperatures. At low temperatures the plots are nearly linear (on a log-log scale) with relatively small slopes. At intermediate temperatures the low partial pressure region exhibits an increased slope. This slope becomes characteristic of the entire curve at high temperatures. These plots are actually isothermal sections from Fig. 2. Comparison of Fig. 2 and 4 reveals that the regions where the rate is most sensitive to arsenic partial pressure variations, *i.e.*, at low arsenic partial pressures and high temperatures, correspond to regions of Fig. 2 where the growth rate decreases with increasing temperature. This illustrates the value of obtaining the rate-partial pressure data at several temperatures. Certainly, erroneous conclusions would be obtained if rate-partial pressure variations were interpreted in terms of a kinetic model when at low partial pressures the rate is no longer kinetically limited. For example, only the high partial pressure points of the 754° curve in Fig. 4 actually correspond to the kinetically limited region.

Interesting results are obtained when the growth rate is plotted as a function of the gallium monochloride partial pressure. This is shown in Fig. 5 where the curves for several deposition temperatures are given. It is apparent that, at least at the lower temperatures, the rate passes through a maximum with increasing gallium monochloride partial pressure. As in the preceding case, it is important to identify those portions of these curves which correspond to the kinetically limited region. Again this may be ascertained by comparison with Fig. 3. Although there might be a small region of the ascending portions of the curves in Fig. 4 which represent kinetic control, only the descending regions beyond the maximum definitely correspond to the activated regions in Fig. 3. Although not shown in Fig. 5, the growth rates actually

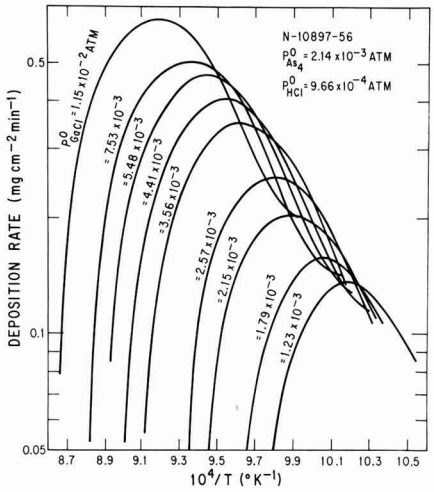

Fig. 3. Growth rate as a function of reciprocal temperature at several gallium monochloride input partial pressures in atmospheres.

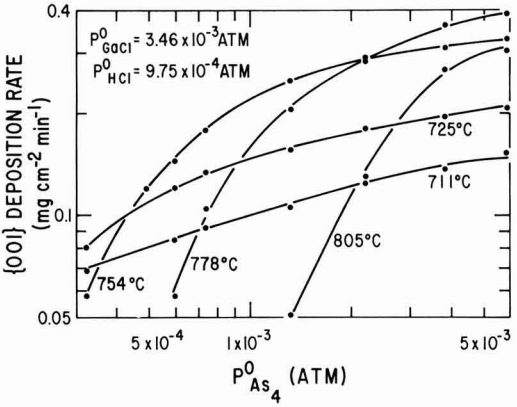

Fig. 4. Growth rate as a function of arsenic input partial pressure for several substrate temperatures.

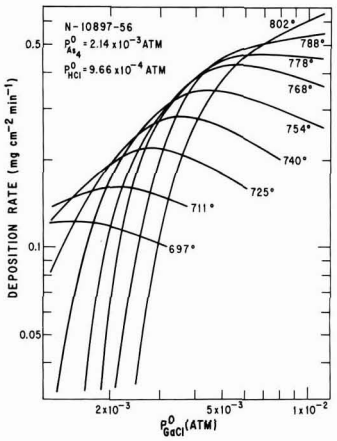

Fig. 5. Growth rate as a function of gallium monochloride input partial pressure for several substrate temperatures.

pass through a minimum at high partial pressures considerably in excess of the value for the rate maximum. This is due to two-dimensional nucleation on the fused silica hangdown fiber which results in extraneous growth as previously mentioned. Since this is independent of the single crystal epitaxial growth, such data will be excluded from the discussion. The results shown in Fig. 4 and 5 correspond only to conditions where growth is confined to the substrate crystal.

In general the results may be summarized in terms of two unique growth regions. The first region, which corresponds to low partial pressures and high temperatures, is characterized by rates which decrease with increasing temperature and increase when the partial pressure of one reactant is increased while holding the other constant. In the second region, the rate increases with increasing temperature and with increasing arsenic partial pressure, but actually decreases when the other reactant, gallium monochloride, is increased.

Discussion

As previously stated, the low-temperature region where the rate increases with increasing temperature is believed to represent a region where the process operates under kinetic control. This interpretation is supported by the following evidence: (*i*) The deposition rate exhibits a strong orientation dependence (4). (*ii*) An exponential temperature dependence is observed which is contrary to that predicted from equilibrium considerations (1). (*iii*) The rate is independent of the total gas flow rate (1). Having now established the influence of reactant partial pressures on the growth rate in this kinetically controlled region, it is of interest to examine the possibilities of extracting information concerning the nature of the slow surface process. The process might be adsorption of either reactant species, some surface reaction between adsorbed species, or desorption of the products.

The inverse dependence of the rate on the gallium monochloride partial pressure may indicate a competitive adsorption process whereby GaCl competes with arsenic for adsorption sites. Consider, for example, that As_4 is in gas phase equilibrium with As_2 which in turn is adsorbed dissociatively on the {001} surface. If GaCl should compete for these sites, perhaps by attraction of the Cl portion of the molecule to the surface, the amount of surface available for arsenic adsorption would be reduced. By assuming a Langmuir type adsorption process, the fraction of the surface covered by arsenic atoms could be expressed by the following equation

$$\theta_{As} = \frac{\beta_{As_2}{}^{1/2} P_{As_2}{}^{1/2}}{(1 + \beta_{As_2}{}^{1/2} P_{As_2}{}^{1/2} + \beta_{GaCl} P_{GaCl})} \quad [1]$$

where β_{As_2} and β_{GaCl} represent the Langmuir adsorption coefficients for the subscripted species. If the rate-limiting process involves a reaction of adsorbed arsenic atoms, then the rate may significantly begin to decrease with increasing gallium monochloride partial pressures when

$$\beta_{GaCl} P_{GaCl} > 1 + \beta_{As_2}{}^{1/2} P_{As_2}{}^{1/2} \quad [2]$$

Actually, several different rate-limiting surface processes may be imagined which involve adsorbed arsenic atoms. General rate expressions were derived for many of these processes in an attempt to describe the actual growth mechanism in the kinetic region. However, the resulting equations all involve several undetermined constants. Although many of the rate expressions appear to agree with the experimental results, the undetermined constants precluded identification of which if any of the mechanisms was the most valid. Consequently, one cannot determine the true nature of the rate-limiting process in the region of kinetic control. However, a competitive adsorption process between arsenic and gallium monochloride for the arsenic adsorption sites can qualitatively account for the experimental observations.

The high temperature-low partial pressure regions where the rate exhibits a negative temperature dependence could be due to an activated etching process which becomes significant at higher temperatures. However, this is unlikely since earlier results (1) indicated that the orientation dependence diminishes markedly in this region. Another possibility is that, at high temperatures or low partial pressures, the entire gas stream approaches equilibrium with the condensed phase. In order to investigate this possibility, equilibrium calculations were carried out for conditions which corresponded to our experiments. In these calculations, the composition of a mixture was determined which represented the minimum free energy of the system subject to the mass balance constraints. Thermodynamic values employed in the calculations were taken from Day's (6) compilation. However, comparison of the experimental rates described earlier with the calculated values revealed a large discrepancy. Yet when the two results were plotted, the curve shapes were very similar, particularly in the regions of high temperatures and low reactant partial pressures.

Sedgwick (7) described a method for treating silicon epitaxial deposition in which a "quasi-equilibrium" is assumed. In this case, only a fraction of the incoming gas stream equilibrates with the condensed phase, while the remainder passes by unreacted. Silvestri (8) has successfully applied this approach to germanium deposition from $GeCl_4$ and H_2. Actually the quasi-equilibrium approach is very similar to models which assume diffusion control, where all diffusing species have the same diffusion coefficients and the rate is determined by the difference between the bulk stream partial pressure of a given species and its equilibrium value at the crystal surface.

According to Sedgwick, the deposition rate for a process operating in the quasi-equilibrium mode may be expressed as

$$D = J \cdot \alpha \cdot \beta \quad [3]$$

where J is the flux of the species being deposited, α is a theoretical efficiency factor which represents the fraction of the flux which would be deposited if complete equilibrium were achieved between the entire gas stream and the substrate, and β is the fraction of the incoming gas stream which actually equilibrates with the condensed substrate. For the case where the entire gas stream equilibrates with the condensed phase, β is unity. However, for the quasi-equilibrium case, β is less than unity and is a highly geometry dependent factor.

Calculations of the factor $J \cdot \alpha$ were made for portions of the data shown in Fig. 2 through 5. The factor β was then estimated by assuming that the quasi-equilibrium approach was valid at 740°C and the lowest gallium monochloride partial pressure (1.23×10^{-3} atm) shown in Fig. 5. A value of $\beta = 0.093$ was obtained. This value was assumed to remain constant for all the experimental conditions described since the same geometry and linear gas stream velocity were used throughout the study. It should be noted that β should be only weakly dependent on temperature. Using the above mentioned value of β, theoretical curves for the dependence of the deposition rate on the arsenic and gallium monochloride initial partial pressures were determined. These curves, together with points representing the experimental results, are shown in Fig. 6 and 7. The same value of β was used in construction of the curves for both figures.

Very poor agreement between the theoretical and experimental values is obtained at low temperatures, but, as the deposition temperature is increased, the agreement becomes better. Very good agreement is obtained at 768°C at the lower partial pressure values. Comparison of Fig. 6 and 7 with Fig. 2 and 4 reveals that deviations between the experimental and calculated values become significant when the data falls in the activated regions or where the process begins to operate under kinetic control. However, in the high temperature-low partial pressure regions good agreement is apparent, indicating that the quasi-equilibrium model is applicable in the region. The value of $\beta = 0.093$ for the GaAs system may be compared with a value of 0.3 obtained for Ge deposition (8) and the range of values from 0.03 to 0.30 for Si deposition (7).

In summary, with the present system, GaAs can be deposited epitaxially under two unique regimes depending on the temperature and reactant partial pressures. At low temperatures and high reactant partial pressures the GaAs deposition rate is limited by some surface process. The rate is then inversely dependent on the gallium monochloride partial pressure and may indicate a competitive adsorption process between gallium monochloride and arsenic. With lower partial pressures and high deposition temperatures, the rate behavior agrees well with a quasi-equilibrium model.

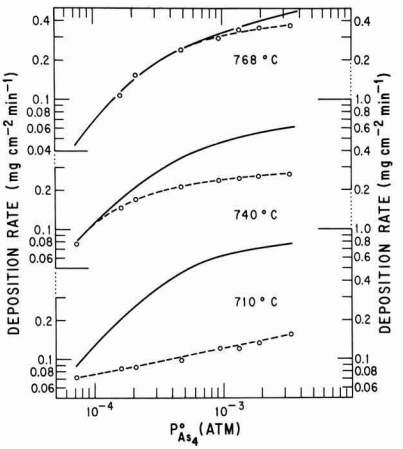

Fig. 6. Theoretical curves of rate as a function of arsenic input partial pressure. Open circles represent experimental data. Ordinate scales on each side of the figure correspond to 710°, 740°, and 768° in ascending order.

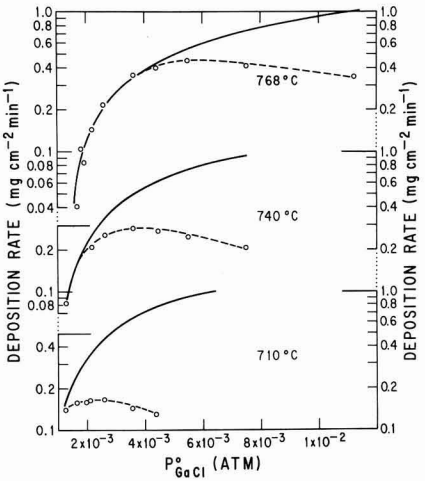

Fig. 7. Theoretical curves of rate as a function of gallium monochloride input partial pressure. Open circles represent experimental data. Ordinate scales on each side of the figure correspond to 710°, 740°, and 768° in ascending order.

These two types of deposition should be accompanied by differences in surface morphologies and electrical characteristics. For example, Silvestri (8) has observed that smooth surfaces are obtained when Ge is deposited under conditions corresponding to the quasi-equilibrium case, while structured surfaces predominate when surface limitations are significant. Differences in the electrical characteristics may also be observed since growth in the high temperature region occurs under conditions which more closely approach equilibrium than in the low temperature kinetically controlled region. Such differences will be the subject of future studies.

Acknowledgments

Appreciation is expressed to Miss Carolyn Banks for her assistance with the experimental work. In addition, the author wishes to thank Drs. L. G. Bailey and B. G. Secrest for their interest and several stimulating discussions.

Manuscript submitted Oct. 27, 1968; revised manuscript received Jan. 27, 1970. This was Paper 172 presented in part at the Detroit Meeting of the Society, Oct. 5-9, 1969.

Any discussion of this paper will appear in a Discussion Section to be published in the December 1970 JOURNAL.

REFERENCES

1. D. W. Shaw, *This Journal*, **115**, 405 (1968).
2. R. E. Ewing and P. E. Greene, *ibid.*, **111**, 1266 (1964).
3. D. W. Shaw, R. W. Conrad, E. W. Mehal, and O. W. Wilson, 1966 Inter. Symp. on GaAs, Inst. of Physics and the Physical Society Conf. Series No. 3, 10-15.
4. D. W. Shaw, 1968 Inter. Symp. on GaAs, Inst. of Physics and the Physical Society Conf. Series No. 6, 50-54.
5. L. Cahn and H. Schultz, *Anal. Chem.*, **35**, 1729 (1963).
6. G. F. Day, "Heterojunction Device Concepts" prepared for Air Force Avionics Laboratory, Contract AF 33(615)1988, Varian Associates, September 1966.
7. T. O. Sedgwick, *This Journal*, **111**, 1381 (1964).
8. V. J. Silvestri, *ibid.*, **116**, 81 (1969).

The Theory of Anomalous Diffusion in Solids Near Diffusant Saturation Concentrations: Example–Phosphorus in Silicon

P. E. Bakeman, Jr.

Rensselaer Research Corporation, Troy, New York

and J. M. Borrego

Electrophysics Division, Rensselaer Polytechnic Institute, Troy, New York

ABSTRACT

This paper presents a diffusion theory for the diffusion of impurities which exhibit solid solubility saturation. The theory is based on a simple assumption for impurity atom interaction which yields a self-consistent result for the diffusion constant and chemical potential of the impurity. The theory predicts the diffusion constant of the diffusing species to be: $D' = D(C_{max} + C)/(C_{max} - C)$, where D is the low level diffusion constant, C is the impurity concentration, and C_{max} is the saturation impurity concentration. The theory is compared with available experimental data on the diffusion of phosphorus in silicon. The theory and experiment are in excellent agreement.

It is the purpose of this paper to advance a theory of diffusion which is capable of explaining the anomalous diffusion behavior observed in the diffusion of impurities which exhibit solid solubility saturation, such as phosphorus diffusing in silicon. The assumption is made that atoms of the diffusing species do interact with each other during diffusion as opposed to the assumption that they move independently, which is implicit in deriving Fick's first law. The rationale for the atomic interaction assumption is presented and the assumed interaction is expressed both phenomenologically and as a term in the chemical potential equation.

A recent communication (1) evaluates the effect of ambipolar or field aided diffusion of impurities in silicon and concludes that this effect is insufficient to cause experimentally observed diffusion anomalies. In fact, it can be shown that ambipolar diffusion effects can account for a maximum increase in D, the impurity diffusion constant, by a factor of 2 in semiconductors if Maxwell-Boltzmann statistics are used (2). In the degenerate case, Shockley (3) has evaluated the ambipolar diffusion effect using Fermi statistics and derived the relation

$$\frac{D^*}{D} = 1 + \left(\frac{\pi}{6}\right)^{1/3}\left(\frac{N_d}{N_c}\right)^{2/3} \qquad [1]$$

This correction still cannot explain the experimentally observed diffusion phenomena.

Theory

Let us derive a one dimensional expression for the impurity atom flux density as a function of concentration and concentration gradient. In the classical derivation, which yields Fick's first law, the following assumptions are made (4).

1. The impurity atoms move in discrete jumps (length $= \alpha$) with a jump frequency Γ (jumps/sec) which is a function of neither concentration nor concentration gradient.
2. Each impurity atom moves at random independent of other diffusing impurity atoms.

The second assumption indicates that there is an equal probability of an impurity atom, at plane x, jumping in the $+x$ and $-x$ directions on any given jump. Thus, the probability, $P(+, x)$, that it jumps in the $+x$ direction is 1/2 and, similarly, the probability, $P(-, x)$, that it jumps in the $-x$ direction is 1/2. By definition

$$P(+, x) + P(-, x) = 1 \qquad [2]$$

These assumptions yield the result that (4)

$$D = 1/2\ \Gamma\alpha^2 \qquad [3]$$

Let us change assumption 2 to account for impurity atom interaction as follows:

2'. Each impurity atom moves at random to available sites within the host material. Also assume that the total concentration of impurity cannot exceed C_{max}.

The effect of the new assumption is to change the values of $P(+, x)$ and $P(-, x)$ so that they are no longer equal, but their sum is still unity.

The probabilities $P(+, x)$ and $P(-, x)$ are mathematically determined by counting the density of empty sites in planes $x + \alpha$ and $x - \alpha$. Since we have assumed that the impurity atom will diffuse into any empty site with equal probability

$$\frac{P(+, x)}{P(-, x)} = \frac{N_{max} - N\ (x + \alpha)}{N_{max} - N\ (x - \alpha)} \qquad [4]$$

where N_{max} = maximum density of impurity in an atomic plane; $N(x)$ = density of impurity atoms in atomic plane at x (number/cm^2); and α = spacing of atomic planes.

Combining Eq. [2] and [4] yields the values of $P(+, x)$ and $P(-, x)$

$$P(+, x) = \frac{N_{max} - N(x + \alpha)}{[N_{max} - N(x + \alpha)] + [N_{max} - N(x - \alpha)]} \qquad [5a]$$

$$P(-, x) = \frac{N_{max} - N(x - \alpha)}{[N_{max} - N(x + \alpha)] + [N_{max} - N(x - \alpha)]} \qquad [5b]$$

Referring to Fig. 1, we calculate the atom flux density $J(x)$ across plane x. The net flux equals the number of impurity atoms flowing from plane $x - \alpha/2$ to plane $x + \alpha/2$ minus those moving from $x + \alpha/2$ to $x - \alpha/2$

$$J = N\left(x - \frac{\alpha}{2}\right) P\left(+, x - \frac{\alpha}{2}\right)\Gamma - N\left(x + \frac{\alpha}{2}\right) P\left(-, x + \frac{\alpha}{2}\right)\Gamma \qquad [6]$$

where Γ = impurity jump frequency.

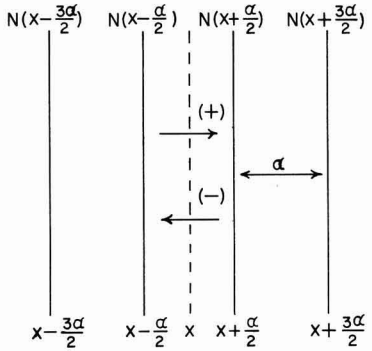

Fig. 1. Atomic flux density across plane x

By transforming the value of x in Eq. [5a] and [5b], we find

$$P\left(+, x-\frac{\alpha}{2}\right) = \frac{N_{max} - N\left(x+\frac{\alpha}{2}\right)}{\left[N_{max} - N\left(x+\frac{\alpha}{2}\right)\right] + \left[N_{max} - N\left(x-\frac{3\alpha}{2}\right)\right]} \quad [7a]$$

$$P\left(-, x+\frac{\alpha}{2}\right) = \frac{N_{max} - N\left(x-\frac{\alpha}{2}\right)}{\left[N_{max} - N\left(x-\frac{\alpha}{2}\right)\right] + \left[N_{max} - N\left(x+\frac{3\alpha}{2}\right)\right]} \quad [7b]$$

The relationship between area concentration, $N(x)$, and volume concentration, $C(x)$ is

$$N(x) = C(x)\,\alpha \quad [8]$$

Combining Eq. [6] through [8] yields

$$J = -1/2\,\Gamma\alpha^2 \frac{dC(x)}{dx} \frac{C_{max}^2 - C(x)^2 + \left(\frac{\alpha}{2}\frac{dC(x)}{dx}\right)^2}{[C_{max} - C(x)]^2 - \left(\frac{\alpha}{2}\frac{dC(x)}{dx}\right)^2} \quad [9]$$

but

$$\frac{\alpha}{2}\frac{dC(x)}{dx} << C_{max} - C(x) \quad [10]$$

therefore

$$J = -\tfrac{1}{2}\Gamma\alpha^2 \frac{dC(x)}{dx}\frac{C_{max} + C(x)}{C_{max} - C(x)} \quad [11]$$

Thus, from Eq. [3] and [11], the effective diffusion constant D', is a function of concentration and equals

$$D' = D\frac{C_{max} + C(x)}{C_{max} - C(x)} \quad [12]$$

where, D = the impurity diffusion constant at low impurity concentrations. Equation [12] shows that the diffusion constant, D', of an impurity in a material is a function of the actual concentration of the impurity relative to its saturation concentration. At low concentrations [$C(x) << C_{max}$] the impurity diffusion constant equals D and is independent of concentration; at high impurity levels Eq. [12] must be used to calculate D' as a function of concentration.

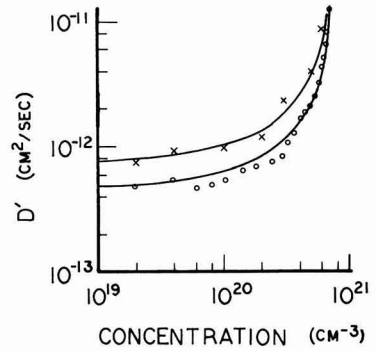

Fig. 2. Diffusion constant, D', of phosphorus in silicon as a function of phosphorus concentration. Data points are experimental measurement of two samples diffused at 1050°C for 30 min each, from Tannenbaum (5). Curves are as calculated from Eq. [12] using $D = 7.4 \times 10^{-13}$ cm²/sec and $C_{max} = 7.4 \times 10^{20}$ cm^{-3} (upper) and $D = 4.8 \times 10^{-13}$ cm²/sec and $C_{max} = 7.7 \times 10^{20}$ cm^{-3} (lower).

It should be noted that Eq. [12] can be derived using the random-walk approach to diffusion theory (7) and the directional jump probabilities presented in Eq. [5a] and [5b].

Discussion

Figure 2 is a graph of effective diffusion constant *vs.* impurity concentration for the diffusion of phosphorus in silicon. The data points were obtained by Tannenbaum (5) from experimental radioactive tracer data of two diffusion runs under identical conditions. The upper and lower curves are calculated from the theory presented herein using values for D of 7.4 and 4.8 x 10^{-13} cm²/sec and for C_{max} of 7.4 and 7.7 x 10^{20} atom/cm³, respectively. It can be seen that the theory and experiment show remarkable agreement. Similar experimental verification can be shown using recent experimental data by Vick and Whittle (6) for the diffusion of boron in silicon.

The chemical potential for an impurity in a solid with the assumption of no impurity atom interaction is

$$\phi = +kT \ln C(x) + \text{constant} \quad [13]$$

It can be shown from Eq. [12] that the chemical potential in the system based on assumption 2′ is

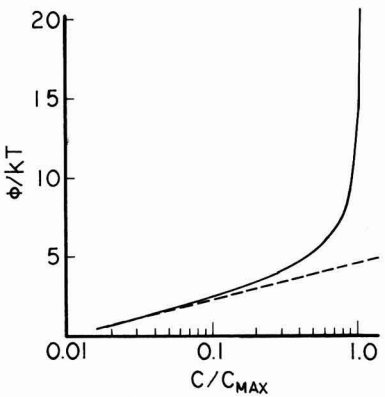

Fig. 3. Graph of chemical potential *vs.* impurity concentration for the two diffusion theories. Dotted line is from Eq. [13]. Solid line, corrected for impurity atom interaction, is from Eq. [14].

$$\phi = +kT \ln \frac{C(x)}{\left[1 - \frac{C(x)}{C_{max}}\right]^2} + \text{constant} \quad [14]$$

These equations are plotted in Fig. 3. The abrupt rise in ϕ' at $C = C_{max}$ is precisely what is required of an impurity for it to exhibit a maximum solid solubility at a concentraton C_{max}.

Acknowledgment

The authors wish to thank Dr. H. B. Huntington for his assistance in reviewing the manuscript.

Manuscript submitted Aug. 29, 1969; revised manuscript received *ca.* Jan. 5, 1970.

Any discussion of this paper will appear in a Discussion Section to be published in the December 1970 JOURNAL.

REFERENCES

1. D. P. Kennedy, *Proc. IEEE (Letters)*, **57**, 1202 (June 1969).
2. F. M. Smits, *Proc. IRE*, **46**, 1049 (1958).
3. W. Shockley, *J. Appl. Phys. (Letters)*, **32**, 1402 (July 1961).
4. P. G. Shewmon, "Diffusion in Solids," pp. 41-42, McGraw-Hill Book Co., New York (1963).
5. E. Tannenbaum, *Solid-State Electron.*, **2**, 123 (1961).
6. G. L. Vick and K. M. Whittle, *This Journal*, **116**, 1142 (1969).
7. J. R. Manning, "Diffusion Kinetics for Atoms In Crystals," D. Van Nostrand Co., Inc. (1968).

New Data on Basic Lead Sulfates

H. W. Billhardt[1]

Mineralogisches Institut der Universität (TH), Karlsruhe, Germany

ABSTRACT

High-temperature x-ray and DTA investigations of the lead oxide-lead sulfate system confirmed the phase relations established by Esdayle and Lander. In order to elucidate discrepancies in the literature and to insure positive identification of the three basic lead sulfates $PbO \cdot PbSO_4$, β-$2PbO \cdot PbSO_4$, and $4PbO \cdot PbSO_4$, single crystals were prepared and investigated by several x-ray techniques. Indexed x-ray powder data, cell parameters, and also IR-absorption spectra are presented. A high-temperature x-ray pattern is given for α-$2PbO \cdot PbSO_4$.

During the investigation of lead silicate sulfate glasses and their crystallization products, the well-known system PbO-SO_3 (1-6) was re-investigated. Discrepancies were found between the x-ray data given in previous papers and those obtained from our own measurements. In order to insure positive identification of all basic lead sulfates, single crystals were prepared and investigated by means of several x-ray techniques. IR-absorption spectra were also recorded.

Pure PbO and $PbSO_4$ were used for the preparation of the basic lead sulfates. The oxides in stoichiometric relation were fused in Pt crucibles, taking into account the loss caused by evaporation. To protect the Pt crucible from reaction with Pb a small amount of NH_4NO_3 was added to the sample in order to get an oxidizing atmosphere [Merker and Wondratschek (7)] and then the batch was heated very slowly. A serious attack of the crucibles by Pb-rich melts was never observed. After each preparation the Pt crucibles were cleaned by a soda-borax melt. The loss of Pt was always less than 1 mg.

In the lead oxide-lead sulfate system, the monobasic, the α- and β-dibasic and the tetrabasic lead sulfate are the only phases which are observed. The phase diagram established by Esdaile (3) and Lander (4) has been confirmed (Fig. 1). It stands in strict contradiction to the newly published paper of Margulis and Kopylov (6). Our repeated DTA-analyses and high-temperature x-ray measurements under different heating and cooling rates, revealed that the diagram given by Margulis and Kopylov is based on systems not in equilibrium and on cooling-curves with retarded crystallization effects and should, therefore, be rejected.

Monobasic Lead Sulfate

Monobasic lead sulfate obtained by slow cooling of a $PbO \cdot PbSO_4$ melt in Pt crucibles was found to be identical with the mineral lanarkite. The crystallographic space group is C2/m and the monoclinic cell parameters tabulated in Table I are in close agreement with the data of lanarkite described by Richmond and Wolfe (8) and Binnie (9). The cell parameters presented in this paper are the result of refinement of the x-ray powder data in Table II (AEG-Guinier camera, $CuK\alpha_1$-radiation, intensities photometrically measured) with the help of a least-squares computer procedure.

Dibasic Lead Sulfate

Dibasic lead sulfate exists in two modifications (3, 10). High-temperature x-ray investigations (Nonius-Guinier camera) revealed that this compound is unstable below about 640°C and decomposes at this temperature to mono- and tetrabasic lead sulfate. This decomposition takes place very slowly. Even at cooling rates of 10°C/hr, α-$2PbO \cdot PbSO_4$ is stable down to 450°C and then it forms metastable β-$2PbO \cdot PbSO_4$.

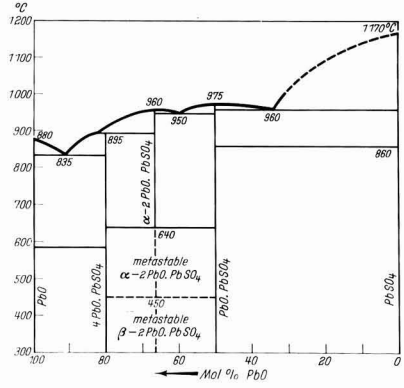

Fig. 1. Lead-oxide sulfate system after Esdaile (3), Lander (4), and the author's measurements.

[1] Present address: Forschungsinstitut der Zementindustrie, Düsseldorf-Nord, Germany.

Table I. Single-crystal data of $PbO \cdot PbSO_4$ and lanarkite

	$PbO \cdot PbSO_4$	Lanarkite	
	Present work	Binnie	Richmond and Wolfe
Probable space group	C2/m	C2/m	C2/m
a in Å	13.753 ± 0.02	13.75 ± 0.04	13.73
b in Å	5.697 ± 0.02	5.68 ± 0.02	5.68
c in Å	7.064 ± 0.02	7.05 ± 0.02	7.07
β in °	115.9 ± 0.2	116.2 ± 0.2	116°13′
V in Å^3	498	494	495
z	4	4	4
ρ calc. in g/cm^3	7.02	7.08	7.07
ρ meas.	7.08 ± 0.1	6.92	

Table II. Indexed x-ray pattern of monobasic lead sulfate

I/I_0	$d_{meas.}$	$d_{comp.}$	h k l	I/I_0	$d_{meas.}$	$d_{comp.}$	h k l
25	6.31	6.36	0 0 1	15	2.228	2.230	$\bar{6}$ 0 2
25	6.14	6.19	2 0 0	4	2.190	2.192	$\bar{4}$ 2 1
20	5.85	5.90	$\bar{2}$ 0 1			2.214	$\bar{2}$ 2 2
10	5.14	5.17	1 1 0	6	2.167	2.169	$\bar{3}$ 1 3
45	4.40	4.43	$\bar{1}$ 1 1	10	2.120	2.121	0 2 2
20	3.69	3.70	1 1 1			2.119	0 0 3
15	3.50	3.51	$\bar{3}$ 1 1	5	2.100	2.100	$\bar{1}$ 1 3
80	3.34	3.34	3 1 0			2.096	4 2 0
20	3.18	3.18	0 0 2	20	2.063	2.062	$\bar{6}$ 0 0
		3.093	$\bar{4}$ 0 0	30	2.048	2.050	$\bar{4}$ 2 2
100	2.957	2.959	$\bar{1}$ 1 2	5	1.967	1.968	$\bar{6}$ 0 3
		2.952	$\bar{4}$ 0 2	5	1.910	1.909	5 1 1
50	2.860	2.863	$\bar{3}$ 1 2	25	1.849	1.850	$\bar{4}$ 0 2
4	2.844	2.848	0 2 0			1.848	2 2 2
7	2.603	2.603	3 1 1	15	1.835	1.835	$\bar{4}$ 2 1
7	2.585	2.587	$\bar{2}$ 2 0	5	1.828	1.832	$\bar{7}$ 1 1
7	2.563	2.566	$\bar{2}$ 2 1	4	1.810	1.809	$\bar{2}$ 2 3
20	2.473	2.474	$\bar{5}$ 1 1	5	1.778	1.777	$\bar{6}$ 2 1
25	2.429	2.429	2 0 2	7	1.760	1.759	$\bar{4}$ 0 4
10	2.400	2.400	$\bar{4}$ 0 1	8	1.757	1.756	$\bar{6}$ 2 2
5	2.354	2.343	$\bar{5}$ 1 2	5	1.749	1.750	6 0 1
8	2.339	2.342	$\bar{2}$ 0 3	20	1.726	1.725	3 3 0
15	2.271	2.270	5 1 0	10	1.682	1.681	$\bar{8}$ 0 1
5	2.254	2.257	2 2 1	15	1.671	1.671	6 2 0

This low-temperature modification has the monoclinic space group $P2_1/m$ or $P2_1$, in agreement with Boivin, Thomas, and Tridot (10), but we could not confirm all the cell parameters given by these authors (a = 7.814Å, b = 5.803Å, c = 8.035Å, β = 102.64°, ρ_{calc} = 6.98 g/cm^3, ρ_{exp} = 7.08 g/cm^3). Our repeated density measurements and x-ray single-crystal investigations led to the following cell parameters: a = 8.06 ± 0.02Å, b = 5.79 ± 0.02Å, c = 7.17_5 ± 0.02Å, and β = 103°C ± 0.02°.

The calculated density is 7.63 g/cm^3, assuming two formula weights per unit cell. This density is close to our experimentally determined density of 7.6 ± 0.05 g/cm^3. The β-2PbO · $PbSO_4$ single crystals are twinned about a twofold [101] rotation axis or a ($10\bar{1}$) twin plane. The angle between a_1^* of the one cell and c_2^* of the other cell is about 8.4 ± 0.3°.

DTA-heating curves and high-temperature x-ray measurements reveal that the metastable β low-temperature modification exists up to about 450°C and then decomposes to mono- and tetrabasic lead sulfate. At or above 640°C, 2PbO · $PbSO_4$ recrystallizes from the two basic lead sulfates, but now in the α-form. It is remarkable that the inflection point at 640°C is not strictly

Table III. X-ray powder diffraction of α-2PbO·$PbSO_4$ at 700°C

I/I_0	d, Å	I/I_0	d, Å
10	7.56	20	2.996
15	6.00	3	2.82
4	4.84	5	2.728
10	4.74	6	2.712
10	4.27	6	2.583
3	3.78	15	2.427
100	3.21	20	2.354
30	3.16	12	2.184
12	3.13	10	2.139
60	3.06	5	2.002

Table IV. Indexed x-ray pattern of β-dibasic lead sulfate

I/I_0	$d_{meas.}$	$d_{comp.}$	h k l
20	7.85	7.86	1 0 0
2	6.99	6.99	0 0 1
10	5.92	5.93	$\bar{1}$ 0 1
7	4.74	4.72	1 0 1
2	4.64	4.66	1 1 0
7	4.46	4.46	0 1 1
5	4.13	4.14	$\bar{1}$ 1 1
7	3.80	3.81	$\bar{2}$ 0 1
10	3.67	3.66	1 1 1
2	3.50	3.50	$\bar{1}$ 0 2
2	3.49	3.495	0 0 2
100	3.25	3.25	2 1 0
2	3.18	3.18	$\bar{2}$ 1 1
75	3.00	2.995	1 1 2
	2.991	2.993	0 1 2
30	2.971	2.963	$\bar{2}$ 0 2
20	2.952	2.957	1 0 2
60	2.894	2.896	0 2 0
10	2.767	2.758	2 1 1
10	2.713	2.717	1 2 0
8	2.631	2.633	1 1 2
7	2.471	2.468	1 2 1
2	2.414	2.414	$\bar{3}$ 1 1
20	2.387	2.386	3 1 0
25	2.375	2.367	$\bar{3}$ 0 2
20	2.357	2.361	2 0 2
25	2.300	2.305	$\bar{2}$ 2 1
4	2.231	2.231	$\bar{1}$ 2 2
		2.230	0 2 2
6	2.206	2.206	$\bar{1}$ 1 3
3	2.199	2.191	$\bar{3}$ 1 2
3	2.184	2.186	2 1 2
3	2.166	2.162	0 1 3
4	2.135	2.129	3 1 1
7	2.123	2.127	2 2 1
25	2.074	2.071	$\bar{2}$ 2 2
20	2.067	2.069	1 2 2
20	1.966	1.964	4 0 0
10	1.899	1.901	$\bar{4}$ 1 1
		1.901	3 0 2

Table V. Indexed x-ray pattern of tetrabasic lead sulfate

I/I_0	$d_{meas.}$	$d_{comp.}$	h k l
15	8.30	8.17	1 1 0
8	7.37	7.31	0 0 1
8	6.21	6.20	0 1 1
7	5.77	5.83	0 2 0
		5.72	2 0 0
7	5.43	5.42	1 1 1
2	5.17	5.14	2 1 0
2	4.47	4.48	$\bar{2}$ 0 1
2	4.26	4.25	$\bar{1}$ 2 1
2	3.48	3.49	0 1 2
3	3.44	3.43	0 3 1
4	3.32	3.32	1 1 2
8	3.28	3.28	1 3 1
100	3.22	3.23	3 1 1
3	3.21	3.21	$\bar{2}$ 3 0
80	3.10	3.10	$\bar{2}$ 0 2
		3.099	0 2 2
80	3.06	3.06	$\bar{2}$ 0 2
5	3.01	3.00	$\bar{1}$ 2 2
3	2.962	2.962	$\bar{2}$ 1 2
3	2.940	2.939	$\bar{3}$ 2 1
3	2.924	2.918	0 4 0
55	2.880	2.862	4 0 0
2	2.838	2.826	1 4 0
3	2.716	2.711	2 2 2
90	2.665	2.664	0 3 2
2	2.646	2.651	4 0 1
8	2.601	2.600	$\bar{1}$ 3 2
		2.598	2 4 0
6	2.572	2.568	4 2 0
5	2.558	2.557	3 1 2
2	2.394	2.391	$\bar{3}$ 2 2
2	2.342	2.343	$\bar{1}$ 1 3
2	2.328	2.330	1 1 3
4	2.319	2.317	3 4 0
2	2.293	2.286	1 5 0
2	2.279	2.280	0 4 2
2	2.262	2.268	$\bar{4}$ 0 2
2	2.257	2.255	$\bar{2}$ 0 3
4	2.241	2.240	$\bar{1}$ 4 2
		2.238	4 0 2
3	2.228	2.227	$\bar{4}$ 1 2
3	2.212	2.213	$\bar{1}$ 2 3
5	2.199	2.198	4 1 2
4	2.189	2.190	4 3 1
2	2.149	2.155	$\bar{5}$ 1 1
4	2.130	2.130	5 2 0
3	2.113	2.115	$\bar{4}$ 2 2
4	2.065	2.066	0 3 3

Table VI. IR-absorption spectra of lead sulfates

SO_4^{2-}	$PbSO_4$	$PbO \cdot PbSO_4$	β-$2PbO \cdot PbSO_4$	$4PbO \cdot PbSO_4$
(Siebert)		311 cm^{-1} st	345-365 cm^{-1}	350 cm^{-1} st (b)
		367 m (b)	387 st	
			397 st	390 sh
		420 st		437 (b)
ν_2: 451 cm^{-1}		454 sh	453 sh	460 m
				471 m
			520 st	
ν_4: 613	595 st	599 st	605 st	600 st
		607 sh (?)	613 st	610 st
				615 sh
ν_1: 981	900-1200 (max. at 1030-1090)	900-1200 (max. at 1066)	955 st	960 m
				1050 st (b)
			1050 st	1100 sh
ν_3: 1104			1146 st	1133 m

reversible at normal cooling rates and may be easily overlooked.

The transformation of α-$2PbO \cdot PbSO_4$ (which is metastable below 640°C) to the β-form occurs even during quenching at 450°C. The high-temperature x-ray data of α-$2PbO \cdot PbSO_4$, recorded in Table III, are similar to those of β-$2PbO \cdot PbSO_4$. In order to index these data, further high-temperature single-crystal investigations are necessary and are planned.

Tetrabasic Lead Sulfate

Zimkina and Shchemelev (11) gave for tetrabasic lead sulfate the following rhombic, pseudotetragonal crystal data: a = 11.5Å, b = 11.7Å, and c = 7.3Å, obtained from electron diffraction patterns. Pinsker and Farmakovskaya (12) determined the hexagonal cell parameters a = 8.98Å and c = 24.8Å. The material had been obtained by deposition from an aqueous suspension by dusting it through a silk screen. The data of Pinsker and Farmakovskaya (12) are similar to those of a basic lead carbonate $2PbCO_3 \cdot Pb(OH)_2$ described by Cowley (13).

In the course of our investigation, it was possible to synthesize the incongruently melting compound $4PbO \cdot PbSO_4$ in large single crystals out of a ternary silicate sulfate melt having the over-all composition 60 m/o (mol per cent) PbO, 15 m/o $PbSO_4$, and 25 m/o $PbSiO_3$. Oscillation, Weissenberg, and precession photographs revealed that the data of Zimkina and Shchemelev (11) are only approximate. The new cell dimensions are: Probable space group: $P2_1/a$ and a = 11.443 ± 0.02Å, b = 11.666 ± 0.02Å, c = 7.316 ± 0.02Å, and β = 90.82 ± 0.2°. The calculated density is 8.13_5 g/cm^3, assuming the number of formula weights per unit cell, Z = 4. The experimental density is 8.1 ± 0.1 g/cm^3. With these cell parameters, the powder diffraction pattern in Table V could be indexed completely. We have never observed the hexagonal modification of $4PbO \cdot PbSO_4$ described by Pinsker *et al.* (12), nor any other basic lead sulfate with hexagonal cell parameters.

The $4PbO \cdot PbSO_4$ data in Table V has, like the other basic lead sulfates in Tables II and IV, many more d-values than the (unindexed) ASTM-cards 6-0275, 308, 382, 388; 2-1276 and 12-775. Furthermore, the differing intensities reveal that possibly the ASTM-cards are based on samples which were not free of texture.

The IR-absorption data of all basic lead sulfates are collected in Table VI. They are compared with those of $PbSO_4$, anglesite, and those of the free SO_4^{2-} anion (14). The typical SO_4^{2-} absorption bands appear in all basic lead sulfates, but they show relatively large splitting (*e.g.*, ν_4) which indicates that the SO_4^{2-} ion in the basic lead sulfates has lower site-symmetry than in lead sulfate.

Acknowledgments

The author expresses his thanks to Professor Dr. H. Wondratschek for his interest and support of this work. He is grateful to Dr. G. Weitz and Dr. W. E. Klee (Mineralogisches Institut der Universität Karlsruhe) for many helpful discussions.

Manuscript submitted Sept. 8, 1969; revised manuscript received *ca.* Dec. 29, 1969.

Any discussion of this paper will appear in a Discussion Section to be published in the December 1970 JOURNAL.

REFERENCES

1. F. M. Jäger and H. C. Germs, *Z. anorg. allgem. Chem.*, **119**, 152 (1921).
2. G. L. Clark, J. N. Mrgudich, and N. C. Schieltz, *ibid.*, **229**, 401 (1936).
3. J. D. Esdaile, *This Journal*, **113**, 71 (1966).
4. J. J. Lander, *ibid.*, **95**, 174 (1949).
5. H. H. Kellogg and S. K. Basu, *Trans. Met. Soc. AIME*, **218**, 70 (1960).
6. E. V. Margulis and N. I. Kopylov, *Russ. J. Inorg. Chem. (English Transl.)*, **9**, 423 (1964).
7. L. Merker and H. Wondratschek, *Glastech. Ber., Sonderband*, **30**, 473 (1957).
8. W. E. Richmond and C. W. Wolfe, *Amer. Mineralogist*, **23**, 799 (1938).
9. W. P. Binnie, *Acta Cryst.*, **4**, 471 (1951).
10. J.-C. Boivin, D. Thomas, and G. Tridot, *Compt. Rend.*, Ser. C, **267**, 532 (1968).
11. T. M. Zimkina and V. N. Shchemelev, *Fiz. Tverd. Tela Akad. Nauk SSSR*, **2**, 1646 (1960) [Solid-State Physics, Acad. Sci., USSR, **2**, 1489 (1960)].
12. G. Z. Pinsker and G. J. Farmakovskaya, *Kristallografiya*, **6**, 268 (1961).
13. J. M. Cowley, *Acta Cryst.*, **9**, 391 (1956).
14. H. Siebert, "Anwendung der Schwingungsspektroskopie in der Anorganische Chemie," p. 68, Springer Verlag, Berlin, (1966).

The Deposition of Molybdenum and Tungsten Films from Vapor Decomposition of Carbonyls

L. H. Kaplan

IBM Components Division, East Fishkill Laboratory, Hopewell Junction, New York

and F. M. d'Heurle

IBM Thomas J. Watson Research Center, Yorktown Heights, New York

ABSTRACT

Molybdenum and tungsten films formed by the pyrolytic decomposition of the respective carbonyls were investigated to determine their usefulness as conductors in microcircuit devices. The relations between deposition variables (such as pressure of carbonyls, pressure of the carrier gas, rate of gas flow, and substrate temperature) and deposition parameters (such as rate of film growth) or film properties (such as resistivity) were studied. The effects of carrier gas substitution on molybdenum film resistivity were determined. At a carbonyl pressure of 0.001 Torr, a hydrogen pressure of 0.01 Torr, a gas flow of 12 std cc/min, and a substrate temperature of 500°C, molybdenum films were deposited with a resistivity close to that of bulk (5.6 μohm cm), at a rate of 3.7 Å/sec. In molybdenum films deposited at lower substrate temperatures the resistivity increased, presumably because of increased carbon within the films. The resistivity of tungsten film is always greater than the resistivity of Mo films deposited under equivalent conditions. The lowest resistivity achieved in a tungsten film was approximately twice the value for bulk tungsten (5.5 μohm cm). The structures of both molybdenum and tungsten films deposited under conditions that favored the formation of films with the lowest resistivities were examined by x-ray diffraction as well as replica electron microscope techniques. Measured lattice parameters, when corrected for independently determined stress, were approximately equal to the parameters reported for pure molybdenum and tungsten. In all tungsten films studied, tensile stresses were found, but in molybdenum films the stresses were tensile for substrate temperatures greater than 500°C and compressive for lower temperatures.

Molybdenum and tungsten are potentially interesting materials for semiconductor device applications because of their relative inertness, high-temperature stability, satisfactory electrical resistivity, low thermal expansion coefficients, and good etching properties. Since damage to the semiconductor surface should be minimal during deposition of metal interconnections, chemical vapor deposition is preferable to sputtering or electron-bombardment evaporation. Of several ways to vapor-deposit molybdenum and tungsten, the most attractive are hydrogen reduction of metal halides and thermal decomposition of carbonyls. The latter process has the advantage of a starting material that is a fairly inert, volatile solid, which allows a relatively simple system design. It does, however, require operation at reduced pressure, in contrast to halide reductions (1-6), which usually proceed at atmospheric pressure.

In the pioneering study of molybdenum and tungsten carbonyl decomposition by Lander and Germer (7, 8) the main emphasis was placed on the mechanical properties of thick coatings used to protect bearing surfaces against wear. Electrical properties were not considered and deposition rates were not systematically studied. A general article on carbonyl metallurgy by Carlton and Goldberger (9) considers thermodynamics and kinetics. Carlton and Oxley (10) have determined the kinetics of iron carbonyl decomposition. Matyuskenko *et al.* (11) have investigated the morphology of molybdenum and tungsten films deposited via carbonyl decomposition. More recently, Cuomo (12) has described preliminary work on molybdenum and tungsten films formed from their respective carbonyls.

In the present work, the carbonyl decomposition process was characterized with regard to deposition rate and to properties (resistivity, stress, orientation, grain size) of the films produced. The effects were investigated of varying the parameters (temperature, pressure, and rate of gas flow) and of modifying the chemistry of the system. A specific aim of some of these experiments was to reduce carbon in molybdenum films.

Apparatus and Method

All films were deposited as follows in an apparatus shown schematically in Fig. 1. The apparatus consisted of a diffusion-pumped vacuum system 1 connected to a vertical reactor tube 2. A cylindrical molybdenum susceptor 3, supported and rotated from below, was heated inductively through use of a coil mounted outside the tube. The substrate, generally an oxidized silicon wafer, was placed on the susceptor and was perpendicular to the direction of the incoming gas. The gas (hydrogen or other carrier gas at reduced pressure, containing a known partial pressure of metal carbonyl) entered through the top of the tube. The carbonyl pressure was established by regulating the temperature of solid carbonyl in a reser-

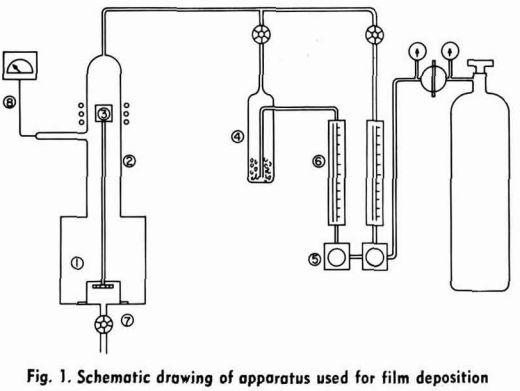

Fig. 1. Schematic drawing of apparatus used for film deposition

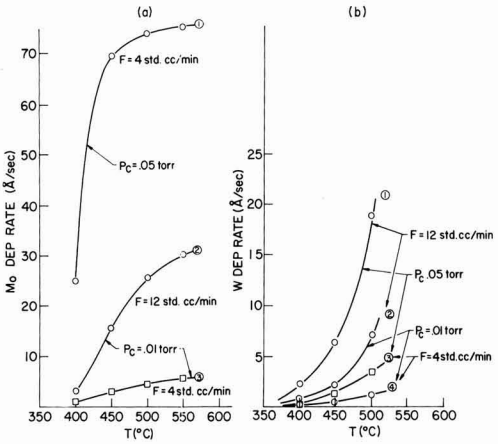

Fig. 2. Rate of metal deposition vs. deposition temperature. a. P_H = 0.07 Torr; b. P_H = 0.23 Torr.

voir 4 through which the carrier gas passed. This reservoir (shown in the diagram as a single chamber) consisted of a superheated carbonyl source followed by an equilibrating chamber maintained at the desired temperature. The rate of flow was regulated by a needle valve 5 and calibrated flow meter 6. Pressure in the tube was determined by setting the vacuum valve 7 and was read by a calibrated Pirani gauge 8.

The temperature of the molybdenum susceptor was read from a thermocouple rigidly fastened to it. The substrate was thermally coupled to the susceptor by a layer of liquid gallium which maintained susceptor and substrate at essentially identical temperatures. To prevent reaction between the gallium and the molybdenum susceptor, the upper surface of the susceptor was coated with reactively sputtered silicon nitride. The hydrogen and argon (Matheson research grade, 99.995% pure, with nitrogen the main impurity) were used without further purification. The molybdenum carbonyl (99.5% purity)[1] was found by emission spectroscopy to contain less than 0.01% metallic contaminants.

Typically, film deposition would begin with evacuating the reactor tube to a pressure of 2 x 10^{-5} Torr. Carrier gas was then admitted through a by-pass at low flow rate and pressure, while the substrate temperature was raised to the desired point. The carrier gas was then allowed to flow through the carbonyl powder and into the reactor at the desired flow rate, while the vacuum valve was used to adjust reactor pressure. After the desired deposition time, gas flow and heat were turned off, and the substrate was cooled to room temperature, while carrier gas flow was maintained. The most important process parameters that could be varied independently were substrate temperature, carbonyl partial pressure, carrier gas pressure, and carrier gas flow rate. Each significantly affected the rate of deposition, but deposition temperature appeared to affect the resistivity of the films formed most significantly.

Thickness measurements were made with a Talysurf instrument and/or a Tolanski interferometer. Film resistivities were derived from resistance measurements obtained from a linear four-point probe and a Keithley 503 milliohmeter. A qualitative evaluation of film adhesion was obtained by means of the so-called "Scotch-tape test."

Results and Discussion

Process rate studies.—Figure 2a and b show the effect of substrate temperature on deposition rates of Mo and W, respectively, for several typical sets of operating parameters. Although the conditions for the two metals were not fully equivalent, it may be noted that deposition rates for Mo were higher than those for W. As the deposition temperature is increased, the deposition rate tends to rise sharply at first but then levels off at high temperatures. However, the leveling off effect shown by the Mo rate curve at higher temperatures is not exhibited by the W curves. Additional results have shown that for deposition temperatures lower than 400°C, the rates of growth of Mo films appear to increase slightly with decreasing temperatures. A maximum in deposition rate is reached at about 300°C. Since this unexpected increase in deposition rate occurs under conditions where molybdenum carbide rather than molybdenum films are obtained, it is likely due precisely to the formation of molybdenum carbide. At temperatures below 300°C the rate of deposition falls rapidly to zero.

The effect of carbonyl partial pressure P_c on deposition rate is shown in Fig. 3a and b for Mo and W, respectively, for various conditions of temperature and flow. In all cases approximate linearity is observed in the initial portions of the curves, generally followed by a leveled-off portion. The importance of carrier gas flow rate F, at constant P_c and total pressure, in determining the rate of Mo and W deposition is clearly shown in Fig. 4a and b, for low and high levels of temperature and carbonyl pressure.

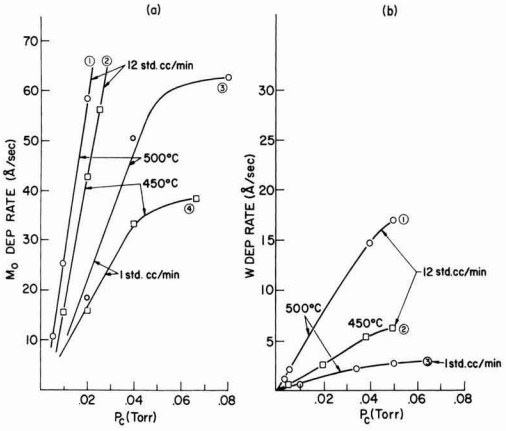

Fig. 3. Rate of metal deposition vs. carbonyl partial pressure. a. P_H = 0.07 Torr; b. P_H = 0.23 Torr.

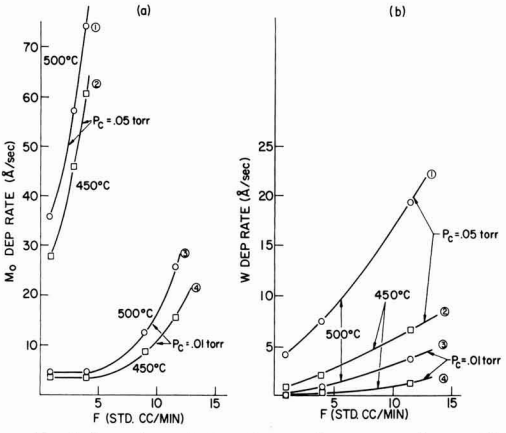

Fig. 4. Rate of metal deposition vs. flow rate. a. P_H = 0.07 Torr; b. P_H = 0.23 Torr.

[1] Purchased from Gallard-Schlesinger Chemical Manufacturing Corporation, Carle Place, New York.

In vapor decomposition processes such as those considered here, two mechanisms are generally expected to play a rate-controlling role: (*i*) the chemical decomposition of the carbonyl, and (*ii*) gaseous diffusion of carbonyl vapor to the deposition surface. Also, in this latter diffusion mechanism one should include the diffusion of by-products, in this case CO, away from the same surface.

The individual processes should each exhibit a different temperature dependence. Thus, as the temperature is raised, the rate of the chemical decomposition will increase as $\exp(-Q/kT)$ (where Q is the activation energy), while the rate of a gaseous diffusion will vary only as the $\sqrt{T}$ (13). Hence, while the carbonyl decomposition might be the rate-limiting step at some lower temperature range (here, apparently 200°-400°C), the diffusion steps would limit the rate at higher temperatures.

It should also be noted that an experimental limitation can be caused by the carbonyl depletion of the gas at high deposition rates. A quick calculation indicates that under the deposition conditions used here, such a depletion effect contributes to the leveling-off in the deposition rates recorded in curves 1 and 2 of Fig. 2a.

The shape of the curves (deposition rate *vs.* carbonyl pressure) in Fig. 3 suggests that gaseous diffusion of carbonyl molecules to the substrate surface is rate-limiting. The rate of such diffusion should be linear with carbonyl concentration until the concentration becomes high enough that diffusion is no longer the slowest process. At higher carbonyl pressure the overall rate should be much less affected by pressure, and the curves should level off.

The effect of flow rates on the rate of deposition is shown in Fig. 4. The curves do not extrapolate to a deposition rate of 0 at 0 flow rate. This undoubtedly reflects the diffusion of carbonyl vapor from the source to the reactor. The approximate proportionality observed between deposition rate and pressure (at equal temperature) at the lowest flow rates substantiates this point. The more than linearly increasing variation of deposition rate at high flow rate in curves 3 and 4 of Fig. 4a remains unexplained.

From the temperature dependence as shown in Fig. 2, one may attempt to calculate an over-all activation energy for the reactions. The form of these curves indicates that, in the case of Mo, carbonyl decomposition is rate-limiting only at the lower temperature ranges. Figure 5 shows an Arrhenius-type plot of the rate/temperature data for a typical set of conditions (0.05 Torr of Mo $(CO)_6$ flowing at 0.9 std. cc/min). For Mo $(CO)_6$ an activation energy of 23 kcal/mole was found, while the corresponding value for W $(CO)_6$ was 18 kcal/mole. These figures are roughly in the same range as the value of 14 kcal/mole reported (14) for the decomposition of nickel carbonyl, Ni $(CO)_4$.

Lander and Germer (7) found that Mo deposition on an iron surface stops totally when the temperature is lowered to 160°C. In the course of this study, a similar behavior was found to occur at temperatures which varied with choice of substrate surfaces. In each case, the expected exponential decay of deposition rate with temperature was interrupted by a sudden cutoff of deposition. In order to initiate deposition at temperatures in the range immediately above the cutoff, it was found necessary to raise the system pressure to several Torr for a few seconds. Once deposition began, pressure could be lowered to the desired level (usually about 0.01 Torr) and deposition continued. Minimum Mo deposition temperatures were established for oxidized silicon surfaces, as well as for various polymer surfaces. On SiO_2, Mo deposition cuts off between 180° and 170°C. On oxidized silicon wafers coated with AZ1350, a photosensitive varnish used in semiconductor technology,[2] deposition does not occur below 210°C. Although not all deposition parameters were studied for all cases, it was found that the cutoff temperature for SiO_2 surfaces was not significantly dependent upon carbonyl pressure or flow rate.

[2] Distributed by the Shipley Corporation, Wellesley, Massachusetts.

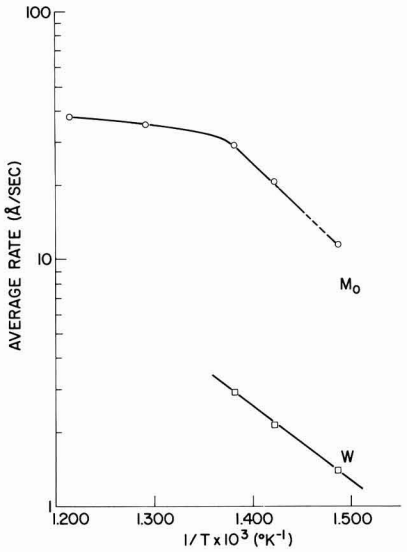

Fig. 5. Log (rate) vs. 1/T

Film properties.—Adherence.—Adherence of films to a substrate is a function of two types of opposing forces. One arises from the bonding between film and substrate and the other from the state of stress of the film. If the stresses in the film are effectively independent of film thickness, adhesion will decrease with increasing film thickness because of the increased shearing force at the film-substrate interface. On the other hand, the increase in film adhesion usually observed with increasing temperature of deposition may be attributed to the formation of chemical bonds between substrate and film material. In general, films formed above 500°C were perfectly adherent. Molybdenum films with thicknesses of 13,000Å or less deposited at 450°C were satisfactory according to the "Scotch-tape test." The Mo films deposited at lower temperatures were unsatisfactory. The same finding is essentially true for tungsten films of the same thickness.

To obtain adherent films in the lower temperature ranges so that other film properties might be evaluated, several potentially useful methods were developed. The addition during the first minute of deposition of a partial pressure (1-2 Torr) of an oxidizing gas (O_2 or H_2O) greatly improved adhesion to SiO_2 surfaces and allowed deposition temperatures as low as 325°C. Similarly low temperatures were made practical by first depositing at a very low rate (0.1-1.0 Å/sec) up to a thickness of several hundred angstroms. Deposition at normal rates following this step yielded adherent films at substrate temperatures as low as 325°C. Adherence of films depends strongly on the nature of the substrate surface. Ultrathin coatings (*e.g.*, 100Å) of AZ1350, or other photosensitive varnishes, on the oxidized silicon wafers allowed deposition of adherent Mo films at all substrate temperatures down to the 210°C cutoff temperature. Aside from the effects of such coatings, no relationship between film adhesion and substrate preparation procedures could be established.

Electrical resistivity.—The resistivity of metal films is of paramount importance for most microelectronic applications. The most probable cause for high resistivities in the films produced by carbonyl decomposition is the incorporation of carbon into the metal struc-

Table I. Resistivity and carbon content for various deposition conditions

Carrier gas	Deposition Temperature, °C	Rate, Å/sec	P_{H_2O}, mm	Resistivity, μohm cm	Carbon content, ppm
H_2	430	5	0	28	4400
H_2	480	5	0	10.1	2800
CO_2	480	5	0	9.5	1600
H_2	480	5	0.0003	8.8	1100
H_2	430	5	0.0003	9.0	1100
Ar	480	5	0	9.0	1000
H_2	500	5	0.0003	6.2	700
H_2	530	5	0	5.8	700
H_2	480	0.8	0	5.8	<260

ture either as interstitial atoms or in the form of a finely divided carbide. Such a cause/effect relationship is strongly suggested by the data in Table I. Here, the average carbon content, obtained by chemical analysis (oxidation followed by micro-gas-analysis), is listed with average resistivity for various deposition conditions, including the presence of water vapor in the plating gas. A good correlation between carbon content and resistivity is evident.

Figure 6a and b show the effect of deposition temperature on resistivity for films of Mo and W formed via carbonyl decomposition. It may be noted that resistivity of films deposited in the high range of substrate temperature is essentially invariant with temperature. For any given pressure and flow conditions, however, there will be some substrate temperature below which the resistivities of deposited films are found to increase. In fact, a decrease of 50°C in substrate temperature in this range can cause the resistivity of the resultant film to be 10-100 times as high as that of films formed at higher temperatures. Indications are that resistivity may level off again for still lower deposition temperatures. However, diffraction studies indicate that a carbide phase is deposited at such temperatures.

The dramatic effect of deposition temperature on resistivity of the deposited films shown in Fig. 6 can be explained, at least qualitatively, in terms of the thermodynamics of the CO/CO_2 equilibrium. When thermodynamic equilibrium is assumed, the ratio of carbon to metal deposited in the films can be derived from a consideration of the following reactions

$$M(CO)_6 = M + 6\,CO \qquad [1]$$

$$C + CO_2 = 2\,CO \qquad [2]$$

Clearly, the number of moles of deposited carbon will be equal to the number of moles of CO_2. From the knowledge of the equilibrium constant K for Eq. [2] one may then calculate the ratio of moles of deposited carbon to moles of deposited metal. This is expressed by the relation

$$\frac{n_m}{n_c} = \frac{K}{6} \cdot \frac{1}{P_{co}} + \frac{1}{3} \qquad [3]$$

where n_m and n_c are the numbers of moles of deposited metal and carbon, respectively. Calculated values of the ratio n_c/n_m, together with values of K (15) as a function of T are listed in Table II. At least in the lower concentration range, n_c/n_m should be linear with resistivity. The values of CO pressure used were obtained by assuming a carbonyl pressure of 0.0076 mm (a typical pressure here) and using the derived relationship

$$P_{co} = \frac{K}{4}\,(-1 \pm \sqrt{1 + 48\ P_c/K}) \qquad [4]$$

It is apparent that an increasingly sharp rise in the ratio n_c/n_m is to be expected as the deposition temperature is lowered. In practice, as is seen in Fig. 6, this effect reaches noticeable proportions below 450°C in molybdenum and generally below about 500° for tungsten.

Although no correlation between resistivity and any one deposition parameter other than deposition temperature was established, the resistivity of molybdenum films was found to change with deposition rate, as illustrated in Fig. 7. These films were deposited on substrates at 400°C and had relatively high resistivities. Results obtained with films deposited at 500°C might be expected to show a similar relationship between resistivity and rate. However, because the resistivities of such films were so close to bulk value, they were almost indistinguishable. The more sensitive parameter of resistivity ratio ($\rho_{\text{room temperature}}/\rho_{\text{liquid } N_2}$) was used in an attempt to discover a relation-

Table II. Calculated deposition of carbon in films as function of temperature
(For $P_c = 7.6 \times 10^{-3}$ mm $= 10^{-5}$ atm)

Temperature, °C	Equilibrium constant, $K = p_{co}^2/P_{co_2}$	P_{co}, atm	n_m/n_c	n_c/n_m, $\times 10^6$
800	10.0	6.23×10^{-5}	9.95×10^5	1
750	2.98	5.96×10^{-5}	2.96×10^5	3
700	1.01	6.06×10^{-5}	1.02×10^5	10
650	0.347	6.07×10^{-5}	3.52×10^4	28
600	0.079	5.99×10^{-5}	7.90×10^3	127
550	0.019	5.98×10^{-5}	1890.0	552
500	3.7×10^{-3}	6.01×10^{-5}	369.0	2,710
450	5.6×10^{-4}	5.07×10^{-5}	47.6	21,000
400	9.2×10^{-5}	3.45×10^{-5}	5.60	179,000

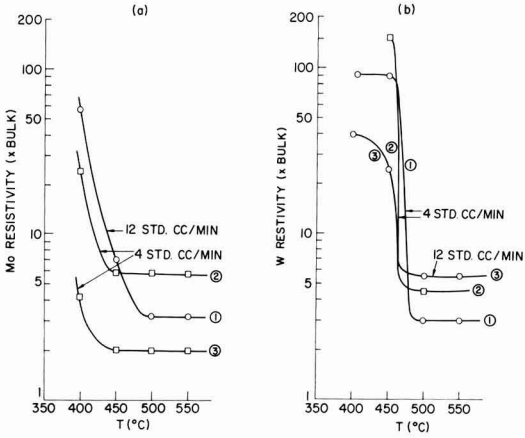

Fig. 6. Resistivity vs. deposition temperature. Resistivities are given as number of times bulk value, taken as 5.7 μohm cm for Mo and 5.5 μohm cm for W. a. $P_H = 0.074$ Torr; b. $P_H = 0.23$ Torr.

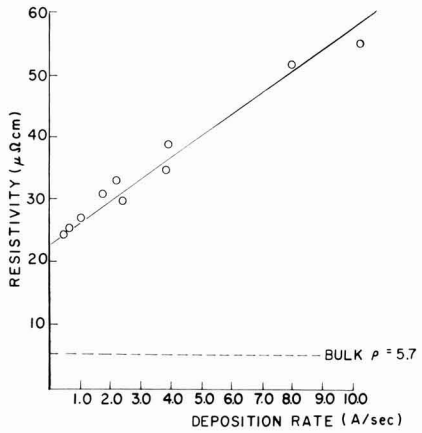

Fig. 7. Resistivity vs. deposition rate

ship between the resistivity and rate of growth of films deposited at 500°C, but no clear-cut relation was found. The dependence of resistivity on deposition rate, observed in films deposited at 400°C, is possibly explained by the physical incorporation of adsorbed carbon-containing molecules (CO and CO_2) into the growing film. If the rate of deposition is high enough that an adsorbed biproduct molecule is covered before it can move away, the molecule will become an impurity in the film. Lower rates of deposition might allow a greater portion of biproduct molecules to escape before entrapment and thus yield films with lower resistivity.

An investigation aimed at determining the optimum deposition parameters for molybdenum films deposited at the lowest possible substrate temperature, but still displaying a resistivity of approximately 6 μohm cm (close to that of pure bulk molybdenum), yielded the following results: substrate temperature 500°C, carbonyl pressure 0.001 Torr, hydrogen pressure 0.01 Torr, rate of gas flow 12 std. cc/min, rate of film growth 3.7 Å/sec. Attempts to obtain films with as low resistivities, but deposited at lower substrate temperatures, were all unsuccessful.

Some alloys of Mo and W were formed by simultaneous decomposition of the two carbonyls in appropriate molar ratios. Alloys prepared from such mixtures containing 0, 2, 5, 10, and 50% W had resistivities of 6.9, 7.3, 7.7, 8.6, and 14.7 μohm cm. Experience with chromium impurities in certain batches of molybdenum carbonyl in this work indicated that Cr exerts a deleterious influence on the resistivity of Mo films. This effect, which appears quite large, may be partly due to the formation of chromium carbide.

Structure, orientation, and stress.—Films deposited at different substrate temperatures were examined by the usual replica electron microscopy technique and by x-ray diffraction. In some instances, the stresses in the films were determined by the "wafer bending technique," (16) in which stresses are evaluated from the optically determined bow imparted to the underlying silicon substrate.

Measurements made on an XRD-5 diffractometer with a Cu target yielded information about structure, preferred orientation, and particle size; and through lattice parameter (17) determination (with an accuracy of ± 0.0015Å) gave values for the homogeneous film stresses. Strains measured from lattice parameter measurements were correlated with stresses determined by optical means, according to the formula

$$\epsilon_z = \frac{2\nu}{E}\sigma_x \qquad [5]$$

where ϵ_z is the strain normal to the surface of the film, ν is the Poisson ratio, E the modulus of elasticity, and σ_x is the homogeneous film stress in the direction parallel to the film surface. The values (18) of ν and E are 0.32 and 3.2 x 10^{12} dynes/cm^2, respectively, for pure molybdenum.

For tungsten $E = 3.5 \times 10^{12}$ dynes/cm^2, and $\nu = 0.27$, from the listed values (19) of E and G, the modulus of rigidity. The diffraction line broadening was partitioned into two parts, respectively proportional to $1/\cos\theta$ and $\tan\theta$, which yielded values of particle size and heterogeneous film stresses. A few samples were also examined by electron diffraction.

Molybdenum films used for structural studies were deposited under conditions that produced films with the lowest value of film resistivity obtained. The carbonyl pressure was 0.0015 Torr, hydrogen pressure 0.01 Torr, and rate of gas flow 12 std. cc/min; only the substrate temperature was varied for the different film depositions.

The residual stresses measured by optical means at room temperature were tensile for films deposited at high substrate temperatures (1.5 to 2 x 10^9 dynes/cm^2, 580°C) and compressive, with quite high values, for films deposited at lower substrate temperatures. Compressive stress values of 2 x 10^9 dynes/cm^2, 1.3 x 10^{10} dynes/cm^2, and as high as 2.3 x 10^{10} dynes/cm^2 were determined for films deposited at substrate temperatures of 530°, 480°, and 430°C, respectively.

Figure 8 shows the surface topography of a film deposited at 580°C, as shown by the microscope. X-ray diffraction indicates that such a film has a very strong (100) orientation. The lattice parameter measured on a similar film was found to be 3.1456Å, and 3.1468Å after correction for a film stress of 2 x 10^9 dynes/cm^2. (The listed lattice parameter (20) is 3.1466Å for pure molybdenum.) The particle size, from x-ray measurements, was $\sim$ 2500Å in a direction normal to the film surface. If one assumes that Fig. 8 gives a good indication of the grain size in a direction parallel to the film surface, it would appear that the grain structure is approximately equiaxed. Values of heterogeneous stresses, approximately $\pm 3.5 \times 10^9$ dynes/cm^2, appear quite high.

Figure 9 is an electron micrograph of a replica taken from a 5000Å thick film of molybdenum deposited at a substrate temperature of 530°C. This film showed a mixed (100)-(211) orientation, with the (211) part predominant. The combination of orientations, as well as an apparently smaller grain size, probably accounts for the more complex surface aspect displayed in Fig. 9 as compared with Fig. 8. The high lattice-parameter value, measured as 3.1490Å (corresponding to 3.1475Å after correction for a stress of 2.3 x 10^9 dynes/cm^2) corroborates indications that the film is in a state of compressive stress. Diffraction-determined grain size and heterogeneous stress values are about equal to those reported above for a film deposited at 580°C. Film orientations do not correspond to those observed by Lander and Germer (7) who reported mostly (111) orientations.

Films deposited at a substrate temperature of 480° and 430°C displayed nondistinctive surface structures on examination by electron microscopy.

When films deposited at a substrate temperature of 480°C were studied by x-ray diffraction, strong (211) and (111) peaks were obtained, while (200) peaks were either absent or extremely weak. The lattice parameter of one such film was 3.1562Å, or 3.1480Å after correction for a compressive stress of 1.3 x 10^{10} dynes/cm^2. The diffraction peaks were quite wide. If

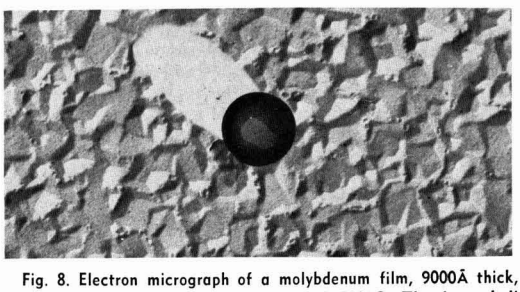

Fig. 8. Electron micrograph of a molybdenum film, 9000Å thick, deposited at a substrate temperature of 580°C. The latex ball has a diameter of 5000Å (as on the other photographs).

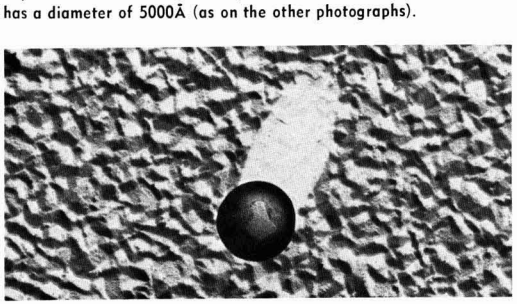

Fig. 9. Electron micrograph of a molybdenum film, 5000Å thick, deposited at a substrate temperature of 530°C.

one assumes, as was found in films deposited at higher temperatures, that the line broadening can be partitioned equally between grain size and heterogeneous stress effects, the grain size would be of the order of 600Å and the heterogeneous stress approximately $\pm 5.5 \times 10^9$ dynes/cm^2.

Several films were deposited at a substrate temperature of 430°C. Unfortunately, because of poor adhesion and other difficulties, these had to be used independently for optical stress measurements and for x-ray studies. A compressive stress with a magnitude of 2.3×10^{10} dynes/cm^2 was observed in one of these films. This apparently corresponds to a lattice parameter of 3.1622Å determined in a similar film with a (100) orientation, which would give a value of 3.1477Å after correction for stress. However, most films deposited under similar conditions appeared to have a random orientation and a lattice parameter of 3.1510Å. This latter value would fit quite well with a stress value of 3.6×10^9 dynes/cm^2 which was also measured in a film deposited at 430°C under identical conditions. It was not possible to determine the cause of the two orientations and of the relation between film stress and film orientation. In all of these films, regardless of substrate temperature during deposition, the lattice parameters (after correction for stress), agree within the accuracy of these measurements with the lattice parameter of pure molybdenum. Impurities, therefore, do not contribute significantly to the lattice parameter of the films.

When the substrate temperature during deposition is below 400°C, molybdenum carbide films rather than molybdenum metal films are obtained. The transition between deposition temperatures that correspond to molybdenum films and those that correspond to molybdenum carbide films occurs rather sharply at about 400°C. Only in films deposited at this temperature were diffraction lines characteristic of molybdenum and molybdenum carbide obtained simultaneously. Films deposited at 415°C appeared to be essentially "pure" molybdenum and films deposited at 370°C "pure" carbide. This value of the transition temperature appears in rough agreement with the one that can be extrapolated from the work of Lander and Germer. In spite of rather strong preferred orientations in carbide films, enough diffraction peaks were obtained to establish that the carbide phase is the cubic form reported by the same authors.

Molybdenum carbide films deposited at substrate temperatures of 375°C or below had very strong (100) orientations, although in films deposited at 300°C this orientation was somewhat less pronounced. Figure 10 is an electron micrograph of a replica taken from a 5000Å film deposited at 345°C. The apparent grain size is commensurate with a value of 1200Å determined in a similar film by x-ray diffraction. In general, carbide films had remarkably sharp diffraction lines, indicating that grain size did not decrease much below 1000Å and that heterogeneity either of stress or composition was limited. The lattice parameter, which seems to increase with decreasing temperature of deposition, may be influenced by lack of carbon stoichiometry. Values of 4.136, 4.146, and 4.160Å were found for films deposited at 370°, 350°, and 300°C, respectively.

For purposes of structural examination, tungsten films were deposited at a carbonyl pressure of 0.002 mm, at a hydrogen pressure of 0.01 mm, at a flow rate of 12 std. cc/min, and at substrate temperatures of 450°, 400°, 350°, and 300°C. X-ray diffraction examination of the films showed that all of them were "pure" tungsten, without detectable carbide lines. These results were confirmed by electron diffraction for the films deposited at 450°, 400°, and 300°C. Thus, as previously observed by Lander and Germer, the tendency to form carbides is much less in tungsten films than in molybdenum films. The film deposited at 450°C had a (100) orientation, while the others were randomly oriented. For both tungsten and molybdenum films, higher temperatures of deposition favor (100) orientations. However, for equal temperatures of deposition, tungsten films show tensile stress, whereas molybdenum films show compressive stresses. From two tungsten films deposited at 400°C, the value of the tensile stress was found to be $4.6 \pm 1 \times 10^9$ dynes/cm^2. In a film deposited at 450°C the lattice parameter was 3.1616Å, which, when compared with a lattice parameter of 3.1650Å for pure tungsten (21), corresponds to a tensile stress of 5.3×10^9 dynes/cm^2. Diffraction line broadening showed the film had heterogeneous stresses of $\pm 4 \times 10^9$ dynes/cm^2 and a particle size of 1200Å. Comparison of this value with the apparent grain size of the same film in Fig. 11 indicates that the structure might be slightly columnar.

The stress level in the tungsten films is approximately twice the 2.6×10^9 dynes/cm^2 value that would be expected on the basis of differential contraction between tungsten and silicon, for films deposited at about 400°C. It appears, therefore, that the films are deposited with intrinsic tensile stresses. The molybdenum films, however, display compressive stresses, which probably are due to carbide precipitation.

Effects of gaseous additions and substitutions.—Since low resistivity is desired for conducting films in microelectronic devices, different techniques were used to try to decrease the resistivity of molybdenum films. Generally speaking, the aim was to improve the resistivity by decreasing the carbon incorporated in the films during deposition.

Addition of water vapor and hydrogen sulfide to carrier gas.—The removal of carbon from metals, according to the reaction

$$H_2O + C = H_2 + CO \qquad [6]$$

is well established. However, excessive concentrations of H_2O in a system could lead to oxidation of the host material, according to a reaction such as

$$Mo + 3\,H_2O = MoO_3 + 3H_2 \qquad [7]$$

which would be expected to deleteriously affect the resistivity. Hence, with increasing water vapor, the resistivity passes through a minimum. In fact, the oxidation of Mo by mixtures of H_2 and H_2O is thermodynamically favored up to 800°C for the minimum

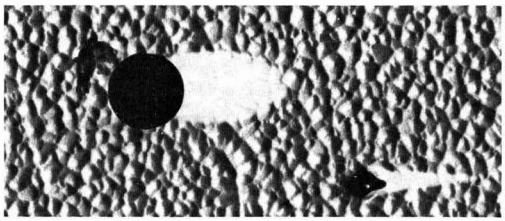

Fig. 10. Electron micrograph of a molybdenum carbide film, 5500Å thick, deposited at a substrate temperature of 345°C.

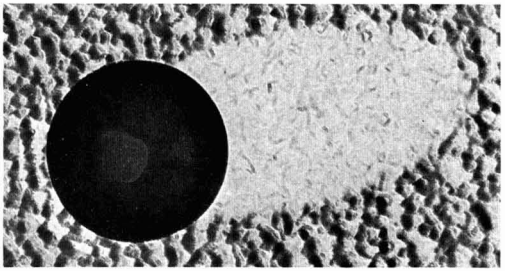

Fig. 11. Electron micrograph of a tungsten film, 3000Å thick, deposited at a substrate temperature of 450°C.

H_2O/H_2 ratio (0.01) used in this work. Calculations indicate that an H_2O/H_2 ratio at 2 x 10^{-6} is just oxidizing at 400°C. These calculations were based on the data of Glassner (22) for MoO_3 ($\Delta F = -157$ kcal/mol at 300°K and -115 kcal/mol at 800°K) and for MoO_2 ($\Delta F = -116$ kcal/mol at 300°K and -89 kcal/mol at 800°K) and on the method described in Darken and Gurry (23). [The substantial disagreement between this value and the 0.062 mentioned by Lander and Germer (7) probably is due to their use of unreliable data for the free energies of formation of the two molybdenum oxides.] Results of experiments on adding water vapor to the hydrogen carrier gas are shown in Fig. 12. Although resistivity improved substantially at low deposition temperatures, where resistivity values generally are high, very little improvement occurred in films deposited at 500°C, which had a resistivity close to that of bulk molybdenum even when deposited without added water vapor. To determine whether reaction [6] plays a significant role in the resistivity of films deposited in the presence of water vapor, several films deposited at a substrate temperature of 480°C (with water vapor pressure of 0.001-0.002 Torr) were subsequently annealed in hydrogen at 600°C. This treatment had no effect on the resistivity of the films. It is possible that the negative result is due to the difficulty in reaching equilibrium at this comparatively low temperature for molybdenum.

Removal of carbon by H_2S could be envisaged according to the following reaction

$$2H_2S + C = 2H_2 + CS_2 \qquad [8]$$

Although such a reaction is not thermodynamically favored, under equilibrium conditions, decreases in the carbon content of molybdenum films deposited in the presence of H_2S were reported by Lander and Germer (7).

Results obtained here indicate that although the addition of H_2S produces a substantial decrease in resistivity at a deposition temperature of 350°C, no advantage is gained for deposition at 500°C. In fact, it has been observed that even extremely small concentrations of H_2S cause the resistivity to rise for films deposited at this temperature.

Substitution of argon or carbon dioxide for hydrogen. —The water-carbon reaction of Eq. [6] suggests another means for reducing the carbon content in these films. When hydrogen is used as a carrier gas, it tends to drive this reaction to the left, causing carbon to form by the reduction of the CO biproduct from the carbonyl decomposition. Hence, substitution of an inert gas such as Ar might be expected to reduce carbon content. Figure 13 compares the electrical resistivity of films made with H_2 with that of films made with Ar carrier gases at various temperatures.

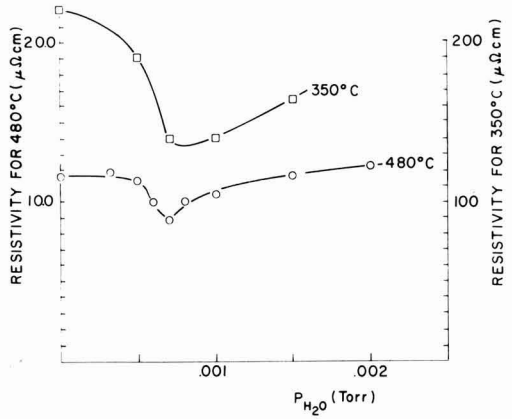

Fig. 12. Resistivity vs. water vapor pressure

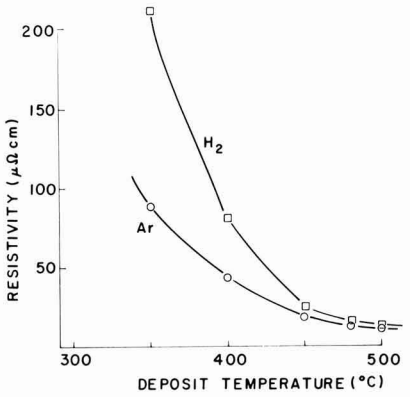

Fig. 13. Resistivity vs. deposition temperature for two carrier gases.

Although at low deposition temperatures the carrier gas substitution has a definite advantage, improvement falls off rapidly with increasing temperature. Carbon analysis of films deposited at 480°C shows no substantial differences in carbon content when the carrier gas is changed.

The disproportionation of carbon monoxide, shown in Eq. [2] to be a likely source of carbon in the films, theoretically should be reversed by an increase in concentration of CO_2. As in the case of water, however, too much CO_2 can constitute an oxidizing atmosphere and react with the depositing metal M, according to the reaction

$$M + 3\,CO_2 = MO_3 + 3\,CO \qquad [9]$$

It was to be expected then that pure CO_2 carrier gas would lead to large resistivities. A mixture of CO_2 and H_2 might minimize both oxide and carbon impurities. Figure 14 shows resistivity as a function of mole fraction of H_2 in the carrier gas for films deposited at 400°C. A minimum is evident in the region of 30 m/o (mole per cent) H_2.

Conclusions

Molybdenum films with a resistivity approaching the bulk value can be deposited from decomposition of molybdenum carbonyl at temperatures of 500°C, or above, and at growth rates of 3-4 Å/sec. At lower deposition temperatures films with bulk resistivity cannot be obtained, presumably because of carbon incorporation within the films, as evidenced by the correlation between film resistivity and carbon content.

In molybdenum films the stress changes from a tensile value of 1.5-2 x 10^9 dynes/cm^2 for films deposited at 580°C to a compressive value of 2.3 x 10^{10} dynes/cm^2 for films deposited at 430°C. In tungsten films deposited in a similar range of temperatures,

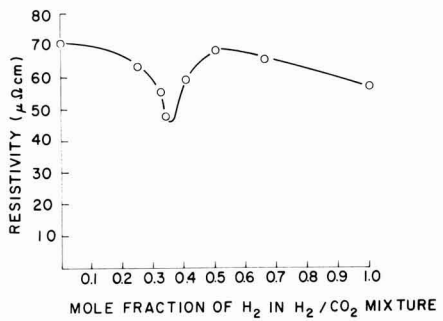

Fig. 14. Resistivity vs. mole fraction of H_2 in H_2/CO_2 mixtures

only tensile stresses were observed, with a value of 4.6 x 10^9 dynes/cm^2 for a film deposited at 400°C. This difference between tungsten and molybdenum films is probably related to the formation of a carbide phase, which was found to form much more readily in molybdenum than in tungsten.

Attempts to produce films with low resistivity by making chemical deposition conditions more oxidizing were most successful at deposition temperatures of about 400°C. However, the improvements obtained were not sufficient to reduce resistivity to values approaching bulk value. Additions of water vapor, hydrogen sulfide, carbon dioxide, and argon to hydrogen, and various combinations of these were not effective in the temperature range of 450°-500°C, where the unmodified carbonyl decomposition in hydrogen gives films with resistivities of 1.5-2 times bulk value. Thus it must be concluded that production of molybdenum films with bulk resistivity by carbonyl decomposition at substrate temperatures below 500°C is unlikely.

Acknowledgments

The authors are pleased to acknowledge the help of Mr. W. C. Metzger who accomplished most of the experimental work involved in depositing the films and in making the stress determinations. Mr. C. Aliotta made the replicas and obtained the electron micrographs. Comments by T. Sedgwick were extremely helpful.

Manuscript received Oct. 2, 1969.

Any discussion of this paper will appear in a Discussion Section to be published in the December 1970 JOURNAL.

REFERENCES

1. W. J. Childs *et al., Trans. ASM,* **43,** 105 (1951).
2. S. T. Wlodek and J. Wulff, *This Journal,* **107,** 565 (1960).
3. S. H. Smiley, D. C. Brater, and H. L. Kaufman, *J. Metals,* **17,** 605 (1965).
4. G. Kano *et al., J. Appl. Phys.,* **37,** 2985 (1966).
5. J. G. Donaldson and H. Kenworthy, U.S. Dept. of Interior, Bureau of Mines, Report 6853 (1966).
6. G. F. Wakefield, *This Journal,* **116,** 5 (1969).
7. J. J. Lander and L. H. Germer, *Trans. Met. Soc.-AIME,* **175,** 648 (1948).
8. J. J. Lander, U.S. Patent 2,690,980 (October 1954).
9. H. E. Carlton and W. M. Goldberger, *J. Metals,* **17,** 611 (1965).
10. H. E. Carlton and J. H. Oxley, *A.I.Ch.J.,* **11,** 79 (1965).
11. N. J. Matyushenko, A. A. Rozen, and V. V. Sagalovich, *Fiz. Metal. Metalloved.,* **21,** 403 (1966).
12. J. J. Cuomo, To be published.
13. S. Dushman, "Scientific Foundations of Vacuum Techniques," pp. 10 and 74, John Wiley & Sons, Inc., New York (1949).
14. R. K. Chan and R. McIntosh, *Can. J. Chem.,* **40,** 845 (1962).
15. J. B. Austin and M. J. Day, *Ind. Eng. Chem.,* **33,** 23 (1941).
16. R. Glang, R. Holmwood, and R. L. Rosenfeld, *Rev. Sci. Instr.,* **36,** 7 (1965).
17. F. d'Heurle, *Trans. Met. Soc.-AIME,* **236,** 314 (1966).
18. H. R. Clauser, "The Encyclopedia of Engineering Materials and Processes," p. 430, Reinhold Publishing Corp., New York, (1963).
19. *Ibid,* p. 686.
20. W. P. Pearson, "A Handbook of Lattice Spacings and Structure of Metals and Alloys," p. 752, Pergamon Press, New York (1963).
21. *Ibid.,* pp. 884-885.
22. A. Glassner, "Thermochemical Properties of Oxides, Fluorides and Chlorides," Argonne National Laboratory, Contract W 31-109-eng-38 (1957), L.C. 58-62015.
23. L. S. Darken and R. W. Gurry, "Physical Chemistry of Metals," p. 349, McGraw-Hill Book Co., Inc., New York (1953).

The Ga-GaP-GaAs Ternary Phase Diagram

G. A. Antypas

Varian Associates, Palo Alto, California

ABSTRACT

The ternary phase diagram of Ga-GaP-GaAs has been calculated using Darken's quadratic formalism for a ternary liquid in equilibrium with a regular solid solution. Liquidus isotherms have been calculated from 900° to 1450°C in 50°C increments. GaP distribution curves have also been calculated for 0.95, 0.9, 0.8, 0.7, 0.6, 0.5, 0.4, 0.3, and 0.1 mole fraction of GaP. The calculated ternary and pseudobinary phase diagrams are in excellent agreement with available experimental data.

Since it was demonstrated that the GaP-GaAs system forms continuous solid solutions (1) the system has attracted great attention, primarily because a portion of the system has a bandgap corresponding to the visible region of the spectrum. Initially, the GaAs-GaP crystals were prepared by vapor transport techniques, using AsH_3 and PH_3 as the source materials (2). It has been demonstrated, however, that III-V compounds grown from solution have a lower native defect density (3) and in general have more efficient radiative recombination properties. Thus an understanding of the thermodynamic properties of both the liquid and solid solutions is necessary for establishing optimum growth conditions. The model to be presented has already been applied to the In-Ga-As and Ga-As-Sb (4) systems where it gave excellent agreement with available experimental data. It can also be applied to all III-V ternary solids forming continuous solid solutions.

Phase Equilibria of III-V Ternary Compounds

Ternary-phase diagrams of III-V compounds have been calculated using the quasi-chemical equilibrium treatment (5) and the regular solution treatment (6). In computing the conditions for equilibrium between a ternary liquid solution A, B, C (Ga, P, As) and a pseudobinary solid solution AB-AC (GaP-GaAs), Stringfellow and Greene (5) derived the following equations

$$\ln \gamma_{AB}x = \ln 4N_AN_B + \ln (\gamma_A\gamma_B/\gamma_A^{STC}\gamma_B^{STC}) + \Delta S^F_{AB}(T^F_{AB} - T)/RT \quad [1]$$

$$\ln \gamma_{AC}(1-x) = \ln 4N_AN_C + \ln (\gamma_A\gamma_C/\gamma_A^{STC}\gamma_C^{STC}) + \Delta S^F_{AC}(T^F_{AC} - T)/RT$$

where γ_{AB} and γ_{AC} are the activity coefficients of AB and AC in the solid solution, x is the mole fraction of AB, N_i and γ_i (i = A, B, C,) are the atom fraction and

activity coefficient of i in the liquid solution, respectively, γ_i^{STC} is the activity coefficient of N_i at the stoichiometric composition, ΔS^F_{AB} is the entropy of fusion of AB, T^F_{AB} is the temperature of fusion of AB, R is the universal gas constant, and T is the temperature in °K.

Under the restriction

$$N_A + N_B + N_C = 1 \qquad [2]$$

Eq. [1] can be solved numerically on a computer to yield two sets of curves, one describing the liquidus isotherms and the other describing the solidus isoconcentration curves of the system.

In previous investigations the activity coefficients were determined by the quasi-chemical equilibrium (5) approach and by considering the ternary liquid as a strictly regular solution (6). In the present communication, however, the determination of the activity coefficient in the liquid phase is based on Darken's quadratic representation, which for a binary liquid is

$$\ln \gamma_A = \alpha_{AB} N_B^2$$
$$\ln (\gamma_B/\gamma^0_B) = \alpha_{AB}(-2N_B + N_B^2) \qquad [3]$$

where A is the solvent and B is the solute, γ^0_B is the activity coefficient of B at infinite dilution, and α_{AB} is the interaction parameter of the system. Equation [2] reduces to that describing a regular solution if $\ln \gamma^0_B = \alpha_{AB}$. This formalism has been satisfactorily applied by Darken (7) and Turkdogan and Darken (8) to a number of liquid metallic solutions for concentration of up to 60%. This formalism is consistent with the Gibbs-Duhem equation and satisfies Raoult's and Henry's laws as the limiting cases. The quadratic formalism was also extended by Darken (9) to ternary systems, which results in activity coefficients given by

$$\begin{aligned}
\ln\gamma_A &= \alpha_{AB}N_B^2 + \alpha_{AC}N_C^2 + (\alpha_{AB} + \alpha_{AC} - \alpha_{BC})N_BN_C \\
\ln(\gamma_B/\gamma^0_B) &= -2\alpha_{AB}N_B + (\alpha_{BC} - \alpha_{AB} - \alpha_{AC})N_C \\
&\quad + \alpha_{AB}N_B^2 + \alpha_{AC}N_C^2 + (\alpha_{AB} + \alpha_{AC} - \alpha_{BC})N_BN_C \\
\ln(\gamma_C/\gamma^0_C) &= -2\alpha_{AC}N_C + (\alpha_{BC} - \alpha_{AB} - \alpha_{AC})N_B \\
&\quad + \alpha_{AB}N_B^2 + \alpha_{AC}N_C^2 + (\alpha_{AB} + \alpha_{AC} - \alpha_{BC})N_BN_C
\end{aligned} \qquad [4]$$

where component A is the solvent and components B and C are the solutes, γ^0_C is the activity coefficient of component C at infinite dilution, and α_{i-j} are the interaction energies of the various binary systems. The above formalism is also consistent with the Gibbs-Duhem equation, and furthermore it reduces to the binary quadratic formalism as one of the solutes in the ternary approaches infinite dilution.

The solid solution in equilibrium with the ternary liquid was assumed to be regular, i.e., $\Delta F^{xs} = \alpha_{AB\text{-}AC}x(1 - x)$, where $\alpha_{AB\text{-}AC}$ is the interaction energy and x is the mole fraction of one of the components in the solid. The activity coefficients are thus given by

$$\ln \gamma_{AB} = \alpha_{AB\text{-}AC}(1 - x)^2$$
$$\ln \gamma_{AC} = \alpha_{AB\text{-}AC}x^2 \qquad [5]$$

Substituting Eq. [4] and [5] in Eq. [1] the ternary phase diagram can be calculated numerically to yield the liquidus and solid distribution curves.

Calculation of the Ga-GaP-GaAs Phase Diagram

The parameters necessary in calculating the ternary phase diagram are the temperatures T^F and entropies ΔS^F of fusion of the III-V compounds and the interaction parameters α_{AB}, α_{AC}, α_{BC}, and $\alpha_{AB\text{-}AC}$. T^F and ΔS^F for GaP and GaAs can be obtained directly from the literature and are shown in Table I. Vieland (10) has used regular solution theory to calculate the liquidus of III-V compounds. The interaction parameter obtained from such a treatment is

$$\alpha = \frac{\Delta S^F\,(T - T^F)\,[1 + R/\Delta S^F \ln 1/4x(1 - x)]}{2(x - 0.5)^2} \qquad [6]$$

Table I. List of thermodynamic parameters used in calculating the Ga-GaP-GaAs phase diagram

	GaP	GaAs	As-P	GaP-GaAs
α (cal/mole)	7900-7.00 T (11)	−3.7 T (12)	2000	1000
ΔS^F (eu)	15 (11)	16.64 (12)	—	—
T^F (°C)	1470	1238	—	—

where x is the column V element in solution. For a regular solution α should be independent of temperature and composition. Thurmond (11), however, demonstrated that for GaAs and GaP α is a linear function of temperature given by

$$\alpha_{GaAs} = 9960 - 11.15\ T$$
$$\alpha_{GaP} = 7900 - 7.00\ T \qquad [7]$$

When the interaction parameter α is divided by RT so that it will be thermodynamically consistent with Darken's formulation it takes the form of

$$\omega = \frac{\mathcal{L}}{RT} - \frac{\mathcal{S}}{R} \qquad [8]$$

which is of the form derived by Turkdogan and Darken (8), where $\mathcal{L}$ and $\mathcal{S}$ have the units of enthalpy and entropy, respectively.

In calculating α_{GaAs}, Thurmond assumed a ΔS^F_{GaAs} value of 14.0 eu. Arthur (12) pointed out that when a recently measured value for ΔS^F_{GaAs} of 16.64 eu is used, then

$$\alpha_{GaAs} = 5160 - 9.16\ T$$

Arthur has also calculated the activity coefficient of As from As vapor pressure measurements, and using a regular solution treatment found that the interaction parameter is accurately given by

$$\alpha_{GaAs} = -3.7\ T$$

The interaction parameter of the As-P system was calculated to be 2000 cal/mole by fitting the liquidus curve to a regular solution model and comparing it to available experimental data (13). Similarly, the interaction parameter of the GaP-GaAs system was determined by fitting the solidus to recently published data of the GaP-GaAs pseudobinary (14). Calculations performed by Moon (15) on GaP-GaAs were in good agreement for $\alpha_{GaP\text{-}GaAs} = 1000$ cal/mole.

Figure 1 represents the calculated ternary phase diagram. Solid lines represent the liquidus isotherms from 900° to 1450°C by 50°C increments, while dotted lines represent GaP isoconcentration curves at 0.95, 0.9, 0.8,

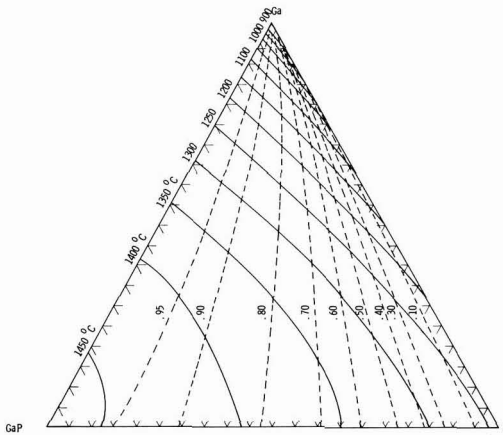

Fig. 1. Ga-GaP-GaAs ternary-phase diagram. ———, Liquidus isotherms, - - - - -, GaP isoconcentrations curves.

0.7, 0.6, 0.5, 0.4, 0.3, and 0.1 mole fraction of GaP. The pseudobinary obtained from Fig. 1 is shown on Fig. 2 along with available experimental data (14). Figures 3, 4, and 5 compare the experimental results reported by Thurmond for the GaAs and GaP compounds, and by Panish (16) for the Ga-GaP-GaAs solution growth and solution epitaxy results. Figure 3 is a portion of Fig. 1, plotted in cartesian coordinates, showing the

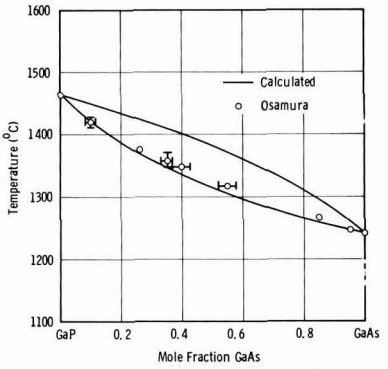

Fig. 2. GaP-GaAs pseudobinary-phase diagram

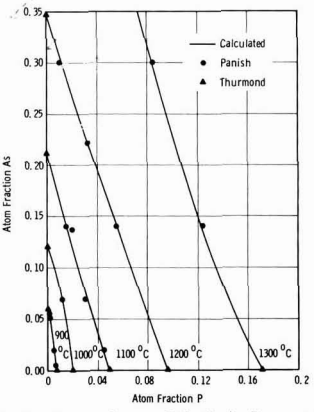

Fig. 3. Liquidus isotherms of the $GaAs_xP_{1-x}$ system

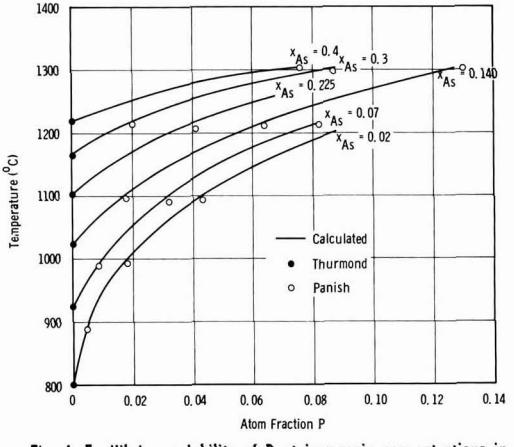

Fig. 4. Equilibrium solubility of P at isoarsenic concentrations in the ternary liquid solution.

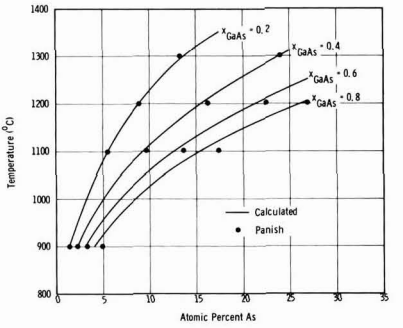

Fig. 5. GaAs isoconcentration curves plotted as a function of temperature and As concentration in the melt.

equilibrium solubility of P as a function of the As concentration in the melt for 900°, 1000°, 1100°, 1200°, and 1300°C isotherms. Excellent agreement is obtained between calculated and experimental results. Figure 4 also shows a portion of the ternary-phase diagram in greater detail, on which the solubility of P is plotted as a function of temperature at isoarsenic concentrations. Figure 5 represents the distribution of GaAs in equilibrium with the ternary melt as a function of the As present in the liquid solution. The distribution coefficient is defined by

$$D = \frac{\gamma_{GaP}}{\gamma_{GaAs}} \frac{x_{GaAs}/x_{As}}{x_{GaP}/x_P}$$

where γ_{GaAs}, x_{GaAs}, and x_{As} are the activity coefficient of GaAs in the solid solution, the GaAs mole fraction, and the atom fraction of As in the liquid solution, respectively. For the 1100°C isotherm, D varied between 0.13 for $x_P = 0.045$ and 0.27 for $x_P = 0.002$.

Conclusions

It has been shown that ternary phase diagrams of III-V compounds calculated by Darken's phenomenological quadratic formalism are in excellent agreement with available experimental data. The parameters used in calculating the Ga-GaP-GaAs phase diagram were either directly obtained from the literature, or were obtained by fitting the model to available experimental data. Although this model is derived to describe the solution in the vicinity of the major component (in solution epitaxy and solution growth of GaP_xAs_{1-x} in the vicinity of the Ga corner of the ternary diagram), the agreement between the calculated and experimental results of the pseudobinary phase diagram indicate that the quadratic formalism accurately describes the ternary phase diagram of Ga-GaP-GaAs for concentration of up to 50%.

Manuscript submitted Oct. 30, 1969; revised manuscript received Dec. 18, 1969.

Any discussion of this paper will appear in a Discussion Section to be published in the December 1970 JOURNAL.

REFERENCES

1. N. A. Goryunova, "The Chemistry of Diamond-Like Semiconductors," Chapman and Hall Ltd. (1965).
2. J. J. Tietjen and J. A. Amick, *This Journal*, **113**, 724 (1966).
3. C. S. Kang and P. E. Greene, *Appl. Phys. Letters*, **11**, 171 (1967).
4. G. A. Antypas and L. W. James, Accepted for publication in *J. Appl. Phys.*, 1970.
5. G. B. Stringfellow and P. E. Greene, *J. Phys. Chem. Solids*, **30**, 1779 (1969).
6. M. Ilegems and G. L. Pearson, "Proceedings of the Second International Symposium on GaAs," C. I. Pedersen, Editor, p. 3, Institute of Physics and the Physical Society, London (1969).

7. L. S. Darken, *Trans. Met. Soc. AIME*, **239**, 80 (1967).
8. E. T. Turkdogan and L. S. Darken, *ibid.*, **242**, 1997 (1968).
9. L. S. Darken, *ibid.*, **239**, 90 (1967).
10. L. J. Vieland, *Acta Met.*, **11**, 137 (1963).
11. C. D. Thurmond, *J. Phys. Chem. Solids*, **26**, 798 (1965).
12. J. R. Arthur, *ibid.*, **28**, 2257 (1967).
13. M. Hansen, "Constitution of Binary Alloys," McGraw-Hill Book Co., New York (1958).
14. K. Osamura and Y. Murakami, *Japan J. Appl. Phys.*, **8**, 967 (1969).
15. R. L. Moon, Private communication.
16. M. B. Panish, *J. Phys. Chem. Solids*, **30**, 1083 (1969).

Properties of Aluminum Oxide Obtained by Hydrolysis of $AlCl_3$

T. Tsujide, S. Nakanuma,* and Y. Ikushima

IC Division, Nippon Electric Company, Tokyo, Japan

ABSTRACT

A study has been made of aluminum oxide films prepared by the hydrolysis of mixtures of $AlCl_3$, H_2, and CO_2. Positive shifts of the flat band voltage of the MAS structure occur independently of the polarity and type of the applied bias when this is higher than a critical voltage. This phenomenon can be explained by electron injection and trapping. The trapped electrons have a long lifetime, but are excited by radiation such as x-rays and electron beam without introduction of damage.

One of the most important processes in the fabrication of semiconductor devices is the passivation of the semiconductor surface. For this purpose, various dielectric films have been examined, among which the most studied has been thermally grown silicon dioxide, because of its ease of preparation. Unfortunately, it exhibits instabilities such as shifts in device characteristics due to the migration of impurities, especially Na ions through the oxide at elevated temperatures under bias conditions (1) and degradation of device characteristics under irradiation environments (2); more demanding requirements have therefore led to the need for insulating films superior to this oxide.

It is a reflection of such requirements that recently silicon nitride and aluminum oxide have been receiving a great deal of attention. These materials were found to have properties superior to silicon dioxide films, in that the ion migration effect has been shown to be sufficiently negligible that they may be used as a barrier for contamination (3, 4), making it possible to fabricate capless devices. In addition, they have a high radiation resistance (5, 6). However, silicon nitride has some disadvantages of high surface charge density and crack generation during subsequent heat-treatment. On the other hand, it has been reported that aluminum oxide makes the silicon surface more p-type due to the negative charge (7, 8). This is pertinent to the fabrication of insulated gate field effect transistors with low threshold voltage as well as n-channel enhancement mode devices. Moreover, there are several applications of the aluminum oxide such as a diffusion mask, passivating film for bipolar type devices, and other new structures.

There are various methods for formation of aluminum oxide: pyrolysis of organic compounds such as $Al(C_3H_7O)_3$ (3, 9) and $Al(C_2H_5O)_3$ (10), anodization of aluminum in oxygen plasma (11), reactive evaporation (12), and reactive sputtering (13, 14). The films obtained by the above methods are structureless, *i.e.*, amorphous, but some of these aluminum oxide films have instabilities under thermal stress which are found to be reduced by post annealing at temperatures as low as 400°C. On the other hand, deposition of polycrystalline aluminum oxide films on silicon by the hydrolysis of $AlCl_3$ at about 800°C was reported by Nigh (15) and Doo and Tsang (16). The properties of such polycrystalline films, namely refractive index, etch rate, infrared absorption, and dielectric constant, have been studied by us as a function of deposition conditions, and the MAS (metal-aluminum oxide-silicon) structures have been used to evaluate the electrical properties of the Si-Al_2O_3 interface. All of these results are discussed here.

* Electrochemical Society Active Member.

Experimental

The system used for the deposition of aluminum oxide films on silicon wafers was similar to that reported by Nigh (15) in which H_2O vapor, formed by the reaction of CO_2 with hydrogen, hydrolyzes $AlCl_3$ vapor. All deposition runs were carried out using the following conditions: the flow rates of CO_2, hydrogen saturated with $AlCl_3$ vapor and make-up hydrogen were 326 cc/min, 2 l/min, and 20 l/min, respectively, and the temperature of the silicon wafers was measured by means of an optical pyrometer and was kept at 850°C. The deposition rate of aluminum oxide was approximately 70 Å/min. The silicon wafers with (100) orientation and resistivities of $3 \sim 5$ ohm-cm, either p-type or n-type, were mechanically-chemically polished and carefully cleaned. The cleaning procedure involved rinses in trichlorethylene and acetone using ultrasonic agitation immediately prior to the deposition.

The refractive index and the thickness of the aluminum oxide films were measured by ellipsometry. The etch rate was determined by measuring thickness after each successive etching.

For the evaluation of the electrical properties of the aluminum oxide films and the Si-Al_2O_3 interface, the MAS structure was constructed by the deposition of aluminum oxide on silicon, followed by the evaporation of aluminum electrodes of 1 mm diameter and mounting on TO-5 headers. The C-V characteristics of the MAS structure were measured at 1 MHz. From the area of the electrode, the thickness of the film, and the capacitance of the MAS structure under accumulation conditions the dielectric constant was obtained. The I-V characteristics of the aluminum oxide were also measured by the same MAS structure using a Keithley electrometer in order to analyze the conduction mechanism in the aluminum oxide.

Results

Ellipsometric measurements on the aluminum oxide yielded values for the relative permittivity of $7.6 \sim 7.8$. These are consistent with 7.6 for the film obtained by anodization in oxygen plasma (11), but are less than

those of 8.9 ~ 9.3 (15) and 11 (17) for the films formed by the hydrolysis of $AlCl_3$.

The dielectric strength measured using the MAS structure was found to depend on the polarity of the applied voltage. When positive voltage was applied to the Al electrode, dielectric breakdown occurred at fields of $6 \sim 7 \times 10^6$ and $8 \sim 9 \times 10^6$ V/cm at room and liquid nitrogen temperature, respectively, while for negative polarity it occurred with time dependence, *i.e.*, when a somewhat lower field than $1.1 \sim 1.2 \times 10^7$ V/cm was applied for a few minutes, a thermal current fluctuation of nA order was observed and finally the film underwent breakdown. Similar phenomena have been observed for steam-grown silicon dioxide films, though the polarity dependence was opposite (18).

Figure 1 shows the capacitance-voltage characteristics of an Al_2O_3 film of 1200Å in thickness on n-type silicon substrate at three different temperatures, −196°, 25°, and 250°C. It should be noted that this unit has a nearly zero flat band voltage at room temperature in coincidence with the ideal MIS diode characteristic; the C-V curve shifts in the positive voltage direction at liquid nitrogen temperature and in the negative direction at 250°C. The MAS structure with p-type silicon, however, showed the opposite shifts to that with n-type silicon, indicating that fast surface states exist in the energy gap of silicon. These shifts can be explained by the existence of acceptor- and donor-type surface states near the band edge of the conduction and valence bands, respectively, as reported by Gray and Brown (19) for the thermal grown oxide film. With decreasing temperature down to liquid nitrogen temperature the acceptor-type states above the room temperature Fermi level are filled with electrons so as to make the surface of the silicon more p-type. The amount of scatter in the flat band voltages at room temperature is in the range $0 \sim 0.5$V for n-type silicon and $0.4 \sim 3.0$V for p-type. These positive flat band voltages imply that negative charges of $10^9 \sim 10^{11}$ electron charges/cm^2 exist either at the Si-Al_2O_3 interface or within the Al_2O_3 film. The origin of the negative charge has been explained in terms of the existence of negative ions in the Al_2O_3 film (10), but the negative charge reported here is believed to be due to electrons, as will be discussed later.

The MAS structure exhibited an interesting behavior in that the C-V curves shifted in the positive direction after application of voltages higher than a critical voltage, below which the C-V curves are very stable and reproducible. This positive shift occurred independently of the polarity and type of the bias, such as +d.c., −d.c., a.c., and pulse. Figures 2(a) and 2(b) show the effects of positive and negative bias, respectively, applied to the metal electrode on the C-V

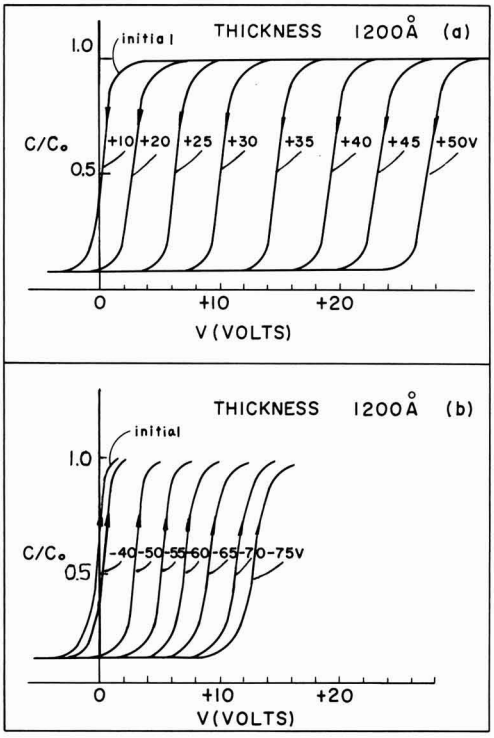

Fig. 2. Capacitance-voltage characteristics after application of various voltages to the Al electrode at room temperature for 1 min: (a) the effect of positive bias; (b) the effect of negative bias.

characteristics of the MAS structure with an Al_2O_3 film of 1200Å in thickness. These curves were taken after application of the bias indicated in the figures at room temperature for 1 min. Figure 3 shows the voltage shifts *vs.* the applied bias, where the critical voltages for the negative and positive bias were +15 and −40V, respectively. With positive bias, voltage shifts continue to increase linearly with applied bias until dielectric breakdown occurs, while with negative voltage linear positive shifts above the negative critical voltage followed by a decrease of the positive shifts are observed. This decrease is always accompanied by increasing current through the aluminum oxide film, which will be discussed later. Such positive shifts were also observed at liquid nitrogen temperature as shown

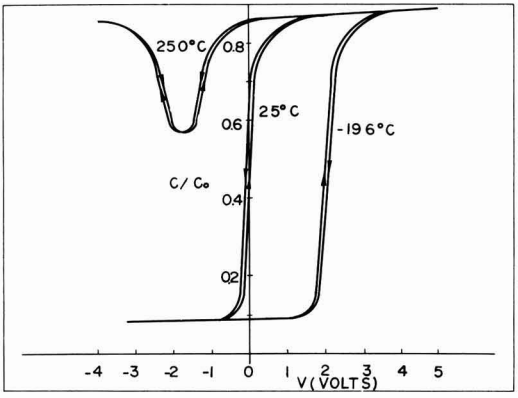

Fig. 1. Capacitance-voltage characteristics of the MAS structure at −196°, 25°, and 256°C, 3 ohm-cm n-type silicon substrate.

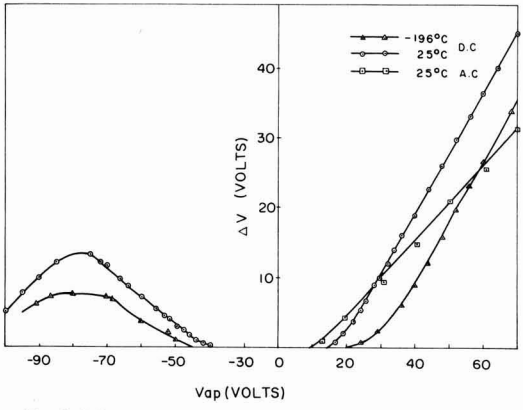

Fig. 3. Relationship between positive shift ΔV and applied voltage (d.c. and a.c., 50 Hz) at room and liquid nitrogen temperature. A-C bias shows peak value; initial flat band voltage is +0.2V.

in Fig. 3, but the lower the temperature, the higher are the critical voltages.

Figure 4 shows the change in the positive shifts when the negative bias is applied to the MAS structure after the positive shifts caused by the positive bias, and when positive bias is applied after the positive shifts by the negative bias. This means that the shifted voltages are kept constant to the same values when the voltage is reversed.

The time dependence of the positive shifts in the C-V characteristics of a typical sample with a 1200Å aluminum oxide film at room temperature for bias values of +40 and −60V is shown in Fig. 5. Although there seems to be a broad distribution of time constant, saturation was observed about 100 min after the application of the bias in both cases. The decay of the shift was studied as a function of film thickness, temperature, and polarity of the applied bias and the results are shown in Fig. 6 and 7. Figure 6 shows a typical decay curve of the positive shift at room temperature, where the shift was caused by application of +100V for 1 min to the MAS structure with a 2400Å aluminum oxide film. An initial decrease of the shift is followed by a very slow decay, where it takes 10^{14} hr to decay by a half of the shift. Figure 7 shows decay curves of the MAS structure with a 1200Å aluminum oxide film at several temperatures, the shifts of which were caused by the application of positive bias as well as negative bias, where samples having nearly the same values of the shift were used. Apparently the decays consist of two parts; 1, a rapid decay for the first several minutes especially for the samples with the shift caused by a positive bias, which

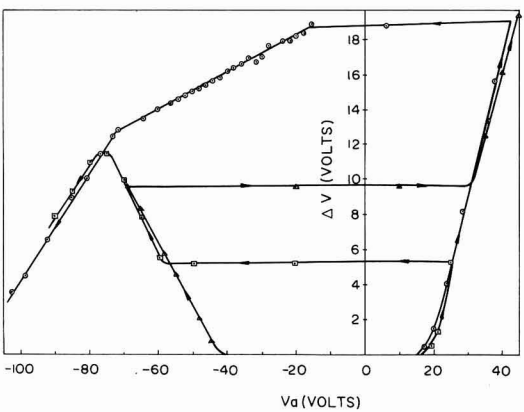

Fig. 4. Dependence of positive voltage shift ΔV of MAS structure with previous bias history on subsequent voltage applications.

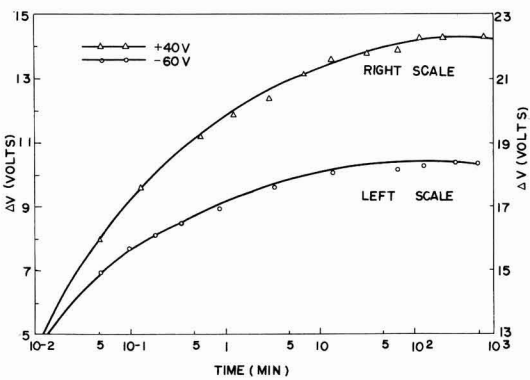

Fig. 5. Plots of positive voltage shift ΔV of an MAS structure with initial flat-band voltage of +0.2V.

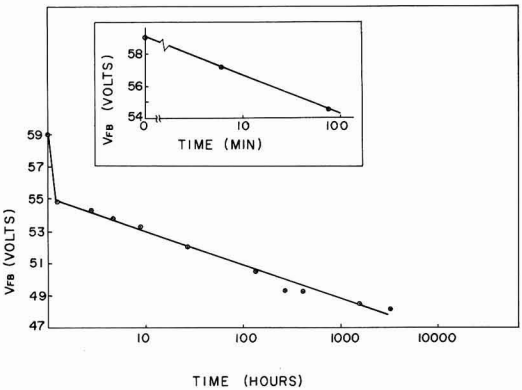

Fig. 6. Decay of positive shift of flat-band voltage with time at room temperature. Insert illustrates initial decay. Film thickness is 2400Å, and p-type silicon substrate is used.

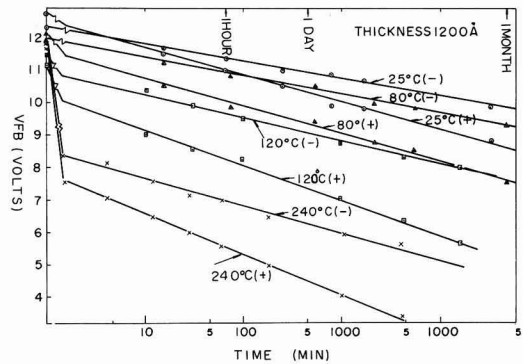

Fig. 7. Thermal annealing of positive shift of MAS structure with initial flat band voltages of +0.2V. Film thickness is 1200Å, and 3 ohm-cm n-type silicon substrate is used.

compares with the initial rapid increase of the shift shown in Fig. 5 and has considerably large temperature and polarity dependencies; 2, a subsequent slow decay which is in proportion to the logarithm of time, the temperature dependence of which is less sensitive than that of the rapid decay and the slope of which is larger for the positive bias than the negative bias.

Figure 8(a) and (b) show the effect of x-rays on C-V characteristics of the as-grown MAS structure

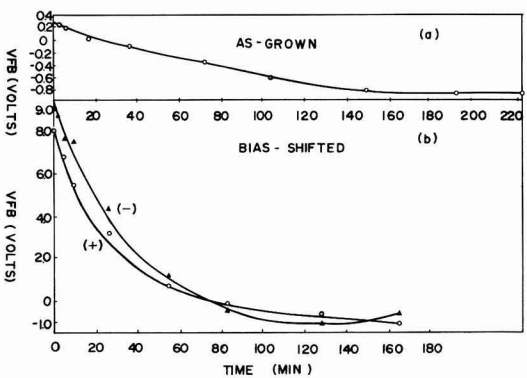

Fig. 8. Effect of x-rays on C-V characteristics of (a) as-grown and (b) shifted MAS structure.

and the shifted one, respectively, where x-rays from a copper target tube operated at 25 kV and 2 mA were irradiated through the aluminum electrode at a distance of 5 cm. No difference of the decay constants for the shift by positive bias and by negative bias was observed. Logarithm of flat-band voltage *vs.* radiation time gave a straight line, indicating exponential decay. The shapes of the C-V curves before and after irradiation were unchanged and an MAS structure which had been returned to the initial state by irradiation with x-rays or an electron beam showed the same positive shift on application of bias greater than the critical voltage as it did in the first place.

In addition to the large positive shifts for the MAS structure, a very slight C-V hysteresis of the order of 0.05V was observed, as shown in Fig. 1, which at room temperature occurred in the same direction of shift as that due to ion migration or polarization, but in the opposite direction at liquid nitrogen temperature. This was also observed on the positive shifted C-V curve with the same order of the hysteresis, that is, this is independent of the positive shift.

A time dependence of the I-V characteristics of the MAS structure was observed. When the applied voltage exceeds the critical voltage above which the positive shift of the C-V curve occurs, the current through the aluminum oxide film decreases gradually for 15 min or longer, then reaches a steady state. An additional I-V measurement of this MAS structure gave lower currents than the previous ones regardless of the polarity. Below the critical voltage, neither a time dependence nor a polarity dependence of the I-V characteristic was observed with ohmic currents in the picoampere range.

Figure 9 shows a typical I-V characteristic of the MAS structure with a 1400Å aluminum oxide film for positive and negative bias, where each point indicates the current measured 20 min after application of the bias. At higher voltages than the critical voltage, the current increases exponentially with the square root of the applied voltage over several decades of current.

The temperature dependence of the current through aluminum oxide films is shown in Fig. 10 and 11.

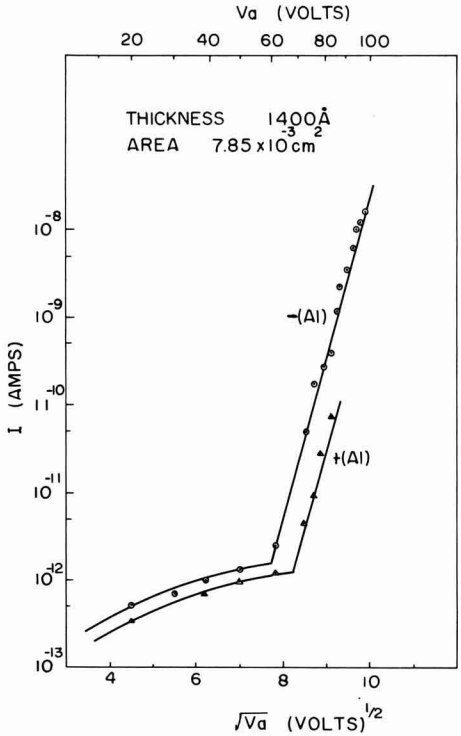

Fig. 9. Current *vs.* square root of applied voltage for both polarities at room temperature for MAS structure with 1400Å aluminum oxide film and electrode area of 7.85×10^{-3} cm^2. Positive bias is applied after measurement of I-V characteristic with negative bias.

Discussion

Positive shifts by bias voltages have been reported in MIS structures with insulators such as phosphosilicate glass (20), silicon nitride (21, 22), and reactively sputtered aluminum oxide (12) by several workers. Those of the phosphosilicate glass, the silicon nitride, and the aluminum oxide have been explained in terms of polarization of the glass, injection of electrons, and mobile negative ions, respectively. The aluminum oxide in this work shows a different type of positive shift, that is, the positive shifts occur independently of the type and polarity of the applied bias such as +d.c., −d.c., a.c., and pulse, and are observed in the same direction even at liquid nitrogen temperature. This means that these shifts are neither due to ionic transport nor to ionic polarization, but to electronic phenomena. Therefore, the positive shifts of the aluminum oxide are based on a different origin than those for the reactively sputtered aluminum oxide because ionic migration is quite improbable at liquid nitrogen temperature. These shifts can be explained by electron trapping in the aluminum oxide as follows: when a positive bias is applied to the MAS structure, electrons are injected from the semiconductor into the aluminum oxide by tunneling (23) and some of them are trapped in trapping states. This injection needs some energy which results in the critical field as reported in silicon nitride by Deal *et al.* (22). However, when a negative bias is applied, electrons are injected from the metal to the aluminum oxide to cause the positive shifts. Similar explanations have been proposed for sputtered silicon nitride, although the

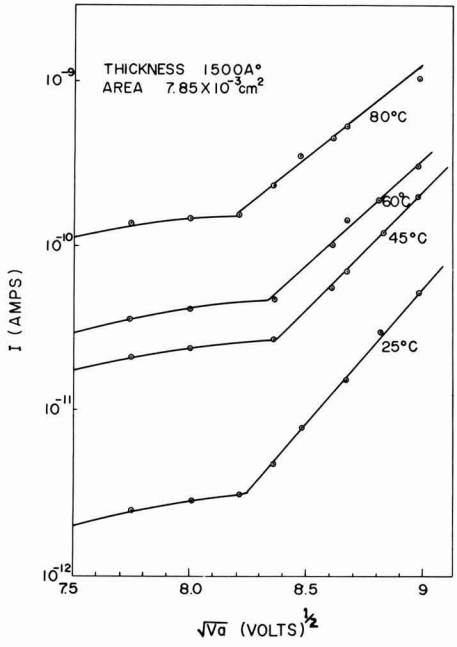

Fig. 10. Current *vs.* square root of applied positive voltage at four different temperatures with 1500Å aluminum oxide.

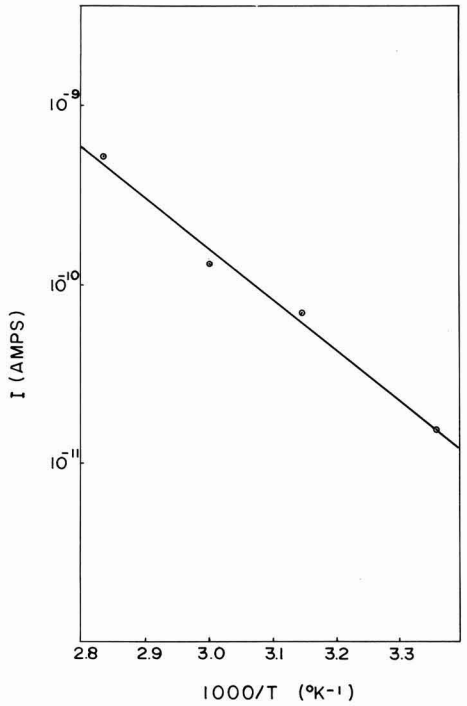

Fig. 11. Current vs. $1/T$ at voltage of + 75V in Fig. 10

carriers injected were holes rather than electrons (24). As the electron trapping near Si-Al_2O_3 interface is efficient, it takes more energy to trap electrons at negative than at positive bias. This model for the positive shifts is supported (*i*) by the fact that the positive shifts by negative bias decay more slowly and have smaller initial decay than those by positive bias as shown in Fig. 7, that is, the trapped electrons near the interface are more easily released than those away from the interface; and (*ii*) by the fact that the trapped electrons by negative bias as well as by positive bias can be excited by radiation such as x-rays and electron beam without introduction of damage. Although several radiation effects have been reported and explained by radiation damage in MIS structures (25), with the excitation of trapped electrons the drift due to the built-in field in the aluminum oxide is responsible for the exponential decay of the positive shifts by x-rays, as shown in Fig. 9.

The decrease of the positive shifts by higher negative bias as shown in Fig. 3 is always accompanied by an exponential increase of the current through the aluminum oxide, so that this is due to the release of trapped electrons by the rapid increase in current. A similar decrease was reported for a MOS structure with three different SiO_2 films (26).

The aluminum oxide film used in this work did not show any distinguishable change in its electrical properties when it was heated below the deposition temperature. Further, under bias temperature stress of the MAS structure, no appreciable change was observed in its flat band voltage below a critical voltage at the temperature of the bias temperature stress.

The critical voltage for the positive shifts is temperature dependent. As shown in Fig. 3, the critical voltages increase with decreasing temperature with negative bias as well as with positive bias because of the increase of the barrier height for injection.

The initial decay of the positive shifts with a strong temperature dependence as shown in Fig. 7 is also explained by the barrier height lowering at elevated temperature. The decay of the positive shifts depends on the distribution of trapped electrons, so the application of higher negative voltage after positive shift by a positive bias produces a redistribution of trapped electrons, that is, the trapped electrons near the interface are easily released to the semiconductor. Therefore, positive shifts thus obtained are more stable than those by the positive bias alone. Similar redistribution occurs when positive shifted MAS structures are exposed to x-rays and electron beams.

On the other hand, the time dependence of I-V characteristics previously mentioned can be interpreted by the change of space charge distribution due to electron injection. This is closely related to the time dependence of the C-V characteristics. This means that the electric field in the aluminum oxide has a spatial distribution due to the electron injection, particularly, near the Si-Al_2O_3 interface. This is one of the reasons why we describe the positive shifts as a function of applied voltage rather than electric field.

The I-V characteristics obtained in this work are very similar to those reported by Sze for silicon nitride (27) due to hopping of thermally excited electrons from one isolated state to another at lower voltages. Assuming the rapid increase in current as internal Schottky or Poole-Frenkel current, a static dielectric constant of 3.4 is obtained which is in approximate agreement with the square of the refractive index of 1.78. Furthermore, from the slope of ln I *vs.* $1/T$, an activation energy of 1.3 eV is obtained which is to be compared with 1.3 and 1.5 eV for Si_3N_4 obtained for the $SiCl_4$-NH_3 system and the SiH_4-NH_3-H_2 system (28), respectively.

The MNOS structure has been extensively investigated for memory devices (29). This MAS structure also has been utilized for the fabrication of a read-only memory (30) consisting of MAS FET's, which can be written by electron injection from the semiconductor as well as from the metal. The amount of current through the Al_2O_3 film is 2 orders smaller than that through Si_3N_4 films and, as can be seen from Fig. 8, both the positive-shifted MAS structure and the as-grown one are very stable between $\pm$20V which corresponds to an electric field of 2×10^6 V/cm.

Conclusions

The properties of aluminum oxide films prepared by the hydrolysis of $AlCl_3$ have been evaluated by using a MAS structure. The positive shifts of the flat band voltages of the MAS structure occur independently of the polarity and type of the applied bias when this is higher than a critical voltage, under which the MAS structure has stable C-V characteristics. These positive shifts can be explained by electron injection and trapping in the aluminum oxide. The trapped electrons persist for a long time before discharge. However, they can be excited by radiation such as x-rays and electron beams without damage to the MAS structure and, as they drift and discharge, the positive shift decays exponentially. These aluminum oxide films are suited for the insulator in nonvolatile field-effect memory devices.

Acknowledgments

The authors wish to thank Drs. A. Ohuchi, S. Tsuneki, Y. Matsukura, Y. Haneta, and K. Kobayashi for many stimulating discussions. Thanks are also due to Messrs. S. Konno and M. Nakagiri for their assistance with the experimental work.

Manuscript received Nov. 10, 1969; revised manuscript received Jan. 20, 1970.

Any discussion of this paper will appear in a Discussion Section to be published in the December 1970 JOURNAL.

REFERENCES

1. S. R. Hofstein, *Solid-State Electronics*, **10**, 657 (1967).
2. E. H. Snow, A. S. Grove, and D. J. Fitzgerald, *Proc. IEEE*, **55**, 1168 (1967).

3. N. C. Tombs, H. A. Wegener, R. Newman, B. T. Kenny, and A. J. Coppola, *ibid.*, **54**, 87 (1966).
4. S. K. Tung and R. E. Caffrey, Paper 477 presented at the Montreal Meeting of the Society, Oct. 6-11, 1968.
5. A. G. Holmes-Siedle and K. H. Zaininger, *Solid State Tech.*, **12**, 40 (1969).
6. K. H. Zaininger and A. S. Waxman, *IEEE Trans.*, **ED-16**, 333 (1969).
7. J. A. Aboaf, *This Journal*, **114**, 948 (1967).
8. H. Matsushita and Y. Koga, Paper 90 presented at the Boston Meeting of the Society, May 5-9, 1968.
9. S. Krongelb, *This Journal*, **116**, 1583 (1969).
10. S. Nishimatsu, T. Tokuyama, and M. Matsushita, Paper 480 presented at the Montreal Meeting of the Society, Oct. 6-11, 1968.
11. A. Waxman and K. H. Zaininger, *Appl. Phys. Letters*, **12**, 109 (1968).
12. E. Ferrieu and B. Pruniaux, *This Journal*, **116**, 1008 (1969).
13. R. G. Frieser, *ibid.*, **113**, 357 (1966).
14. T. Tanaka and S. Iwauchi, *Japan J. Appl. Phys.*, **7**, 1420 (1968).
15. H. E. Nigh, Paper 476 presented at the Montreal Meeting of the Society, Oct. 6-11, 1968.
16. V. Y. Doo and P. J. Tsang, Paper 16 presented at the New York Meeting of the Society, May 4-9, 1969.
17. H. Teshima, Y. Tarui, and T. Matsuoka, Inst. Electronics Comm. Engrs. Japan Mtg. Oct. p. 765 (1967).
18. F. L. Worthing, *This Journal*, **115**, 88 (1968).
19. P. V. Gray and D. M. Brown, *Appl. Phys. Letters*, **15**, 31 (1966).
20. E. H. Snow and B. E. Deal, *This Journal*, **113**, 264 (1966).
21. S. M. Hu, *ibid.*, **113**, 693 (1966).
22. B. E. Deal, P. J. Fleming, and P. L. Castro, *ibid.*, **115**, 300 (1968).
23. E. P. Herman and G. Warfield, *IEEE Trans.*, **ED-12**, 167 (1965).
24. S. M. Hu, D. R. Kerr, and L. V. Gregor, *Appl. Phys. Letters*, **10**, 97 (1967).
25. J. P. Mitchell, *IEEE*, **ED-14**, 764 (1967).
26. K. Kobayashi and Y. Haneta, Japan Appl. Phys. Soc. Fall Mtg. (1969).
27. S. M. Sze, *J. Appl. Phys.*, **38**, 2951 (1967).
28. G. A. Brown, W. C. Robinette, Jr., and H. G. Carlson, *This Journal*, **115**, 948 (1968).
29. E. C. Ross and J. T. Wallmark, *RCA Rev.*, **30**, 366 (1969).
30. S. Nakanuma, T. Tsujide, R. Igarashi, K. Onoda, T. Wada, and M. Nakagiri, IEEE International Solid-State Circuits Conference, Session VI (6.2), (1970).

Technical Notes

Divalent Rare Earth Activated 96% SiO_2 Glass

A. Wachtel

Westinghouse Electric Corporation, Bloomfield, New Jersey

Doping of porous 96% silica glass (1, 2) with organic dyes or transition metal ions, the latter followed by heat-treatment, is a well-known process for the preparation of color filters (3). Claffy, Ginther, and Arnold (4) reported on Ce, Sm, Mn, and Cu activated phosphors based on this material.

The present note describes the fluorescence of the divalent rare earths Eu^{2+}, Yb^{2+}, and Sm^{2+}, which is obtained only if Al^{3+} is also present. The glasses are therefore related to the high-SiO_2 form ("Phosphor I") of aluminosilicates which was described in an earlier publication (5), the principal differences in composition being only the B^{3+} content and the lower Al^{3+} content of the glasses.

The purpose of this note is twofold: (*i*) it shows that the effect of B^{3+} provides additional evidence concerning the nature of the Eu^{2+} activator center (5), and (*ii*) it attempts to explain the large effect of particle size on the spectral energy distribution of the Eu^{2+} emission in terms of optical cascade energy transfer.

Experimental

The raw material consisted of Corning No. 7930 glass ("thirsty Vycor") which contained 6.9×10^{-3} g atoms Al/mole. In the few instances where Al-free glass was required (Al = 0 points in Fig. 2), a raw material was prepared, in this laboratory, from 55 w/o (weight per cent) SiO_2-10 w/o Na_2O-35 w/o B_2O_3 glass by annealing at 575°C for 20 hr, and leaching in dilute HCl. The glasses were activated by impregnating with aqueous $RE^{3+}(NO_3)_3 + Al(NO_3)_3$ solutions of appropriate concentrations, followed by firing in a reducing atmosphere.

Fluorescence intensity of Eu-activated glass was measured by use of an integrating sphere in which specimens were excited through a 254 nm transmitting interference filter. Measurements were also taken on ground samples, using conventional powder plaques for which the intensity of 254 nm excitation was standardized with $CaWO_4$:Pb, NBS No. 1026. The detector used was the Spectra Brightness Spot Meter[1] set on "blue" ($\bar{z}$ sensitivity). Emission and excitation spectra were obtained as described by Thornton (6).

Results and Discussion

Figure 1 shows fluorescence intensity as a function of Eu for low or high Al concentrations. The former represent samples not intentionally doped with Al, *i.e.*, containing 6.9×10^{-3} Al/mole. The latter were prepared by impregnation, at 95°C, with fused salt mixtures $Al(NO_3)_3 \cdot 9H_2O + Eu(NO_3)_3 \cdot 6H_2O$. While fluorescence intensities of the samples prior to and after grinding are measured differently and are therefore not directly comparable, it can be seen that in both cases, maxima occur near 4×10^{-4} and 5×10^{-3} Eu. At approximately three times higher Eu concentrations, the samples acquired a yellow body color caused by a broad absorption band which is otherwise not present. At still higher Eu concentrations, the glasses devitrified. Note that the fluorescence intensity of unground specimens is highest at low Al and Eu concentrations, while the opposite holds true for powders.

Figure 2 shows fluorescence intensity, at three Eu concentrations, as a function of Al up to the highest

[1] Photo Research Corporation, Hollywood, California.

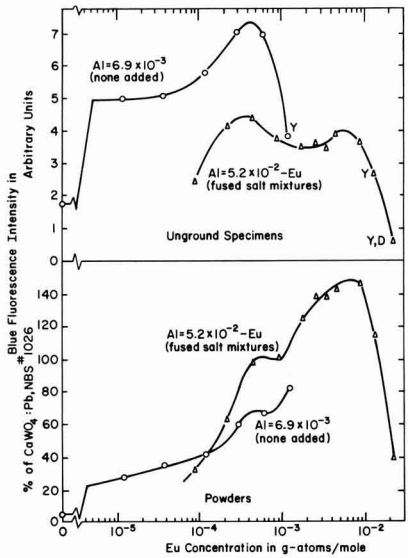

Fig. 1. Fluorescence intensity of 96% SiO_2 glass as a function of Eu^{2+} concentration. Y, yellow discoloration; D, devitrification.

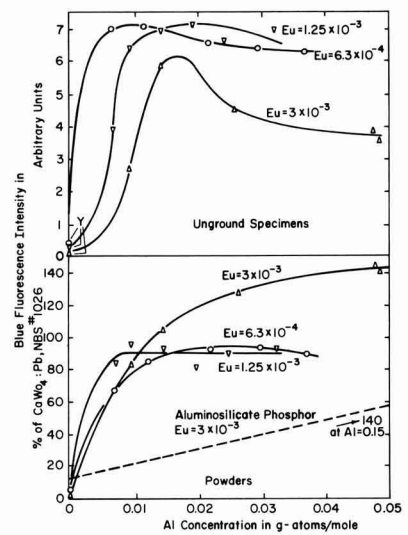

Fig. 2. Fluorescence intensity of Eu^{2+} in 96% SiO_2 glass as a function of Al concentration. Y, yellow discoloration.

attainable with the fused salt mixtures. In contrast to phosphors with varying Eu concentration (Fig. 1), single maxima are obtained; however, we note again that grinding shifts these to higher doping levels. The actual fluorescence intensity of powders prepared with 3×10^{-3} Eu becomes comparable to that of aluminosilicate phosphor I (5). It can be seen that in the powdered glasses, this fluorescence intensity level is obtained at somewhat less than 5×10^{-2} Al/mole, *i.e.*, at three times lower Al concentration than in the aluminosilicate phosphor,[2] and the shape of the curve suggests that at still higher Al concentrations, it would not be appreciably increased. At lower Eu concentrations, maximum fluorescence intensity in powders is obtained within the concentration range employed, but again, the fluorescence increases rapidly with increasing Al concentration. At Al = 0, the data were obtained on samples prepared with the Al-free raw material. These samples were essentially nonluminescent and showed a yellow body color even at the lowest Eu concentration.

A search for crystalline inclusions (mullite) which, in the case of the aluminosilicate phosphor, were proposed to be instrumental in the luminescence process, was unsuccessful. Even highly doped glasses failed to show distinct x-ray reflections or revealed significant inhomogeneities in electronphotomicrographs taken by transmission through thin edges.

The principal differences between the present glasses and the aluminosilicate phosphor, therefore, are the B^{3+} content of the glasses, and the lower Al^{3+} concentration which is required to produce the same fluorescence intensity observed in the aluminosilicate phosphor. The relatively large Eu^{2+} ion is a network modifier and therefore occupies interstitial sites. Charge compensation of network modifiers in silicate glasses by Al^{3+} or B^{3+} leads to formation of network forming (substitutional) $[AlO_4]$ or $[BO_4]$ tetrahedra (7-9). Each Eu^{2+} ion then requires two M^{3+} according to $2M^{3+} + Eu^{2+} = 2Si^{4+}$. The present experimental evidence, however, indicates that the activator center involves network modifying (interstitial) $[AlO_6]$ groups. This evidence may be summarized as follows: (*i*) Boron does not give rise to Eu^{2+} luminescence. Unlike Al^{3+}, it enters the SiO_2 network only substitutionally, an excess over low-valence modifiers forming triangularly coordinated $[BO_3]$ groups (9, 10). It is likely, therefore, that Eu^{2+} charge-compensated by substitutional Al^{3+}, is also nonluminescent. (*ii*) At low concentrations, Al^{3+} normally tends to occupy substitutional sites; in the presence of B^{3+}; however, some of the Al is displaced into interstitial sites (11, 12). The more rapid rise of fluorescence intensity with Al concentration in the (B-containing) glasses, as compared with the aluminosilicate phosphor, can therefore be explained by the more rapid rise in concentration of interstitial Al. (*iii*) Even in the glasses, maximum fluorescence intensity obtains at Al/Eu ratios which are substantially higher than the 2/1 ratio suggested by charge compensation. Again, such excess Al is known to occupy interstitial sites (9, 12, 13).

These arguments suggest that the luminescence center in the (homogeneous) glasses is basically no different from that proposed for the heterogeneous aluminosilicate phosphor in which Eu^{2+} replaces Al^{3+} at a mullite surface, and is charge compensated by Si^{4+} at the adjacent amorphous SiO_2 phase (5). In both cases, Al is a cation, and only the size of $[AlO_6]$ aggregates and the degree of crystalline order of interstitial aluminosilicates is different.

Emission spectra consist of bands with widths at half maximum averaging 77.1 nm in unground, and 75.6 nm in ground glasses. Variations in Eu concentration primarily affect the peak emission wavelengths as seen in Fig. 3. This figure shows the same low and high Al series shown in Fig. 1. In both cases, it can be seen that at high as well as low Eu concentrations, the emission spectra are independent of particle size. At moderate Eu concentrations, however, differences become pronounced, particularly in the high Al glasses. At 2.7×10^{-3} Eu, this difference is at a maximum of 10 nm. A displacement of the emission band is also observed by shifting the excitation of powders to longer wavelengths, as shown in Table I. Here it can be seen that in going from 254 to 405 nm excitation, the emission peak is shifted to longer wavelengths by 15.6 nm. The table also shows that the width at half maximum does not decrease (as expected by lack of emission below 405 nm), but actually increases by 2.2 nm.

Figure 4 shows the emission of the 2.7×10^{-3} Eu glass under 254 nm excitation. The excitabilities of the

[2] In ref. (5), Al was expressed as Al_2O_3 with the optimum at 0.075, *i.e.*, 0.15 Al.

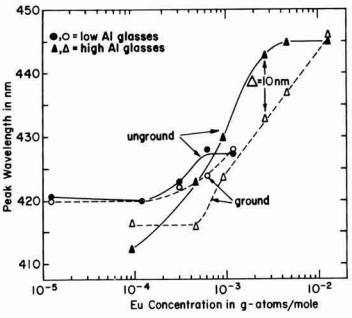

Fig. 3. Peak emission wavelength of 96% SiO_2 glass, under 254 nm excitation, as a function of Eu^{2+} concentration.

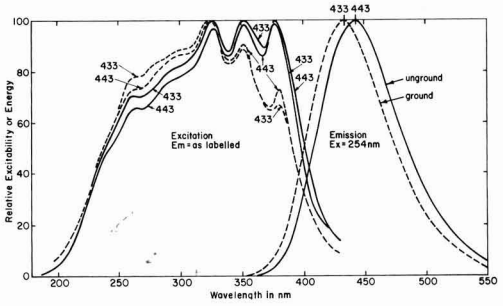

Fig. 4. 254 nm—excited emission spectra, and excitation spectra of 96% SiO_2 glass containing 2.7 x 10^{-3} Eu^{2+}/mole. Numbers in figure denote wavelength of measured emission.

two peak emission wavelengths, shown by the numbers in the figure, are also included. The relative heights of these are seen to vary with the observed emission wavelengths in the direction one would expect, and even more strongly with the particle size. In the latter case, the displacement is in the direction of greater excitability of powders at shorter wavelengths.

The 10 nm shift to longer wavelengths of the emission of the unground glass, as compared to that of the powder, is not due to self-absorption alone, since the emission band width is not narrower. It is therefore caused by excitation energy at longer wavelengths which is present in addition to the 254 nm radiation employed. Figure 4 shows that this energy originates from the 254 nm-excited emission of the glass, and that radiation near 400 nm (the center of overlap between the excitation and emission spectra) is primarily responsible for this process. Since pure 405 nm excitation of the powder caused a shift of 15.6 nm (Table I), it follows that in the present case, the shift should be smaller. The observed value of 10 nm, therefore, indicates that about 2/3 of the emission of the unground glass originates from optical cascade energy transfer. A detailed treatment of powder-optical processes which contribute to the present discussion is given by Melamed (14).

Table I. Emission properties of powdered 96% SiO_2 glass doped with 4.9 x 10^{-2} Al^{3+} and 2.7 x 10^{-3} Eu^{2+}

Excitation wavelength, nm	Emission peak wavelength, nm	Emission width at half maximum nm
254	433.0	76.0
365	435.5	75.2
405	448.6	78.2

96% silica glass (as well as the aluminosilicate phosphor) can also be activated by Yb^{2+} or Sm^{2+}, although these elements proved to be more difficult to reduce to the divalent state than Eu. Figure 5 shows excitation and emission spectra of an unground specimen of glass doped with 4.4 x 10^{-3} Al + 2.2 x 10^{-3} Yb/mole and fired in H_2 for 20 hr. The excitation spectrum, taken with Hg lines, is corrected for equal quanta of exciting radiation, but may contain more detail than indicated in Fig. 5. Nevertheless, it appears that there may be four excitation bands in addition to the pronounced increase in excitability towards short wavelengths. The broad emission band is unproportionally high on the short wavelength side, and therefore may consist of a number of unresolved bands. Figure 6a shows excitation and emission spectra of a glass doped with 4.4 x 10^{-3} Al + 2.2 x 10^{-3} Sm, fired in air, and Fig. 6b shows the same glass fired in H_2 for 20 hr. The excitation spectra in Fig. 6a and 6b were taken with a continuous source of uv, and are also corrected for equal quanta of exciting radiation. It can be seen that at 77K, neither the excitation nor the emission spectra of Sm^{2+} are significantly better resolved, although the vibronic side bands are markedly decreased. In this respect, the emission line widths of Sm^{2+} in the glasses differ from those in many crystalline matrices (15-19) where usually, broad bands are observed at room temperature. It should also be noted that the emission of the H_2-fired glass includes weak lines at 602 and 649 nm due to Sm^{3+}; with 254 nm excitation (not shown) these are considerably enhanced. This is caused by incomplete reduction in spite of the prolonged firing, and due to the relatively high reduction potential of Sm (20). For this reason, optimum doping with Sm (or Yb) is somewhat higher than with Eu, and detailed measurements of fluorescence as a function of actual Sm^{2+} or Yb^{2+} concentration have not been carried out.

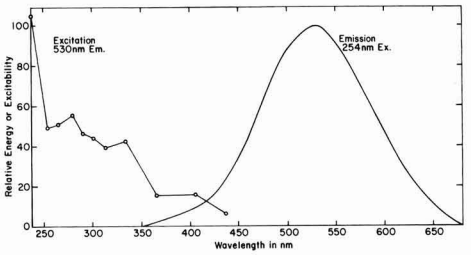

Fig. 5. Excitation and emission spectra of 96% SiO_2 glass doped with 4.4 x 10^{-3} Al + 2.2 x 10^{-3} Yb/mole, fired in H_2 at 1150°C for 20 hr.

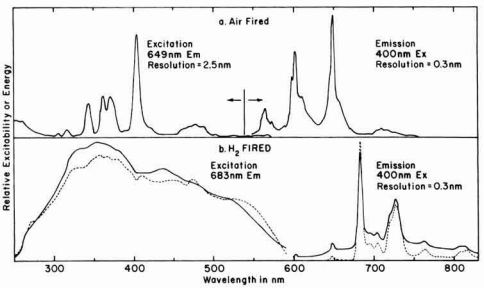

Fig. 6. Excitation and emission spectra of 96% SiO_2 glass doped with 4.4 x 10^{-3} Al + 2.2 x 10^{-3} Sm/mole; a, fired in air at 1150°C for 3 hr; b, fired in H_2 at 1150°C for 20 hr. Solid lines = spectra at room temperature; broken lines = spectra at 77K.

Acknowledgments

The writer wishes to thank Miss I. Walinski for sample preparation and measurements, and W. A. Thornton, N. T. Melamed, W. B. White, and C. Hirayama for spectra and helpful discussions. E. P. Riedel kindly determined the spectra of the Sm activated glasses.

Manuscript submitted June 30, 1969; revised manuscript received *ca.* Jan. 26, 1970. This was Paper 87 presented at the New York Meeting of the Society, May 4-9, 1969.

Any discussion of this paper will appear in a Discussion Section to be published in the December 1970 JOURNAL.

REFERENCES

1. H. P. Hood and M. E. Nordberg, U.S. Pat. 2,106,744, Feb. 1, 1938; 2,215,039, Sept. 17, 1940; 2,221,709, Nov. 12, 1940; 2,286,275, June 16, 1942.
2. K. Kühne and W. Skatulla, *Silikattechnik*, **10**, 105 (1959).
3. M. E. Nordberg and H. E. Rumenapp, U.S. Pat. 2,303,756, Dec. 1, 1942; 2,315,329, March 30, 1943; 2,340,013, Jan. 25, 1944; 2,355,746, Aug. 15, 1944; and H. P. Hood and M. E. Nordberg, U.S. Pat. 2,315,329, March 30, 1943.
4. R. J. Ginther, J. H. Schulman, and G. W. Arnold, Extended Abstract 26, New York, Meeting of the Society May 4-9, 1959.
5. A. Wachtel, *This Journal*, **116**, 61 (1969).
6. W. A. Thornton, *ibid.*, **116**, 286 (1969).
7. R. H. Doramus, *Phys. Chem. Glasses*, **10**, 28 (1969).
8. M. W. Safford and A. Silverman, *J. Am. Ceram. Soc.*, **30**, 203 (1947).
9. A. A. Appen, The Structure of Glass, Proc. All-Union Conf. Glassy State, Leningrad (1953). Consultants Bureau Trans. pp. 75-82 (1958).
10. Tosio Abe, *J. Am. Ceram. Soc.*, **35**, 284 (1952).
11. E. I. Galant, The Structure of Glass, Proc. All-Union Conf. Glassy State, Leningrad (1953). Consultants Bureau Trans. pp. 451-3 (1960).
12. N. I. Vlasova, E. I. Galant, and A. A. Kefeli, *ibid.*, Vol. 2, pp. 327-30 (1960).
13. Sook Lee and P. J. Bray, *Phys Chem. Glasses*, **3**, 37 (1962).
14. N. T. Melamed, *J. Appl. Phys.*, **34**, 500 (1963).
15. G. H. Dieke and R. Sarup, *J. Chem. Phys.*, **36**, 371 (1962).
16. A. W. Smith, *Appl. Optics*, **3**, 147 (1964).
17. J. P. Axe and P. P. Sorokin, *Phys. Rev.*, **130**, 945 (1963).
18. V. H. Konyukhov, V. M. Marchenko, and A. M. Prokhorov, *Opt. and Spectros*, **20**, 299 (1966).
19. B. I. Bykovskii and V. F. Pisarenko, *ibid.*, **26**, 271 (1969).
20. W. Noddak and A. Brukl, *Angew. Chem.*, **50**, 362 (1937).

Beryllium as an Acceptor in Silicon

E. A. Taft and R. O. Carlson

General Electric Research and Development Center, Schenectady, New York

The high oxygen content of Czochralski grown silicon crystals is well known (1), and some study has been made of the reactions of group III acceptors with this oxygen (2). The high free energy of formation and great thermal stability of BeO is also well established (3). The possibility of beryllium combining with oxygen in liquid or solid silicon to form a stable, electrically inactive impurity led to our investigation.

Experimental

Beryllium has been added to 500 ohm-cm silicon to be pulled from quartz crucibles. Single-crystal material was difficult to grow by this method because of nucleation from oxides on the melt surface, but specimens which could be studied were obtained. A beryllia crucible was also found to be suitable for use in pulling doped single-crystal silicon. However, the reaction of molten silicon with the crucible wall supplied the dopants, and the amount of dopant obtained could not be controlled. Also beryllium was diffused into oxygen-containing n-type and p-type silicon wafers at 1170°C for times up to 16 hr. It was found that consistent results could be obtained only if the beryllium metal was not directly exposed to the quartz walls of the furnace. The silicon test sample was, therefore, enclosed with beryllium in a cavity of silicon while the diffusion proceeded. In addition, float-zoned crystal of 1 ohm-cm beryllium doped oxygen-free silicon was made available by R. J. Mulligan. These variously doped crystals were then studied in infrared absorption, resistivity, Hall effect, and heat treatment.

Results

The oxygen content of undoped silicon crystals pulled from small quartz crucibles is typically 10^{18} atoms/cm^3. The oxygen is readily determined by infrared absorption (1). Beryllium doped crystals pulled from similar quartz crucibles typically contained 10^{17} atoms/cm^3 of oxygen, a moderate reduction. There is possibly some gettering of oxygen by beryllium in the melt, but, more likely, the formation of a beryllium silicate on the quartz crucible wall reduced the reaction rate of molten silicon with quartz. Crystals pulled from beryllia crucibles were found to contain oxygen in amounts comparable to that found for the beryllium doped crystals pulled from quartz crucibles. This oxygen level does not approach the concentrations of 10^{15} atoms/cm^3 found in float zoned silicon.

The distribution coefficient, k, of Be in silicon was obtained for a number of crystals pulled from quartz crucibles. The impurity concentration, C_S, of acceptors was obtained from traveling probe resistivity data at room temperature (4). (Most of the acceptors are ionized at the low concentrations obtained.) C_S is plotted against the atom fraction, g, of the initial charge solidified in a pulled crystal in Fig. 1. The curve $C_S = kC_L/1 - g$ contains the initial concentration, $C_L = 3.2 \times 10^{19}$ atoms/cm^3 of beryllium in the liquid obtained from the initial weighed charges of beryllium and silicon. For best fit to the points, k was selected at 1.3×10^{-4}. The consistency in results for several crystals measured, and the excellent fit to the curve, indicate that the dopant losses during the crystal growth were not significant. All crystals were "p" type showing values between 1.3 and 1.6×10^{-4} for k.

N-type silicon of 50 ohm-cm and of 0.06 ohm-cm was converted to p-type after Be was diffused at 1170°C for up to 16 hr, indicating the acceptor nature of the Be center. As the resistivity of these crystals was no longer changing with time of diffusion, the silicon appeared to be saturated with Be after this treatment. The resistivity *vs.* temperature for one of these crystals, Be 3, is shown in Fig. 2. Also in this figure are the data for K-97, a Be-doped crystal pulled from a quartz crucible. These p-type crystals prepared by different methods show the same deep-lying acceptor level of Be. The carrier concentration derived from Hall effect data for these same two crystals is given in

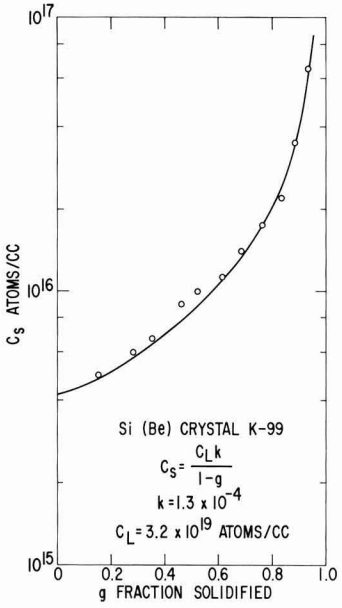

Fig. 1. Distribution coefficient of beryllium in silicon; k is chosen for best fit to the data points.

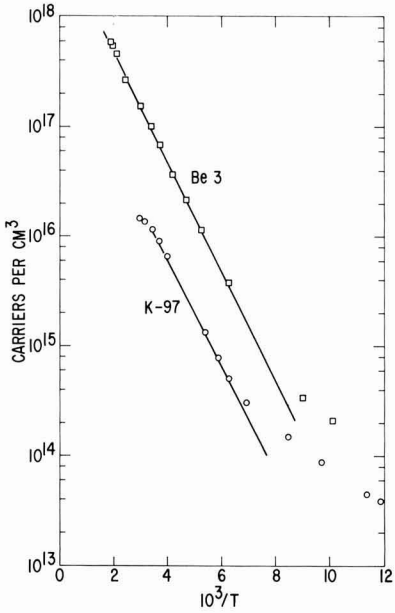

Fig. 3. Temperature variation of hole concentration in beryllium doped silicon derived from Hall effect data.

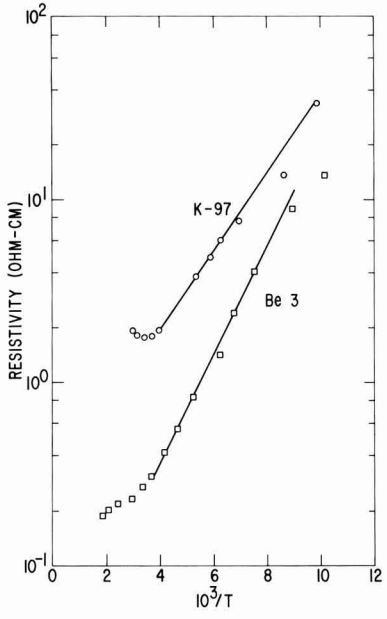

Fig. 2. Temperature variation of resistivity for beryllium doped silicon. K-97 is a grown crystal containing Be; Be 3 is a Be diffused silicon sample.

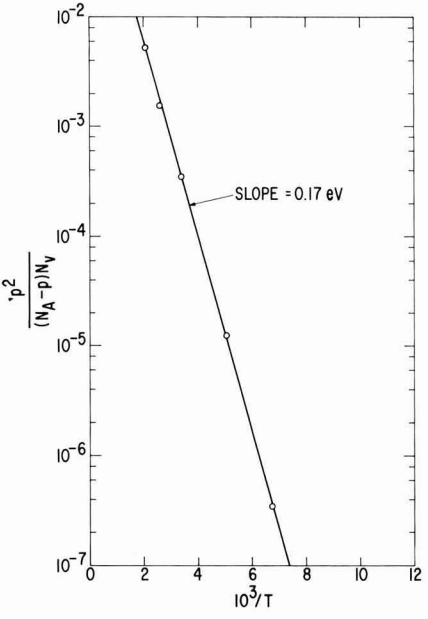

Fig. 4. Acceptor level determination from Hall effect data using corrections for total acceptor sites and for temperature variation of valence band density of states.

Fig. 3. A room-temperature mobility of 230 $cm^2\ V^{-1}\ sec^{-1}$ with an exponential temperature dependence of -2.4 for Be 3 shows that this crystal exhibits reasonable behavior for doped silicon. K-97 also exhibits normal mobility values.

Further analysis of the Hall effect data, such as that used by Hutson (5), yields the curve of Fig. 4. All crystals analyzed were similar in showing an activation energy of 0.17 eV for the Be acceptor center. Following Hutson, the intercept of Fig. 4 can be used to estimate the degeneracy of the Be center. As Fig. 4 was derived from a crystal with $< 10^{14}$ donor centers, compensation was negligible and the simpler equation is used.

$$\frac{p^2}{(N_A - p)N_V} = \left(\frac{m}{m}\right)^{*3/2} D^{-1} \exp\left(\frac{-E_o}{kT}\right)$$

The intercept is 0.25, $(m/m)^{*3/2}$ is 0.45 for holes in silicon leaving a degeneracy factor $D = 1.8$ or closely 2.

The possibility that Be contributes two levels in silicon has been considered but not investigated. The chemically similar element, zinc, is known to give two levels (6). If beryllium is considered to be a well-behaved solute in silicon, the distribution coefficient can be used to estimate the solid solubility at any temperature (7). Our coefficient of 1.3×10^{-4} would give an equilibrium concentration of 5×10^{17} Be atoms/cm^3 at 1170°C. As the data of the diffused sample Be 3 of Fig. 3 do not show a saturation of carriers, the room-temperature value has been utilized. Assuming an acceptor level of 0.17 eV in silicon, the number of acceptors needed to get the 10^{17}/cm^3 room-temperature carriers observed in Fig. 3 is calculated in the usual textbook approach. The value of 1.2×10^{18}/cm^3 acceptors obtained is higher than, but in reasonable agreement with, the value obtained from the distribution coefficient. Our data are not considered to be of sufficient accuracy to deduce an arguable meaning, such as two energy levels, from these differences in acceptor concentration.

Further trying to take advantage of the affinity of beryllium for oxygen, some of the crystals were subjected to heat treatment at 1000°C. The crystals contained initially 10^{16} atoms/cm^3 of Be and 10^{17} atoms of O_2 as determined from resistivity and from infrared absorption, respectively. The room-temperature resistivity of the samples rose by a factor of over 100 after only a few hours of heating. The Be was no longer active electrically and only background impurities of $< 10^{14}$/cm^3 were in evidence. The oxygen content changed little, if at all, but the oxygen was of course in great excess relative to the beryllium. A short heat treatment at 1300°C did not return the resistivity to the original value as is the case for the more usual dopants upon interaction with dissolved oxygen (8). The beryllium was thus not available for redissolution (9). In this case, it is not clear whether the Be actually left the crystal by means of diffusion to the surface or whether a Be-O combination is too tightly bound to be dissociated to any extent at 1300°C.

A 2 mm thick piece of oxygen-free beryllium doped ($\sim 10^{16}$/cm^3) crystal was heated in argon at 1050°C for 1 hr. The room-temperature resistivity doubled after this treatment, the Be presumably going to the surface to react with the surface oxide. From this result, we have an estimate of the diffusion coefficient of Be in silicon at 1050°C of $\sim 10^{-7}$ cm^2/sec. In this case, it is clear that the Be is leaving the silicon and not reacting with dissolved oxygen as could be expected with the pulled crystal samples. Diffusion or clustering of O_2 is not significant for these short times and low temperatures.

To sum up, beryllium in silicon is a fast diffuser giving an acceptor level at 0.17 eV. The distribution coefficient is 1.3×10^{-4}. A Be-O combination has not been observed.

Acknowledgment

We wish to acknowledge the interest and encouragement of the late F. H. Horn who suggested this study.

Manuscript submitted Sept. 23, 1969; revised manuscript submitted Jan. 28, 1970. This was a Recent News Paper presented at the New York Meeting of the Society, May 4-9, 1969.

Any discussion of this paper will appear in a Discussion Section to be published in the December 1970 JOURNAL.

REFERENCES

1. W. Kaiser and P. H. Keck, *J. Appl. Phys.*, **28**, 822 (1957).
2. C. S. Fuller, F. H. Doleiden, and Katherine Wolfstein, *Phys. Chem. Solids*, **13**, 187 (1960).
3. D. W. White, Jr., and J. E. Burke, "The Metal Beryllium," p. 599, The American Society for Metals, Cleveland, Ohio (1955).
4. J. C. Irvin, *Bell System Tech. J.*, **41**, 387 (1962).
5. A. R. Hutson, *Phys. Rev.*, **108**, 222 (1957).
6. R. O. Carlson, *ibid.*, **108**, 1390 (1957).
7. R. N. Hall, *J. Phys. Chem. Solids*, **3**, 63 (1957).
8. C. S. Fuller and F. H. Doleiden, *J. Appl. Phys.*, **29**, 1264 (1958).
9. J. B. Robertson, *Bull. Am. Phys. Soc.*, **13**, 1475 (1968).

Selected Area Electron Diffraction Study of α-Fe_2O_3 Platelet Growths Twinned on Twist Grain Boundaries

In this paper by R. L. Tallman and E. A. Gulbransen which appeared in the February 1970 issue of the Journal, the diffraction patterns in Fig. 3 and 4 on page 252 were completely obscured by snow-storm-like additions.

Figures 3 and 4 are shown below as they should be.

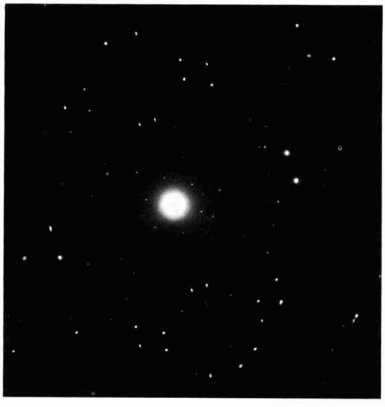

Fig. 3

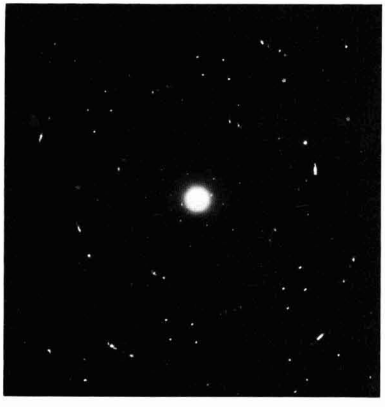

Fig. 4

JOURNAL OF THE ELECTROCHEMICAL SOCIETY

ELECTROCHEMICAL TECHNOLOGY

MAY 1970

High-Surface-Area Electrodeposited Aluminum

Richard J. Roethlein

Research and Development Laboratories, Sprague Electric Company, North Adams, Massachusetts

ABSTRACT

Aluminum was electrodeposited from a nonaqueous organic hydride electrolyte, $AlCl_3$ and $LiAlH_4$ in ethyl ether, which produced aluminum deposits ranging from smooth compact to rough and highly porous. Formation of high-surface-area Al substrates has been obtained by the application of high current densities. High-capacity values are explained on the basis of fine particle formation incurred under these plating conditions. Current-voltage curves for the anodic and cathodic reaction are indicative of a diffusion-controlled process.

The preparation of high-surface-area aluminum electrodes for electrolytic capacitors has always been a major concern in order to obtain the maximum capacitance values per unit geometric area or volume. Increasing the surface area of aluminum has been done for the most part either by chemical or electrolytic etching. Recently, however, large surface gains have been reported (1) through the electrodeposition of aluminum.

By means of an organic aluminum plating solution (2) and varying current density, aluminum dendritic growths have been reported to produce a surface gain factor over smooth aluminum of one to two orders of magnitude, depending on the formation voltage of the sample. Due to the possible advantages such a method may have in producing high-surface-area aluminum substrates, an investigation was undertaken to determine the feasibility of electrodepositing aluminum.

The formation of dense compact aluminum deposits has received considerable attention in the literature (2-7); however, highly dispersed porous aluminum deposits which would produce maximum surface roughness have been avoided. Parameters were therefore studied which would affect the nature of the aluminum deposit and tend to produce high-capacitance values. Electroplating was carried out in a nonaqueous electrolyte on aluminum wire electrodes.

Experimental

Due to the detrimental effects moisture has on aluminum plating baths, all experiments were carried out in a dry box containing an atmosphere consisting of 9 parts N_2 and 1 part H_2. Reagent-grade anhydrous materials used in the plating solutions were weighed inside of the dry box to avoid contact with water vapor in the atmosphere. The aluminum plating bath was an organic electrolyte (5, 6) which was operable at room temperature and consisted of an ethyl ether solution of 3M $AlCl_3$ and 0.4M $LiAlH_4$. The addition of anhydrous ether to the alkali halides must be done slowly, otherwise foaming and undesirable side reactions occur which affect properties of the plating solution. The plating cell consisted of a cylindrical Pyrex glass vessel 6 in. in length formed from a 60/50 joint; the top portion consisted of an array of equally spaced 10/30 joints which served as inlet ports for the study, reference, and counter electrodes. The study electrode was a section of 47 mil diameter aluminum wire, 99.99% purity, which was sealed to a section of Pyrex tubing by means of heat shrinkable Flo-tite[1] Teflon[2] tubing. The aluminum electrode, with an exposed geometric area of approximately 0.5 cm^2, could then be adjusted in the plating cell by means of a 10/30 Teflon gland. The counterelectrode consisted of a spiral section of either aluminum or platinum wire which provided an even current distribution on the study electrode. A Luggin capillary was sealed to one of the 10/30 joints into which a section of platinum wire was inserted which served as the reference electrode.

Aluminum electrodes were precleaned by the following sequence: immersion into acetone, rinsed, concentrated solution of 85% H_3PO_4-15% HNO_3 at 85°C for 2 min, rinsed, 1N-NaOH 2 min, rinsed, then dried at 90°C. After immersion into the plating solution, it was necessary to preanodize the electrode at a high current density, 200 mA/cm^2, for about 1 min; failure to preanodize the electrode in the plating solution produced nonadherent deposits. After anodization was complete, the current was immediately reversed to the appropriate cathodic plating current.

Both capacitance and RC product values were measured with a conventional a-c bridge having a few millivolts' signal. The electrodeposited wire was suspended in a cylindrical glass tube, the sides of which were lined with a platinum black counterelectrode. The measuring electrolyte had a resistivity of 12 ohm-cm and was used previously by Burger and Cheseldine (8). Oxide formations were carried out in a solution of 17% ammonium pentaborate in ethylene glycol. Values of the capacity measured at "zero voltage" were taken on the unformed wire which has a thin natural oxide on its surface.

Results

The use of this organic aluminate plating solution provides uniform adherent electrodeposits of Al and has the added advantage of being operable at room temperature. Conductometric studies (9) have shown that an ethereal solution of $AlCl_3$ will increase in conductivity with addition of $LiAlH_4$ up to approximately 17% equivalence. The formation of ionized species,

[1] Trade-mark, Pope Scientific Company.
[2] Trade-mark, Du Pont Corporation.

$Al_2Cl_5^+ + AlH_4^-$, has been postulated to produce this conductivity maximum; further addition of the hydride causes a destruction of the ionic species and lowering of the conductivity. A contrary view has been held by several authors (13, 14) in that the presence of excess $AlCl_3$, or the formation of $AlHCl_2$ or trichlorodialane $AlH_2Cl \cdot AlHCl_2$ is considered more favorable. Recent studies (15) have postulated the existence of several chemical species present in the plating solution and the possibility that the plating current is carried by three or four different ions. They conclude that an anion containing hydride exists and that the Li etherate is the principal current-carrying ion. The exact nature of the ionic species in solution has still, however, not been definitely proved.

In the presence of moisture, oxygen, and carbon dioxide the bath rapidly deteriorates; hydrogen gas is liberated at both electrodes during electrolysis, but to a much greater extent at the anode. Brenner (6) concluded that the bath was not regenerative due to a different ionic species formed during the dissolution of aluminum. More extensive studies (15) of bath life, extending over an 8 month period, have shown that the Al anode does dissolve to some extent in a manner which replaces the deposited aluminum. We have found that reproducible plating results can be maintained by a periodic addition of solid $AlCl_3$ and $LiAlH_4$ to the plating solution.

Surface roughness of the electrodeposited material can be varied to a considerable extent by variations in the plating current density. Generally, a current density less than 50 mA/cm^2 tends to give a smooth deposit. As the current density is increased the deposits tend to become nodular, and for values greater than 100 mA/cm^2 dendritic growth becomes rapid. At current density values greater than 300 mA/cm^2, a black powdery-like deposit forms on the electrode surface. Values of the capacity showed a large variation with changes in the surface morphology of the electrodeposited aluminum.

A series of aluminum electrodes having an apparent geometric area of 0.5 cm^2 were electroplated at various cathodic current densities both at constant cathodic charge (Q), and also for varying periods of time with current density constant. For electrodes plated at current densities ranging from 50 to 300 mA/cm^2, capacity measurements taken at zero formation voltage fell into a limited range from 4 to 15 μfd/cm^2. Depending on the amount of charge passed, deposit thickness for these electrodes ranged from 1 to 10 mils, the thicker deposits exhibiting the higher capacity values.

Larger values of the capacity were not realized until the plating current density was increased to values greater than 300 mA/cm^2. At these extremely high current densities, a black deposit forms on the electrode surface accompanied by gas evolution. Capacity measurements gave values in excess of 150 μfd/cm^2 on the unformed wire, and plots of the reciprocal of capacity *vs.* formation voltage were linear (Fig. 1). Microscopic inspection of the dark deposit at magnifications up to 500X show the growth of crystals. Spectrographic comparison of the electrodeposited material and an Al wire showed traces of B, Si, Fe, and Cu to be present in both samples. Lithium, which is one of the constituents of the plating solution, was not detected in the sample of electrodeposited aluminum using a method accurate to 10 ppm. Photomicrographs taken on a cross section of an Al wire that was electroplated at a current density of 500 mA/cm^2 for 7 min are shown in Fig. 2. The photos show that electrodeposited material consists of a highly porous deposit, 3-4 mils in thickness, containing dendritic growths of varying diameter.

Figure 3 is a plot of capacity/cm^2 *vs.* formation voltage comparing the results we obtained for a wire electrodeposited at 300 mA/cm^2 for 5 min with that reported by Muhlhausser (1). In the low-voltage region, <10V, Muhlhausser's data indicate a considerable increase in capacitance over what we have found on

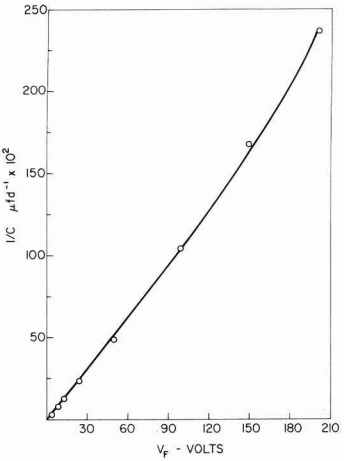

Fig. 1. Reciprocal capacity *vs.* formation voltage: electrodeposited Al, 300 mA/cm^2, 5 min.

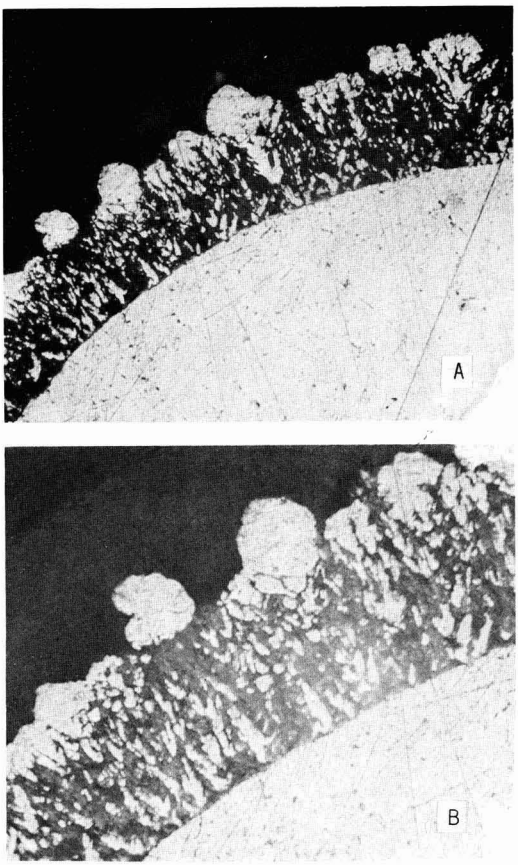

Fig. 2. Photomicrographs of electrodeposited Al plating. Conditions: 500 mA/cm^2, 7 min. Magnification (A) 200X, (B) 385X.

electrodeposited wires; at higher formation voltages, the capacities he reports are considerably less than what we have observed.

The capacity of unformed wire was studied for Al deposits obtained at several high current densities for varying periods of time. Figure 4 indicates a sharp rise in capacitance with the amount of Al deposited

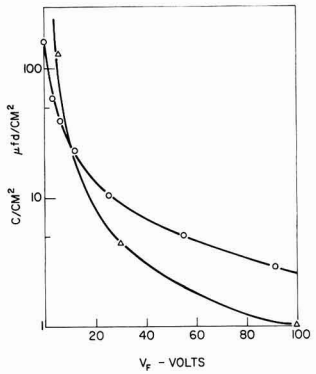

Fig. 3. Comparison of capacity/cm² for various Al structures. ○—Electrodeposited wire, 300 mA/cm², 5 min. △—Muhlhausser's data, 8 mA/cm², 30 min; 60 mA/cm², 1.5 min; 15 mA/cm², 30 min.

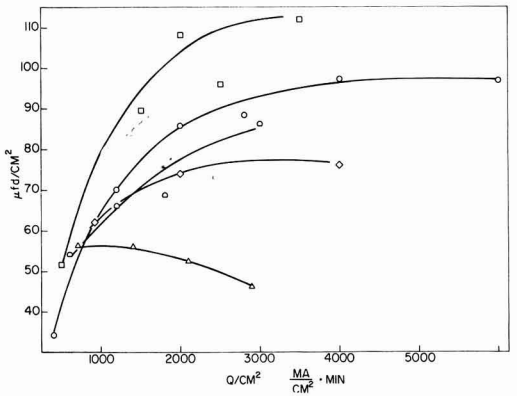

Fig. 4. Variation of capacitance for electrodeposits obtained at different current densities and total charge. Plating current density, mA/cm: ◇—300, ○—400, □—500, ⌓—600, △—700; zero formation voltage.

which tends to level off as the charge increases. The capacity also seems to be a function of the plating current density, the highest values being obtained for a current density the order of 500 mA/cm². The lower capacity values obtained at higher plating current density are due to a lack of adherence of the depositing material which becomes increasingly worse as the current density is raised. Adherence of the electrodeposited Al at high current density can be somewhat enhanced if a periodic short current reversal is applied during the plating sequence, *e.g.* 5 sec anodic/60 sec cathodic. During current reversal, the species formed could be aluminum hydride (16).

Values of the capacity measured as a function of formation voltage for three different deposit thicknesses (Fig. 5) indicate less of a capacity loss is incurred at higher formation voltages for thicker electrodeposits of aluminum. This does not contradict the previous findings, for if the samples used in Fig. 4 were formed at a higher formation voltage a more linear rise in capacity with charge increase would be observed.

Steady-state current voltage curves for the deposition and dissolution of aluminum were taken galvanostatically, potential differences being measured between the study electrode and a platinum reference electrode. A linear relationship exists between current and potential for both the anodic and cathodic electrode process; polarization values are similar to

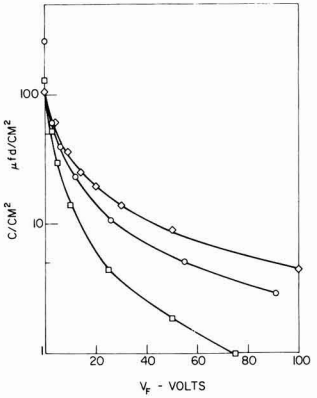

Fig. 5. Capacity/cm² vs. formation voltage as a function of deposit thickness. ◇—9 mils, 300 mA/cm², 20 min; ○—3 mils, 300 mA/cm², 5 min; □—1 mil, 300 mA/cm², 1 min.

those reported by Hayashi (10). A semilog plot, Fig. 6, gives a low value of the slope for the linear portion of the curve between 5 and 10 mV/decade. The low value of the slope eliminates the possibility of activation control and indicates that the reaction is most probably diffusion controlled. Measurements of the difference in potential between the extended linear portion of the curve and the potential observed at a certain current density gave a constant value for the resistance, $\Delta E/I$, over the range of currents studied. Although the shape of the curve indicates a limiting current region, most of the polarization is due to an ohmic drop incurred through the electrolyte. This is further emphasized by the small decrease in polarization that was observed when the electrolyte was stirred. For the concentrations used in these experiments, a true limiting current is not observed until current densities from 200 to 300 mA/cm² are reached.

Discussion

Since the largest capacity increases were observed for aluminum electrodeposits obtained at high current densities, the discussion is concerned mainly with that region of the experimental results. The formation of very fine crystals or powder metals by electrolysis is well known in the powder metallurgy industry, and these forms have been prepared from a wide variety of metals in both aqueous and nonaqueous systems (11). These deposits often appear black because of the very small size of the particles. The structure of these deposits depends strongly on the formation of new nuclei and the rate of growth of the already existing crystals. If the rate of nucleation is

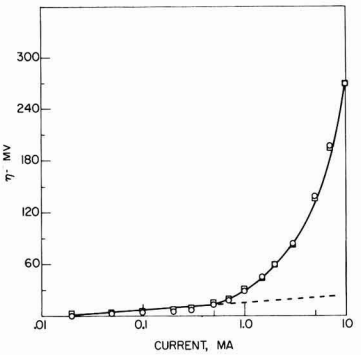

Fig. 6. Semilog current-voltage curve, deposition ○ and dissolution □ of Al.

large and crystal growth is inhibited, the formation rate of powder metals will be increased. Those factors that tend to reduce interfacial concentration, such as increased current density or decreasing metal ion concentration, will favor a high nucleation rate. As the concentration of metal ions in solution approaches zero, at limiting current, the onset of powder deposition begins.

We have observed experimentally that, upon application of a current sufficiently high to cause powder deposition, a black deposit does not begin to form until after a few seconds' time have elapsed. This lag is due to the time necessary to reduce the concentration of Al ions to near zero at the electrode solution interface. Initially, a bright metal deposits on the electrode but, as the concentration of Al ions at the interface approaches zero, a black powder begins to form. Consequently, those factors (current density, temperature, rate of stirring) that influence mass transport phenomena influence the formation of both powder deposition and particle size. After the onset of a black powdery deposition, we have observed that for current densities between 300-500 mA/cm^2 the deposits tend to become metallic again after several minutes of plating. This is probably due to an increase in the surface area of the electrode which in turn reduces the true current density. Thus, the Al ion concentration at the surface is increased favoring the deposition of larger metallic aluminum particles. This view is supported by the photomicrographs in Fig. 2 which show that larger particles tend to grow as the thickness of the electrodeposit increases.

The aluminum deposits we have studied in this work which have exhibited high capacities are a combination of very fine black Al particles overgrown by a porous dendritic deposit. Aluminum deposits grown at current density below the formation of powdered Al exhibit capacities that are an order of magnitude lower even though they are dendritic in nature and of the same or greater thickness. Capacity measurements for the deposition of copper (12) have also shown that a steep rise in capacity occurs with the onset of powder formation at limiting current.

The adhesion of these powder deposits is favorable for current densities below approximately 500 mA/cm^2; for higher current density values, the black particles fall off the electrode easily. It is therefore necessary to maintain a current density in the region where the particles will adhere to the aluminum substrate; this can be enhanced to some extent by a periodic reversal of current for a short duration.

Conclusions

1. A nonaqueous organic plating solution has been used successfully in electrodepositing aluminum to obtain high-surface-area Al electrodes.
2. The increased capacity values observed for these deposits have been related to the formation of fine black Al crystals which are obtained in the region of limiting current density.
3. Current-voltage curves indicate that the electrodeposition of Al from this electrolyte is probably diffusion controlled.

Acknowledgments

The author wishes to thank Drs. Robert S. Alwitt and Glenn M. Cook for their advice and help during the course of this project.

Manuscript submitted Oct. 28, 1969; revised manuscript received Feb. 3, 1970.

Any discussion of this paper will appear in a Discussion Section to be published in the December 1970 JOURNAL.

REFERENCES

1. M. Muhlhausser, *Electrochem. Technol.*, **6,** 183 (1968).
2. K. Ziegler and H. Lehmkuhl, *Z. Anorg. Allgem. Chem.*, **283,** 414 (1956).
3. W. J. Kroll, *Trans. Electrochem. Soc.*, **87,** 551 (1945).
4. K. H. Hurley, and T. P. Wier, U.S. Pat. 2,446,349, Aug. 3, 1948; *This Journal*, **98,** 204 (1951).
5. D. E. Couch and A. Brenner, *This Journal*, **99,** 234 (1952).
6. J. H. Connor and A. Brenner, *ibid.*, **103,** 657 (1956).
7. A. L. Levinskas and A. Yu. Simanauichus, *Electrokhimiya*, **2,** 200 (1966).
8. F. Burger and D. Cheseldine, 1st Semiannual Report, Contract DRB9596-S3811 Defense Research Board (Canada) (1964).
9. G. Evans, J. Kennedy, Jr., and F. DelGreco, *J. Inorg. Nucl. Chem.*, **4,** 40 (1957).
10. T. Hayashi and T. Ishida, *Bull. Univ. Osaka Pref., Ser. A*, **7,** 43 (1959).
11. N. Ibl, *Advan. Electrochem. Electrochem. Eng.*, **2,** 49 (1962).
12. M. Loshkarlv, A. Ozerov, and N. Kudrautsev, *Zhur. Priklad. Khim.*, **22,** 294 (1949); *Chem. Abs.*, **43,** 5674g (1949).
13. Yu. M. Kessler, N. M. Alpatova, and O. R. Osipov, *Russian Chem. Rev.*, **33,** No. 3, 119 (1964).
14. E. C. Ashby and J. Prather, *J. Am. Chem. Soc.*, **88,** 729 (1966).
15. F. A. Clay, W. B. Harding, and C. J. Stimetz, *Plating*, **56,** 1027 (1969).
16. *Russian Chem. Rev.*, **57,** No. 2, 99 (1968).

Electrodeposition of Resin

S. Mercouris and W. F. Graydon

Department of Chemical Engineering and Applied Chemistry, University of Toronto, Toronto, Ontario, Canada

ABSTRACT

The electrodeposition, under constant voltage, of an emulsion of a polyacrylic resin is studied. The coulombic yield of the process is examined at different voltages and for different deposition times. The coating is analyzed for iron, and the iron content/coulombs relationship was found to be linear. An addition of a small amount of Cl^- in the bath highly increased the iron content of the coating. The role of the electrodissolved anodic metal is examined by comparative deposition on steel and platinum. The water content of the coating was studied and the "gassing" effect at the anode was related to the resistance of the resulting film.

Electrocoating, as a method of applying primers or finishes on metalic surfaces, has attained wide application in recent years. Several patents cover the use of different electrocoating baths and conditions of deposition. However, in spite of the numerous publications in this field, the actual mechanism of the electrodeposition process is not yet clearly understood, and the continuous operation of the electrocoating tanks still involves many problems.

The composition of an electropainting bath is very complex. It may consist of resin, pigment, extenders, and a crosslinking agent as well as other compounds

which give specific properties to the coating. All those constituents must be deposited at the same rate or special care must be taken to keep the composition of the bath constant. The problem is solved mainly by special formulation of the bath, so that equal rates of deposition are attained.

Due to the complexity of the electropainting bath, and the fact that a knowledge of behavior under simple conditions is a prerequisite to the understanding of complex technological problems, a relatively simpler system of an emulsion of a polyacrylic resin was studied. Moreover, the resin undergoes all the reactions leading to the deposition of the paint. The resin was solubilized in water by use of triethylamine and the suspended particles of the emulsions were aggregates of polymeric molecules charged by the ionization of some carboxyl groups of the molecules located on the surface of the particle.

Tawn and Berry (1) discussed the application of the theories of Pauli and Helmholtz to the above systems and they stressed the difficulties in studying them in terms of fundamental physicochemical properties alone. Following their ideas in the present work, the relationship among some of the less fundamental variables of the electrodeposition process was studied. The rest of the variables had to be kept constant and this caused some problems when the degree of dispersion was to be kept constant. In the emulsion of the resin, there is a wide distribution of particle sizes and size/charge ratios. This distribution cannot be exactly reproduced and, even for a given solution, changes with time. This difficulty can be easily overcome in many cases by taking all the measurements within a short time interval, but nothing can be done in the case where the concentration of the resin is the independent variable. The dependent variable then does not depend only on the given concentration, but also on the degree of dispersion of the prepared emulsions. Consequently, a higher variance is expected.

This can be clearly demonstrated in Fig. 5. Each point of the three lines is the mean of two measurements with a mean deviation less than 1% and all the points of each line come from measurements taken in a short time interval. However, the repetition of the same experiment, using the same emulsion on three different days, produces three distinct curves and this must be attributed to the change in the degree of dispersion of the emulsion since all the other variables can be considered reproducible.

Electrode reactions.—The species moving toward the anode by the applied electrical field are negatively charged colloidal particles of resin (colloid-R) COO^- and OH^-. It is generally accepted that the deposition is not due to the immediate discharge of the colloidal particles at the anode, and the main arguments are as follows:

1. Deposition can take place on diaphragms interposed between the anode and the emulsion which do not permit immediate contact between the colloidal particles and the anode [Fink and Feinleib (2)].
2. If deposition were due to immediate discharge of the particles, we would not be able to explain the deposition after the first layer is formed, since the particles cannot reach the anode any more [Finn and Mell (3)].
3. Tawn and Berry (1) reported a delay period before deposition could be observed and a progressive increase of the concentration of resin in the film adjacent to the anode (dipped film) during this period. This cannot be explained if the particles are immediately discharged and deposited.
4. Immediate discharge of the particles should be followed by a Kolbe Electrolytic Synthesis producing a condensation of the resin ions with an evolution of carbon dioxide. Gloyer, Hart, and Cutforth (4) have not detected either carbon dioxide evolution at the anode or significant reduction in acid value of the deposited resin.

It is generally accepted in literature that deposition is due to the following reactions.

$$(\text{Colloid-R})\text{COO}^- \xrightarrow{Fe^{2+}} [(\text{Colloid-R})\text{COO}]_2\,\text{Fe} \quad [1]$$

$$(\text{Colloid-R})\text{COO}^- \xrightarrow{H^+} (\text{Colloid-R})\text{COOH} \quad [2]$$

Fe^{2+} come from electrodissolution of the anode, and H^+ come from a local drop of the pH after the discharge and consequent removal of the OH^-.

Fink and Feinlieb (2) and, later, Olsen (5) proved that the iron is dissolved in the form of Fe^{2+} by adding thiocyanate or ferricyanide ions in the bath. The same was proved in this work more quantitatively by analyzing the coating for Fe^{2+} and Fe^{3+}.

May and Smith (6) tried to calculate the ratio of the amounts deposited, according to reactions [1] and [2], from the ratio of the electrical charges involved in each of them. The number of coulombs used for reaction [1] was calculated from the amount of iron determined by analysis of the coating. The charges involved in reaction [2] were calculated from the weight of the deposited coating and the acid number of the resin. The sum of the two numbers, as above calculated, was less than the total number of coulombs used for the deposition. They called this difference "unaccounted current."

Results and Discussion

Iron content of the coating.—A spectrophotometric method was used to analyze the coating for iron after dissolution with alcohol. The iron was determined in alcoholic solutions and in the presence of the resin. The number of coulombs used for the deposition was calculated from the area under the current/time curve obtained by the use of a recorder.

The lower curve of Fig. 2 shows the weight deposited *vs.* coulombs relationship, for different deposition times. A straight line, followed by a downward curve at higher deposition times (*i.e.*, beyond 4 min), is obtained. The slope of the straight line represents the coulombic yield of the deposition. A very small increase of the coulombic yield was observed with increasing concentration of the bath and a number 8-12 mg/coulomb was obtained for concentrations of 2-12% solids.

The amount of iron *vs.* the number of coulombs relationship for different times of deposition is linear as shown in Fig. 1. Since the coulombic yield is constant for different deposition times, a constant concentration of iron for different deposition times must be concluded. This concentration of iron was calculated to be of the order of 0.006%; the bath had a concentration of 2% solids. The relationship between the amount of iron and coulombs was also found to be linear for a solution of 12% solids and a similar iron concentration was calculated.

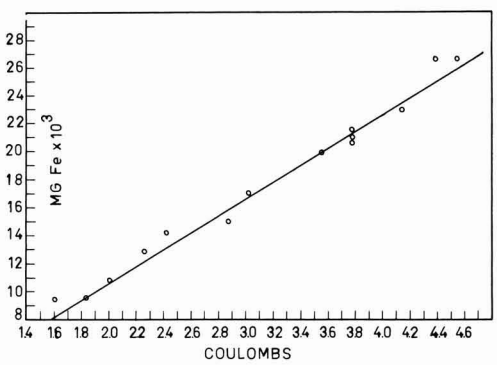

Fig. 1. Iron *vs.* coulombs plot: 2% solids, 60% neutralization

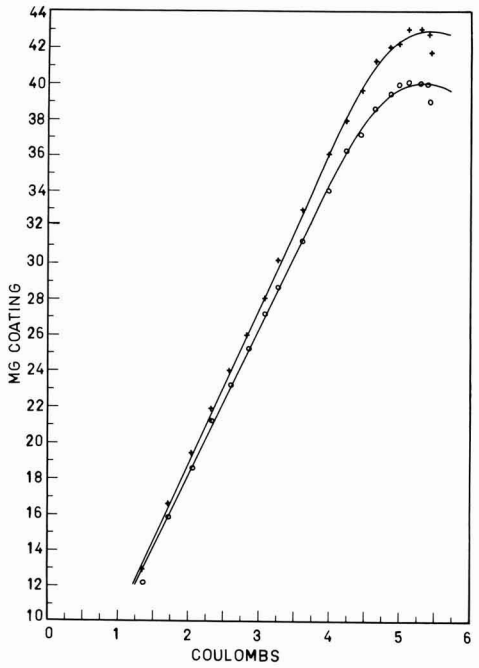

Fig. 2. Weight vs. coulombs plot: 2% solids, 60% neutralization. ○, Weight of baked coating; +, weight of unbaked coating.

The effect of the contamination of the bath with foreign anions was studied by adding a small amount of NaCl (50 mg/liter). The iron/coulombs relationship was again linear, but the concentration of iron was highly increased from 0.006 to 2%. The high concentration of iron is quite evident by the brown color of the coatings obtained.

Comparative deposition on iron and platinum was studied under identical conditions. The rates of deposition were found to be the same and identical coulombic yields were obtained. The equality of the coulombic yields is demonstrated in Table I. A pair comparison of the tabulated values must be considered (Fe-Pt), since the values for each pair are the result of experiments conducted under identical conditions (in a short time interval).

Role of iron in the electrodeposition process.—The percentage of the total current used to dissolve the iron can be calculated from the previous data. Table II shows the results for different runs.

Table I. Comparison of the coulombic yields for deposition on Fe and Pt

Conditions: 2% solids (+ 50 mg NaCl/liter)
60% neutralization
110V
3 min deposition time

Run No.	Coulombic yield Fe	Pt
1	8.24	8.30
2	7.83	7.61
3	7.25	7.55

Table II. Percentage of coulombs used to dissolve the iron

	% Coulombs for iron
2% solids, 60% neutralization	2.07
12% solids, 60% neutralization	1.86
2% solids, 35% neutralization	3.37
2% solids (+ 50 mg/liter NaCl), 60% neutralization	72.8

The percentage of the current used for the iron dissolution seems to be independent of the concentration and has a higher value for a lower degree of neutralization.

From the acid number of the resin and the weight of the coating, the percentage of the current used to deposit the resin, according to reaction [2], can be calculated. This method of calculation, however, is not correct for the following reasons. The emulsion used for the electrodepositions consists of colloidal particles formed by aggregates of polymeric molecules. The charge of the particles is due to ionization of some carboxyl groups of molecules which are at the surface of the particle. However, there is a large number of other carboxyl groups which, being in the mass of the particle, are not ionized. Consequently, they do not take part in the electrodeposition reactions, but are deposited because of the deposition of the whole particle.

Tawn and Berry (1) represented the deposited species in the form

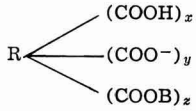

where B represents the neutralizing base.

x, y, and z can have different values depending on the ionization constants of the carboxyl groups and the base. Water insolubility or coagulation will result from an increase in the value of x, with a corresponding decrease in y, and will also be promoted by loss of base, *i.e.* fall in z. The above discussion shows that a particle can be deposited even when some of the carboxyl groups are still ionized or are neutralized with an equivalent amount of base.

It would be expected, thus, that by adding the percentage of the current used to dissolve the iron plus the percentage of the current calculated by counting all the carboxyl groups of the resin a number much higher than 100 would be obtained.

This was not verified by the experiments for they gave a sum much lower than 100. The difference from 100 is the unaccounted current reported by May and Smith (6).

Using an average value for the coulombic yield equal to 10, the percentage of the coulombs for the resin is calculated as being equal to 19. The unaccounted current, having been calculated equal to 79%, shows a very bad efficiency for reactions [1] and [2].

In the case of the bath contaminated with chlorides, the percentage of electrochemical equivalents for the iron was found equal to 72.8 (Table II). This is much higher than the percentage of the electrochemical equivalents of the resin calculated in the previous paragraph. That means that the amount of iron in the coating is much higher than the one required from the stoichiometry of reaction [1], even if we assume that this is the only deposition reaction. Consequently, questions arise as to the form in which the rest of the iron exists in the coating.

The results shown in Table I proving equal coulombic yields for deposition on iron and platinum cannot be explained by the previous theory. In the case of deposition on platinum, a large amount of current is used to discharge the chlorine ions producing chlorine gas. This amount of current does not result in any deposition. In the case of deposition on iron, the discharged chlorine ions dissolve the anode, producing iron ions, which deposit a certain amount of resin. Consequently, a higher coulombic yield for deposition on iron would be expected.

Sullivan (7) explains the existence of iron in the coating as being due to the formation of stable iron oxides by the reaction of the ferrous and ferric ions with the hydroxyl ions traveling toward the anode.

$$Fe^{+2} + 2\,OH^- \rightarrow Fe(OH)_2 \qquad [3]$$

$$Fe^{+3} + 3\,OH^- \rightarrow Fe(OH)_3 \qquad [4]$$

The main reaction explaining the deposition of resin in all cases is reaction [5].

$$(\text{Colloid} - \text{R})\text{COO}^- + \text{H}^+ \rightleftarrows (\text{Colloid} - \text{R})\text{COOH} \quad [5]$$

This reaction must be considered as having the form of equilibrium, and deposition occurs when $[(\text{Colloid}-\text{R})\text{COO}^-]\ [\text{H}^+] > k$, where k is the ionization constant of the resin. The drop of the pH close to the anode cannot be local, as often reported in literature, and a concentration gradient from the anode up to the bulk of the solution must be considered. Due to this concentration gradient, a large number of H^+ do not take part in the deposition reactions but are transferred to the bulk of the solution. This is a possible explanation of the "unaccounted current" since the current used to produce the above H^+ does not lead to any deposition.

Tawn and Berry (1) reported a higher concentration for the resin in the dipped film. An immediate discharge of the particles, as was already discussed, cannot be accepted. Consequently, a similar concentration gradient to H^+ for resin must be considered.

The delay period reported by Tawn and Berry (1) can be explained as the time required for the above two concentration gradients to build up. Deposition starts when the product $[(\text{Colloid-R})\text{COO}^-]\ [\text{H}^+]$ becomes greater than k. This also explains the progressive increase of the concentration of resin in the dipped film during the delay period reported by the same authors and the decrease of the delay period with an increase of the applied voltage reported by Yeates (8). The higher the voltage, the faster the formation of the two concentration gradients.

Finally, the curvature of the weight/coulombs curve after a long time of deposition, shown in Fig. 2, can be explained by the above proposed scheme. After a long time of deposition, the anode is almost isolated and there is a large potential drop through the film. The remaining potential difference is not sufficient to maintain the above concentration gradients. Thus, $[(\text{Colloid-R})\text{COO}^-]\ [\text{H}^+] < k$, and dissolution of the film occurs instead of deposition.

Water content of the coating.—The investigations of the water content of the film and the gassing effect, which will be discussed later, are of great technological importance since the studied variables are directly related to such qualities of the coating produced as appearance and resistance. For example, the higher the water content of the film, the higher the possibility of getting pinholes in the coating because of the escape of water bubbles during the baking process.

The water content of the film was calculated as the difference between the weight of a baked and an unbaked film under identical conditions. The unbaked film was dried by putting it in a desiccator under vacuum conditions.

Figure 2 shows the weight/coulombs plot of the baked and unbaked film for different times of deposition for a 2%-solids bath. It is interesting to note that even the weight of the unbaked film changes linearly with the number of coulombs. A problem arising here is that the difference in the weight of the unbaked and baked film, which gives the amount of water in the film, can be of similar magnitude as the variance of the distributions of the two numbers used for the subtraction. Consequently a great variance for the distribution of the water content is expected, making the results inconclusive.

The above problem was solved by drawing the regression lines and taking the differences between corresponding points. Each point of the regression line represents the mean of the distribution of the individual measurements, whose variance is eliminated in this way. A large number of points were used for the construction of the two regression lines in order to have a higher degree of confidence.

The values of the water content of the film at different times of deposition were calculated from Fig. 2.

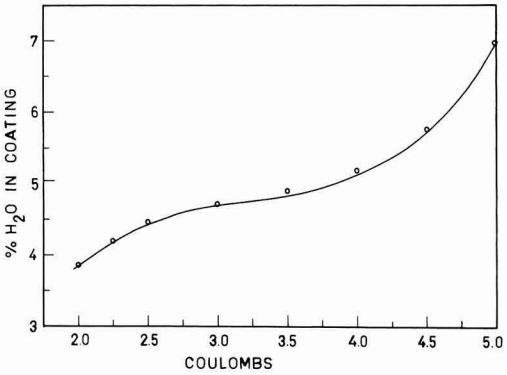

Fig. 3. Water content *vs.* coulombs plot: 2% solids, 60% neutralization.

The plot of the water content *vs.* the number of coulombs is shown in Fig. 3. An increase in the water content of the coating is observed with an increase in the number of coulombs at different deposition times.

The same work was repeated using a 12%-solids bath. The same increase of the water content was observed with increasing deposition time, but the actual numbers were higher (almost double).

The conclusion from the above results is that a film with lower water content can be obtained by using a lower concentration of resin and a shorter deposition time.

Gassing effect.—Tasker and Taylor (9) and, more recently, Curtis, Pugh, and Taylor (10) reported a peak in their resistance of the film/weight deposited plots. The experiment was conducted under constant current conditions. They examined the film with the aid of a microscope and proved that the peak occurred at the point at which the film originally laid down disrupted in order to allow the trapped anodic gas to escape.

Similar peaks were observed in the current/time curves under constant voltage conditions, as shown in Fig. 4. The peaks are inverted since the current is inversely proportional to the resistance.

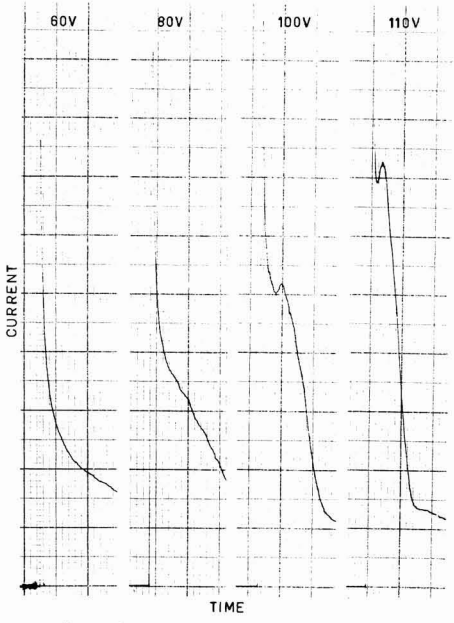

Fig. 4. Gassing effect at different voltages.

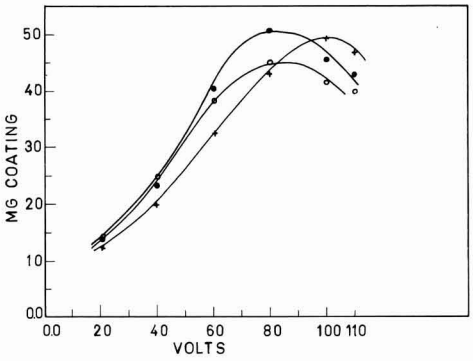

Fig. 5. Weight *vs.* voltage for 3 min deposition time: 4% solids, 60% neutralization. ○, First day; ●, second day; +, third day.

In Fig. 5, the weight of coating is plotted *vs.* the corresponding voltage of deposition for 3 min deposition time. The three curves represent three runs at three different days. An almost linear increase for each curve is observed followed by a curvature at 80-110V. This curvature of the weight/voltage plots starts almost at the same voltage at which the resistance "peaking" starts to appear. Possibly, there is a connection between the two phenomena.

After about 90V, a higher voltage deposits a lower weight for the same deposition time (3 min). That means that the higher the voltage, the higher the resistance of the deposited film. This can be considered a justification for the high voltages used in technical applications (100-300V). In the above experiment, a 4%-solids solution was used. For lower concentrations the above gassing effect was not observed, whereas for higher concentrations it was even more clearly evident (Fig. 5).

Conclusions

The coulombic yield of the electrodeposition was found to be constant for different voltages and at different deposition times. Almost constant coulombic yield was found for different concentrations of resin and for deposition on different metals. The iron content of the film, for deposition on steel, was proved to be almost constant for different concentrations of resin and different deposition times.

The electrochemical current used to dissolve the iron was proved to be a small percentage of the total current. The iron content of the film and the percentage of the total current used to dissolve the iron were highly increased after a small contamination of the bath with chlorides. The role of the ferrous and ferric ions in the electrodeposition reactions is not as yet clearly understood. More work must be done in order to elucidate the exact form of iron in the coating.

A small amount of water was found in the film. This increases with deposition time and is higher for higher concentrations of resin.

A rupture of the film due to the escape of trapped anodic gas was observed at a certain time during the deposition. This rupture occurred for higher concentrations and voltages greater than 80. In addition, an increase in the resistance of the film obtained was observed with a voltage greater than 80.

Manuscript received Sept. 29, 1969.

Any discussion of this paper will appear in a Discussion Section to be published in the December 1970 JOURNAL.

REFERENCES

1. A. R. H. Tawn and J. R. Berry, *J. Oil Colour Chemists' Assoc.*, **48**, 790 (1965).
2. C. G. Fink and M. Feileib, *J. (and Trans.) Electrochem. Soc.*, **94**, 309 (1948).
3. S. R. Finn and C. C. Mell, *J. Oil Colour Chemists' Assoc.*, **47**, 219 (1964).
4. S. W. Glover, D. P. Hart, and R. E. Cutforth, *Off. Digest J. Paint. Technol. and Eng.*, **37**, No. 481, 113 (1965).
5. D. A. Olsen, *J. Paint Technology*, **38**, No. 499, 429 (1966).
6. C. A. May and G. Smith, *ibid.*, **40**, No. 526, 494 (1968).
7. M. R. Sullivan, *ibid.*, **38**, No. 499, 424 (1966).
8. R. L. Yeates, "Electropainting," Robert Draper Ltd. (1966).
9. L. Tasker and J. R. Taylor, *J. Oil Colour Chemists' Assoc.*, **48**, No. 2, 121 (1965).
10. W. B. Curtis, J. A. Pugh, and J. R. Taylor, *Chem. Ind. (London)*, **1967**, 1858.

Preparation and Evaluation of Spreading Resistance Probe Tip

E. F. Gorey, C. P. Schneider, and M. R. Poponiak

IBM Components Division, East Fishkill Facility, Hopewell Junction, New York

ABSTRACT

The spreading resistance technique used to evaluate various types of silicon structures is dependent primarily on the probe point. Data are presented on point preparation and loading of different point materials. A method for preparation and evaluation of point characteristics for effective use on thin silicon structures is described.

The spreading resistance technique (1-3) is the most versatile technique used to characterize impurity profiles of multilayered structures.

An improved spreading resistance probe (4) which utilized balance beam probe arms, weight loading, and controlled velocity of impact emphasized contact reproducibility as one of its most important parameters. It has been implied in the previous papers that a spreading resistance probe will function properly if a particular type of probe point is used.

The most critical part of the technique is the probe point. It must have the capability of making thousands of measurements without deteriorating and must maintain certain characteristics that make it useful in measuring both n- and p-type silicon structures.

This paper describes a method of preparing and evaluating a probe point for its use in the spreading resistance technique.

Probe Point Characteristics

A good probe point has the following characteristics: the effective penetration of the probe into the silicon surface must be kept to a minimum, and the spreading resistance measured in the forward and reverse

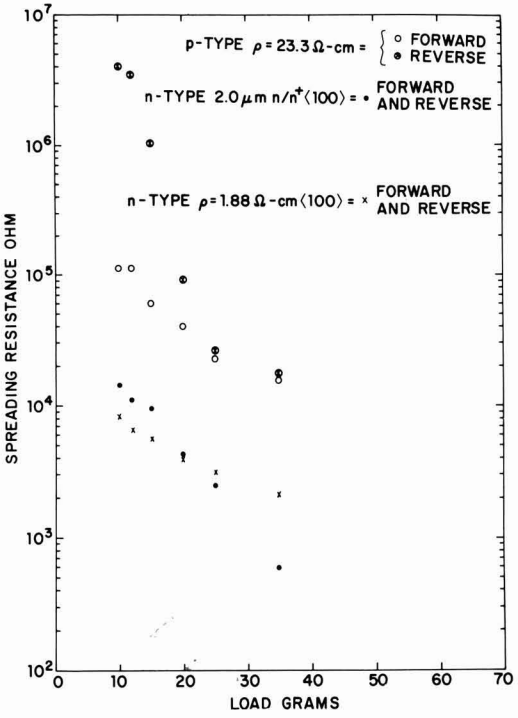

Fig. 1. Spreading resistance as a function of loading for a new K-75 point as received from vendor.

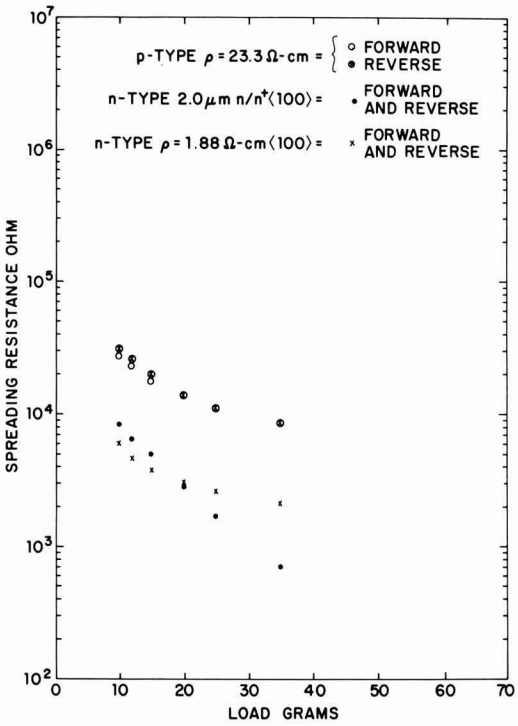

Fig. 2. Spreading resistance as a function of loading for a K-75 point prepared by 3 sec abrasion.

direction of current must not differ by more than 5% of the average. Experimental data indicate that a probe can function on n-type silicon but can give inconsistent results on p-type.

An experiment designed to study these characteristics and the behavior of n- and p-type silicon wafers was performed on 3 wafers. A 23.3 ohm-cm p-type mechanical polished bulk wafer was used to indicate when good contact was achieved. Good contact exists when the spreading resistance in the forward and reverse direction of current is within 5% of the average. A 1.88 ohm-cm n-type bulk wafer was used as a control wafer. A 3.0 ohm-cm n-type epitaxial layer of 2.0 μm thickness on a 0.001 ohm-cm n-type substrate was used to indicate effective probe penetration. In the range of loading where the ratio of the spreading resistances of the epitaxial wafer to the n-type bulk wafer remains constant, no effective penetration is considered to exist.

Spreading resistance was plotted as a function of probe point loading. All measurements were made utilizing the spreading resistance apparatus described in Ref. (4). Figures 1 through 4 show the results obtained from tungsten-ruthenium probe points with tip radius of 0.0007 in.

Figure 1 represents the results of a point as received from the vendor.[1] From 10 to 15g loads, bad contact is made on the p-type wafer. Good contact is made on both n-type wafers and no effective penetration exists. At 20g, the ratio of the two n-type wafers now changes and effective probe penetration is observed. The difference between the forward and reverse spreading resistance from the average on the p-type sample is 40%. Greater effective probe penetration of the epitaxial layer and good contact on the p-type wafer is observed at 25g loading. Deep effective penetration of the thin epitaxial layer and good contact on the p-type wafer was observed at 35g loading. From results obtained, it can be seen that at no one loading of the probe point did the point exhibit good contact and no effective penetration.

The probe in Fig. 2 was prepared by an abrasive blasting of 3 sec. The spreading resistance probe point is prepared by an abrasive blasting technique in the following manner. A series of probe points to be prepared are positioned in a holder with their points exposed. An air abrasive unit is then used to abrade the point with 27.5 μm aluminum oxide with a 50 psi pressure. The unit has a 1/16 in. nozzle orifice.

The nozzle of the unit is placed approximately 1 in. from the probe points. After abrading, each probe is immersed in trichlorethylene for 5 min. The probes are then wiped with cotton swabs saturated with acetone. This procedure gives the probe tips the proper finish to make good contact to the sample.

It was evident that the abrasive blasting technique changes the results significantly. Good contact was made on the p-type wafer with only 10g loading. This probe point will operate properly if used between 10-15g loading.

Figure 3 shows the results of abrading for 5 sec. Effective penetration starts at 15g. The probe point represented in Fig. 4 was the result of abrasion for 10 sec. In Fig. 3 and 4, the tips exhibited large spikes due to the abrasion which caused deep effective penetration.

Figure 5 shows the results of an osmium alloy probe point with a tip radius of 0.0007 in.[2] Effective penetration did not occur until 35g, but poor contact was made to the p-type wafer. This point will not meet all the requirements of a good point. Figure 6 represents a ruthenium alloy probe point with a tip radius of 0.0007 in.[3] which exhibited characteristics similar to the osmium point.

A convenient method to insure a good probe point is as follows. Measurements are made on 3 wafers: No. 1, a thin ($\sim$ 2.0 μm thick) n-type epitaxial layer of

[1] Fidelitone K-75 PIVOT, tungsten ruthenium alloy.

[2] Fidelitone #741 PIVOT, osmium alloy.

[3] Fidelitone #347 PIVOT, ruthenium alloy.

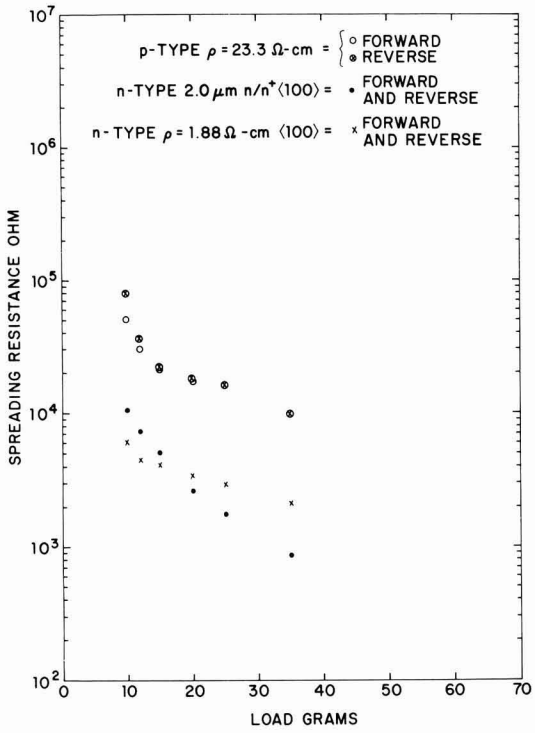

Fig. 3. Spreading resistance as a function of loading for a K-75 point prepared by 5 sec abrasion.

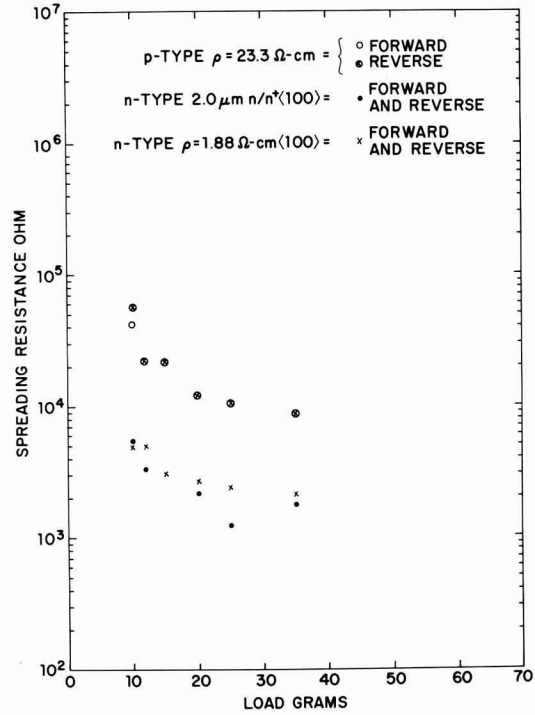

Fig. 4. Spreading resistance as a function of loading for a K-75 point prepared by 10 sec abrasion.

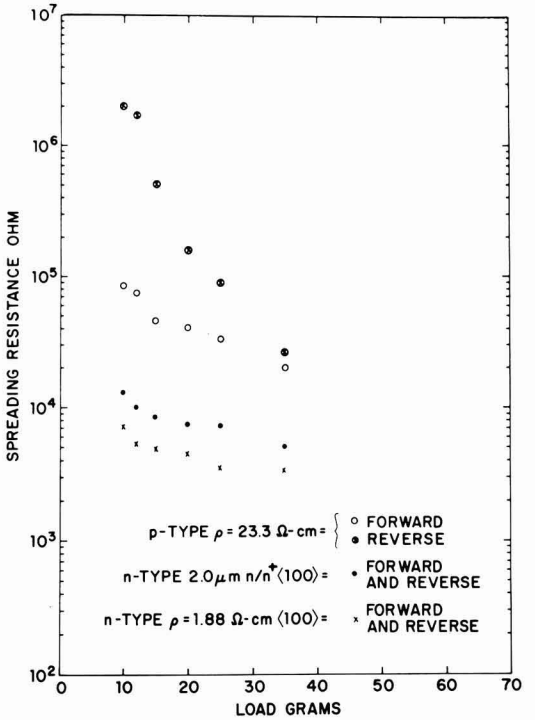

Fig. 5. Spreading resistance as a function of loading for a #741 osmium alloy point.

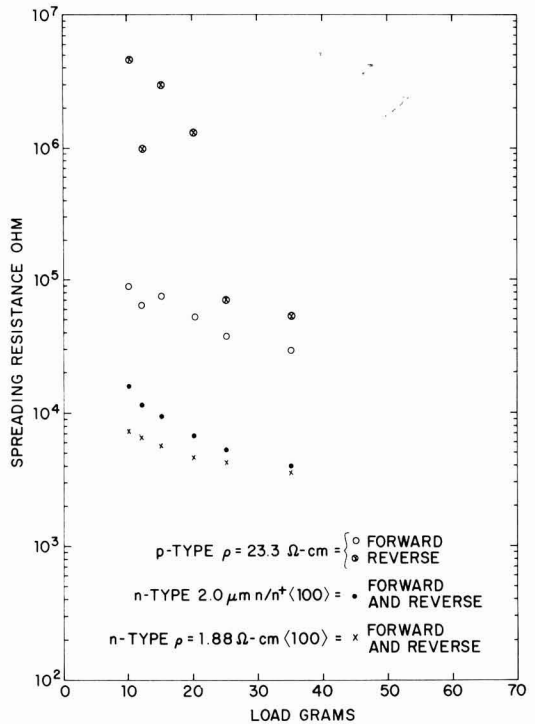

Fig. 6. Spreading resistance as a function of loading for a #347 ruthenium alloy point.

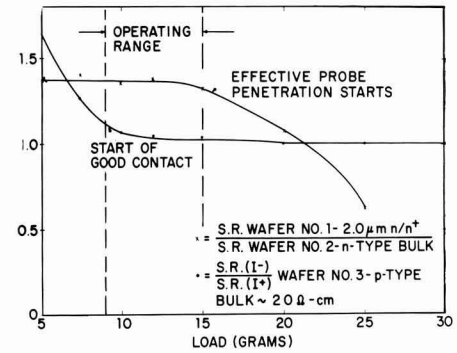

Fig. 7. Ratios of spreading resistances of n/n+ to n-type bulk wafers and spreading resistances in the reverse direction to the forward direction of current as a function of loading for a typical prepared K-75 probe point.

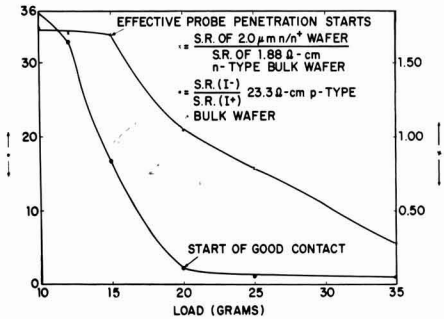

Fig. 8. Ratios of spreading resistances of n/n+ to n-type bulk wafers and spreading resistances in the reverse direction to the forward direction of current as a function of loading for an unprepared K-75 probe point.

some ρ on an N+ substrate exhibiting a certain spreading resistance; No. 2, an n-type bulk wafer with approximately the same spreading resistance as wafer 1; and No. 3, a p-type mechanical polished bulk wafer of ~ 20.0 ohm-cm. Starting with a probe point loading of 5.0g, the ratios of the spreading resistances of the n/n+ wafer to the n-type bulk and the spreading resistances in the reverse direction of current to the forward direction of current of the p-type wafer are plotted as a function of loading.

Figure 7 represents a probe point which will be operable in the range of 9-15g loading. The selection of the load for proper operation is limited to the regions where both ratios have a slope of 0. For comparison, Fig. 8 presents the same ratios for the probe point used in Fig. 1. In this case, the regions where the slopes are 0 do not coincide for any loading of the probe point indicating that the point cannot be used effectively in a spreading resistance apparatus.

At this point, the loading should be set at the midpoint of the operating range. Previous experience indicated that final conditioning of the point required repeated use under operating conditions to insure stability. Experimental data showed that a minimum of 250 measurement cycles are required to stabilize the probe point. Stabilization is a wearing-in process that removes probe point spikes that are not strong enough to withstand repeated operations. These manifest themselves by rapid changes in the spreading resistance.

Figure 9 is a test profile of a n/n+ epitaxial wafer. The wafer was beveled at a 1° angle and spreading resistance was measured on the bevel at intervals of

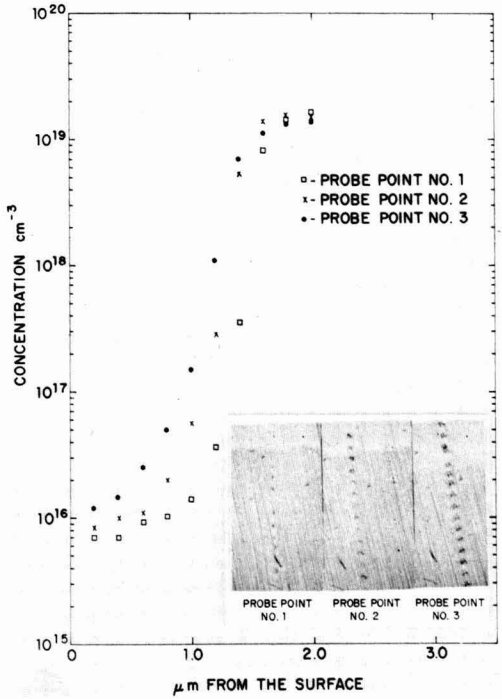

Fig. 9. Concentration *vs.* depth profile of a thin n/n+ epitaxial layer measured with three different K-75 probe points.

0.0005 in. resulting in depth increments of 0.20 μm. Three probe points, using the apparatus described in Ref. (4), were used to determine concentration *vs.* depth profiles. Probe point 1 was considered to have minimal effective penetration and probes No. 2 and 3 had increasing effective penetration, respectively. Visual inspection of the photographs of the three points' indentations on the bevel corroborate this finding. Probe point No. 1 was the only probe that would qualify as a good point using the method described previously.

Discussion

The method has been developed that produces probe points to be used in the measurement of spreading resistance of silicon with good precision. The requirements that a probe point must have are little effective penetration and good contact. A probe point with, and only with, these characteristics enables concentration *vs.* depth profiles of thin layers of any type structure to be measured.

Acknowledgments

The authors wish to acknowledge the help of Mr. P. A. Schumann, Jr., for his helpful discussions in preparation of this paper and Mr. P. Amato for some of the experimental data presented in this paper.

Manuscript submitted Sept. 15, 1969; revised manuscript received Jan. 26, 1970. This was a Late News Paper presented at the New York Meeting, May 4-9, 1969.

Any discussion of this paper will appear in a Discussion Section to be published in the December 1970 JOURNAL.

REFERENCES

1. R. G. Mazur and D. H. Dickey, *This Journal*, **113**, 255 (1966).
2. E. E. Gardner, "Symposium on Manufacturing In-Process Control and Measuring Techniques for Semiconductors," Phoenix, March 9-11, 1966.

3. E. E. Gardner, P. A. Schumann, and E. F. Gorey, "Measurement Techniques for Thin Films," p. 258, B. Schwartz and N. Schwartz, Editors, The Electrochem. Soc. (1967).

4. J. M. Adley, M. R. Poponiak, C. P. Schneider, P. A. Schumann, and A. H. Tong, Paper 324 presented at Electrochem. Soc. Meeting, New York, May 4-9, 1969.

Technical Note

Electrical Properties of Flash Evaporated Thin Film CdSe-CdTe Alloys

Tung H. Weng

School of Engineering, Oakland University, Rochester, Michigan

The work described in this paper was undertaken to determine the feasibility of forming thin film solid solutions of CdSe and CdTe by means of flash evaporation techniques and evaluate their electrical properties. One of the outstanding features of this alloy is the continuous variation of energy band gap and electrical properties with the composition of the constituent compounds. This means that a semiconductor with specific properties can be prepared simply by changing the composition. Such a wide range of properties would undoubtedly widen the scope of application which could not be achieved otherwise with a simple compound semiconductor.

Film preparation.—The apparatus used for flash evaporation is similar to that suggested by Müller (1), but with different design in the part of the powder feeder assembly as shown in Fig. 1. Instead of using mechanical vibration as in Müller's system, the powder is fed into the evaporator by a relay-operated plunger. When the relay is energized or de-energized by a variable square wave generator, the plunger strikes the reservoir so that the powder falls through a small opening located at the bottom of the reservoir into the funnel of the evaporator. This method provides a continuous and uniform rate of feeding which is essential if a homogeneous film with the original composition is to be obtained. One of the advantages of this system is that the rate of feed, and hence the rate of deposition, can be easily controlled by merely changing the frequency of the generator when the other physical settings, such as the diameter of the opening and the weight of the plunger, remain unchanged. This is desirable because it provides a simple means for controlling the crystalline structure as well as the properties of the deposit which is known to depend heavily on the deposition rate.

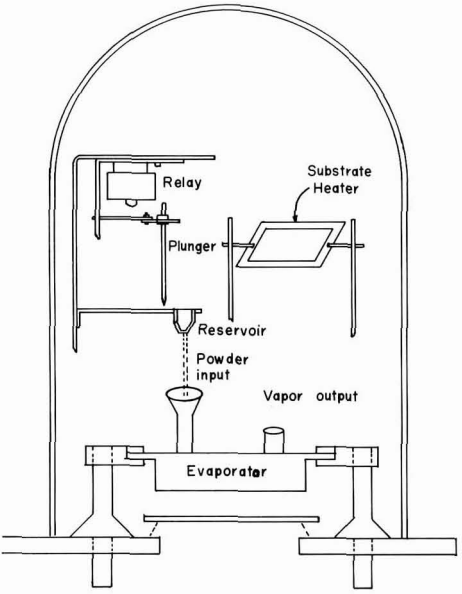

Fig. 1. The flash evaporation system

A folded molybdenum sheet was used as substrate heater. The glass substrate was inserted between the two sheets and clamped to the heater by metal screws. A Chromel-Alumel thermocouple for measurement of substrate temperature was placed adjacent to the substrate heater and made direct contact to the glass. The substrate was located about 8 in. from the evaporator with the hope that such a large distance between substrate and evaporator would minimize the heating effect generated by the heat radiating from the evaporator and produce a uniform thickness of the deposit. The vacuum system used is a 4 in. diffusion pump system with a liquid nitrogen trap. The pressure was maintained at 5×10^{-6} Torr during the entire evaporation. The evaporator which was designed specifically for the flash evaporation of compound semiconductors was kept at 1200°C. This assures a rapid and complete evaporation of each grain of the CdSe-CdTe powder which reaches the heater source.

CdSe and CdTe powders having a purity of 99.999% were supplied by Semi-elements, Inc. These powders were well mixed and sieved through a 0.088 mm opening before being put into the reservoir of the powder feeder assembly. For a given physical setting of the assembly, the rate of feed was approximately 10 mg/min which produced a 5 Å/sec deposition rate. A lower rate was also used, but the film resistivity was substantially higher than those obtained at 5 Å/sec. This is presumed to be caused by the absorption of oxygen during the crystal growth even though the vacuum pressure was in the 10^{-6} Torr range. In order to obtain a wide range of solid solutions, the composition used in this investigation varied from 10 to 90% of CdSe by weight. The substrates used were Corning's Type 7059 glass with dimensions of 3 in. x 1 in. x 0.048 in. Microslides with the same dimensions as the 7059

glass were also used. It was found that no significant difference in the characteristics of the deposited films was observed when these two types of glasses were interchanged. The substrates were cleaned, baked, and preheated to the designated temperature before evaporation took place. A set of four films with different substrate temperatures ranging from 50° to 200°C was prepared at a single pump down. This was intended to reveal the properties of the films as a function of the substrate temperature without being affected by other parameters which could conceivably have a pronounced effect on the properties of the deposits. A lower substrate temperature could not be obtained because of the heat radiating from the evaporator even with the substrate located far from the heater source. At higher substrate temperatures, however, the film resistivity was so high that the electrical measurement became increasingly difficult to perform and in many cases a thicker film could not be obtained. This is believed to be due to either re-evaporation or to a low sticking coefficient at a higher temperature.

Film properties.—The lattice type and constants of the CdSe-CdTe films were determined using x-ray diffraction. The diffractometer patterns were taken at room temperature and the output showed a single peak with a Bragg angle which varied with the composition of the constituent compounds. No trace of either CdSe or CdTe was detected regardless of their composition and preparation conditions. Since the as-deposited films showed a strong preferred orientation which would not give the information needed for an accurate result, the diffraction of randomly oriented powder was then performed. This was done by first stripping the films from their substrates and then pulverizing them before x-ray data were taken. Based on diffraction from various [hkl] planes, it was possible to determine their crystal type and lattice parameters rather accurately. The results are tabulated in Table I, and are similar to those obtained by Stucks and Farrell (2) for pure CdSe-CdTe alloys. The film containing 50 w/o (weight per cent) of CdTe could not be positively identified. This presumably was due to the presence of both hexagonal and cubic structures as reported elsewhere (2). There were no notable changes between the interplanar distance for a given composition when the substrate temperature was changed from 50° to 200°C. The relative intensity distributions for the powdered CdSe-CdTe alloys were estimated by measuring the peak heights directly on the diffractometer tracings. These data showed that the intensities for [002] (hex.) and [111] (cubic) directions are stronger than other reflections. These were also the preferred orientations of the films as deposited where a single peak was observed.

Table I. Lattice type and constants of thin film CdSe-CdTe alloys

Percentage of CdSe in CdSe-CdTe alloys	Hexagonal structure a Å	c Å	Cubic structure a Å
100	4.290	7.010	
75	4.352	7.146	
60	4.390	7.200	
50			
40			6.301
25			6.336
10			6.387
0			6.471

The carrier mobility and conductivity of CdSe-CdTe films with thickness of about 2000Å were determined using the Hall effect measurements. The dimensions of the Hall sample were 3/16 in. x ⅜ in. with evaporated indium films as ohmic contacts. All films regardless of their composition were N-type with carrier mobility and concentration varying with both composition and substrate temperature. In general, both mobility and carrier density decreased with increasing substrate temperature and varied appreciably from one set of films to another. Since reproducible properties of these films cannot be obtained without strict control of the preparation conditions, no attempt was made to pin down their electrical properties as a function of the preparation conditions. However, the mobilities of the films containing 25-50 w/o of CdSe prepared at the substrate temperature around 50°C were in the vicinity of 30 cm^2/V-sec. This figure is comparable to those of pure CdSe films (3).

On the basis of experimental results, one concludes that the flash evaporation technique can indeed be used to form polycrystalline thin film solid solutions of CdSe and CdTe and similar alloys (4). This technique offers simplicity and could be easily adopted for epitaxial growth of these alloys onto various single-crystal substrates, provided that suitable growth condition could be established. One of the immediate applications of these thin film alloys is in the area of thin film transistors. These have been fabricated successfully (5) and showed similar characteristics as CdSe and CdTe insofar as the stability and frequency response are concerned.

Manuscript submitted Sept. 10, 1969; revised manuscript received *ca.* Jan. 26, 1970. This was Paper 179 presented at the Detroit Meeting, Oct. 5-9, 1969.

Any discussion of this paper will appear in a Discussion Section to be published in the December 1970 JOURNAL.

REFERENCES

1. E. K. Müller, *J. Appl. Phys.*, **35**, 580 (1964).
2. A. D. Stuckes and G. Farrell, *J. Phys. Chem. Solids*, **25**, 477 (1964).
3. F. V. Shallcross, *RCA Review*, **24**, 676 (1963).
4. Tung H. Weng and H. J. Yu, *Solid-State Electron.*, **12**, (1969).
5. Tung H. Weng, *Proc. IEEE*, **57**, 1780 (1969).

Brief Communication

Porosity in Electrodeposited Gold-Alumina Alloys

E. S. Chen and F. K. Sautter

U. S. Army Watervliet Arsenal, Watervliet, New York

Porosity is an important factor which affects the properties of all materials. In recent years, the emphasis of many investigations was on the effect of porosity in relation to fracture (1), creep (2), and ductility (3, 4) of materials. However, it is frequently overlooked that test materials inherently contain pores as a consequence of the fabrication process. This is particularly true in the case of dispersion strengthened

alloys regardless of whether the manufacturing process is one of powder technique or electroforming. This report presents the results of a study on the porosity in electroformed Au-Al_2O_3 alloys before and after high-temperature heat treatment and the attending implications of porosity in the creep strength of these alloys.

Experimental

Electrodeposited Au-Al_2O_3 alloys were prepared from solutions containing

$KAu(CN)_2$	10 g/liter
KCN	10 g/liter
α-Al_2O_3 (1.0μ)	2-25 g/liter

using the techniques reported by Sautter (5). The plating was conducted at a *p*H of 10.5, current density of 3.5 mA/cm^2, and temperature of 60°C using pure gold as soluble anodes and electropolished copper tubings, 0.4 cm diameter, as cathodes. The solutions were agitated by Teflon-coated magnetic stirrers. Only one plate was prepared from each solution. For a cathode with a total surface area of 10 cm^2, the thickness of the deposit was on the average 180μ after 16 hr of plating. Tubular Au-Al_2O_3 alloy samples are obtained on removing the copper substrate by dissolution in 50% HNO_3.

The porosity in our electroformed alloys was studied through density measurements since such studies are commonly used to measure residual porosity in sintered materials and are also applicable to studying porosity in dispersion-hardened alloys (6). The density of Au-Al_2O_3 samples weighing 1.5g each were determined with an immersion technique using an analytical balance with a sensitivity of 0.1 mg. The immersion solution was doubly distilled water with added Triton X-100 surfactant to lower the surface tension to 35 dynes/cm thereby reducing solution damping effects. The precision of the density measurements is better than $\pm$0.03 g/cm^3. The density for each sample was determined at room temperature before and after annealing for 1 hr at 1000°C in air. The Al_2O_3 content in the alloy specimens was determined gravimetrically.

In the course of preparing the alloy samples for density measurements, the observation was made that all annealed samples show permanent length increases. This unique behavior in the electrodeposited Au-Al_2O_3 alloys was further investigated with a Leitz dilatometer, using a heating rate of 2°C/min.

Results

Typical results of the density measurements as a function of Al_2O_3 content are shown in Fig. 1. The upper curve shows the density of the as-plated alloy to be a linear function of oxide volume per cent (v/o) and that the measured densities would superimpose on the theoretical values (not illustrated) predicted by the rule of mixtures using the densities of pure gold and aluminum oxide as 19.3 and 3.97 g/cc, respectively. The lower curve shows the effect of the heat treatment. The initial decrease in density is very pronounced up to an oxide concentration of 1.5 v/o at which point the density appears to vary linearly with further increases in oxide content. Figure 2 shows the expansion behavior typical of the Au-Al_2O_3 alloys tested. The curve shows the linear expansion *vs.* temperature of an alloy specimen 1.0 cm long containing 10.5 v/o 1μ Al_2O_3 particles against a 5.0 cm pure gold reference. Distinct discontinuities in the expansion-temperature curve were observed at 240°, 330°, and 450°C, indicating the release of different gas impurities from the metal matrix as well as adsorbed impurities from the surface of the oxide particles. Impurity analysis using mass spectrometry showed that the composition of the evolved gas was mainly hydrogen and water and that gas evolution commences at about 300°C.

Discussion

The difference between the densities of the plated alloys before and after heat treatment can be attributed to the presence of adsorbed impurities on the surface of the oxide particles. These impurities may be water, hydroxyl groups, or organic additives present in the plating electrolyte and are codeposited with the

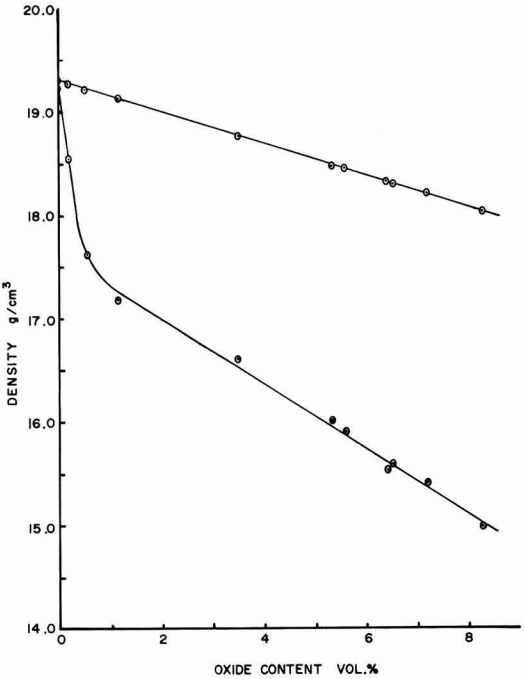

Fig. 1. Density as a function of volume per cent oxide in Au-Al_2O_3 (1.0μ) alloys. (Upper curve—as-plated alloys; lower curve—annealed alloys, 1 hr at 1000°C.)

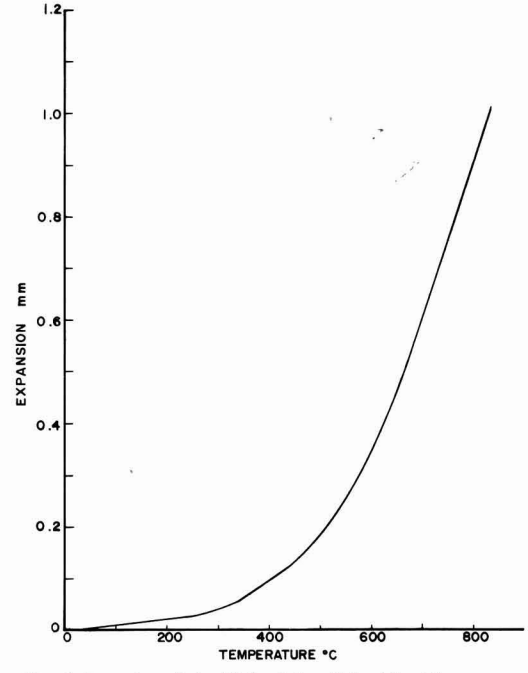

Fig. 2. Expansion of Au-Al_2O_3 (1.0μ, 10.5 v/o) with temperature for a heating rate of 2°C/min.

oxide particles. It has been calculated that an adsorbed monolayer on powders with a specific surface area of 100 m^2/g represents an impurity level of 5-10 v/o (7). The adsorbed monolayer occupies little volume in the condensed state. As such, the as-plated density should not deviate from the theoretical value; however, gasification of the impurities at high temperatures introduces porosity resulting in a subsequent decrease in alloy density. A simple calculation can illustrate this point more clearly. Consider an alloy sample containing 8 v/o oxide that is annealed at 950°C. The 1μ Al_2O_3 powder has an estimated specific surface area of 2 m^2/g. At 950°C, the gasified impurities build up sufficient pressure to cause irreversible deformation in the alloy. The resulting pore volume can be estimated by neglecting the effects of surface energy and assuming the ideal gas law holds. Using the pressure $P = 72$ psi or 4.9 atm which is the stress at zero strain (threshold stress for creep deformation) for a gold alloy containing 8 v/o oxide (8), $T = 1223$°K, $R = 82$ cc atm/°mole and 0.00016/18 moles of water, the pore volume is estimated to be 0.18 cc or 18 v/o. This compares favorably with our experimental value of 16.4 v/o measured at a slightly higher temperature of 1000°C. In view of the crude nature of the foregoing calculation, the significance of the illustration should not be attached to the agreement obtained but rather to the probability of pore formation proceeding in this manner. The initial sharp decrease in density of the heat-treated alloys is difficult to interpret without further investigation; however, one possible explanation is that should the relative degree of oxide particle agglomeration in the plating solution be greater when the solution is less concentrated in oxide, the resulting electrodeposit will also contain more agglomerated particles. Because occluded electrolyte is more prevalent in the agglomerated case, such system will show more porosity when the alloys are heat treated. Optical microscopic examination of polished alloy specimens indicates that a difference in degree of agglomeration does exist in the electrodeposits prepared from plating solutions of varying oxide concentrations. To eliminate the effects of particle agglomeration entirely, we are currently conducting experiments whereby electrodeposits are prepared under ultrasonic agitation to achieve optimum oxide dispersion.

The amount of porosity in the electrodeposited Au-Al_2O_3 alloys as calculated from our density measurements was as high as 16.5 v/o. A similar but smaller increase in porosity was observed after heat treatment of extruded and drawn Au-Al_2O_3 samples prepared by powder metallurgy. Furthermore, we have qualitatively studied alloy samples which were heat treated to produce porosity followed by cold working, extruding, and wire drawing whereby the density approached 99.9% of the theoretical value only to find that subsequent annealing will restore the porosity. This effect is a consequence of residual gases which can be eliminated only by completely melting the sample. In terms of high-temperature properties, the important criterion is therefore no longer the nucleation but the growth of existing pores that will determine the creep strength of these dispersion strengthened alloys. The presence of nonassociated pores anchored by uniformly distributed oxide particles will require creep deformation to be accompanied by the growth of these pores. Thus any gaseous impurities which can lower the internal metal surface energy must also be considered. The gasification of impurities, particularly that of water, at the indicated temperatures is in general agreement with the findings of other investigators (9), who deduced that surface hydration does occur on suitable parts of the α-Al_2O_3 surface and that ignition to 400°C results in the dehydration of physically bound water, while ignition above 400°C eliminates chemically bound water. Additional work is in progress using differential thermal analysis techniques to gain insight on the dehydration and gasification of adsorbed impurities in these alloys.

Manuscript submitted Aug. 29, 1969; revised manuscript received Jan. 28, 1970.

Any discussion of this paper will appear in a Discussion Section to be published in the December 1970 JOURNAL.

REFERENCES

1. D. Hull and D. E. Rimmer, *Phil. Mag.*, **4**, 673 (1959).
2. R. C. Boettner and W. D. Robertson, *Trans. AIME*, **221**, 613 (1961).
3. J. O. Stiegler, K. Farrell, B. T. M. Lok, and H. E. McCoy, *Trans. ASM*, **60**, 494 (1967).
4. H. Kellerer and G. Piatti, *J. Matls. Sci.*, **3**, 222 (1968).
5. F. K. Sautter, "Electrodeposition of Au-Al_2O_3 Alloys," Tech. Report WVT-RR-6321, Dec. 1963.
6. P. Bonnet, H. Kellerer, G. Piatti, and H. W. Schleicher, *Scripta Met.*, **2**, 689 (1968).
7. R. K. Stringer, C. E. Warble, and L. S. Williams, "Kinetics of Reaction in Ionic Systems," Material Science Research, Vol. 4, p. 74, Plenum Press (1969).
8. F. K. Sautter and E. S. Chen, "Oxide Dispersion Strengthening, Metallurgical Society Conferences," Vol. 47, p. 495, Gordon and Breach (1968).
9. D. J. O'Connor, P. G. Johansen, and A. S. Buchanan, *Trans. Faraday Soc.*, **52**, 229 (1956).

JOURNAL OF THE ELECTROCHEMICAL SOCIETY

REVIEWS AND NEWS

MAY 1970

Chemical Approaches to the Approximate Prediction of Band Gaps of Binary Semiconductors and Insulators

Ashok K. Vijh*

Hydro-Quebec Institute of Research, Varennes, Quebec, Canada

ABSTRACT

The chemical approaches to the approximate prediction of band gaps of binary inorganic semiconductors and insulators have been briefly reviewed with special emphasis on relatively recent work. These approaches involve establishment of correlations between band gaps and various other quantities, *e.g.* heats of formation, bond energies and electronegativities, *etc.* It has been shown that some of these correlations provide semiquantitative means for the estimation of band gaps of several materials for which it is either too difficult or impossible to compute accurate band gaps on the basis of methods of theoretical physics. The possible theoretical foundations of some of these correlations, as examined previously, have also been presented. Some of the recently proposed correlations, *e.g.* between band gaps and heats of formation per equivalent, even though rough, have universal validity in that they are applicable to all types of binary inorganic compounds covering a wide range of ionicity, crystal type, and band gaps.

It is generally recognized that the methods of theoretical physics are either inadequate or cumbersome for computing the width of forbidden gaps of all but the simplest semiconductors, *e.g.* Ge. The width of the forbidden gap is, of course, an extremely important parameter for the case of semiconducting compounds since it constitutes the basis for the calculation of band structure and the computation of the number of intrinsic carriers, and other properties. This situation has prompted a number of investigators to predict, albeit approximately, the band gaps of semiconductors by chemical approaches involving a variety of correlations (1-8). For example, band gaps have been related to heats of formation per mole (1), heats of formation per equivalent (7), electronegativities (3), atomic numbers (6), heats of atomization per atom (5), single bond energies (4), and average bond energies (8). Many of these correlations are purely empirical in nature. In some cases, however, attempts have been made to present some theoretical justifications (1, 5, 8-10).

In the present article, an attempt is made to present an outline of the more significant of these approaches with special emphasis on relatively recent work. It is assumed that the reader is familiar with the qualitative description of the band theory of solids as presented, *e.g.* in a recent lucid article (11). Other excellent articles on the band theory of solids, at a relatively elementary level, are also available in the literature (2, 3, 12-16).

It may be added that the fundamental contributions of Mooser and Pearson (17), Goodman (18), Suchet (19), and Welker (20) to the subject of prediction of semiconductivity in materials are not included in this article since their work has already been reviewed previously in some detail (10).

Correlation of Band Gaps to Various Quantities

It was demonstrated by Ruppel, Rose, and Gerritsen (1) that band gaps, E_g, of several semiconductors and insulators lie between one and two times the heats of formation per *mole* of the corresponding compounds (Fig. 1). It was pointed out (7), however, following Sanderson (21), that in correlations of the type shown in Fig. 1 the thermodynamic data must be "normalized," *i.e.* the heats of formation should be plotted as per equivalent (*i.e.* neither as per mole nor as per atom but as per atom equivalent). This correlation (Fig. 1) was extended to several more compounds by including this concept of normalization (7), and the results are shown in Fig. 2. It is clear from Fig. 2 that, *roughly,* a very large variety of semiconductors and insulators obey the relation:

$$E_g = 2\,\Delta H_e \qquad [1]$$

where ΔH_e is the heat of formation per equivalent. For the case of polyatomic compounds formed between polyvalent ions, it is particularly glaring that (Table I) the proposal of Ruppel *et al.* (1) is not sustained, whereas Vijh's relation (Fig. 2) gives rather satisfactory predictions of approximate values of the band gaps (Table I).

In a correlation proposed by Hooge (Fig. 3), band gaps of several binary compounds may be satisfactorily estimated from electronegativities by means of an empirical equation. This correlation (3) does not, however, include polyatomic compounds.

In a very interesting paper, Manca related the single bond energies of several compounds, calculated by Pauling's empirical equation (22), to their band gaps,

* Electrochemical Society Active Member.

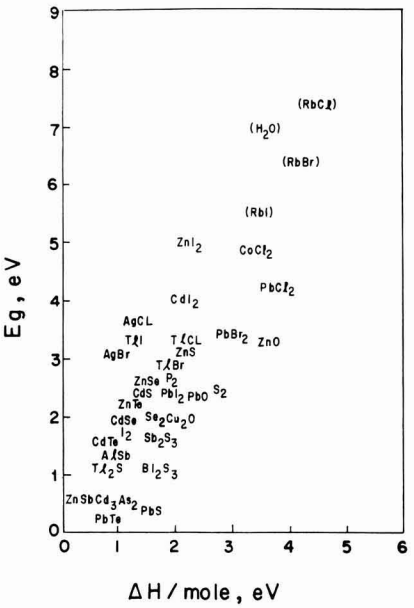

Fig. 1. Correlation between band gaps and heats of formation (standard state) per *mole* for several compounds, after Ruppel, Rose, and Gerritsen (1).

Table I

Compound	E_g (Ruppel *et al.*), eV	E_g (Vijh), eV	E_g (experimental), eV
Al_2O_3	17-34	5.67	7
Ta_2O_5	21.75-43.5	4.35	4.6
TiO_2	9.46-19.92	4.73	3.0
Ga_2O_3	11.19-22.38	3.73	4.4
In_2O_3	9.63-19.26	3.21	2.8

through an empirical relation of the type:

$$E_g = a\,(E_s - b) = 2\,(E_s - b) \qquad [2]$$

where E_g is the band gap value; E_s is the single bond energy; a and b are constants characteristic of a given class (*e.g.* $A^{IV}\,B^{IV}$, $A^{III}\,B^{V}$, *etc.*) of semiconductors. For the compounds examined by Manca, the value of a is roughly equal to 2. Manca's results showing the validity of Eq. [2] for several compounds have been presented in Fig. 4. In another paper, Bailly and Manca (5) have shown that for several compounds the following relation is obeyed:

$$E_g = \overline{A}\,(\Delta G^s - \overline{B}) \qquad [3]$$

Here ΔG^s is the free energy of sublimation per atom of the semiconducting compounds and $\overline{A}$ and $\overline{B}$ are parameters characteristic of each series of semiconducting material. It may be seen from Fig. 5 that Eq. [3] holds for a typical series of compounds. Bailly and Manca have also analyzed the factors that determine the magnitude of parameters $\overline{A}$ and $\overline{B}$ for several series of inorganic compounds (5).

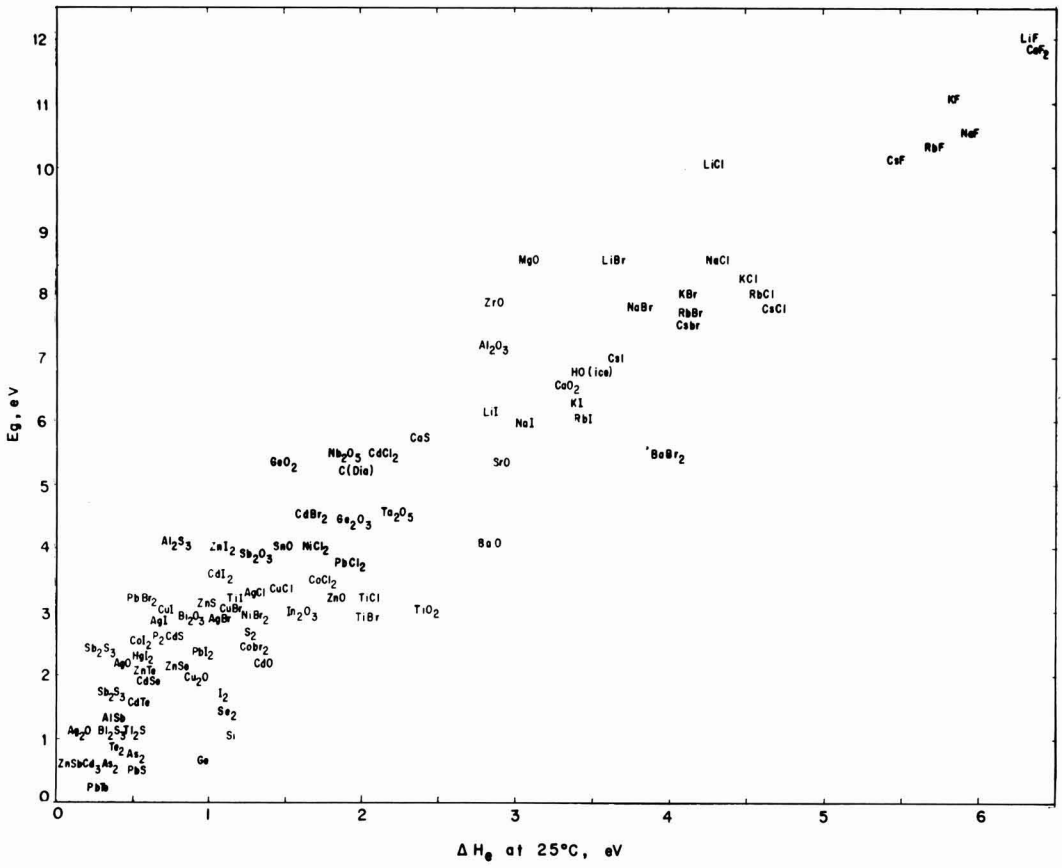

Fig. 2. A plot of band gaps *vs.* heats of formation (standard state) per equivalent for a large number of inorganic binary compounds (7)

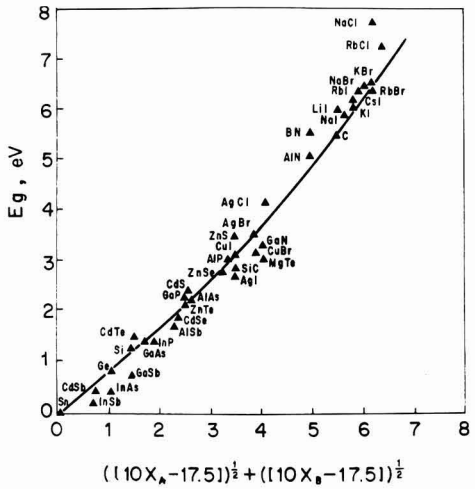

Fig. 3. Hooge's (3) relationship between band gaps and a function of electronegativities, X, for some semiconductors and insulators.

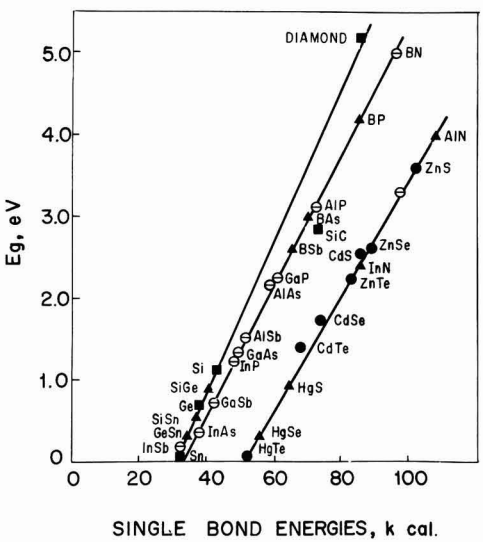

Fig. 4. Manca's correlation between single bond energies, as estimated by Pauling's method, and band gaps for several series of inorganic substances (4).

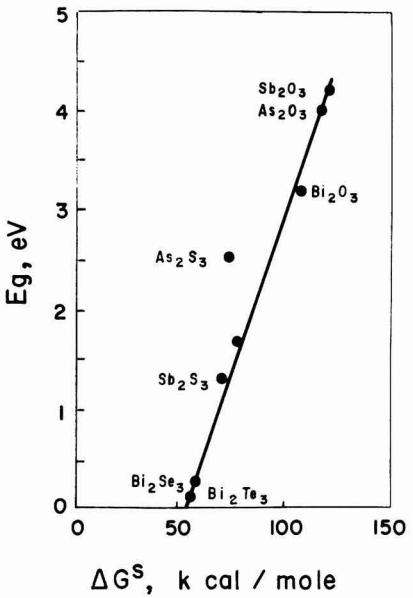

Fig. 5. A typical plot of free energy of sublimation per atom against band gaps for a given series of semiconductors, as presented by Bailly and Manca (5).

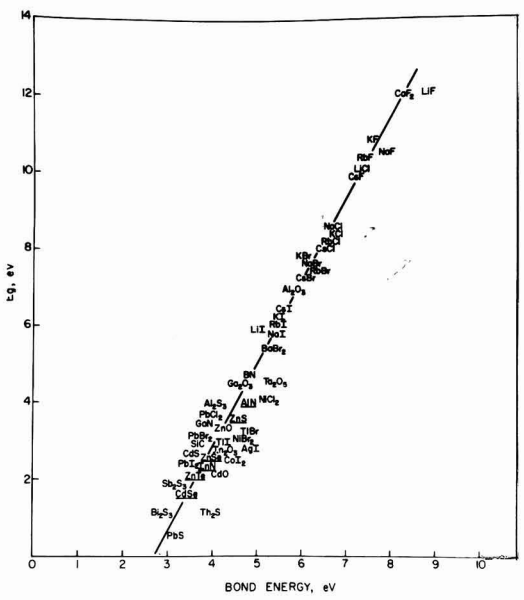

Fig. 6. A plot depicting correlation of average bond energies with band gaps for a wide range of inorganic binary compounds. Bond energies for CdSe, ZnTe, InN, ZnSe, ZnS, and AlN are single bond energies estimated by Pauling's empirical equation since reliable thermodynamic data are not available for calculation of average bond energies (8).

All the foregoing correlations (Fig. 1-5) have a serious limitation in that they are empirical in nature. Further, most of them (Fig. 1, 3-5) are restricted to certain special classes of compounds and lack universal applicability. However, the relationship presented in Fig. 2 is an exception in this particular respect; *i.e.* it has general applicability. A point that may be emphasized here is that most of these correlations are rather approximate in nature.

Recently, Vijh (8) has presented a correlation (Fig. 6) between average bond energies and band gaps, E_g, of several inorganic binary compounds. In fact it has been shown that Manca's Eq. [2] is applicable to a large variety of compounds (Fig. 6) if E_s in Eq. [2] is assumed to denote an average bond energy as calculated by a thermochemical procedure, instead of representing a single bond energy value. It is important to note that this correlation (Fig. 6) is *not* restricted to some particular class of semiconductors and is in fact a general one and includes compounds which cover the following spectrum of behavior:

(i) Inorganic compounds which range from highly covalent (Sb_2S_3) to those which are highly ionic (NaF).

(ii) Semiconductors and insulators representing a rather large range of band gap values, *e.g.* 0.5 to 12 eV.

(iii) There are several substances in Fig. 6 (and Table I) which are polyatomic binary compounds formed between *polyvalent* ions, *e.g.* Sb_2S_3, Bi_2S_3, Al_2O_3, Ta_2O_5, *etc.*

(iv) A wide range of crystal structures as represented in Fig. 6, *e.g.* Wurzite, zinc blende, Corundum, cuprite, fluorite, NaCl, and CsCl.

The relationship presented in Fig. 6 is not only a rather general one but it can also be derived theoretically (8) for the case of ionic compounds, *e.g.* alkali halides. The theoretical basis of Fig. 6 and Fig. 2 has been outlined in the following section.

Some Theoretical Considerations

In this section, an attempt is made to indicate the theoretical basis of Eq. [2] and [1] for the case of alkali halides, assuming that E_s in Eq. [2] represents an average bond energy value. It is important, however, to precede this analysis by a discussion of some matters related to the question of proper definition of bond energies and band gaps.

Bond energies.—There are two procedures frequently used for the calculation of bond energies:

1. *Pauling's method—single bond energies*

The bond energy of an isolated diatomic molecule formed between two univalent atoms, *e.g.* NaCl, may be estimated by Pauling's empirical equation:

$$D(\text{Na-Cl}) = \tfrac{1}{2}\{D(\text{Na-Na}) + D(\text{Cl-Cl})\} + 23(X_{\text{Na}}-X_{\text{Cl}})^2 \quad [4]$$

Here, D(Na-Cl) is the bond energy between Na and Cl in NaCl; D(Na-Na) is the bond energy between Na atoms; D(Cl-Cl) is the bond energy between two chlorine atoms; X_{Na} and X_{Cl} are the electronegativities of Na and Cl, respectively, on the Pauling Scale (22). This method gives fairly accurate estimates of bond energy between two univalent atoms held together by a single bond, *e.g.* NaCl. However, when more than one bond is involved, *e.g.* in CH_4, Pauling's procedure does not give a good estimate of the average C-H bond energy, but only yields a value for the last dissociation energy, *i.e.* C-H bond, when only one H is present on C. When applied to cases involving either divalent or multivalent atoms, *e.g.* Ta_2O_5, Sb_2S_3, GaN, this method gives an estimate of the energy of the last bond in the molecule after all other bonds have been removed. It is believed that such a quantity is not a very good measure of the *general* magnitude of binding in a complex molecule, which must be represented by an average bond energy. The average bond energy thus obtained, it is believed, is more pertinent to the discussion of relation between binding and band gaps in inorganic compounds. This bond energy is calculated from the appropriate thermochemical data, as follows.

2. *Thermochemical procedure—average bond energies*

The bond energy of a compound, *e.g.* NaCl, may be obtained from the equation:

$$D(\text{Na-Cl}) = \Delta H_S + \tfrac{1}{2}\,\Delta H^\circ_{\text{diss}} + H^\circ_f \quad [5]$$

Here, D(Na-Cl) is the required bond energy; ΔH_S is the heat of sublimation of Na metal per *mole*; ΔH_{diss} is the heat of dissociation of Cl_2 molecule into Cl atoms, again, per mole; ΔH°_f is the heat of formation of NaCl in its standard state, again per mole. The quantity given by Eq. [5] (*i.e.* bond energy) is, of course, the heat of atomization of NaCl. In the case of NaCl, only one shared electron pair is involved in the bonding. For complex compounds, *e.g.* Al_2O_3, several bonds (*i.e.* shared electron pairs) are involved and hence an appropriate normalizing factor must be used to obtain from Eq. [5] the bond energy per *bond* and not the total energy for all the bonds in Al_2O_3. This is done by computing, first from Eq. [5], the heat of atomization per mole which is then normalized with respect to the participating valences in order to obtain heat of atomization per equivalent, which is, of course, the bond energy. For example, the heat of atomization per equivalent (*i.e.* the bond energy) for Al_2O_3 is 1/6 of the heat of atomization per mole as calculated from Eq. [5]. Further details on these and related matters are available elsewhere (7, 8, 21-23).

The heat of atomization per equivalent thus obtained, after some second-order corrections (*e.g.* spin correlation stabilization energies, coordinate valence) as discussed by Howald (23), are the actual values of the average bond energies as obtained from the experimental thermochemical data.

These average bond energy values have been used in constructing Fig. 6 (see, however, caption to Fig. 6). The accuracy of these bond energies is limited only by the accuracy of the thermodynamic data which were used in their calculation. These data have been obtained from reliable compilations (23-25). In obtaining these average bond energies, corrections to the heats of atomization per equivalent were applied only for spin correlation stabilization energies (23). The possible presence of coordinate valence has been ignored because unambiguous estimates of the extent of participation of coordinate valence in compounds are not always easily obtained as discussed by Howald (23). Since the theoretical derivation of Eq. [2] and [3] (see below) is claimed to be strictly valid for alkali halides only, this neglect of coordinate valence in the calculation of bond energies is not serious, because alkali halides do not involve any coordinate bonds.

Band gaps.—These band gaps (Fig. 6) refer to k space at $k = 0$. It may be mentioned that precise definition and determination of band gaps involves some real difficulties. For example, in large band gap semiconductors like alkali halides, experimental values quoted are strongly influenced by coulomb effects, even though there is no significant difference between the direct and indirect gap since the bands are very narrow. This is because of the reason that the optical absorption is determined rather by the exciton structure in front of the energy gap than by the energy gap itself (8). In small band gap semiconductors, on the other hand, there are appreciable differences between direct and indirect gaps since the bands are rather wide (8). The significance of values of band gaps used in Fig. 6 must be accepted only in relation to these difficulties. It is believed, however, that the aforementioned difficulties in the precise definition and determination of band gaps are not serious enough to render values of band gaps in Fig. 6 so uncertain as to make the relationship presented invalid.

Derivation of Eq. [2] and [3] for ionic compounds.—As shown previously by Mark (26), the forbidden gap E_g of an ionic compound like NaCl is given by:

$$E_g = 2M - (I_m - A_x) \quad [6]$$

where M is the Madelung energy, I_m is the ionization potential of Na; A_x is the electron affinity of Cl. From Eq. [6],

$$E_g = 2(U - R) - I_m + A_x \quad [7]$$

where U is the experimental (thermochemical) lattice energy and R is an energy term which includes repulsive, London, and other components (*e.g.*, crystal field stabilization energy) of theoretical lattice energy (12) so that

$$M = (U - R) \quad [8]$$

is quite valid.

It may be readily shown, by means of a Born-Haber thermochemical cycle, that (12):

$$\Delta H^\circ_f = \Delta H_s + I_m + \tfrac{1}{2}\,\Delta H_D + A_x + U \quad [9]$$

where,

ΔH°_f is the heat of formation, *e.g.* of NaCl
ΔH_s is the heat of sublimation of Na
I_m is the ionization potential of Na

ΔH_D is the energy of dissociation of Cl_2 (g) into atoms
A_x is the electron affinity of Cl
U is the lattice energy of NaCl

The quantities defined above are all as per *mole* of the corresponding substance.

On obvious rearrangement, Eq. [9] gives:

$$-U = \Delta H_s + I_m + \tfrac{1}{2}\Delta H_D + A_x - \Delta H^o_f \quad [10]$$

Now we note that U, A_x, and ΔH^o_f are exothermic quantities (hence with $-$ sign) and ΔH_s, I_m, and ΔH_D are endothermic quantities (hence with $+$ sign) for alkali halides. On making these substitutions for exothermicity and endothermicity in Eq. [10], we obtain:

$$U = \Delta H_s + I_m + \tfrac{1}{2}\Delta H_D + \Delta H^o_f - A_x \quad [11]$$

Substituting Eq. [11] in Eq. [7],

$$E_g = 2\Delta H_s + 2I_m + \Delta H_D + 2\Delta H^o_f - 2A_x - 2R - I_m + A_x \quad [12]$$

or

$$E_g = 2\Delta H_s + I_m + \Delta H_D + 2\Delta H^o_f - A_x - 2R \quad [13]$$

On making an approximation that I_m is roughly equivalent to A_x in magnitude, one obtains:

$$E_g = 2\Delta H_s + 2\Delta H^o_f + \Delta H_D - 2R \quad [14]$$

or

$$E_g = 2(\Delta H_a - R) \quad [15]$$

where ΔH_a is the heat of atomization per *mole*, and for a diatomic molecule formed between two univalent ions (*e.g.* NaCl) is identical with the heat of atomization per equivalent, which is, of course, the average bond energy (8, 21-23).

When considering a polyatomic compound formed between either univalent or polyvalent ions, Eq. [15] has to be suitably modified. This is owing to the fact that Eq. [6] and [7] refer to the transfer of *one* valence electron only, *i.e.* from Na to Cl; in order to maintain the validitiy of Eq. [12], U in Eq. [11] must also be taken as per valence electron, *i.e.* as per equivalent. As a result, the ΔH_a term in Eq. [15] must be changed from ΔH_a/mole to ΔH_a/eq. for a polyatomic compound. As mentioned earlier, ΔH_a/eq. is, of course, the bond energy E_s. Hence,

$$E_g = 2(E_s - R) \quad [16]$$

For a closely related series of compounds, *e.g.* alkali halides, R may roughly be treated as a constant. Hence, Eq. [15] may be written as:

$$E_g = 2(E_s - b) \quad [17]$$

where "b" is a constant. This Eq. [17] is identical with Manca's equation, *i.e.* Eq. 2 in this paper.

The approximation made in the derivation of Eq. [17] may now be considered. If I_m is not roughly equivalent to A_x, then R in Eq. [16] may be transformed into R' where,

$$R' = R + \tfrac{1}{2}I_m - \tfrac{1}{2}A_x \quad [18]$$

For structurally related compounds, R' may again be assumed as, *roughly*, a constant. For example, for several alkali halides, values of R' lie close to 2.5 ± 0.5 eV. It is obvious, of course, that Eq. [18] must be appropriately modified for compounds involving positive electron affinities.

On the basis of the foregoing analysis, the possible theoretical basis of Fig. 2 may now be explored. Rewriting Eq. [14], by substituting Eq. [18] into it, one obtains:

$$E_g = (2\Delta H_s + \Delta H_D - 2R') + 2\Delta H^o_f \quad [19]$$

For several compounds, it turns out, fortuitously, that quantities in the parentheses of Eq. [19] either roughly cancel each other out or assume rather small net value (8). Hence, Eq. [19] may be approximated as:

$$E_g \simeq 2\Delta H^o_f \quad [20]$$

As mentioned in the foregoing discussion, in all such discussions the quantities must be properly normalized (7, 8, 21-23), *i.e.* taken as per equivalent which for a diatomic substance formed between uni-univalent ions is, of course, the same thing as per mole. Hence, Eq. [20] may be written as:

$$E_g \simeq 2\Delta H_e \quad [21]$$

Equation [21] is identical with Eq. [1], and it constitutes the possible theoretical basis of Fig. 2.

Limitations of the foregoing theoretical analysis.— It is clear that the foregoing analysis is invalid for elementary semiconductors since lattice energy for these substances has no significance. Also, molecular semiconductors like anthracene are not covered by the foregoing discussions. Further, theoretical foundations of Fig. 2 and 6 for the case of predominantly covalent binary compounds like Sb_2S_3 are not completely clear.

For the case of some covalent compounds, however, *e.g.* those included in Fig. 6, it is possible that the increase in cohesive energy due to homopolar binding approximately cancels out the decrease in lattice energy that may result from partial ionicity of the compound (8, 26). In these cases, experimental lattice energy values, U, will be nearly equivalent to the $(M + R)$ values that would have been obtained, had the compound been predominantly ionic. In some fortuitous cases of this type, the entire analysis presented here would still be valid, despite significant covalent bonding.

In some other cases of covalent compounds, the present analysis may be extended by modifying Eq. [17] to give:

$$E_g = 2(E_s - b) \pm \Delta U \quad [22]$$

where ΔU is the difference between the thermochemical and theoretical lattice energies (12) again taken as per equivalent.

It is important to emphasize that it is rather fortuitous that several covalent compounds obey the relationship shown in Fig. 6, despite the fact that no correction for homopolar bonding has been applied to them.

Concluding Remarks

It has been shown in the foregoing discussion that it is possible to obtain by chemical approaches some significant, semiquantitative correlations between band gaps and other properties, *e.g.* heats of formation and bond energies. The important points that have been brought out in this article are as follows:

(A) These correlations (Fig. 2 and 6) need not necessarily be limited to certain restricted classes of compounds.

(B) They yield semiquantitative results and not just qualitative trends.

(C) These correlations also lend themselves to some theoretical analysis.

It is obvious, of course, that these correlations are not very exact yet and would need considerable improvements and more sophisticated theoretical analysis before yielding procedures for accurate prediction of band gaps of materials.

Manuscript submitted Nov. 3, 1969; revised manuscript received Jan. 19, 1970.

Any discussion of this paper will appear in a Discussion Section to be published in the December 1970 JOURNAL.

REFERENCES

1. W. Ruppel, A. Rose, and H. J. Gerritsen, *Helv. Phys. Acta*, **30**, 238 (1957); see also, A. Rose, "Concepts in Photoconductivity and Allied Problems," last chapter, Interscience (1963).
2. H. Gatos and A. Rosenberg, "The Physics and Chemistry of Ceramics," C. Klingsberg, Editor, Gordon and Breach, New York (1963).
3. F. N. Hooge, *Z. Physik. Chem. Neve Folge*, **24**, 275 (1960).

4. P. Manca, *J. Phys. Chem. Solids*, **20**, 268 (1961).
5. F. Bailly and P. Manca, *ibid.*, **27**, 783 (1966).
6. R. H. Bube, "Photoconductivity of Solids," John Wiley & Sons (1966).
7. A. K. Vijh, *J. Phys. Chem. Solids*, **29**, 2233 (1968).
8. A. K. Vijh, *ibid.*, **30**, 1999 (1969); *idem, Solid State Commun.*, **7** (9), Vi (1969).
9. S. A. Semenkovich in "Chemical Bonds in Semiconductors and Solids," N. N. Sirota, Editor, Consultants Bureau, New York (1967).
10. J. P. Suchet, "Chemical Physics of Semiconductors," London (1964); see also, J. P. Suchet and F. Bailly, *Ann. Chim. (Paris)*, **10**, 517 (1965).
11. E. F. Gurnee, *J. Chem. Ed.*, **46**, 81 (1969).
12. W. J. Moore, "Seven Solid State," W. A. Benjamin, Inc., New York (1967).
13. Sir Nevill Mott, "The Solid State" in "Materials," W. H. Freeman and Co., San Francisco (1967).
14. L. V. Azaroff, "Introduction to Solids," McGraw-Hill Book Co., New York (1960).
15. L. H. Van Vlack, "Elements of Materials Science," Addison-Wesley Publishing Co., Inc. (1966).
16. A. J. Dekker, "Solid State Physics," Prentice Hall, Inc., Englewood Cliffs, N. J. (1957).
17. E. Mooser and W. B. Pearson, *J. Electron.*, **1**, 629 (1956).
18. C. H. L. Goodman, *J. Phys. Chem. Solids*, **6**, 305 (1958).
19. J. P. Suchet, *ibid.*, **12**, 74 (1959).
20. H. Welker, *Z. Naturforsch.*, **7a**, 744 (1952); **8a**, 248 (1953).
21. R. T. Sanderson, "Chemical Periodicity," Reinhold Publishing Co., New York (1960).
22. L. Pauling, "The Nature of the Chemical Bond," Cornell Press, Ithaca, N. Y. (1960).
23. R. Howald, *J. Chem. Ed.*, **45**, 163 (1968).
24. R. Rossini *et al.*, "Selected Thermodynamic Properties," N.B.S. 500, U.S. Govt. Printing Office, Washington, D.C. (1952).
25. "Handbook of Chemistry and Physics," 47th Ed., The Chemical Rubber Co. (1966).
26. P. Mark, *J. Phys. Chem. Solids*, **29**, 689 (1968).

SECTION NEWS

Columbus Section

A symposium on battery separators was held in Columbus, Ohio, on February 18-19, 1970 under the sponsorship of the Columbus Section of The Electrochemical Society. 19 papers covered separator materials and performance in lead-acid, nickel-cadmium, silver-zinc, and silver-cadmium batteries and rechargeable fuel cells. Approximately 100 scientists and engineers from the United States, Canada, England, and Sweden were in attendance.

The proceedings of the symposium will be published in a softbound book in approximately two months. A limited number of copies are still available at $7.00 each. Orders for copies of the proceedings should be sent to Dr. H. L. Goering, Battelle Memorial Institute, 505 King Avenue, Columbus, Ohio 43201. Checks should be made payable to Columbus Section of The Electrochemical Society.

The program consisted of the following papers:

"General Requirements and Characterization of Secondary Battery Separators,"—J. J. Lander, Air Force Aero Propulsion Laboratory, and E. J. Casey, Defense Research Establishment;

"A New Type of Microporous Polymeric Separator,"—Erik Sundberg, Tudor Sweden, and J. Q. Selsor, Amerace, Esna Corporation;

"Characterization of Anisotropic Films for Battery Separators,"—Michael J. Lysaght, Amincon Corporation;

"The Selection of Textile Fibers and Fabricating Techniques in Separator Design,"—Phoenix N. Dangel, Kendall, Fiber Products Division;

"Characterization and Performance of Separators for Ni-Cd Aircraft Batteries,"—Louis Belove and Paul Scardaville, Sonotone Corporation;

"QC Procedures and Measurements —Polypropylene Separators for Sealed Ni-Cd Batteries,"—T. E. King, Defense Research Establishment;

"Separators for Heat Sterilizable Ni-Cd Batteries," —R. Lutwack, Jet Propulsion Laboratory;

"Ultrafine Porous Polymer Membranes as Battery Separators,"—J. L. Weininger, General Electric Company;

"Cellulosic Separators for Alkaline Batteries—A Review,"—G. A. Dalin, Yardney Electric Corporation;

"Silver-Zinc Battery Separator Material Development,"—E. V. Kirkland, Monsanto Research Corporation;

"Improved Separator Materials for Alkaline Batteries,"—H. E. Hoyt, Borden, Inc., Chemical Division;

"Preparation and Properties of Separators for Silver-Zinc Cells,"—A. Langer and L. C. Scala, Westinghouse Electric Corporation;

"Preparation and Properties of Grafted Membrane Separators for Silver-Zinc Cells,"—V. D'Agostino, RAI Research Corporation;

"Performance of Organic Membranes and Inorganic Coatings as Separators in Silver-Zinc Cells,"—T. J. Hennigan, Goddard Space Flight Center;

"Charged Stand and Cycle Life Test Results on Separator Systems for Alkaline Cells,"—R. S. Bogner, Jet Propulsion Laboratory;

"QC for Heat Sterilizable Silver-Zinc Separator Materials,"—W. von Hartmann, Jet Propulsion Laboratory;

"Chemical and Physical Analysis of Grafted Membranes for Silver-Zinc Batteries,"—E. F. Cuddihy and J. Moacanin, Jet Propulsion Laboratory;

"Separator Developments for Rechargeable H_2O_2 Fuel Cells,"—M. G. Klein, Electro-Optical Systems, Inc.;

"Recent Advances in Ion Exchange Membranes for Use in Rechargeable Fuel Cells,"—A. P. Fickett, General Electric Company.

Concluding the program was a panel discussion chaired by Arthur Fleischer, with panelists T. J. Hennigan, R. Lutwack, T. E. King, and J. J. Lander.

Detroit Section

The Detroit Section held a meeting on March 19, 1970, at the McGregor Memorial Conference Center, Wayne State University. The guest speaker was Dr. C. V. King, Vice-President of the Society, and also President of American Gas & Chemicals, Inc. Dr. King gave a very interesting and lucid account of methods for determining gas leaks. Most of the methods described were chemical tests, involving the use of color-change tapes or papers, which could be used for rocket and missile fuels and oxidizers, for carbon monoxide, ammonia, hydrazine, unsymmetrical dimethyl hydrazine, hydrogen sulfide, for engine fuels, oils, and hydraulic fluids. A simple bubble test for butane lighters was described which involved immersion in water containing a suitable detergent. Dr. King also described a few electrochemical methods for determining leaks. The presentation was illustrated with several demonstrations.

Prior to the technical part of the meeting Dr. King spent fifteen minutes or so discussing Society affairs. The main topics covered were the transfer of the National Office to Princeton, N. J., the running of National Meetings by the National Office, and the Society's membership and financial standing.

Raymond Thacker
2nd Vice Chairman

National Capital Area Section

Jeanne Burbank receives 6th Annual William Blum Award

The National Capital Area Section recently presented its 6th William Blum Award to Mrs. Jeanne Beadle Burbank of the Naval Research Laboratory, Washington, D.C. The award was presented to Mrs. Burbank for her fundamental contribution to the science of electrochemistry and in particular to her fundamental research on storage battery and storage cell phenomena.

The award dinner, held at the Washingtonian Motel, Gaithersburg, Md., was attended by many members, guests, and friends. Among the distinguished guests were Mr. N. Corey Cahoon, President of The Electrochemical Society, Dr. J. C. White of the Naval Research Laboratory, and Dr. William Blum, for whom the award is named.

The program included opening remarks from the Chairman of the National Capital Area Section, Frank X. McCawley, who described the award purposes and criteria. Some pertinent remarks were made by Mr. Cahoon on behalf of the National Society. Dr. J. C. White then described Mrs. Burbank's career.

Jeanne Burbank received an A.B. degree from American University and an M.S. from the University of Pennsylvania. She spent some years at Peacock Laboratories in Philadelphia, Pa. in metallic coatings research. She was later employed at the Naval Research Laboratory where she has continued a long and distinguished career. She worked as a physical chemist in the Electrochemical Power Sources Section and later became Head of the Crystal Chemistry Section of the Electrochemistry Branch, Chemistry Division. She has received the American Institute of Chemists Award for undergraduate work and the Electrochemical Society Battery Division Research Award in 1966. In her researches she has applied X-ray and electron microscopy to the materials and components of the lead acid and silver zinc systems. She has also made substantial contributions to the understanding of battery grid corrosion and the active materials' reactions. She has over 35 papers on battery systems to her credit.

Twenty Years in the LAB

Having been asked many times why a woman would devote so much of her life to the lead-acid battery (LAB) she seized this unique opportunity to reply:

"The story of this lead box really begins close to 400 years ago. Shakespeare clearly foresaw and built the plot of his "Merchant of Venice" around the joy consequent to risking life and giving fortune for the unknown contents of a lead box, eschewing the alternate choices of gold and silver. This was another of his famous instances of precognition, for gold, the most noble metal known to his time, obviously stood for fuel cells, the silver box for the silver cells, but the real prize was in the lead box. Just so today, the reliable work horse of the storage batteries is the lead-acid cell. Likely to remain so too, because of the plentiful supply of lead.

"Despite the promises of Shakespeare, 300 years passed before Gaston Plante opened his lead box and discovered the lead-acid cell. Plante was considered a saint by those who knew him, he dedicated his life and fortune to his experimental work, he endowed a retirement home for penniless scientists, he gave his invention to the world free and clear of any patent restrictions. His invention changed the course of men's lives. Plante hooked his lead cell to Gramme's machine and electric motors became a working reality. With electric power and lighting, the working man began to perceive freedom from miserable drudgery and a life spent in essential bondage. This was the greatest treasure hidden in Plante's little lead box. But the promise of more treasure lingers on.

"One hundred years later, a privileged few of us still seek more treasure in these lead boxes. We find in our work the ecstatic joy of discovery, detective work more engrossing than any Sherlock Holmes mystery, and tiny crystals of surpassing beauty. Though it has been said that diamonds are a girl's best friend, these lead oxide crystals have been mine. Some of us are so fortunate as to find in these lead boxes an occasion such as this tonight.

"These are the personal treasures one find in these lead boxes. But there is a greater store of treasure yet to be uncovered. We must keep working and searching and developing. Why? Because we have in the lead box the promise of help with some urgent problems of today. Air pollution, exploration, expanded data storage and communication systems, national defense, and control and monitoring systems. We need quiet clean power for our automobiles, more people need more telephones, we cannot afford massive power black-outs, nuclear submarines and computers need batteries. Even a solid gold Cadillac can't be started without its homely battery. As modern culture patterns spread to more parts of the world, the lead-acid cell must of necessity go along, not for the ride, but to provide the ride and keep the wheels turning. We need every treasure in the lead box that we can uncover.

"And that's why this woman has spent the best twenty years of her life in the L.A.B. Thank you."

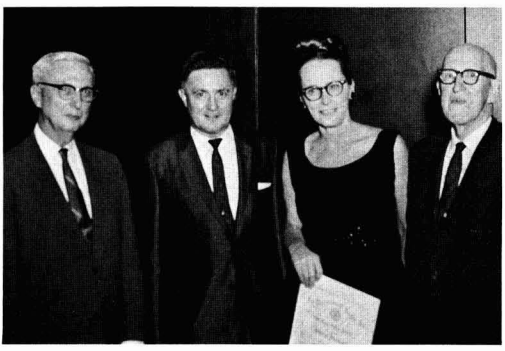

(from left to right):
Mr. N. Corey Cahoon
Dr. Frank X. McCawley
Mrs. Jeanne Burbank
Dr. William Blum

Metropolitan New York Section

The Metropolitan New York Section of The Electrochemical Society held its third meeting of the 1969-1970 year at the Stonehall Inn, New York, on March 11, 1970, with 24 members and guests attending. Following a cocktail hour and dinner, the meeting was opened by Dr. Eric Rau, Chairman. He apologized to those members who showed up for the meeting on January 11, 1970 without a reservation, because it was impossible to notify them in advance that the meeting was cancelled because of the threat of a heavy storm.

Dr. Rau then called upon Dr. Henry B. Linford to give a report on behalf of the Nominating Committee. Dr. Linford reported that the following men were proposed as officers of the Metropolitan New York Section for the year 1970-1971:

Eric Rau—Past Chairman
Dodd S. Carr—Chairman
D. Gardner Foulke—Vice Chairman
Palmer H. Langdon—Secretary-Treasurer.

He said that this slate would be presented for election at the business meeting on April 8, 1970.

The Chairman then called upon Dr. Cecil V. King to give a brief status report on the new National Headquarters Building of The Electrochemical Society. Dr. King reported that the building will be located on Route 1 in Princeton, N. J. and that it was scheduled for occupancy by the summer of 1970. The building will have two levels for offices and storage with dining facilities on lower level.

The meeting was then turned over to the Vice Chairman, Dr. Dodd S. Carr, who introduced the guest speaker, Dr. Thomas B. Reed of Lincoln Laboratory, MIT, Lexington, Mass., who gave an interesting presentation on the growth of single crystals by three methods. Using slides and a color movie, Dr. Reed explained the techniques of growing single crystals of EuO, EuS, EuSe, and EuTe, by the use of vapor deposited tungsten crucibles in refractory fur-

naces in the 2000-3000°C range; the use of electric arcs for material synthesis, purification, and crystal growth; and new methods for vapor growth of single crystals of ZnTe, using a "transparent furnace" especially suited for vapor growth of crystals. After a lively period of questions and answers, Dr. Reed demonstrated a model of the transparent furnace. Dr. Carr presented the speaker with a telescoping pocket pointer as a token of the appreciation of the Section for the fine lecture and the meeting was closed with a rising vote of thanks for Dr. Thomas B. Reed.

Dodd S. Carr
Vice-Chairman

North Texas Section

The winter meeting of the North Texas Section was held on January 26, 1970 in the Meadows Building Cafeteria in Dallas.

The speaker was Dr. Charles Tobias of the University of California. Dr. Tobias conducted an informal discussion of several aspects of Electrochemical Society activities such as the new location of the national headquarters. Following this discussion he made a technical presentation on "Electrolysis at High Rates."

Active and transpassive anodic dissolution modes of copper are characterized by different overpotentials and different resulting surface textures. Voltage transients observed during these dissolution processes are related to current densities and electrolyte flow rates. Passivation phenomena and the formation and removal of solid anodic reaction products are likely controlled by mass transport.

David F. Cole
Chairman

Pacific Northwest Section

The Pacific Northwest Section held its third meeting at Andy's Diner, Seattle, Wash., on March 16, 1970. After a social hour and dinner, Robert Glockling, Chairman, introduced David Roe, the guest speaker. Dr. Roe is on the faculty of the Oregon Graduate Center, Portland, Oreg. His illustrated talk was entitled "An Electrochemical and Mass Spectrometric Investigation of Platinum Electrodes."

In spite of their extensive use in electrochemistry, platinum electrodes show some unusual characteristics which eluded thorough explanations. The literature of the past ten years, in particular, is replete with electrochemical investigations of the surface oxidation of platinum and studies of oxidation of organic compounds on "activated" platinum. Deductive development of rigorous, or even consistent molecular models from such information is hampered by incomplete knowledge of, for example, true surface area, "active" surface area, adsorption sites, surface contamination, and the chemical nature of surface oxides.

Further insight in some of these problems has been obtained from combining mass spectrometry with electrochemical measurements. From these results it can be shown how to obtain a clean platinum surface, free of organic adsorbants. Also, anodic oxidation of platinum does not produce an oxide with any of the properties of PtO_2, as noted by decomposition behavior in vacuum. However, exposure of platinum to oxygen and water vapor at 210°C does result in detectable surface oxidation. This oxide can be reduced electrochemically and compared with anodically-formed oxide. Rate and equilibrium measurements of the vapor phase oxidation at 210°C leads to identification of the reaction as requiring one water molecule per atom of oxygen, i.e. $Pt + \frac{1}{2}O_2 + H_2O \rightarrow Pt(OH)_2$.

Sidney Gross
Secretary

1971 Palladium Medal Award, ECS

The tenth Palladium Medal of The Electrochemical Society will be awarded at the Fall Meeting of the Society to be held in Cleveland, Ohio, October 3-8, 1971. The medal was established in 1951 by the Corrosion Division.

The candidate shall be distinguished for his original contributions to theoretical electrochemistry or to fundamental scientific knowledge of corrosion processes. He need not be a member of the Society. There shall be no restrictions or reservations made regarding his citizenship, age, or sex.

To be eligible, the candidate shall agree to receive the award in person at the designated national meeting of the Society. He shall also agree to present a general lecture before the Society, at the above designated national meeting, to be called the Palladium Medal Address. This address will in general describe some area of the candidate's researches, and will be presented at a time and place during the meeting to be specified in each instance by the Board of Directors.

Previous medalists have been: Carl Wagner, Max Planck Institut fur Physikalische Chemie; N. H. Furman, Princeton University; U. R. Evans, Cambridge University; K. F. Bonhoeffer, Max Planck Institut fur Physikalische Chemie (posthumous award); A. N. Frumkin, Electrochemical Institute of the USSR; H. H. Uhlig, Massachusetts Institute of Technology; Norman Hackerman, University of Texas; Paul Delahay, New York University; and Thomas P. Hoar, Cambridge University.

Sections, Divisions, and members of the Society are invited to send suggestions for candidates, accompanied by supporting information, to Mr. Ernest G. Enck, Executive Secretary, The Electrochemical Society, 30 East 42nd St., New York, N. Y. 10017, for forwarding to the Committee Chairman. Deadline for submission of suggestions is August 31, 1971.

BOOK REVIEWS

"Thin Film Technology," by R. W. Berry, P. M. Hall, and M. T. Harris. Published by D. Van Nostrand Co. Inc., Princeton, N. J., 1969. 206 pages; $15.00.

"Thin Film Phenomena," by K. L. Chopra. Published by McGraw-Hill, New York, 1969. 793 pages; $24.50.

Both of the above books are introductions in a way to thin film activities. The former, prepared by the staff of Bell Telephone Laboratories, is perfect for the novice who wishes to engineer a thin film operation. Bare on fundamentals but heavily loaded with specific equations for various topics, it covers the entire gamut, in a surface manner, from the vacuum system itself to generation of the film assembly line. As such it is excellent, but it only covers the thin film capacitors and resistors with its main emphasis on tantalum components. It is, in essence, an engineering manual.

The latter book, by Chopra, could be considered a manual also—but of a different type. Dr. Chopra collects all the phenomena that could occur in thin films, their properties and their experimental aspects, briefly and sparsely covers them and then presents a fantastic amount of references (over 2000). The book is really an encyclopedia of phenomena, techniques and properties. As such it is a surface coverage for someone wishing to enter into thin film research.

Both books serve useful functions. However, I prefer the series on "Physics of Thin Film" published by Academic Press as a more comprehensive starting point.

Julius Klerer
The Cooper Union, New York

NEW MEMBERS

It is a pleasure to announce the following new members of the Electrochemical Society as recommended by the Admissions Committee and approved by the Board of Directors in February, 1970.

Active Members

Aylward, C. F., Danvers, Mass.
Bohunovsky, Otto, Ft. Saskatchewan, Alb., Canada
Brannan, J. R., Mentor, Ohio
Budenstein, P. P., Auburn, Ala.
Clark, R. W., Murfreesboro, Tenn.
Cunningham, A. J., Decatur, Ga.
Curtis, B. J., Zurich, Switzerland
Di Gregorio, Joseph, Houston, Texas
Gardner, W. R., Dallas, Texas
Gentry, F. E., Skaneateles, N. Y.
Harding, R. P., S. Windsor, Conn.
Hruden, W. R., Windsor, Ont., Canada
Justice, B. H., Houston, Texas
Kelly, Jr., G. J., R.D. Port Murray, N. J.
Leigh, R. L., Marion, Ind.
Meuli, W. P., Sunnyvale, Cal.
Ogawa, Nobuo, Anan Tokushima, Japan
O'Leary, K. J., Cleveland Heights, Ohio
Richman, David, Princeton, N. J.
Schaer, G. R., Columbus, Ohio
Simpson, W. I., Rowland Heights, Cal.
Stadler, H. L., Dearborn, Wis.
Turrill, F. G., Silver Spring, Md.
Wengert, P. R., Toledo, Ohio

Associate

Van Zant, Peter, Dallas, Texas

Student

Bhalla, Ranbir, J.R.S.B., State College, Pa.
Mirza, Z. I., Los Angeles, Cal.
Place, B. G., Champaign, Ill.
Rajdev, Dilip, Los Angeles, Cal.

Transfer

Michel, D. J., Gaithersburg, Md.
Paddock, Arnold, Dallas, Texas

PEOPLE

Myron E. Browning has joined the staff of American Chemical & Refining Company as technical director. He will coordinate ACR research activities with production and field services and will be responsible for programming long range research and development in the areas of aerospace, pollution abatement, and electronics.

Mr. Browning is an active member of The Electrochemical Society, as well as the Deutsche Bunsen-Gesellschaft für Physikalische Chemie. He is also a member of the American Electroplater's Society, the Deutsche Gesellschaft für Galvanotechnik, American Society for Metals, American Chemical Society, and ASTM.

Robert Bakish has become consultant to Pechiney. His former part time association in the Aluminum Industry was with Republic Foil, Inc., Danbury, Conn.

Herman S. Preiser, principal research scientist of Hydronautics, Inc. in Laurel, Md. for the past eight years and licensed practicing engineer in the State of Maryland, has been granted sabbatical leave for the year 1970.

Mr. Preiser will be retained as a corrosion consultant with Hydronautics,

Inc. and will engage in a limited private practice. He is a member of many professional societies and has authored, or co-authored, numerous papers (including co-editing a translation from the Russian of Tomashov's book "Theory and Protection of Metals" MacMillan 1966) and holds 20 patents related to cathodic protection of ships.

During the sabbatical year, he will take up the position as coordinator of the Antioch Child Study Program at Antioch Columbia College. This community-oriented program, just in its infancy, will address itself immediately to training of teachers and other professionals to work with handicapped children and later on plan to expand into areas of developing new programs and conducting research into diagnosis and remediation of developmental disabilities in children.

Harvey Seiger has been appointed director of Electrochemical Technology at Heliotek, a division in the Aerospace Group of Textron, Inc., Sylmar, Cal. He will be responsible for the production and research and development of an aerospace nickel/cadmium battery.

One of the country's foremost authorities on nickel/cadmium batteries, Dr. Seiger has done extensive work in atmospheric physics, high temperature measurements and thermodynamics. Prior to joining Heliotek, Dr. Seiger was associated with Gulton Industries, Metuchen, N. J. as director of electrochemical research.

He has several patents to his credit and is the author of numerous technical papers which have been presented to technical conferences and published in technical journals.

A Fellow of the American Institute of Chemists, Dr. Seiger is an active member of The Electrochemical Society and the honorary chemical society Phi Lambda Upsilon.

Karl S. Willson has been appointed senior research associate for the Industrial Chemical Department of the Harshaw Chemical Company, Cleveland, Ohio; he will undertake long range electrochemical research relating to electroplating and metal corrosion.

During his 16 years at Harshaw, Dr. Willson has served in various capacities including manager of Electroplating Research. In addition to receiving the George W. Heise Award for contributions to The Electrochemical Society and the Arthur Logozzo Chrome Plating Award, he has authored numerous papers and holds several patents in the area of electrochemistry.

Dr. Willson holds B.A., M.S. and Ph.D. degrees in Chemistry from Western Reserve University, where he was a member of Phi Beta Kappa and Sigma Xi honorary scientific fraternity. His professional memberships include The Electrochemical Society, the American Electroplaters Society, American Chemical Society, and American Institute of Chemistry. He is a charter member of the Cleveland Association of Research Directors.

NEWS ITEMS

Electrical Double Layer Conference

A Conference on the Electrical Double Layer and its Influence on Electrode Processes will be held at the University of Kentucky, Lexington, Ky., from September 10-11, 1970.

The speakers will be:—Drs. F. C. Anson, J. O'M. Bockris, M. Bonnemay, D. Inman, R. de Levie, D. M. Mohilner, R. Payne, and J. E. B. Randles. There is a nominal charge for three meals and social hour.

For further information please contact: Dr. Gary D. Christian, Chemistry Department, University of Kentucky, Lexington, Ky. 40506.

International Union of Pure and Applied Chemistry

(IUPAC) Commission on Electrochemistry

The IUPAC Commission on Electrochemistry aims at being broadly representative of the international scientific community which is currently active in various fields of pure and applied electrochemistry. The Commission solicits the cooperation of societies, groups and individuals concerned with significant aspects of electrochemistry. Comments, suggestions and active participation are cordially invited. The current program of the Commission is focused on matters of nomenclature and authoritative compilation of reference data.

1. Electrochemical Nomenclature.—The Commission is laying the groundwork for an "Electrochemical Appendix" to the IUPAC "Manual of Symbols and Terminology for Physicochemical Qualities and Units." The immediate objective is standardization and codification of a consistent set of definitions and terms for describing electrochemical cells under conditions of finite flow.

2. Electrochemical Thermodynamic Data.—A comprehensive tabular compilation of electrode potentials and related thermodynamic quantities (heats, Gibbs Free Energies and entropies) is planned. Data including assignments in molten salts and other non-aqueous solvents are expected to be available for publication in 1971.

3. Electrochemical Kinetics.—In the wake of important recent theoretical developments, a set of "Guidelines for the Design of Mechanistically Significant Experiments in Electrode Kinetics" is being prepared for imminent publication. Concomitantly a questionnaire is being distributed to authors of papers on electrode kinetics, seeking to identify the type of experimental information currently available. Retrieval and critical reinterpretation of a wealth of information is envisioned in the light

of contemporary knowledge of diffusion theory, physicochemical hydrodynamics and electric double layer phenomena.

4. A Symposium on Non-Aqueous Electrochemistry—has been cosponsored by the Commission. The meeting is scheduled for July 8-10, 1970, in Paris. Coverage will encompass solvation, electroanalytical methods, ionic equilibria (acid-base, redox, complexation, etc.) and organic electrode reactions.

Relevant inquiries and communications may be directed to the secretary of the Commission on Electrochemistry: Professor J. Koryta, Czechoslovak Academy of Sciences, J. Heyrovsky Institute of Polarography, Opletalova 25, Prague 1, Czechoslovakia, Telephone 22 59 97. Other members of the Commission are: V. S. Bagotsky (USSR); H. Brusset (France); I. Epelboin (France); A. N. Frumkin (USSR), Vice-Chairman; H. Gerischer (Germany; R. Haase (Germany; W. J. Hamer (USA); J. Jordan (USA), Chairman; E. Levart (France); G. Milazzo (Italy); R. Parsons (UK); A. Sanfeld (Belgium); R. Tamamushi (Japan); H. Tannenberger (Switzerland); E. Yeager (USA).

On matters of mutual interest the Commission on Electrochemistry is cooperating with other appropriate IUPAC Commissions, viz.: with the Commission on Electroanalytical Chemistry (I. M. Kolthoff, Chairman) on items 1, 2 and 4 of the aforementioned program; with the Commissions on Physicochemical Symbols, Terminology and Units (M. L. McGlashan, Chairman), on Analytical Nomenclature (H. M. N. H. Irving, Chairman) and the Interdivisional Committee on Nomenclature and Symbols (K. A. Jensen, Chairman) on item 1.

NEW PRODUCTS

pH-Indicator Paper—A pH indicator paper, covering the entire range from 0.1 to 14.0 in units of 0.5, is again available. Each strip is a pH tester in itself and it gives you immediate readings.

For details write to Pfaltz & Bauer, Inc., 126-02 Northern Blvd., Flushing, N. Y. 11368.

Semiconductor Surface Stabilizing Glass—Yields of discrete semiconductor devices can be significantly improved by a new surface stabilizing glass. The glass, IP 650, is designed for semiconductors on which surface states are critical—power devices, or where there is a need to control performance characteristics such as matching transistor parameters, guaranteeing excellent leakage current stability, or insuring long term reliability.

For further information contact: INNOTECH Corporation, 181 Main Street, Norwalk, Conn. 06851.

New Positions in Battery Manufacturing

San Francisco Bay Area

Experience in Button and Cylindrical Cells:

1—Production Manager
2—Chief Products Design Engineer
3—Senior Design Engineer
4—Senior Process Design Engineer
5—Sales Manager
6—Assistant Sales Manager

Please send resume to the Personnel Department Electrochimica Corporation, 1140 O'Brien Drive, Menlo Park, Cal. 94025.

POSITIONS AVAILABLE

Please address replies to the box number shown, c/o The Electrochemical Society, Inc., 30 East 42 St., New York, N.Y. 10017.

Electrochemist—M.S. or comparable experience. Direct own research program aimed at an understanding of copper and copper alloy system principally in non-aqueous media. Use the latest equipment in new research facilities located adjacent to Case Western Reserve University. Extensive computer facilities in same building available computer facilities in same building available plus electronics consultant. Reply Box B-54.

POSITIONS WANTED

Please address replies to the box number shown, c/o The Electrochemical Society, Inc., 30 East 42 St., New York, N.Y. 10017.

Solid State Scientist—PhD 1970—Research on surface preparation and characterization including etching processes, thin film formation, defect characterization and device fabrication. Seeks R & D or teaching position. Publications. Resume available. Reply Box C-32.

Solid State Chemist/Physicist—Ph.D. Solid State Sciences 1970, Ph.D. Physics 1968. Specialized in Characterization and properties using electron microprobe, scanning electron microscope, X-ray, etc. Cathodoluminescence thesis. Desire challenging position in materials characterization and properties. Age 26. Reply Box C-33.

Book Reviewers Needed

The Electrochemical Society needs competent individuals to review books for the Journal.

Any Society member who wishes to volunteer his services should send his name, address, and field of competence to the attention of the Book Review Editor, Dr. Julius Klerer, c/o The Electrochemical Society, 30 East 42 Street, New York, N. Y. 10017.

Positions Wanted

Society members of any class may, at no cost and for the purposes of professional employment, place not more than three identical insertions per calendar year, not to exceed 8 lines each. Count 43 characters per line, including box number, which the Society will assign.

ADVERTISER'S INDEX

ATTENTION, MEMBERS AND SUBSCRIBERS

Whenever you write to The Electrochemical Society about your membership or subscription, please include your Magazine address label to ensure prompt service.

Mail to the Circulation Department, The Electrochemical Society, Inc., 30 East 42 St., New York, N. Y. 10017.

ATTACH LABEL HERE

Change of Address

To change your address, place magazine address label here. Print your NEW address below. If you have any question about your subscription or membership, place your magazine label here and clip this form to your letter.

name

address

city state zip code

The Electrochemical Society, Inc.

30 East 42nd St. • New York, N. Y. 10017 • 212 TN 7-4430

INSTRUCTIONS TO AUTHORS OF PAPERS

(Revised 4/1/69)

Statements of Editorial Content

JOURNAL OF THE ELECTROCHEMICAL SOCIETY is the official journal of the Society and contains four sections totaling some 2500 editorial pages annually:

Electrochemical Science the fundamental research section serves the interdisciplinary needs of chemistry, physics, biology, and medicine, as they pertain to electrochemistry and to electrochemical phenomena. Its editorial interests include research work in such areas as batteries, fuel cells, corrosion, electrothermics and metallurgy, electrodeposition, electro-organic reactions and phenomena, and allied work of a theoretical electrochemical nature. Written for the research scientist in industry, government, the independent laboratory, and the university, it contains contributed Papers, Notes, and Brief Communications describing current basic research of original character.

Solid State Science the fundamental research section serves the interdisciplinary interests of chemistry, physics, electronics, biology, and medicine, as they pertain to solid state electrochemistry and to solid state electrochemical phenomena. Its editorial interests include such areas as dielectrics and insulation, electrothermics and metallurgy, semiconductors, luminescence, and related solid state investigations. Written for the research scientist in industry, government, the independent laboratory, and the university, it contains contributed Papers, Notes, and Brief Communications describing current basic research of original character.

Electrochemical Technology the applied section serves the scientific and engineering interests of those responsible for research and development of electrochemical procedures, and in design and production of products and systems which rely on electrochemical phenomena for their function. It is written for the researcher, engineer, designer, and scientist concerned with such products and processes as: batteries and fuel cells, corrosion, dielectrics and insulation, eletrodeposition, electrothermics and metallurgy, electro-organic reactions, industrial electrolysis, and the electrochemical aspects of solid state technology including luminescence and semiconductors. It contains original contributed Technical Papers, Technical Notes, and Brief Communications describing current application of electrochemistry and electrochemical phenomena to products and systems. Its editorial interest is current progress in the application of electrochemistry and electrochemical phenomena to new and improved processes for the preparation of materials and devices and to the solution of manufacturing and processing problems.

Electrochemical Society Reviews and News is the section serving the interdisciplinary interests of chemistry, physics, electronics, metallurgy, biology, medicine, and engineering, as they pertain to electrochemistry and to electrochemical phenomena. Written for the scientist and engineer in industry, government, the independent laboratory, and the university, it publishes invited and contributed reviews of current research in such areas as batteries, fuel cells, corrosion and corrosion mechanisms, electrothermics and metallurgy, electrodeposition, electro-organic reactions and phenomena, semiconductors, luminescence, dielectrics and insulation, and related solid state investigations. The normal review should not exceed 20 manuscript pages and furnish a current and critical analysis with citation only of truly pertinent references. Also included is the Electrochemical Society News Section, keeping the readers appraised of Society activities, news of its 19 sections and 9 divisions, book reviews, symposium plans, personals, etc.

Printed in U.S.A.

SAMPLE CURVE DRAWING FOR REDUCTION TO $\frac{1}{2}$ SIZE

$6\frac{1}{4}$" max (May be less)

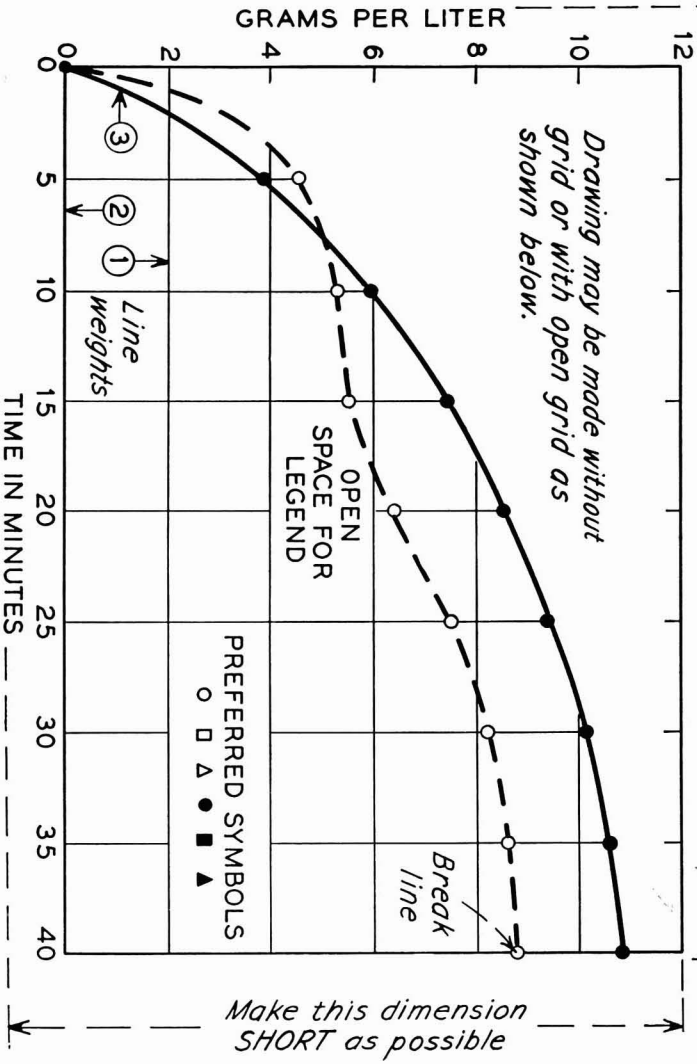

GENERAL

Manuscripts must be submitted in triplicate to expedite review. They should be typewritten, double-spaced, on one side, with 2½-4 cm (1½ in.) margins.

Titles should be brief, followed by the author's name and professional connection. Text should be as brief as is consistent with clarity and should omit introductory or explanatory material which may be regarded as familiar to specialists in the particular field. Proprietary and trade names should be generally avoided; if used with discretion, they should be capitalized to protect the owners' rights.

Authors are encouraged to suggest qualified reviewers for their manuscripts, the Editor reserving the right to final choice. It is helpful if the author tells which ECS Division would be most interested in his paper.

Present Society policy permits manuscript review in several weeks. Manuscripts returned to the author for revision should be resubmitted promptly to allow publication in five months or less from date of original receipt.

TYPES OF ARTICLES

Fundamental Papers describe original research of basic nature and must have adequate scientific depth. **Applied Technical Papers** may deal with any practical aspect of the fields of interest to the Society, e.g., plant design or operation, production and control methods, economics. Articles of wide diversity of interest are acceptable, but subjects primarily covered in other specialized journals (e.g., analytical or nuclear chemistry) are not considered appropriate. **Review Papers** furnish a current and critical analysis of the subject with only pertinent references cited. Each paper should begin with an **Abstract** which should state the scope of the paper and summarize fully its results and contents. Suitable headings and subheadings should be included, but sections should not be numbered. Articles in recent issues should be consulted for current style.

Notes are used for reporting briefer research, developmental work, process technology, new or improved devices, materials, techniques, or processes which do not involve more extensive basic scientific study. No abstract is required.

Brief Communications are used only to report new information of scientific or technological importance which warrants rapid dissemination. They need not necessarily reflect a complete research project; interim reports are acceptable. Length should be a nominal 700 words, with up to two illustrations. No abstract is required. Publishing time is normally less than three months.

EQUATIONS

Mathematical Equations should be written on a single line if possible, and parentheses, brackets, the solidus (/), negative exponents, etc., may be used freely for this purpose. Authors are urged to consult Chapter VI of the "Style Manual" of the American Institute of Physics (available for $1.00 at American Institute of Physics, 335 East 45 Street, New York, N. Y. 10017) and to follow the patterns described there.

SYMBOLS

Authors are encouraged to use symbols extensively. These should be defined in a list at the end of the paper, with units given. For example:

$a, b \ldots$ = empirical constants of Brown equation
f_i = fugacity of pure ith component, atm
D_v = volume diffusion coefficient, cm²/sec

KEY WORDS

Authors are responsible for supplying a list of key words, to facilitate information retrieval. Generic terms generally are to be avoided. Key words acceptable to **Chemical Abstracts** are also generally acceptable in Society publications. List key words in the margin of the first page of the manuscript.

ABBREVIATIONS UNITS

The AIP "Style Manual" referred to here gives a suitable list of common **Abbreviations.** Units usually will be abbreviated without periods throughout the text, as sec, min, hr, cm, mm, etc. **Metric Units** should be used throughout, unless English units are clearly more appropriate in the area of discussion.

POTENTIAL SIGNS

Electrode Potentials: Authors are urged to state and make use of the polarity of test electrodes with respect to the reference electrode used, **i.e.,** Zn is normally negative, Cu normally positive with respect to the standard hydrogen electrode. The sign for the emf of a cell should conform to the free energy change of the chemical reaction as written or implied, in accordance with the definition $\Delta G = -nFE$. These suggestions agree with the IUPAC conventions adopted in 1953.

REFERENCES

Literature References should be listed on a separate sheet at the end of the paper in the order in which they are cited in the text. Authors' initials must be given, and the style and abbreviations adopted by **Chemical Abstracts** should be used. Any recent issue of Society journals may be consulted. Literature cited should be readily available; consequently personal communications, Department of Defense (DOD), and Office of Technical Services (OTS) citations should be minimized. When references are not readily accessible, **Chemical Abstracts** citation numbers must be supplied.

PUBLICATION CHARGE

A charge of $40 per printed page is made for publication of technical material in Society journals. A 10% reduction is allowed if at least one author of an article is an ECS member or an employee of a Patron or Sustaining Member firm. However, acceptance of a manuscript is in no way dependent on such payment, and the charge may be waived in individual cases.

ILLUSTRATIONS

Photographs should be used sparingly, must be glossy prints, and should be mailed with protection against folding. **Micrographs** should have a labeled length unit drawn or pasted on the picture. On both, label "top" where any uncertainty might arise. **Captions** for figures (including photographs) must be included on a separate sheet. Figure numbers must **not** appear in the body of the figure; they will be removed if they do. **Numerical Data** should not be duplicated in tables and figures.

Drawings and **Graphs** ordinarily will be reduced to 8.3 cm (3¼ in.) column width, and after such reduction should have lettering no less than 0.15 cm high. Lettering must be of letter-guide quality. India ink on tracing cloth or paper is preferred, but India ink on coordinate paper with blue ruling is acceptable. Line weight 2 is used for borders and zero lines. When several curves are shown, each may be numbered and described in the caption. Lettering shown is approximately ⅛ in. In plotting current or potential as ordinate, increasing negative values should go down. The sample graph shown conforms to suggestions of the United States of America Standards Institute (USA Report Y15.1-1959).

NEW SYMPOSIA VOLUMES

HIGH TEMPERATURE METALLIC CORROSION BY SULPHUR AND ITS COMPOUNDS.

The Corrosion Division sponsored a symposium on "High Temperature Sulphur Corrosion" in Detroit, Fall 1969. The edited papers will be published in a soft bound volume in the summer 1970. To obtain your copy, use appropriate order form on next page with payment.

PROCEEDINGS OF THE SECOND INTERNATIONAL CONFERENCE ON CHEMICAL VAPOR DEPOSITION.

The Electrothermics and Metallurgy Division is sponsoring in Los Angeles the "Second International Conference on Chemical Vapor Deposition". The edited papers will be published in a soft bound volume in May 1970. To obtain your copy, use appropriate order form on next page with payment.

PROCEEDINGS IVth INTERNATIONAL CONFERENCE ON ELECTRON AND ION BEAM SCIENCE AND TECHNOLOGY

The Electrothermics and Metallurgy Division is sponsoring in Los Angeles the "IVth International Conference on Electron and Ion Beam Science and Technology". The edited papers will be published in a soft bound volume in the summer 1970. To obtain your copy, use order form on next page with payment.

SEE FOLLOWING PAGE FOR ORDER FORMS

NEW SYMPOSIA ORDER FORMS

CONTENTS BOOKS

Return Postage Guaranteed

From –
The Electrochemical Society, Inc.
30 E. 42nd St.
New York, N. Y. 10017

lame _____
ddress _____
ity _____ State _____
ip Code _____ Country _____

Do Not Use
HTM

Insert Your Order No. Here

HIGH TEMPERATURE METALLIC CORROSION BY SULPHUR AND ITS COMPOUNDS

I Wish to Order

	No. of Copies	Total Cost
Copies @ $9.00		

Payment in U.S. funds must accompany order.

Name _____
Address _____
City _____ State _____
Zip Code _____ Country _____

Forward this order form with full payment to
THE ELECTROCHEMICAL SOCIETY, INC.
30 E. 42nd St. New York, N. Y. 10017.

P.O. #
CK. #
RECAP

CONTENTS BOOKS

Return Postage Guaranteed

From –
The Electrochemical Society, Inc.
30 E. 42nd St.
New York, N. Y. 10017

Name _____
Address _____
City _____ State _____
Zip Code _____ Country _____

Do Not Use
CVD

Insert Your Order No. Here

SECOND INTERNATIONAL CONFERENCE ON CHEMICAL VAPOR DEPOSITION

I Wish to Order

	No. of Copies	Total Cost
Copies @ $15.00		

Payment in U.S. funds must accompany order.

Name _____
Address _____
City _____ State _____
Zip Code _____ Country _____

Forward this order form with full payment to
THE ELECTROCHEMICAL SOCIETY, INC.
30 E. 42nd St. New York, N. Y. 10017.

P.O. #
CK. #
RECAP

ONTENTS BOOKS

eturn Postage Guaranteed

From –
The Electrochemical Society, Inc.
30 E. 42nd St.
New York, N. Y. 10017

Name _____
ddress _____
ity _____ State _____
ip Code _____ Country _____

Do Not Use
EI4

Insert Your Ordor No. Here

ELECTRON AND ION BEAM SCIENCE AND TECHNOLOGY 4th

I Wish to Order

	No. of Copies	Total Cost
Copies @ $15.00		

Payment in U.S. funds must accompany order.

Name _____
Address _____
City _____ State _____
Zip Code _____ Country _____

Forward this order form with full payment to
THE ELECTROCHEMICAL SOCIETY, INC.
30 E. 42nd St. New York, N. Y. 10017.

P.O. #
CK. #
RECAP

THE ELECTROCHEMICAL SOCIETY PATRON MEMBERS

Aluminum Co. of Canada, Ltd., Montreal, Que., Canada

Dow Chemical Co.
Inorganic Chemicals Dept., Midland, Mich.

General Electric Co.
Electronic Capacitor & Battery Dept., Irmo, S. C.
Battery Business Section, Gainesville, Fla.
Chemical Laboratory, Knolls Atomic Power Laboratory, Schenectady, N. Y.
Research and Development Center, Physical Chemistry Laboratory, Solid State Physics Laboratory, Schenectady, N. Y.
Direct Energy Conversion Operation, West Lynn, Mass.
Lamp Div., Cleveland, Ohio
Materials & Processes Laboratory, Large Steam Turbine-Generator Dept., Schenectady, N. Y.

The International Nickel Co., Inc., New York, N. Y.

Olin Corporation
Chemicals Div., Research Dept., New Haven, Conn.

Union Carbide Corp.
Divisions:
Carbon Products Div., New York, N. Y.
Consumer Products Div., New York, N. Y.

Westinghouse Electric Corp.
Electronic Tube Div., Elmira, N. Y.
Lamp Div., Bloomfield, N. J.
Molecular Electronics Div., Elkridge, Md.
Semiconductor Div., Youngwood, Pa.
Research Laboratories, Pittsburgh, Pa.

THE ELECTROCHEMICAL SOCIETY SUSTAINING MEMBERS

Airco Speer Electrodes and Anodes, St. Marys, Pa.

Allen-Bradley Co., Milwaukee, Wis.

Allied Chemical Corp., General Chemical Div., Morristown, N. J.

Aluminum Co. of America, New Kensington, Pa.

American Cyanamid Co., Stamford Research Laboratories, Stamford, Conn.

American Gas & Chemicals, Inc., New York, N. Y.

American Metal Climax, Inc., New York, N. Y.

American Potash & Chemical Corp., Los Angeles, Calif.

American Smelting and Refining Co., South Plainfield, N. J.

American Zinc Co., St. Louis, Mo.

The M. Ames Chemical Works, Inc., Glens Falls, N. Y.

Ampex Corp., Redwood City, Calif.

Applied Electrochemistry Inc. Mountain View, California

Beckman Instruments, Inc., Fullerton, Calif.

Bell Telephone Laboratories, Inc., Murray Hill, N. J. (2 memberships)

Bethlehem Steel Corp., Bethlehem, Pa. (2 memberships)

Boeing Co., Seattle, Wash.

Burndy Corp., Norwalk, Conn.

Canadian Industries Ltd., Montreal, Que., Canada

Carborundum Co., Niagara Falls, N. Y.

Chrysler Corp., Detroit, Mich.

Clevite Corp., Burgess Battery Div., Freeport, Ill. (2 memberships)

Cominco Ltd., Trail, B. C., Canada

Dargo Technical Research Ltd. London N.W.9, England

The Detroit Edison Co., Detroit, Mich.

Diamond Shamrock Corp., Painesville, Ohio

Wilbur B. Driver Co., Newark, N. J.

E. I. du Pont de Nemours & Co., Inc., Wilmington, Del.

Eagle-Picher Industries, Inc., Electronics Div., Joplin, Mo.

Eastman Kodak Co., Rochester, N. Y.

Electrode Corporation Chardon, Ohio

Eltra Corp., Prestolite Div., Toledo, Ohio
C&D Batteries, Conshohocken, Pa.

Engelhard Industries, Inc., Newark, N. J.

The Eppley Laboratory, Inc., Newport, R. I.

ESB Inc., Philadelphia, Pa. (2 memberships)

Esso Research and Engineering Co., Engineering Technology Div., Florham Park, N. J.

Exmet Corp., Bridgeport, Conn.

SUSTAINING MEMBERS (CONTINUED)

Fairchild Semiconductor Corp.,
Palo Alto, Calif.

Falconbridge Nickel Mines Ltd.,
Thornhill, Ont., Canada

FMC Corp.,
Inorganic Chemicals Div.,
Buffalo, N. Y.
Inorganic Chemicals Div.,
South Charleston, W. Va.

Foote Mineral Co.,
Exton, Pa.

Ford Motor Co.,
Dearborn, Mich.

General Motors Corp.,
AC Electronics Div., Milwaukee, Wis.
Allison Div., Indianapolis, Ind.
Delco-Remy Div., Anderson, Ind.
Research Laboratories Div., Warren, Mich.

General Telephone & Electronics Laboratories, Inc., Bayside, N. Y.

Globe-Union, Inc.,
Milwaukee, Wis.

B. F. Goodrich Chemical Co.,
Cleveland, Ohio

Gould-National Batteries, Inc.,
Minneapolis, Minn.

Great Lakes Carbon Corp.,
New York, N. Y.

Harshaw Chemical Co.,
Cleveland, Ohio (2 memberships)

Hill Cross Co., Inc.,
West New York, N. J.

Honam Electric Industrial Co.,
Kwangju City, Korea

Honeywell, Inc.,
Minneapolis, Minn.

Hooker Chemical Corp.,
Niagara Falls, N. Y. (2 memberships)

HP Associates,
Palo Alto, Calif.

Hughes Research Laboratories, Div. of Hughes Aircraft Co., Malibu, Calif.

International Business Machines Corp.,
New York, N. Y.

International Minerals & Chemical Corp.,
Skokie, Ill.

IRC, Division of TRW, Inc.,
Philadelphia, Pa.

Jones & Laughlin Steel Corp.,
Pittsburgh, Pa.

K. W. Battery Co.,
Skokie, Ill.

Kaiser Aluminum & Chemical Corp.,
Div. of Metallurgical Research,
Spokane, Wash.

Kawecki Chemical Co.,
Boyertown, Pa.

Kennecott Copper Corp.,
New York, N. Y.

Leesona Moos Laboratories, Div. of Leesona Corp., Great Neck, N. Y.

Arthur D. Little, Inc.,
Cambridge, Mass.

Lockheed Aircraft Corp.,
Missiles & Space Div.,
Sunnyvale, Calif.

Mobil Oil Corp.,
Dallas, Texas

Molybdenum Corporation of America,
New York, N. Y.

Motorola Inc.,
Phoenix, Ariz.

Monsanto Chemical Co.,
St. Louis, Mo.

M&T Chemicals Inc.,
Detroit, Mich.

Nalco Chemical Co.,
Chicago, Ill.

National Cash Register Co.,
Dayton, Ohio

National Lead Co.,
New York, N. Y.

National Steel Corp.,
Weirton, W. Va.

Nortec Electronics Corp.,
Santa Clara, Calif.

North American Rockwell Corp.,
El Segundo, Calif.

Northern Electric Co.,
Montreal, Que., Canada

Norton Research Corp.,
Cambridge, Mass.

Nova Devices, Inc.
New York, N. Y.

Owens-Illinois Glass Co.,
Toledo, Ohio

Park Electrochemical Corp.,
Great Neck, N. Y.

Pennwalt Corp.,
Philadelphia, Pa.

Phelps Dodge Refining Corp.,
Maspeth, N. Y.

Philips Laboratories, Inc.,
Briarcliff Manor, N. Y.

PPG Industries, Inc.,
Chemical Div.,
Pittsburgh, Pa.

Radio Corp. of America,
Electronic Components and Devices,
Lancaster, Pa.

Republic Foil Inc.,
Danbury, Conn.

Reynolds Metals Co.,
Richmond, Va.

Shawinigan Chemicals Ltd.,
Montreal, Que., Canada

Sonotone Batteries,
Marathon Battery Co.,
Cold Spring, N. Y.

Sprague Electric Co.,
North Adams, Mass.

Stackpole Carbon Co.,
St. Marys, Pa.

The Standard Oil Company of Ohio,
Cleveland, Ohio

Stauffer Chemical Co.,
Dobbs Ferry, N. Y.

Syncro Corp.,
Oxford, Mich.

Teletype Corp.
Skokie, Ill.

Texas Instruments Inc.,
Dallas, Texas

3 M Company
St. Paul, Minn.

Titanium Metals Corp. of America,
Henderson, Nev.

Tyco Laboratories, Inc.,
Waltham, Mass.

Udylite Corp.,
Detroit, Mich. (4 memberships)

United States Steel Corp.,
Pittsburgh, Pa.

Varian Associates,
Palo Alto, Calif.

Western Electric Co., Inc.,
Chicago, Ill.

Wyandotte Chemicals Corp.,
Wyandotte, Mich.

Yardney Electric Corp.,
New York, N. Y.

Zenith Radio Corp.,
Chicago, Ill.